

**ONR GRANT N00014-95-1-0539**

*A DoD Multidisciplinary Research Program  
of the University Research Initiative (M-URI)*

**YEAR 2 - ANNUAL REPORT**

---

**INTEGRATED DIAGNOSTICS**

*March 1, 1996 - February 28, 1997*

FOR

**Office of Naval Research**

800 N. Quincy Street  
Arlington, VA 22217-5660

PREPARED BY

Richard S. Cowan, Program Manager  
Ward O. Winer, Principal Investigator

**Georgia Institute of Technology**

MULTIUNIVERSITY CENTER FOR INTEGRATED DIAGNOSTICS  
Woodruff School of Mechanical Engineering  
Atlanta, GA 30332-0405  
Ph: 404-894-3200

SUBGRANTEES

**Northwestern University**

Jan D. Achenbach, Director  
Center for Quality Engineering and Failure Prevention  
Ph: 847-491-5527

**University of Minnesota**

Dennis Polla, Professor  
Department of Electrical Engineering  
Ph: 612-624-8005  
S. Ramalingam, Professor  
Department of Mechanical Engineering  
Ph: 612-625-4017

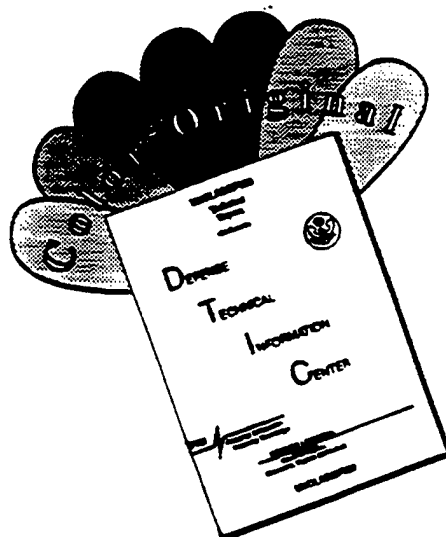
19970424 002

**DTIC QUALITY INSPECTED 3**

**DISTRIBUTION STATEMENT A**

Approved for public release;  
Distribution Unlimited

# DISCLAIMER NOTICE



THIS DOCUMENT IS BEST QUALITY AVAILABLE. THE COPY FURNISHED TO DTIC CONTAINED A SIGNIFICANT NUMBER OF COLOR PAGES WHICH DO NOT REPRODUCE LEGIBLY ON BLACK AND WHITE MICROFICHE.

**ONR GRANT N00014-95-1-0539**

*A DoD Multidisciplinary Research Program  
of the University Research Initiative (M-URI)*

**YEAR 2 - ANNUAL REPORT**

---

# **INTEGRATED DIAGNOSTICS**

*March 1, 1996 - February 28, 1997*

FOR

**Office of Naval Research**

800 N. Quincy Street  
Arlington, VA 22217-5660

PREPARED BY

Richard S. Cowan, Program Manager

Ward O. Winer, Principal Investigator

**Georgia Institute of Technology**

MULTIUNIVERSITY CENTER FOR INTEGRATED DIAGNOSTICS

Woodruff School of Mechanical Engineering

Atlanta, GA 30332-0405

Ph: 404-894-3200

SUBGRANTEES

**Northwestern University**

Jan D. Achenbach, Director

Center for Quality Engineering and Failure Prevention

Ph: 847-491-5527

**University of Minnesota**

Dennis Polla, Professor

Department of Electrical Engineering

Ph: 612-624-8005

S. Ramalingam, Professor

Department of Mechanical Engineering

Ph: 612-625-4017

**DTIC QUALITY INSPECTED 3**

# TABLE OF CONTENTS

Title Page .....	i
Table of Contents .....	iii
List of Tables .....	v
List of Figures .....	vii
<b>EXECUTIVE SUMMARY</b> .....	1
<b>1. INTRODUCTION</b> .....	3
1.1 Mission .....	3
1.2 Organization .....	4
<b>2. RESEARCH ACCOMPLISHMENTS and PLANS</b> .....	8
2.1 Failure Detection and Identification .....	12
2.1.1 Flaw Detection and Characterization .....	13
2.1.2 Crack Detection in Annular Structures by Ultrasonic Guided Waves .....	23
2.1.3 Detection of Mechanical Seal Failure in Turbomachinery .....	28
2.1.4 Study of Acoustic Emission and Transmission from Incipient Fatigue Failure ..	33
2.2 Failure Prediction Methodology .....	43
2.2.1 Structural Fatigue Investigation .....	44
2.2.1.1 Stress Analysis and Stress Intensity Factor Solutions for Cracks .....	46
2.2.1.2 Characterization of Fatigue Behavior and Mechanisms .....	51
2.2.1.3 Remaining Life Estimation Methodology .....	70
2.2.1.4 Project Vision .....	83
2.2.2 Fatigue Reliability .....	86
2.3 Direct Sensing, Analysis, Real-time Diagnosis .....	93
2.3.1 Magnetic-Electrical-Impedance Tomography .....	94
2.3.2 Eddy Current Microsensors for Integrated Diagnostics .....	111
2.3.3 Integrated Microsensors for Aircraft Fatigue and Failure Warning .....	141
2.3.3.1 Microsensor Development .....	142
2.3.3.2 Sensor Electronics .....	158
2.3.3.3 Signal Processing .....	175
2.3.3.4 Project Plans .....	186
2.3.4 Acoustic Emission Modeling for Integrated Diagnostics .....	187
2.3.5 Dynamic Metrology as a Wear Diagnostic .....	218
2.3.6 Monitoring of Harmonic Oscillations in Rotating Machine Elements .....	233
2.4 References .....	252
<b>3. TECHNOLOGY TRANSFER ACHIEVEMENTS</b> .....	259
3.1 Publications .....	259
3.2 Presentations .....	264
3.3 Education .....	265
3.4 Partnerships .....	266
<b>APPENDIX A. Program Participants</b> .....	A-1



## LIST OF TABLES

---

1. Chemical Compositions of 4340 Steel of Different Sources (in %)	78
2. Mechanical Properties of 4340 Steel of Different Sources	79
3. Nanoindentation Test Samples and their Conditions	82
4. Major Project Accomplishments for Year 2	142
5. Dielectric and Ferroelectric Properties of PZT Thin Films	144
6. Bottom Electrode Materials Thicknesses used for MEMS Acoustic Emission Sensor	157
7. Mechanical Properties of Materials Used in MEMS Acoustic Emission Sensor	157
8. Current Status of Electronics	158
9. Future Electronics Work	174
10. 1200 RPM Accelerometer Experiments for Cup Damage	224
11. 1200 RPM Acoustic Emission Experiments for Cup Damage	227
12. 1200 RPM Accelerometer Analysis for Cone Damage	228

## LIST OF FIGURES

1. (a.) Technology Delivery .....	3
(b.) Program Organization .....	5
2. (a.) Allocation of M-URI Year 2 Funding, Participating Institutes .....	6
(b.) Allocation of M-URI Year 2 Funding, Research Focus .....	7
3. Program Organization Diagram, Topical .....	11
4. Optical Set-up of the Fiber-Array Based LBU Generation System .....	15
5. Configuration of the Line Array Ultrasound Source .....	15
6. Comparison of Energy Delivery Capability of the Fiber-Optic LBU Generation System .....	16
7. Laser Generated Ultrasonic Signal (thermoelastic spot array mode) and its Power Spectrum .....	17
8. Laser Generated Ultrasonic Signal (ablative spot array mode) and its Power Spectrum .....	17
9. Laser Generated Ultrasonic Signal (thermoelastic line mode) and its Power Spectrum .....	17
10. Reservoir Hub from an H-46 Helicopter .....	18
11. (a.) Schematic Diagram of a Focusing Fiber-Array .....	19
(b.) Typical Ultrasonic Pulse Generated by the System as in (a.) .....	19
12. Generation of Ultrasound Signal for the Inspection of (a.) an Engineering Component with Irregular and Limited Surface Access. Plot (b.) shows the waveform picked up by PZT .....	19
13. Fiberized Path-matched Sagnac Interferometer .....	20
14. LBU Signal Detected by the Sagnac Interferometer and the Corresponding Power Spectrum .....	21
15. Comparison between the Sagnac Interferometer (left) and the PZT Transducer (right) .....	21
16. Schematic of Project Interaction .....	23
17. Ideal Annular Structure with Machine-made Cracks .....	25
18. Detection Techniques: (a.) Pulse-echo; (b.) Pitch-catch; (c.) Transmission .....	25
19. Schematic of Apparatus .....	29
20. Results of Analytic Model .....	31
21. Results of Bench Tests .....	31
22. (a.) Steady State Test Results I .....	32
(b.) Steady State Tests Results II .....	32
23. Schematic of Project Interaction .....	33
24. Specimen and Half-space Signals Used for Transfer Function .....	35
25. Comparison of Double Pulse in Specimen and Double Pulse Specimen Signal Operated on by Transfer Function .....	35

26. Simulated Phase Array .....	37
27. Fatigue Test Sample, Showing Transducer Location and Stages of Crack Growth .....	38
28. Acoustic Emission Signals from Fatigue Test Sample .....	39
29. Optical Fiber Receiving Array .....	41
30. (a.) Rotor Hub (One-third) Solid Model (Right View) .....	47
(b.) Rotor Hub Loading Components .....	47
31. Mesh of Rotor Hub Model .....	48
32. (a.) Plot of Maximum Principal Stress Results .....	49
(b.) Plot of von Mises Stress Results .....	49
33. Rotor Hub Predicted Failure Locations .....	50
34. (a.) Schematic of Typical Progression of Crack Growth Rate Behavior as a Function of Crack Length and Stress Amplitude .....	54
(b.) Schematic of Kitagawa diagram for HCF thresholds .....	54
35. Predicted $da/dN$ versus $\Delta K_I$ for Small Cracks in 1045 Steel .....	55
36. Uniaxial Tensile Properties of Ti-6Al-4V .....	57
37. Long Crack Growth Data .....	58
38. $da/dN$ vrs. $\Delta K_{eff}$ Curve for Ti-6Al-4V .....	59
39. FASTRAN Large Crack Growth Validation .....	59
40. Pothole at Notch Root of Small-Crack Specimen used as an Initiation Site .....	60
41. (a.) FASTRAN Predictions of the Crack's Aspect Ratio Evolution; 5 $\mu m$ initial crack length .....	61
(b.) FASTRAN Predictions of the Crack's Aspect Ratio Evolution; 10 $\mu m$ initial crack length .....	61
42. (a.) FASTRAN Predictions of the Crack's Life; 5 $\mu m$ initial crack length .....	62
(b.) FASTRAN Predictions of the Crack's Life; 10 $\mu m$ initial crack length .....	62
43. Delta K vs. $dc/dN$ curve, Stress Range: 50 ksi .....	63
44. FASTRAN Small-Crack Growth Prediction .....	63
45. Critical Path Diagram .....	64
46. Crack Growth Behavior of PH 13-8 Mo Stainless Steel .....	69
47. H-46 Helicopter Connecting Link .....	73
48. H-46 Helicopter Connecting Link .....	75
49. (a.) Microstructure of 4340 Steel: Connecting Link Material .....	77
(b.) Microstructure of 4340 Steel: Quenched and Tempered Bar .....	77
(c.) Microstructure of 4340 Steel: As-received Bar .....	78
50. Disk-like CT Specimen .....	79
51. Fatigue Crack Growth Data of 4340 Steel .....	80
52. Interaction of Microstructure and Fatigue Crack; (a.) as-received; (b.) quenched and tempered ....	81

53. Nanoindentation Hardness Profile of Quenched and Tempered Materials.....	82
54. Solution for Quarter Space Domain.....	88
55. (a.) Solution for Circular Domain.....	89
(b.) Solution for Spherical Domain.....	89
56. Probability of Detection Curves.....	90
57. Probability of Failure vs. Inspection Time.....	91
58. Failure Probability vs. Inspection Coefficient .....	91
59. Current Flow between Two Electrodes on a Device under Test with and without a Flaw.....	95
60. Schematic Diagram of the Experimental Test Bed.....	96
61. Drawings of the C, D, and X-type Focusing Probes .....	98
62. Shielded Differential H-type Probe: (a.) Ferrite H Head; (b.) Ferrite Shield; (c.) Assembly.....	99
63. Region Scanned and the Location and Size of the Flaws .....	102
64. Color Graph of the Magnitude of the Differenced Response .....	103
65. Magnitude and Phase of the Differenced Response for Flaw A as a Function of x .....	105
66. Magnitude and Phase of the Differenced Response for Flaw C as a Function of x.....	106
67. Magnitude and Phase of the Differenced Response for Flaw G as a Function of x .....	107
68. Magnitude and Phase of the Differenced Response for Flaw K as a Function of x .....	108
69. Magnitude and Phase of the Differenced Response for Flaw H as a Function of x .....	109
70. Maximum Amplitude of the Differenced Response at each Flaw as a Function of Flaw Size .....	110
71. Eddy Current (EC) Inspection System Assembled for Flaw Detection and Flaw Imaging.....	113
72. Eddy Current Micro Sensor Geometry and the 4 x 4 Array Sensor Implemented in Silicon.....	119
73. Micro Sensor Array Implemented in Silicon and the Complete Single Element Sensor .....	120
74. Model Flaw Reconstructed with Differential EC signals Acquired with Single Element Sensor...121	
75. EC Contour and Images Constructed by Scanning a 300 $\mu\text{m}$ dia. Model Flaw .....	123
76. Three Dimensional EC Image Constructed by Scanning a 300 $\mu\text{m}$ dia. Model Flaw .....	125
77. EC Contour and Images Constructed by Scanning a 100 $\mu\text{m}$ wide EDM Slot, 5 mm in length .....	127
78. Three Dimensional EC Images Constructed by Scanning an EDM Slot and a Keyhole Slot (100 $\mu\text{m}$ wide EDM Slot Emerging from a 2 mm dia. Drilled Hole).....	129
79. EC Image of a 750 $\mu\text{m}$ dia. Model Flaw and a Reconstructed Section through the Flaw .....	131
80. EC Contour and 3-D Image Constructed by Scanning a 100 $\mu\text{m}$ wide x 5 mm long EDM Slot.....	132
81. EC Image of a Blunted Crack-like Flaw (Keyhole Slot) - 100 $\mu\text{m}$ wide EDM Slot Terminating at a 2 mm dia. Drilled Hole and the Reconstructed Section through the Model Flaw .....	133
82. Pole Piece for 4 x 4 Micro Sensor Array and the Simplified FEM Model of the Pole Piece to Calculate Eddy Current Signal Characteristics of the Array Sensor .....	134

83. Calculated Magnetic Field Components $B_x$ , $B_y$ and $B_z$ , with $B_{sum}$ .....	135
84. Calculated Vector Potential and Magnetic Field Components $A_z$ , with $A_{sum}$ and $B_{sum}$ .....	136
85. Calculated Eddy Current Components $J_{ex}$ , $J_{ey}$ and $J_{ez}$ , with $J_{sum}$ .....	137
86. Schematic of a 3-mask, 50-turn Transverse Eddy Current Micro Sensor with a $2\ \mu\text{m} \times 3000\ \mu\text{m}$ Permalloy Flux Concentrator and a Photograph of the Sensor Implemented in Silicon .....	138
87. Pole piece Geometry for Single Element Transverse Sensor and Schematic of the Multi-element Transverse Sensor Array .....	139
88. Schematic of the Set Up for Hall Effect Micro Sensor Evaluation (DC to 50 kHz excitation) for Eddy Current Inspection and Imaging.....	140
89. Pole Piece Geometry (Hall effect sensor) for Flux Focusing to Enhance Spatial Resolution.....	140
90. Demanding Flaw Geometries Proposed for EC Imaging & Flaw Resolution in Field of Cracks ...	140
91. Integrated Diagnostic Coupon.....	141
92. (a.) Preparation of a Metal Organic PZT Solution.....	143
(b.) Preparation of PZT Coatings .....	143
93. SEM Micrograph of the Surface of a PZT Thin Film .....	144
94. Typical Structure of Electrode PZT Thin Films .....	145
95. Acoustic Emission Spectra for (a.) a $0.6\ \mu\text{m}$ -thick Thin Film PZT Microsensor; and (b.) a Physical Acoustic Model S9220 Commercial AE Sensor.....	147
96. Microbeam Vibration Sensor .....	148
97. SEM of Vibration Sensor .....	148
98. Acoustic Emission in Multi-layered Isotropic Solids .....	149
99. Theoretical Reflection Curves (Longitudinal Reflected Waves).....	151
100. Theoretical Reflection Curves (Vertical Polarized Shear Reflected Waves) .....	151
101. Theoretical Transmission Curves (Longitudinally Transmitted Waves).....	152
102. Theoretical Transmission Curves (Vertically Polarized Transmitted Waves) .....	152
103. Energy Ratio for Longitudinal Reflected Wave to Longitudinal Incident Wave .....	153
104. Energy Ratio for Reflected Shear Wave (Vertically Polarized) to Longitudinal Incident Wave..	153
105. AE Waveforms from Initiation of Plasticity in Fe-3% Si.....	154
106. Relationship between Measured Acoustic Energy and Elastic Energy Released from an Event..	155
107. Voltage Amplifier .....	160
108. Charge Amplifier.....	160
109. Modified Charge Amplifier Circuit .....	160
110. Plot of Power vs. Capacitance for MOS and Bipolar Transistors.....	161
111. Noise Spectral Density vs. Capacitance.....	162

112. AC Response of the Charge Amplifier Circuit .....	163
113. Temperature Sensor Block Diagram .....	163
114. Bandgap Temperature Sensor Principles .....	164
115. Linear Resistance Based Bandgap Voltage Reference .....	165
116. Switched-Capacitor Implementation of Temperature Sensor .....	165
117. Comparison of Silicon Area for Linear Resistor vs. Switched-Capacitor Implementation.....	166
118. Simulation Results for Switched-Capacitor Temperature Sensor .....	166
119. Weak Inversion PTAT Cell.....	167
120. Simulation Results for Weak Inversion PTAT Cell.....	167
121. Telemetry Block Diagram .....	168
122. Microsensor Block Diagram .....	168
123. Transceiver Block Diagram .....	169
124. Low Noise Amplifier Schematic.....	170
125. LNA Frequency Response.....	170
126. On-chip Spiral Inductors .....	171
127. Down-conversion Mixer .....	171
128. Automatic Gain Control Circuit.....	172
129. AGC Simulation .....	173
130. Transmitter Circuit .....	173
131. Prototype Block Diagram.....	174
132. Data Recorded over One Cycle .....	178
133. Data Recorded over the Next Cycle.....	178
134. Block Diagram of Proposed Signal Processing Approach.....	179
135. An Optimal Taper.....	181
136. Spectral Compactness of Tapers .....	181
137. Output of Channel that Contains the AE Signals.....	182
138. De-noised Time Series of One Channel.....	182
139. De-noising of a Single AE Event .....	182
140. ROC Curves for $k = 5$ to $15$ .....	184
141. Source Waveform and Data Measured at Two Sensors.....	184
142. Comparison of Power Spectra of Actual and Estimated Source Waveforms .....	185
143. Stress-Strain Curves for Annealed and Heat Treated 4340 Steel .....	189

144. Compact Tension Specimen.....	190
145. Compact Tension Specimen with AE Sensors and Crack Propagation Gages .....	191
146. Spatial Filtering Technique for Noise Suppression .....	192
147. Cumulative AE Counts and Crack Extension vs. Fatigue Cycles.....	195
148. Normalized Cumulative AE Counts and Crack Length vs. Normalized Number of Fatigue Cycles for 4340 Steel Specimens.....	196
149. Cumulative AE Counts and Crack Length vs. Number of Fatigue Cycles; $K_{\max} = 0.15K_{IC}$ .....	197
150. Cumulative AE Counts and Crack Length vs. Number of Fatigue Cycles; $K_{\max} = 0.20K_{IC}$ .....	198
151. Cumulative AE Counts and Crack Length vs. Number of Fatigue Cycles; $K_{\max} = 0.25K_{IC}$ .....	199
152. Cumulative AE Counts and Crack Length vs. Number of Fatigue Cycles; $K_{\max} = 0.35K_{IC}$ .....	200
153. Cumulative AE Counts vs. Loading Cycle Phase; Stage 1 .....	201
154. Cumulative AE Counts vs. Loading Cycle Phase; Stage 2 .....	202
155. Cumulative AE Counts vs. Loading Cycle Phase; Stage 3 .....	203
156. Cumulative AE Counts vs. Loading Cycle Phase; Stage 4 .....	204
157. Cumulative AE Counts vs. Loading Cycle Phase; Stage 5 .....	205
158. Cumulative AE Counts vs. Loading Cycle Phase; Stage 6 .....	206
159. Cumulative AE Counts and Corresponding Phase Distributions at Several Stages .....	207
160. Loading Phase Distribution of AE Activity .....	208
161. Fracture Morphology and Stages of Crack Propagation .....	209
162. Probability Density Function of AE Cumulative Counts; $K_{\max} = 0.15K_c$ .....	210
163. Probability Density Function of AE Cumulative Counts; $K_{\max} = 0.175K_c$ .....	211
164. Probability Density Function of AE Cumulative Counts; $K_{\max} = 0.2K_c$ .....	212
165. Probability Density Function of AE Cumulative Counts; $K_{\max} = 0.25K_c$ ; Specimen 1 .....	213
166. Probability Density Function of AE Cumulative Counts; $K_{\max} = 0.25K_c$ ; Specimen 2 .....	214
167. Probability Density Function of AE Cumulative Counts; $K_{\max} = 0.3K_c$ .....	215
168. Probability Density Function of AE Cumulative Counts; $K_{\max} = 0.35K_c$ .....	216
169. Probability Density Function of AE Cumulative Counts by Region .....	217
170. Signal Processing Diagram .....	220
171. High Frequency Resonance Technique Processing .....	220
172. Experimental Schematic.....	223
173. Peak Value Relationship for Cup Damage, 1200 RPM .....	224
174. Accelerometer Data Analysis for 15.39 $\mu$ m Cup Scratch at 1200 RPM.....	226
175. Accelerometer Data Analysis for 349.32 $\mu$ m Cup Scratch at 1200 RPM.....	226

176. AE Analysis for Cup Damage.....	227
177. Accelerometer Relationship for Cone Defects with PR Consideration .....	229
178. Kurtosis and Crest Factor to Defect Relationship for Cone Defects .....	229
179. Accelerometer Analysis for 408 $\mu$ m Cone Defects .....	230
180. Flow Chart for Future Research .....	231
181. Schematic of the Noncontacting FMR Seal Test Rig .....	237
182. Stator Coning Mechanism .....	237
183. Seal Model and Coordinate System .....	238
184. Relative Position between Rotor and Stator.....	239
185. Vector Representation of the Complete Response.....	240
186. Misalignment and Precession of a Plane.....	241
187. (a.) Rotor Dynamic Response Orbit (noncontacting operation) .....	244
(b.) Rotor Dynamic Response Orbit (having seal face contact).....	244
188. Rotor Dynamic Response (noncontacting operation) .....	245
189. (a.) Rotor Dynamic Response (seal having face contact) .....	246
(b.) Rotor Dynamic Response (seal having face contact) .....	247
(c.) Rotor Dynamic Response (seal having face contact) .....	248



## EXECUTIVE SUMMARY

---

Faculty and staff from the Georgia Institute of Technology, Northwestern University, and the University of Minnesota are pleased to submit this document, summarizing second year activities of Office of Naval Research (ONR) Grant N00014-95-1-0539, *Integrated Diagnostics*. Supported through the Department of Defense (DoD) Multidisciplinary Research Program of the University Research Initiative (M-URI), this program was initiated to promote basic research in the technologies and methodologies used in determining how mechanical failures occur, and how they can be detected, predicted, and diagnosed in real-time.

To accomplish the objectives set forth by the M-URI program, the MULTIUNIVERSITY CENTER FOR INTEGRATED DIAGNOSTICS was formed. Under the direction of Principal Investigator Ward Winer, Regents' Professor and Chair of the Woodruff School of Mechanical Engineering at Georgia Tech, research is being conducted by nineteen (19) faculty associated with four schools from the Georgia Tech College of Engineering, four (4) faculty from Northwestern University, and eleven (11) from the University of Minnesota. Dr. Dennis Polla and Dr. S. Ramalingam of the University of Minnesota, and Dr. Jan Achenbach of Northwestern University are the Subgrant Principal Investigators for their respective schools. Georgia Tech's Richard Cowan serves as the Center's Program Manager.

Using material, load, and vibration information from critical rotorcraft components, experiments have been designed and conducted so as to collect information of relevance in understanding the mechanisms of failure for use in developing failure models. These models can serve as a guide in the selection and development of sensors to detect faults and pending failures. Effort has been placed on micro-sensor development, and achieving the means to analyze and correlate reliable sensor output for operator use. Organizationally, this activity is being accomplished through sixteen (16) projects, categorized by three (3) thrust areas:

- Failure Detection and Identification.
- Failure Prediction Methodology (Failure Mechanisms, Life Estimation).
- Direct Sensing, Analysis, Diagnosis (Sensor Development, Real-time Diagnosis).

The broad range of cross-disciplinary research topics addressed by the Integrated Diagnostics program has necessitated an effective communication network encompassing both the faculties and sponsors. A number of activities have been engaged to facilitate the flow of information including traditional publication channels, meeting presentations, monthly updates, partnerships, and electronic reporting (<http://www.me.gatech.edu/Diagnostics/>). Of course, the primary mode of transfer is through students, who upon entering an engineering profession, will be trained in an aspect of integrated diagnostics. During this reporting period, the program has accommodated ten (10) post-doctoral researchers, thirty-five (35) graduate students, and seven (7) advanced undergraduate students.

# 1. INTRODUCTION

Office of Naval Research (ONR) Grant N00014-95-1-0539, *Integrated Diagnostics*, was initiated on March 1, 1995, following approval of a research proposal submitted to the Department of Defense Multidisciplinary Research Program of the University Research Initiative (M-URI). To accomplish the objectives set forth by the M-URI program, the MULTIUNIVERSITY CENTER FOR INTEGRATED DIAGNOSTICS was formed, supported by faculty and staff from the Georgia Institute of Technology, University of Minnesota, and Northwestern University. Funded for a basic period of three years, with a potential for two additional years, this document reports on the Center's second year of activity.

## 1.1 MISSION

America's military machines (e.g., ships, aircraft, and land vehicles) are growing old. Many of the systems that are confidently relied upon today were designed and built twenty and thirty years ago. Given the present economic climate, replacement with next generation equipment can no longer be taken for granted. As a result, an expectation of keeping aging machines in service well into the next century has emerged, which has elevated concern that poor performance, inadequate safety, and increasingly expensive maintenance will result.

To respond to this technological challenge, pending failures must be identified before disastrous consequences occur. Incipient failures, however, are hard to locate, and current maintenance systems have limited capabilities to do so. Today's systems rely mainly on time-based inspection, which requires that parts be inspected at specified intervals, and be replaced when deemed unfit for service. A more effective and efficient alternative to time-based inspection is to continuously monitor critical components. This necessitates an understanding of *Integrated Diagnostics*, a term associated with the technologies and methodologies used to determine how mechanical failures occur, and how they can be detected, predicted, and diagnosed in real-time.

As shown in Fig. 1a, a systematic approach has been implemented to enable innovative ideas to reach maturity with respect to mechanical system diagnostics and prognostics. Provided funding through the Department of Defense M-URI, a technical organization has been built to facilitate and combine the various disciplines required to generate the payoff of a system capable of being installed on a commercial or defense service vehicle. Researchers, representing a variety of engineering disciplines at the Georgia Institute of Technology, Northwestern University, and the University of Minnesota have been assembled, offering expertise with respect to material fatigue, fracture, nondestructive testing, sensors, and signal processing. To gain first-hand knowledge of the problems that maintenance personnel face, engineering support has been obtained through the Cherry Point Naval Aviation Depot. Additional experience has been made available through industrial partnerships.

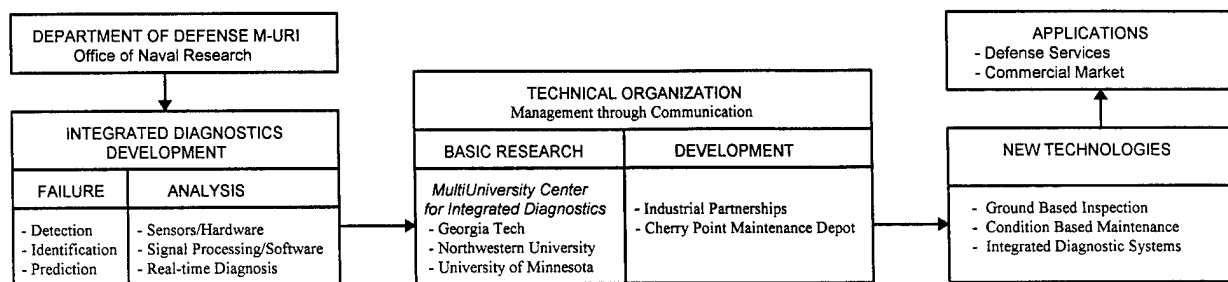


Figure 1a. Technology Delivery

The MultiUniversity Center for Integrated Diagnostics is committed to perform studies associated with three major Integrated Diagnostic needs: the need to detect and identify incipient failures, the need to reliably predict the occurrence of failures, and the need to monitor the condition of a component or system in real-time. Organizationally, this has led to the formation of three research thrust areas, the objectives of which are defined below.

- I. **Failure Detection and Identification:** perform studies pertaining to deterioration mechanisms and techniques for detecting the initiation of fractures or other failures.
- II. **Failure Prediction Methodology:** perform studies pertaining to the methodology for failure prediction in real-time, including modeling fault initiation and failure signatures, and observing the propagation and fracture phases of fatigue-based failure.
- III. **Direct Sensing, Analysis, Real-time Diagnosis:** perform studies with respect to the responses of signals early in fault inception, including research on sensors that can be placed at critical sites on mechanical systems for responses to change in variables of state or vibration.

## 1.2 ORGANIZATION

To provide an overview of what is needed for developing the new technologies associated with integrated diagnostics, Fig. 1b is offered. This basic research "delivery system" begins through the understanding of Department of Defense (*DoD*) needs and is ultimately cultivated to produce payoffs in *decision technology*. The MultiUniversity Center for Integrated Diagnostics has focused attention on *sensor development*, the results of which are of use in accomplishing the Center's mission in furthering the understanding of *failure mechanisms* and the ability to reliably address *failure detection*. It is anticipated that such knowledge will further the development of the two major components needed for the advancement of diagnostic/prognostic technologies: *life estimation* and *real-time diagnosis*.

A technical organization built on effective management and efficient communication has been formed to facilitate and combine the various disciplines required to develop the needed scientific and engineering foundation outlined above. The participating faculty and staff, representing the Georgia Institute of Technology, Northwestern University, and the University of Minnesota, are recognized for their significant contributions with respect to structural fatigue, fracture, nondestructive testing, acoustics, ultrasonics, sensors, and signal processing. Identified in Appendix A, Integrated Diagnostics research is being carried out by nineteen (19) faculty associated with four schools from the Georgia Tech College of Engineering, four (4) faculty from Northwestern University, and eleven (11) from the University of Minnesota. In addition, during this reporting period, the program has accommodated ten (10) post-doctoral researchers, thirty-five (35) graduate students, and seven (7) advanced undergraduate students.

In this second year of M-URI support, studies continue with respect to understanding the mechanisms of failure (through detection, identification, and prediction) and the means to detect, identify and analyze them (through sensors/hardware, signal processing/software, and real-time diagnosis). Figures 2a and 2b provide an indication as to how M-URI monies have been distributed to the participating institutions and prioritized with respect to research area. Sections 2 and 3 of this annual report summarize the second-year accomplishments obtained by this financial commitment.

## Program Organization Diagram

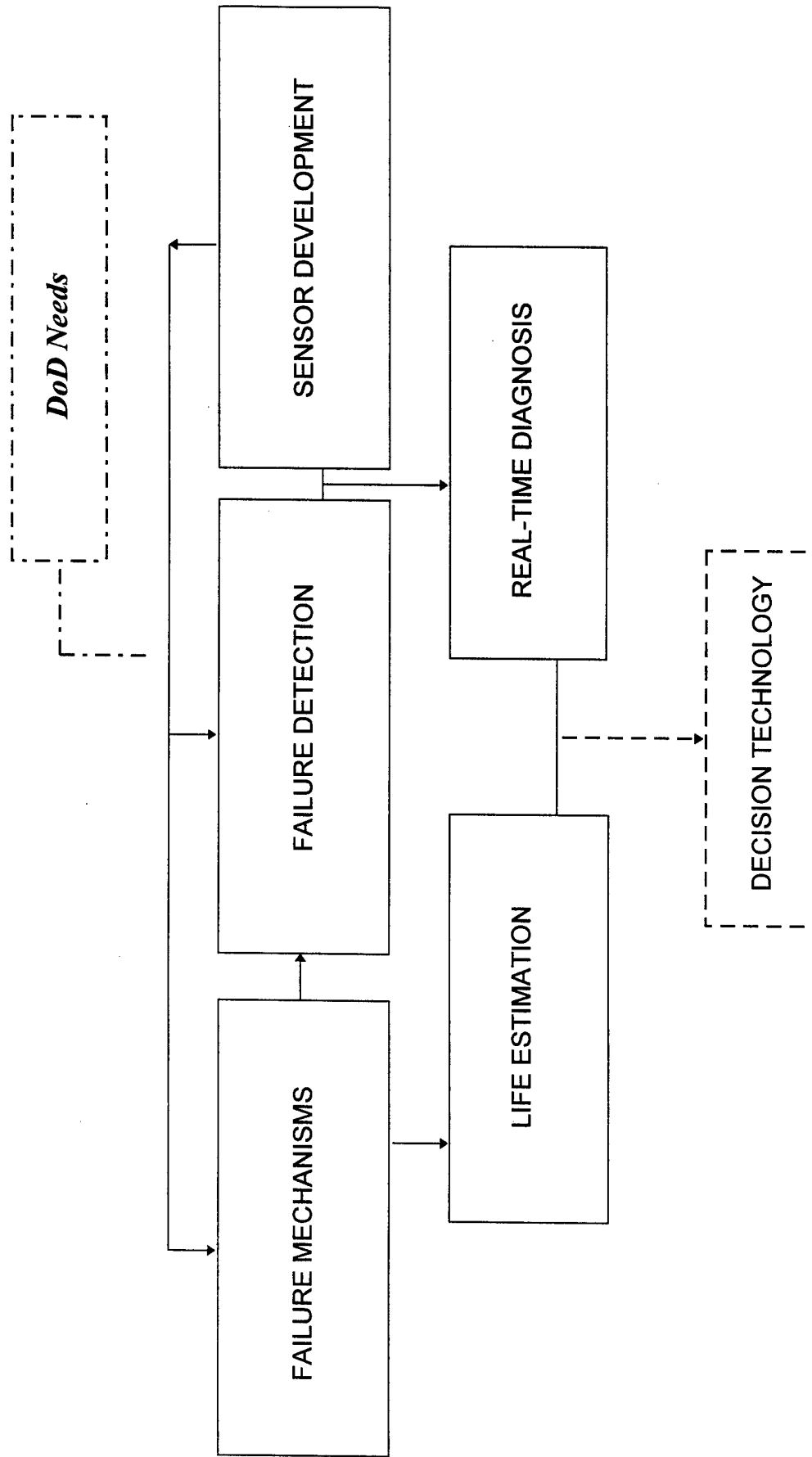


Figure 1b.

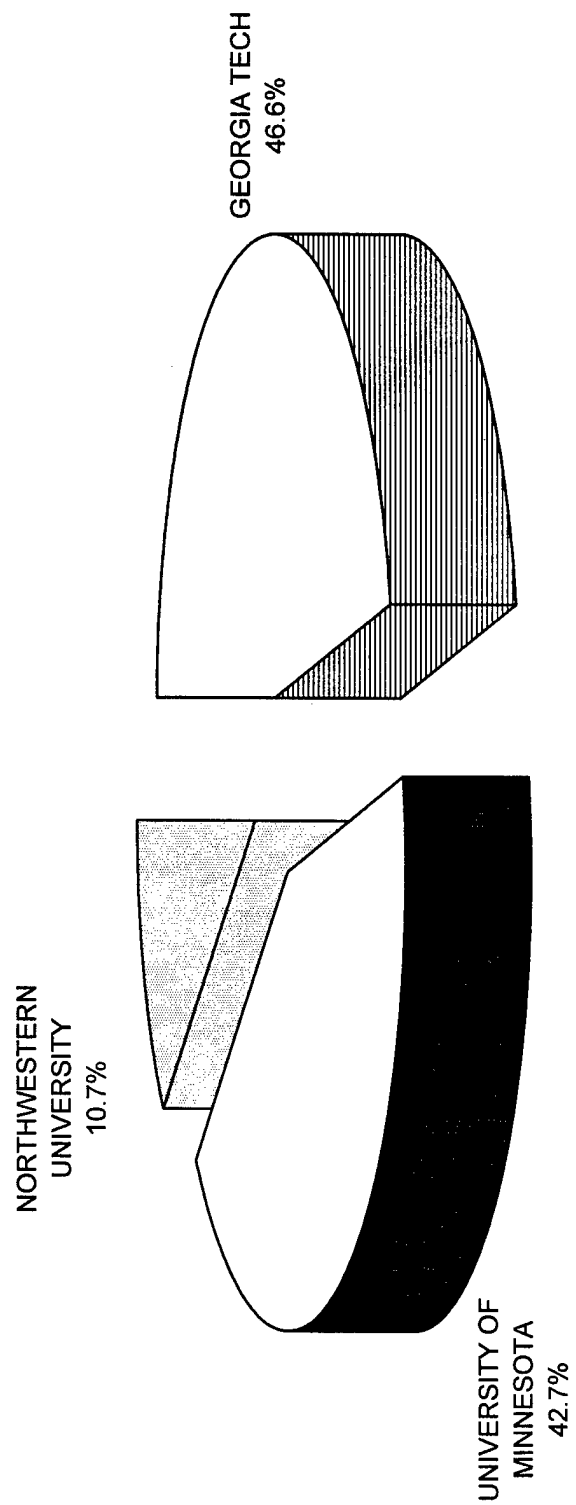


Figure 2a. Allocation of M-JRI Year 2 Funding (Participating Institutes)

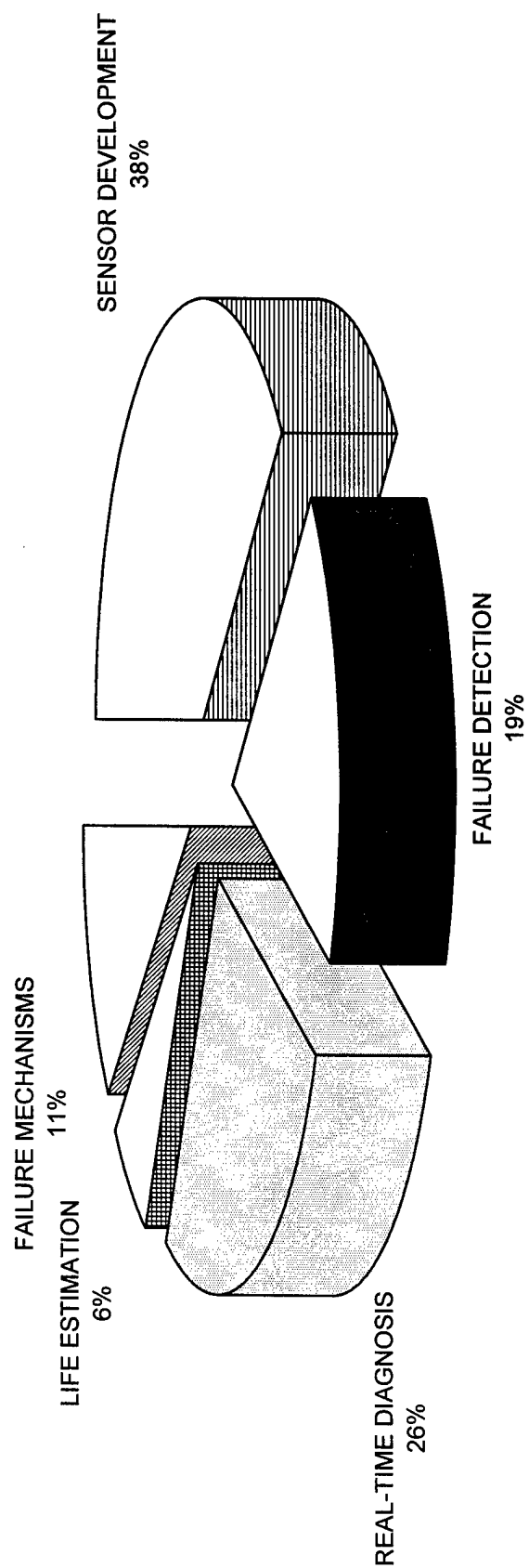


Figure 2b. Allocation of M-URI Year 2 Funding (Research Focus)

## 2. RESEARCH ACCOMPLISHMENTS and PLANS

---

The MultiUniversity Center for Integrated Diagnostics is focused on providing a meaningful program of research for use in minimizing the impact and or occurrence of *critical failures* in mechanical systems, including vehicle platforms and machinery. In the Predictive Maintenance community, a failure is identified as critical when it results in serious injury, loss of life, or significant financial burden.

As discussed in Section 1, a cross-discipline team has been formed to address an assortment of research projects, organized according to thrust areas that overlap in responsibility. This enables the faculty and staff to focus on a particular integrated diagnostic need, while maintaining an awareness of the progress achieved through the overall program.

During this reporting period, experiments based on material, load, and vibration information from critical rotorcraft components have been designed and conducted so as to collect data of relevance in understanding the mechanisms of failure for use in developing failure models. These models can serve as a guide in the selection and development of sensors to detect faults and pending failures. Effort has been placed on micro-sensor development, and achieving the means to analyze and correlate reliable sensor output for operator use.

The following pages summarize the accomplishments, plans and vision for the basic integrated diagnostic research pursued during this reporting period. Project titles, associated with a particular thrust area, are listed below with an indication as to what significant milestones have been achieved to date. These projects are similarly identified with their respective coordinators in the organization diagram of Fig. 3.

### I. Failure Detection and Identification

1. Flaw Detection and Characterization (Ultrasonics)
  - Developed a laser based ultrasonic system for remote nondestructive inspection.
  - Achieved the generation and detection of ultrasound by a fiber-array based delivery system and a fully path-matched Sagnac interferometer.
2. Crack Detection in Annular Structures by Ultrasonic Guided Waves
  - Validated the feasibility of crack detection in thick annular structures by ultrasonic waves.
  - Developed theoretical models (dispersion curves and normal mode theory) for propagation in thick annular structures.
  - Obtained an extended database of ultrasonic waveforms for various configurations (source/receiver positions, wave angles, frequency, etc.) in an uncracked ideal structure.
3. Detection of Mechanical Seal Failure in Turbomachinery
  - Assembled instrumentation and transducers for use in detecting ultrasonic transmission and ultrasonic noise as a function of seal gap.
  - Obtained data (on-going), which upon examination, is consistent with expectations.
4. Study of Acoustic Emission and Transmission from Incipient Fatigue Failure
  - Developed and tested PVF2 and PZT sensors for measuring acoustic emission and transmission in samples undergoing fatigue fracture tests.
  - Developed a useful transfer function technique to remove geometrical effects from received signals, so as to recover transmitted waveform.
  - Constructed a nonrotating fatigue test fixture.

## II. Failure Prediction Methodology

### 1. Structural Fatigue Investigation

#### *Stress Analysis and Stress Intensity Factor Solutions for Cracks*

- Developed a numerical simulation post-processor for the visualization of stress fields in complex 3D components (e.g., helicopter rotorhub).

#### *Characterization of Fatigue Behavior and Mechanisms*

- Developed a novel small crack propagation approach that unifies elements of strain-life and fracture mechanics methods.
- Developed experimental methodology for growing small cracks from notch.
- Conducted parametric study on small crack growth.
- Prepared test specimens of materials representative of helicopter components (e.g., 4340 steel, 304 stainless, PH 13-8 Mo-stainless, titanium alloy).

#### *Remaining Life Estimation Methodology*

- Completed analysis of damage for in-service H46 helicopter rotor connecting link.
- Completed heat treatment, microstructural characterization, and specimen preparation for fatigue crack initiation and propagation studies with test material acquired from the Cherry Point Naval Aviation Depot.

### 2. Fatigue Reliability

- Determined that accurate fatigue reliability calculations for problems in three-dimensional fracture (with multiple random variables) can be addressed using the developed direct integration methodology with the first-order reliability method (FORM).

## III. Direct Sensing, Analysis, Real-time Diagnosis

### 1. Magnetic-Electrical-Impedance Tomography

- Improved focusing probes used to locate small internal flaws.
- Automated the experimental test bed with an x-y positioner.
- Developed and improved computer models.

### 2. Eddy Current Microsensors for Integrated Diagnostics

- Performed eddy-current microsensor computer simulations.
- Constructed single and multi-element microsensors on Silicon wafers.
- Built and tested (for automated operation) a two-axis, computer controlled scanning system, for use in conjunction with eddy current microsensor arrays.
- Achieved sensor element spatial resolution of 100 micron.

### 3. Integrated Microsensors for Aircraft Fatigue and Failure Warning

#### *Microsensors*

- Fabricated a silicon-based piezoelectric acoustic emission sensor, and demonstrated its functionality.
- Conducted process development of an integrated (sensor and amplifier) sensor for acoustic emission detection.

#### *Signal Processing*

- Characterized helicopter noise baseline data, applying several processing methods to the acoustic emission detection.

### 4. Acoustic Emission Modeling for Integrated Diagnostics

- Determined that the loading phase is a very important parameter in correlating acoustic emission and damage state or age of a specimen or part.



5. Dynamic Metrology as a Wear Diagnostic
  - Built bearing test stand.
  - Established and coded envelope spectrum with adaptive in-line enhancing methodology for digital signal processing.
  - Performed vibration measurement and analysis for bearing fault diagnostics, including peak ratio analysis for bearing health.
6. Monitoring of Sub or Higher Harmonic Oscillations in Rotating Machine Elements
  - Reactivated test rig.
  - Reproduced high harmonic oscillations (HHO), evaluating a mechanical seal.

# Program Organization Diagram

*Coordinators identified in parentheses*

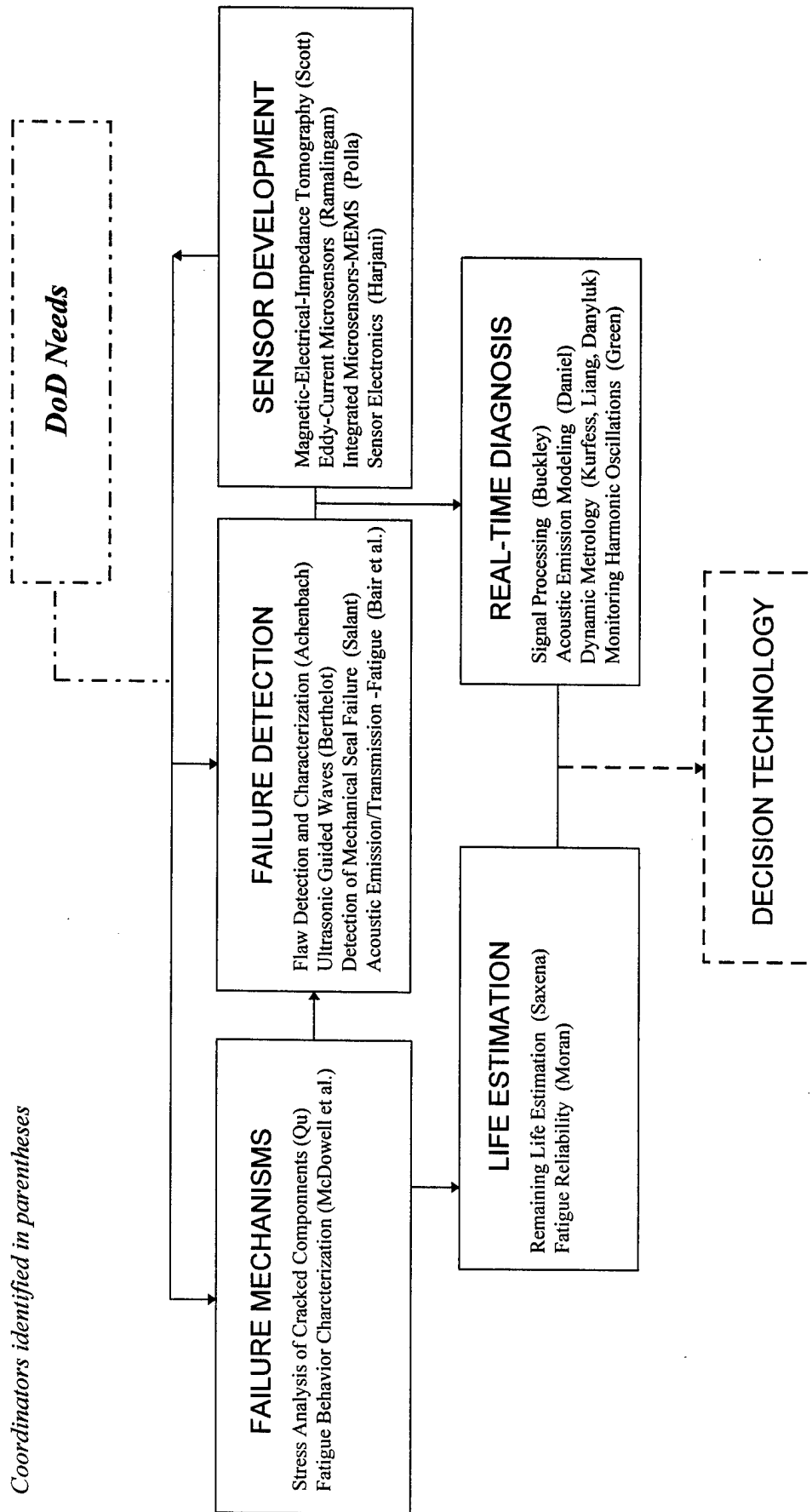


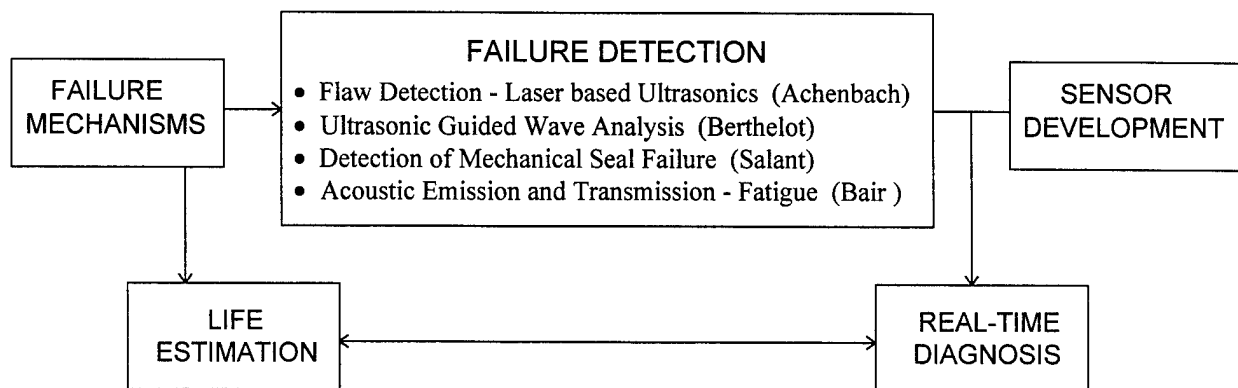
Figure 3

## Thrust Area I

### 2.1 FAILURE DETECTION AND IDENTIFICATION

*Perform studies pertaining to deterioration mechanisms and techniques for detecting the initiation of fractures or other failures.*

2.1.1	FLAW DETECTION AND CHARACTERIZATION .....	13
	Project Overview .....	13
	Accomplishments of M-URI Year 2.....	14
	Plans for M-URI Year 3.....	22
	Vision for Years 4 and 5 .....	22
2.1.2	CRACK DETECTION IN ANNULAR STRUCTURES BY ULTRASONIC GUIDED WAVES .....	23
	Project Overview .....	23
	Accomplishments of M-URI Year 2.....	24
	Plans for M-URI Year 3.....	27
	Vision for Years 4 and 5 .....	27
2.1.3	DETECTION OF MECHANICAL SEAL FAILURE IN TURBOMACHINERY .....	28
	Project Overview .....	28
	Accomplishments of M-URI Year 2.....	29
	Plans for M-URI Year 3.....	30
	Vision for Years 4 and 5 .....	30
2.1.4	STUDY OF ACOUSTIC EMISSION AND TRANSMISSION FROM INCIPIENT FATIGUE FAILURE.....	33
	Project Overview .....	33
	Accomplishments of M-URI Year 2.....	33
	Plans for M-URI Year 3.....	40
	Vision for Years 4 and 5 .....	42



### 2.1.1 FLAW DETECTION AND CHARACTERIZATION

Co-investigators: Jan D. Achenbach and Liusheng Wang (Northwestern)

M-URI Year 2 Funding Allocation: 4.3%

#### PROJECT OVERVIEW

Surface acoustic waves are commonly used to nondestructively investigate the near-surface region of a solid component for cracks (and other defects). One particularly attractive method of generating and detecting such ultrasonic signals is the use of laser based techniques. By directing a high-energy pulse of light at the surface of interest, ultrasound is generated through the rapid thermal expansion of the surface material. Conversely, a propagating ultrasonic disturbance (whether actively or passively generated) can be detected and measured using laser interferometry. Conventional laser based ultrasonics (LBU) methods provide a number of advantages over conventional ultrasonic systems (e.g., point generation/detection, non-contact, high bandwidth, scanning ease, applicable to high temperature/hostile environments etc.). Although LBU has acceptable high-bandwidth sensitivity, further enhancement of that sensitivity is possible by narrowing the detection bandwidth, as the signal-to-noise ratio for such a shot-noise limited laser detection system is given by [1] as

$$SNR \propto \delta^2 \frac{P}{B} \quad (1)$$

where  $\delta$  is the ultrasonic displacement amplitude,  $P$  is optical detection power and  $B$  is the detection bandwidth. To maximize the gain achieved by bandwidth reduction, the generation bandwidth should be narrowed to match the detection bandwidth as closely as possible. Narrowband generation and detection is also a particularly desirable alternative when inspecting for particular resonance modes or guided waves. However, the most attractive feature of LBU for the current study (i.e., use in real-world applications) is its ability to use fiber optics for system miniaturization. This would allow access to even internal components, requiring only enough access to allow the passage of optical fibers to the surface of interest (i.e., only a few millimeters). Furthermore, the surface need not be polished, but need only to reflect light and be free of oil and debris (though this requirement is primarily critical only for the detection of ultrasound).

Detection of ultrasound using laser interferometric techniques has been achieved by using a heterodyning interferometer or stabilized Michelson interferometer. The former is a costly and bulky system though it works for rough surfaces. A conventional Michelson interferometer requires stabilization due to the fact that the solid wave amplitude is far below the wavelength of the detection laser unit used. A fiberized Sagnac interferometer can overcome the above limitations due to its relatively small size and its fully path-matched feature.

#### Approach

Other researchers [2,3] have used fiber optic systems to enhance signal strength and directivity for both bulk and surface waves. However, these systems use a "star-coupler" device in which a pulse of light is focused into a single fiber, and then distributed to a series of fibers. A star-coupler device is therefore limited by the amount of light which can be focused into a single fiber. The approach undertaken for the effort reported here employs a binary diffraction grating to separate the single laser pulse into 10 equal but spatially separated laser pulses which can then be focused into 10 individual fibers. Because the detection signal-to-noise ratio is proportional to the square of the surface displacement, which is in turn directly proportional to the optical generation power (within limits), this fiber optic method will improve detectability by two orders of magnitude. When combined with an interferometer, the resulting system will act both as a sensor in support of guided wave based defect detection and as a defect detection system.

A linear fiber-array laser light delivery system for ultrasound generation works fine when the detection unit is aligned with the direction of the array. The ultrasound waveform picked up in this configuration is of a tone-burst form. In some special situations when the access space is very limited, the above arrangement for generation-detection units would be difficult. A modified output fixture of the fiber array has therefore been developed, whereby the fibers in the array are arranged in an annular form rather than a linear array. A similar system but using bulk optics has been reported [4]. Such a bulk optics system lacks, however, flexibility, which is a primary requirement for applications with limited access.

On the detection side, an improved Sagnac interferometer has been used. This point-wise fully fiberized interferometric system employs an acousto-optical modulator to bias the interferometer to its quadrature operating point for the detection of ultrasound signals [5]. This detection unit has been integrated with a laser-based ultrasound generation system for routine laboratory use.

## **ACCOMPLISHMENTS OF M-URI YEAR 2**

Effort for this second year of the project has been focused on the following aspects: (i) the improvement of the previously developed fiber-optic narrowband laser ultrasound generation system; (ii) the development of a technique for laser generation of broadband ultrasound signals with enhanced amplitude; (iii) the development of a fiber-optic laser interferometric detection system whose frequency response is optimized to close to that of the generation system, in order to (a) take full advantage of the bandwidth reduction of the narrowband generation system, and (b) provide greater speed and simplicity (compared to the application of Wiener filtering process [6,7]).

### **Narrowband Generation**

For completeness, a brief description of the LBU generation system is provided here. A Q-switched Nd:YAG laser operating at a 1064 nm wavelength (infrared) with a pulse duration of approximately 10 ns and pulse energies of up to 300 mJ was used as the laser source (see Fig. 4). Research from year 1 has demonstrated that a fiber array consisting of 10 high-power 200  $\mu$ m core diameter fibers can be used to deliver laser light to a remote location for ultrasound generation. While each fiber was not able to transmit the full 10 mJ of energy for which it was designed (primarily due to spatial non-uniformity of the input laser pulse), the array was able to transmit sufficient energy to allow three types of ultrasound generation: (1.) maximum point source thermoelastic ultrasonic generation (in which the surface is undamaged), (2.) ablative ultrasonic generation (in which the ultrasound is substantially stronger than that generated thermoelastically but the surface is slightly burnished), or (3.) maximum line source thermoelastic ultrasound generation (the lines are about 5 mm long perpendicular to the desired direction of propagation / measurement).

Details of the experimental arrangement for the 10-fiber delivery system are shown in Fig. 4. Two high damage-threshold neutral density attenuators (ND) with fixed transmission rates of 30% and 60% respectively were used to adjust the input energy to the fibers while maintaining a fairly uniform beam profile. This beam was then focused by a positive lens, with a focal length of 250 mm. Between the lens and its focal plane, a binary diffraction grating was placed to diffract the beam so as to generate 10 spatially separated (by 5.5 mrad) but equal energy pulses. These 10 separated spots were then launched into 10 multi-mode fibers (of 200  $\mu$ m core diameter) which were rigidly mounted at 1 mm spacings.

At the output end of the fiber array fixture, the spacing between fibers was set to 0.58 mm for the generation of 5 MHz ultrasound signals on aluminum materials (with Rayleigh wave speed of 2960 m/s). Figure 5 shows details of the configuration for line source generation by using a positive lens  $L_p$  and a cylindrical lens  $L_c$ . Adjusting the lenses along the arrow directions can change the frequencies of the ultrasound signals generated.

## **FAILURE DETECTION AND IDENTIFICATION**

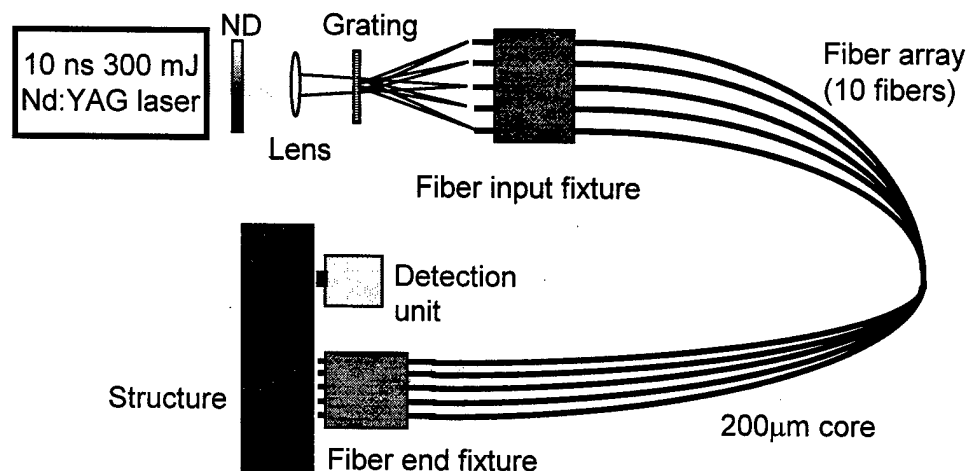


**Figure 4.** Optical setup of the fiber-array based LBU generation system. ND: two high damage-threshold neutral-density filters with transmission rates of 30% and 60% respectively. Only five fibers are shown here though the array consists of 10 fibers.

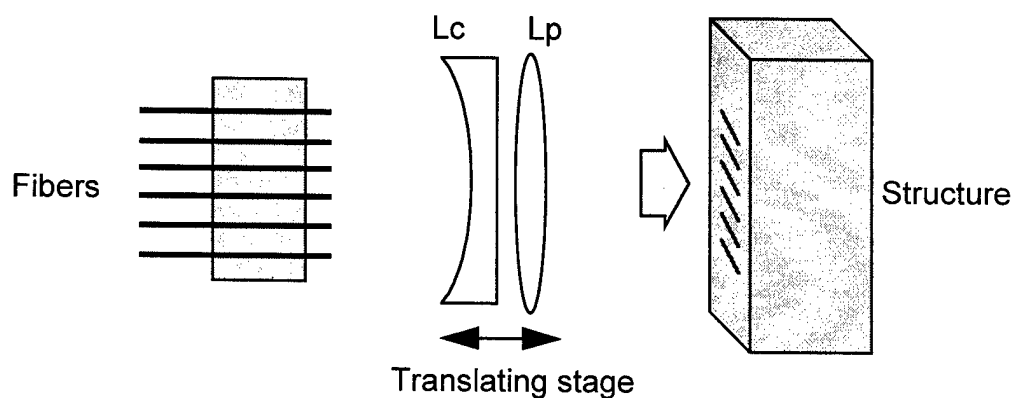


**Figure 5.** Configuration of the line array ultrasound source by using a combination of a cylindrical lens (Lc) and a positive lens (Lp). Translating the optical components can adjust the frequency of the generated ultrasonic signal.

The current arrangement using 10 fibers can deliver 100 times as much energy, within a narrow bandwidth, as would a single fiber system or a system employing a star-coupler. This effect can be seen from the plots in Figure 6 where the solid line shows the power spectrum for a simulated 10-fiber LBU system optimized for 2.3 MHz. In comparison, the dotted line shows that in order to achieve the same level of energy at 2.3 MHz, 100 times as much energy would be needed in a single fiber (broadband) system. For the same energy input, the fibers of our array are less likely to be damaged than would be a single fiber. Moreover, the array improves the signal detectability or SNR by 100 times as depicted by Eqn. (1).

Following the work from M-URI Year 1, a piezo-electric transducer (PZT) was first employed as the ultrasonic detection unit. Figure 7 shows the tone-burst ultrasound waveform generated by the fiber-array delivery system operating in the thermoelastic regime. The results were obtained for an aluminum block of 115x24x12 mm and the distance between the laser generation site and the 5 MHz PZT sensor was about 55 mm. Also shown in Fig. 7 is the power spectrum of the ultrasonic signal. By adjusting the positive lens  $L_p$  along the arrow directions shown in Fig. 5 (no cylindrical lens was needed for point source generation), the ablative operation regime was achieved. Figure 8 shows a tone-burst signal and its power spectrum. Note that compared to Fig. 7, due to the adjustment of the lens position, an ultrasonic signal with a different frequency was readily generated.

Using the optical arrangement shown in Fig. 5, a line array of sources was obtained. Figure 9 shows a typical waveform generated by such an array in the thermoelastic mode and the corresponding power spectrum of the waveform. The central frequency of the signal in this case was 5.0 MHz. It can be seen that, although the line source was operating in the thermoelastic generation regime, the resulting ultrasonic signal amplitude reached the same level as that by the ablative spot array source (Figure 8), but no surface burnish was produced in this arrangement.

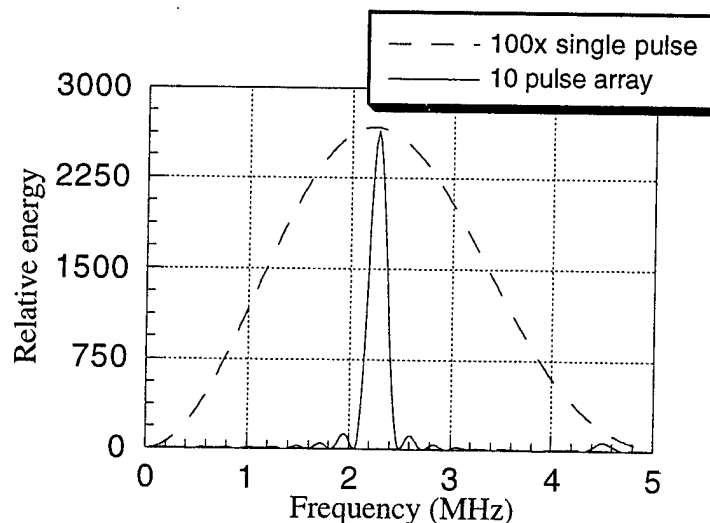


**Figure 6. Comparison of energy delivery capability of the fiber-optic LBU generation system.** The curves show the power spectra for simulated ultrasonic signals generated by a 10-fiber array (solid line) and a single fiber (dashed line), but with a 100 times as large energy input.

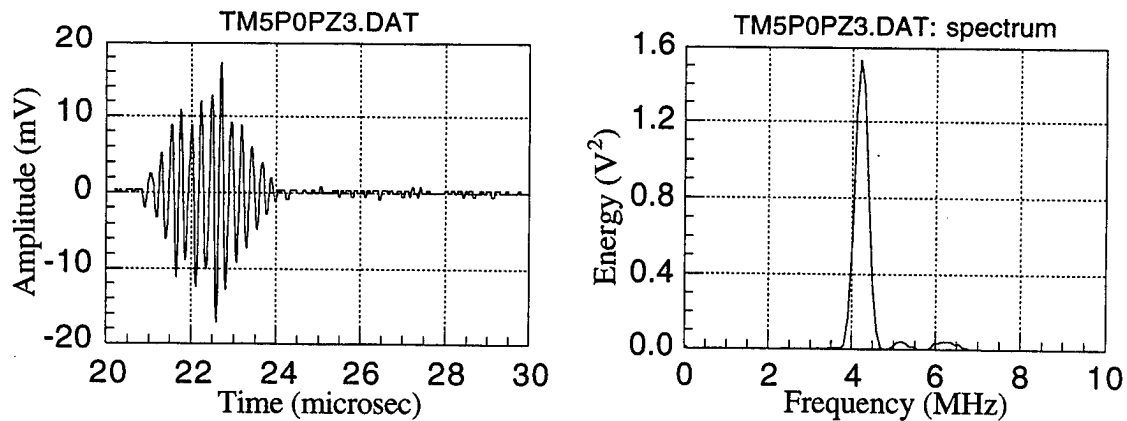


**Figure 7.** Laser generated ultrasonic signal (thermoelastic spot array mode) and its power spectrum. The central frequency of the tone-burst waveform was 4.2 MHz.

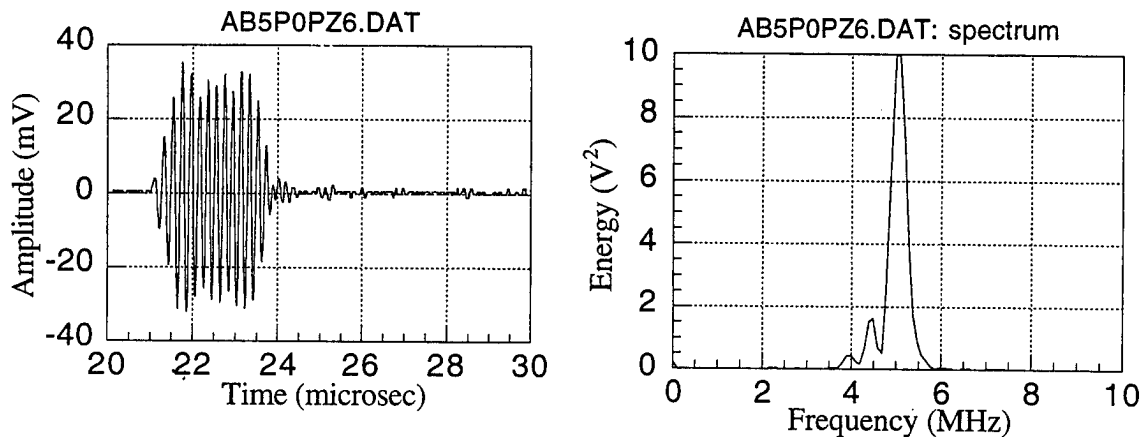


**Figure 8.** Laser generated ultrasonic signal (ablative spot array mode) and its power spectrum. The central frequency of the tone-burst waveform was 5.1 MHz.

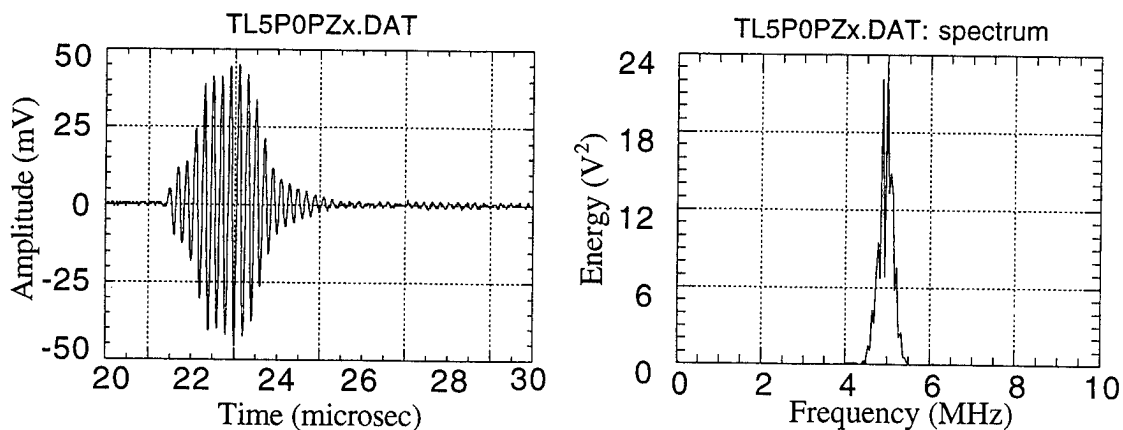


**Figure 9.** Laser generated ultrasonic signal (thermoelastic line mode with the length of the lines about 5mm) and its power spectrum. The central frequency of the tone-burst waveform was 5.1 MHz.



### **Broadband Generation**

For the above generation unit using a linear fiber-array source, the detection sensor must be placed along the direction of the array. This requirement may be hard to meet in some applications where the testing component is geometrically irregular. For example, to apply the LBU system for the inspection of a reservoir hub (Fig. 10) with a stepped cross-section profile, it would be difficult to employ the linear array to detect flaws emanating from the corners on the surface profile.

A broadband ultrasound generating system has been developed to suit this type of applications. The system is based on the configuration shown in Fig. 4 but with a modified output fixture for the fiber-array. The fibers in the array are arranged in an annular form as depicted in Fig. 11(a). Each fiber source generates an ultrasonic pulse due to the rapid heating of the surface of the material under inspection. When  $N$  fibers are used, then at the central point (focus) of the annular ring, the amplitude of the ultrasound signal would be  $N$  times that due to a single fiber, because of wave superimposition. Figure 11(b) presents an ultrasonic pulse generated by an array of eight fibers of 0.4 mm core diameter (operating in ablative regime). The radius of the annular array was 12.7 mm. It can be seen that as high as 400 mV peak-to-peak amplitude value has been achieved (picked up by a 2.25 MHz PZT sensor without any pre-amplification).

To demonstrate the capability of this broadband generation system, it has been applied to the reservoir hub shown in Fig. 10 for ultrasound generation. The focusing fiber-array was placed on the top surface of the component (see Fig. 12(a)). The ultrasound was detected by a PZT on the inner surface of the cylinder-like component. Figure 12(b) shows the signal picked up by the PZT. Because of the shape of the top surface which has a sharp stepped cross-section profile, there exists some tailing noise following the pulse due to complex reflections.

The focusing fiber-array system works best if the signal detection is performed point-wise at the central location of the annular ring of the array. This may be achieved by using a Sagnac laser interferometer as described next.

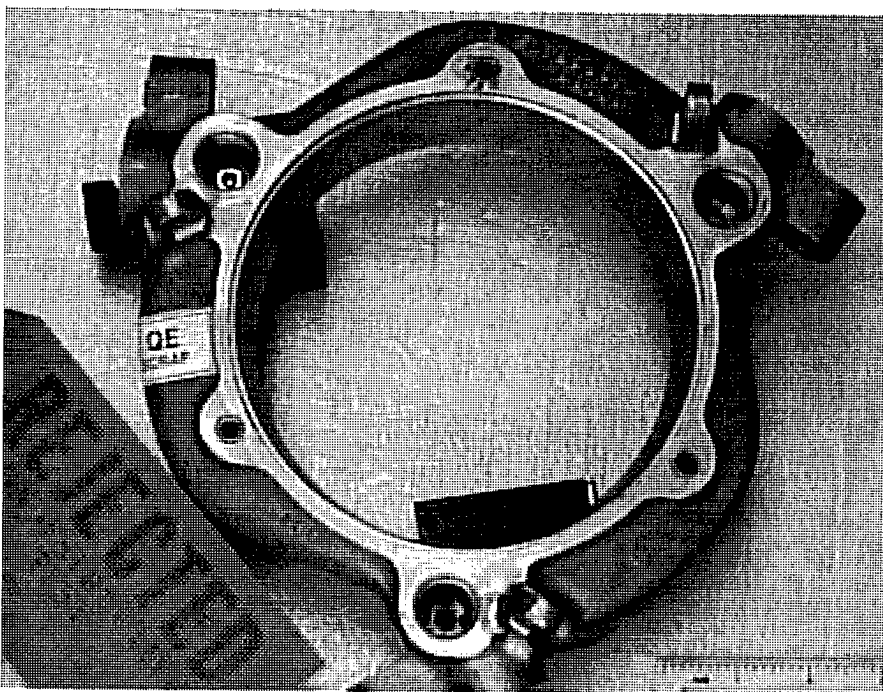


**Figure 10.**

A reservoir hub from an H-46 helicopter. This component is geometrically irregular and therefore prevents the practice of using a linear fiber-array for laser ultrasound generation and a detector along the array direction for ultrasound reception.

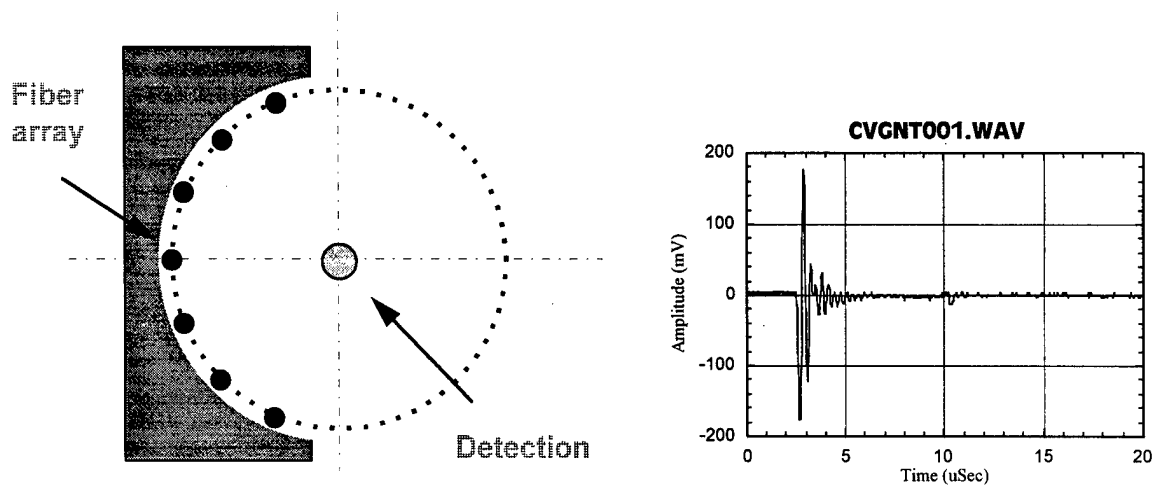


**Figure 11.** (a.) Schematic diagram of a focusing fiber-array for the generation of broadband ultrasound with enhanced amplitude; (b.) A typical ultrasonic pulse generated by the system as in (a.), operating in the ablative regime (eight 0.4 mm core diameter fibers were used). Detection of the waveform was performed by a 2.25 MHz PZT at the center of the ring as shown in (a.).

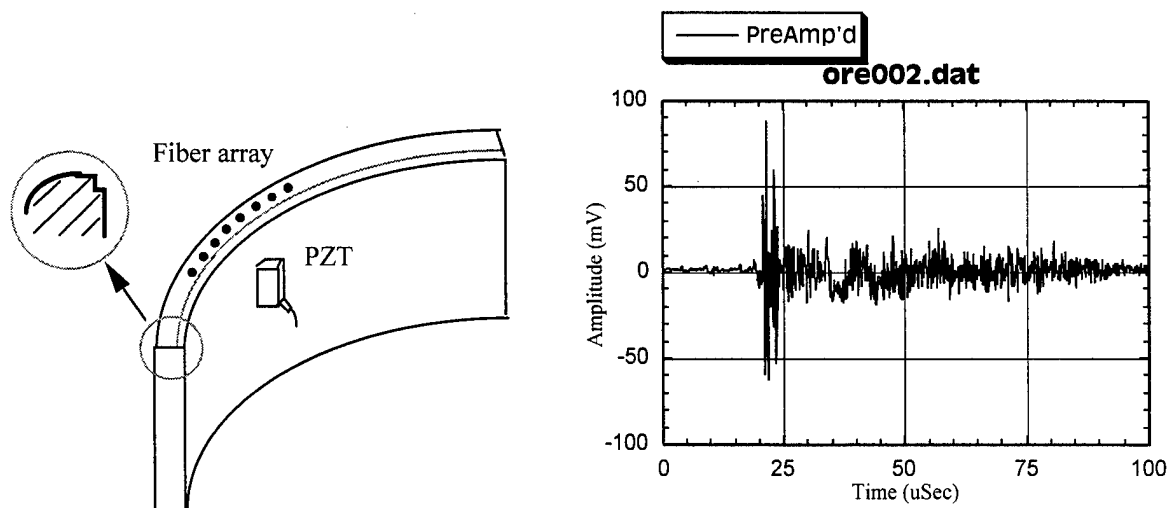


**Figure 12.** Generation of ultrasound signal for the inspection of (a.) an engineering component with irregular and limited access surface. Plot (b.) shows the waveform picked up by a PZT.

### Laser-Based Detection System

For ultrasound detection a non-contact highly accurate laser-based interferometer was used. This fully fiberized path-matched Sagnac laser interferometer was described in [5]. As shown in Fig. 13, this detection unit employs a HeNe laser operating at 633 nm as the coherent light source. The beam is first launched into a single-mode polarization-maintaining fiber and then split into two equal parts by a directional fiber coupler (A). The two parts travel respectively through paths L1 and L2 and are combined at coupler B to illuminate the structure surface (S) under examination. The reflected beam travels back via L1 and L2 and re-combined by coupler A to subsequently reach the photo-detector (PD). Note that path L2 has a 20 m long fiber loop so that among the four possible beam arrivals at the PD, only the two which travel in the order via the two sequential paths A-L1-B-S-B-L2-A-PD and A-L2-B-S-B-L1-A-PD can interfere (path-matched). In addition, an acousto-optic modulator was installed in path L2 to shift the laser beam frequency. The use of this component is to bias the two interfering beam frequencies by an amount of 70 MHz while the other two unwanted beams are not shifted. This can reduce the optical noise in the detected signal.

The length of the delay loop was optimized for the detection of 5 MHz narrowband ultrasonic signals. This matches the narrowband generation system as mentioned earlier. Such a design is important in terms of maximizing the efficiency of the generated ultrasound energies.

The fiberized Sagnac interferometer has been applied to the detection of LBU signals. For simplicity, a binary grating generated array source was used to produce the ultrasound signal. Shown in Fig. 14 is a typical tone burst waveform detected (averaged 100 times) by the Sagnac interferometer. The corresponding power spectrum of the waveform is also shown. For the comparison of spatial resolution between the point detection Sagnac interferometer and a PZT transducer, a waveform was recorded by each of the two detection units and the results are presented in Fig. 15. They correspond to a single laser line source. The actual single pulse form generated by the Nd:YAG laser should have only one spike as the Sagnac interferometer correctly demonstrates, but the PZT showed two spikes due to its finite sensing area and possibly due to internal reflection in the PZT.

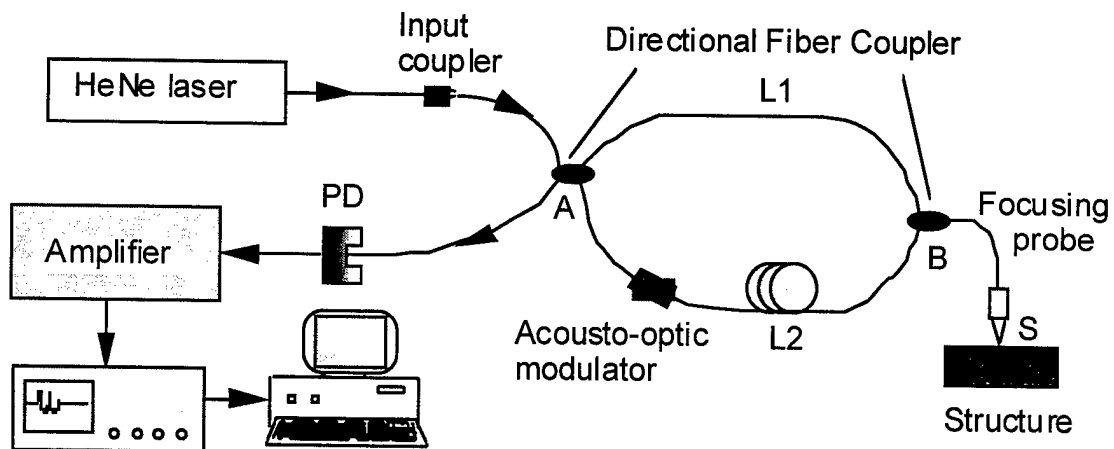


**Figure 13.** A fiberized path-matched Sagnac interferometer used for the detection of laser-generated ultrasonic signals.

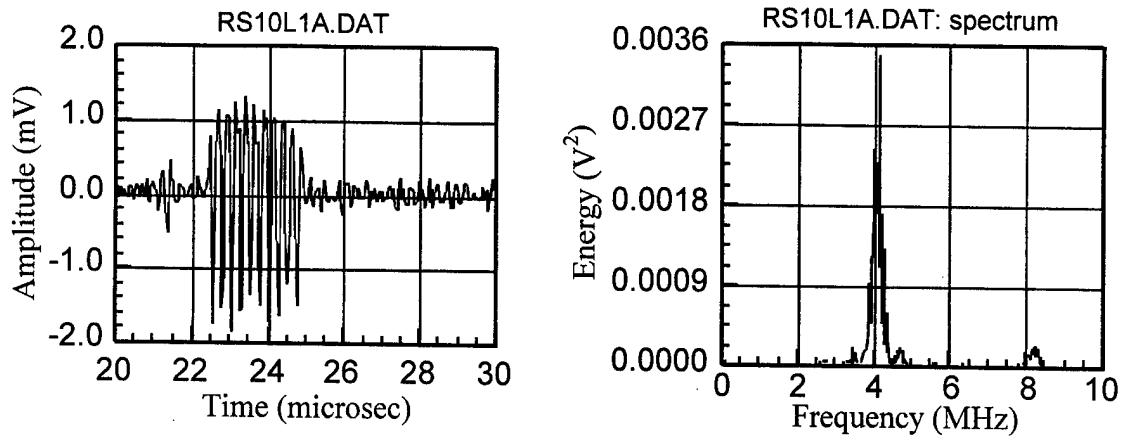


**Figure 14.** LBU signal detected by the Sagnac interferometer and the corresponding power spectrum.

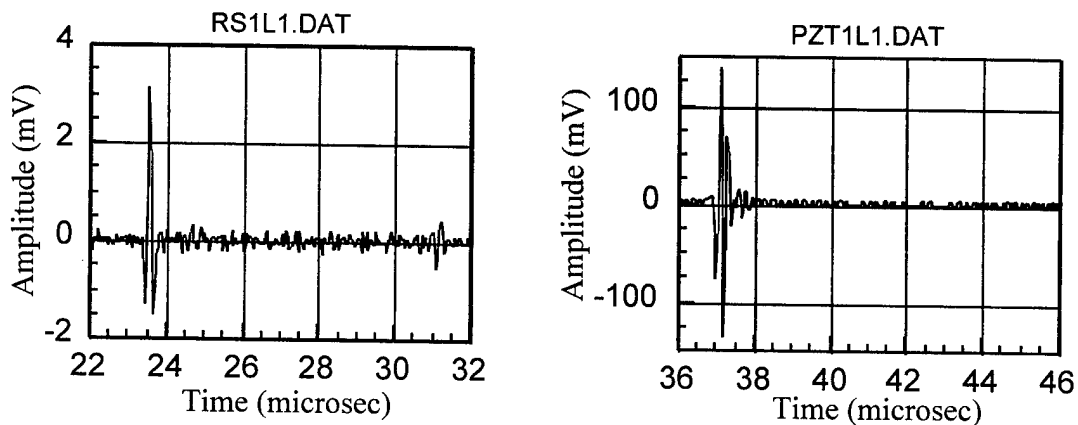


**Figure 15.** Comparison between the Sagnac interferometer (left) and the PZT transducer (right). The ultrasonic signal was generated by a single line laser source and the Sagnac interferometer picked up the signal correctly (one spike) but the PZT output shows two spikes due to its finite sensing area and possibly internal reflection.

### **Conclusion**

Improvements and refinements of the fiber-optic laser-based ultrasonic system have been pursued. A method using an annular array of fibers for the generation of broadband ultrasound signals with enhanced amplitudes has been developed. This broadband system has been demonstrated to work for the case of an irregular surface. Point-wise non-contact detection of ultrasound has been achieved with a recently developed fiberized Sagnac interferometer.

### **PLANS FOR M-URI YEAR 3**

The laser-based generation and detection system has been integrated into a unit for laboratory use, but improvement will be needed for its consistency and reliability. In addition, further applications of the system to components with limited access or irregular surfaces will be pursued. Since it must be expected that in field use, damage to the input end of the LBU generation fiber-array will happen from time to time, a technique which allows simple replacement of a damaged fiber in a field test will be investigated. A fully portable system for field application will require a small size of the complete system. Therefore miniaturization, especially of the output fixture of the laser delivery unit, will be another aspect for Year 3 studies.

### **VISION FOR YEARS 4 AND 5**

It is expected that a portable system with combined laser generation and detection system will be finalized for field tests. Development of a time-delay array of fibers for ultrasound generation will be initiated. A time-delay array can be applied to steer beams for the inspection of the interior of components. Signal analysis by use of measurement models and use of neural network techniques for signal classification will also be investigated.

## 2.1.2 CRACK DETECTION IN ANNULAR STRUCTURES BY ULTRASONIC GUIDED WAVES

Co-investigators: Yves Berthelot, Jianmin Qu, Laurence Jacobs (Georgia Tech)

M-URI Year 2 Funding Allocation: 6.0%

### PROJECT OVERVIEW

The goal of this research project is to understand how to design an efficient diagnostic/prognostic capability for the failure of components of annular shapes. Specifically, the proposed research is to develop robust techniques using ultrasonic guided waves to detect and monitor cracks in thick annular structures (e.g., the pitch-shaft or rotor hub of a military helicopter). In the development of a device used for practical applications, it is intended that the basic research approach performed under this project be integrated with research on (a.) new integrated miniature, and possibly wireless, sensors and actuators for diagnostics (cf. Sections 2.1.4, 2.3), (b.) structural fatigue for prognostics (cf. Section 2.2) and (c.) integration with signal processing schemes and intelligent algorithms (cf. Section 2.3.3.3).

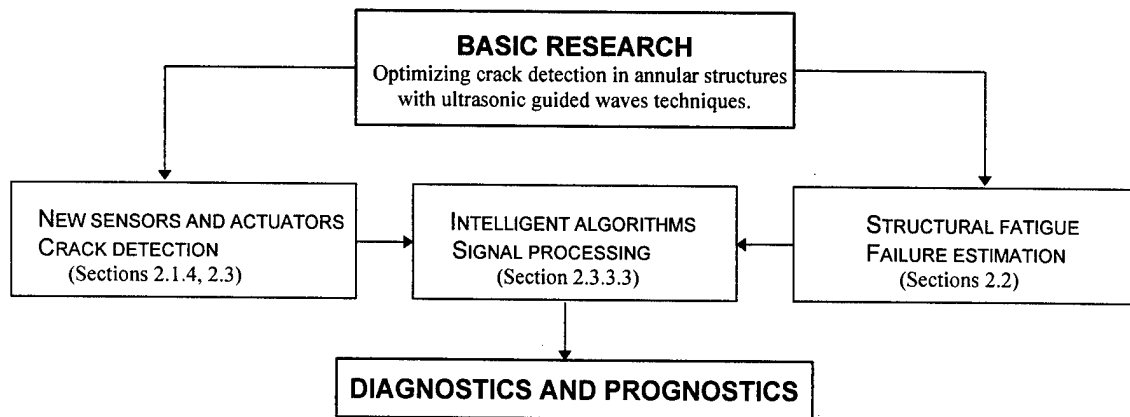


Figure 16. Schematic of Project Interaction

### Ultrasonic Guided Waves versus Conventional Ultrasonics

Conventional ultrasonic techniques by transmission and reflection are impractical because much of the structure is often inaccessible for transducer mounting. In addition, conventional methods are often very time consuming. Ultrasonic guided waves offer the advantage of probing the entire path of propagation at once. The challenge of the methods lies in understanding and, if possible, reducing the complexity of the received waveforms with a judicious choice of the operating parameters (position of source/receiver, frequency, angles at which ultrasound is launched and detected, etc.)

### Specific Objectives

- Develop theoretical models (dispersion curves, normal mode theory) for the propagation of ultrasonic waves in thick, ideal, annular structures.
- Develop models that predict how a judicious choice of the operating parameters (frequency, source/receiver positions, wedge angles) may be used to control the propagating modes, and therefore help optimize crack detection on the inner surface of the annulus.

- Build extensive experimental data base of waveforms in cracked or uncracked annular structures in either transmission mode, pitch-catch mode, or pulse-echo mode for various configurations: source/receiver positions, wedge angles, frequency, etc. Assess the feasibility of controlling the generation/detection of a few modes that are particularly appropriate for crack detection on the inner surface of the annulus.
- Assess the feasibility of the method when an inner pin is inserted (tight fit) in the annular structure.
- Develop efficient computational algorithms for the simulation of wave fields scattered by cracks in the annulus, with and without an inner pin. Compare with experiments.
- Test the method; e.g., on the (disassembled) pitch-shaft of an H-46 helicopter.

## ACCOMPLISHMENTS OF M-URI YEAR 2

- Validated the feasibility of crack detection in an ideal annular structure by ultrasonic guided wave techniques.
- Developed the appropriate (2D) theoretical and computational models for propagation in thick annular structures: (i) dispersion curves, (ii) normal mode theory for transient point source excitation, (iii) effect of transducer wedge and curvature matching piece.
- Validated experimentally that 2D models are indeed appropriate.
- Established that the wavelet transform of the signals can be used to determine the group velocities of the modes present in the signal. This information is useful in controlling the propagating modes in the structure.
- Built an extensive experimental data base of waveforms in cracked or uncracked annular structures in either transmission mode, pitch-catch mode, or pulse-echo mode for various configurations: source/receiver positions, wedge angles, frequency, etc.

### Crack Detection in an Ideal Annular Structure

#### *Experimental Criteria:*

- Transducers: 0.5 MHz, 1.0 MHz, and 2.25 MHz (longitudinal)
- Samples (see Fig. 17):
  - 2 through-wall cracks (1.5 and 3.0 mm)
  - 2 half-wall cracks (3.0 mm) at 90 and 45 degrees.
- Detection techniques (see Fig. 18):
  - a) *pulse-echo method* (with curvature matching piece)
    - incident/receiving angles:  $\beta=20^\circ$  to  $60^\circ$  by increment of  $5^\circ$
    - detection positions:  $\theta=10^\circ$  to  $280^\circ$  by increment of  $30^\circ$
  - b) *pitch-catch method* (without curvature matching piece)
    - incident/receiving angles:  $\beta=20^\circ$  to  $60^\circ$  by increment of  $5^\circ$
    - excitation position:  $\theta_2=280^\circ$
    - detection positions:  $\theta_1=10^\circ$  to  $190^\circ$  by increment of  $30^\circ$
  - c) *transmission method* (without curvature matching piece)
    - incident/receiving angles:  $\beta=20^\circ$  to  $50^\circ$  by increment of  $5^\circ$
    - excitation position:  $\theta_2=280^\circ$ , and  $190^\circ$
    - detection positions:  $\theta_1=10^\circ$  to  $160^\circ$  by increment of  $30^\circ$

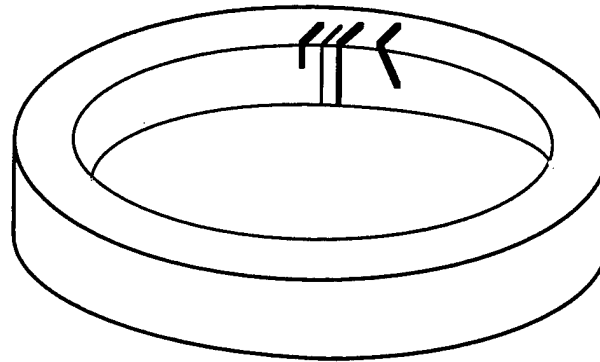


Figure 17. Ideal annular structure with machine-made cracks

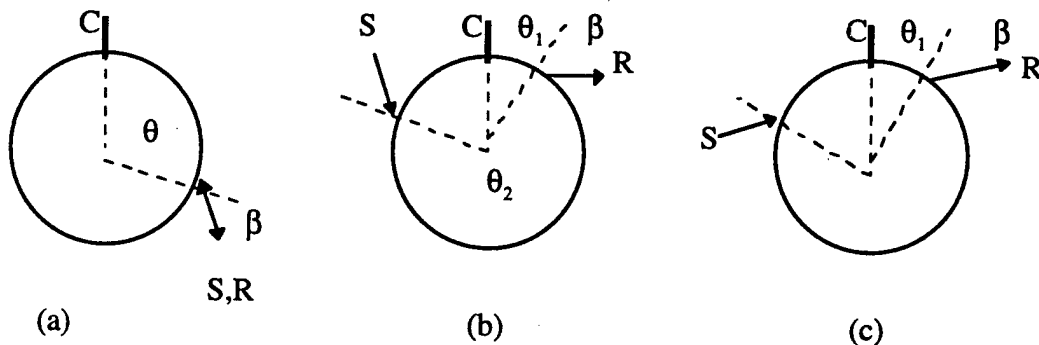


Figure 18. Detection techniques: (a.) pulse-echo; (b.) pitch-catch; (c.) transmission  
(C: crack; S: send; R: receive)

#### *Empirical Results:*

- Pulse-echo method:

To optimize the detection, the receiver wedge angle  $\beta$  has to match the wedge angle of the incident pulse. The range of acceptable values for the wedge angle is  $25^\circ$  to  $45^\circ$  (for the 1 MHz transducer). The best value is at  $30^\circ$ . It is also observed that the best angle for higher frequency transducers is larger than for lower frequency transducers.

The distance at which the crack is detectable is in the range  $\theta=10^\circ$  to  $180^\circ$  with all three transducers. (The distance is actually the product of the outer radius by the angle  $\theta$ ). It extends to  $250^\circ$  with the 2.25 MHz transducer). Higher frequency transducers give higher sensitivity and resolution for crack detection in the sense that the detected backscattered waveforms have higher amplitudes and exhibit less complexity. However, in our experiments, the  $45^\circ$  inclined crack was not detectable by the pulse-echo technique.



- Pitch-catch method:

Same conclusions as for the pitch-catch method. However, it is preferable to use two transducers, if possible, rather than one, because the detected signal is less affected by the presence of multiple reflections in the wedge of the source transducer.

- Transmission method:

The optimum wedge angle is in the range of  $30^\circ$  to  $40^\circ$ . For small cracks, the best angle is around  $30^\circ$  but for larger cracks, the best angle is around  $40^\circ$ . The distance at which cracks are detectable is in the range of  $\theta=20^\circ$  to  $240^\circ$ . Better results are obtained with the high frequency transducers. (Detection is almost impossible with the 0.5 MHz transducer, for all four cracks). The  $45^\circ$  inclined crack can be detected in the range of  $40^\circ$  to  $150^\circ$ , but the resolution is poorer than with the other cracks.

### **Crack Detection in an Ideal Annular Structure with an Inner Pin**

#### *Experimental Criteria:*

- Transducers: 2.25 MHz
- Samples: Two annular structures imbedded with an interference fit (average overlap  $\sim 0.1$  mm).  
Outer radius: 2.5 in, interference radius: 2.0 in, inner radius: 1.5 in.  
3 mm crack (through wall) on the inner surface of outer annulus.
- Pulse-echo method:  
Incident receiving wedge angles:  $\beta=30^\circ, 35^\circ, 40^\circ$ .  
Receiver positions:  $\theta=10^\circ$  to  $190^\circ$  by increment of  $30^\circ$ .
- Pitch-catch method:  
Incident receiving wedge angles:  $\beta=30^\circ, 40^\circ$ .  
Source position with respect to crack:  $280^\circ$ .  
Receiver positions:  $\theta=10^\circ$  to  $190^\circ$  by increment of  $30^\circ$ .

#### *Preliminary Conclusions (empirical):*

- Pulse-echo method:  
The best wedge angle is  $30^\circ$ . (Detection is almost impossible at  $40^\circ$ ).  
The maximum distance at which the crack is detectable is  $190^\circ$  (with a wedge angle of  $30^\circ$ ) and detection is best in the range  $100^\circ$  to  $150^\circ$ .
- Pitch-catch method:  
The best wedge angle is  $40^\circ$ .  
The maximum distance at which the crack is detectable is  $200^\circ$  (with a wedge angle of  $40^\circ$ ) and detection is best at positions  $40^\circ, 100^\circ$ , and  $160^\circ$ .

### **Crack Detection in a Helicopter Pitch Shaft**

- Work in progress.

### **PLANS FOR M-URI YEAR 3**

A major effort during Year 3 will be to connect the theoretical work with the experimental results. The combination of theoretical predictions and purely empirical knowledge (obtained from the large data base presented above) will provide the best possible guidelines for the selection of the optimum parameters for crack detection (frequency, wedge angles, positions, etc.). To do so will involve: (a.) using the finite element method to obtain the 2-D transient wave propagation solution incorporating realistic transducer geometry and wedge angle; (b.) developing analytical models for the shaft/inner pin assembly; and (c.) studying parametricly the wave files scattered by radial cracks of various sizes and orientations. The goal is to optimize the transducer configuration and the frequency/mode selection.

The experimental work will focus on the pitch-shaft of the H-46 helicopter with calibrated machine-made cracks. Signal processing techniques will be implemented to enhance the detection of cracks. In addition, laser interferometric detection will be used (instead of piezoelectric detection) to (a.) provide precise in-plane and out-of-plane measurements at the detection spot, and thus infer the modal nature of the signal, and (b.) assess the feasibility of using the optical transducer being developed at Northwestern University (see Section 2.1.1) for ultrasonic guided wave applications.

### **VISION FOR YEARS 4 AND 5**

- Improve the signal to noise ratio in the system to enhance the threshold of crack detection. This includes implementing improved signal processing techniques.
- Apply the method to other parts with annular geometry (e.g., helicopter rotor hub, pitch shaft, etc.).
- Explore other important effects: crack face roughness, crack tip closure due to fatigue, corrosion induced cracks, lubricants, rough boundaries, etc.
- Integrate with research on (a.) new integrated miniature (and possibly wireless) sensors and actuators (Projects reported in Sections 2.1.4, 2.3) for diagnostics; (b.) structural fatigue (Projects of Section 2.2) for prognostics; and (c.) integration with intelligent algorithms.

### 2.1.3 DETECTION OF MECHANICAL SEAL FAILURE IN TURBOMACHINERY

Co-investigators: Richard F. Salant and Jacek Jarzynski (Georgia Tech)

M-URI Year 2 Funding Allocation: 4.9%

#### PROJECT OVERVIEW

**M**echanical (face) seal failure is one of the principal causes of breakdown in such turbomachines as centrifugal pumps, compressors, turbines, turbopumps, propeller shaft assemblies, and gas turbine engines. In this project, a real-time monitoring system for detection of the precursor to seal failure is being developed. Such a system will allow preventive action to be taken to avoid failure.

Mechanical seals generally fail as the result of the collapse of the lubricating film between the two seal faces. The goal of this project is to develop a system to detect the collapse of the film before mechanical and thermal damage is sustained.

The approach involves placing piezoelectric transducers behind the seal faces and monitoring (and processing) the output of the transducer(s) in real time. Two modes of operation have been investigated: passive and active modes.

*Passive Mode.* When the lubricating film collapses, the relative motion of contacting asperities will generate ultrasonic waves in the face, which will be detected by the transducers. The primary challenge is to correlate the detector signal characteristics with the degree of contact between the mating seal faces. The primary problem is the ultrasonic wave generation characteristics (frequency-amplitude) is very dependent on the particular seal being investigated, and on the physical state of the seal. Since one does not have control over the signal characteristics, it may be difficult to distinguish it from machinery noise.

*Active Mode.* When the lubricating film collapses, mechanical contact between the two seal faces occurs, providing a transmission path for ultrasonic waves. To utilize this effect as a means for detecting film breakdown, one of the transducers is used as a receiver, while the other is used as a source. A continuous series of wave packets of a specified primary frequency and amplitude are generated by the source, using a wave generator. The signal amplitude detected by the receiver will indicate whether or not mechanical contact between the seal faces has occurred. The advantage of this approach is it is relatively independent of the particular seal characteristics. Furthermore, since the amplitude of the signal generated by the source can be controlled, it can be made large enough to be distinguished from machinery noise.

The primary test apparatus consists of a double mechanical seal contained within a housing. It is shown schematically in Fig. 19. A single tungsten carbide rotating face is fixed to the shaft. Two non-rotating controllable face assemblies float in the axial direction. Each of the latter assemblies consists of a carbon graphite face bonded to a PZT-5H piezoelectric actuator (in the form of a ring), a piezoelectric transducer, a boron nitride holder, O-ring secondary seals, and coil springs, as shown. The actuator crystal is poled in the radial direction, so that when a voltage is applied across the crystal (in the axial direction), the crystal undergoes shear deformation and causes the carbon face to cone. The larger the applied voltage, the larger the coning. The interface between the carbon and the tungsten carbide faces consists of a fluid film. It can be shown that the larger the coning, the higher the average fluid pressure in the film (for a fixed film thickness), and therefore the thicker the film. As the applied voltage and the coning is reduced, the film thickness will be reduced, until there is contact between the faces. Thus, by adjusting the applied voltage, one can control the occurrence of contact. The seal tester is driven by a motor, through a belt drive.

Results obtained indicate that the active mode of operation is superior to the passive mode, and therefore future work will concentrate on the former. Ultimately, it is anticipated that this approach will be developed into an onboard, continuous, active monitoring system for any piece of turbomachinery containing mechanical seals (engines, pumps, compressors, etc.). Such a system will give a positive indication when the lubricating film in the seal breaks down, allowing replacement or repair of the seal before seal failure.

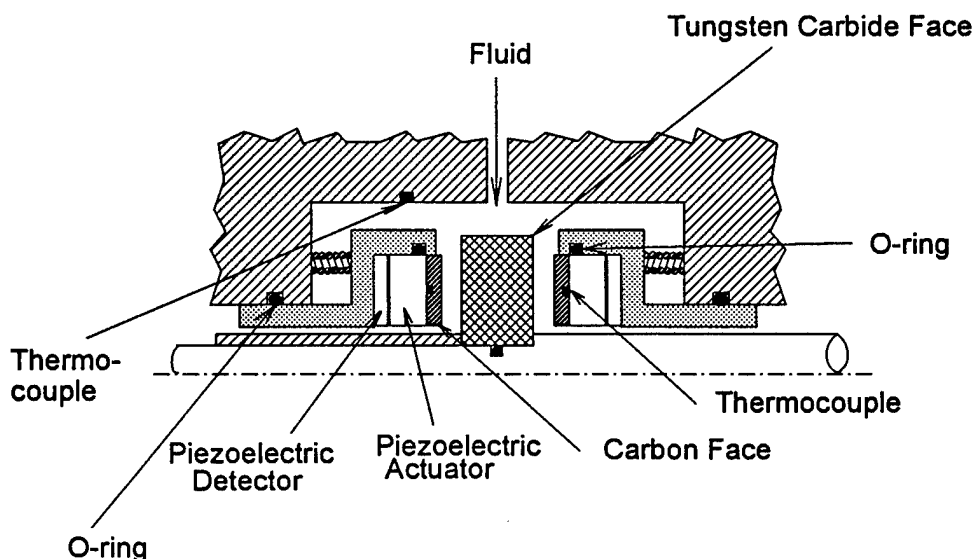


Figure 19. Schematic of Apparatus

## ACCOMPLISHMENTS OF M-URI YEAR 2

The principal activities for this project over the three-year grant period include: (1.) rebuilding and modifying the existing seal tester, with air as the sealed medium; (2.) developing a mathematical model of wave generation and detection; (3.) designing, analyzing and constructing a piezoelectric detector; (4.) developing signal processing methods; (5.) performing shakedown tests of the system; (6.) performing steady state tests with varying degree of face contact; (7.) performing transient tests; and (8.) performing destructive tests to failure.

During year 1, task 1 and most of task 3 were completed. During year 2, the remainder of task 3 was completed, as well as tasks 2 (wave detection), 4, 5, and part of task 6. (The wave generation part of task 2 was curtailed, since emphasis has shifted to the active mode). Results obtained so far follow, discussed with respect to mode.

### **Passive Mode**

The passive mode was initially tested in a series of experiments in which the shaft was turned by hand. In these tests, ultrasonic waves generated by face contact in the seal were detected. However, in dynamic tests in which the motor was run, it was found that any possible ultrasonic wave generation by the seal was masked by the motor. It was therefore decided to concentrate effort on the active mode.

### **Active Mode**

An analytical model to predict the amplitude of the receiver signal, for a given source signal, was constructed and implemented in the form of a MATLAB computer program. The one-dimensional, normal plane wave transmission model includes all of the important interfaces of the actual system. Typical results are shown in Fig. 20. It is seen that the system is essentially binary: either the receiver signal amplitude is substantial, indicating mechanical contact, or it is very small, indicating the presence of a film, essentially independent of film thickness. This is a very desirable characteristic, which will make interpretation easier than if there was a film thickness dependence.

A series of bench tests was performed to aid in interpreting the seal tests and to verify the analytical model. All of the seal components, except the housing, were assembled in a jig, and Mylar spacers were used to set a predetermined film thickness. For a given source signal, at 4 MHz., the receiver signal was measured as a function of film thickness. The results are shown in Fig. 21, and are consistent with the analytical model: either the receiver signal amplitude is substantial, indicating mechanical contact, or it is very small, indicating the presence of a film, essentially independent of film thickness.

Steady state tests were performed on the actual seal, utilizing a 4 MHz. signal. The voltage to the actuator was varied to vary the film thickness, as described above. Typical results are shown in Figs. 22a and 22b, which contain plots of the signal amplitude detected by the receiver. In the test illustrated in Fig. 22a, with an applied voltage of -2 kV there is mechanical contact between the faces. When the voltage is increased to -1, 0, and +1 kV, a substantial drop in amplitude indicates the presence of a lubricating film. Fig. 22b shows similar behavior, except the amplitude at -1 kV indicates partial contact.

The above results provide strong validation of the active mode as a successful condition monitoring approach.

### **PLANS FOR M-URI YEAR 3**

In year 3, task 6 (steady state tests) will be completed. In particular, the tests run in year 2 will be repeated, with improved insulation of the source and receiver transducers. It is expected that the latter will result in cleaner signals. Task 7 (transient tests), involving monitoring of such processes as startup and shutdown, will be performed. Finally, task 8 (destructive tests to failure) will be performed. In this task, the sequence of events from normal operation to breakdown of the lubricating film and detection by condition monitor to failure of the seal, will be observed.

### **VISION FOR YEARS 4 AND 5**

Years 4 and 5 will be devoted to extending the present monitoring system (viz., the active mode) to liquid applications. Note, in years 1 through 3, the working fluid was air. For test purposes, the working fluid will be water. A completely new test apparatus will be built. It will be similar to the existing apparatus, but will be designed to handle the special problems associated with liquid systems, i.e., corrosion and insulation of electronic components. Tests, similar to those of years 1 through 3 on the gas system, will be performed. At this time, it is expected that the tests will be confined to the active mode.

### **FAILURE DETECTION AND IDENTIFICATION**

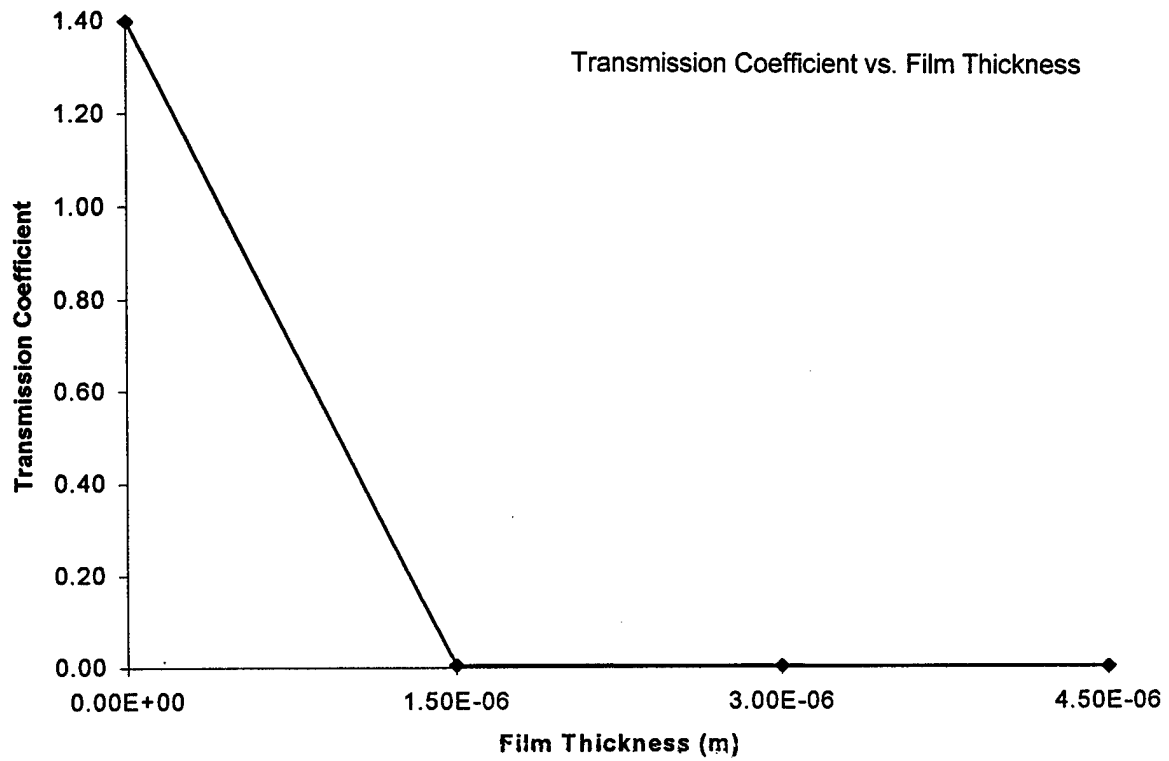


Figure 20. Results of Analytic Model

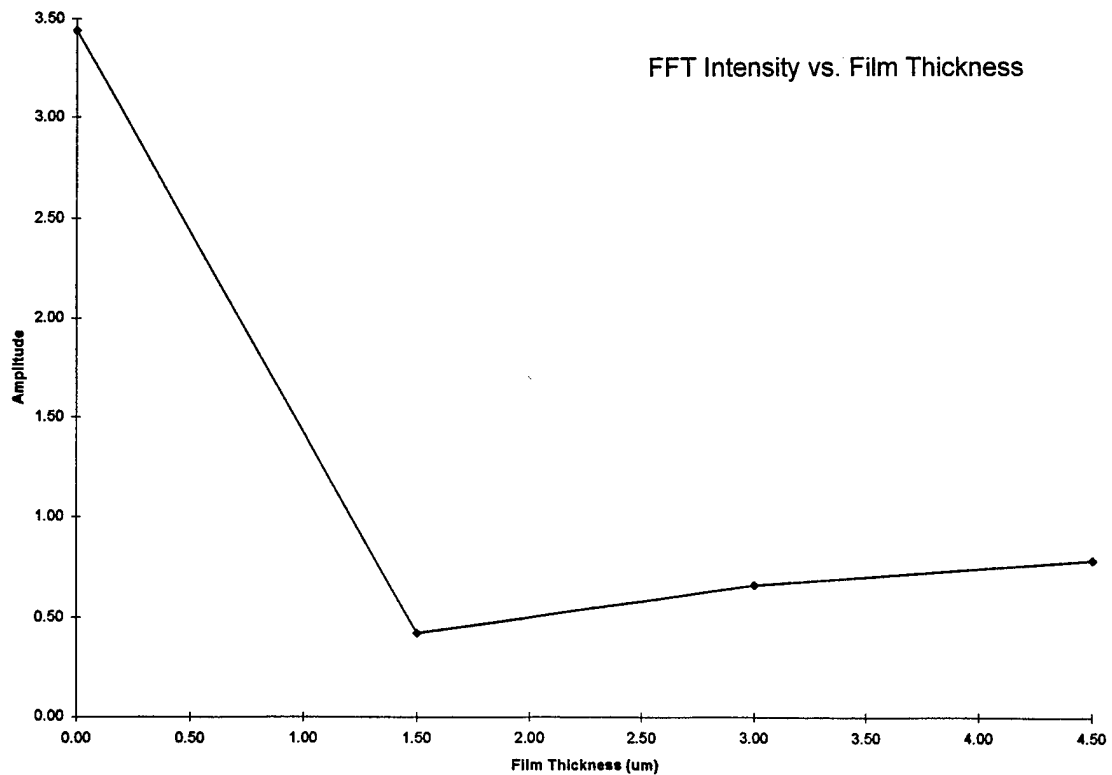
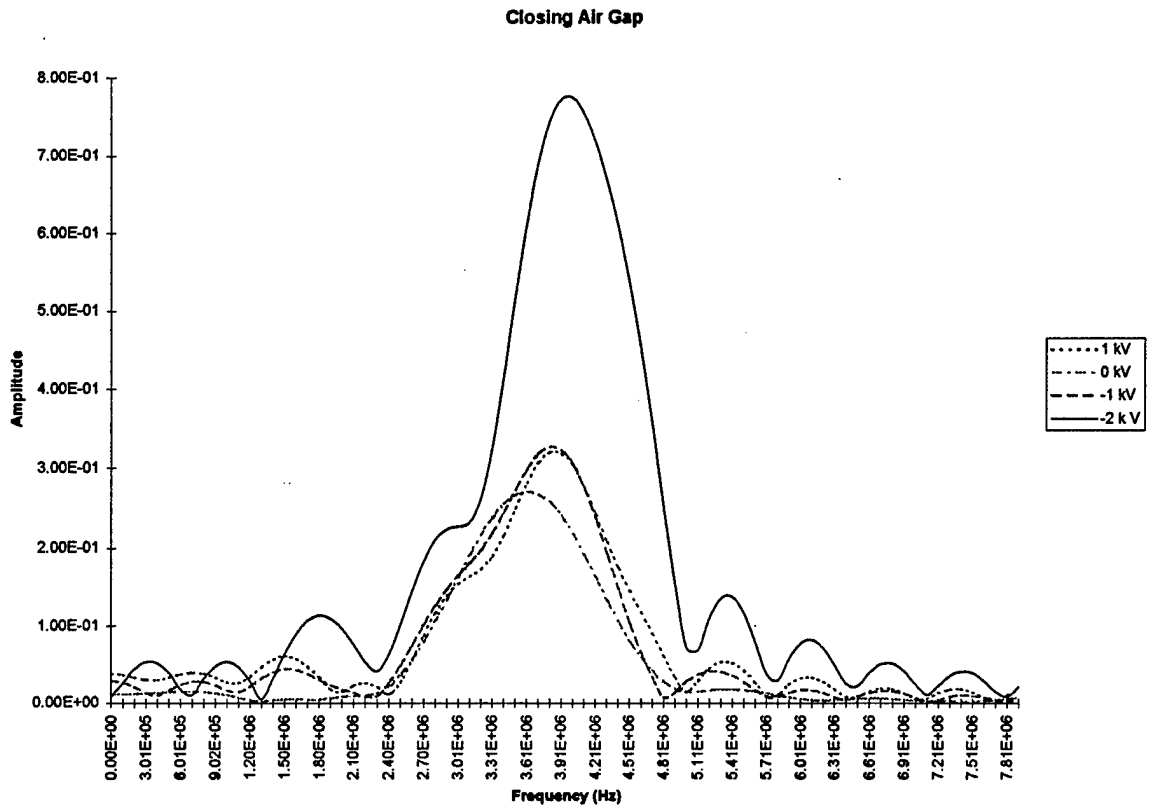
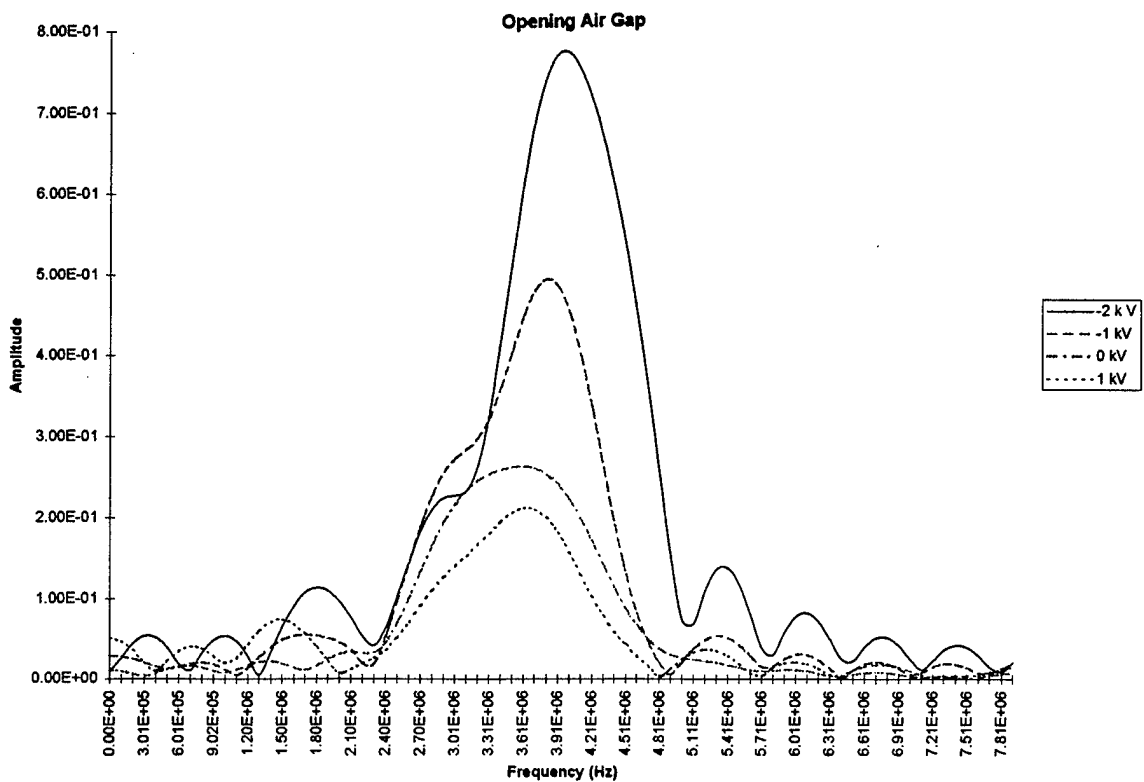


Figure 21. Results of Bench Tests



**Figure 22a. Steady State Test Results I**



**Figure 22b. Steady State Test Results II**

#### 2.1.4 STUDY OF ACOUSTIC EMISSION AND TRANSMISSION FROM INCIPIENT FATIGUE FAILURE

Co-investigators: Scott Bair, Jacek Jarzynski, Laurence Jacobs (Georgia Tech)  
M-URI Year 2 Funding Allocation: 5.1%

#### PROJECT OVERVIEW

The objective of this project is to develop both active (ultrasonic transmission) and passive (acoustic emission detection) techniques to determine incipient failure in vehicle platform and machinery components. During FY 96, this research focused on (1) acoustic emission methods, and (2) development of transducer arrays for both active and passive failure detection techniques.

Acoustic emission (AE) techniques offer a distinct advantage over other methodologies because they allow for the *real-time* monitoring of in-service components. However, to be effective, acoustic emission methods must be able to identify an emission source and characterize the severity of damage associated with that source. One of the primary difficulties in the application of acoustic emission techniques is in interpreting and categorizing the large quantity of data and in removing erroneous information, such as signals caused by environmental noise. In this project, two approaches are investigated for reducing environmental noise: (1) A transfer function technique to remove geometric effects, and (2) Development of transducer arrays. Time delays are introduced between outputs from individual array elements so that the array has peak response along some given direction. Therefore, the array can be designed to have peak response along the direction from which AE signals are expected, and suppress noise signals from other directions.

To design optimum sensors and signal processing techniques for AE detection (Sections 2.1.2 and 2.3), it is necessary to have detailed information about the AE signals generated during fatigue failure - their amplitude, duration and shape at various stages of the fatigue process. This is the objective of a joint study with the Structural Fatigue Investigation group (Section 2.2.1).

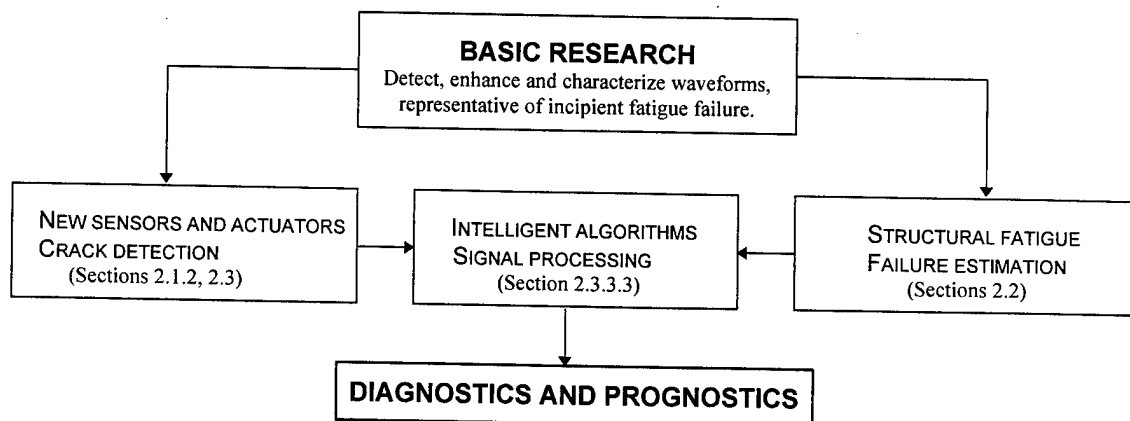


Figure 23. Schematic of Project Interaction

#### ACCOMPLISHMENTS OF M-URI YEAR 2

##### Equipment

A state of the art digital data acquisition system was purchased from Digital Wave Corporation. This system is now used for all AE measurements. The unique features of this system are: (1) A wide bandwidth, extending from 3kHz to 4Mhz, which allows capture of individual AE waveforms. A trigger threshold control allows the unit to be set to capture only waveforms whose amplitude exceeds a preset



value; (2) The above system is designed for fast data acquisition (several signals per second). Each captured waveform is transferred, as a data file, to a desktop computer where it is available for further processing; (3) The system will also record up to four parametric signals, such as the output from a load cell. During cyclic fatigue testing, the load cell signal can be used to determine the stage of the stress cycle at which a given AE signal occurs.

### **Discrimination Against Noise to Characterize AE Signals**

#### *Transfer Function Technique:*

The specimen geometry changes the original acoustic emission signal as it propagates from its source to the receiving sensor. These changes, which are caused by reflection, transmission and mode conversion at interfaces and boundaries, have a significant impact on the acoustic emission wave that is measured by the receiving sensor. The geometry effects (which do not contain any useful information for acoustic emission testing) tend to swamp and mask the initial signal, making it difficult to uniquely identify the original source of the acoustic emission. Work in the previous year developed a transfer function that quantifies and removes these geometric effects from measured acoustic emission signals. This transfer function is developed using a repeatable, broad band (synthetic) acoustic emission source, a pulsed laser, and a broad band, high fidelity sensor, a laser interferometer. The steps in the development of the transfer function are as follows: an acoustic emission signal is generated and detected in a specimen whose geometry is being characterized; this experiment (same source) is repeated in a "geometry-less specimen," one that contains no geometric features; and the "geometry-less" signal is divided by the specimen signal (in the frequency domain) to form the transfer function. This transfer function can operate on an acoustic emission signal, measured in the same specimen, but caused by a different source. The accuracy of this transfer function is demonstrated by operating on different acoustic emission sources such as a pencil lead break and removing the unwanted geometric features.

The specific specimen examined is the fatigue crack specimen being used by the Structural Fatigue Investigation group (Section 2.2.1). Since all measurements in the fatigue crack specimen are made with the source and receiver on the same side (surface), the corresponding "geometry-less specimen" is a half-space. Signals measured in this half-space only contain the effect of the source, they are not influenced by any specimen geometry features. The geometric features exhibited by the fatigue crack specimen (which are very complicated) are dominated by the multiple reflections of the Rayleigh waves off the side edges, as well as the body waves that propagate into the specimen and are reflected and mode converted off the bottom surface. An accurate accounting of the arrival of each of these features, which are shown in Fig. 24, is not necessary for the development or application of the transfer function. However, the key peaks and arrival times are identified in [8].

The validity and robustness of the transfer function developed in this research is demonstrated by operating on different, prescribed sources in the fatigue crack specimen. In this application, the "reproduced" half-space signal (in the time domain) is compared with an "actual" half-space signal, the signal created by the new (different) generation source in a half-space. This procedure is used to remove the fatigue crack specimen geometric effects (and thus isolating the source signal) from a number of new sources such as a double laser pulse or a pencil lead break. For example, this transfer function is used to remove the geometric effects from a signal created with a double pulse (ablation) source. Figure 25 compares the double pulse signal in the specimen and this same specimen signal operated on by the transfer function. The specimen signal operated on by the transfer function shows the accuracy of the transfer function in removing the effect of the specimen geometry from the measured signal; the transfer function is effective in removing the geometric features, but it adds spurious noise to the new signal.

Results of this study show that the concept of the transfer function is most effectual when the unknown source is similar to the original source (the source that is used to make the transfer function).

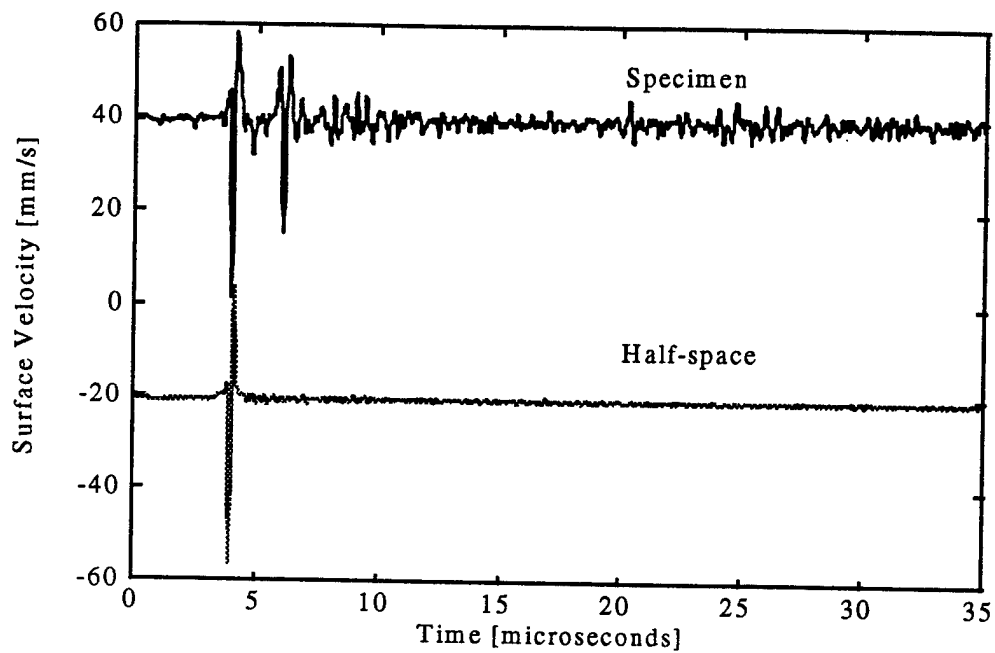


Figure 24. Specimen and Half-space Signals Used for Transfer Function

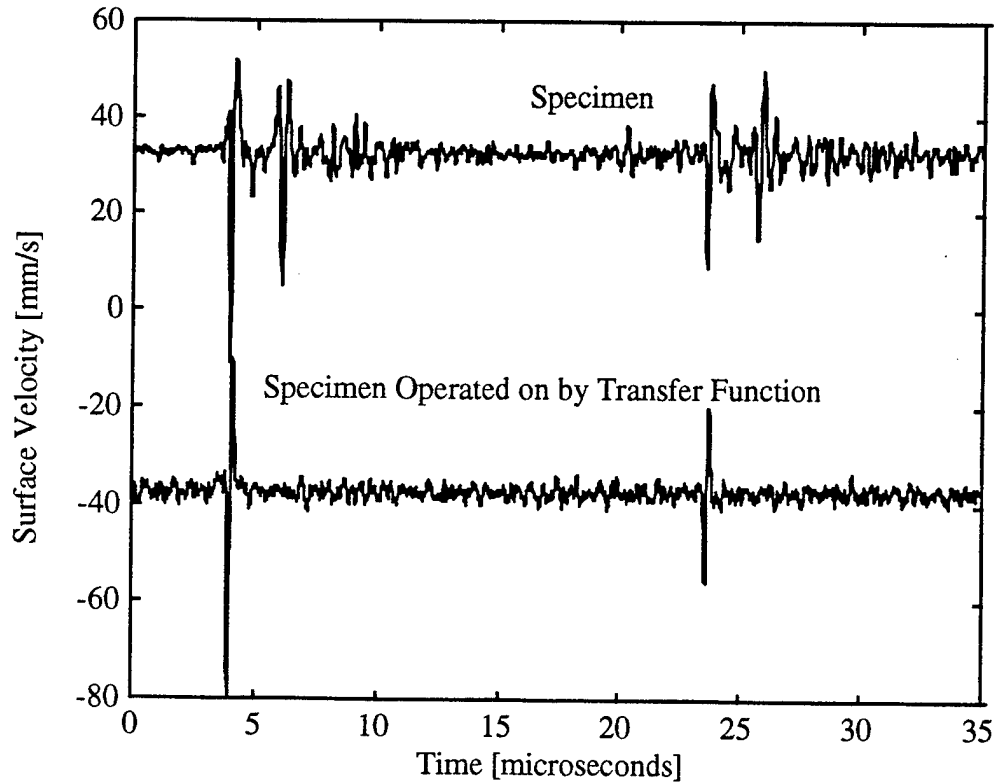


Figure 25. Comparison of Double Pulse in Specimen and Double Pulse Specimen Signal Operated on by Transfer Function

Important parameters when defining source similarities are: location and size, similitude in the loading force type and direction, as well as the relative amplitude ratios of the different signal components created. Moreover, the transfer function is very robust when the geometric features are relatively uncomplicated; this is the case for a 90° corner specimen [9]. However, difficulties arise when the methodology is applied to a vastly different source (as compared to the original) or if there is excessive noise in the signal. These difficulties are magnified when the specimen geometry is complicated (as is the case with the fatigue crack specimen).

#### **Arrays:**

Receiving transducer arrays, with four elements, were assembled and tested. Each element is a strip, 6 mm x 2mm, 28  $\mu\text{m}$  thick of the piezoactive plastic PVF<sub>2</sub>. All four elements are mounted on a single neoprene rubber backing. Each element is a broadband transducer (dc to ~ 10 Mhz) which detects elastic waves by responding to the out-of-plane surface motion produced by the wave. At this stage of the project the arrays were tested by digitally recording the output from each element, and the array operation was simulated in the computer by assigning appropriate time shifts to the data files and adding them. An example of this simulation is shown in Fig. 26. The simulated AE source for testing the array was the breaking of a thin graphite pencil lead, and the array was placed on a thin aluminum plate sample of the same dimensions as the samples used in cyclic fatigue tests (see Fig. 27). The first three signals in Fig. 26 are outputs from individual array elements, and they are delayed with respect to each other by a constant amount (2.1  $\mu\text{sec}$ ). When these delays are compensated digitally and the three signals are added, to simulate array operation, the result is the bottom signal in Fig. 26. This signal shows that the array is working since the front part of the signal, which is the simulated AE, is enhanced by a factor of ~ 2.5 relative to the later part of the signal, which is the reverberation and noise in the sample.

#### **Basic Research on AE Signals**

This work includes the joint research with the Structural Fatigue Investigation group of Section 2.2.1. Transducers for receiving AE signals are attached to steel samples which are subjected to a known cyclic stress until the sample fails through rapid crack growth. The formation and growth of the cracks is monitored by optical and other techniques. These experiments provide a unique opportunity to obtain data on the amplitude and other characteristics of AE signals at various stages of the fatigue process. Also, the characteristics of the AE signals can be related to the crack growth rate and the applied stress.

Much of the initial work in FY 96 involved trying different transducers and different trigger threshold and filter settings, on the Digital Wave data acquisition system, to determine the optimum conditions for receiving AE signals and suppressing noise. It was found that environmental noise, such as flexural vibrations of the sample, is strongest below ~ 100 kHz. The best arrangement so far is to use a tuned 1Mhz piezoactive ceramic (PZT) transducer and a high pass filter in the trigger channel, set to 500 kHz. This transducer is positioned as shown in Fig. 27. Also shown in Fig. 27 is the initial growth of the crack across the edge of the plate and the final growth to failure along the plate. AE signals at the above two stages of the fatigue process are shown in Fig. 28. Thus, at the end of FY 96 the conditions have been established for continuing AE measurements during the controlled fatigue tests.

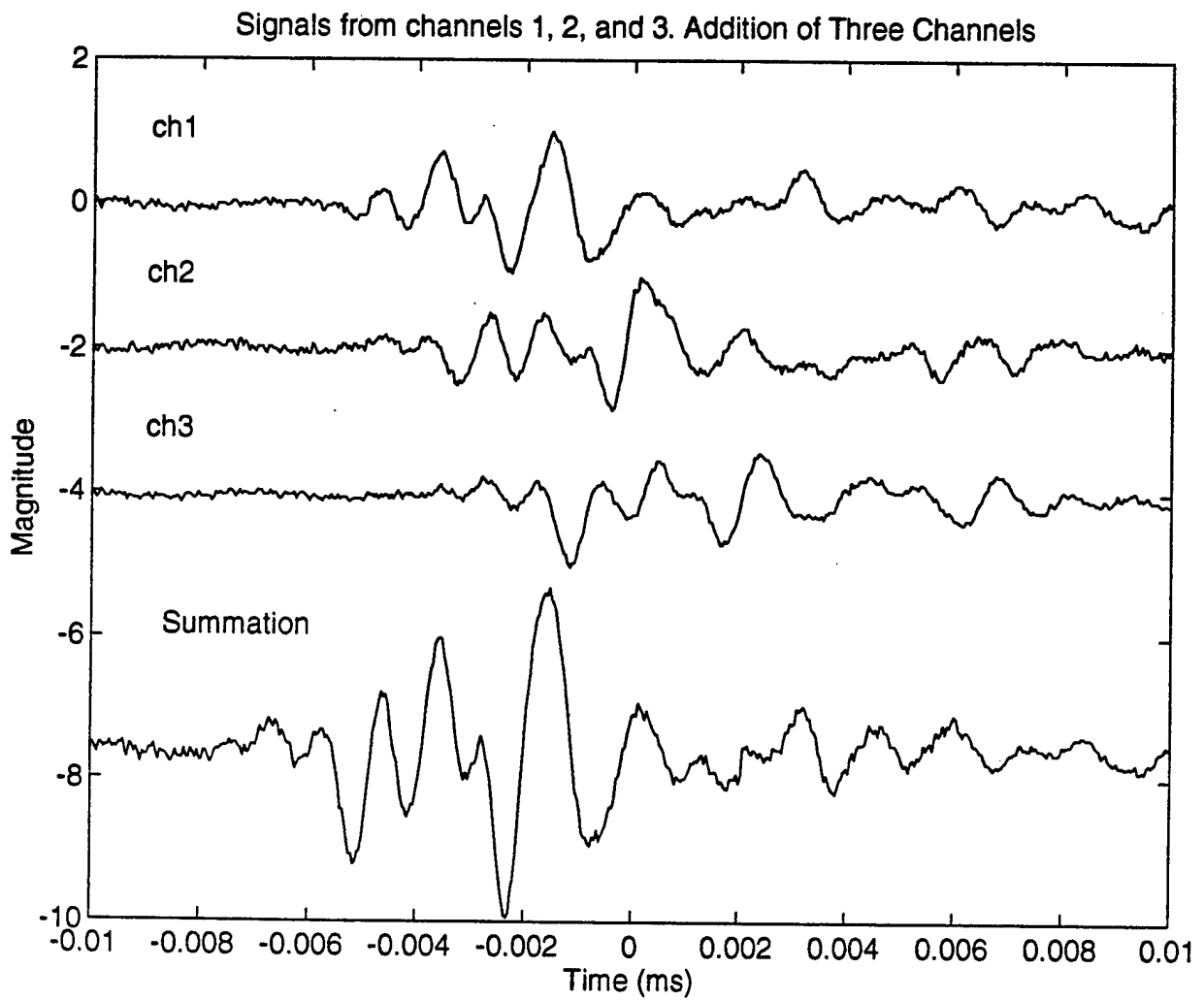
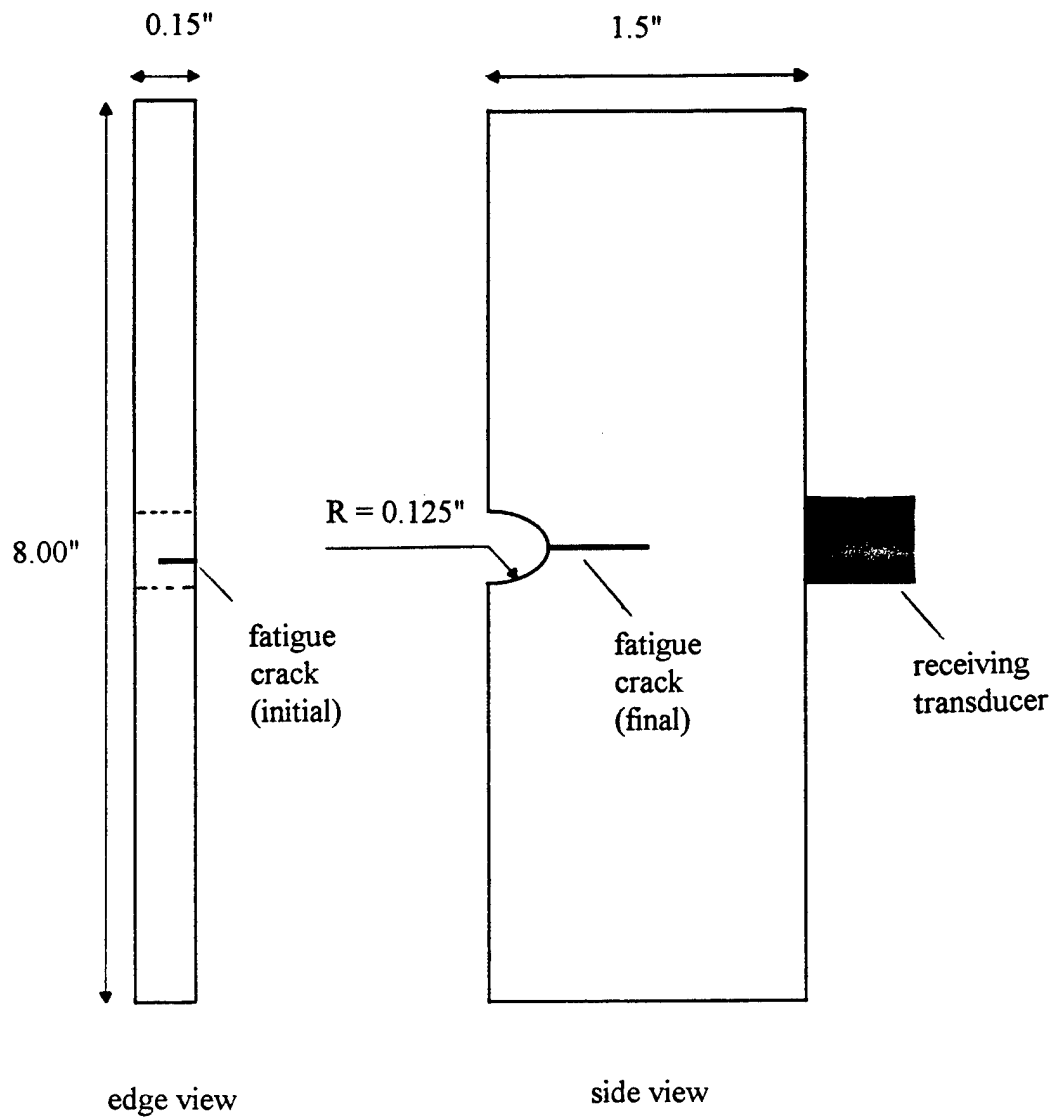
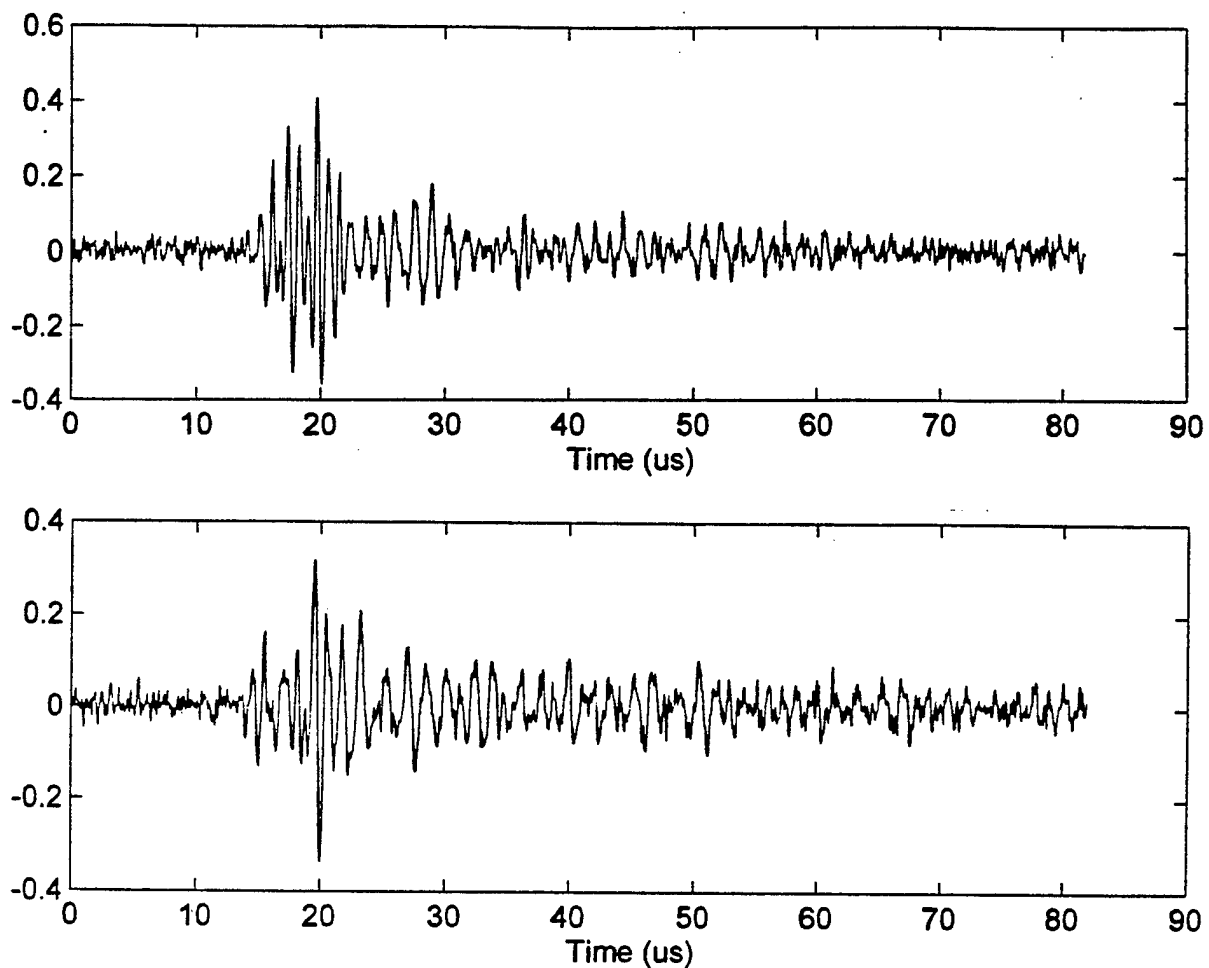


Figure 26. Simulated Phase Array



**Figure 27. Fatigue Test Sample, showing location of transducer, and initial and final stages of crack growth**



**Figure 28.** Acoustic Emission Signals from Fatigue Test Sample. The top figure is a signal at the initial stage of crack growth. The bottom figure is a signal during the final stage of crack growth.

## PLANS FOR M-URI YEAR 3

### Discrimination Against Noise to Characterize AE Signals

#### *Transfer Function Technique:*

While the current study used very sophisticated experimental techniques, the accompanying signal processing tools are somewhat naive; the thrust of the current effort is in making accurate experimental measurements of wave propagation in finite specimens. As a result, work in the next year will investigate the application of more advanced signal processing techniques such as short time Fourier Transforms (SFT), wavelets and neural networks in developing the proposed transfer functions. However, the experimental measurements already made are applicable to any new signal processing method. Consequently, a more robust transfer function can be developed by combining the measurements made in this research with more accurate signal processing and inversion techniques.

A complementary thrust area will be to develop a numerical model that validates the accuracy and robustness of the experimental transfer function. This procedure will use a three-dimensional boundary element method (BEM) model to study the interaction of elastic waves with a variety of fatigue specimen geometries. Additional computational work will investigate the effectiveness of commercial finite element (FEM) codes for this application. Furthermore, analytical source models will be developed for a variety of acoustic emission events, such as a Mode I crack. It is important to note that the goal of all of these studies is to be able to separate signals caused by damage events (such as crack growth) from those due to noise and extraneous sources.

#### *Arrays:*

Four element arrays will be assembled, with appropriate compensating delays between the elements permanently hard-wired. These arrays will be used for AE measurements in the cyclic fatigue tests. Also the arrays will be tested on a helicopter. New developments in the area of PZT sensors will be investigated. There have been major improvements recently in the fabrication of plastic-PZT composite sensors. These sensors retain the high sensitivity of PZT but do not have the disadvantage of being hard or brittle. They can be fabricated to conform to curved surfaces. Arrays with composite PZT elements will be assembled and tested.

#### *Optical Sensors:*

Optical sensors have potential advantages for both active and passive detection in a helicopter. One advantage is freedom from electromagnetic pickup. A second advantage is that these sensors can be configured to measure the in-plane component of wave motion at the detection point. This can help to discriminate against noise, since it has been shown [10] that typical sources of noise in elastic structures produce signals with dominant out-of-plane component.

One optical sensor which will be investigated is the optical fiber array sensor shown in Fig. 29. The fiber array consists of short lengths of fiber bonded to a thin plastic base which is coupled mechanically to the test sample. Strains due to elastic waves are transferred to the fiber and change the phase of the light through the fiber. This phase change is detected by interfering the signal light beam with a second reference beam. The above optical fiber array is a narrowband sensor with peak response at the frequency at which the bonded length of fiber is equal to one half of the trace wavelength (along the sample surface) of the elastic wave in the sample. Thus, the fiber array measures the in-plane component of surface motion, with peak response in the direction for which the trace wavelength of the elastic wave matches the spacing between adjacent bonded lengths of fiber. The sensitivity of the array is proportional to the number of bonded fiber segments, and initial estimates show that with six bonded segments the minimum detectable displacement in the test sample is  $\sim 5 \times 10^{-14}$  meters.

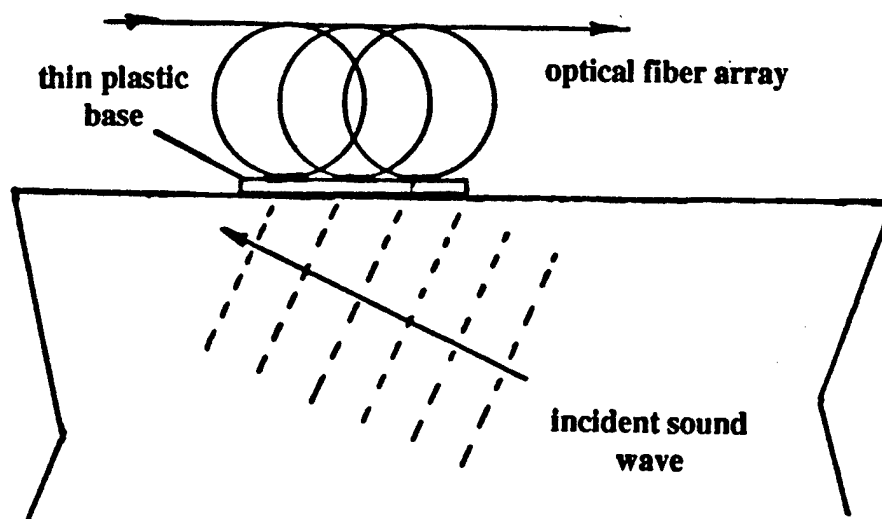


**Figure 29. Optical Fiber Receiving Array**

A second optical sensor which will be investigated will be a non-contact laser Doppler vibration probe. This type of sensor has now been used for several years by the acoustics group at Georgia Tech for vibration measurements. The laser Doppler probe can be configured for measurement of in-plane surface motion.

The above sensors will be initially tested in the laboratory. However, both sensors can be configured to be portable for testing in a helicopter at a later stage.

### **Basic Research on AE Signals**

#### *Interface with Structural Fatigue Group:*

Measurements of acoustic emission will continue to be recorded during most of FY 97 in steel samples undergoing cyclic fatigue tests designed and monitored by the Structural Fatigue Investigation group (Section 2.2.1). The samples will be 4340 steel, which is a common material used in helicopter rotor components. These measurements will build a data base on acoustic emission under a known, prescribed loading spectrum. The amplitude, duration, frequency and other characteristics of the AE signals will be established as a function of fatigue test duration and crack growth. This data will be used to develop a model for acoustic emission in the above steel during fatigue. Also, the above data will be used to optimize transducers and signal processing for detection of acoustic emission.

#### *Interface with Signal Processing Group:*

The Signal Processing Group (Section 2.3.3.3) requires realistic waveforms for the development of signal processing algorithms. Selected data obtained through experiments identified in the preceding paragraph will be sent to this group.



#### Source Model:

A measured acoustic emission signal depends upon three factors: its source; wave propagation from the source to the receiver (component geometry); and receiving sensor and instrumentation. Each of these three elements must be understood in order to effectively identify and characterize measured AE waveforms. The source of an AE waveform determines its initial shape and frequency content; AE waveforms are transient and broad band in nature. In this project the integral equation method will be used to develop a source model for acoustic emission from a fatigue crack.

#### Field Tests in a Helicopter

A test is planned to characterize the signal environment that is present in an operating helicopter. A compact, safe, non-intrusive experimental procedure is being developed to examine a realistic acoustic emission source from a crack growth event in an operating helicopter. A pre-cracked specimen will be loaded in tension-tension fatigue by a unique pneumatic device. Power will be derived from bottled nitrogen. In the interest of safety, the volumes of all the pneumatic devices will be kept small ( $< 1 \text{ in}^3$ ) to minimize stored energy. This is possible because all of the displacements will be very small ( $\sim 10^{-2} \text{ in}$ ). It is possible to construct a device such that no electric power is required.

### **VISION FOR YEARS 4 AND 5**

#### Transducer Arrays

The transducer arrays and the data base on AE developed during the first three years will be tested on selected helicopter components and on location in a helicopter.

Tests will be made on helicopter rotor assembly components. The transducer arrays will be used in an active mode to transmit and receive ultrasound for detection of cracks. Transducer arrays may have an advantage for detection of cracks in complex components, such as the rotor assembly, because the arrays can be steered to transmit and receive ultrasound along specified directions and thus discriminate against reverberation and noise. These tests will use the data base developed by the Guided Wave Propagation group (Section 2.1.2).

#### Passive Mode Detection of AE

Tests will be made in a passive mode for detection of AE. The focus of the experimental, analytical and numerical modeling work in years 1 through 3 concentrated on characterizing acoustic emission signals in laboratory specimens, while effort in years 4 and 5 will extend these results to distinguish and quantify acoustic emission signals in real helicopter components. The proposed research will utilize the results completed by the Guided Wave Propagation group (Section 2.1.2) concerning the propagation of elastic waves in annular structures. The dispersion curves developed by this group will be combined with the source model results from the fatigue crack experiments to develop techniques that can identify acoustic emission signals in annular structures.

#### Corrosion Detection

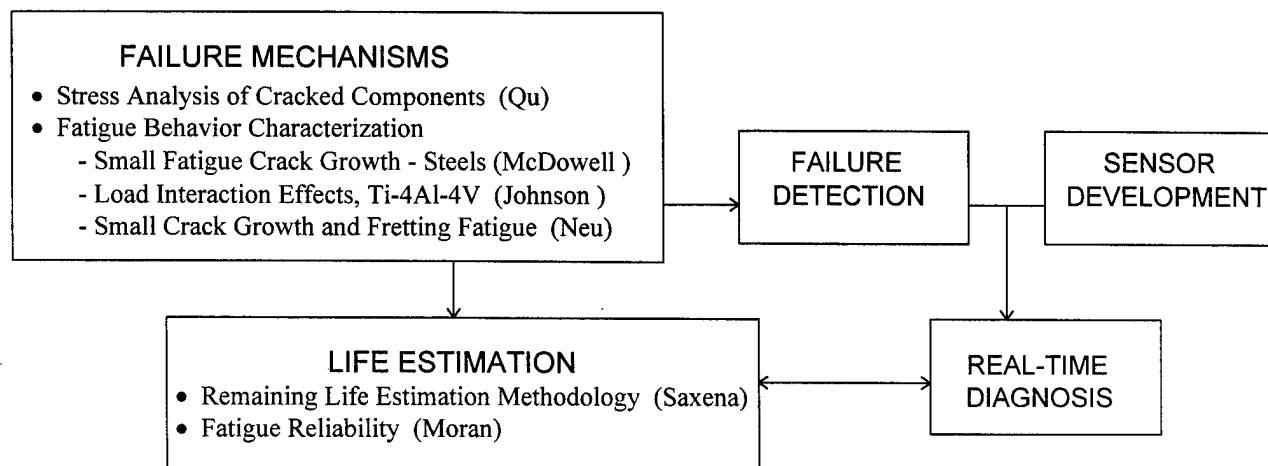
A new area of application for transducer arrays, which will be investigated, is detection of corrosion. In this case, the arrays are used in an active mode to transmit and receive ultrasound from an area where corrosion may occur. Corrosion at the interface of bolted joints is an acute problem for sea-going vehicles. Using the techniques developed for the passive acoustic arrays, a bench-top test of an active system for the detection of a gap between bolted structures will be developed. This bench-top test will employ accelerated corrosion by applying an electrolyte between dissimilar materials to make an effective battery.

## Thrust Area II

### 2.2 FAILURE PREDICTION METHODOLOGY

*Perform studies pertaining to the methodology for failure prediction in real-time, including modeling fault initiation and failure signatures, and observing the propagation and fracture phases of fatigue-based failure.*

2.2.1	STRUCTURAL FATIGUE INVESTIGATION .....	44
	Project Overview .....	44
	Sub-task 1: Stress Analysis and Stress Intensity Factor Solutions.....	46
	Accomplishments of M-URI Year 2.....	46
	Plans for M-URI Year 3.....	50
	Sub-task 2: Characterization of Fatigue Behavior and Mechanisms.....	51
	a. Small Fatigue Crack Growth in Steels.....	51
	Accomplishments of M-URI Year 2.....	51
	Plans for M-URI Year 3.....	56
	b. Load Interaction Effects in Ti-6Al-4V .....	56
	Accomplishments of M-URI Year 2.....	56
	Plans for M-URI Year 3.....	64
	c. Small Crack Growth and Fretting Fatigue.....	64
	Accomplishments of M-URI Year 2.....	64
	Plans for M-URI Year 3.....	69
	Sub-task 3: Remaining Life Estimation Methodology .....	70
	Accomplishments of M-URI Year 2.....	70
	Plans for M-URI Year 3.....	72
	Vision for Years 4 and 5 .....	83
2.2.2	FATIGUE RELIABILITY.....	86
	Project Overview .....	86
	Accomplishments of M-URI Year 2.....	88
	Plans for M-URI Year 3.....	92
	Vision for Years 4 and 5 .....	92



### 2.2.1 STRUCTURAL FATIGUE INVESTIGATION

Co-investigators: D. L. McDowell, W. S. Johnson, R. C. Neu, J. Qu, A. Saxena (Georgia Tech)

M-URI Year 2 Funding Allocation: 11.8%

#### PROJECT OVERVIEW

The objective of condition based maintenance relies on the integration of appropriate diagnostics technology directly into rotorcraft components. Maintenance and retirement decisions are ultimately based on the conditions as assessed by an algorithm which interprets the outputs of various diagnostic sensors. Accordingly, understanding the fatigue behavior of rotorcraft materials is foundational. There are several important aspects of fatigue crack development that are not yet sufficiently developed to perform remaining life assessment, including:

- propagation of microstructurally and physically small cracks, including transition to mechanically small conditions and growth from notches.
- mixed mode growth.
- load interaction effects under variable loading.
- three-dimensional crack effects.
- algorithms for multi-site/multi-scale fatigue damage to interface with transducer/sensor outputs.

The first four items form the gist of the work for the initial three years of the program, while the last topic will integrate these issues into system diagnostics and extrapolation procedures in program years 4 and 5.

One of the key issues in current procedures for maintenance of platforms and machinery is the ability to accurately estimate the remaining life and to set safe inspection intervals for the critical structural parts of complex systems such as helicopters. A successful strategy should employ a design which is damage tolerant so that detectable fatigue cracks form in critical parts prior to catastrophic failure. This requirement is typically met in aircraft components which are designed to damage tolerant specifications. However, it is often not possible to avoid cases where cracks grow rapidly after reaching some relatively small length beyond detection. A maintenance strategy depends on periodic inspection during service for continued safe operation as well for avoiding costly unscheduled outages. The inspection interval, the choice of inspection technique(s) and the inspection criterion must be specified as part of an overall strategy which provides the basis for making decisions such as continuation of operation, retirement, replacement at present or replacement at a future date (possibly during a scheduled maintenance outage). Such a periodic inspection covers the risk due to the uncertainties in the predicted component life related to:

- detection of small cracks,
- propagation of small cracks in fatigue, and
- service loading conditions.

The estimation of remaining life of in-service components based on such an inspection methodology is an important component of fleet maintenance for either military or commercial transportation vehicles. Remaining life estimates of components subjected to spectrum fatigue loading has traditionally been coupled with a non-destructive inspection scheme to ensure that no flaws should grow to critical dimensions between inspection intervals. This philosophy has formed the basis of the so-called damage tolerant methodology currently employed by military aircraft maintenance procedures. Such inspections are relatively effort intensive, requiring a substantial investment in inspection facilities and manpower.

Various components in rotary aircraft, for example, can sustain different allowable degrees of cracking prior to compromise of overall structural integrity and performance of the vehicle. In some cases, the cracks are easily visible well in advance of catastrophic consequences. In other cases, however, the cracks may be essentially undetectable by optical methods, due either to length or lack of accessibility, until after the crack has reached critical dimensions. This is particularly true of metallic components subjected to high frequency, relatively low amplitude fatigue loading such as rotor and drive components of helicopters. Under such conditions, fatigue cracks may remain very small (e.g.  $< 0.5$  mm) for over 90% of the life,

#### FAILURE PREDICTION METHODOLOGY (FATIGUE)

propagating to catastrophic dimensions only near the very end of life. In components, the determination of whether or not a crack is on the verge of catastrophic propagation depends on the rate of change of the driving force for crack growth as a function of crack length (e.g.  $dK/da$ ). Consequently, the operator may be faced with the relatively rapid in-flight onset of deleterious structural performance, include loss of control, landing capabilities, etc.

Addressing such rapidly developing failures in more thorough fashion requires modification of the inspection scheme outlined earlier to provide for a higher frequency of feedback in the loop between "inspection" and estimation of remaining life. In the limit, something close to real-time sampling and assessment of remaining life may be necessary for certain components. For example, the helicopter pilot must make very quick decisions concerning landing a helicopter in which the rotor drive-train or guidance components have sustained damage which compromises performance. Passive and active on-board sensors which can detect the presence and growth of crack-like defects offer a means to achieve nearly continuous feedback. In turn, this information must be provided to an on-board computational device for assessment of remaining life based on material fatigue mechanisms under spectrum loading and stress analysis of cracks in critical components from which the signals emanate. In this project, the elements of structural fatigue and remaining life estimation essential to a successful integrated diagnostics system are being addressed, based on the concept of *Condition Based Maintenance*. Specifically, the assessment of material fatigue behavior, cracked component stress analyses, and algorithms for fatigue damage under spectrum loading are underway. State-of-the-art computational tools for fatigue modeling are being employed. Cooperation is also underway with the component level testing and sensor development efforts of the program with an eye towards an integrated system capability.

### Organization of Sub-tasks

For implementing Condition Based Maintenance as described above for dynamically loaded airframe and drive-train components, the STRUCTURAL FATIGUE TASK is decomposed into three closely linked areas:

- I. Stress analysis & stress intensity factor solutions for cracks in notched components & specimens (Qu)  
OBJECTIVES: Perform stress analyses to provide necessary component level stress and stress-intensity factor information to enable the application of fatigue crack growth laws for remaining life estimation, including 3-D aspects of crack analysis.
- II. Experimental characterization and models for correlating the growth of microstructurally small and mechanically small fatigue cracks (McDowell, Johnson, Neu)  
OBJECTIVES: Assess material fatigue mechanisms, developing fatigue crack growth models which employ state-of-the-art technology and address those technology deficiencies noted in the last section.
- III. Development of remaining life estimation methodology for components (Saxena, McDowell)  
OBJECTIVES: Develop methodologies to incorporate fatigue crack initiation/growth models to assess remaining life, including small crack growth effects and crack growth under variable loading. Develop appropriate algorithms for remaining life to interface with the NDE output, providing a rapid evaluation of the condition of cracked components.

The efforts of individual faculty are distributed across these sub-tasks as follows, led by D.L. McDowell:

*W.S. Johnson* - fatigue crack growth modeling; loading spectrum and interaction effects.

*D.L. McDowell* - growth laws for small fatigue cracks under multiaxial stress states; remaining life algorithms for multi-site/multi-scale damage.

*R.W. Neu* - experimental study of fatigue crack growth mechanisms and modeling; notch effects and fretting fatigue.

*J. Qu* - analysis of cracked components; 3-D crack growth models.

*A. Saxena* - remaining life algorithms for fatigue of components; quantification of fatigue damage in components and in cracked specimens.

Component level fatigue testing which makes use of appropriate sensor technology to measure the extent of fatigue damage is one part of developing a viable system for condition based maintenance. It is particularly useful for (i) determining "hot-spots" in the structure which favor fatigue crack initiation/propagation and (ii) establishing correlation between signals from various sensors and fatigue damage in specific components.

It is important to point out, however, that fatigue life exhibits considerable scatter for the same loading conditions, particularly at long lives. Accordingly, remaining life estimates invariably have some associated confidence level. Establishing this confidence level generally requires insight into the mechanisms of fatigue failure, which in turn depend on material and loading conditions. The local approach to fatigue crack initiation and fracture mechanics have both progressed substantially over the past two decades. Any robust technology for condition based maintenance of in-service components must integrate such assessment tools, along with structural characteristics and material properties, into the scheme for assessment of remaining life. In particular, cumulative damage concepts (e.g. crack growth) for small cracks must be addressed.

#### 2.2.1.1 Sub-Task I

##### **STRESS ANALYSIS AND STRESS INTENSITY FACTOR SOLUTIONS FOR CRACKS IN ROTOR AND DRIVE SYSTEM COMPONENTS AND TEST SPECIMENS**

*J. Qu*

The objectives of this sub-task are to:

- i. Calculate the "Driving" force (SIF) for crack growth in rotor and drive system components of the H-46 helicopter. (Connecting Link, Pitch Shaft, and Rotor Hub).
- ii. Study the effects of crack-tip mode mixity on 3-D crack growth and develop a computational algorithm to compute the 3-D crack-front parameters under complex state of stresses. These parameters including the local energy release rate and the local stress intensity factors can be used to characterize the behavior of a growing 3-D crack under complex loading conditions.
- iii. Develop a simulation and visualization program for the growth of 3-D cracks by combining crack initiation, small crack growth, and large crack growth models in conjunction with material fatigue properties. The simulation program *Data Explorer* is being used for this purpose.

#### **ACCOMPLISHMENTS OF M-URI YEAR 2**

##### **Stress Analysis**

A visualization program was developed to enable improved understanding of component behavior under various loading conditions. The visualization program allows the user the ability to look inside the finite element model of a complex structure and see how the field quantity of interest develops. In particular, the visualization program provides for a more complete assessment of the stress field, providing insight to the driving force behind crack initiation and the growth of small cracks. To demonstrate the effectiveness of this program, a stress analysis was performed on an H-46 helicopter rotor hub.

The H-46 rotor hub was chosen to be modeled due to its complex geometry. Assuming the rotor blades exert identical forces on the rotor hub independent of time, periodicity can be used to reduce the rotor hub to a one-third model (Fig. 30a). Subjecting the rotor hub to load, the forces were identified according to the three components of lift, centrifugal, and drag, with drag being neglected when assuming low speed conditions (Fig. 30b). The final finite element model contained 32,296 tetrahedral elements (Fig. 31). Two finite element models were solved, one with a unit lifting load and one with a unit centrifugal load. From the two finite element models, component behavior under various loading conditions can be simulated using the principle of superposition.

#### **FAILURE PREDICTION METHODOLOGY (FATIGUE)**

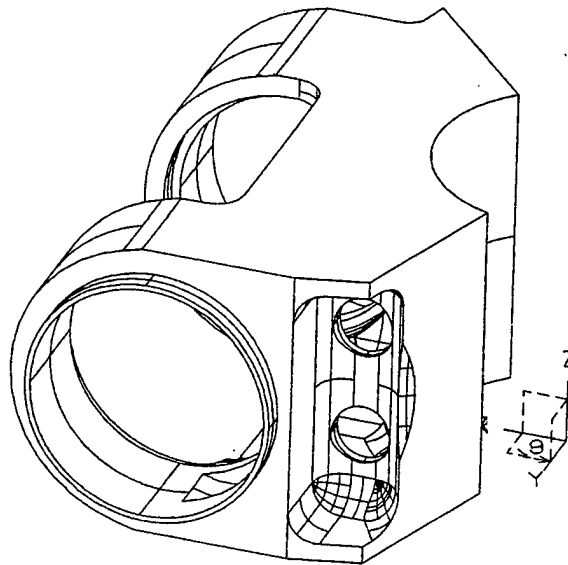


**Figure 30a. Rotor Hub (One-third) Solid Model (Right View)**

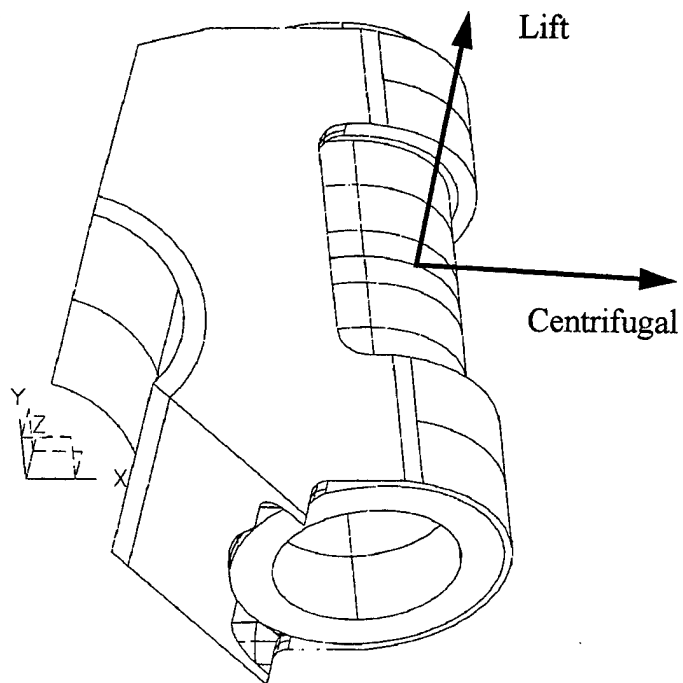


**Figure 30b. Rotor Hub Loading Components**

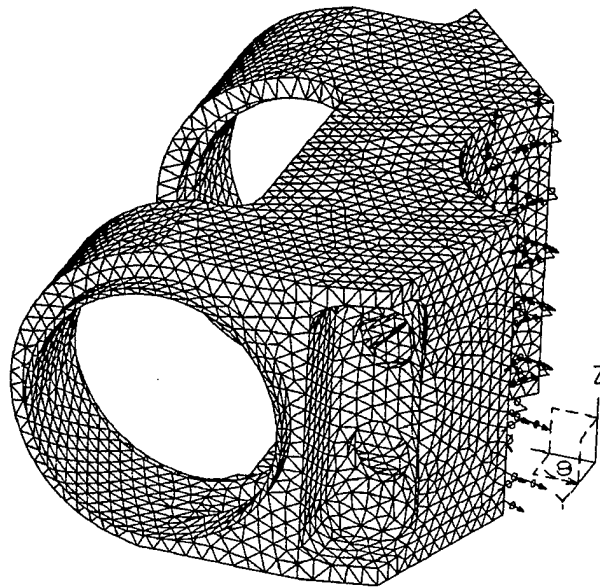


**Figure 31. Mesh of Rotor Hub Model (Right View)**

A parametric study was performed in order to determine the relationship between the maximum normal stress and the maximum von Mises stress versus combination of centrifugal and lifting loads. These results are shown in graphical form in Figs. 32a and 32b.

Using the results of the finite element analysis, predictions of possible failure locations were made based on two criteria: Maximum Principal Stress and Maximum von Mises Stress. The maximum principal stress criterion assumes a crack will initiate at a point with the largest maximum principal stress and propagate perpendicular to the maximum principal direction (Mode I growth). The von Mises Stress Criterion assumes a crack will initiate at a point with the largest von Mises stress. Fatigue crack initiation site are predicted to occur in elements with both large maximum principal stress and large von Mises stress. Case 24 of the parametric study provided the most severe loading of the rotor hub and is used to predict possible failure sites. Four locations were established as potential failure sites (Fig. 33). One important observation is that the four predicted sites are all located near through holes in the rotor hub. Additionally, element one coincided with the location of an actual failure recorded at the Cherry Point Naval Aviation Depot.

### **3-D Crack Front Parameters**

The ability to calculate the energy release rate of a three-dimensional crack front is crucial in order to determine crack growth behavior. In general, the local energy release rate varies along the crack front, thus crack growth behavior also varies with position. It was found through our extensive literature search that one of the most promising techniques is the Virtual Crack Extension Method (VCEM) developed by Parks [11], with subsequent improvements by Bakker [12] and Claydon [13]. VCEM allows the energy release rate to be numerically determined for an arbitrary three-dimensional crack front, including non-planar cracks. The energy release rate can be used to determine the direction and extent of local crack growth.

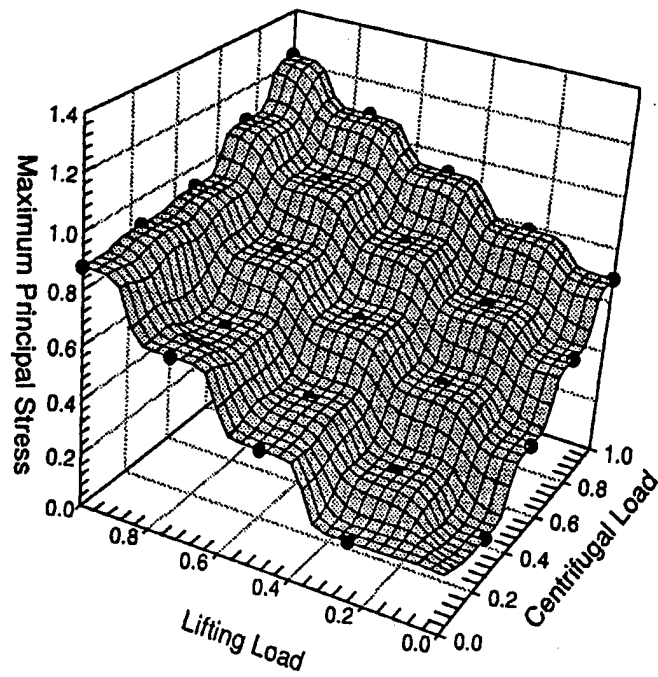


Figure 32a. Plot of Maximum Principal Stress Results

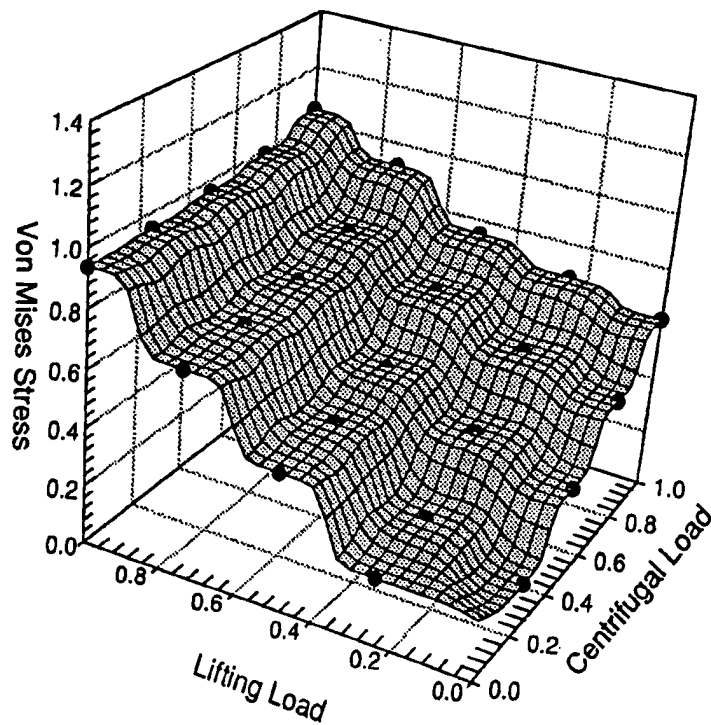
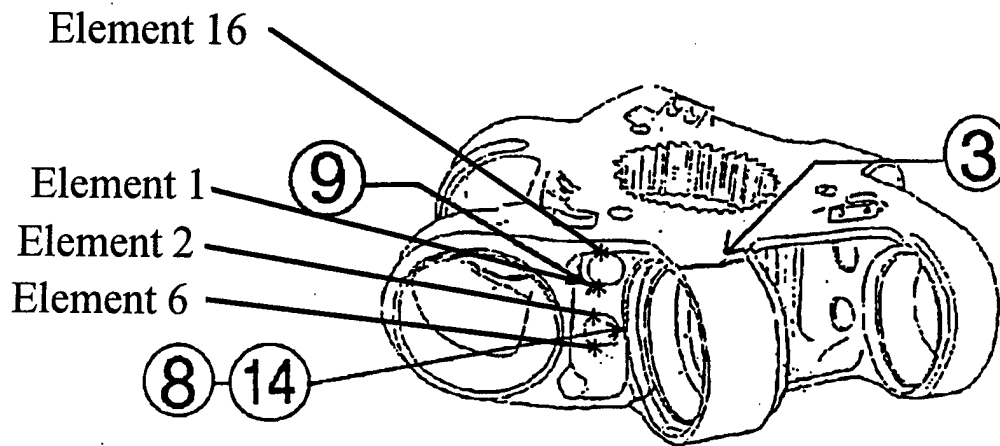


Figure 32b. Plot of von Mises Stress Results





**Figure 33. Rotor Hub Predicted Failure Locations**

### **PLANS FOR YEAR 3**

- Integrate the Virtual Crack Extension Method (VCEM) into a commercially available finite element code (ABAQUS); interact with Brian Moran of Northwestern University (co-PI of Section 2.2.2) regarding alternative methods for computing mode mixity of 3-D cracks.
- Use the VCEM algorithm to simulate a 3-D corner crack in a specimen with simple geometry and compare the results with experimental measurements. (In addition to the energy release rate, the mixed mode stress intensity factors are important for characterization of the crack front.)
- Develop a modified VCEM algorithm to include elastic-plastic crack growth.

### 2.2.1.2 Sub-Task II

#### **CHARACTERIZATION OF FATIGUE BEHAVIOR AND MECHANISMS**

*D. McDowell, S. Johnson, R. Neu*

To conduct remaining life assessments based on fatigue crack growth and fracture, associated material properties must be known. We expect to make use of existing data (from ONR, other DoD agencies, industrial vendors, etc.) regarding the fracture and fatigue properties of the appropriate materials, as well as data to be generated in this task. First, the driving forces and criticality conditions of cracks must be well understood for each component; this requires appropriate stress analysis as well as fracture toughness information. Depending on the length of cracks that must be detected prior to criticality, several fatigue methodologies must be considered. For small cracks (length  $< 0.5$  mm), it is generally observed that the rate of propagation exceeds that of longer cracks based on correlation with the cyclic stress intensity factor,  $\Delta K$ . This correlation for growth of small cracks, including effects of biaxial stress fields, is an important consideration. For cracks growing from notches, there may be additional crack growth rate deceleration effects associated with the reduction of crack driving force. For longer cracks which are suitably treated with linear elastic fracture mechanics principles, there is still the issue of propagation which depends upon the mean stress (R-ratio) and biaxiality of the stress fields (i.e. mixed mode loading). Load interaction effects will be investigated for microstructurally small and mechanically small cracks to aid in developing appropriate crack growth methodology for a variable loading spectrum. It is important to note that the numerous crack growth models which have been developed for long cracks do not necessarily apply to small/short cracks. Crack growth models for the latter are not mature, and considerable attention must be devoted to such models, particularly under high cycle fatigue conditions or sequences of low and high cycle fatigue amplitudes.

Fatigue crack growth experiments will be carried out on smooth and standard fracture mechanics specimens in the Mechanical Properties Research Laboratory (MPRL) to the extent necessary to supplement already existing data in support of component lifetime estimation (Sub-Task III, Section 2.2.1.3). One or two metallic materials will be considered, as appropriate. These procedures will be verified by conducting selected component fatigue testing and interfacing with the NDE/NDI effort, using the stress analysis results from Sub-Task I of Section 2.2.1.1.

In addition to the component materials, another concern is the degradation of the sensors with fatigue loading. It will be necessary to support sensor development and stability studies with selected fatigue testing of isolated and in-situ sensors. Degradation of signal due to sensor fatigue processes must be quantified and considered, along with instrumentation of selected laboratory specimens to assess the resolution, accuracy and repeatability of different NDI methods.

#### **A. SMALL FATIGUE CRACK GROWTH IN STEELS (D. L. MCDOWELL)**

##### **ACCOMPLISHMENTS OF M-URI YEAR 2**

A suitably general engineering model for the growth of cracks from a length on the order of a grain size to detectable dimensions (perhaps 200 to 1000  $\mu\text{m}$ ) does not presently exist, particularly under multiaxial loading conditions. Such a model will provide a fundamental advance relative to the current cyclic stress- and strain-based crack initiation approaches. The model must facilitate a consistent treatment of the growth of fatigue cracks ranging in length from microstructurally small to mechanically long cracks; the latter can be correlated using traditional LEFM or EPFM fracture mechanics principles. This model will facilitate practical algorithms for remaining life assessment for areas where small cracks dominate life estimation. This approach will lead to innovative advances in fatigue design/analysis methodology by introducing a hybrid form which seeks to unify the currently distinct methodologies of fatigue crack "initiation" and "propagation."

We are extending the multiaxial fatigue microcrack propagation approach of McDowell & Berard to span regimes of microcrack growth ranging from microstructurally small cracks to physically small cracks governed by standard fracture mechanics correlations. The first regime represents strongly microstructurally-influenced crack propagation, typically applicable to cracks of length on the order of several grain diameters. The second regime reflects a diminished role of microstructure.

The goals of this research are to:

- (i) establish a framework for correlation/prediction of fatigue crack growth of small fatigue cracks consistent with concepts of elastic-plastic fracture mechanics and critical plane theories of multiaxial fatigue, focusing on growth of microstructurally small cracks and physically small cracks;
- (ii) develop crack length-, amplitude- and stress state-dependent criteria for the transition from one regime to the next to denote limits of applicability of certain correlative forms;
- (iii) understand the propagation behavior of small cracks as a function of stress state and amplitude and develop appropriate modeling concepts based on computational crystal plasticity; and
- (iv) introduce threshold conditions for cyclic microplasticity and nonpropagating cracks (i.e. fatigue limits) into the framework of a multiaxial HCF fatigue theory.

#### **Modeling: Multi-regime Small Crack Propagation and Computational Crystal Plasticity**

Further efforts to improve the accuracy of life estimation which addresses LCF, HCF and LCF-HCF interaction must consider various factors that are not presently addressed by traditional elastic plastic fracture mechanics (EPFM) or linear elastic fracture mechanics (LEFM) approaches based on long, self-similar cracks in homogeneous materials, nor by conventional HCF design tools such as the  $\epsilon$ -N curve, the S-N curve, modified Goodman diagram and the fatigue limit.

Development of microstructure-sensitive fatigue crack propagation relations relies critically on deeper understanding of (a.) small crack behavior including interactions with microstructure, (b.) heterogeneity and anisotropy of cyclic slip processes associated with the orientation distribution of grains, and (c.) local mode mixity effects on small crack growth. The basic technology is not yet sufficiently advanced to implement damage tolerant design for HCF. In this work, we have developed a model which approximates the results of slip transfer models that describe crack blockage by microstructure barriers; the model is consistent with critical plane concepts for Stage I growth of small cracks, standard cyclic stress-strain and strain-life equations, and the Kitagawa diagram for HCF threshold behaviors. The model is able to correlate the most relevant trends of small crack growth behavior, including the fatigue limit, load sequence effects, and stress state effects.

It is convenient and physically consistent to consider the growth of small cracks in polycrystalline metals to be subject to several characteristic regimes, as shown in Fig. 34a. Microstructurally small cracks are subject to strong interactions with microstructural barriers. The solid line in Fig. 34a. illustrates typical results from a distributed dislocation model which characterizes small crack growth in terms of a series of periodic activations of slip in adjacent grains of different orientation, followed by dislocation blockage by grain boundaries and associated deceleration of  $da/dN$  [14-16]. Oscillatory  $da/dN$  behavior is commonly observed for microstructurally small cracks; it is experimentally well-established that this behavior is linked to microcrack interaction with microstructure features such as grain or phase boundaries [15,17]. Typically, the experimentally observed spacing for the strongest barrier,  $d$ , is somewhat higher than the characteristic grain size,  $d$ . If the applied stress is insufficient to produce cyclic slip in grains adjacent to the crack tip, then small cracks will decelerate and arrest at this length scale, giving rise to a fatigue limit. In general,  $d$  depends on the particular composition and arrangement of microstructure, and does not simply correspond simply to optical identification [15]. If cracks propagate past the strongest barrier, they continue to be subject to a diminishing influence of microstructure for several multiples of this length scale ( $a < kd$ ,  $k$  in the range of 2 to 7) [14, 18, 19]. Finally, the propagation rate is only slightly affected by microstructure for  $a > kd$ . The dashed line in Fig. 34a represents the idealization of this oscillatory slip transfer model offered by the model originally proposed by Hobson [20, 21].

Application of the class of linear elastic fracture mechanics (LEFM) or elastic-plastic fracture mechanics (EPFM) solutions which presume material isotropy, homogeneity and often self-similar crack extension to small fatigue cracks involves strong assumptions. First, microstructure affects the fatigue crack growth rate (FCGR) of small cracks very substantially, whereas long crack LEFM solutions for homogeneous materials lack incorporation of appropriate length scales and arrest mechanisms. Second, the assumptions of planarity and self-similarity of crack growth often made in LEFM solutions applied to growth of long fatigue cracks is generally far from reality as small cracks meander among slip systems across grains. Third, the intrinsic nature of mixed mode crack tip opening and sliding displacements, distinct from remote load mixity, is most often neglected in the application of conventional LEFM to fatigue crack growth. Fourth, the ratio of the cyclic plastic zone or fatigue damage process zone to crack length for small cracks is often too large for small scale crack tip damage arguments to hold; this represents a potential fundamental limitation of singularity-based fracture mechanics. Although effects of both plasticity and roughness-induced closure have been observed in growth of small cracks, the incorporation of these phenomena into fracture mechanics-based growth laws is often accompanied by quite simplified assumptions, such as the applicability of LEFM solutions for long, planar cracks in homogeneous materials.

In addition to the behavior shown in Fig. 34a, there are several other phenomena that should be recognized in development of a realistic small crack propagation models:

- (i) The observation of threshold behavior under HCF conditions is important. For cracks on the order of microstructural dimension, the conventional smooth specimen fatigue limit is observed, while LEFM threshold conditions prevail for somewhat longer cracks that are insensitive to the influence of microstructure, as shown in the Kitagawa diagram [16, 18, 19] in Fig. 34b for the completely reversed, uniaxial loading case. Crack length  $a_0$  represents the intersection of the smooth specimen fatigue limit,  $\sigma_{FL}$ , and the LEFM trajectory. These two limiting threshold conditions differ mechanistically, as the fatigue limit represents a stress level below which cracks are arrested at strong microstructural barriers, whereas the LEFM threshold is associated with the mechanical conditions established within the crack tip field which encompasses a number of microstructural units [16, 19].
- (ii) In the finite life regime, above threshold conditions, the strain-life relations form the basis for empirical description of combined crack nucleation/propagation lifetime to a predetermined crack length, typically on the order of 0.5 mm to 1 mm.
- (iii) Any comprehensive model for small crack behavior in fatigue of metallic polycrystals should predict (or at least successfully correlate) the ubiquitous empirical observations (i)-(ii). Furthermore, it is essential to characterize small crack behavior in terms of mixed mode local conditions, regardless of remote loading mode, in view of the role of crystallographic anisotropy and the slip-driven nature of the fatigue process. To this end, critical plane models for multiaxial fatigue offer a framework in which characteristic behavior of small cracks under various stress states are catalogued.

A three-regime small fatigue crack propagation framework has been developed that incorporates basic modeling elements of crack interaction with microstructural barriers and accordance with HCF thresholds at different length scales. These crack growth laws are a non-dimensionalized generalization of the critical plane-based microcrack growth law of McDowell and co-workers which obey the cyclic stress-strain and strain-life equations in uniaxial and torsional fatigue. The fatigue limit is defined by an approximate model for slip blockage due to microstructure after Hobson [20, 21].

Figure 35 shows the predictions of the model for  $da/dN$  versus the EPFM  $\Delta K_I$  parameter for small cracks under completely reversed conditions for 1045 steel. Long crack data for  $R = 0$  appears as the dashed line. Note that crack deceleration and arrest occurs for a stress amplitude below the smooth specimen fatigue limit, as is experimentally observed.

In order to enhance the predictive capability of this model framework, we are conducting novel 2-D crystal plasticity solutions for cyclic deformation within a set of grains in the vicinity of the free surface, with and without cracks. Topics of principal interest include:

1. Effect of orientation distribution of grains near the surface on shakedown limits for cyclic microplasticity.
2. Effect of misorientation of neighboring grains on crack tip opening and sliding displacements (CTOD and CTSD) under cyclic loading as a function of stress state and amplitude.
3. Effect of free surfaces on constraint on cyclic CTOD and CTSD.
4. Mechanical conditions for transition from Stage I to Stage II growth.

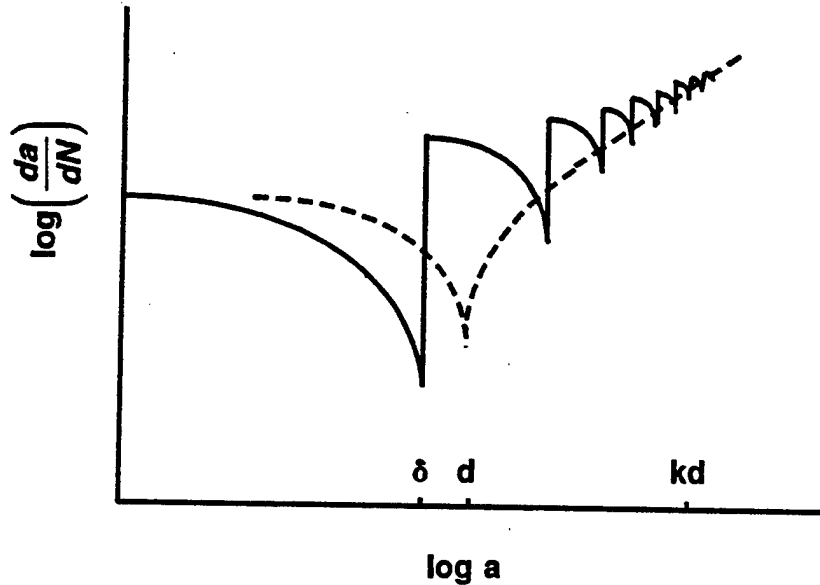


**Figure 34a.** Schematic of typical progression of crack growth rate behavior as a function of crack length and stress amplitude for microstructurally small ( $a < d$ ) and physically small ( $a > kd$ ) cracks, with the transition regime in-between.

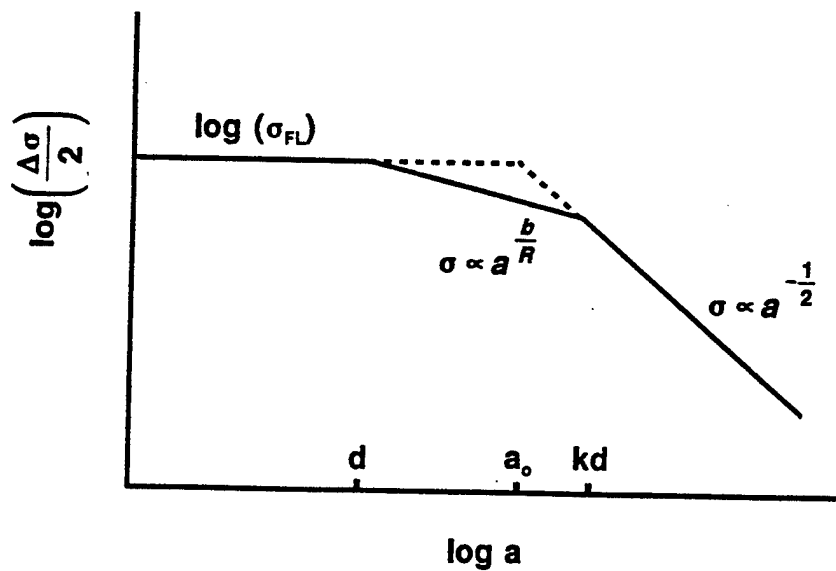


**Figure 34b.** Schematic of Kitagawa diagram for HCF thresholds, separating into Regime I ( $a < d$ ), Regime II ( $a = d$  to  $a = kd$ ) and Regime III ( $a > kd$ ), with the LEFM threshold applicable to Regime III.

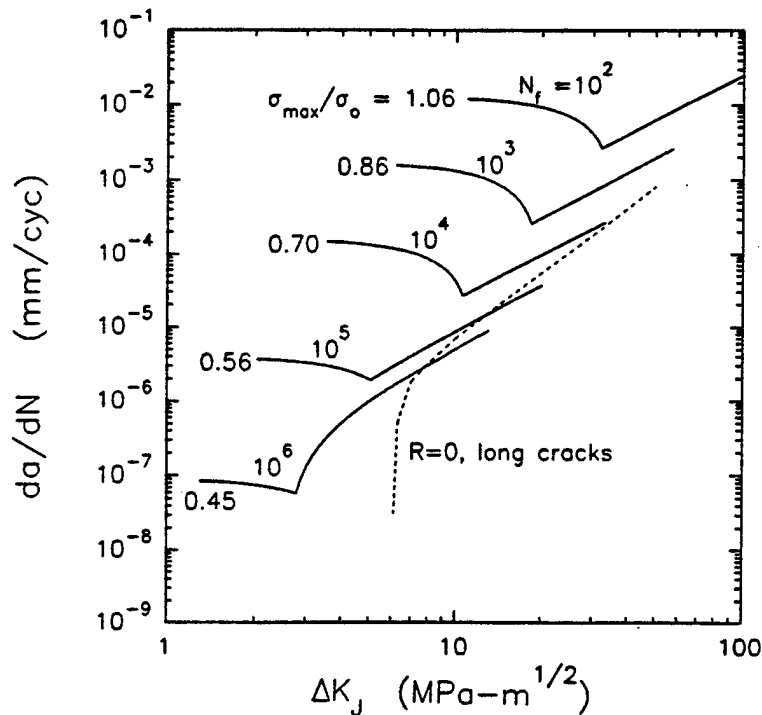


**Figure 35.** Predicted  $da/dN$  versus  $\Delta K_I$  for small cracks in 1045 steel for a range of completely reversed uniaxial stress amplitudes ( $R = -1$ );  $\sigma_o = 548$  MPa is the mean flow stress in the cyclic plastic regime.

#### **Experiments: Multiaxial Small Crack Growth, Sequence and Mean Stress Effects**

To stimulate model development and verify model concepts a series of axial-torsional experiments are underway on tubular specimens to study the formation and growth of microstructurally and physically small cracks under combined stress states. In addition to completely reversed loading, we are considering load amplitude and mean stress effects as well. The results of these experiments will be compared with the model predictions to verify that nonlinear crack growth and its dependence on stress state is adequately treated. Four materials are being studied, including 1045 steel, 304 stainless steel, PH 13-8 Mo stainless steel and 4340 steel. The first two have already been thoroughly characterized under uniaxial and torsional conditions in the literature, so limited sequence and mean stress tests will be useful in testing the capabilities of the model. The latter two materials are commonly employed in rotor hub applications and are less well characterized in multiaxial fatigue. Machining and polishing has been completed on nearly 50% of tubular axial-torsional specimens.

The fatigue tests are designed to offer a critical evaluation of certain model features:

- (i) Baseline constant amplitude, proportional loading experiments with fatigue lives ranging from  $10^3$  to  $10^6$  cycles.
- (ii) High-low and low-high amplitude sequence tests under proportional loading to establish sequence effects for the same crack systems.
- (iii) Stress state sequence tests involving sequences of torsion followed by tension and vice versa to establish sequence effects for stress states with the same target fatigue life.
- (iv) Mean stress tests to involving axial mean stress with cyclic shear and other states of stress.

Fatigue tests will be periodically interrupted to apply cellulose acetate tape to obtain replicas of surface cracking, a technique which has proven highly successful in tracking the process of orientation and growth of microcracks and crack systems from a sub-grain length scale on the order of 5-10 microns. All fatigue tests will be conducted at room temperature and in laboratory air. Selected specimens will have a 10-20  $\mu\text{m}$  diameter circular notch (pit) either etched or micro-machined to contrast with the naturally-occurring crack results.

The experimental program is being carried out in Georgia Tech's Mechanical Properties Research Laboratory (MPRL). The MPRL is equipped with two computer-controlled servohydraulic axial-torsional load frames for testing tubular specimens. One machine presently employs well-aligned hydraulic collet grips. A biaxial extensometer is available for measurement of axial and shear strains in cyclic tension-compression-torsion tests.

An AASERT proposal was submitted in November 1996 to support an additional student to conduct the second phase of the experimental study involving 4340 steel and PH 13-8 Mo stainless steel. With this support, progress could be enhanced relative to meeting projected milestones for testing since the additional graduate student would be responsible for addressing the modeling, material acquisition and testing aspects. To date, an undergraduate student has been engaged to assist in the experimental program.

### **PLANS FOR YEAR 3**

#### **Modeling**

April 1997: complete first set of calculations on shakedown and CTOD/CTSD based on crystal plasticity.

May 1997: submit paper for international conference on multiaxial fatigue to be presented in Poland in Sept. 1997.

July 1997: fit baseline parameters for 4340 steel and PH 13-8 Mo stainless steel.

October 1997: refined calculations for free surface effects.

January 1998: CTOD/CTSD solutions for various crack lengths relative to grain size.

February 1998: incorporate micromechanical computations into small crack model.

#### **Experimental**

August 1997: experimental results for baseline and sequence tests for 1045 steel and 304 stainless steel.

September 1997: conduct experiments jointly with NDI faculty; e.g., co-PI's Bair (Sect. 2.1.4) and Polla (Sect 2.3.3) to instrument/monitor fatigue cracking some specimens used in biaxial testing.

December 1997: baseline and sequence tests on 4340 steel.

February 1998: baseline and sequence tests on PH 13-8 Mo stainless steel.

### ***B. LOAD INTERACTION EFFECTS IN Ti-6Al-4V (W. S. JOHNSON)***

#### **ACCOMPLISHMENTS OF M-URI YEAR 2**

The objective of this effort is to understand fundamental load interaction effects on small-cracks in a titanium alloy, Ti-6Al-4V. Almost all small-crack research up to this point has focused on constant amplitude loading. Small crack growth rates exhibit significant scatter, and therefore small-crack growth must be characterized by a band encompassing the upper and lower limits of crack growth rates under a specified loading and stress intensity range. In addition, large cracks behave in a self-similar fashion and the effects of load interaction can be readily explained by crack closure arguments due to a fully-developed plastic zone at the crack tip. Small-cracks do not have developed plastic zones and their growth pattern depends on encounter with microstructural features. This research aims to determine how metallurgical structures influence the growth pattern of small-cracks during load interactions in Ti-6Al-4V and how this behavior differs from large crack growth associated with load interactions in the same material.

Graduate student R. Hamm spent summer 1996 at the NASA Langley Research Center. During that period, an extensive literature search was conducted on a wide range of topics including the small-crack effect in various materials under a range of conditions and loadings, load interaction effects on

### **FAILURE PREDICTION METHODOLOGY (FATIGUE)**

large cracks and small-cracks, modeling of large cracks and small-cracks under those conditions, and studying how metallurgical features interact with crack growth. In addition, the knowledge of Newman's crack closure model was developed through direct interactions with Dr. Newman. The computational version of the model, FASTRAN [22], was used to predict S-N curves for various projects underway there. A parametric study was performed to determine how the model treats load interaction effects as well as how it predicts small crack growth.

While at NASA, tensile tests were conducted to determine static properties of the Ti-6Al-4V sheets from which the small-crack specimens were machined. The tensile properties were determined from three dogbone specimens. The stress-strain curve for the material is shown below in Fig. 36, along with the material's uniaxial static properties. The material's static properties were required as input to predict small-crack growth in Ti-6Al-4V using Newman's FASTRAN code. The predictions will be discussed later.

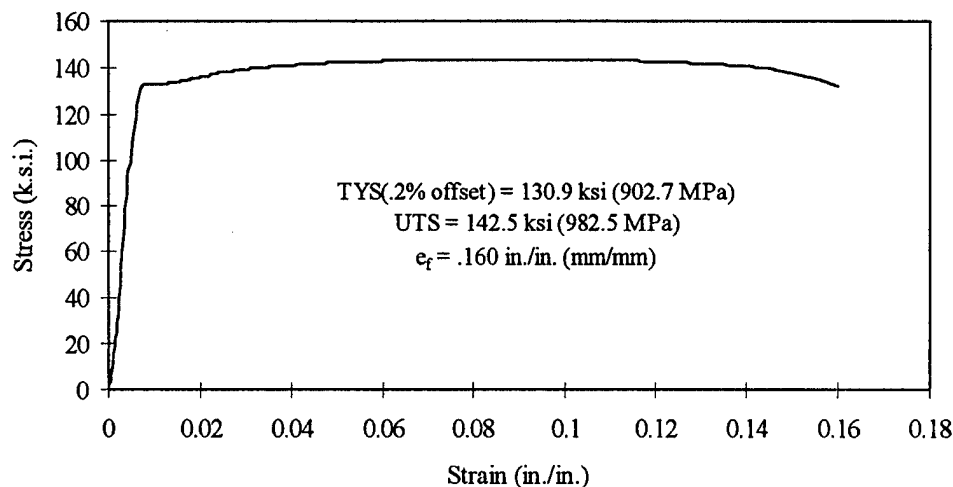


**Figure 36. Uniaxial Tensile Properties of Ti-6Al-4V**

In conjunction with a literature search on small-cracks, an international survey was conducted by ASTM committee E08.06.04 and was executed by the investigators to determine the state of small-crack research and knowledge. The survey consisted of short answer questions regarding the nature of the research, the materials studied, applications of the investigators' research, smallest crack size monitored, techniques used to monitor crack growth, testing environment, surface conditioning/preparation, and models used to predict crack growth. In addition, survey participants were asked to identify critical issues they were addressing in their research and some important unresolved questions in the area of small-cracks. The replies from the survey were compiled and a paper is currently being written. Some results from the survey that apply to the current project are as follows:

- Titanium alloys comprise 41% of all the materials studied by the survey participants, but only 8% of all replies indicate that small-crack research is being done on Ti-6Al-4V.
- Only 15% of all replies indicated that load interaction effects were being investigated on small-cracks. The most common type of loading was constant amplitude loading with different stress ratios, totaling 83% of how loading was characterized by survey participants.
- 49% of replies stated that the smallest crack size being monitored was smaller than or equal to ten microns in length. The current research is considering cracks starting from machined potholes between five and ten microns in diameter.
- 70% of all small crack specimens are being mechanically polished with only 3% incurring no polish. Of the specimens that are mechanically polished, 26% are being electropolished as well. Specimens for the current research are mechanically polished and electropolished.



Some of the unresolved issues noted by survey participants included load interaction effects on small crack growth, modeling of these effects and precisely how metallurgical features influence small-crack growth. These are questions being addressed by the current research.

During the fall, the literature search continued. In addition, supplies were obtained to run tests. Training was completed on a load frame as well as on a scanning electron microscope. During December, the load frame was shut down for repair. Consequently, training was completed on a second load frame. "Dummy" aluminum specimens were obtained for practicing the replication technique and to become proficient with the Questar microscope so that crack growth can be monitored. A study was conducted using FASTRAN to predict how a crack would grow under various conditions with different initial crack sizes. In order to use FASTRAN, a large amount of information on the material was needed including tensile properties, the material's fracture toughness and its effective stress intensity range vs.  $da/dN$  curve. The material's tensile properties were obtained while at Langley Research Center, as noted earlier. The material's other properties were obtained from damage tolerance handbooks [23]. The handbooks contain several different data sets on Ti-6Al-4V because of the range of heat treatments. The particular data sets taken from the handbooks were chosen based on exhibiting material tensile properties close to the properties gathered at NASA Langley. Such data is shown in Fig. 37 for various R.

The data were reduced to an effective  $da/dN$  vs.  $\Delta K_{eff}$  curve with an equation consistently found in several papers. The resulting curve is shown in Fig. 38. The waviness of the  $\Delta K_{eff}$  curve is commonly observed. During the growth of cracks, several mechanisms can lead to this waviness, including the loss of constraint. Once this relationship was found, an input file for FASTRAN was generated. To validate the input file, it was input into FASTRAN to predict the large crack growth data gathered from the damage handbooks. As shown in Fig. 39, FASTRAN predicted the large crack data very accurately using the developed input file. This was true at all R ratios.

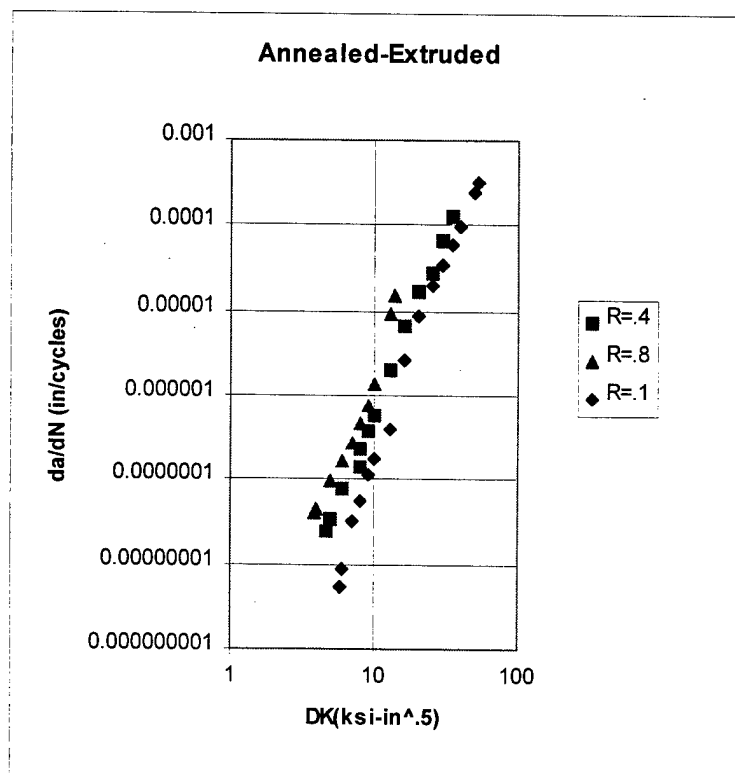


Figure 37. Long Crack Growth Data [23]

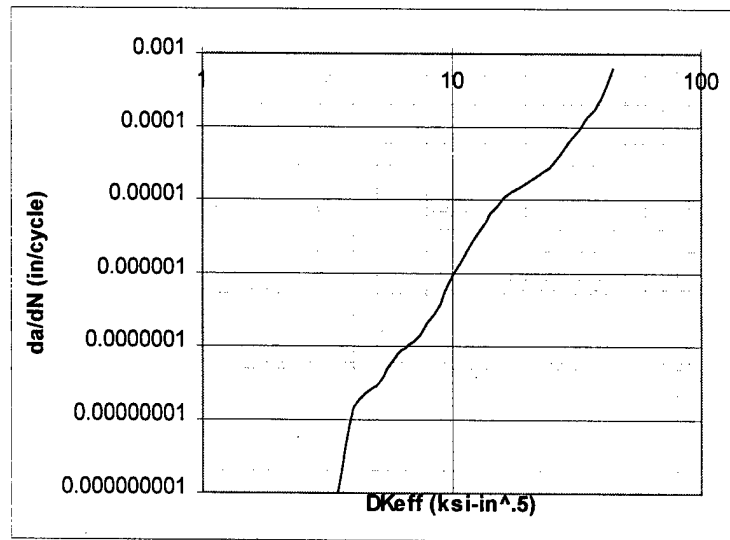


Figure 38.  $da/dN$  vs.  $\Delta K_{eff}$  curve for Ti-6Al-4V

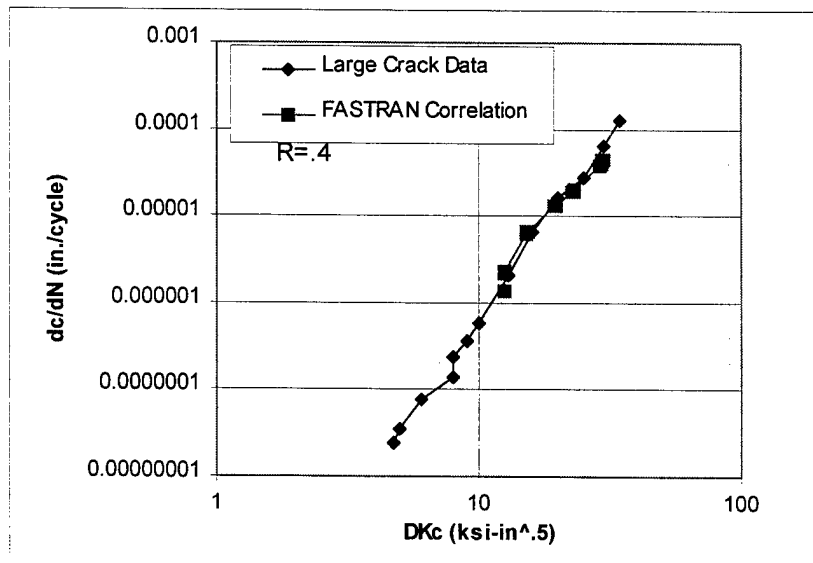


Figure 39. FASTRAN Large Crack Growth Validation

The most beneficial aspect of the large crack data is that the amount of the small-crack effect can be determined qualitatively. This effect is seen as cracks growing either below the large crack thresholds for identical conditions or growing at faster rates than large cracks at the same nominal stress intensity range. In addition to this, the large crack data provides information about when testing on the small-crack specimens can be stopped (i.e. when a crack no longer exhibits the small crack effect and grows out of the small crack regime).

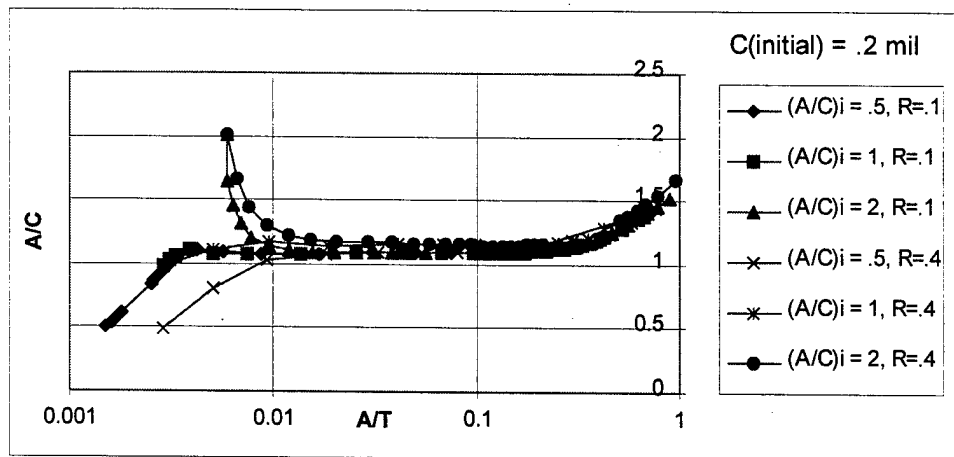
Once the FASTRAN input file was validated, it was used to predict some growth rates under numerous conditions. The study included growing cracks with three different initial aspect ratios ( $a/c$ ), two different  $R$  ratios and two different initial crack lengths. The initial aspect ratios were 0.5, 1, and 2. These values were chosen because the lower and upper ratios are close to the geometric limits allowed by FASTRAN and Newman's stress intensity solution. The two  $R$  ratios picked were 0.1 and 0.4. These  $R$  values were selected since they can be correlated to the  $\Delta K_{eff}$  curve easily. The initial crack lengths ( $C$  initial) were set to 5 and 10 microns (approximately .2 and .4 mils) which corresponded to the size of the potholes that were put at the notch root of the specimens that will be tested. The potholes will serve as initiation sites for the small-cracks. A picture of one of the potholes, this one ten microns in diameter, is shown below in Fig. 40. Some of the results of the FASTRAN trials are shown in Figs. 41-43.

Once the study was completed, a constant amplitude test matrix was developed using FASTRAN. The test matrix will serve as baseline data for load interaction tests. In order to design the load interaction tests, information must be known regarding the small crack growth at a nominal stress level and stress ratio. The test matrix consists of cycling specimens at maximum stresses of 30, 40 and 50 ksi at stress ratios of -0.1, 0.1, 0.4 and 0.7. These values are similar to ones found in damage tolerance handbooks. Thus, the information in the handbooks can readily be used to assist in verification of any small crack effects. A sample of the FASTRAN predictions for the constant amplitude test matrix is shown in Fig. 44.

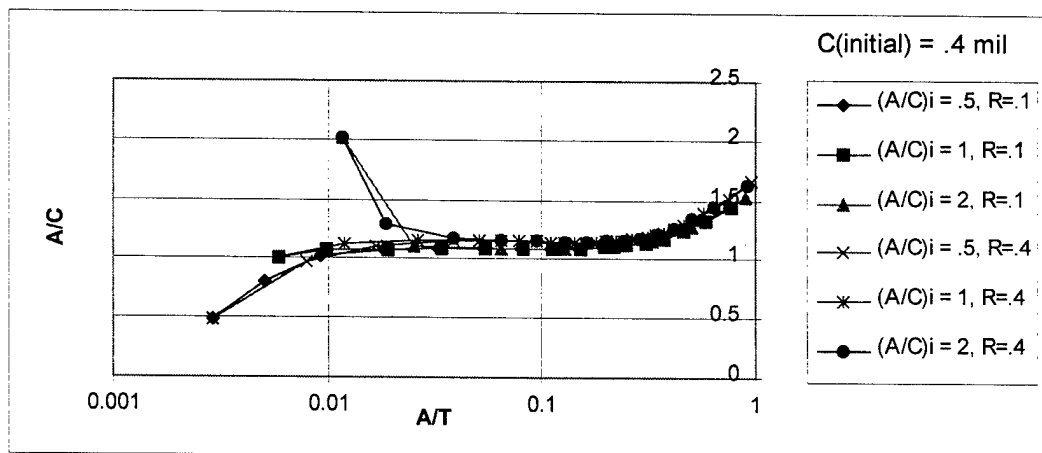
As data is gathered on this particular material, the FASTRAN input file will be refined to fit the results obtained and to consequently predict future results. Currently, the first test in the constant amplitude matrix is underway. This data will offer guidance as to whether or not micron sized potholes should be put in the notch root to help start cracks.



Figure 40. Pothole at Notch Root of Small-Crack Specimen used as an Initiation Site



**Figure 41a.** FASTRAN Predictions of the Crack's Aspect Ratio Evolution; 5 microns initial crack length, 50ksi stress range.



**Figure 41b.** FASTRAN Predictions of the Crack's Aspect Ratio Evolution;  $10\mu\text{m}$  initial crack length, 50ksi stress range.

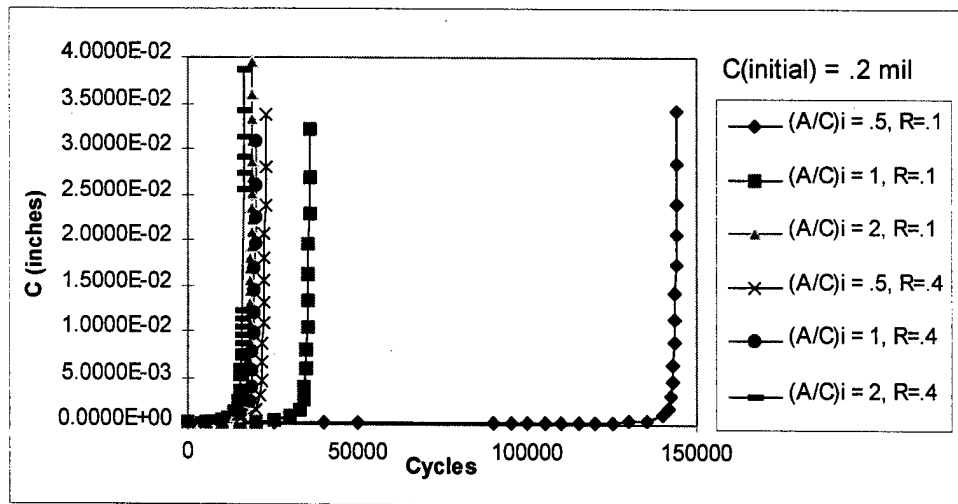


**Figure 42a.** FASTRAN Predictions of the Crack's Life; 5 microns initial crack length, 50ksi stress range.

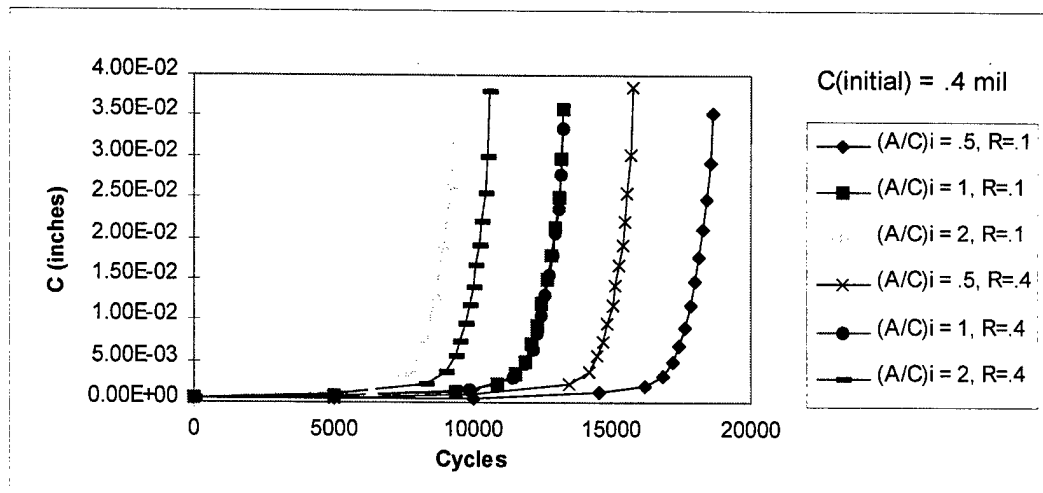


**Figure 42b.** FASTRAN Predictions of the Crack's Life; 10 microns initial crack length, 50ksi stress range.

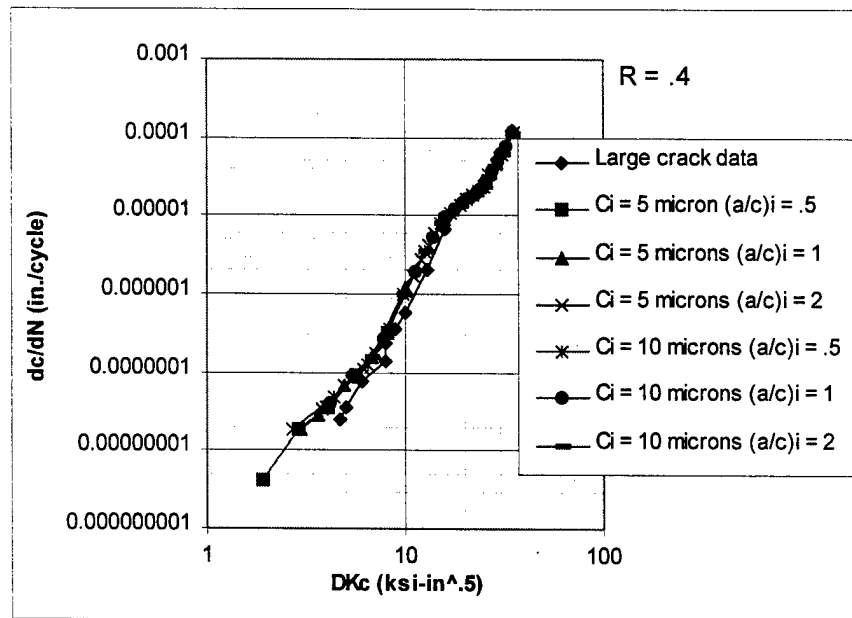


Figure 43. Delta K vs.  $dc/dN$  curve, Stress Range: 50 ksi

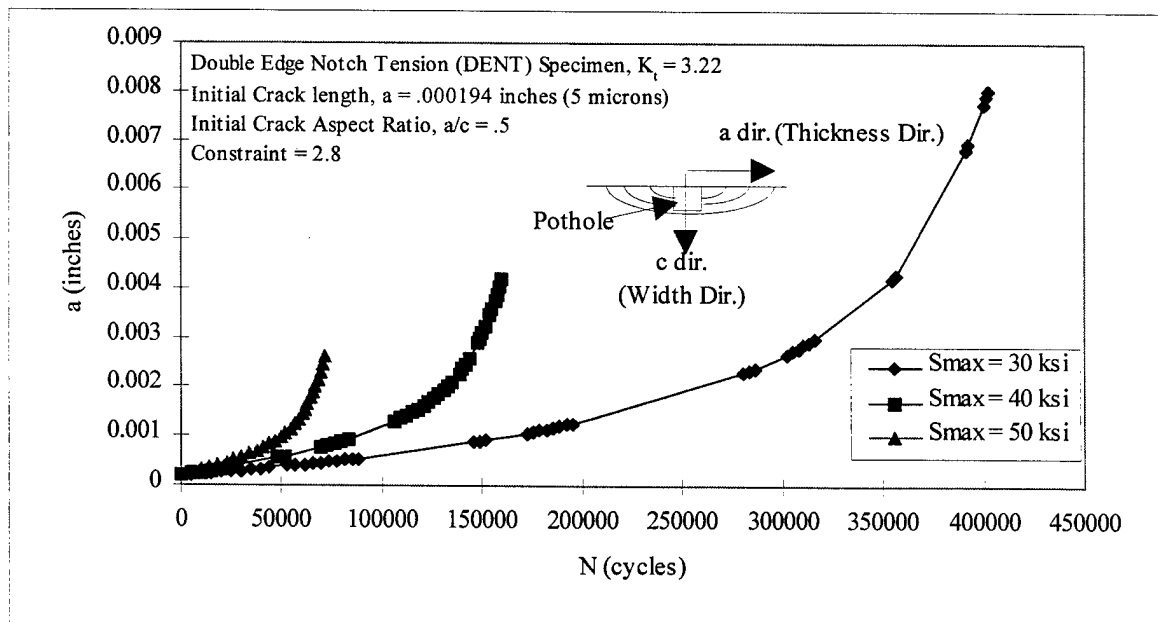


Figure 44. FASTRAN Small-Crack Growth Prediction

### PLANS FOR YEAR 3

Within the coming year, the constant amplitude test matrix, overload/underload tests and load interaction tests will be completed. The overload/underload stage will consist of spike overloads and underloads at stress ratios used in the constant amplitude tests. The load interaction stage will consist of stress ratio excursions between those used in the constant amplitude matrix. Predictions will be made on the data using FASTRAN. In addition, the influence of metallurgical features on crack growth subjected to load interaction effects will be investigated. All of this is scheduled as shown in the critical path diagram of Fig. 45.

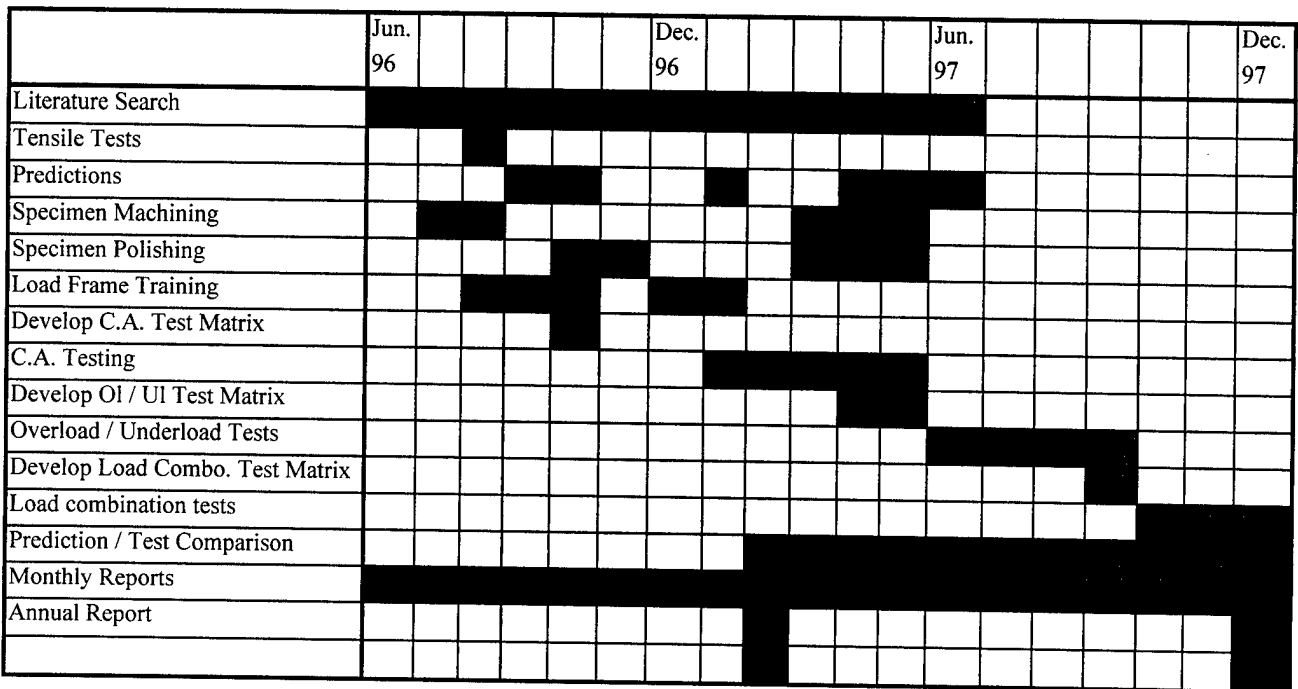


Figure 45. Critical Path Diagram

### C. SMALL CRACK GROWTH AND FRETTING FATIGUE (R. W. NEU)

#### ACCOMPLISHMENTS OF M-URI YEAR 2

Even though fretting fatigue has been attributed to recent major failures, there is surprisingly little basic scientific research to elucidate the important fretting fatigue mechanisms. Fretting fatigue is the small amplitude oscillatory sliding between two bodies when one of the bodies is undergoing a bulk alternating stress. It commonly occurs in clamped joints or joints with interference fits. Generally, fretting alone or fatigue alone will not cause catastrophic damage propagation, but the synergism between fretting and fatigue is especially severe. Fretting fatigue consists of a crack nucleation stage and various crack growth stages from small cracks growing in mixed-mode ( $< 1$  mm in length) to cracks that are nearly mode I and are well-represented by linear elastic fracture mechanics based on long crack behavior.

There has been much success in detecting and monitoring long cracks with various traditional sensors. Improved sensors may be able to capture small crack growth, though it may be easier to capture the precursor processes leading to the formation of a crack. Consequently, prognostic tools must not only acknowledge the crack growth process but also the nucleation process. In fact, sensors will potentially have success in capturing the characteristics of the contact between the two bodies undergoing fretting fatigue during the nucleation process more easily than detect the small crack growth.

In order to develop applicable prognostic tools that will be used in conjunction with sensor signals, a better understanding of the nucleation process and early crack growth under fretting fatigue are basic research needs. First, the limit of applicability of well-developed long crack growth models based on fracture mechanics to the modeling of small crack growth from notches will be determined for two steels (PH 13-8 Mo stainless steel and 4340 steel) commonly used in aircraft components. When the crack is small, the crack growth rate is generally greater than that predicted using the long crack growth models without accounting for the small crack growth effect or mode mixity. Experiments will be conducted to confirm this and applicable short crack growth models for these two steels will be identified. Then these models will be applied to small cracks growing under the influence of fretting fatigue where in addition to the bulk alternating stress, the frictional force and contact pressure contribute to the crack driving force. It is hypothesized that by accounting for the cyclic bulk stress, tangential force, and contact pressure on the crack driving force, the small crack growth models will predict both plain fatigue and fretting fatigue. Experimental investigations on the small crack growth under both plain fatigue and fretting fatigue on the same material have rarely been conducted and will be conducted to verify the current crack growth models.

A long-term objective is the better understanding of the nucleation process under fretting fatigue and the development of nucleation models. These models are not as well developed as the crack growth models. The fretting fatigue apparatus will also be used to elucidate the nucleation mechanisms through local characterization of the subsurface material in the fretting region. The sensor signals need to be correlated to the mechanical, physical, and chemical fretting fatigue nucleation mechanisms. Until these mechanisms can be identified and quantified, the sensor signals are difficult to interpret. The proposed experiments will enable us to hypothesize and corroborate fretting fatigue nucleation mechanisms and models. In addition, this understanding will lead to improved palliatives for fretting fatigue as well as tools for predicting the performance and life of components. The investigation will take advantage of the sensors developed by other tasks to elucidate the stages of fretting fatigue process. Combined with other characterization tools, this may lead to new predictive models that can link the sensor signals to the physical fretting fatigue mechanisms.

It is envisioned that the fatigue crack growth models as well as models that describe the dominant nucleation mechanisms will be one of numerous inputs into a remaining life prediction scheme or an on-line prognostic scheme.

#### **Literature Review of Fretting Fatigue**

An extensive literature review of fretting fatigue was conducted. A complete review will be reported in a future report and paper. Fretting fatigue is a diverse and widespread phenomenon since it occurs in a vast number of engineering components where two bodies are in contact and can undergo a small oscillatory slip. Some examples include fasteners such as bolted, riveted, and clamped joints; press-fit components; keyways, splines, and dovetails; steel ropes and springs. In gas turbine engines, cracks in blades and disks may only grow a physically short distance before catastrophic failure occurs. Because of this, the number of hours required for inspection of military aircraft is nearly the same or even greater than the number of flight hours. Consequently, on-board sensors which can reduce the inspection interval will provide a tremendous cost savings. The acoustic emission characteristics of fretting and long crack growth are clearly separable [24], but no work has been conducted to relate the physical nucleation process and mechanisms to crack nucleation and small crack growth.



Fretting fatigue involves a highly complex interplay among a number of mechanical, physical, and chemical factors. The primary influencing factors in fretting fatigue are (1) amplitude of relative slip, (2) magnitude and distribution of contact pressure, (3) fatigue loading, (4) mechanical properties of the contacting materials, (5) corrosion resistance (environment), (6) friction forces and near surface stresses, (7) surface condition, (8) cyclic frequency, and (9) temperature. Not much progress in linking these factors has been made beyond empirical relationships based on bulk parameters.

Fretting fatigue cracks are not always associated with regions of maximum fretting damage. The maximum rate of fretting fatigue damage occurs when the relative slip is near 20 mm [25]. When the relative slip is near this value, the contact is characterized by regions of stick and microslip. In fact, Spink [26] found that fretting fatigue cracks nucleated and propagated where surface wear damage was minimal, typically near the interface between the stick and microslip regions [27]. Fretting fatigue cracks have been shown to nucleate at a very early stage in the fretting fatigue life [28]. Various qualitative nucleation mechanisms or stages of fretting fatigue have been hypothesized: for example, (1) asperity accommodation process involving cohesion and breaking of cohesion of the surfaces, (2) abrasive pit-digging action, (3) asperity-contact microcrack initiation, (4) subsurface cyclic shear stresses leading to surface delamination, (5) friction-generated cyclic stresses leading to the formation of microcracks, and (6) abrasive action removing adherent oxide layers, which permits intermetallic welding on a scale sufficient to produce high stresses and extensive plastic deformation. Each hypothesized nucleation process will result in a characteristic local nonhomogeneity of the subsurface material, though there may be some overlapping among them. These mechanisms describe how the global parameters influence the local driving forces for fretting damage.

Once a crack has nucleated, it can be treated as a small crack growing through a nonuniform stress field. It is convenient to separate fretting fatigue into two stages: a nucleation process and a crack growth process. Nucleation involves all the processes leading to the formation crack, typically of the order of 10  $\mu\text{m}$ . The crack growth process describes the additional crack driving forces under fretting fatigue. Since near-term prognostic tools may be based on models of crack growth, propagation is currently being addressed. Nucleation will be addressed in M-URI year 3 and beyond.

#### *Propagation of Fretting Fatigue Cracks:*

It is well known that the growth of small/short cracks is accelerated when compared to backward extrapolated long crack growth behavior. However, the acceleration of the small cracks under fretting fatigue is even greater when compared to the long crack growth behavior. The crack driving force is proportional to the stress intensity factor at the tip of the crack. Under fretting fatigue, it is composed of three individual contributions. The first is the contribution from the cyclic loading in the main body undergoing fatigue. The second is from the alternating frictional force due to fretting. The third contribution is from the normal contact pressure. The latter contribution is typically static and compressive, and therefore tends to be more beneficial than the other more damaging contributions. The stress intensity can further be divided between an alternating component and a mean component [29, 30]. Since the small crack growth behavior is significant to the fretting fatigue problem, the small crack growth effect on the threshold stress intensity factor can be taken into account [31-34].

By using three parameters to describe the crack driving force under fretting fatigue, a number of trends of the actual crack growth behavior are predicted. The same models can be used to predict both plain and fretting fatigue. The methodology has been shown [29, 32, 35] to satisfactorily predict crack growth rates and to determine critical crack sizes [30] in laboratory fretting fatigue tests for a few material combinations and loading conditions. The limited success of the modeling suggests that such an approach may be suitable for an engineering model that can be input into a comprehensive prognostic tool.

## **Experimental Results**

### *Methodology:*

In order to verify and tailor these crack growth models for use in a remaining life estimation scheme, experimental crack growth data on the relevant steels is needed. The data should span a number of scales including long crack growth, small crack growth in plain fatigue, as well as small cracks growing under a more complex loading (e.g., variable amplitude and fretting fatigue). Long crack growth methods and models are well-developed and long crack growth data is generally available. Therefore, just a couple of verification tests for comparing to our more unique small crack growth tests were conducted. Experimental techniques have been developed to measure small crack growth. First, small crack growth tests under uniaxial loading without fretting were conducted at different mean stress levels and stress amplitudes. These tests will be followed by additional tests that will be periodically interrupted with an overload or underload to evaluate the variable amplitude effects in the small crack growth regime. Then fretting fatigue experiments will provide a more complex, though controllable, cyclic mixed-mode loading. Current small crack growth models breakdown under these more complex loadings. The necessary small crack growth data needed to verify and hypothesize these crack growth models is generally not available, especially under both plain and fretting fatigue.

A number of small fatigue crack growth tests along with two long fatigue crack growth tests on PH 13-8 Mo stainless steel were conducted in year 2. Also, the fretting fatigue apparatus was designed and specimens were prepared in year 2. In addition, we continue to collaborate with the co-investigators of Section 2.1.1 who measure acoustic emission signals during a number of these crack growth experiments. Together, we are more capable of linking the sensor signals and the physical crack growth mechanisms.

### *Materials and Specimens:*

PH 13-8 Mo stainless steel falls under a category of materials known as maraging stainless steels. These materials are precipitate hardenable martensitic stainless steels with a low carbon content. Typical compositions of this material consist of 12.39 - 12.9 (wt %) Cr, 7.87 - 8.58 Ni, 1.73 - 2.45 Mo, 0.8 - 1.18 Al, as well as minimal amounts of Si, C, Mn, and other elements [36-42]. Corrosion resistance of stainless steel is primarily due to the Cr content which enables the formation of a passivation layer. However, this passivity can often break down in severe marine environments. The presence of Mo strengthens the passive film and greatly reduces the incidences of pitting in salt water environments.

In general, heat treatment of PH 13-8 Mo stainless steel is performed as follows: Initially, the material is solution treated in the fully austenitic region at temperatures greater than 850 C. It is then quenched to create a b.c.c. martensitic matrix. Finally, it is aged at temperatures resulting in the formation of fine b-NiAl precipitates. The typical solidification structure of the material consists of two phases that form a cellular dendritic structure. There is a lath martensitic matrix structure and  $\delta$ -ferrite. At higher aging temperatures ( $> 566$  C), significant amounts (1.6 to 16.2 wt %) of reverted austenite are found in the martensite matrix [37,42]. The grain size ranges from 20 - 50  $\mu\text{m}$  depending on solution treatment [37].

The microstructure of PH 13-8 Mo stainless steel is particularly sensitive to aging temperature and thus a wide range of mechanical properties can be attained. Our material has been aged for 4 hours at 566 C (H1050). At this aging temperature, a balance of strength and ductility is achieved. A broad range of tensile yield strengths have been reported for the H1050 aging: 165 - 197 ksi [[36,41-44]. The respective ultimate strengths were only slightly higher. The critical stress intensity for this material at H1050 falls in the range of 88 - 103 ksi [36].

The test specimens are single edge notch tension (SENT) specimens. The gross section width is 1.0 in., the thickness is 0.15 in., and the notch radius is 0.125 in. The specimens were fabricated from an aged 0.375 in. plate using a low stress grind to minimize the surface residual stresses due to machining. The notch root and other locations where cracks will grow were mechanically polished with 9 and then 3  $\mu\text{m}$

diamond paste. The specimens were then electropolished to remove the surface residual stresses due to the polishing.

#### *Small Crack Growth Experiments:*

A 20-kip SATEC uniaxial servohydraulic fatigue test system is used to conduct the fatigue tests. The small crack growth is measured by periodically interrupting the fatigue test and taking an acetate replica of the notch root where crack nucleation will occur. The cracks imprinted on the replicas are measured using an optical microscope.

Using the optical microscope, the smallest cracks that have been detected are about 30  $\mu\text{m}$ , though angle sputtering techniques and SEM analysis are currently underway in hopes of increasing the detection limit. Figure 46a shows some typical experimental results from our study. Growth rates of  $1 \times 10^{-4}$   $\mu\text{m}/\text{cycle}$  in the figure should be considered as no growth. The microstructurally sensitive regime appears to lie within 100  $\mu\text{m}$ . The oscillatory growth rate behavior is consistent with previous studies on microstructurally small cracks. Within this regime, there are strong interactions with microstructural features such as grain boundaries, which for our material is on the order of 20-50  $\mu\text{m}$ . These cracks are subject to local mode mixity effects due to the heterogeneity and anisotropy of the cyclic slip processes associated with the orientation distribution of the grains [45]. As the length of the crack increases, a transitional behavior is observed as microstructural features have a diminishing effect and the crack growth rate no longer oscillates. After growing through this transitional regime, the microstructural effect is minimal and traditional linear-elastic fracture mechanics can effectively be applied to characterize the remaining crack growth.

A knowledge of the long crack growth behavior of our material is essential to ascertain when the transition from small crack growth to long crack growth has occurred. Although some long crack growth data on PH13-8 Mo is available, it is unclear how well this information relates to the crack growth conditions in our small crack specimens. Accordingly, two long crack growth tests were conducted so that variations due to specimen thickness and material rolling direction could be eliminated. The data obtained is shown in Fig. 46b. Crack lengths were measured optically at certain increments of crack growth. The raw data was reduced using the seven point incremental polynomial method described in ASTM Standard E647 to obtain the  $da/dN-\Delta K$  curves. Linear curve fits to the data shown in Fig 46b reveal the Paris constants to be  $C = 1.9 \times 10^{-9}$  and  $m = 2.52$  for a stress ratio of 0.5, and  $C = 2.2 \times 10^{-10}$  and  $m = 3.11$  for a stress ratio of 0.1. This data will be used to identify the transition between the small crack growth and long crack growth regimes obtained from the notched specimens.

#### *Fretting Fatigue Experiments:*

A fretting fatigue apparatus has been developed that is similar to the designs reported in [46]. It consists of a uniaxial fatigue specimen with a rectangular cross section similar to our notched specimen. Two pads which each have two feet spaced a distance  $L$  apart are attached to opposite sides of the fatigue specimen through a calibrated proving ring. The normal contact pressure is transmitted through the feet. The feet can either be flat or be convex. The test parameters include the cyclic stress amplitude and mean stress, the normal pressure, and the specimen dimensions, particularly the geometry of the feet. The flat feet have a near uniform pressure distribution except near the ends where the contact pressure is elevated due to the theoretical singularity. The convex feet produce an overall Hertzian pressure distribution. The combination of the pad span ( $L$ ) and stress amplitude ( $sa$ ) controls the relative slip at each foot. Therefore, we can control the degree of microslip and stick at the contact interface. The frictional force is determined experimentally by measuring the strain in the pad between the two feet. The crack lengths will be measured using optical and acetate replica techniques along with switching DC electric potential.

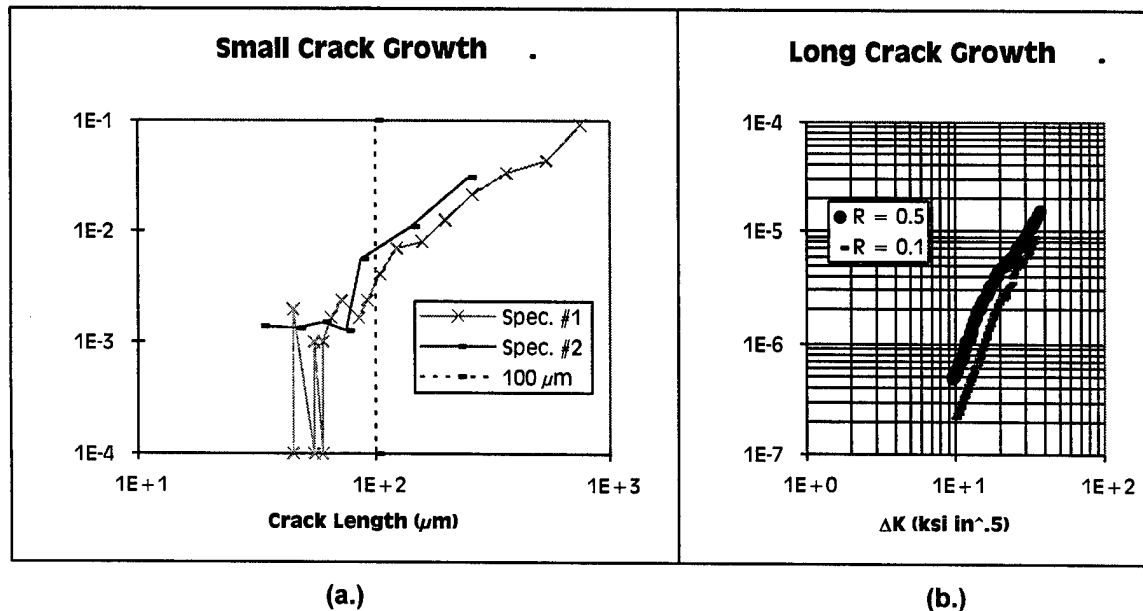


Figure 46. Crack Growth Behavior of PH 13-8 Mo Stainless Steel

### PLANS FOR YEAR 3

Small and long crack growth models suitable for the remaining life estimation and other prognostic schemes will be verified and any needed modifications will be developed. They will be verified using the small and long crack growth test data on PH 13-8 Mo stainless steel. In addition, the effect of variable amplitude loading on small crack growth by imposing single overloads and/or underloads and measuring the effect on the subsequent crack growth will be conducted. This will aid in identifying events leading to a nonpropagating cracks and is critical data for evaluating the applicability of various small crack growth models to variable amplitude loading.

We will then investigate cracks growing under fretting fatigue. We will verify that small crack growth models developed from plain fatigue can be extended to this mixed-mode condition. Similarities between notched (plain) and fretting fatigue in these steels will be identified. With the different pad feet geometries, the influence of the local subsurface stress distribution on nucleation and crack growth will be investigated. In the first set of experiments, the fretting fatigue cracks will be allowed to nucleate and grow until the influence of the frictional force on the crack driving force diminishes. We also will conduct selected plain fatigue and fretting fatigue experiments on 4340 steel for comparing to the PH 13-8 Mo stainless steel and determining the universality of the crack growth modeling.

Two M.S. students will graduate this year. One is funded by the ONR grant and one funded internally. A Ph.D. student will begin working on this project this year. An undergraduate student will also be employed as a research assistant.

### 2.2.1.3 Sub-Task III

#### **REMAINING LIFE ESTIMATION METHODOLOGY**

*A. Saxena and D. McDowell*

The objectives of this task are (i) to understand the damage modes, crack growth mechanisms and crack locations and to develop algorithms for predicting the risk of fatigue failures in helicopter parts and (ii) to recommend strategies by which the results of the risk analyses can be used to predict remaining useful life, minimizing the risk of fatigue failure and avoid catastrophic failures.

#### **ACCOMPLISHMENTS OF M-URI YEAR 2**

In this section, the results of tests performed for characterizing the fatigue crack initiation and growth mechanisms in AISI 4340 steel which is used extensively in cyclically loaded helicopter components are described. The issues related directly to the development of a methodology for predicting remaining life of components are also discussed.

##### **Test Material**

Two pieces of materials were received from the Cherry Point Naval Aviation Depot. The first was a retired helicopter rotor connector link and the second was a round bar of 50.8 mm diameter. Both were American Iron and Steel Institute (AISI) grade 4340 steel. A picture of the retired connector link is shown in Fig. 47. The inside surface of the pin hole in the connector link was examined in detail to detect signs of fatigue damage. An optical examination revealed signs of cracks. A detailed examination, however, showed that the cracks were limited to the surface coating and did not extend into the base material, Fig. 48. Metallography samples were taken from the connector link to characterize the microstructure and the hardness, and the chemical composition of the material was also determined. The microstructure of the connector link material is shown in Fig. 49a, the chemical composition is given in Table 1, and the hardness was measured to be approximately 39 HRC.

The test bar received from Cherry Point had a ferrite/pearlite microstructure and a hardness of 209 HRB, indicating that the material was either furnace cooled or the transformation from austenite to ferrite/pearlite occurred under isothermal conditions. Part of the material was heat treated by first annealing at 870 C, oil quenching followed by tempering at 565 C. The microstructure of the heat treated material is shown in Fig. 49b for comparison to the helicopter link material. The two microstructures are very comparable and the hardness values are also comparable. The microstructure of the as received 4340 steel bar is shown in Fig. 49c. The chemical composition of the test bar is shown in Table 1.

##### **Mechanical Testing**

Specimens were machined from the steel bar in both, as- received and in quenched and tempered conditions. The results of the tensile tests performed are given in Table 2 along with the tensile test results for a material used in a previous study on fatigue behavior of quenched and tempered 4340 steels by Swain et al. [47]. The material in the current study had a lower yield strength than the one used by Swain et.al.

Disk shaped compact type (CT) specimens were machined from the bar material for conducting fatigue crack growth testing, Fig. 50. To observe the interaction between the microstructure and the growing crack, the region immediately ahead of the notch tip was polished and etched prior to even precracking to reveal the microstructure. Subsequently, the specimens were precracked and tested under increasing and decreasing K conditions at a load ratio of 0.1. The tests were periodically interrupted and the specimens were removed from the test frame to examine the crack/microstructure interactions using the optical and scanning electron microscopes. Some tests were also interrupted prior to failure to allow the nanoindentations to be obtained ahead of the crack tip.

One uniaxial fatigue test in the quenched and tempered condition was conducted. To reduce surface roughness and residual stresses, the gage length and the fillet area were low stress ground to min-

imize residual stresses and was subsequently electropolished. This specimen was tested at a stress amplitude of 75% of the yield strength. This specimen was also periodically removed from the test machine to characterize the crack initiation and fatigue damage behavior.

Samples for atomic force microscopy (AFM) were obtained from the uniaxial specimen after completion of the fatigue test. Several regions close to the fatigue initiation site were scanned using AFM. This effort is directed at detecting slip bands as possible sites for fatigue crack initiation.

Nanoindentation hardness specimens were prepared from untested and tested fatigue crack initiation and growth specimens. On the crack growth specimens, the measurements were made along the crack plane, in a direction normal to the crack plane and along 45 degrees to the crack plane. The load and displacement of the indenter was recorded. The indentation depth of 280 nanometers was selected. To eliminate surface effects, the hardness was calculated from taking the average of the hardnesses measured at the indent depth of greater than 120 nm.

### **Test Results and Discussion**

Four fatigue crack growth tests were completed. The results from the tests and those from the available literature data are shown in Fig. 51. Despite the difference in the strength levels, the fatigue crack growth rate behavior of the two quenched and tempered materials are very comparable. On the contrary, large differences were found between the fatigue crack growth behavior of quenched and tempered and as received steel with ferrite/pearlite microstructure. The crack path in the pearlite/ferrite microstructure is shown in Fig. 52. The crack prefers to pass through the region between pearlite colonies when this region is normal to the direction of loading and it passes through the ferrite/cementite interface in other regions. Such preferential crack paths were not found in the quenched and tempered microstructure.

The axial fatigue specimen from the quenched and tempered condition was fully fatigue tested to fracture and it sustained 2,586,596 cycles. However, no cracks were observed in this specimen even after 2,315,068 cycles when examined under the optical microscope. The crack initiated at a surface pit with a round bottom. Once the crack initiated, failure was quite rapid. The investigation of this specimen to understand the damage mechanism is still continuing.

Nanoindentation tests (Table 3) were conducted on fatigue crack growth specimens. Figure 53 shows a plot of nanohardness as a function of the distance from the crack tip along the crack plane for a quenched and tempered specimen. The hardness appears to increase with distance, as would be expected from a cyclically softening material. We have completed several more measurements and the results are currently being analyzed and will be reported in a separate report. We will also be etching the specimens used for nanohardness measurements to study the interaction between the indent and the microstructure. We expect to develop this technique further to a point where inhomogeneities in strain distribution between microstructural entities can be detected using this technique.

The applicability of AFM to characterize slip bands during fatigue loading is being explored. Some preliminary runs on the AFM have been carried out. This work will continue in the next few weeks. The AFM has the potential to resolve displacements with a resolution of less than an angstrom making it suitable for such characterization.

### **Remaining Life Estimation Methodology**

The key requirements for such a methodology are:

- A set of algorithms which are needed for estimating fatigue life, systematizing information about the following factors:
  - Component geometry, size and loading configuration.
  - Flaw configuration and size distribution from nondestructive inspection.
  - Material parameters needed for implementing the various crack growth models.
  - Fatigue loading spectra and environment experienced during service.
- Module for estimating failure risk and probabilities and for selecting optimum inspection intervals.

- Module for estimating the crack driving force capable of accounting for the following:
  - 3-D cracks.
  - multiple cracks.
  - mixed-mode stress intensity parameters for small and long cracks.
- Module consisting of various fatigue crack propagation models capable of accounting for the following effects:
  - Small crack behavior including the effects of interactions between small cracks and the microstructure.
  - Fatigue crack propagation under mixed-mode loading.
  - Variable amplitude loading.
  - Effects of surface residual stresses.
- A catastrophic failure prevention strategy which is based on utilizing signals from on-board sensors.

The initial focus of the structural fatigue task has been on the evaluation of the capabilities of existing models and on the development of new models, as necessary, for accurately predicting the fatigue life of helicopter components. This is essential in order to ensure that the models chosen to predict crack growth rates have the necessary capabilities to accurately consider the factors which will influence the fatigue life of helicopter components. Description of the rate of growth of small fatigue cracks in the range of 5 to 100  $\mu\text{m}$  is considered to be a key factor in helicopter components. The models for predicting the growth of small fatigue cracks are not well developed and no single model is widely accepted. By contrast, the models for predicting the behavior of long fatigue cracks (longer than 1 mm size) are quite well developed, apart from complex 3-D effects. Thus, in the various projects being pursued under the structural fatigue task at Georgia Tech, models are being developed to represent the effects of multi-axial loading on the growth of small flaws (D.L.McDowell), the effects of variable amplitude loading on the growth of small and large flaws (W.S. Johnson), the effects of surface residual stresses and fretting fatigue on the growth of small flaws (R.Neu). In addition, a fundamental understanding is being developed on the interaction between the growth of fatigue cracks and the microstructure using new experimental tools such as nanoindentation hardness measurements and atomic force microscopy (A.Saxena). At Northwestern (B.Moran), a direct integration scheme is being developed for probabilistic assessment of fatigue failure risk. This model can be further developed to integrate the effects of small crack behavior. J. Qu of Georgia Tech is developing methods for determining the stress intensity parameters for relevant crack/component geometry for small cracks under complex service conditions. It is anticipated that the preliminary model development and the characterization of the material parameters will be completed by the third year of the project. An additional fourth year can be dedicated to the detailed development of the remaining life prediction methodology algorithms, refinement of the fatigue crack growth models, dealing with issues of interfacing the remaining life algorithm to different categories of sensor outputs with various resolution characteristics, and to the definition and exploratory investigation of a verification problem for evaluating the remaining life estimation methodology. It is expected that the choice of the verification problem will be made in consultation with HONEYWELL CO. and the ONR project director.

### **PLANS FOR YEAR 3**

1. Complete crack growth testing on 4340 steel by characterizing the data over a wider range.
2. Continue evaluation of the nanoindentation and AFM techniques for characterizing inhomogeneity of strain and damage distribution during fatigue loading in dual microstructure steels.
3. Coordinate with B. Moran at Northwestern University (co-investigator of Section 2.2.2) regarding probabilistic aspects of fatigue crack growth.
4. Identify resolution of various NDI techniques to begin establishing hierarchical structure of remaining life algorithm based on sensor information.

### **FAILURE PREDICTION METHODOLOGY (FATIGUE)**

Figure 47. H-46 Helicopter Connecting Link  
(AISI 4340 Steel)

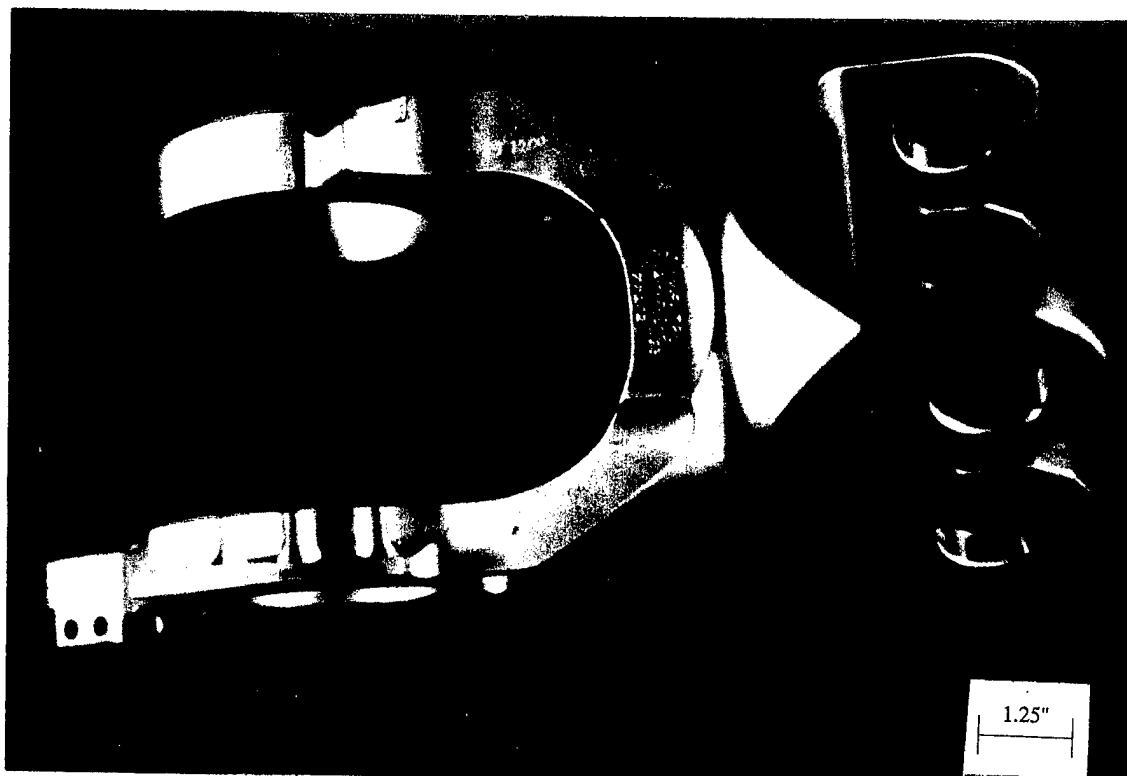




**Figure 48.** H-46 Helicopter Connecting Link  
(AISI 4340 Steel)



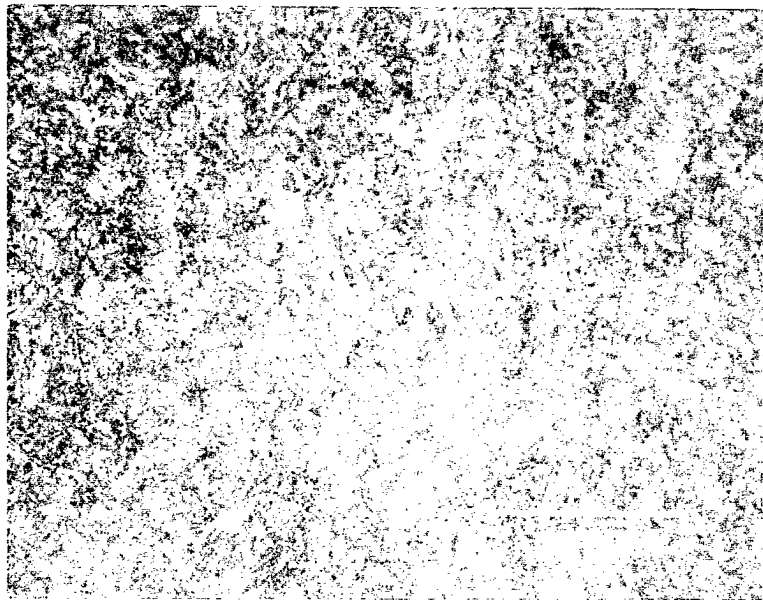


**Figure 49a. Microstructure of 4340 Steel: Connecting Link Material**

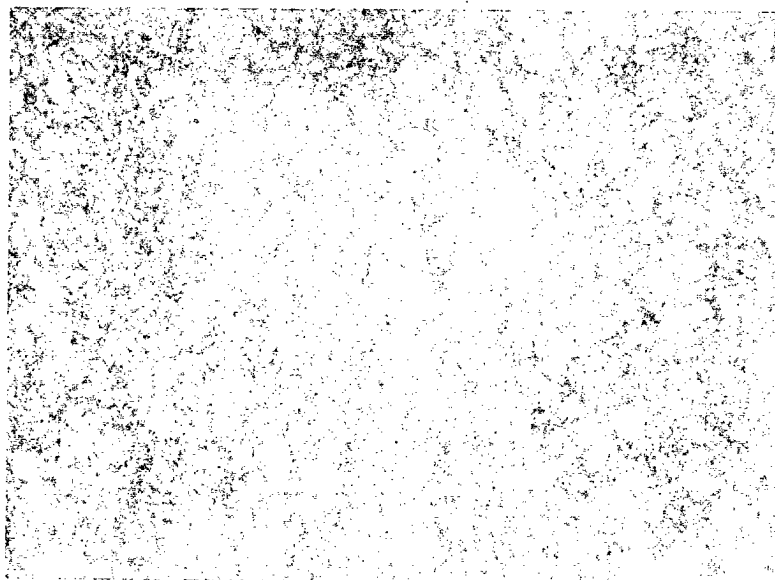


**Figure 49b. Microstructure of 4340 Steel: Quenched and Tempered Bar**

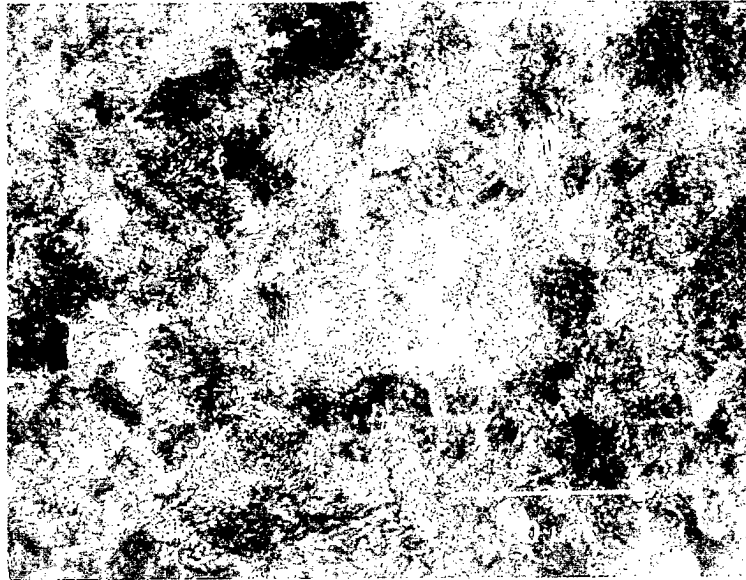


**Figure 49c. Microstructure of 4340 Steel: As-received Bar**

	C	Cr	Mn	Mo	Ni	Si
Connector	0.377	0.78	0.76	0.29	1.79	0.21
Bar	0.390	0.82	0.70	0.26	1.70	0.17
4340(lit.)	0.39	0.79	0.69	0.25	1.75	0.27

**Table 1. The Chemical Compositions of 4340 Steel of Different Sources (in %)**



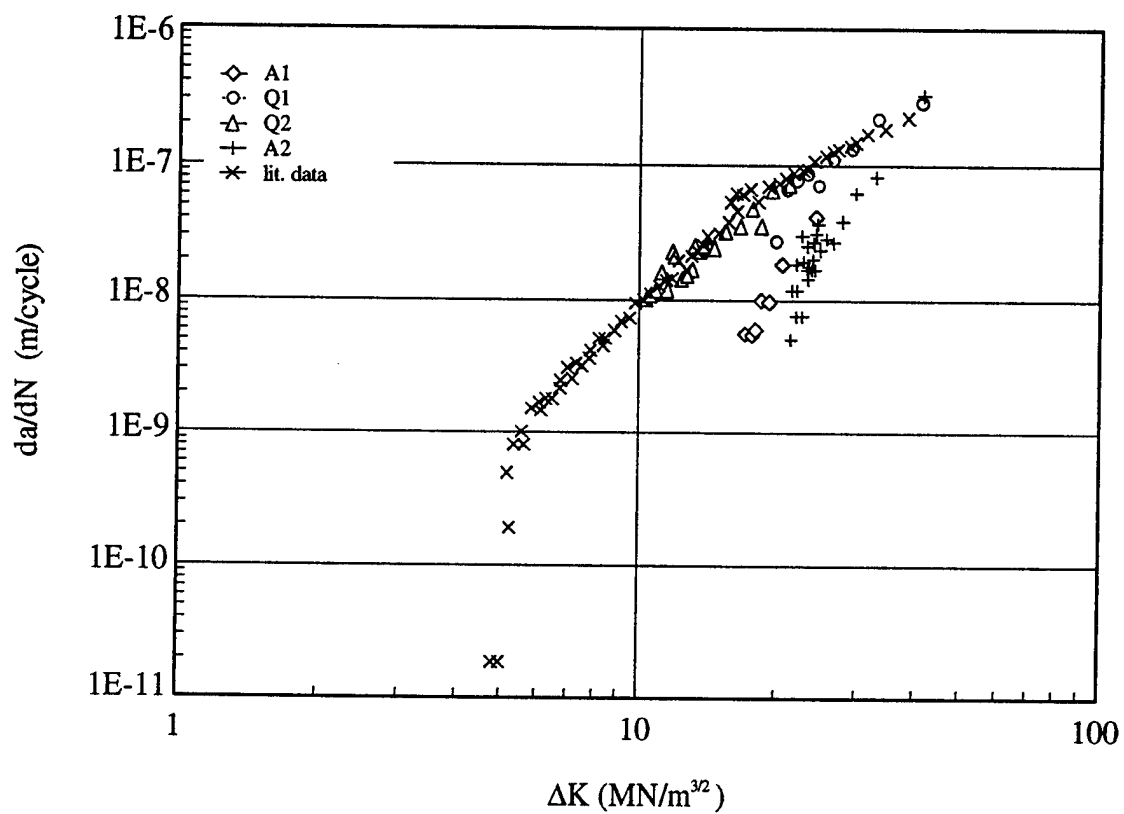
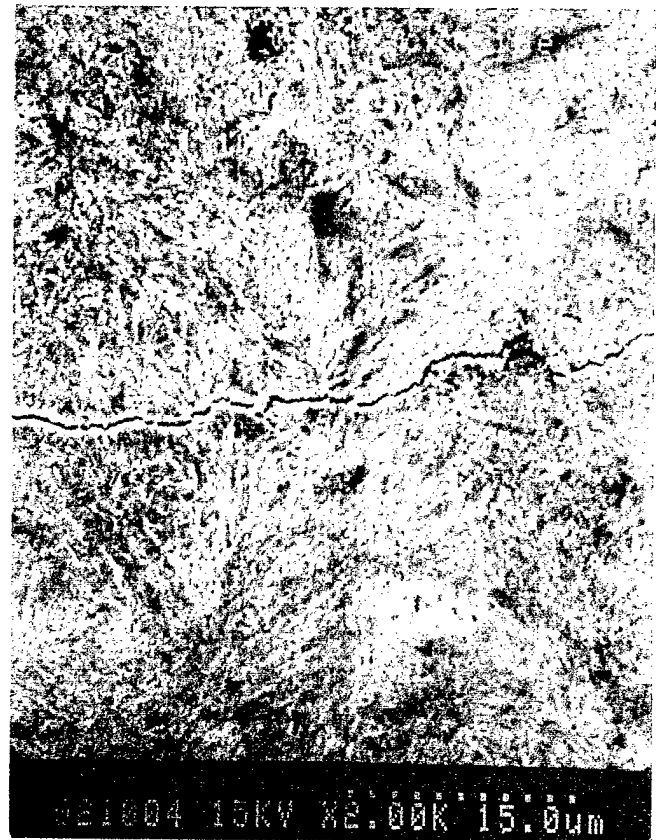


Figure 51. Fatigue Crack Growth Data of 4340 Steel



a.



b.

**Figure 52.** Interaction of Microstructure and Fatigue Crack; **a.)** as-received material; **b.)** quenched and tempered material.

Sample number	Heat treatment	Mechanical test history
FCGA2	as-received	crack tip region of CT specimen, final $\Delta K=50.3\text{MN/m}^{3/2}$
AN	as-received	not tested
AT	as-received	gage region of uniaxial fatigue specimen, monotonically fractured.
FCGQ2	Q + T	crack tip region of CT specimen, final $\Delta K=21.8\text{MN/m}^{3/2}$
QN	Q + T	not tested
QT	Q + T	gage region of uniaxial fatigue specimen, fatigue fractured.

Table 3. Nanoindentation Test Samples and their Conditions

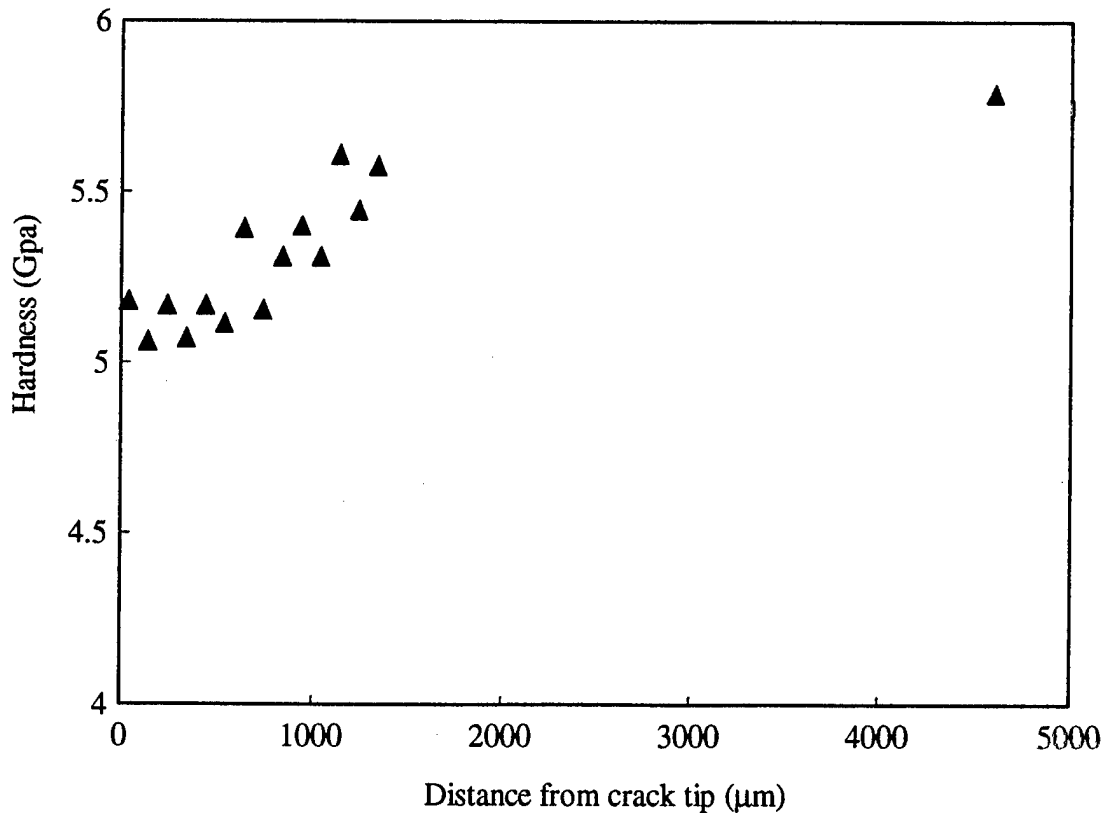


Figure 53. Nanoindentation Hardness Profile of Quenched and Tempered Materials

#### 2.2.1.4 Structural Fatigue Investigation

##### **VISION FOR YEARS 4 AND 5**

The first three years of this project are addressing the technology gaps that exist in the modeling of small cracks interacting with material microstructure, small cracks growing from notches and regions of contact, load sequence effects associated with variable loading conditions common in components, improved methods for visualization of 3-D stress states in components to identify "hot spots," and crack driving forces for 3-D cracks. It is emphasized that the concept of condition-based maintenance implies that given information regarding crack position and crack length, with a specified degree of certainty, the rate of growth of the crack(s) can be estimated at a level of accuracy suitable for ensuring that catastrophic failure will not occur before a maintenance decision can be made. Mechanistically-based models are necessary to satisfy this objective. Addressing these basic science and engineering issues enables the technology necessary to conduct remaining life estimation based on sensor outputs. While work will continue in selected technology-enabling areas to assure technical feasibility of modeling of complex components and to characterize the materials used in "model" components of this study, the integration of sensor information with crack growth theories at various scales is the central feature of the remaining life algorithm. In years 4-5, the Structural Fatigue Task will turn its attention more towards basic scientific and engineering issues to be addressed in a systems level implementation of remaining life assessment for condition-based maintenance, coupling issues addressed by models developed in this Task with issues of resolution and frequency of sensor feedback addressed in other Tasks.

##### **Sub-Task I: Stress Analysis and Stress Intensity Factor Solutions**

The simulation and visualization tools and the 3-D crack growth algorithms will be used to predict crack growth in an actual component, such as the rotor hub. This will incorporate the actual load spectrum and modeling of material fatigue behavior obtained through interaction with other studies of this project. Major issues to be addressed include:

1. *Crack-tip closure for 3-D cracks:* Due to surface roughness or reverse plasticity, crack faces may come into contact. This effect will be incorporated in the elastic-plastic crack growth algorithms developed in year 3.
2. *Multi-site crack propagation effects:* Observation of the cracked components indicates that multiple cracks may co-exist near an area where stress concentration is severe. In this case, interactions between cracks may be significant. Understanding how one singular field may affect the other is crucial for predicting local damage due to multiple cracking. It is conceivable that the following two situations may prevail: (i) One major crack is accompanied by several small cracks near its tip. In this case, an iterative procedure will be used to account for the influence of small cracks on the major crack tip field; (ii) Several cracks of similar size clustered together. In this case, a combined micromechanics-damage mechanics approach will be utilized to describe the damage evolution in such a cracked region.
3. *Crack interaction - surface and boundary interactions:* It is obvious from the cracked components that most of the cracks are initiated from free surfaces. Due to the geometrical complexity and the nature of the fatigue process, many cracks are either growing towards, or near a free surface. Therefore, it is important to understand how free surfaces facilitate the growth of 3-D cracks of various length scales.
4. *Support for remaining life prediction:* A key aspect of Sub-Task I is the support it offers to the remaining life prediction algorithms and their assessment for a model component such as a helicopter rotor hub assembly. To this end, the detailed stress analyses and crack driving force characterizations developed in years 1-3 will be employed.



## **Sub-Task II: Characterization of Fatigue Behavior and Mechanisms**

*D. L. McDowell*

In year 4, we will conclude our computational crystal plasticity studies of the microstructural influence on small fatigue crack growth, and will fully implement the outcome of this modeling into crack propagation models valid for small cracks and the transition to physically long status. The model will be verified by the experimental data obtained in this program and elsewhere, for both uniaxial and multiaxial loading conditions. In year 4, we will introduce several features relevant to system level remaining life prediction: probability distribution of initial crack length, probability distribution of microstructure features, and model approximations for different regimes of crack length, notch root acuities, etc.

*W. S. Johnson*

By the end of year 4, the experimental portion of the project should be completed. This will include all load interaction tests and any additional constant amplitude tests needed for baseline data. Once the experimental work has been completed, the focus of the project will be on modeling the crack growth due to load interaction effects. Specifically, the focus will be to model the role of microstructure in small-crack growth and its influence on mixed mode fracture.

*R. W. Neu*

In years 4 and 5, work will continue on the investigation of small crack growth under the mixed-mode condition of fretting fatigue as well as an additional effort focusing on the nucleation of these small cracks under fretting fatigue.

We plan to characterize the nucleation process by examining the evolution of the subsurface material by repeating and interrupting fretting fatigue experiments and using a number of characterization tools such as optical, scanning electron, and atomic force microscopes, as well as the nanoindentation technique. Through collaboration with other tasks, we expect to gain insight from the analysis of sensor signals taken during the laboratory fretting fatigue tests. The nucleation tests will be conducted on PH 13-8 Mo stainless steel, 4340 steel, and possibly a titanium alloy (Ti-6Al-4V), which are all relevant aircraft materials that experience fretting fatigue.

Based on the characterization, models of the nucleation process or individual nucleation mechanisms will be hypothesized and developed. The objective is to develop models suitable for linking sensor signals to fretting fatigue mechanisms. Compared to crack growth modeling, this is somewhat more exploratory, yet our experience suggests that sensors may detect the changes occurring at the interface more easily than detect the small crack itself.

## **Sub-Task III: Remaining Life Estimation Methodology**

The remaining life prediction methodology will be developed, implemented and verified as described in Section 2.2.1.3. In contrast to airframes and power generation applications, there are additional complexities for the largely HCF problem of integrated diagnostics and condition-based maintenance. Estimation of the remaining life associated with fatigue cracks in helicopter components is a challenging problem, since a fatal flaw may go undetected for the majority of fatigue life with existing technology under high cycle fatigue (HCF) conditions. The problem of modeling growth behavior using either deterministic or stochastic models is quite complex for several reasons:

- uncertainty in measurement of cracks (size, location, initial identification).
- 3-D crack geometries.
- interactions with microstructure and stochasticity of microstructure/properties.
- complex effects of growth from notches.
- surface constraint effects.
- crack closure and crack face interference effects.

This is in marked contrast to the case of mechanically long cracks, which are effectively treated with damage tolerant approaches based on LEFM. In such cases, the problem is generally much better defined and fewer of the above considerations exist simultaneously. Attempts to address the combined effects of these various mechanisms generally rely on fitting of certain deterministic fatigue data/responses, along with judicious selection of driving force parameters. Such approaches can provide a useful engineering tool to estimate remaining lifetime of cracked components, but are generally limited in extrapolative capability. To address the uncertainty inherent at the systems level (i.e. component) due to stochasticity of crack growth combined with stochasticity of crack measurements, it is necessary to develop new concepts related to what one might call an intelligent diagnostics system.

For example, one direction to pursue is the use of artificial neural networks (ANN) to identify patterns of transducer signals and to relate these patterns to specific fatigue mechanisms/models. Another concept is to use an artificially intelligent algorithm such as ANN to train the remaining life estimation to correspond to progressive crack length measurements from embedded sensors, viewing the crack growth model parameters as flexible constraints which may be adapted within stochastic bounds as necessary to match prior history and predict into the future. The accuracy of such predictions would tend to increase with time as more data are available for the training process. Such robust, adaptive fatigue crack growth models and remaining life algorithms would still reflect the physics of various fatigue phenomena through reliance on detailed models, but might be able to effectively incorporate multiple competing mechanisms/sites across multiple scales. Another question to be explored regards what types of sensor information would be necessary as inputs to a neural network which is trained with a set of well-controlled laboratory fatigue experiments in order to have a certain level of confidence in the estimate of remaining lifetime of a cracked component. In essence, fatigue crack growth mechanism maps would be embedded in the neural network composition, inherently containing component-specific information such geometry, stress field solutions, crack driving forces, etc., in much the same manner as humans qualitatively interpret the full scope of complexity of fatigue problems, but at a rate suitable for real time updating of information.

Artificial neural networks are but one example of a systems analysis approach to this problem. We envision that through interaction with the NDI and systems analysis components of the M-URI, we will avail ourselves to other useful technologies as well. Clearly, the scientific challenges are immense, and the territory fertile for basic advances in fatigue modeling/prognostics.

## 2.2.2 FATIGUE RELIABILITY

Co-investigator: Brian Moran (Northwestern)

M-URI Year 2 Funding Allocation: 3.2%

### PROJECT OVERVIEW

The objective of this project is to develop a methodology for fatigue reliability and lifetime prediction of metallic structural components within the framework of condition based maintenance. The method shall be applied to the failure of critical components and systems in military and civilian machinery.

The computation of fatigue life expectancy is an integral part of the condition based maintenance of structural components which experience cyclic loading [48, 49]. Due to the statistical variability in such quantities as material properties and initial flaw sizes, for example, a probabilistic approach is required. Probabilistic fatigue methods can profitably be applied in a setting where critical structural components are monitored by non-destructive techniques so that cracked components can be identified and then repaired or replaced. Such monitoring can significantly reduce the probability of fatigue failure of a structure and increase its useful service life. Quantitative measures of reliability (provided by probabilistic methods) can be used to maximize the effects of inspections through optimization of the inspection schedule and techniques. The First Order Reliability Method (FORM) [50, 51] is a relatively simple and straightforward technique for the evaluation of failure probabilities. The method is particularly useful in a fatigue reliability setting where each random trial or realization requires the integration of a crack growth relation to determine fatigue life. In such situations, Monte Carlo methods may prove unwieldy especially where extreme reliabilities such as those required in the aircraft industry are concerned.

In research carried out at Northwestern University, a First Order Reliability Method (FORM) has been developed which can account for in-service monitoring [50]. Statistical variations in material properties and associated fatigue crack propagation relations are determined in a companion materials thrust. Traditionally, the first order reliability method is applied to one inspection interval at a time which requires characterization of the crack size distribution (i.e., crack size probability density function) at the beginning of each inspection interval, which is costly and difficult. We have extended the traditional FORM to account for the effects of the inspections so that the crack size distribution need only be characterized at an initial state. As in the standard FORM, the probability of failure is evaluated through an integral over the failure set in a standardized Gaussian space, however a novel integration procedure is developed to account for the effects of inspections at discrete times. Numerical results show excellent agreement between the present method and Monte Carlo simulations (where Monte Carlo techniques are feasible and a comparison is possible). The present method also permits the analysis of complex components (involving 3D crack growth) for which the use of Monte Carlo methods at extreme reliabilities is impractical.

In addition to the FORM, Direct Integration methods provide an efficient and robust framework for the determination of fatigue reliability. A Direct Integration scheme will be developed and implemented for fatigue reliability to complement the FORM methodology and comparisons of the Direct Integration method, FORM, and Monte Carlo simulation will be carried out.

The fatigue reliability methodology for condition-based maintenance is to be applied to the failure of critical components and systems identified by the PI in consultation with program monitors and industrial and military personnel. Candidate structural components include gears, drive shafts and rotor hub components in military helicopters, as well as similar hardware in civilian aircraft and in industrial machinery.

### **Optimization of Inspections**

An important link between fatigue reliability modeling and non-destructive evaluation is furnished by the Probability of Detection curve (POD curve). The POD curve characterizes the probability of detection of a crack as a function of crack size for a given inspection technique. A class of POD curves can be written as

$$\text{POD}(a) = \alpha a^{\beta} / (1 + \alpha a^{\beta}) \quad (2)$$

where  $a$  is crack size and the parameters  $\alpha$  and  $\beta$  characterize the NDE inspection technique. In Fig. 56, POD curves for three different sets of parameters are illustrated. For economic and other reasons, only a limited number of inspections may be performed. We have developed a method for determining the optimal inspection time for a given NDE technique (set of POD parameters). In Fig. 57, the probability of failure at 30,000 cycles as a function of time (in cycles) of the performance of a single inspection is given for an edge crack problem. The plot indicates the inspection time of 25,000 cycles is optimum. In this example, early inspections are not particularly advantageous because cracks are still small while later inspection allows cracks to grow too large. A general optimization procedure is being developed to systematically address these questions. A technical report [53] describing the method is being prepared.

### **Inverse Method for Determination of NDE Parameters**

Another important aspect of the NDE-Reliability connection is the choice of NDE technique (or tuning of parameters within a specific technique). The optimum choice of parameters can also be addressed by methods of analysis for inverse or optimization problems. For example, the choice of NDE parameters required to maintain failure probability at or below a specific value can be determined using inverse methods. In Fig. 58, the probability of failure at 20,000 cycles (given an initial inspection at cycle zero) is plotted as a function of the NDE parameter  $\alpha$ —a fixed value of  $\beta=3.5$  is used throughout. It can be seen, for example, that if a failure probability of  $4.0 \times 10^{-6}$  or below is required that the quantity  $1/(1+\alpha)$  must be 0.6 or so. This poses a restriction on the NDE technique (or variable parameters within a technique). A systematic inverse problem approach to these problems is being developed and will be written up as a Technical Report [54].

### **Stress Intensity Factors for Cracks in 3D**

Accurate and efficient methods for determination of stress intensity factors along curved (planar and non-planar) cracks in 3D components are being explored. We will work with Georgia Tech's Jianmin Qu (co-PI of Sections 2.1.2 and 2.2.1) in pursuing this area.

### **Generalized Reliability Index**

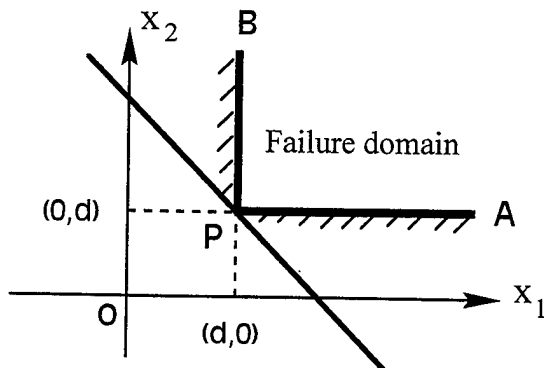
We have investigated the use of generalized reliability indices for application to problems in probabilistic fracture mechanics when statistical information is incomplete. This can happen in engineering practice, when we get a different distribution of the same variable from one researcher to another. For example, in this case, the mean of the resulting reliability indices can be used. This idea can be further extended to "minimum penalty generalized reliability index". In this approach there is a penalty for overestimation of safety. This is because overestimating of safety normally entails tangible or intangible consequences which are far greater in value than the purely economical consequences of underestimating the safety. Furthermore, this method also offers a valuable frame work for incorporating subjective information, such as an expert opinion regarding the parameters of a distribution, which is an indispensable source of information in many engineering applications.

## ACCOMPLISHMENTS OF M-URI YEAR 2

### Limit State Surface Element Method

A limitation of the first-order reliability method is that it can become inaccurate when the curvature of the failure hypersurface becomes large. (The failure surface is a surface which, at the load cycle in question, divides the space of random variables into safe and failure regions.) A method called the Limit State Surface Element Method has been developed and implemented into a general reliability framework. The method involves the discretization of the limit state hypersurface (also called the failure surface) into elements of finite size and using a specially designed integration scheme to integrate the failure probability over the failure region.

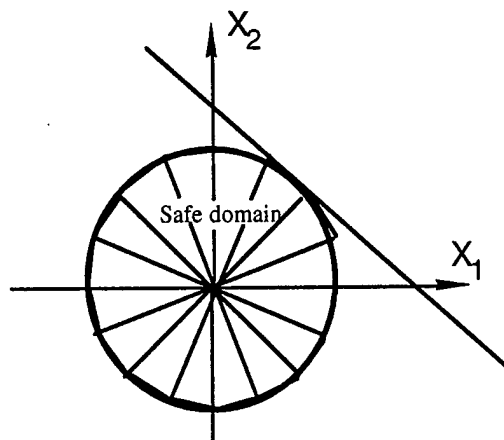
The method is illustrated in Figs. 54 and 55. In Fig. 54, a failure surface with an abrupt corner is discretized using two surface elements of infinite extent. Results from the Limit State Surface Element (LSSE) Method developed here and the previous first order reliability method are compared and the LSSE method is seen to be significantly more accurate with 6-digit accuracy compared to the exact solution. In Fig. 55, results for a circular failure surface and a spherical failure surface are shown and compared to the FORM results. Because of the surface curvature, these examples represent a stringent test case. As can be seen from the results in the tables, the LSSE method is much more accurate than the FORM and gives results within a few percent of the exact solution with a modest number (8) of surface elements. One particular advantage of the LSSE method is that it works very well for complicated failure surfaces whereas methods based on multiple tangent planes quickly become cumbersome because of the necessity to evaluate integrals over intersection regions. In addition, the LSSE method is especially suited to the calculation of failure probabilities for problems involving NDE inspections because the presence of the POD function destroys the standard normal behavior of the (mapped) probability distribution functions and therefore a general integration scheme is required. The method is described in detail in a technical report by Xu and Moran [52].



Solution for quarter space domain

$\sqrt{2} d$	FORM	Exact	LSSE method
1.0	0.841345	<b>0.941605</b>	0.942520
1.5	0.933193	<b>0.979142</b>	0.979142
2.0	0.977250	<b>0.993814</b>	0.993814
2.5	0.993790	<b>0.998513</b>	0.998513
3.0	0.998650	<b>0.999713</b>	0.999713

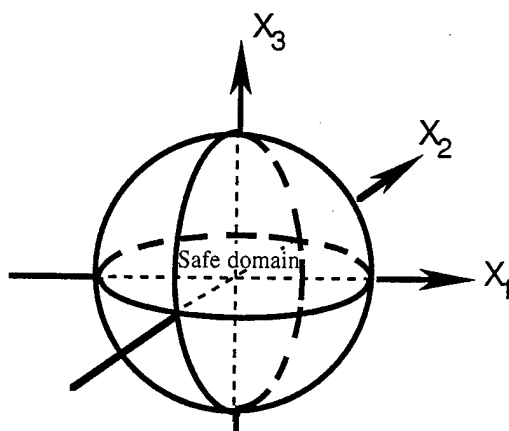
Figure 54. Solution for Quarter Space Domain



Solution for circular domain

a	FORM	Exact	LSSE method
1.0	0.8413	<b>0.3934</b>	0.3965
1.5	0.9332	<b>0.6753</b>	0.6791
2.0	0.9772	<b>0.8646</b>	0.8674
2.5	0.9938	<b>0.9560</b>	0.9574
3.0	0.9987	<b>0.9889</b>	0.9893

Figure 55a. Solution for Circular Domain

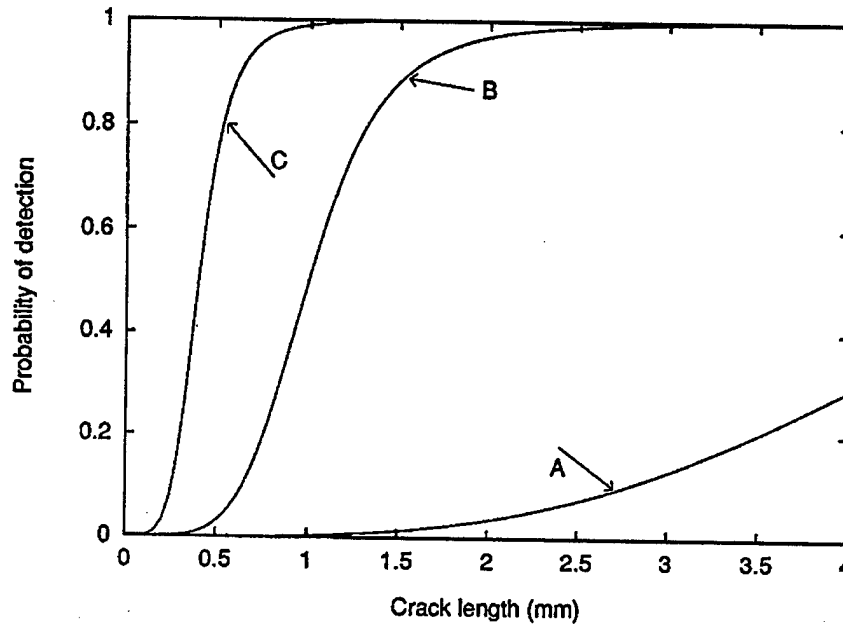


Solution for spherical domain

a	Form	Exact	LSSE method
1.0	0.8413	<b>0.1986</b>	0.2037
1.5	0.9332	<b>0.4778</b>	0.4865
2.0	0.9772	<b>0.7384</b>	0.7473
2.5	0.9938	<b>0.8999</b>	0.9054
3.0	0.9987	<b>0.9708</b>	0.9729

Figure 55b. Solution for Spherical Domain

$$POD(a) = \frac{\alpha a^\beta}{1 + \alpha a^\beta}$$



$A : \alpha = 0.0032 \text{ mm}^{-\beta}, \beta = 3.5;$

$B : \alpha = 1 \text{ mm}^{-\beta}, \beta = 5.0;$

$C : \alpha = 100 \text{ mm}^{-\beta}, \beta = 5.0$

Figure 56. Probability of Detection Curves

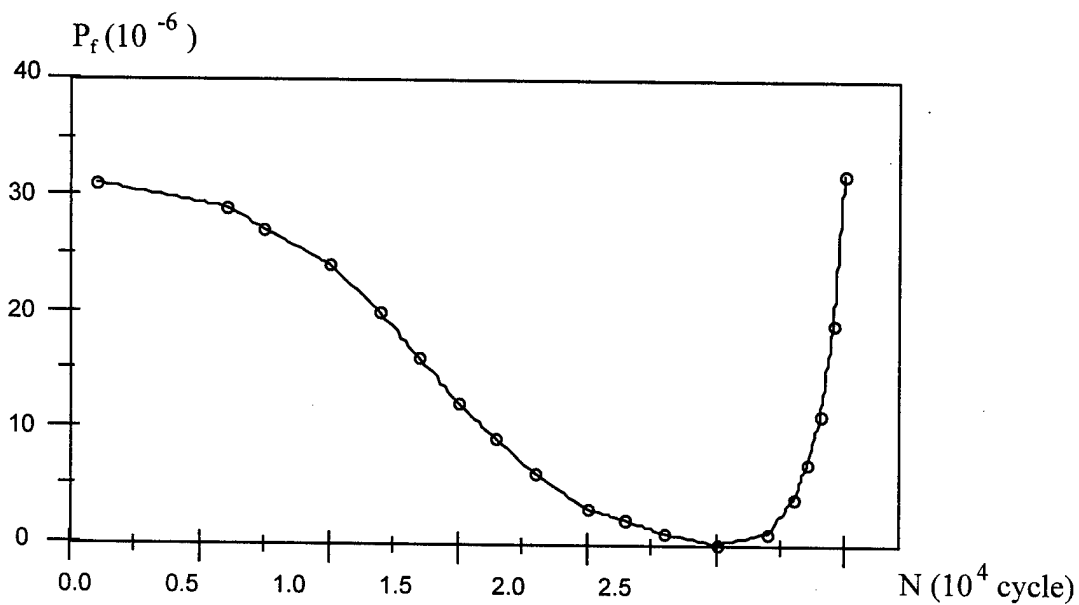


Figure 57. Probability of Failure vs. Inspection Time

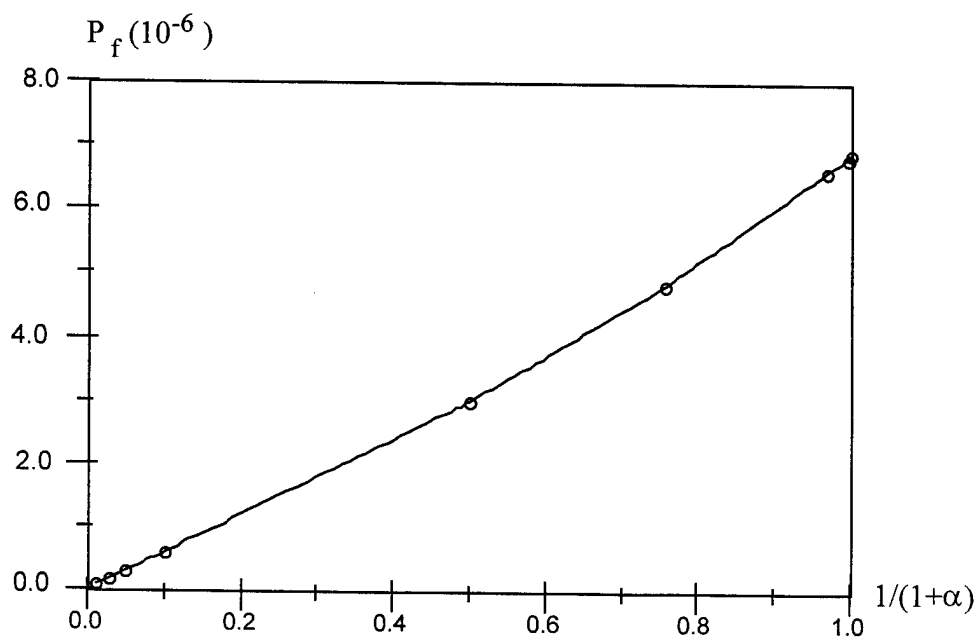


Figure 58. Failure Probability vs. Inspection Coefficient



### **PLANS FOR YEAR 3**

- The direct integration scheme [55] is currently implemented for cracks in 3D components and comparisons of the method with FORM and LSSE will be made for 3D problems. Accurate and efficient methods for determination of stress intensity factors along curved (planar and non-planar) cracks in 3D components will be further pursued.
- Further development of the Limit State Surface Element Method as a general tool for fatigue reliability problems.
- Development of optimization tools (based on probabilistic fracture mechanics) for inspection planning.
- Development of inverse problem methods for NDE technique/parameter determination.
- Application of fatigue reliability methodology to rotary components—discussion with Georgia Tech personnel (McDowell and Qu of Section 2.2.1) are underway in this regard.

### **Deliverables**

Completed research will be published in relevant technical journals on an ongoing basis and made available to interested parties. In addition, annual technical reports (aside from regular progress reports) will be written to summarize the status of the methodology together with details of the developments and applications.

4/30/97 Technical report on Limit State Surface Element Method

6/30/97 Technical report on optimization methods for inspection planning.

Technical Report on inverse problem methods for determination of NDE

2/15/98 Technical report on application of methodology to rotary component.

### ***Milestones***

2/15/98 Application of Methodology to selected component.

### **VISION FOR YEARS 4 AND 5**

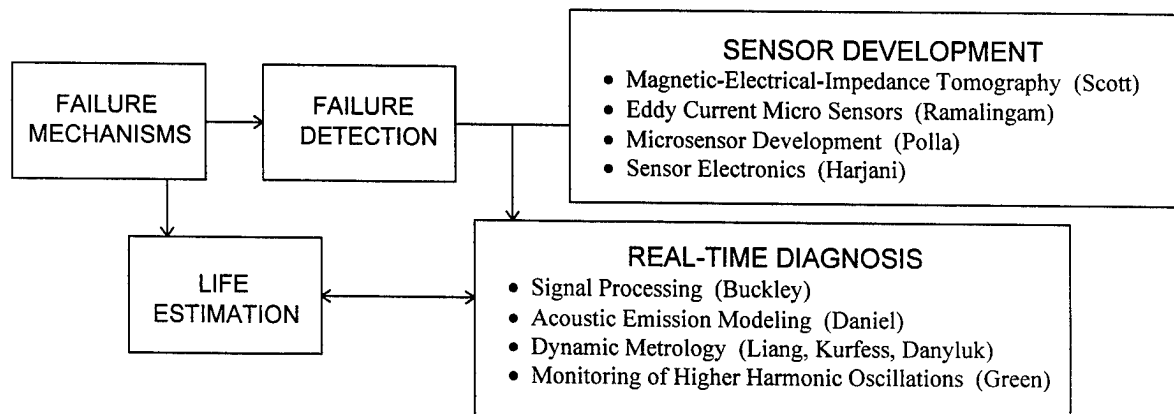
- Further development of probabilistic/fatigue reliability software for transfer to industry.
- Application to additional components.
- Development of Limit State Surface Element Method as a general purpose reliability tool.
- Extension of methodology to stochastic processes.

## Thrust Area III

### 2.3 DIRECT SENSING, ANALYSIS, REAL-TIME DIAGNOSIS

*Perform studies with respect to the responses of signals early in fault inception, including research on sensors that can be placed at critical sites on mechanical systems for responses to changes in variables of state or vibration.*

2.3.1	MAGNETIC-ELECTRICAL-IMPEDANCE TOMOGRAPHY .....	94
	Project Overview .....	94
	Accomplishments of M-URI Year 2 .....	94
	Plans for M-URI Year 3 .....	101
	Vision for Years 4 and 5 .....	101
2.3.2	EDDY-CURRENT MICRO SENSORS FOR INTEGRATED DIAGNOSTICS .....	111
	Project Overview .....	111
	Accomplishments of M-URI Year 2 .....	114
	Plans for M-URI Year 3 .....	117
	Vision for Years 4 and 5 .....	118
2.3.3	INTEGRATED MICROSENSORS FOR AIRCRAFT FATIGUE AND FAILURE WARNING .....	141
	Project Overview .....	141
	Sub-task 1: Microsensor Development .....	142
	Sub-task 2: Sensor Electronics .....	158
	Sub-task 3: Signal Processing .....	175
	a. Data Collection and Analysis .....	176
	Accomplishments of M-URI Year 2 .....	176
	Plans for M-URI Year 3 .....	177
	b. Noise Suppression and Transient Detection .....	179
	Accomplishments of M-URI Year 2 .....	180
	Plans for M-URI Year 3 .....	180
	c. Transient Signal Classification .....	183
	Accomplishments of M-URI Year 2 .....	183
	Plans for M-URI Year 3 .....	185
	Project Plans for M-URI Year 3 and Beyond .....	186
2.3.4	ACOUSTIC EMISSION MODELING FOR INTEGRATED DIAGNOSTICS .....	187
	Project Overview .....	187
	Accomplishments of M-URI Year 2 .....	187
	Plans for M-URI Year 3 .....	194
	Vision for Years 4 and 5 .....	194
2.3.5	DYNAMIC METROLOGY AS A WEAR DIAGNOSTIC .....	218
	Project Overview .....	218
	Accomplishments of M-URI Year 2 .....	219
	Plans for M-URI Year 3 .....	231
	Vision for Years 4 and 5 .....	232
2.3.6	MONITORING OF SUB OR HIGHER HARMONIC OSCILLATIONS IN ROTATING MACHINE ELEMENTS .....	233
	Project Overview .....	233
	Accomplishments of M-URI Year 2 .....	234
	Plans for M-URI Year 3 .....	250
	Vision for Years 4 and 5 .....	251



### DIRECT SENSING, ANALYSIS, REAL-TIME DIAGNOSIS

### **2.3.1 MAGNETIC-ELECTRICAL-IMPEDANCE TOMOGRAPHY**

Co-investigators: Waymond Scott and George Vachtsevanos (Georgia Tech)

M-URI Year 2 Funding Allocation: 4.4%

#### **PROJECT OVERVIEW**

The object of this research is to develop a new technique for noninvasively probing a piecewise homogenous body for small internal flaws on the order of 0.05 mm in size. The technique is a hybrid of two existing techniques - eddy current testing and electrical impedance tomography. In this technique, current is injected into the device under test with electrodes placed on the surface. The injected current flows between the electrodes along the surface of the device under test. Figure 59 is a diagram illustrating the current flowing between two electrodes on a device under test with and without a flaw. When a flaw is not present, the current flows smoothly between the electrodes; however, when a flaw is present, the current changes abruptly near the flaw. The abrupt change in the current will result in a distinctive signature in the magnetic field. A focusing magnetic probe is used to detect the magnetic signature of the flaw. Thus, by scanning the surface of the device under test with the focusing magnetic probe, one can locate a flaw by detecting the magnetic signature of the flaw. Since the depth at which the currents will penetrate into the device under test decreases with increasing frequency, one can also ascertain information about the depth of the flaw by adjusting the frequency of the injected currents.

#### **ACCOMPLISHMENTS OF M-URI YEAR 2**

This has been a very productive year for the project. The two-dimensional experimental test bed has been automated, the focusing probes have been greatly improved, the device under test has been generalized to a more practical geometry, and flaws as small as 0.1 mm have been detected.

##### **Experimental Test Bed**

Figure 60 is a schematic diagram of the experimental test bed designed and constructed for this project. The test bed is being used to demonstrate the viability of the new measurement technique and to evaluate the effectiveness of the focusing probes. The test bed consists of a HP3577a automatic network analyzer, a power amplifier, a matching transformer, a current probe, a differential low-noise amplifier, a focusing probe, a xy positioner, and a device under test. This year, the xy positioner has been added to the test bed and is used to scan the probe over the device under test. Both the positioner and the network analyzer are under computer control, so the probe can be automatically scanned across the device under test while its response is being recorded. The network analyzer is used to generate and analyze the signals for the test bed. Since the amplitude of the signal generated by the network analyzer is insufficient to adequately test and evaluate the system, the power amplifier is used to amplify the signal. Since the impedance of the device under test is much less than the output impedance of the power amplifier, a matching transformer is used to change the impedance level of the signal. The maximum amplitude of the current output by the matching transformer is approximately 45 A. The amplitude of this current is monitored using a current probe that is connected to the reference channel of the network analyzer. When this current is sent through the device under test, it will generate a magnetic field. The distribution of the magnetic fields will depend on the distribution of the currents in the device under test. The focusing probe is used to measure the magnetic fields and is designed to selectively respond to the magnetic signature of a flaw in the device under test. The output of the focusing probe is amplified by a differential, low-noise amplifier and is then input into a signal channel of the network analyzer. The network analyzer displays the magnitude and phase of the ratio of the signal to reference channels. The magnitude of this response is the strongest when the probe is placed over a flaw. Thus, by scanning the probe over the device under test one can determine the location of a flaw by monitoring the response.

#### **DIRECT SENSING, ANALYSIS, REAL-TIME DIAGNOSIS**

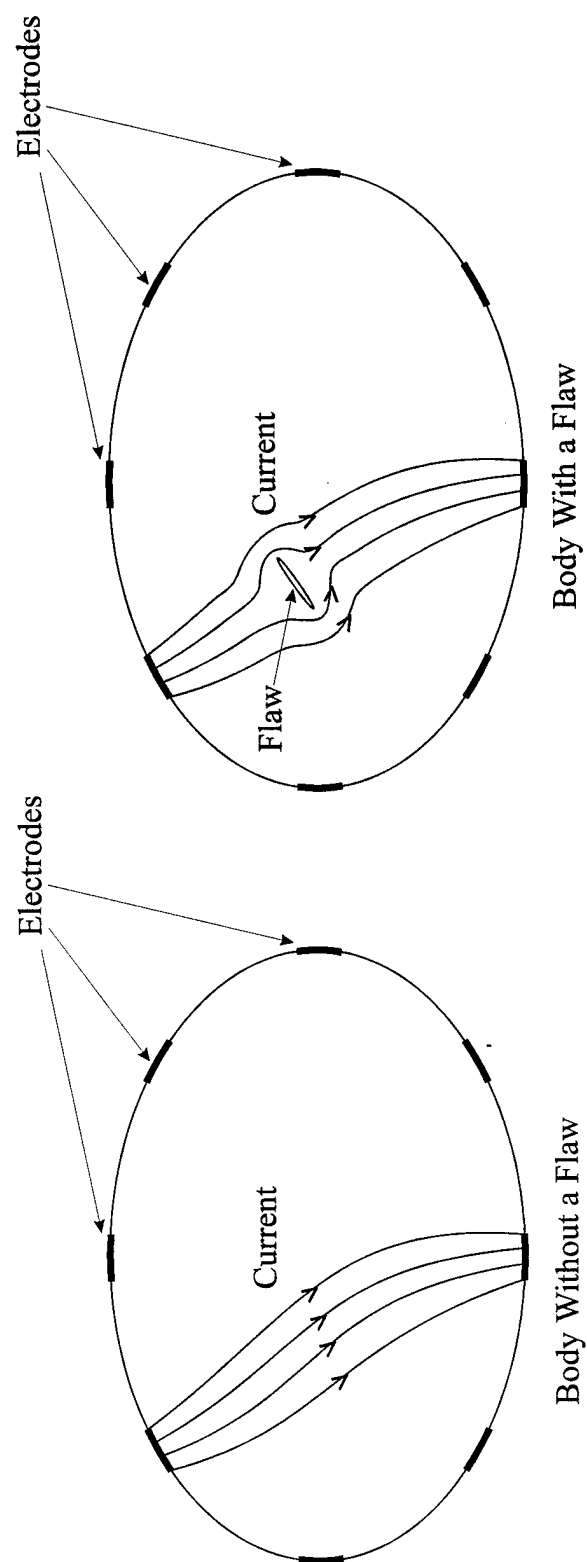


Figure 59. Diagram Illustrating the Current Flowing between Two Electrodes on a Device under Test with and without a Flaw



Two types of device under test were used this year, one with a symmetric return current and one without a symmetric return current. The device under test with the symmetric return current consists of a copper clad, circuit board with flaws machined into the copper cladding. The circuit board is approximately 28 cm wide, 40 cm long and 1.6 mm thick. The copper cladding is approximately 0.07 mm thick. The current is injected at one end of the copper cladding on the top of the circuit board and collected at the same end on the copper cladding on the bottom. The current flows from the top to the bottom cladding by way of a current shunt soldered on to the opposite end. For the initial tests, this geometry was chosen to make the flaws easier to detect. The extraneous magnetic fields generated by currents on the top and bottom claddings approximately cancel, making it easier to detect the magnetic field generated by a flaw in one of the sheets.

The device under test without the symmetric return current consist of a copper clad, circuit board with flaws machined into the copper cladding. The circuit board is approximately 27.3 cm wide, 45.7 cm long and 1.6 mm thick. The current is injected at one end of the copper cladding on the top of the circuit board and collected on the opposite end and returned though a cable as shown in Fig. 60. The extraneous magnetic fields generated by the currents on the cladding are much larger for this configuration. This change in geometry has made it more difficult to detect the flaws and has led to complications in the design of the focusing probes.

### **Focusing Probes**

The focusing probes are the heart of the flaw detection technique. A perfect focusing probe would respond strongly to the magnetic signature of the flaw and would not respond at all to extraneous magnetic fields. Unfortunately, it is not possible to build a perfect probe. Last year a focusing probe was developed that was shown to be very effective. The probe uses magnetic materials to help focus the field in a manner very much like that in the head of a tape recorder or computer disk. This year we have concentrated on improving the performance of the focusing probes, and have greatly improve their performance.

Sketches of a few of the focusing probes that have been investigated are shown in Figs. 61 and 62. The probes will be referred to as C, D, X, and H type as indicated in the figures. The probes are made of a ferrite material with a relative permeability of approximately 5000. The magnetic coils are wrapped around the portion of the core opposite the slit, and the slit portion of the core is placed next to the device under test. Testing has been performed with the probes in two configurations: a single probe which behaves similarly to a magnetic dipole, and a differential pair of probes which behave similarly to a magnetic quadrapole. The differential pair of probes are aligned so that the axes of the probes are along the same line and are located 1 cm apart for the C, D, and X types and 4 mm apart for the H type. In all cases the differential pair of probes has performed better than the single probe.

The C, D, and X type probes were investigated first. The performance of each these probes was roughly equivalent. Overall, the X probe performed slightly better that the others. It had a slightly stronger response to the small flaws than did the other probes and, it had a more localized response to the flaw. However, it had a slightly weaker response to the larger flaws. The X probe is much more difficult to fabricate and is very fragile; these disadvantages seem to outweigh the small performance advantages of this probe. The C and D type probes performed very similarly. However, in practice it was much easier to align and use the D type probes because of their flat bottoms. When used in the differential mode the C, D, and X probes performed well on the device under test with the symmetric return current, however they did not perform nearly as well for the device under test with out the symmetric return current. This is because the extraneous magnetic fields are much larger for the device under test without the symmetric return current.

Shielding was also investigated to improve the performance of the probes for the device under test without the symmetric return current. Shielding was found to be effective for both single and

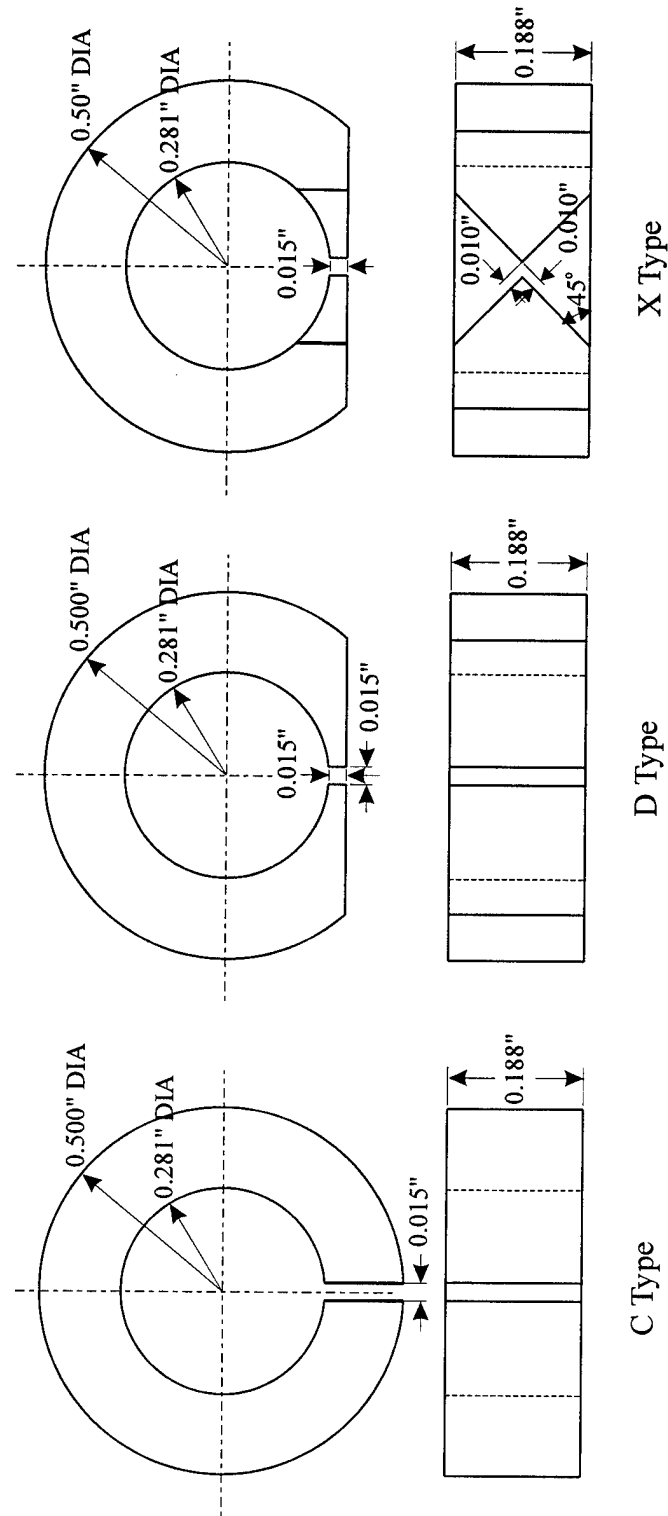


Figure 61. Drawings of the C, D and X-type Focusing Probes

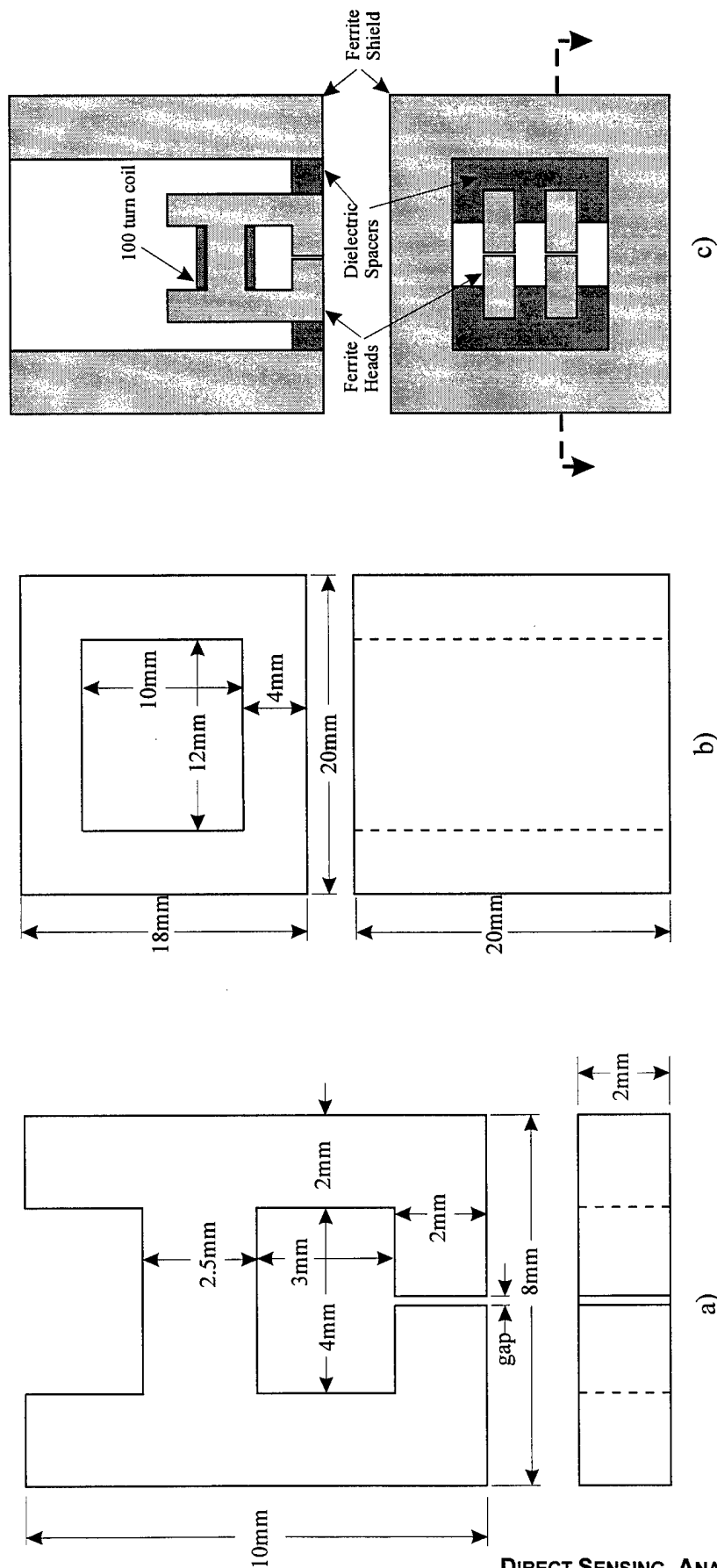


Figure 62. Shielded Differential H-type Probe: a) Ferrite H Head; b) Ferrite Shield; c) Assembly Drawing



differential probes. The differential shielded probes performed the best. Reducing the size of the probes was also found to improve the performance of the probes.

Using these ideas a new probe was designed and fabricated. A sketch of this probe is shown in Fig. 62. It will be referred to as the H type probe. It uses a ferrite shield to partially shield it from the extraneous magnetic fields, and it is smaller so that the extraneous fields that fringe around the shield will be smaller, and it is differential so that the extraneous fields that fringe around the shield are partially canceled. Thus, this probe will be relatively insensitive to the extraneous field. Three of these probes were fabricated with gaps of 0.13 mm, 0.25 mm, and 0.50 mm. Currently only the probe with a gap of 0.25 mm has been tested. These test show that the H type probe performs much better than the other probes that have been investigated.

To demonstrate the performance of the H type probes, measurements were made in which the probe was scanned across the device under test without a symmetric return current in which flaws of known size were machined. The location and size of the flaws in the scanned region of the device under test are shown in Fig. 63. The flaws are labeled A through N and vary in size from 0.1 mm to 2.6 mm. Flaws A through G are in the central portion of the device under test and flaws H through N are in the edges of the device under test. The region over which the scanning was performed is also indicated in Fig. 63. The probe was successively scanned across the device under test in the  $x$  direction with  $y$  being incremented after each scan. The size of the scanned region is 29.4 cm by 23.5 cm.

The magnitude and phase of the response of the probe

$$R(x, y) = \frac{V_p}{I} \quad (3)$$

is recorded as a function of  $x$  and  $y$ . After the scanning is complete, the response is differenced to enhance the signature of the flaws:

$$R_D(x, y) = R(x, y + \Delta y) - R(x, y) \quad (4)$$

where  $\Delta y$  is the differencing increment.

The magnitude of the differenced response  $R_D$  is graphed as a function of  $x$  and  $y$  using a color graph in Fig. 64, where  $\Delta y = 2$  mm and the frequency of the current is  $f = 1$  kHz. The color scale for the graph is also indicated in the figure: levels between -132 dB and -120 dB are shown with the indicated scale, levels below -132 dB are shown in blue, and levels above -120 dB are shown in red. The location of all of the flaws is clearly discernible on this figure, even the 0.1 mm flaw. The response is seen to be very large for the larger flaws, and is seen to be significant for the smaller flaws. The response is also seen to be significant away from the machined flaws at a few locations near the edges; this is believed to be due to small nicks in the edges of the device under test. For the larger flaws, the responses in Fig. 64 are seen to have a very distinctive pattern of nine dots arranged in a three by three array for the flaws in the central portion of the device under test, and the responses are seen to have a very distinctive pattern of six dots arranged in a two by three array for the flaws on the edge of the device under test. For the smaller flaws, the patterns are partially obscured by the response to the extraneous fields. Only one of the dots can be seen for the smallest flaw, G. It is believed that the distinctive nature of the response can be used with a signal processing routine to enhance the sensitivity of the technique to smaller flaws.

The magnitude and phase of the differenced response  $R_D$  of the probe are graphed in Figs. 65 through 69 as a function of  $x$  for selected values of  $y$  in which the probe passes over the flaws labeled A, C, G, K, and H, respectively. In each of the figures, the strongest response is seen to be when the probe is over the flaw, and the response due to the extraneous field is seen to be approximately -135 dB. A portion of this extraneous response is believed to be due to the texture in the circuit board caused by the weave in the fiberglass substrate. The responses are seen to have a very distinctive pattern

of three peaks with the center one being the strongest for the flaws in the central portion of the device under test, and the responses are seen to have a very distinctive pattern of two peaks for the flaws on the edge of the device under test. These distinctive patterns are discernible for all of the flaws even the smallest ones.

The maximum magnitude of the differenced response  $R_D$  at each flaw is graphed in Fig. 70 as a function of the size of the flaw. The amplitude of the differenced response can be seen to strongly depend on the size of the flaw. The response is seen to be slightly stronger for the flaws on the edges. The data on the graph is seen to lie approximately on a straight line. This indicates that it is possible to infer the size of the flaw from the magnitude of the response. This simple relationship between the magnitude of the response and the distinctive pattern of the responses of the flaws, seen in Fig. 64, is strong evidence that it would be possible to develop an algorithm to identify the location and the size of a flaw.

### **PLANS FOR YEAR 3**

1. Investigate the application of the technique to a three-dimensional device under test.
2. Investigate the application of the technique to magnetic (steel) devices.
3. Investigate the measurement of the depth of the flaws, by adjusting the frequency of the injected currents.
4. Improve the focusing probes. This year we have greatly improved the focusing probes, but more improvement may be needed for three-dimensional and magnetic devices under test.
5. Investigate signal processing routines to help in the location and characterization of the flaws.

### **VISION FOR YEARS 4 AND 5**

1. Investigate a technique that has the potential to greatly improve the focusing probes. In this technique, the focusing probe will be vibrated in a plane tangential to the surface of the device under test. These vibrations will modulate the response of the probe and may make it possible to significantly improve the performance of the probes.
2. Investigate the application of the technique to more complex geometries.
3. Continue the investigation of signal processing routines to help in the location and characterization of the flaws.

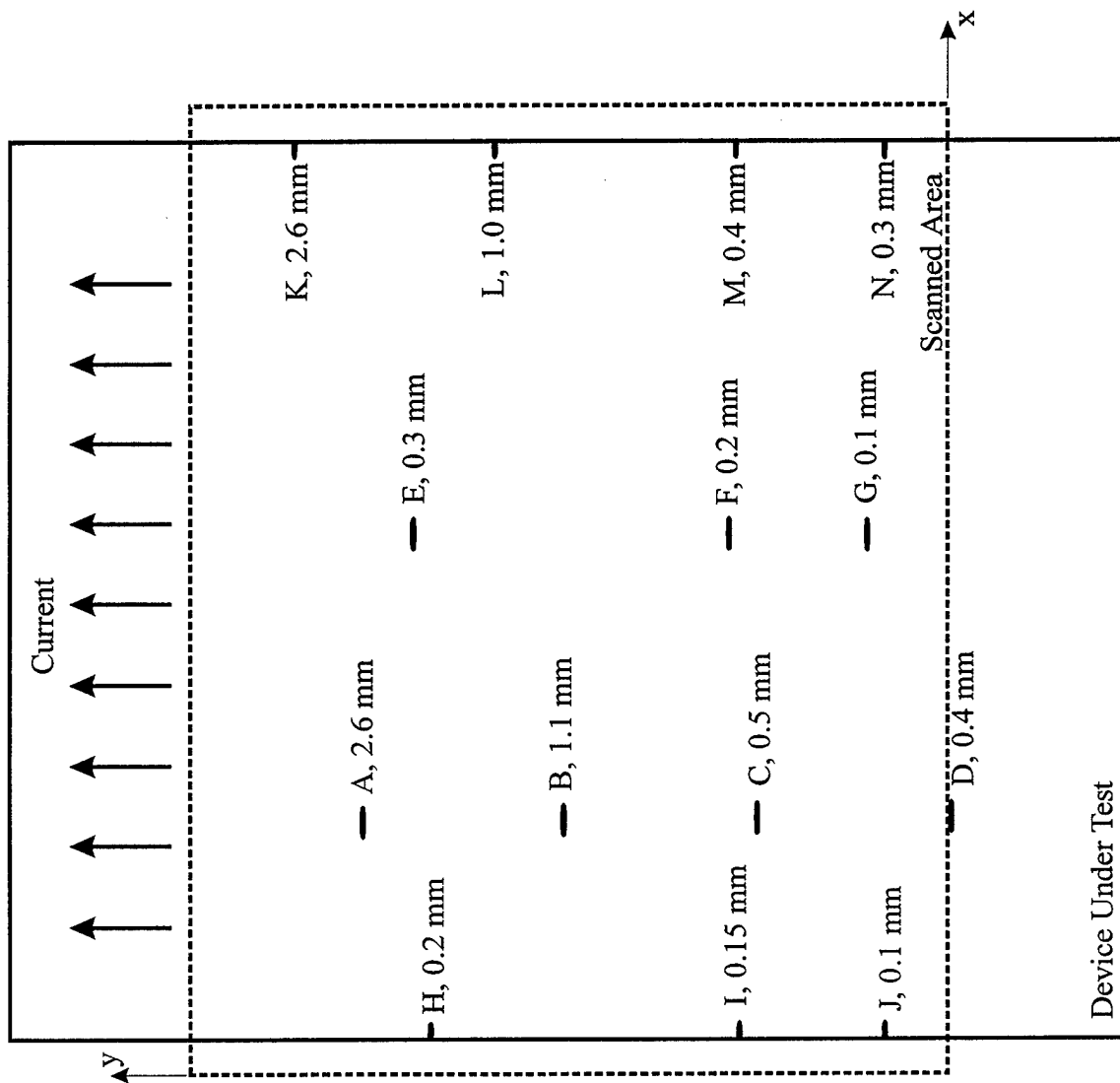


Figure 63. Diagram Indicating the Region Scanned and the Location and Size of the Flaws

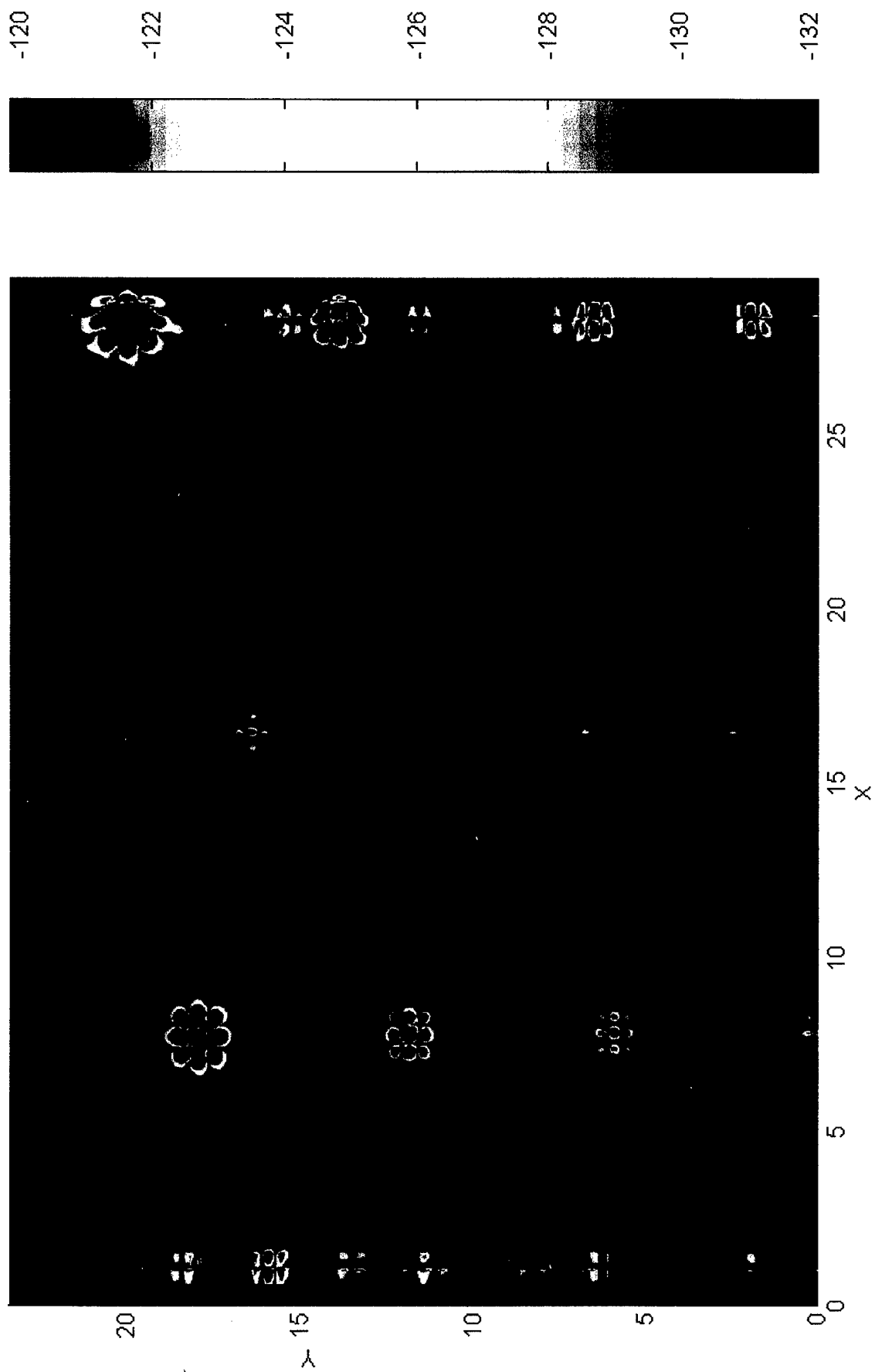
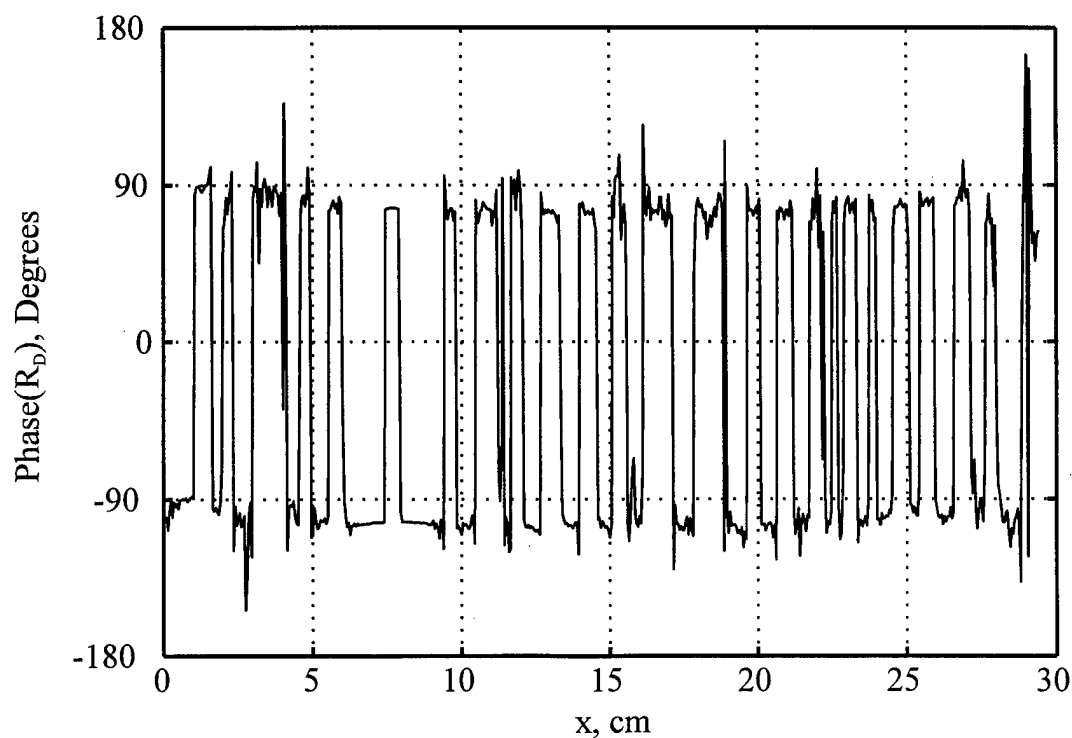
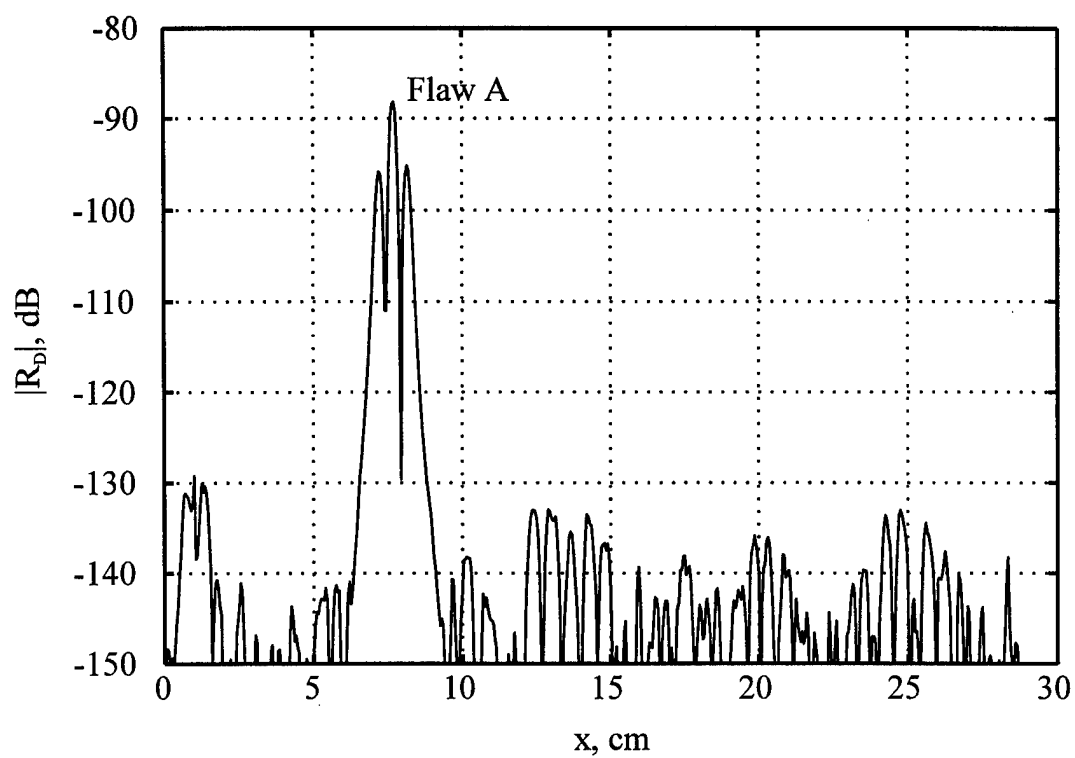
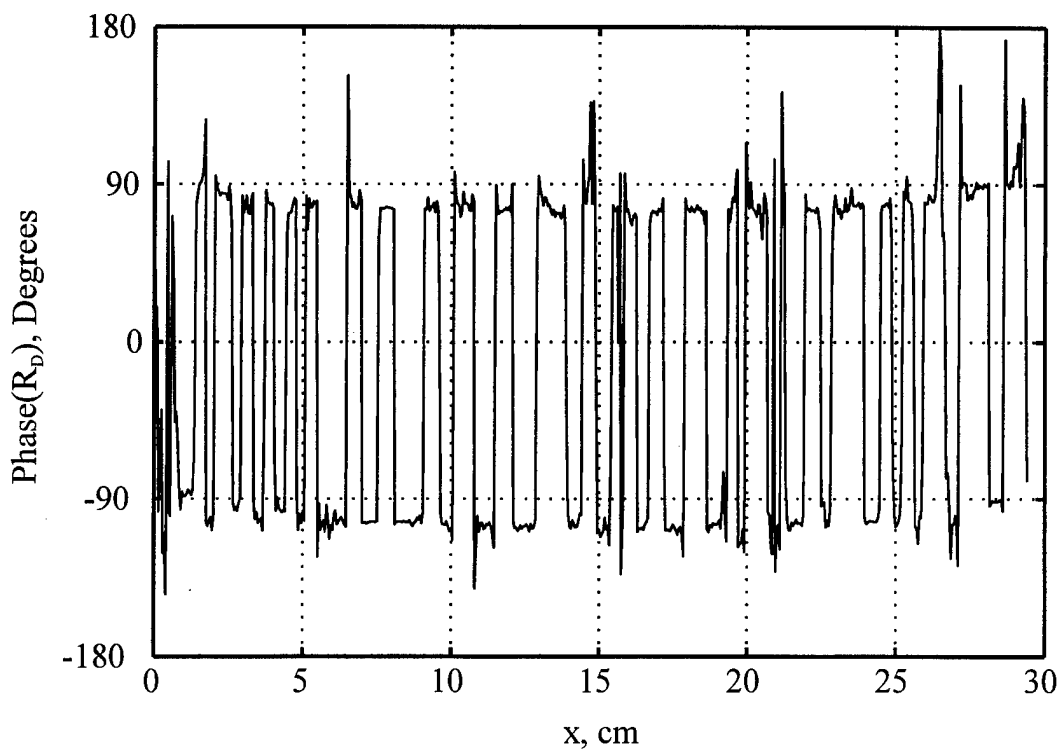
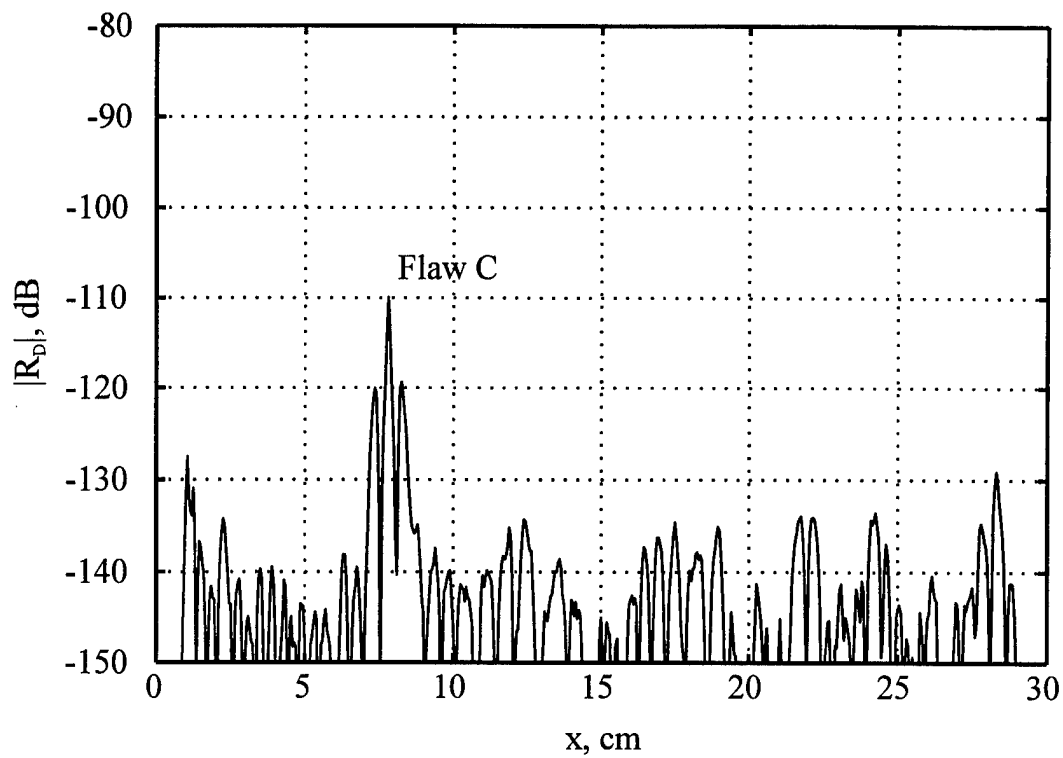


Figure 64. Color graph of the magnitude of the differenced response.



**Figure 65.** Graph of the Magnitude and Phase of the Differenced Response for Flaw A as a Function of  $x$



**Figure 66.** Graph of the Magnitude and Phase of the Differenced Response for Flaw C as a Function of  $x$

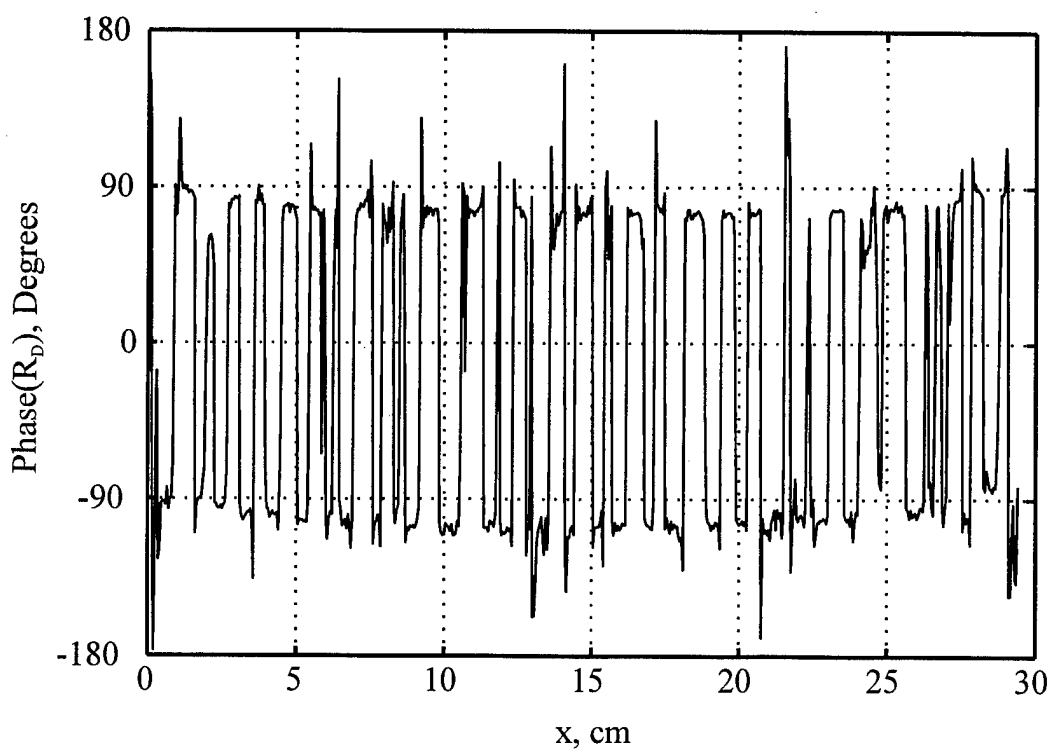
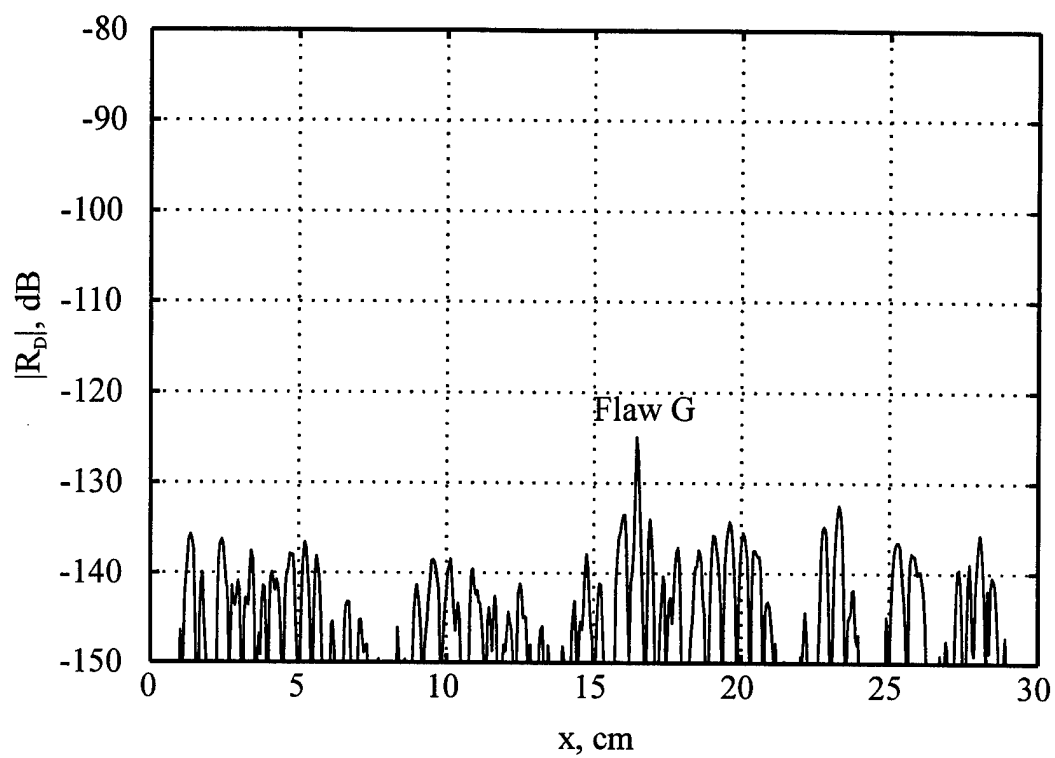


**Figure 67.** Graph of the Magnitude and Phase of the Differenced Response for Flaw G as a Function of  $x$

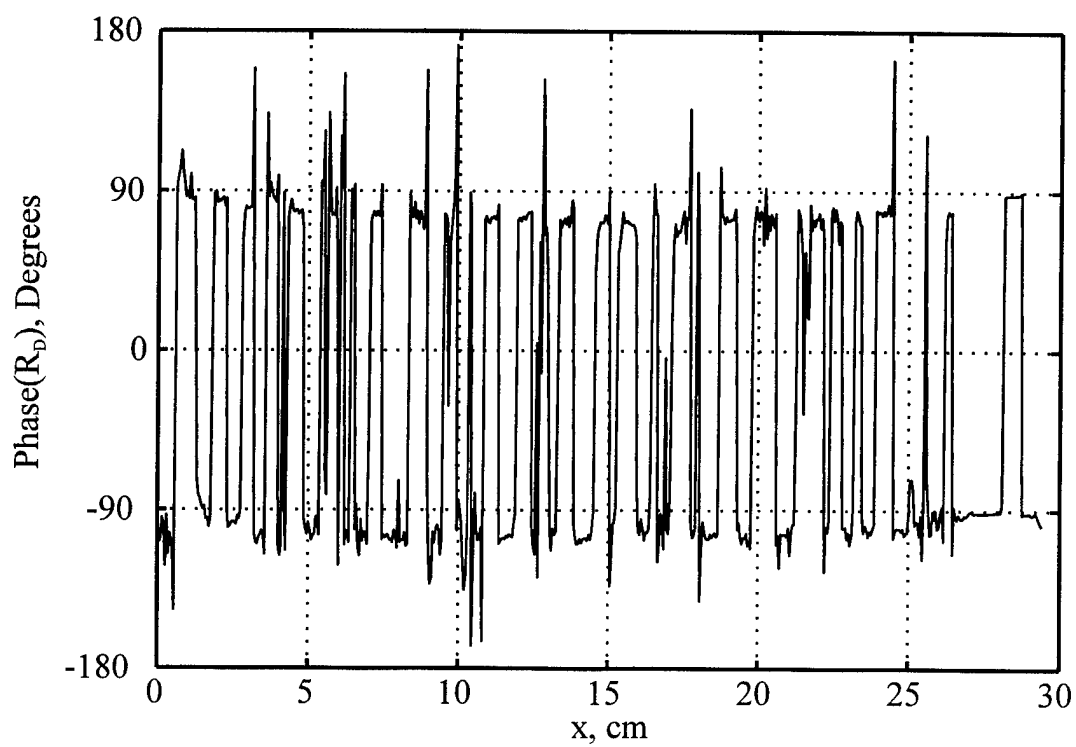
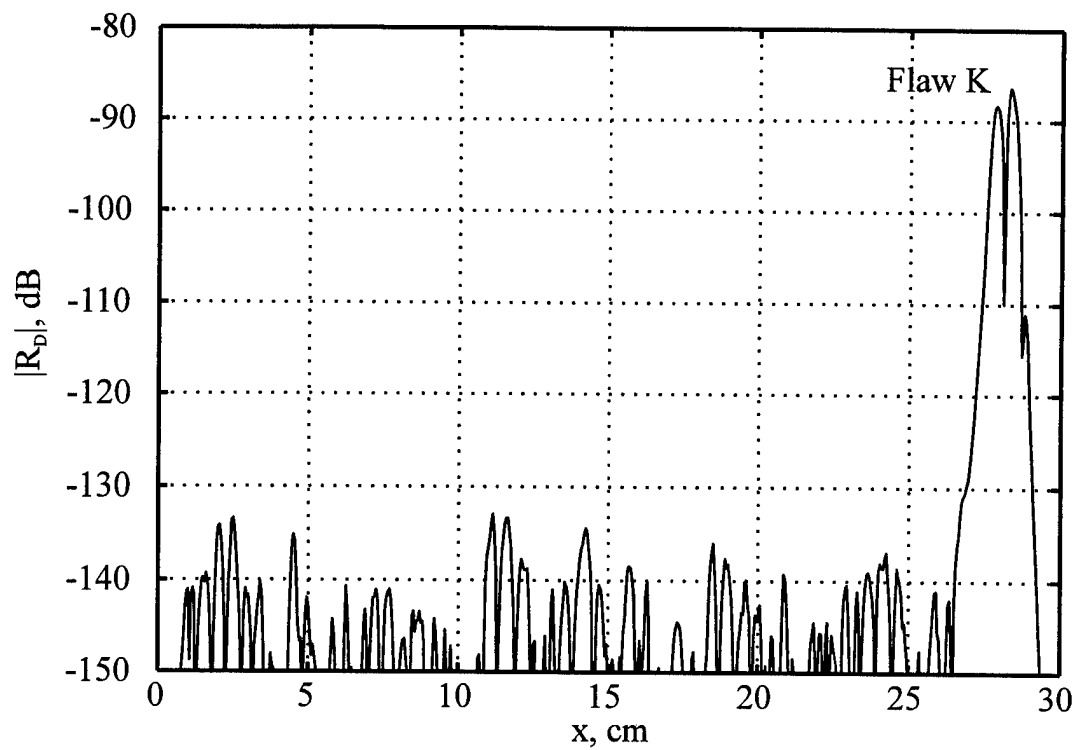


**Figure 68.** Graph of the Magnitude and Phase of the Differenced Response for Flaw K as a Function of  $x$



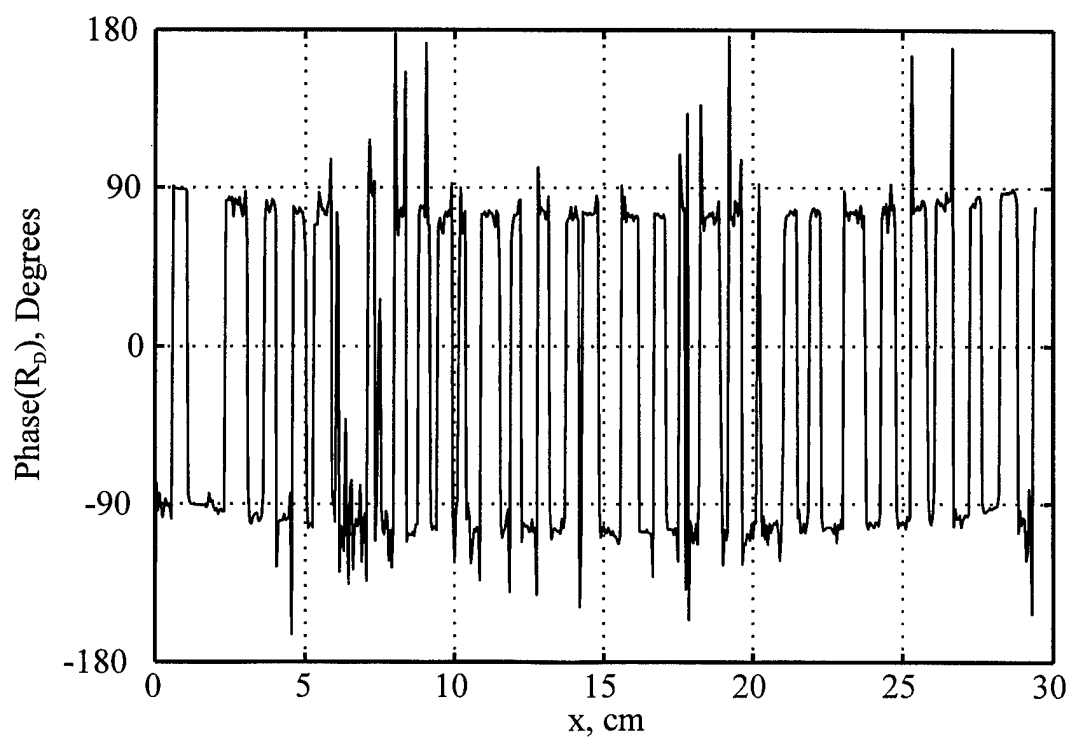
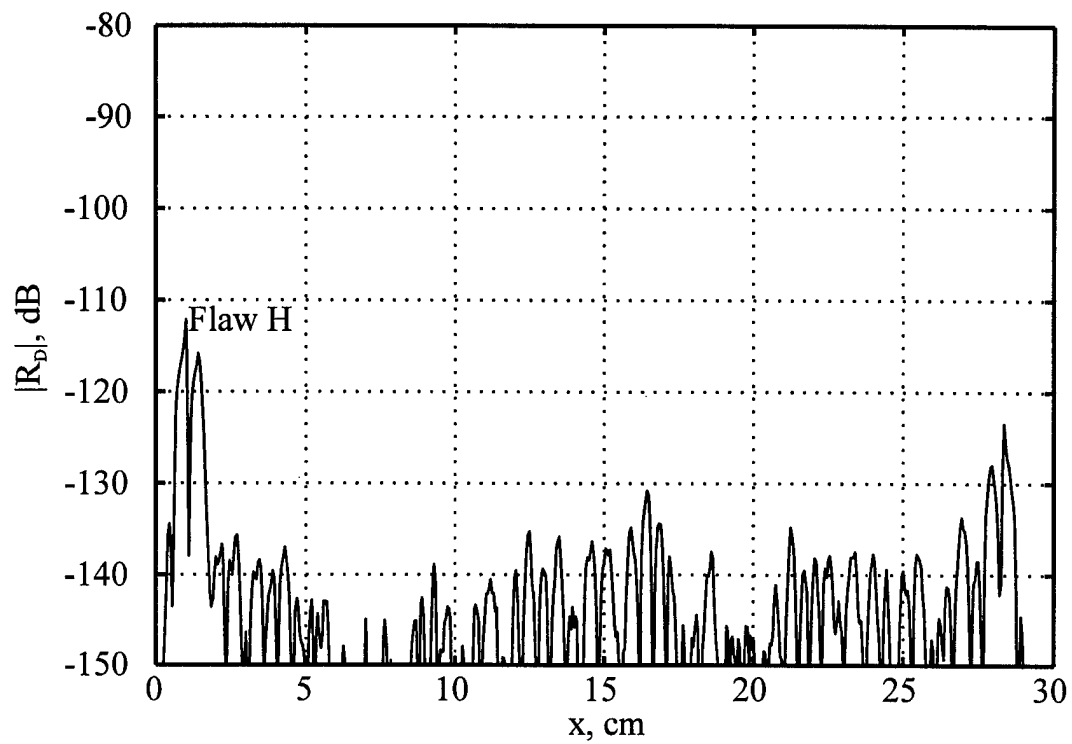


**Figure 69.** Graph of the Magnitude and Phase of the Differenced Response for Flaw H as a Function of  $x$

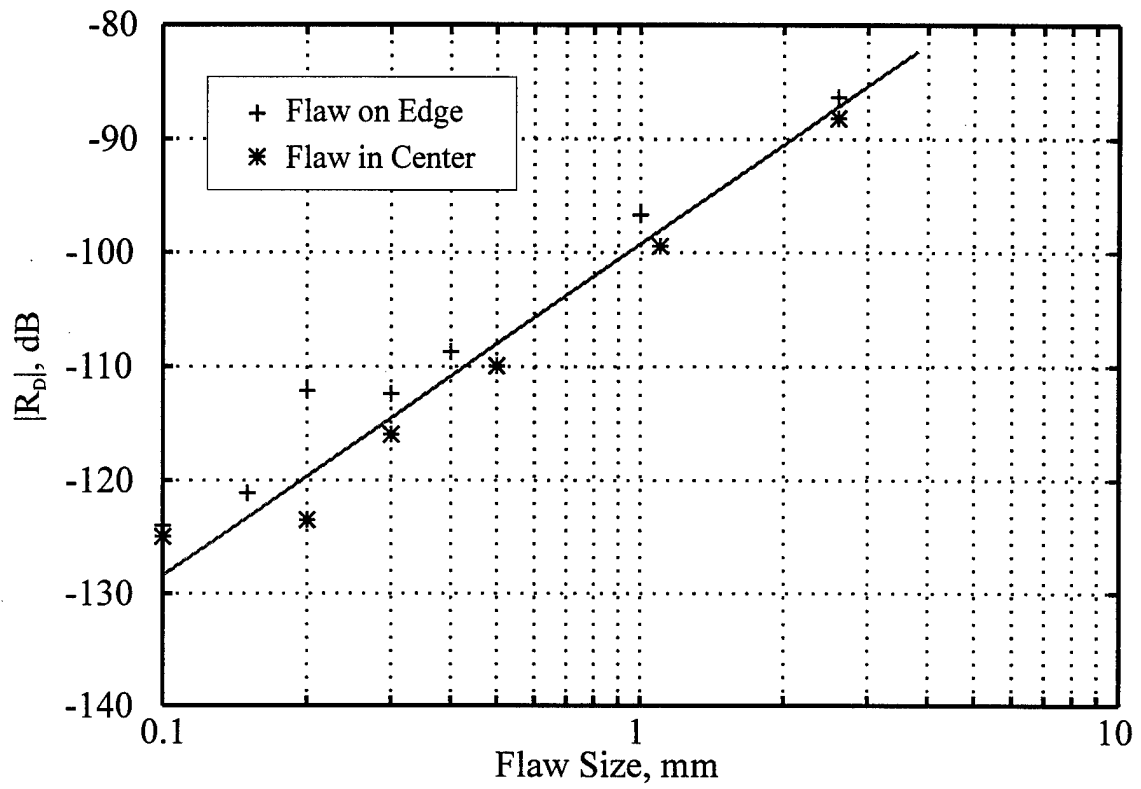


**Figure 70.** Maximum Amplitude of the Differenced Response at each Flaw as a Function of the Size of the Flaw

### 2.3.2 EDDY CURRENT MICRO SENSORS FOR INTEGRATED DIAGNOSTICS

Co-investigator: S. Ramalingam (University of Minnesota)

M-URI Year 2 Funding Allocation: 5.9%

#### PROJECT OVERVIEW

Eddy Current (EC) inspection techniques for flaw detection are well-developed and in wide use. In conventional EC inspection, a co-axial excitation and sensing coil assembly is used to interrogate the test object. Signal detected is due to excitation coil-sensing coil coupling as well as that due to sensor-test object coupling. The direct coupling contribution is large, and it is frequently compensated for using different measurement strategies and with appropriate electronic instrumentation [56-58]. Test object coupling varies with stand-off distance, electron transport and magnetic properties of the test object, and the flaw the characteristics (size, shape and orientation) within the test body. Inspection techniques used must make necessary provisions to compensate for these variations.

Conventional EC inspection is carried out by measuring changes in impedance of the sensor coil with the inspection coil assembly at a fixed stand-off distance. An unflawed test object serves as the reference. Normalized impedance plot is then used for flaw sensing and detection. Use of well-trained operators is necessary to identify and classify flaws since changes in impedance due to flaws are small.

All other factors remaining constant, if now the flaw dimensions are reduced, there is a corresponding reduction in the sensed signal. When, even with high precision signal measurement, the presence of flaws can not be reliably detected, a resolution threshold is said to be reached. Resolution limit in present generation EC measurement systems is a few millimeters.

Critical components of the rotary and fixed-wing aircraft now in use by the Navy and other services are highly stressed components subject to complex aerodynamic and operational loading. High-strength, fracture-resistant materials are used for extended component lives and reliability. Materials used have a longer life in the (fatigue) flaw initiation stage than in the flaw growth or propagation phase of component life. Early flaw detection can permit enhanced operational safety and reliability as well as less expensive repair and reconditioning. Safety and reparability needs can be met with early flaw detection, when the flaw dimensions are well below 1 mm. A detection threshold of tens of microns is therefore sought in this part of the ONR/M-URI program.

Impedance changes accompanying the presence of very small flaws are subtle, requiring highly skilled operators and sensitive instrumentation. Even with these resources, flaw detection is based on subjective judgment. Objective flaw detection methods (flaw imaging, for example) are, hence, preferred in this program to assure EC *inspection reliability*.

EC inspection time increases as the flaw resolution limits are lowered (inversely proportional flaw dimensions). Since, small flaw detection requires large inspection times, reliable flaw detection requires operator alertness over extended time durations. Some form of EC inspection compatible with automation strategies is desirable both to raise flaw detection reliability and to reduce inspection costs.

The objectives of this project of the ONR/M-URI program on Integrated Diagnostics are, therefore, to adapt and enhance the resolution limit of EC inspection techniques for flaw detection in order to enable flaw detection in much earlier stages of a component's life, and at the same time, to develop *automation-compatible EC imaging methods* for reliable flaw sensing.

Two parts of the ONR/M-URI program (this project and the Magnetic-Electrical-Impedance Tomography project described in Section 2.3.1) address the surface and near-surface micro-flaw detection-identification-imaging issues. EC Sensors and imaging techniques developed in this program will be made available to support the Magnetic-Electrical-Impedance Tomography project as well.

### **Objective**

Eddy current micro-sensors are being developed in this part of the ONR/M-URI program to detect small flaws nucleated in the initiation phases of fatigue cracking in highly stressed, critical components of the Navy and other flight systems. Resolution limit sought is in the tens of micron range. To reduce inspection time, cost, and personnel requirements, array sensors are also being developed.

To permit objective flaw identification, imaging techniques are being developed for digital flaw display. Micro sensors and sensor arrays under development are, thus, intended for use in automated inspection systems. The test object(s) are to be scanned with the sensor or sensor array, and the signals acquired are to be digitally displayed for objective flaw imaging. It could eventually lead to automated flaw sensing and identification.

### **Approach**

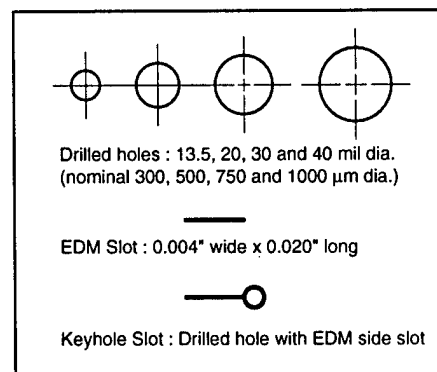
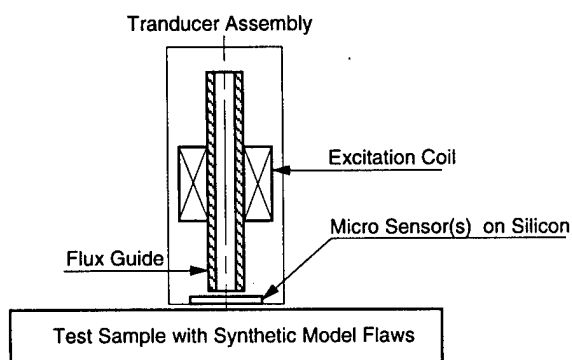
Resolution limit in EC inspection depends on the ratio of test object volume producing the output signal to the total volume interrogated by the excitation coil. Both the coil dimensions and the interrogation frequency can be changed to reduce the interrogation volume. This reduces the excitation power transferred into the test object and the signal from the flawed test object. However, it has been demonstrated that micro sensors and micro sensor arrays can be used to resolve small flaws [58]. But, to transfer sufficient interrogation power to the test object, a large enveloping excitation coil, spanning all the micro sensors, was necessary. Phase-locked loops were also needed to acquire the low level signals in the presence of noise.

To lower measurement complexity and to raise interrogating power transfer, flux-focusing (based on work at NASA-Langley aimed at shielding the sensing coil from the excitation coil) can be used. Computer simulations were used in the First Year of this project to investigate the utility of flux-focusing for EC inspection [59]. Macro-scale sensors with and without a ferromagnetic pole piece were used in analytical and experimental studies. For experimental evaluation, test objects with through-the-thickness and surface-breaking flaws were used.

Calculated results (with high relative permeability iron pole piece and with non-ferromagnetic Al pole piece) showed that a ten-fold improvement in power transfer is feasible by flux focusing and that flux focusing is feasible at low (25 kHz) and moderate (100 kHz) frequencies [59]. Changes in magnitude and spatial location of peak eddy current densities with flaw geometry, and the changes observed in induced current density in the sensing coil, indicated that the flux focusing has a sound physical basis. The results also indicated that although the probe resolution limit will depend on the pole piece/excitation coil dimensions, flux focusing in combination with use of micro sensors for EC inspection can lead to an order of magnitude improvement in spatial resolution.

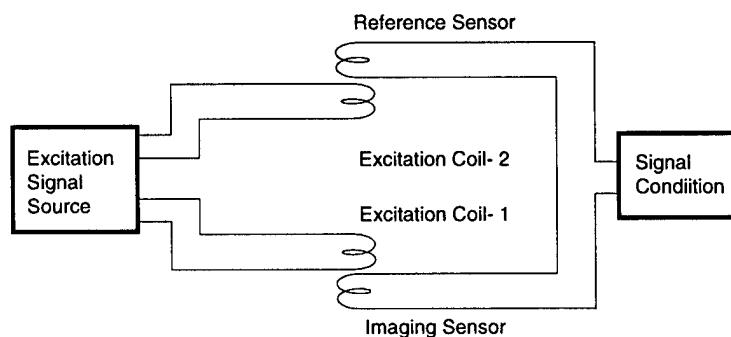
To experimentally validate the calculations, a motor-driven x-y table (Fig. 71) was assembled and an eddy current probe was constructed with the same excitation coil, sensor coil and pole piece dimensions as those used for modeling. Flaw map constructed by scanning a through-the-thickness flaw (drilled hole, 1/4" in diameter) in a steel plate, showed that edge detection dominates, as predicted by numerical simulations, raising the apparent flaw size (Fig. 86a, Ref. 59). Efficient power transfer by flux focusing is attested to by EC signal acquisition requiring no gain.

However, the flaw map constructed by scanning a narrow through-the-thickness flaw in a steel plate (0.008" EDM wide slot, 0.500" in length terminating at a drilled hole, 0.080" in diameter - similar to the keyhole slot shown in Figure 71b) failed to detect the EDM segment of the model flaw. The asymmetric linear flaw mapped as two neighboring hillocks spaced at approximately the flaw length (Fig. 86b, Ref. 59 and Fig. 7b, Ref. 60). A smaller probe (3 mm or 1/8" diameter) was built and used to verify that improved spatial resolution is feasible by scale reduction [59,60].

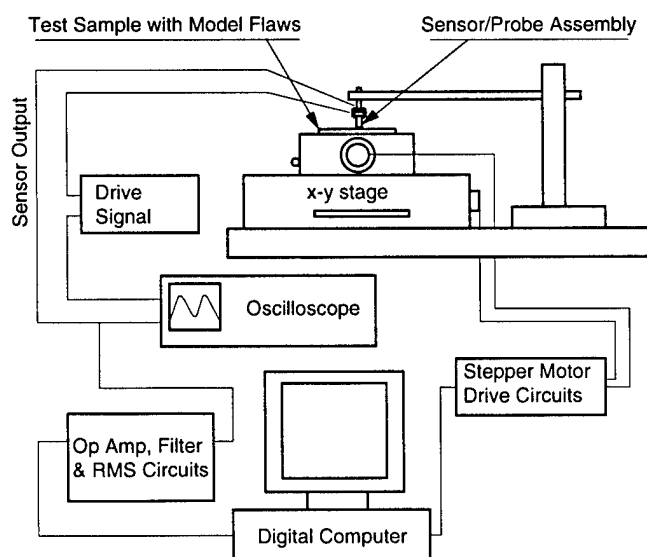


a. Schematic of the Eddy Current Imaging Test Rig

b. Model Flaws in Test Samples Used in 1996-97



c. Dual Probe, Differential Sensing Scheme



d. Schematic of the Eddy Current Imaging Rig

**Figure 71.** Eddy current (EC) inspection system assembled for flaw detection and flaw imaging

## ACCOMPLISHMENTS OF M-URI YEAR 2

To lower the edge domination effects, a dual-probe, differential scanning scheme has been developed this year. It is shown schematically in Fig. 71c. Thin film micro sensors, constructed on Silicon substrates, were used with small diameter flux focusing tubes (flux guide of Fig. 71a) to image the much smaller model flaws (shown in Fig. 71b) using the EC imaging rig shown schematically in Fig. 71d.

Based on the analytical and experimental results obtained in First Year's Effort, the 50 turn x 50 turn coil geometry proposed previously (Fig. 88 of Ref. 59) was implemented this year solely to develop micro sensor fabrication processes. These large (4.5 mm square) micro sensors fabricated on Silicon substrates have now been replaced with sensors using 10  $\mu\text{m}$  technology shown in Fig. 72a. The array sensors implemented in Silicon (1300  $\mu\text{m}$  square sensors; 4 x 4 array; 1.5 mm sensor-to-sensor spacing) are shown in Figs. 72b and 73a. Plan view of a complete single element micro sensor (actually two complete sensors used for differential scanning) is shown in Fig. 73b (cross section shown schematically in Fig. 71a).

The EC Imaging Rig (Fig. 71) developed permitted computerized data acquisition and reconstruction of a model flaw (1 mm or 0.040 dia. drilled hole) in the test object. The dual-probe, differential sensing/scanning scheme implemented substantially reduces edge domination effects. Striking flaw images have been obtained. One example is shown in Fig. 74.

This image was constructed from the EC micro sensor operating under the following conditions.

Device: 1.3 mm x 1.3 mm thin film, 20-turn micro sensors; nominal resistance = 235  $\frac{1}{2}$ .

Ingot iron flux focusing pole piece : Tube OD 0.110" (2.79 mm); ID: 0.086" (2.18 mm) and wall thickness: 0.012" (0.305 mm).

Excitation coil: ~ 200 turns; # 36 copper wire: 4  $\frac{1}{2}$  coil (DC resistance) driven at 50 kHz.

Excitation voltage: 1.0-1.2 VAC; Signal amplifier gain (flat to 50 kHz) ~ 300.

Table scanning speed along X and Y: 4.0 inches/min; Eddy Current signal acquired at Dx = Dy = 0.001" with a sensor lift-off ~ 0.008" (0.2 mm).

With the EC imaging system operating at the measurement conditions enumerated, experimental studies have been carried out to establish the resolution limit of single-element micro sensors. EC contour and 3-D images obtained with test samples containing model flaws are shown in Figs. 75 to 81.

Model flaws used are shown in Fig. 71b. They represent through-the-thickness flaws (drilled holes: 0.040, 0.030, 0.020 and 0.0135 inches in diameter), a shallow linear defect (EDM slot 0.004 in. in width, 0.200 in. in length and 0.040 in. deep) and a keyhole defect representing a 'blunted crack'.

For through-the-thickness flaws, the resolution limit reached is 300  $\mu\text{m}$  or 0.0135", which is more than an order of magnitude better than was possible in M-URI Year 1 (1/4 inch = 6.25 mm dia. drilled hole). EC images constructed using the 300  $\mu\text{m}$  model flaw are shown in Figs. 75 and 76. Similar images constructed using a shallow model defect (EDM slot) representing a surface-initiated crack are shown in Figs. 77 and 78a. EC image of the "blunted crack" is shown in Fig. 78b.

"Surface crack" EC imaging resolution obtained is 100  $\mu\text{m}$  (nominal resolution - see Fig. 80. EDM slot was produced with a 0.004" thick foil. Overcutting may make the flaw width some 10% to 20% larger. This will be evaluated shortly). This is an order of magnitude better than the spatial resolution possible with EC flaw detection systems now in commercial use.

It is found that narrow linear flaws produce images with enhanced signal strength at flaw edge (see Figs. 78a and 80) despite use of differential sensing/measurement schemes. In contrast, whenever the side surfaces of model flaws are better separated, edge domination is largely suppressed (Fig. 79). Planned FEM studies are expected to shed light on this (planned in work for M-URI Year 3).

With the single element micro sensor proved in EC imaging, studies are in progress to complete the design of pole piece for the 4 x 4 array sensor. At any instant when a particular element of the array sensor is in use for EC signal acquisition, any one of the remaining sensors can serve as the differential element. Software selection for choice of differential element is anticipated. Proposed pole piece geometry and a simplified version of the pole (2 x 2 array) now in use for FEM simulations are shown in Fig. 82. Previous FEM simulations [60,61] took advantage of axisymmetry. Full 3-D FEM analysis is now in progress to finalize pole piece design for the array sensors shown in Figs. 72 and 73.

The quantities of interest in FEM simulation are: magnetic flux density, magnetic field intensity and induced eddy current densities within the pole piece, test object and the sensor elements. The unknowns, determined by FEM analysis, are the magnetic potential distributions,  $\{A\}$ . Other field quantities sought are derived from the calculated potential distributions. For harmonic analysis (AC excitation) vector potential formulation is in use.

The magnetic vector potential method used for harmonic analysis is based on Maxwell's equations given by:

$$\nabla \times \{H\} = \{J\} = \{J_s\} + \{J_e\} \quad (5)$$

$$\nabla \times \{E\} = - \left\{ \frac{\partial B}{\partial t} \right\} \quad (6)$$

$$\nabla \cdot \{B\} = 0 \quad (7)$$

where:

$\{H\}$ = magnetic field intensity vector	$\{J\}$ = total current density vector
$\{J_s\}$ = applied source current density vector	$\{J_e\}$ = induced eddy current density vector
$\{E\}$ = electric field intensity vector	$\{B\}$ = magnetic flux density vector

The field equations are supplemented with constitutive relations which describe the behavior of the electromagnetic material:

$$\{B\} = [\mu] \{H\} + \mu_0 \{M_0\} \quad (8)$$

$$\{J\} = [\sigma] \{E\} \quad (9)$$

where:

$\{M_0\}$ = remnant intrinsic magnetization vector, zero for saturable material without magnetic moments
$\mu_0$ = permeability of free space
$\{m\}$ = magnetic permeability matrix, in general, a function of $\{H\}$
$[s]$ = electrical conductivity matrix

Solution is obtained by introducing the magnetic vector potential,  $\{A\}$ , which allows the magnetic field  $\{B\}$  and the electric field  $\{E\}$  to be expressed as:

$$\{B\} = \nabla \times \{A\} \quad (10)$$

$$\{E\} = - \left\{ \frac{\partial A}{\partial t} \right\} \nabla V \quad (11)$$

where  $V$  = electric scalar potential.

These relations satisfy two of the Maxwell's equations (6) and (7). What remains to be solved is Eqn. (5) in conjunction with constitutive relations (8) and (9). These equations are subject to problem-specific boundary conditions.

Once the vector potential distribution  $\{A\}$  has been determined, field quantities of interest are derived. Magnetic flux density is evaluated from vector potential distribution with :

$$\{B\} = \nabla \times [N_A] \{A_e\} \quad (12)$$

Magnetic field intensity is computed from the flux density:

$$\{H\} = [\mu]^{-1} \{B\} \quad (13)$$

Current density due to  $\{A\}$  is calculated with:

$$\{J_e\} = -[\sigma] \left\{ \frac{\partial A}{\partial t} \right\} = -[\sigma] \frac{1}{n} \sum_{i=1}^n [N_A]^T \left\{ \frac{\partial A_e}{\partial t} \right\} \quad (14)$$

The approach used here has been extensively studied in previous research and has a sound analytical basis [61-63].

Simplified 3D model consisting of the coil, flux focusing tube, specimen and surrounding air, is in use for FEM simulation. The dimensions in use are: 1). 10 x 4.55 x 4.55 mm excitation coil with a coil thickness of 0.35 mm; 2). 20 x 3.85 x 3.85 mm flux focusing tube with a wall thickness of 0.35 mm; 3). 2.5 x 4.55 x 4.55 mm specimen; and 4). a 0.35 x 0.7 x 0.7 mm sensor. Quadrilateral solid elements (8-node) are used for analysis. Relative permeability and/or electrical resistivity are defined in the current conducting regions. Material properties used are: copper for coil with resistivity of  $1.67 \times 10^{-8}$  and permeability = 1.0, ferromagnetic tube and specimen with a resistivity of  $1.2 \times 10^{-7}$  and permeability = 3000. Since the ferromagnetic material has finite permeability, the surrounding air is modeled a small distance away from the material. The open boundary is modeled with 3-D infinite boundary element at the edge of the air region. A relative permeability of 1.0 was specified for air. The ferromagnetic flux guide/shield is assumed to be wound with a 350-turn coil carrying 10 mA. Current density of 100 in CGS units is specified over coil elements. The magnetic flux that the coil current produces is assumed to be small enough that no saturation of the ferromagnetic material occurs. Hysteresis effects and the saturation are neglected. This allows a single-iteration, linear analysis. Harmonic analysis at 50 kHz excitation is also in progress. Signal sensed in the sensing coil is calculated from eddy current density generated within the sensing coil

Calculated magnetic field components  $B_x$ ,  $B_y$  and  $B_z$ , and  $B_{sum}$  in regions of interest are shown in Fig. 83. Vector potential and magnetic field components  $A_z$ , and  $A_{sum}$  and  $B_{sum}$  are shown in Fig. 84, with eddy current components  $J_{ex}$ ,  $J_{ey}$  and  $J_{ez}$ , and  $J_{sum}$  in Fig. 85. Flux focusing is found to be non-homogeneous and it may lead to edge dominated EC signals. Promising levels of eddy current densities prevail in the sensor elements. Following a detailed analysis of calculated results, completion of pole piece design with a more permeable material for array sensor pole piece is anticipated in the early part of 1997.

A coil design not entailing space penalties (a 3-metal, 5-mask transverse sensor), was proposed last year (Fig. 89, Ref. 59) with device and coil implementation in a plane normal to the plane of fabrication. Section view of the transverse sensor proposed, and the sensor actually implemented in Silicon are shown in Fig. 86.

The good EC imaging performance demonstrated by the 20-turn, thin film, single element micro sensor suggests that use of transverse sensors can lead to a further gain in spatial resolution of nearly one order of magnitude, with detected flaw dimensions approaching a few tens of microns. The transverse sensor implemented (Figure 86b) has a 3 mm x 2  $\mu$ m Permalloy pole piece for flux concentration (EC signals). Planar excitation or drive coil, also equipped for flux focusing, shown in Fig. 87, will be used in conjunction with single element and transverse array sensors.



It is anticipated that the array sensors can eventually be implemented with  $300\text{ }\mu\text{m} \times 2\text{ }\mu\text{m}$  Permalloy flux concentrators to yield a linear array sensor with a sensor spacing of  $500\text{ }\mu\text{m}$  in the plane of the sensor. Substrate thickness (typically  $500\text{ }\mu\text{m}$ ) determines the sensor spacing along the direction normal to the sensor plane (2 - D sensor array).

Hall Effect Devices (HEDs) have now become widely available. Some of these are integrated field sensors with a measurement range of  $\pm 50\text{ G}$  with acceptable linearity. With modest signal conditioning, these devices can yield sensitivities greater than  $2.5\text{ volts/G}$ . These HEDs are intended for switching applications with small time constants (tens of  $\mu\text{s}$ ). If it can be demonstrated that these devices can detect AC fields at 50 to 100 kHz, HEDs can become useful sensors for low cost and automated EC inspection.

To evaluate the suitability of off-the-shelf HEDs for EC applications, the test rig shown schematically in Fig. 88 was assembled (also needed for Magneto-Resistance and Giant Magneto-Resistance sensor studies that are to follow).

HEDs have been evaluated at solenoidal coil fields at drive frequencies up to 50 kHz (frequency limit of the power amplifier). Sensitivities better than  $1\text{ volt/G}$  have been obtained with inexpensive signal conditioning sub-systems. It is anticipated that with modest flux focusing (proposed geometry is shown in Fig. 89) a further two- to four-fold gain in sensitivity is obtainable. A Helmholtz coil assembly is now in design stages to more thoroughly characterize the AC characteristics of HEDs (as well as the AC characteristics of MR and GMR sensors for EC inspection).

### PLANS FOR M-URI YEAR 3

Micro sensors proposed at the outset of the Integrated Diagnostics program have been implemented in Year 2 with the flux focusing concepts verified in Year 1. Digital flaw imaging methods have been developed and a flaw resolution of  $100\text{ }\mu\text{m}$  has been demonstrated in Year 2.

Planned activities for Year 3 are:

- (1) Demonstrate digital imaging with  $4 \times 4$  array micro sensors to reduce flaw imaging time with automated choice of sensor for differential scanning and display of EC images.
- (2) Implement disposable, single element and array sensors in a flexible (Kapton) substrate.
- (3) Reduce micro sensor scale by a factor of 2 or more and demonstrate  $50\text{ }\mu\text{m}$  resolution.
- (4) Establish EC imaging characteristics for sub-surface flaws and inclined surface-breaking flaws (Fig. 90) with single element and array micro sensors.
- (5) Develop a criterion for spatial resolution in a field of cracks, i.e., to identify individual flaws in a "field of cracks", (comparable to the Abbè criterion of optics) using test samples with closely spaced, parallel cracks (Fig. 90) and branching cracks;
- (6) Complete and demonstrate flaw imaging with transverse micro sensor ( $3\text{ mm} \times 2\text{ }\mu\text{m}$  flux guides and 50 turns); establish resolution limit of transverse sensors; implement and establish the resolution limits of linear, transverse array sensors.
- (7) Based on fracture mechanics research, and using Vicker's indentors for surface cracking, develop test samples with cracks less than  $50\text{ }\mu\text{m}$  wide (indentation cracking of fully hardened materials) for model flaw imaging with micro sensors and sensor arrays.
- (8) Evaluate and document feasibility of Hall effect sensors for flaw sensing and inspection.

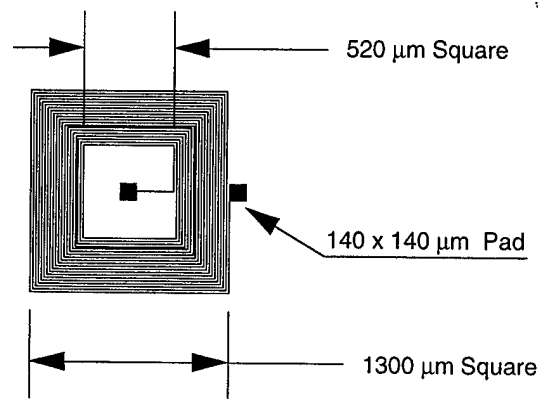
Year 2 effort has shown that the stepper motor driven, scanning system needs updating with servo-drives to avoid vibration problems and for flaw signal acquisition 'on the fly'. Yield problems (wet chemistry processing for device construction) can also be avoided by implementing dry processing (plasma etching). The M-URI Year 3 program will include implementing these improvements.

## **VISION FOR YEARS 4 AND 5**

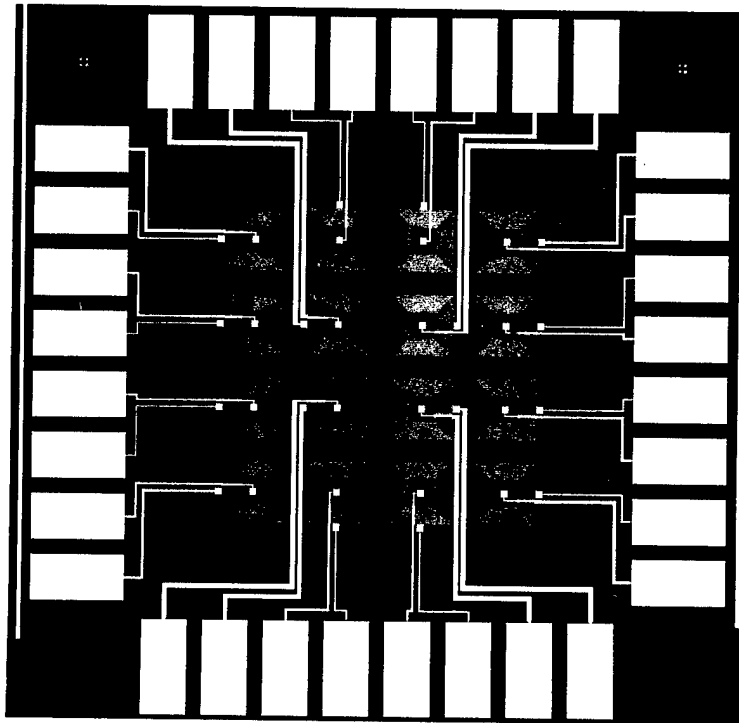
Good progress has been made in the last two decades in understanding and developing magneto-resistance based (MR) devices. MR read-heads are now in commercial use in hard drives for magnetic recording. Large changes in resistance (DR 0.2% to 0.7% at 50 G) have also been reported [64,65] in newly developed Giant Magneto Resistance (GMR) multi-layer films. MR and GMR principles may well permit much simpler next generation micro sensors for EC imaging. Because MR and GMR sensors can be straight forward 2-port devices, micro sensor fabrication can be much less demanding with a very good probability of high process yields. Signal conditioning and SNR are also superior, since well-understood Wheatstone bridge circuits are sufficient. Taking these into consideration, the following activities are proposed for years 4 and 5.

Planned activities for Years 4 and 5 are:

- (1) Validate and evaluate sensors based on Magneto-Resistance (MR) and Giant Magneto Resistance (GMR) for eddy current flaw sensing and imaging requiring simpler signal conditioning and superior signal-to-noise ratio than in current generation micro sensors.
- (2) Design, build and demonstrate simpler MR and GMR micro sensors for EC imaging.
- (3) Establish the resolution limit of MR- and GMR-based micro sensors for EC imaging.
- (4) Build and demonstrate a ruggedized "probe" with micro sensor(s) suitable for automated EC inspection (geometry, functionality and packaging comparable to the Hall probes).
- (5) Demonstrate automated component inspection for flaws and flaw imaging with the "probe" in a 3-axis coordinate measuring machine.
- (6) Demonstrate fully robotic component inspection for flaw imaging under program control .

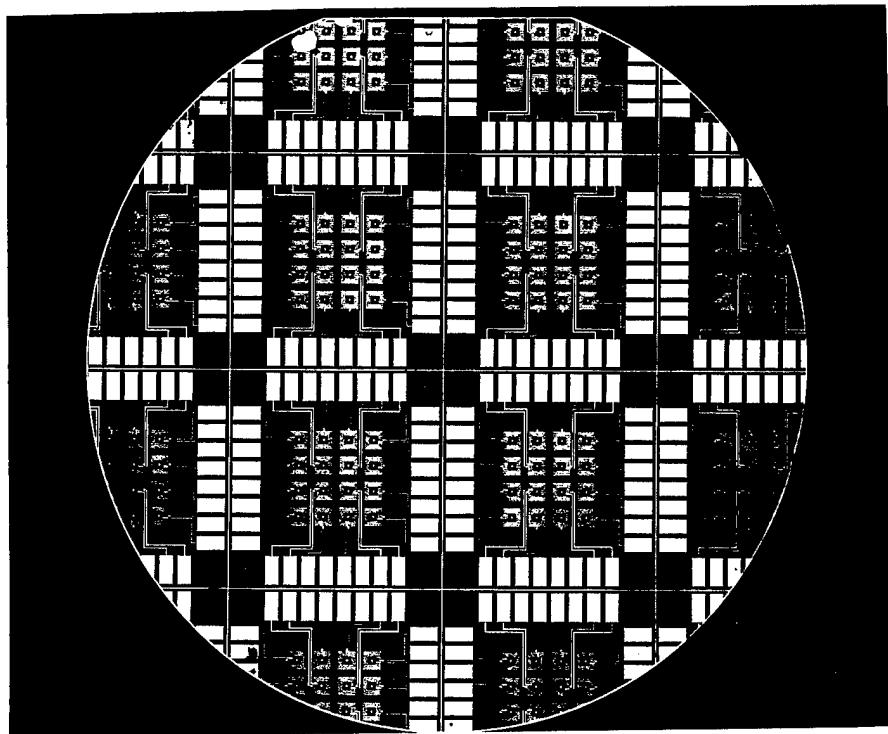


a. Twenty turn Sensor Element with 10  $\mu\text{m}$  lines at 10  $\mu\text{m}$  spacing

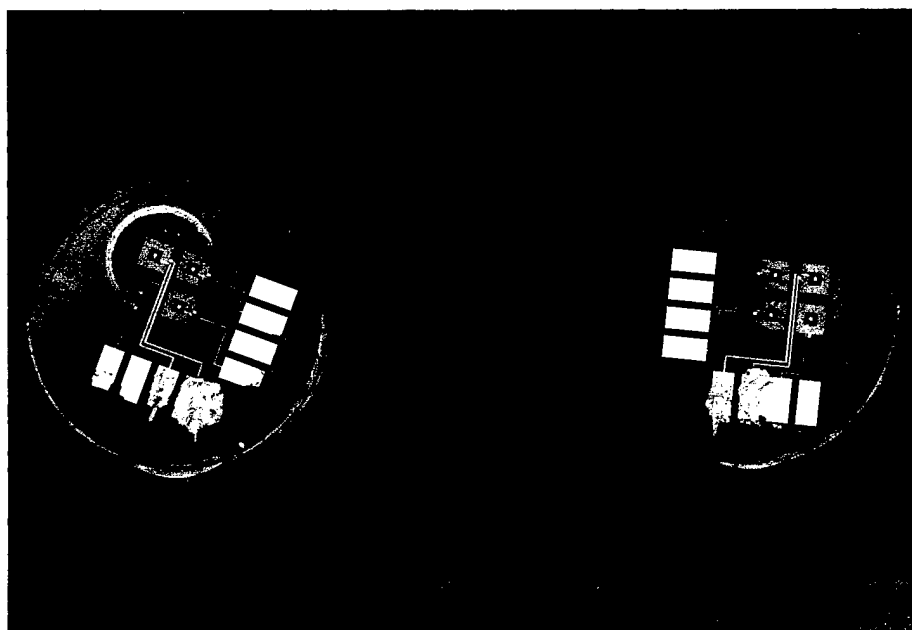


b. Four by Four Sensor Array Mask Layout for Sensor Implementation in Silicon

**Figure 72.** Eddy current micro sensor geometry and the 4 x 4 array sensor implemented in Silicon

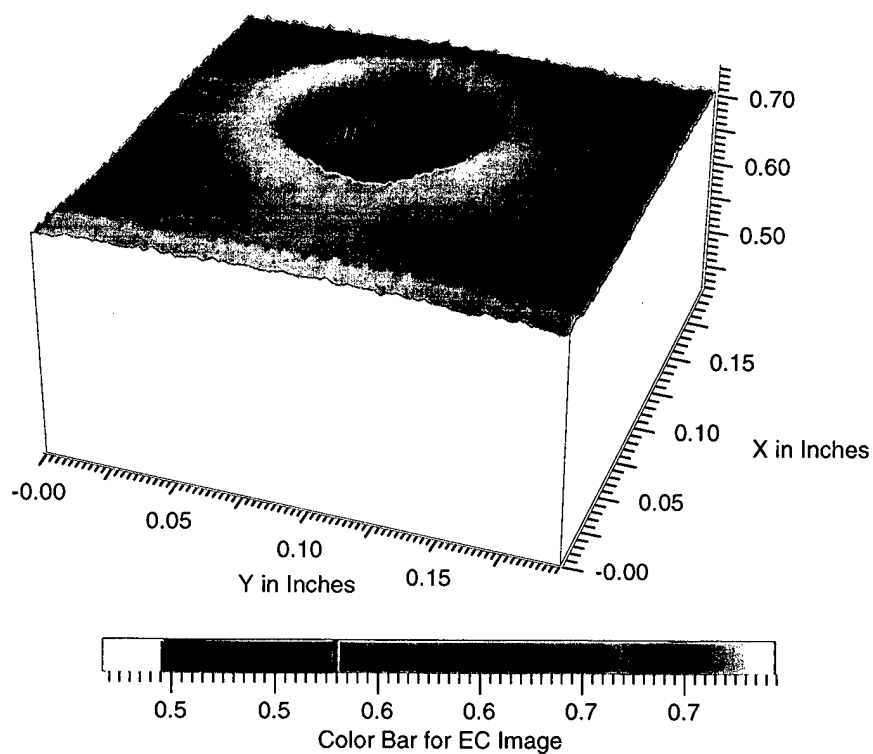


a. Micro sensor array fully implemented in a silicon wafer

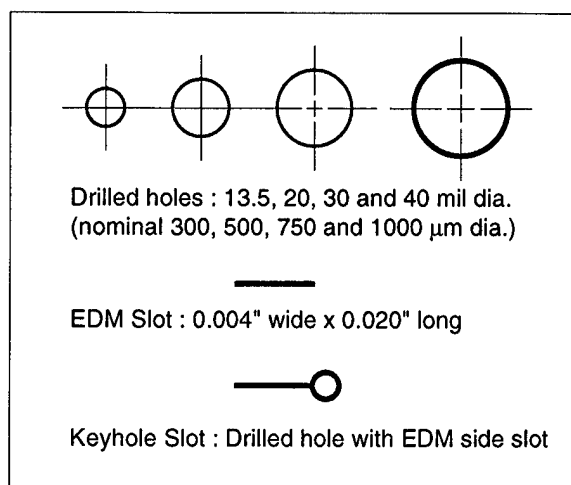


b. A typical single element microsensor used for resolution evaluation  
(implemented by dicing a 4 x 4 array )

**Figure 73.** Micro sensor array implemented in Silicon and the complete single element sensor implemented.



a. Eddy current image of a model flaw - a 0.040 inch diameter drilled hole - in a test sample below .



b. Model flaw used for eddy current imaging is the 0.040" dia. drilled hole shown in the test sample.

**Figure 74.** Model flaw reconstructed with differential EC signals acquired with a single element sensor

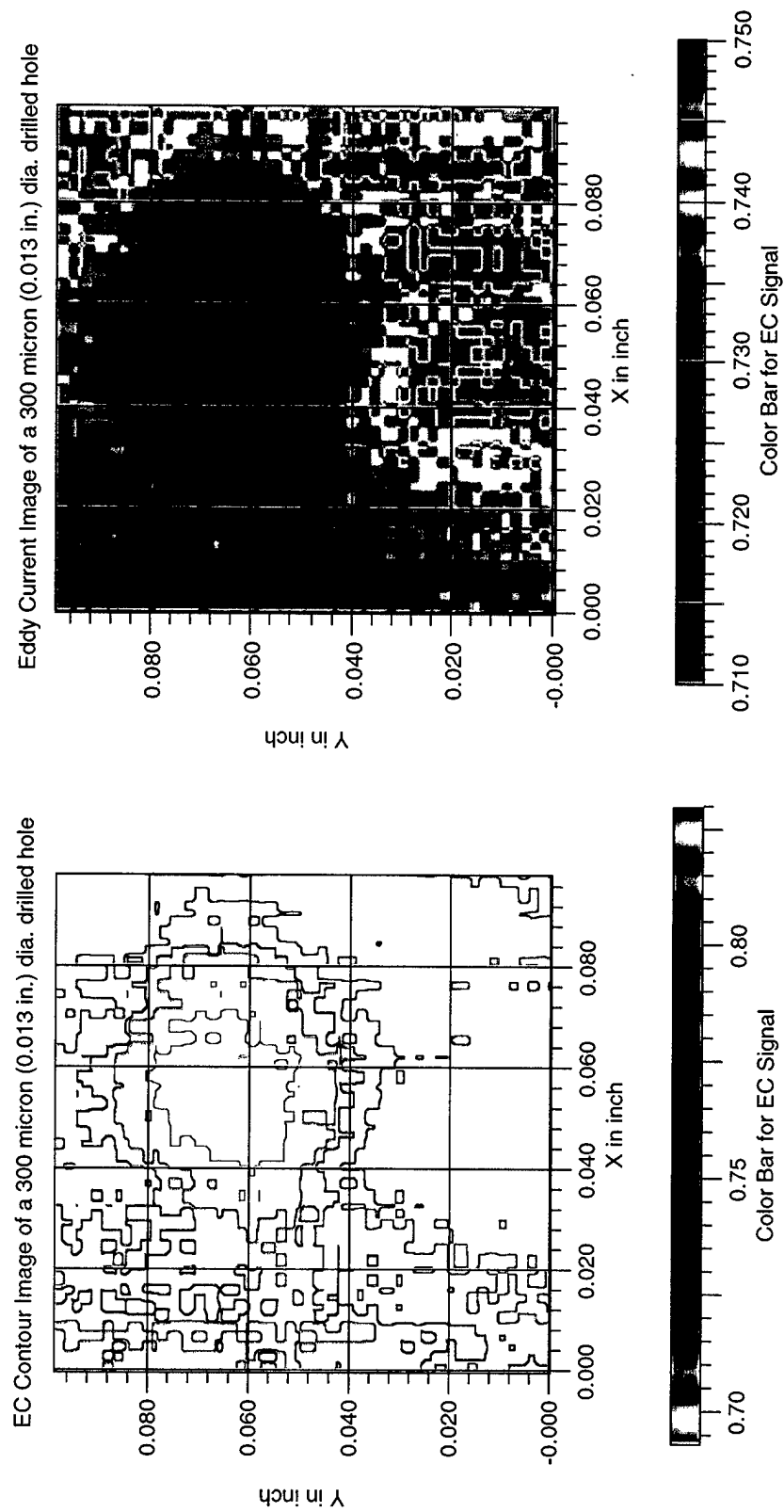


**Figure 75.** EC contour and images constructed by scanning a 300  $\mu$ m dia. model flaw - differential scanning.

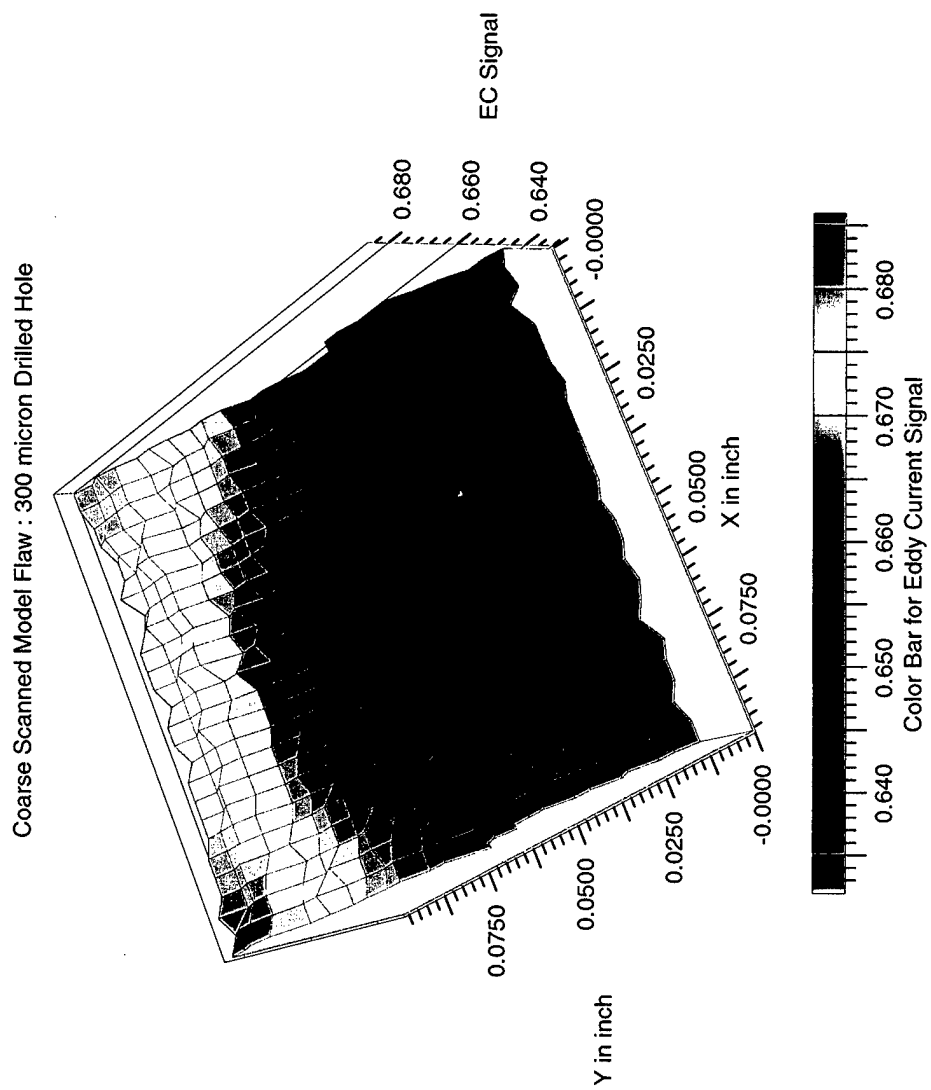
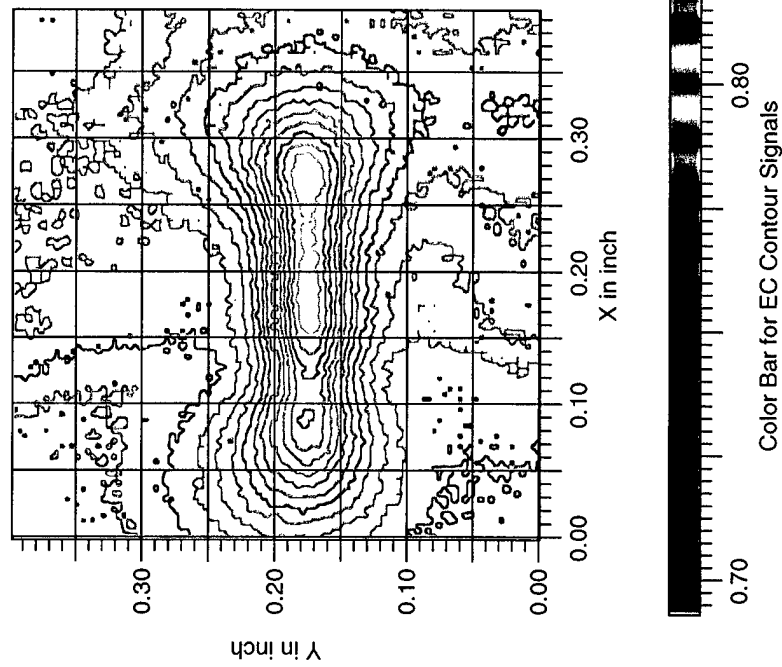


**Figure 76.** Three dimensional EC image constructed by scanning a 300  $\mu$ m dia. model flaw

EC Contour Image of an EDM Slot: 0.004 in. wide x 0.200 in. long



Eddy Current Image of an EDM Slot: 0.004 in wide x 0.200 in. long

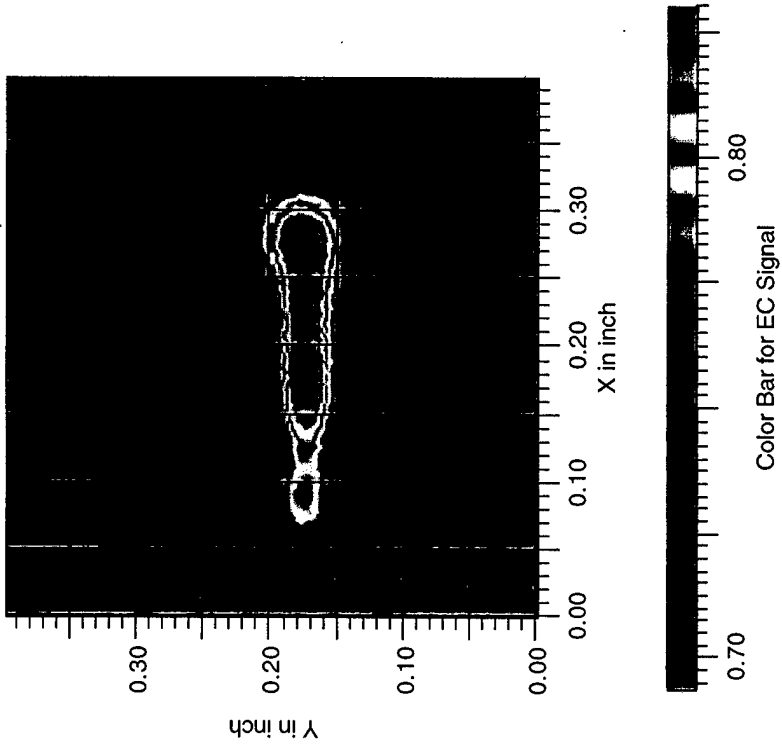
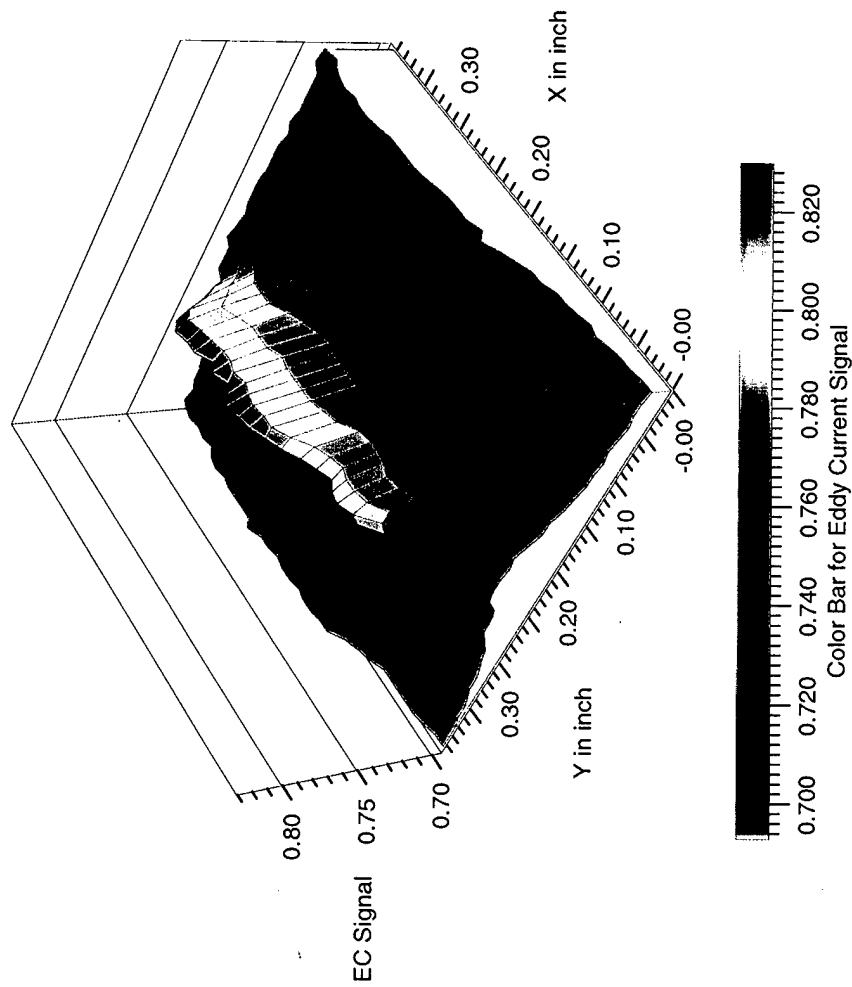
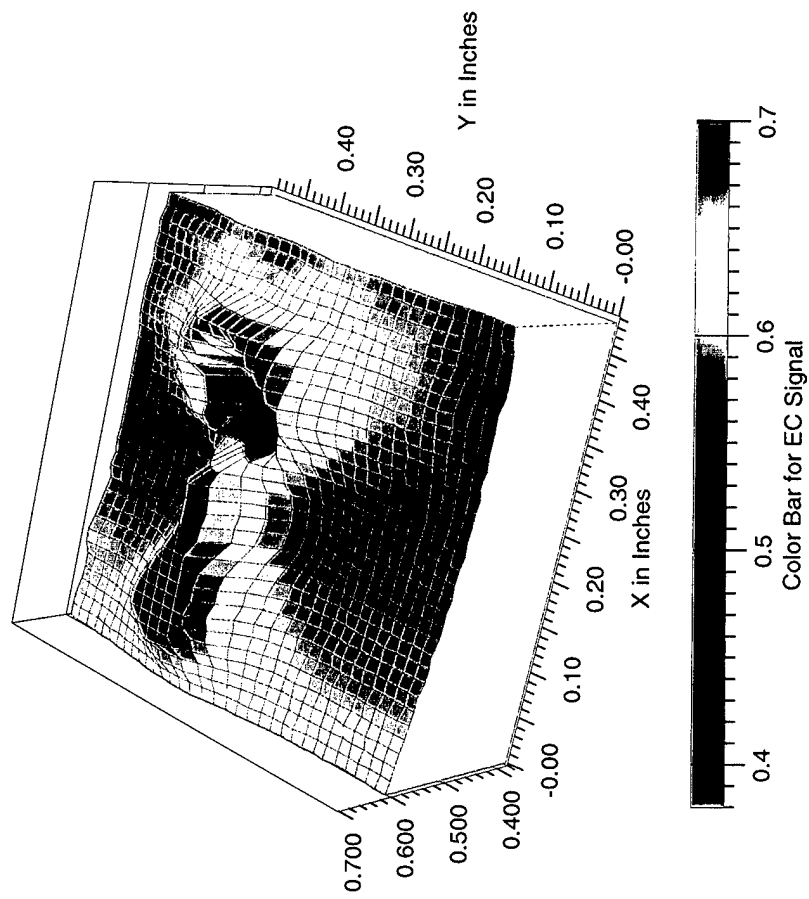


**Figure 77.** EC contour and images constructed by scanning a 100  $\mu$ m wide EDM slot, 5 mm in length



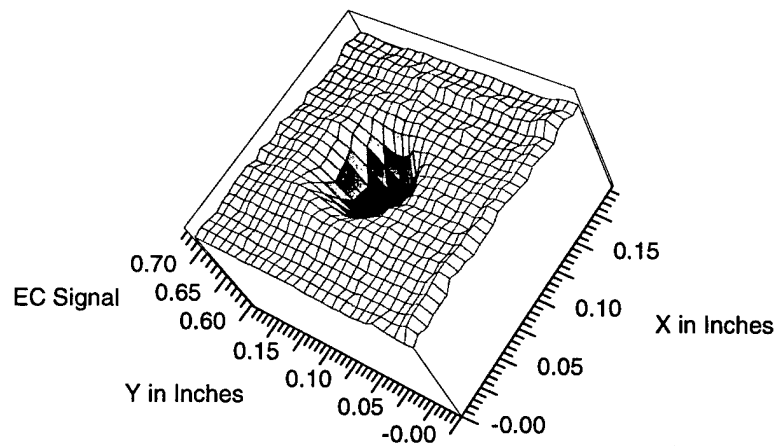


a. EC Image : EDM Slot - 0.004 wide x 5 mm long x 1 mm deep

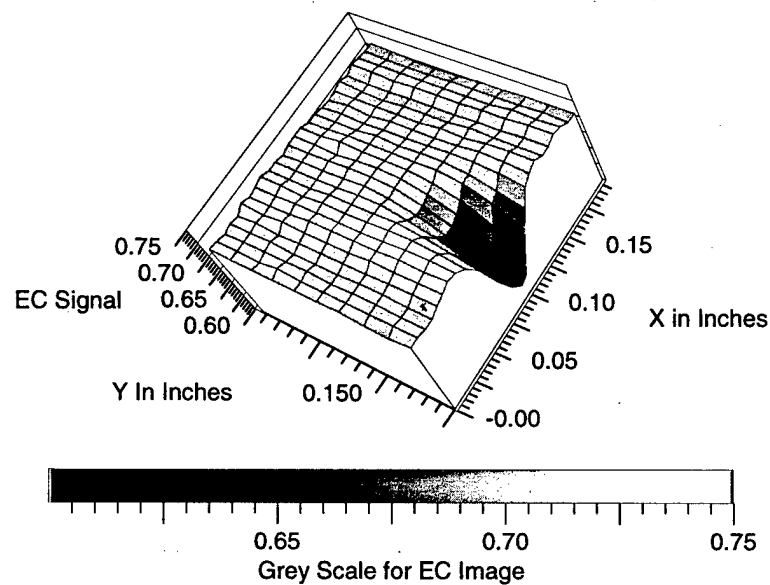


b. EC Image: "Blunted-crack" - EDM Wire-cut Keyhole Slot

**Figure 78.** Three dimensional EC images constructed by scanning an EDM slot and a keyhole slot (100  $\mu\text{m}$  wide EDM slot emerging from a 2 mm dia. drilled hole).



a. Eddy Current Image of A Model Flaw - A 750  $\mu\text{m}$  (0.030") dia. Drilled Hole



b. EC Image of A Section Through The Model flaw - A 750  $\mu\text{m}$  (0.030") dia. Drilled Hole .

**Figure 79.** EC image of a 750  $\mu\text{m}$  dia. model flaw and a reconstructed section through the flaw. Note signal response at flaw edge and flaw center.

EC Image - Model Flaw : An EDM Slot - 0.004" wide X 0.200" long

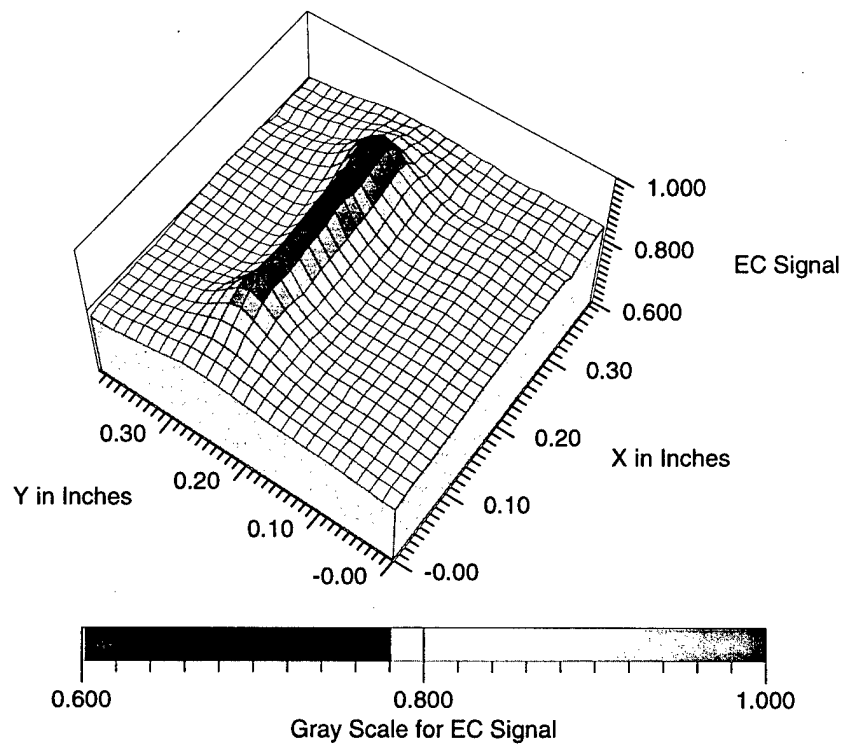
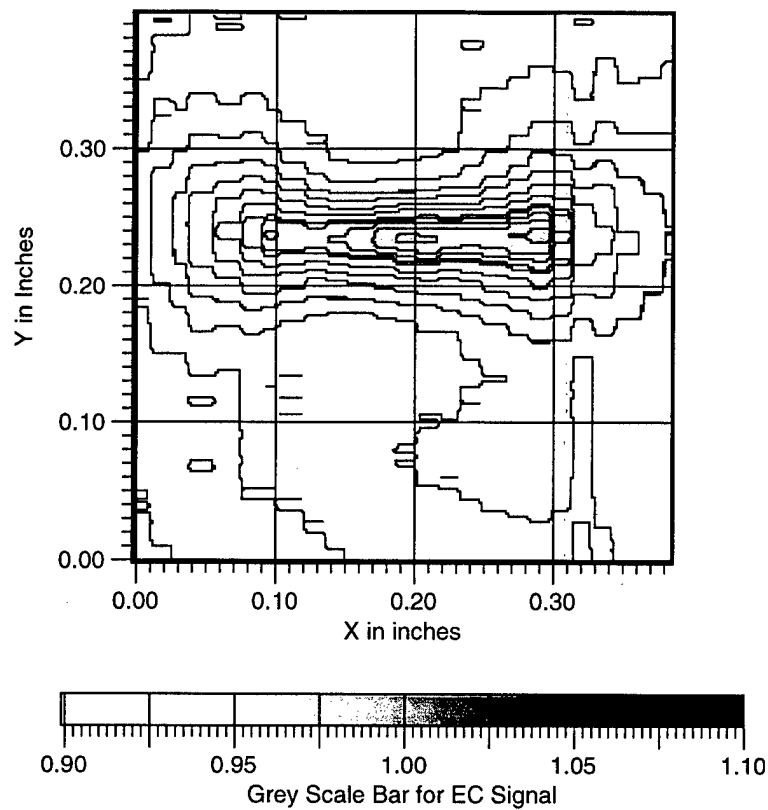
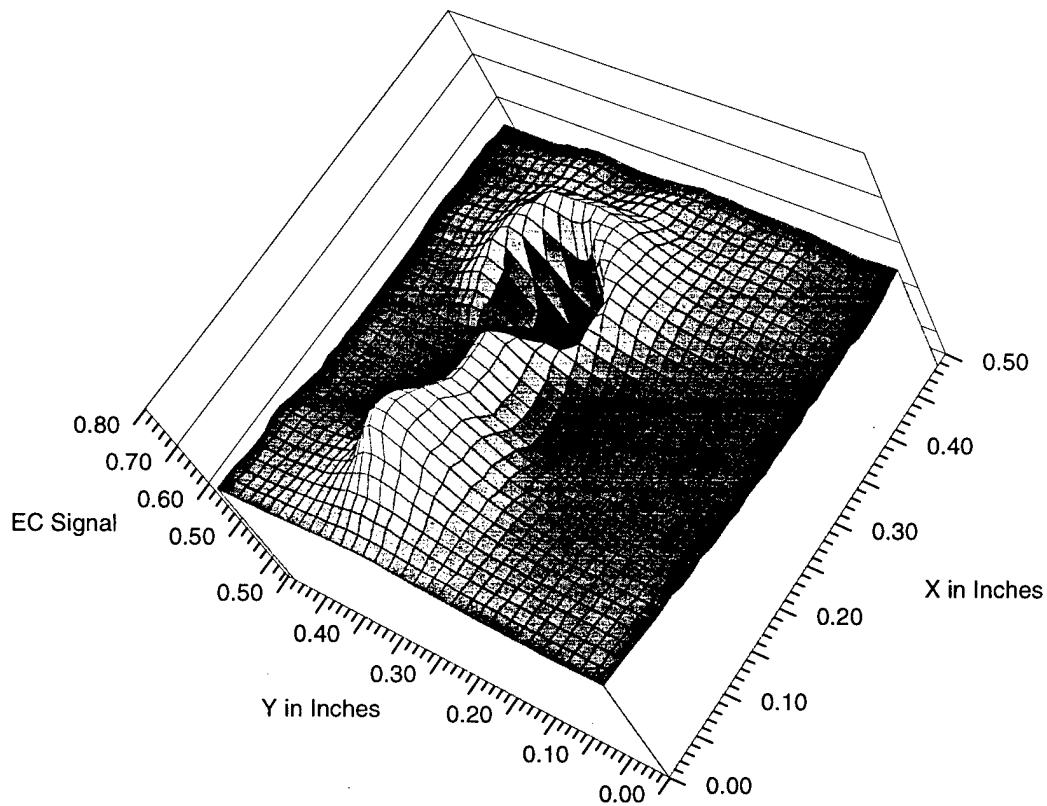
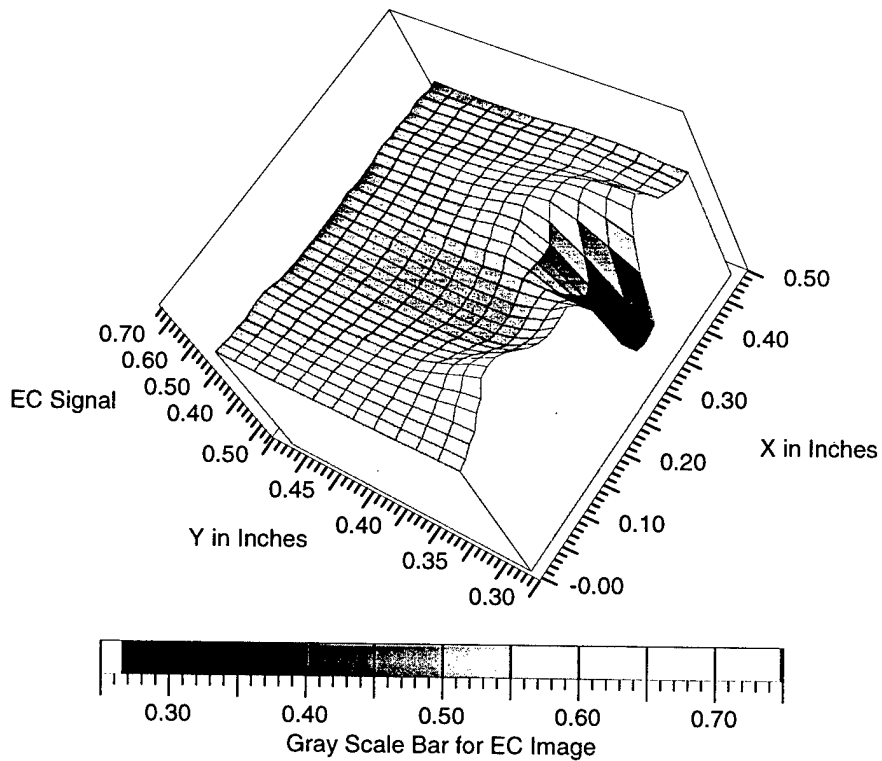


**Figure 80.** EC contour and 3-D image constructed by scanning a 100  $\mu$ m wide x 5 mm long EDM slot. Note enhanced signal response at flaw edge. Flaw resolution demonstrated at 100  $\mu$ m.

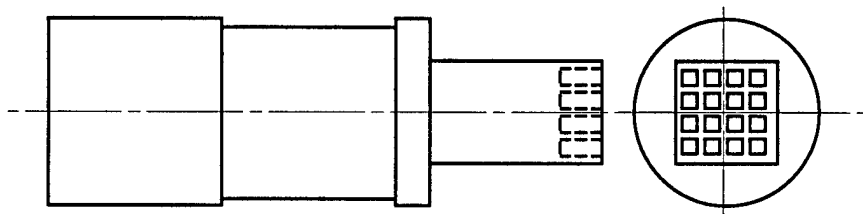


a. EC Image of A Model Flaw - A Keyhole Slot Defect Representing A "Blunted Crack"

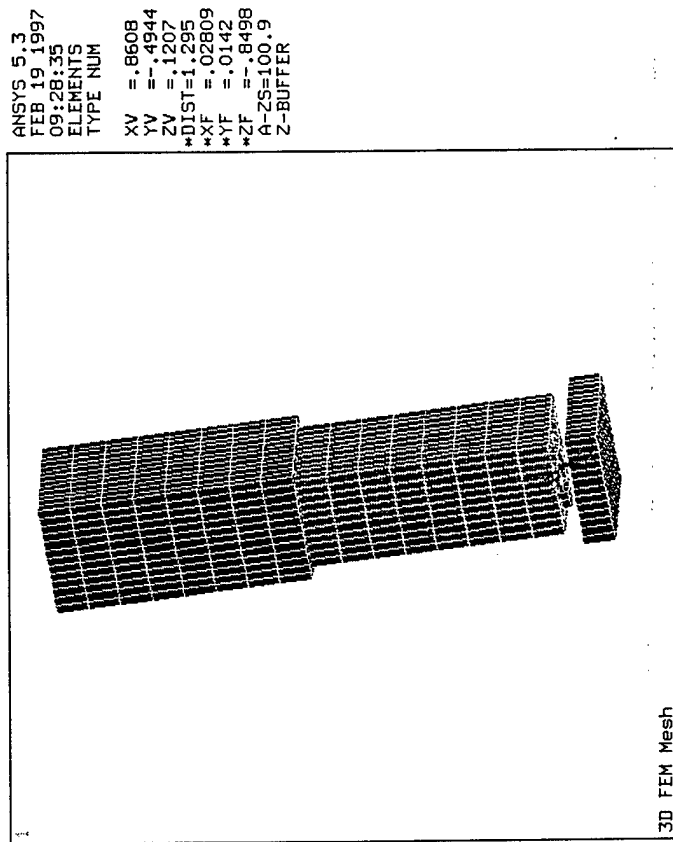


b. EC Image of a section Through The Model Flaw - A Keyhole Slot Defect ("Blunted Crack") .

**Figure 81.** EC image of a blunted crack-like flaw (keyhole slot) - 100  $\mu\text{m}$  wide EDM slot terminating at a 2 mm dia. drilled hole and the reconstructed section through the model flaw.



a. Schematic of the Pole Piece for the 4 x 4 Sensor Array



b. Meshed Model for FEM Analysis : Simplified For a 2 x 2 Micro Sensor Array

**Figure 82.** Pole piece for 4 x 4 micro sensor array and the simplified FEM model of the pole piece to calculate eddy current signal characteristics of the array sensor.

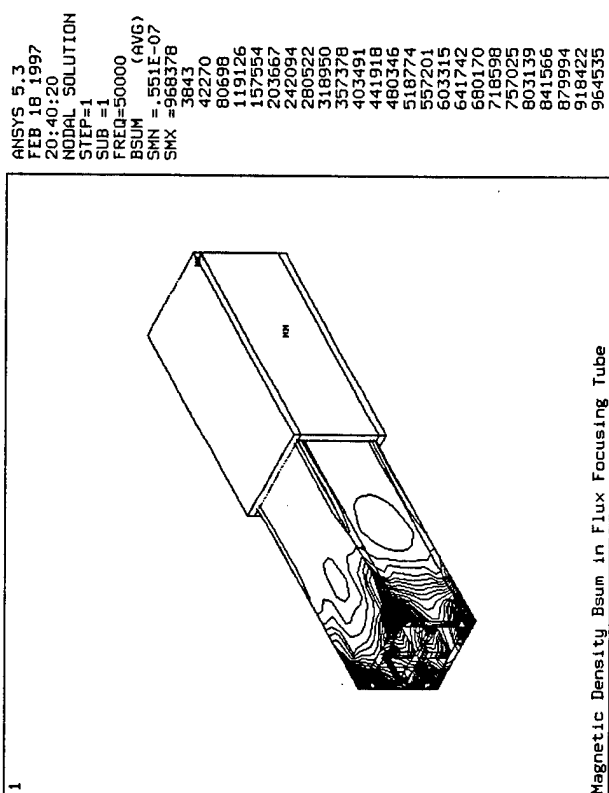
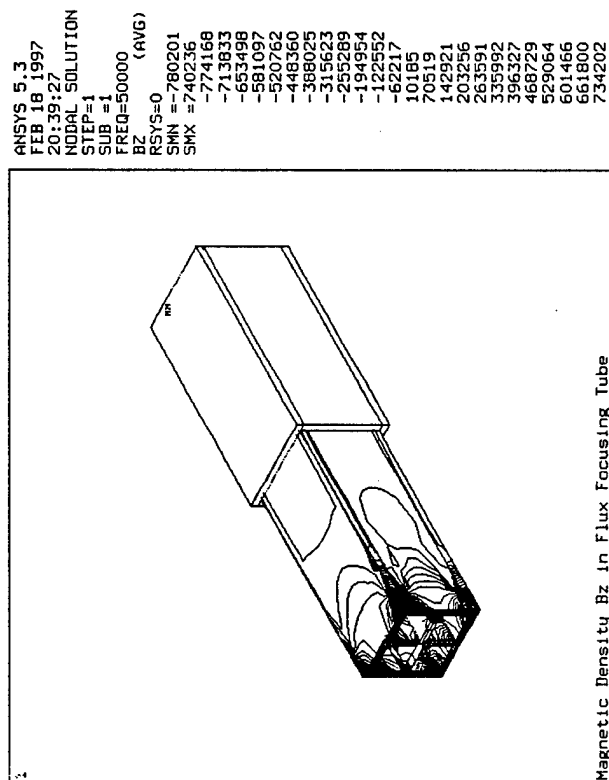
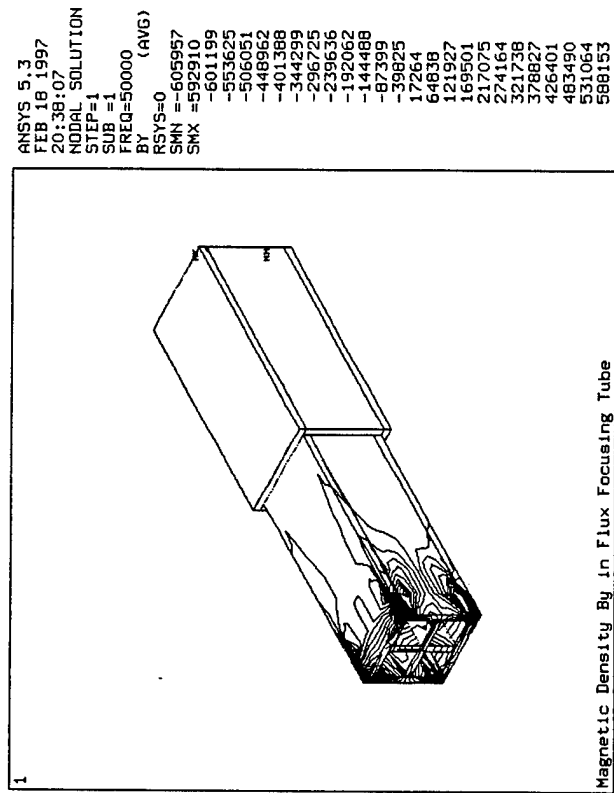
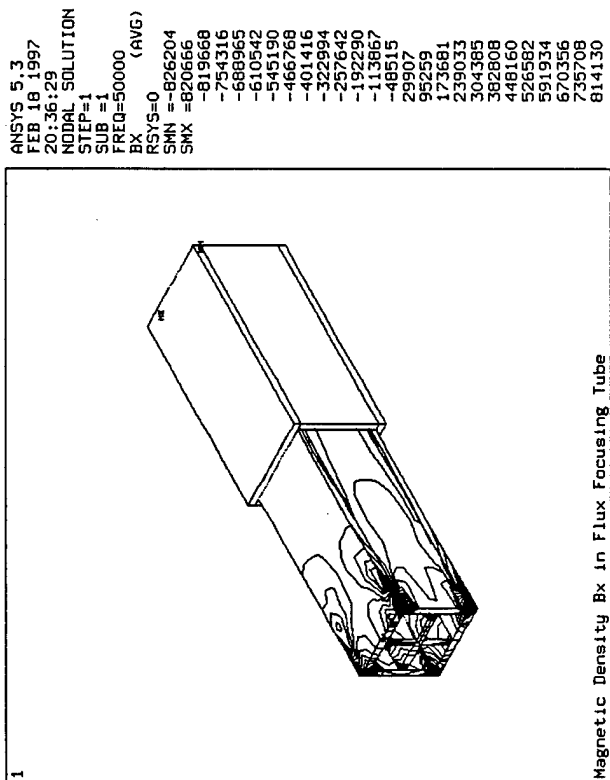


Figure 83. Calculated Magnetic Field Components  $B_x$ ,  $B_y$ , and  $B_z$ , with  $B_{sum}$

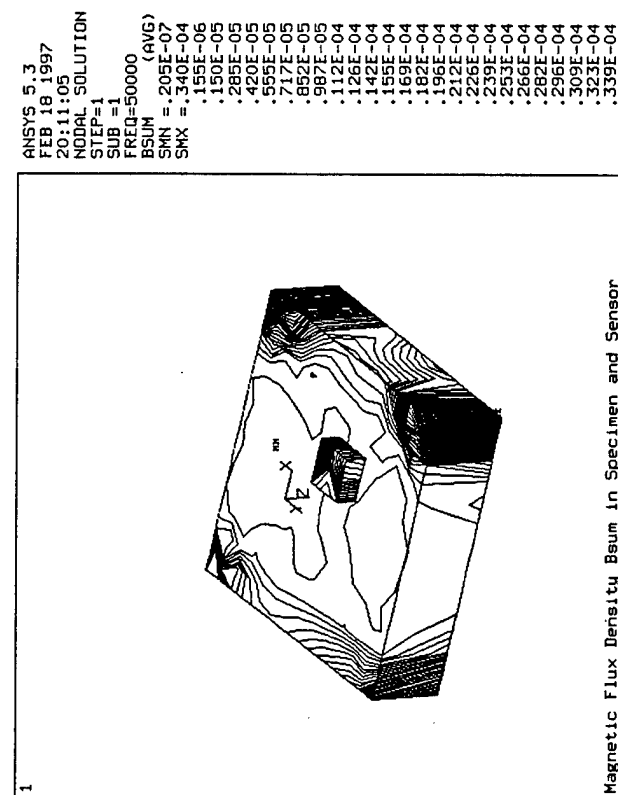
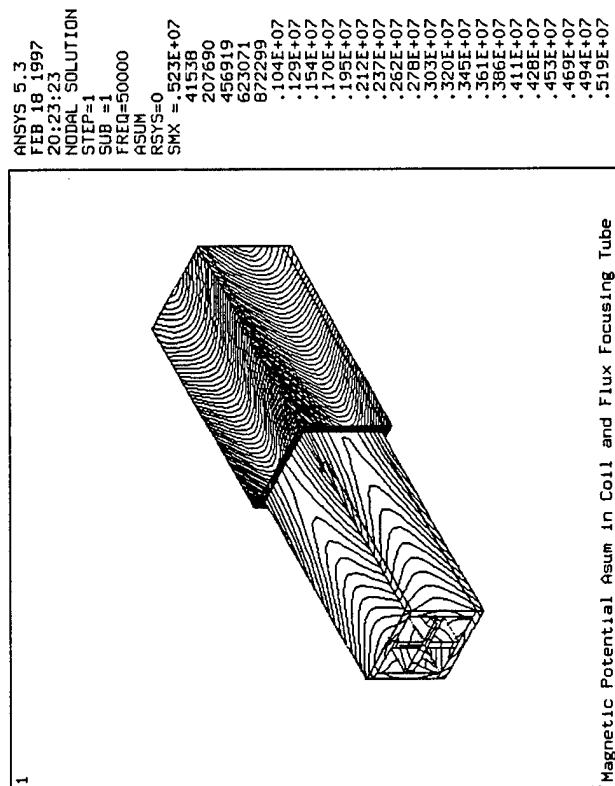
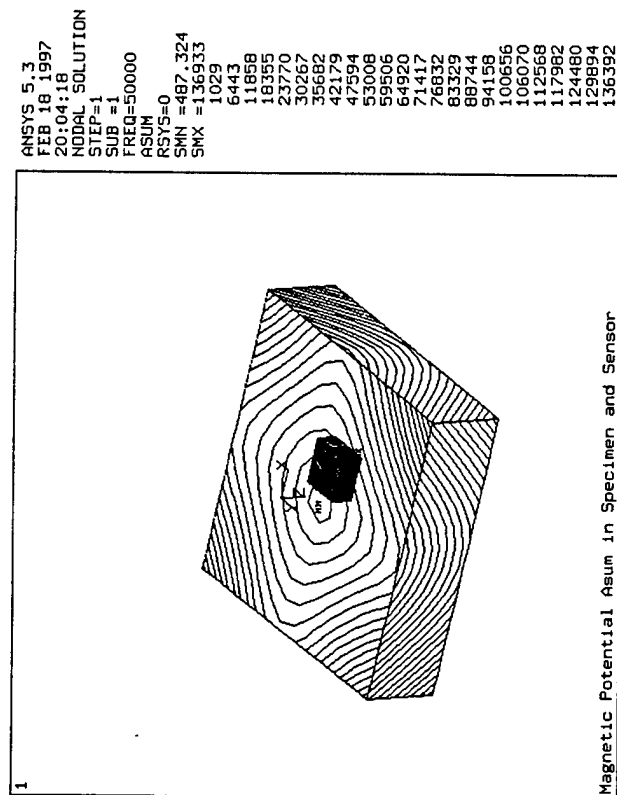
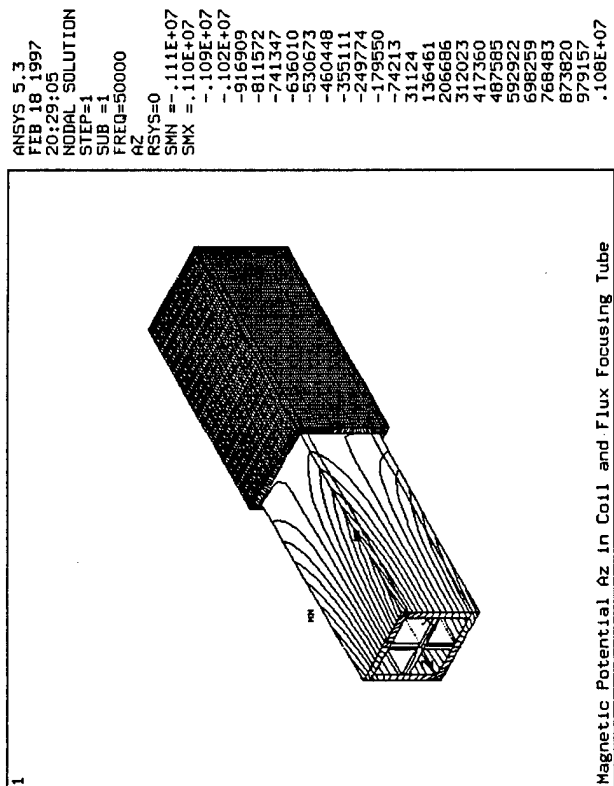


Figure 84. Calculated Vector Potential and Magnetic Field Components  $A_z$ , with  $A_{sum}$  and  $B_{sum}$

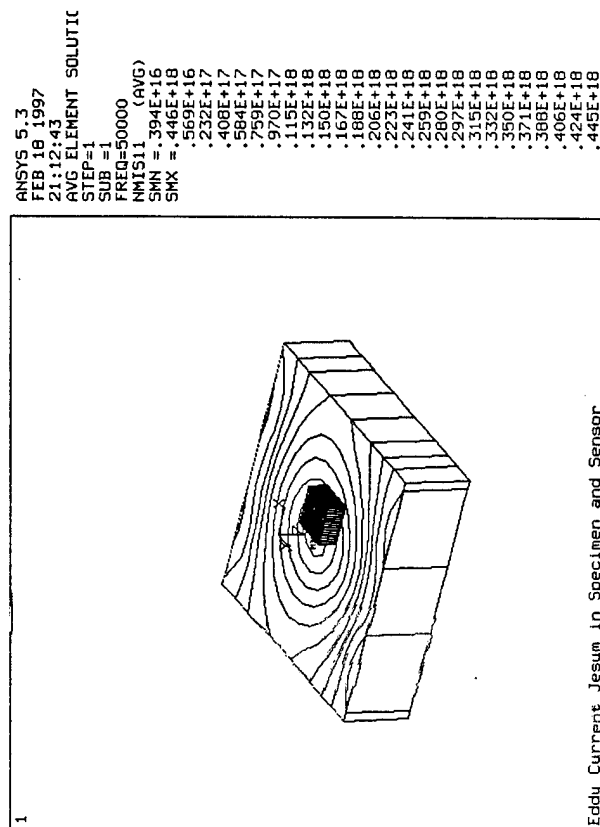
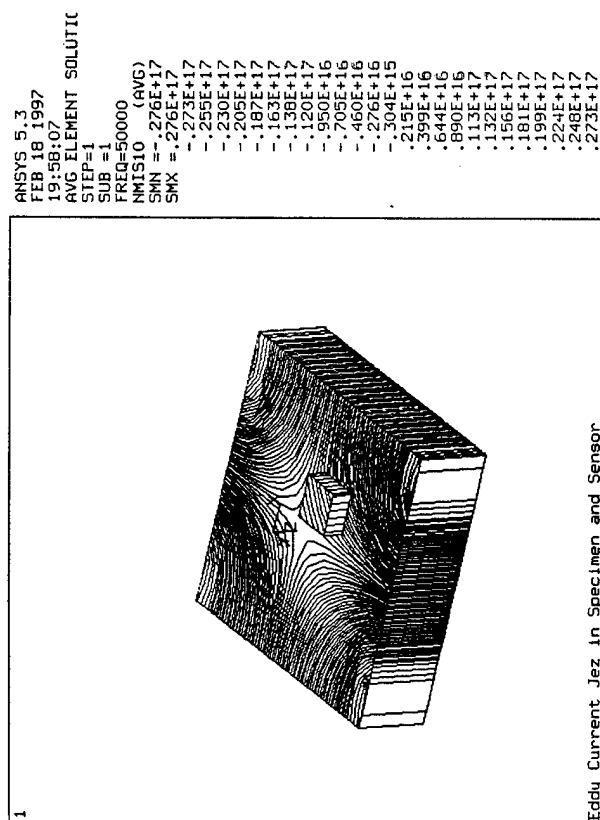
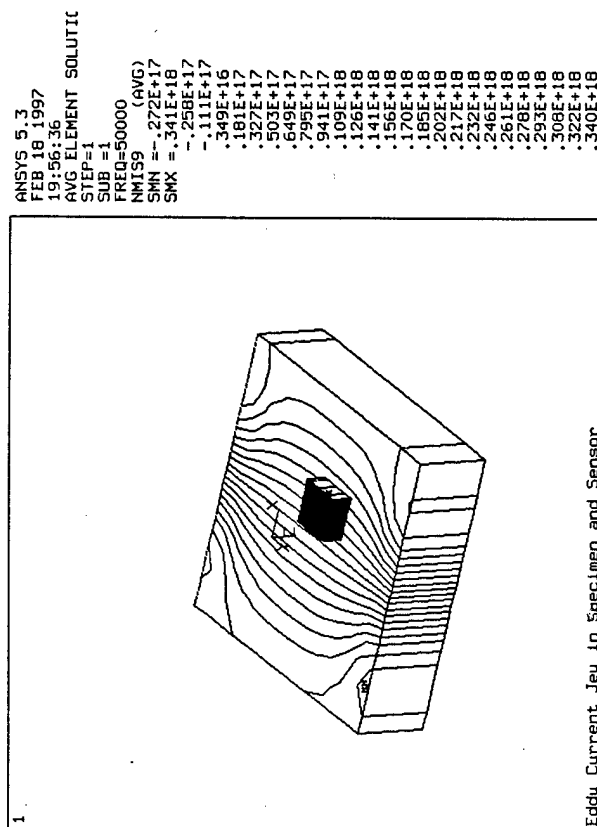
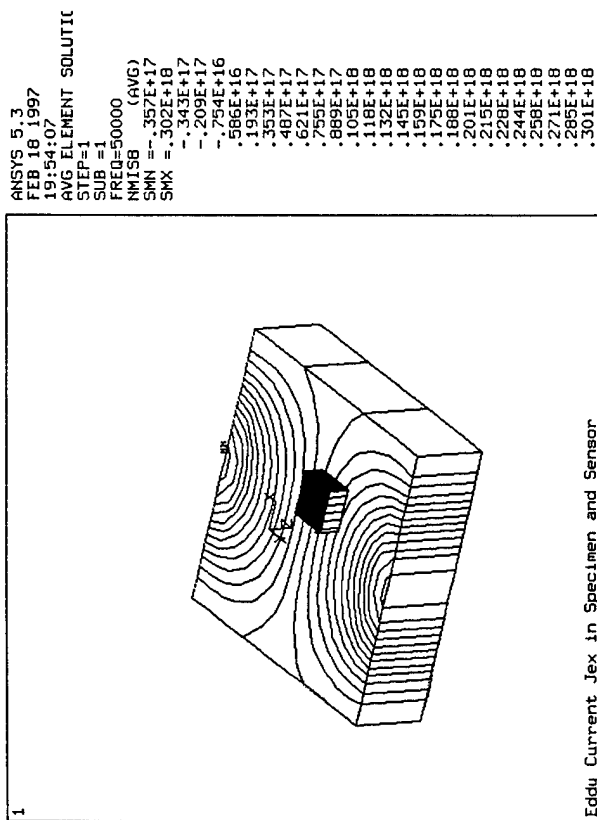
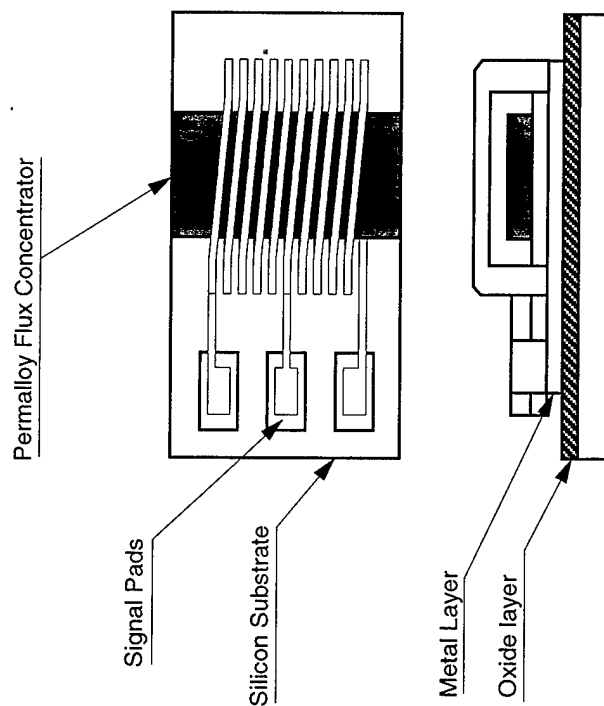
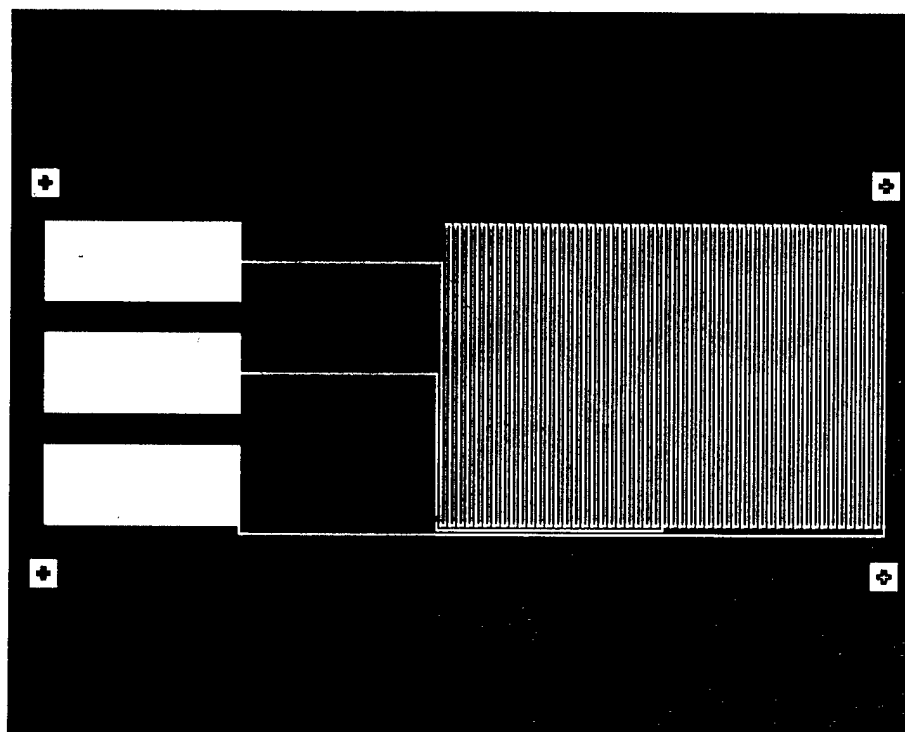


Figure 85. Calculated Eddy Current Components  $J_{ex}$ ,  $J_{ey}$ , and  $J_{ez}$ , with  $J_{sum}$



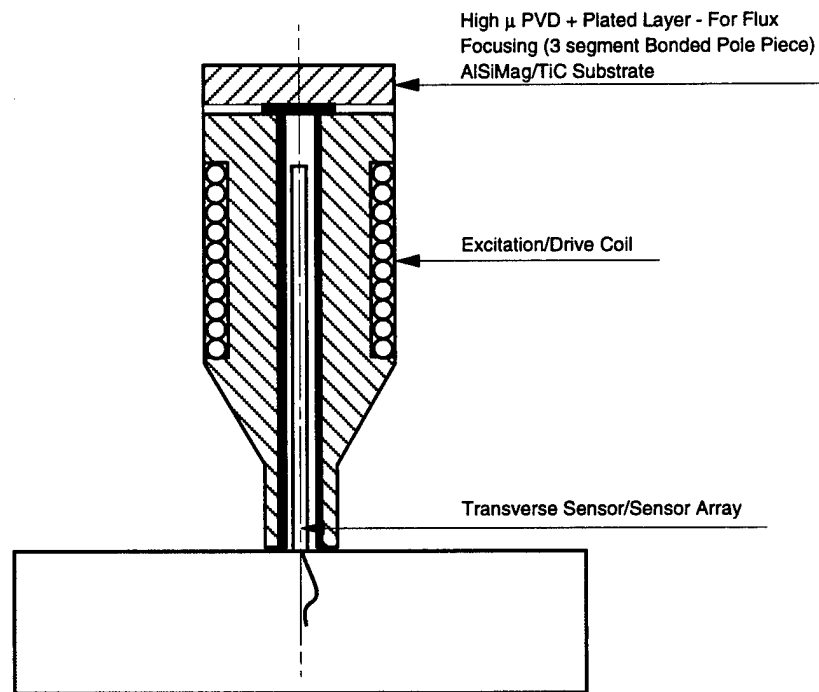


a. Schematic of the Section Through The 3-Mask Transverse Sensor Proposed

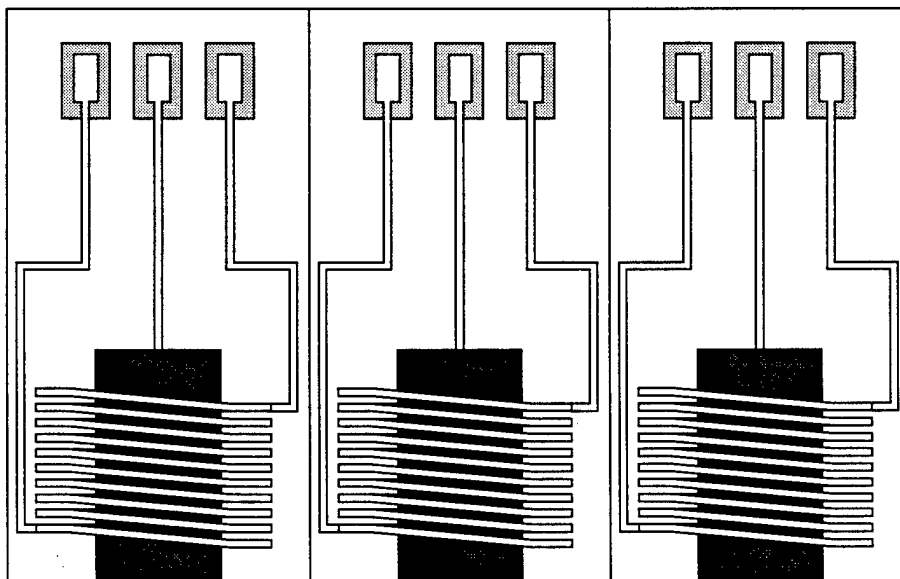


b. Actual Transverse Sensor Implemented on Silicon

**Figure 86.** Schematic of a 3-mask, 50-turn transverse eddy current micro sensor with a  $2\text{ }\mu\text{m} \times 3000\text{ }\mu\text{m}$  Permalloy flux concentrator and a photograph of the sensor implemented in silicon.



a. Schematic of the Flux Focusing Pole Piece for Transverse Sensor/Sensor array



b. Transverse Sensor Array to be Implemented on Silicon

**Figure 87.** Pole piece geometry for single element transverse sensor and schematic of the multi-element transverse sensor array.

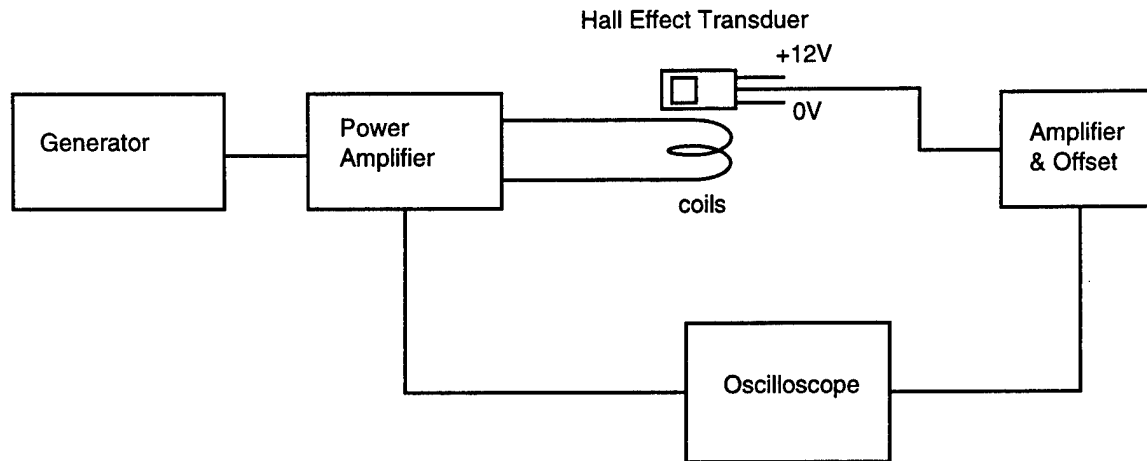


**Figure 88.** Schematic of the set up for Hall effect micro sensor evaluation (DC to 50 kHz excitation) for eddy current inspection and imaging.

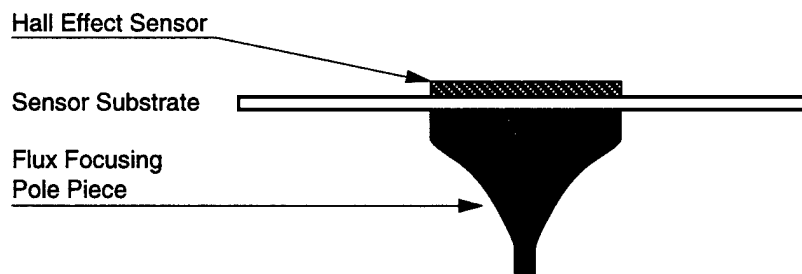


**Figure 89.** Pole piece geometry (Hall effect sensor) for flux focusing to enhance spatial resolution

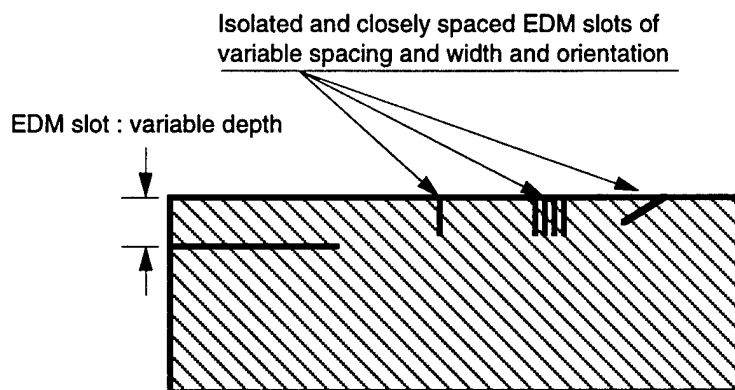


**Figure 90.** Demanding flaw geometries proposed for EC imaging and flaw resolution in a field of cracks.

### 2.3.3 INTEGRATED MICROSENSORS FOR AIRCRAFT FATIGUE AND FAILURE WARNING

Co-investigator: Dennis Polla (University of Minnesota)

M-URI Year 2 Funding Allocation: 36.8%

#### PROJECT OVERVIEW

The objective of this project is to develop real-time sensing devices and methods to accurately identify conditions leading to the imminent and future failure of critical aircraft components. Two key technologies are brought together: solid-state microsensors and advanced signal processing methods. The microsensors include acoustic emission (AE) sensors for the detection of crack development and unusual wear, microbeam accelerometers for the detection of unwanted excessive mechanical vibrations, and temperature sensors for both signal referencing and identification of excessive heating. Several advanced signal processing methods are used to interpret the amplified signals of the variables being sensed. The signal processing effort is directed toward identifying true failure signatures in a real-time in an electrically and acoustically noisy environment. A goal of this project is to realize inexpensive silicon chips, or "coupons" which can potentially be distributed over the critical regions of an aircraft [66]. This coupon might contain a variety of microsensors for detection and cross-confirmation of multiple failure signatures. Based upon some successful milestones achieved in M-URI Years 1 and 2, an effort on wireless communication between the sensor and the remote instrumentation (such as in the cockpit) was initiated. By also integrating analog signal conditioning electronics, A/D converters, digital signal processing circuits, memory, and telemetry with silicon based microsensors, smart microsystems can be formed. The silicon-based coupon concept is represented in Fig. 91.

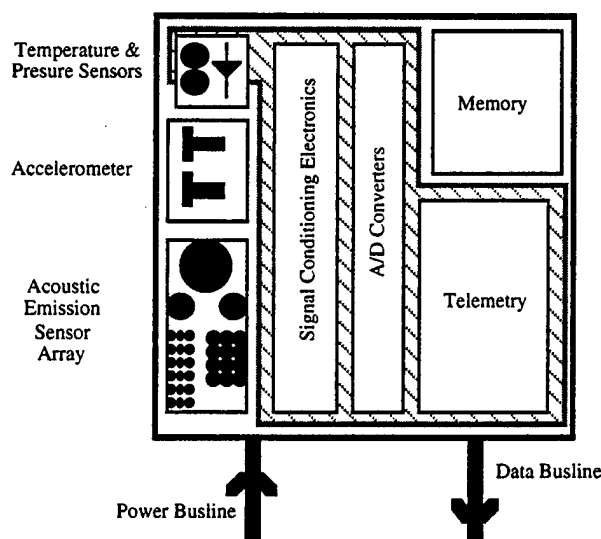


**Figure 91.** Integrated diagnostic coupon containing microsensors, signal conditioning electronics, and telemetry circuitry.

The M-URI Year 2 goals of this project were to 1) demonstrate the integration of acoustic emission microsensors with an analog pre-amplifier, 2) further develop signal processing methods to analyze both AE signals and associated noise background, and 3) demonstrate wireless sensor communication with a remote receiver. The main accomplishments from M-URI Year 2 are summarized in Table 4.

**Table 4. Major Project Accomplishments for Year 2**

- Design and fabrication of AE microsensor amplifiers
- Integration of AE microsensors and amplifiers
- Fabrication of vibration monitoring devices
- Embedding of microsensors in structural composites
- Demonstration of wireless communication with microsensors
- Calibration of AE response with nanoindentation
- Data set analysis to further define signal/noise characteristics
- Development of algorithms for AE signal detection/classification

2.3.3.1 Sub-Task I

**MICROSENSOR DEVELOPMENT**

*D. Polla, L. Francis, W. Gerberich, W. Robbins*

This work on microsensors, for the detection of AE and vibration, is based on the use of piezoelectric thin films [67,68] directly integrated on a silicon chip containing appropriate signal processing electronics. The development of the microsensor effort therefore includes 1) the development and refinement of piezoelectric thin film materials, 2) the design and fabrication of microsensor structures, and 3) the placement and attachment of microsensors onto structures susceptible to fracture.

**Piezoelectric Materials**

Microsensors for acoustic emission and vibration rely on a piezoelectric ceramic thin film. Acoustic emission from crack propagation in a material leads to sound waves [69] which compress the piezoelectric ceramic in the microsensor and creates an electrical signal. For vibration sensors, the piezoelectric film is on top of a cantilever beam which deflects with vibration; deflection in the beam deforms the ceramic and generates an electrical response. Due to its outstanding piezoelectric properties, we use lead zirconate titanate,  $\text{Pb}(\text{Zr}_{0.53}\text{Ti}_{0.47})\text{O}_3$  (PZT), as the piezoelectric material [70]. For these microsensor applications, the demands on the PZT thin film are many. The films must have the appropriate crystal structure, a dense microstructure without cracks and pores, and good adherence to the substrate. Research efforts have been directed at understanding the processing of thin films and how to improve their properties.

In the past year, a convenient process for preparing PZT thin films with good properties has been developed [71,72]. The process involves the synthesis of a metal organic solution, deposition by spin coating and heating to crystallize a ceramic film. Figure 92 shows flow diagrams for these procedures. Unlike routes we have used in the past, this processing route uses non-hazardous solvents and requires

only a short time to prepare. The complex chemistry of this route, however, leads to continued changes in chemical structure with time; this "aging" effect impacts the PZT coating microstructure and its electrical properties, as shown in Table 5. From an investigation of aging, we concluded that the optimum aging time at room temperature is 14 days. Luckily, aging could be accelerated by placing the solution in a 60°C oven. After 2 days of aging, the solutions produced excellent PZT thin films. To arrest the changes in chemical structure, the solutions are placed in a freezer after the 2 day aging. These frozen solutions can then be used as needed with good results.

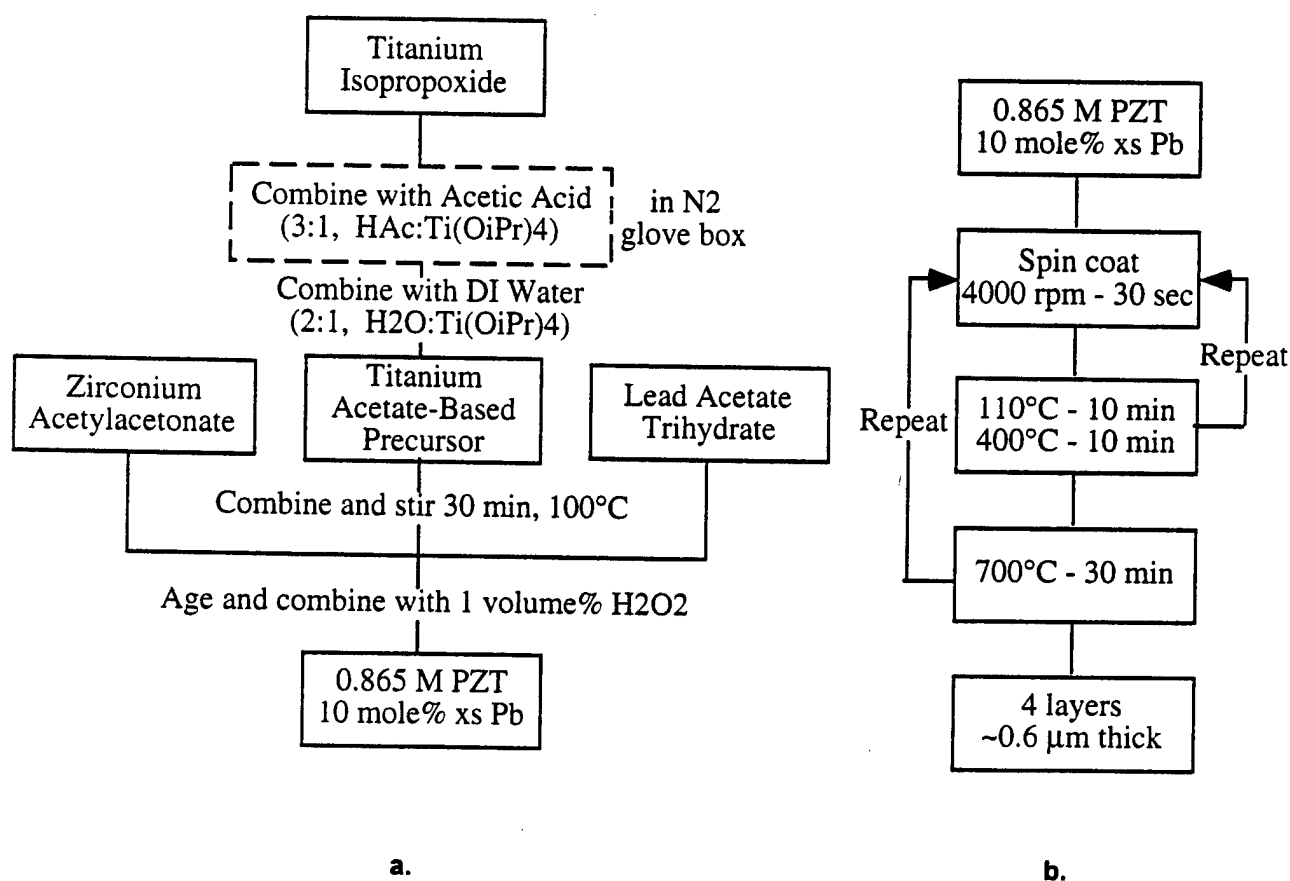


**Figure 92.** (a.) Preparation of a metal organic PZT solution; excess is used to compensate for volatilization that occurs during thermal treatment of the coatings and, (b.) preparation of PZT coatings.

PZT thin films prepared under optimized conditions have the desired Perovskite crystal structure, a dense microstructure and good electrical properties. The Perovskite structure is necessary to develop the dielectric, ferroelectric and piezoelectric properties. The microstructure, as shown in Fig. 93, is dense consisting of submicron grains of PZT. The electrical properties shown in Table 5 are similar to those of bulk PZT and comparable to those achieved in PZT thin films by others working in this field [73-76]. The piezoelectric performance ( $d_{33}$  piezoelectric constant) was determined on some films using a laser interferometer. The results show a  $d_{33}$  of  $\sim 27$  pm/V; this value is slightly lower than that found by other groups on PZT films (50-70 pm/V) [77,78]. Our  $d_{33}$  does rise to  $\sim 80$  pm/V with DC bias of 4V; this effect is currently under investigation. All coatings prepared in this work were deposited on Si with platinum electrodes and intervening Ti, titania, and silica layers (Pt/Ti/TiO<sub>2</sub>/SiO<sub>2</sub>/Si). A representative cross section is shown in Fig. 94. Alternative electrode systems are under investigation with RuO<sub>2</sub> showing promise.

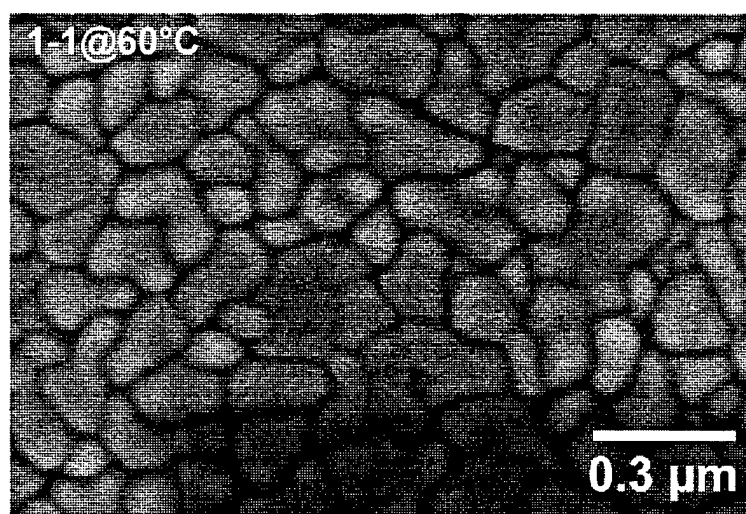
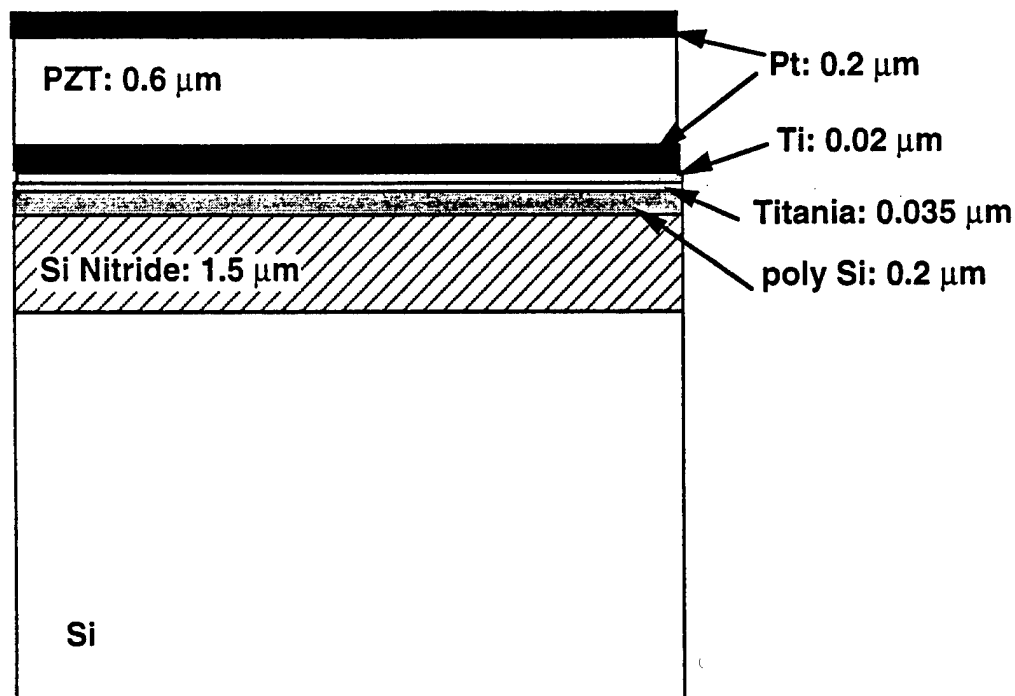


Figure 93. SEM Micrograph of the Surface of a PZT Thin Film.

Table 5. Dielectric and Ferroelectric Properties of PZT Thin Films

Solution Aging*	Relative Dielectric Constant	Loss Tangent	Remanent Polarization ( $\mu\text{C}/\text{cm}^2$ )	Coercive Field (kV/cm)
6 days (20°C)	835	0.040	24.13	54.94
10 days (20°C)	726	0.048	21.32	61.24
14 days (20°C)	898	0.048	27.96	57.40
2 days (60°C)	959	0.039	21.39	40.78
2 days (60°C) then frozen for 1 week	948	0.049	27.18	38.09

\* includes time before and after addition of H<sub>2</sub>O<sub>2</sub>



**Figure 94.** Typical structure of an electroded PZT thin films used for acoustic emission sensing and for characterization of dielectric, ferroelectric and piezoelectric properties.

Research in Year 3 will continue to address improving processing and properties of PZT films and the correlation of PZT composition, properties and microstructure with sensor performance. We are currently trying to implement a PZT processing route developed at Sandia National Laboratory [79]; this route has the advantage of a more gradual heat treatment and hence potentially lower coating stress and improved yield of devices. Another way to improve our thin films is to lower the processing temperature by using a thin layer of lead titanate to enhance the crystallization of the PZT deposited on top of it [80]. We expect to lower the required heat treatment temperature by at least 50°C. Finally, we will also determine the effect of dopants on dielectric, elastic and piezoelectric properties of PZT thin films. For years, small additions of dopants to bulk PZT have been used to tailor properties [69] in commercial bulk sensors; we will implement these strategies with our thin films. In addition to fundamental materials properties, the thin films will be tested for their performance in acoustic emission and vibration sensor. We will therefore gain an understanding of the effect of PZT properties on the sensor operation.

The electrical properties of thin film PZT samples are also characterized. Dielectric properties are measured by impedance analysis, ferroelectric properties (which are related to piezoelectric properties) are determined using a hysteresis set-up, and piezoelectric properties by interferometry. Typical dielectric properties (frequency = 10 kHz) include a dielectric constant of 1000 and a loss tangent of 0.04. Values for the remanent polarization and the coercive field from hysteresis experiments are within the range expected for this PZT composition. A laser interferometer has been built and is operational. We are still in the process of getting data for piezoelectric coefficients and expect that these numbers will be available shortly.



### **AE Microsensor Design and Fabrication**

The objective of the microsensor design and fabrication [81,82] tasks is to develop a thin film wide bandwidth acoustic emission sensor. The sensor needs to be sensitive for the detection of low magnitude acoustic emission events, and also be able to detect high frequency signals (up to 10 MHz or higher). In M-URI Year 1, the basic concept of using thin film PZT capacitor formed on silicon substrates for AE detection was demonstrated. In M-URI Year 2, structural optimization has taken place and processes refined to be compatible with on-chip electronics (commonly referred to as integrated microsensors).

In order to accomplish this, a thin PZT capacitor is used in conjunction with a high frequency amplifier, all in one small package. The amplifier is currently a commercial surface mount device, but is currently being fabricated along with the sensing element on the same chip. The amplifier is used as a charge amplifier with a gain of  $10^9$  volts/coulomb to amplify the charge produced by the piezoelectric sensor in response to the acoustic emission event. This apparatus is contained in small aluminum housing to both protect the sensor from damage and to allow easy use and mounting of the sensor on a variety of structures for characterization and testing.

Thus far, both thin film PZT and small pieces of commercial PZT ceramic disks have been used as the sensing element in the apparatus. The thin film devices (0.6  $\mu\text{m}$  thickness) provide better high frequency response, but a lower sensitivity than the sensors fabricated with the (100  $\mu\text{m}$ -thick) commercial disks. Figure 95 shows the simultaneous response of both the thin film sensor and a commercial acoustic emission sensor (Physical Acoustics S9220) in response to an AE event simulated by the breaking of a 0.5 mm pencil lead on the aluminum block onto which the sensors were mounted. The response of our thin film sensor with integral amplifier shows a significantly faster response to the AE event, although at lower sensitivity than the commercial sensor. In addition, the thin film sensor did not exhibit any ringing after the initial peak, while the commercial sensor output fluctuated for approximately 50  $\mu\text{s}$  (10 oscillations).

Testing is currently underway using the thin film sensor in the Nanoindenter for investigation of acoustic emission produced from microcracking and film delaminations.

### **Vibration Microsensors**

The real-time detection of extraordinary vibration might provide important information in a failure prediction algorithm for a particular system. Vibration microsensors [83] were fabricated in this program using similar piezoelectric thin film microsensors as those used in the AE microsensor above. A main fabrication difference for the vibration microsensor is the need to have a free-standing cantilever oscillate in response to vibration signals. This requires the use of solid-state micromachining techniques to form a deformable microbeam as shown in Fig. 96. The process for making this structure has been developed in Year 1 with details previously reported in the M-URI Year 1 Integrated Diagnostics Annual Report of this program.

In the operation of the vibration sensor, inertial movements produce a time-varying stress across the piezoelectric material thereby producing a spontaneous charge. This charge is sensed by an amplifier or converted to a voltage for subsequent signal processing. Figure 97 shows a scanning electron micrograph of a piezoelectric cantilever measuring  $40 \times 200 \mu\text{m}^2$ .

The PZT vibration sensor is currently being integrated with the identical charge amplifier being used for AE sensing.

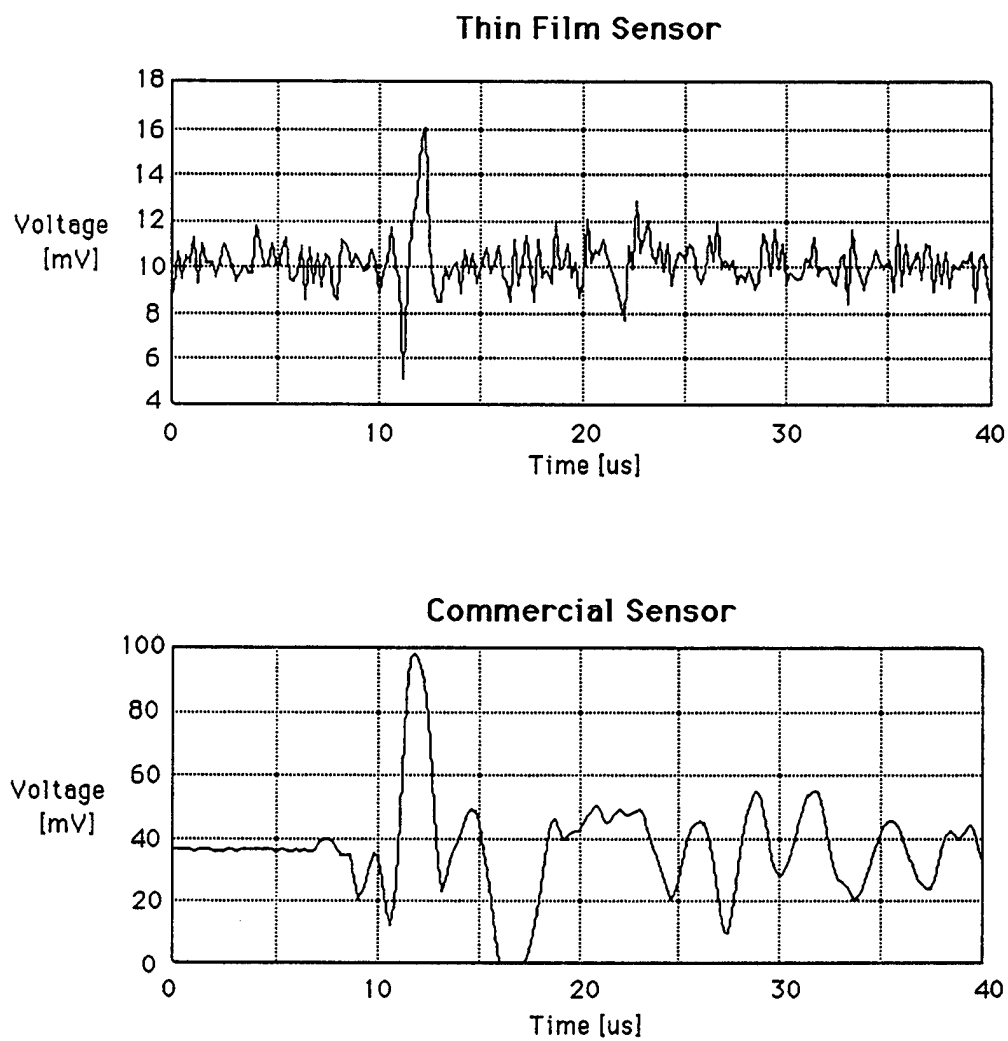


**Figure 95.** Acoustic Emission Spectra for (a.) a 0.6 $\mu$ m-thick film PZT microsensor; and (b.) a Physical Acoustic Model S9220 commercial AE sensor.

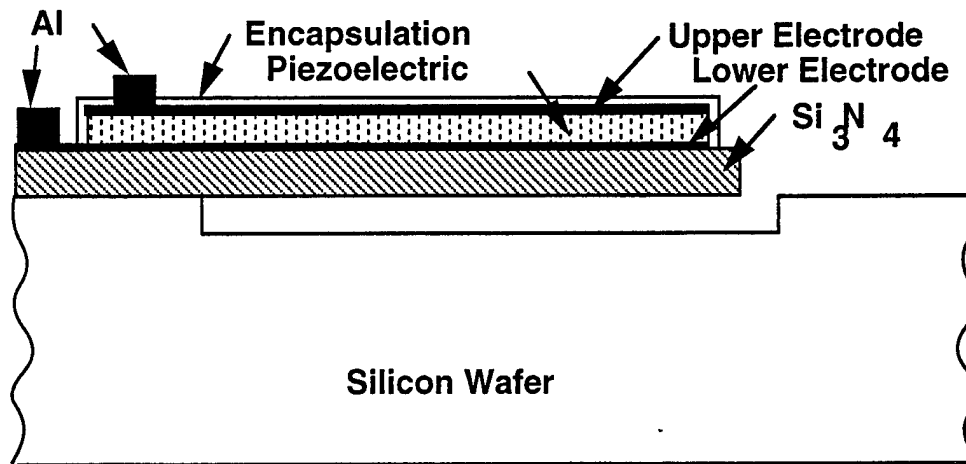


Figure 96. Microbeam Vibration Sensor

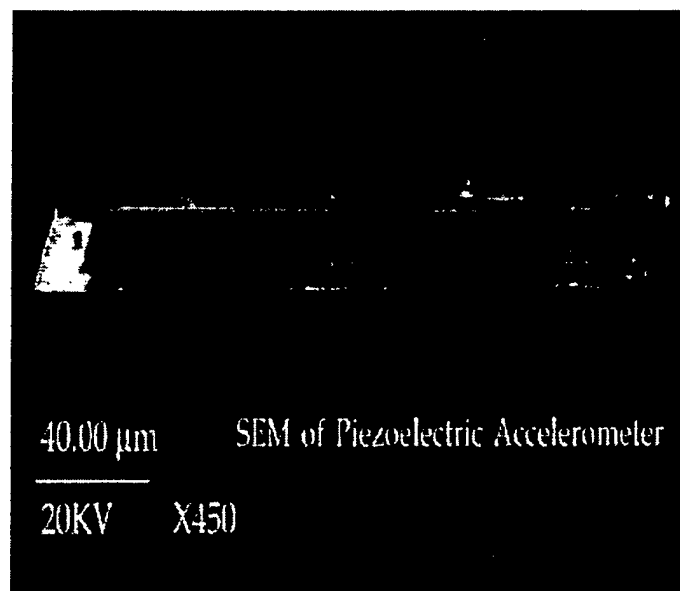


Figure 97. SEM of Vibration Sensor

### Acoustic Emission Microsensor Placement

The acoustic emission in multi-layered isotropic solids is currently being modeled [84]. The goal of this activity is to construct a generalized computer model to account for AE transmission through multi-layered media (helicopter component, adhesive, sensor package, sensor structure, etc.). A theoretical model has been established by considering continuous boundary conditions for the interface between two solids as shown in Fig. 98. Assuming that the wave of acoustic emission is longitudinal, the reflection coefficients,  $R_p$  for longitudinal reflected wave and  $R_s$  for reflected shear wave (vertical polarized) in Region III as shown in Fig. 98, as well as transmission coefficients  $T_p$  for longitudinal transmitted wave and  $T_s$  for transmitted shear wave (vertical polarized) have been obtained by using the theoretical layered model for a range of ultrasonic frequency from 100 kHz to 1 MHz in region of incident angle  $0^\circ$  to  $90^\circ$  (Figs. 99-102). The region of frequency for acoustic emission by material cracking is in 100 kHz to 1 MHz. The energy ratios for the longitudinal reflected wave to longitudinal incident wave,  $E_{rp}/E_{inc}$  and the reflected shear wave to longitudinal incident wave,  $E_{rs}/E_{inc}$  are also given in this report. The reflection and transmission coefficients of horizontally polarized and vertical polarized shear wave incidence also have been obtained. Data analysis is continuing. In M-URI Year 3, the theoretical model will be compared with experimental data obtained from thin film devices.

The acoustic emission in multi-layered isotropic solids is under investigation in our fundamental study of solid acoustic emission microsensor. As shown in Fig. 98, the theoretical model has been established by considering continuous boundary conditions for the interface between two solids. At this stage, the solid materials are treated to be isotropic.

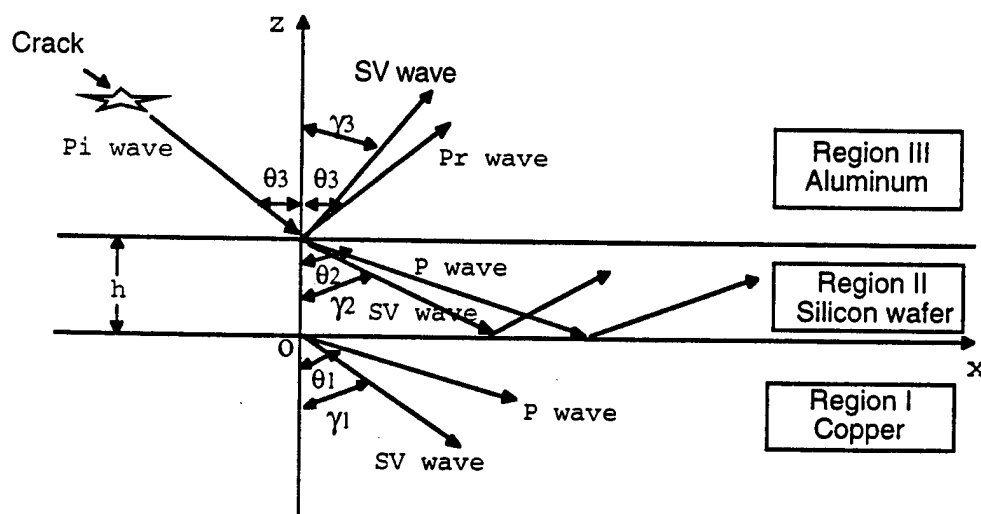


Figure 98. Acoustic Emission in Multi-layered Isotropic Solids

The matrix equation for the reflection coefficients,  $R_p$  for the longitudinal reflected wave and  $R_s$  for shear reflected wave in Region III as shown in Fig. 98, as well as the transmission coefficients,  $T_p$  for longitudinal transmitted wave and  $T_s$  for shear transmitted wave in Region I has been obtained as shown in Eqn. (15). Since Eqn. (15) is a linearly non-homogeneous matrix equation, the reflection coefficients,  $R_p$  and  $R_s$ , as well as transmission coefficients,  $T_p$  and  $T_s$ , can be found by solving the matrix equation and represented in analytical forms.

$$\begin{pmatrix} d_{11} + b_{11} R_p + b_{12} R_s \\ d_{21} + b_{21} R_p + b_{22} R_s \\ d_{31} + b_{31} R_p + b_{32} R_s \\ d_{41} + b_{41} R_p + b_{42} R_s \end{pmatrix} = \begin{pmatrix} a_{11} & a_{12} & a_{13} & a_{14} \\ a_{21} & a_{22} & a_{23} & a_{24} \\ a_{31} & a_{32} & a_{33} & a_{34} \\ a_{41} & a_{42} & a_{43} & a_{44} \end{pmatrix} \begin{pmatrix} c_{11} T_p + c_{12} T_s \\ c_{21} T_p + c_{22} T_s \\ c_{31} T_p + c_{32} T_s \\ c_{41} T_p + c_{42} T_s \end{pmatrix}, \quad (15)$$

where  $d_{ij}$ ,  $b_{ij}$ ,  $a_{ij}$ , and  $c_{ij}$  are known as functions of angles, acoustic frequency, acoustic velocities in solids, thickness of silicon wafer, mass densities of solids, and mechanical properties of solids. The detailed expressions for the coefficients  $d_{ij}$ ,  $b_{ij}$ ,  $a_{ij}$ , and  $c_{ij}$  are not given here because they are complicated and do not lend insight into the objective of this task.

The reflection coefficients  $R_p$  and  $R_s$  as well as transmission coefficients  $T_p$  and  $T_s$  can be obtained from computational calculations of Eqn. (15).

Assuming that the wave of acoustic emission is longitudinal, the reflection coefficients,  $R_p$  for longitudinal reflected wave in Region III as shown in Fig. 98, are given by using the theoretical layered model for a range of ultrasonic frequency from 100 kHz to 1 MHz in region of incident angle  $0^\circ$  to  $90^\circ$  as shown in Fig. 99. For small incident angle, the reflection coefficients of longitudinal reflected wave  $R_p$  for the silicon wafer seem to be independent of frequency and is at about 40%. However, the reflection coefficients for the silicon wafer are decreasing in a region of larger incident angles when frequency is increased. In the region of larger incident angles, the reflection coefficients for the silicon wafer increase as the incident angles increase.

As shown in Fig. 100, the reflection coefficients of the reflected shear wave for the silicon wafer are below 30% in the region of incident angles from  $0^\circ$  to  $90^\circ$ , less than 10% in smaller incident angles. The shear reflected wave may not be important in smaller incident angles. However, in a region of larger incident angles, the shear reflected wave become pronounced.

Assuming that the wave of acoustic emission is longitudinal, the transmission coefficients  $T_p$  for longitudinal transmitted wave for the silicon wafer are given by using the theoretical layered model for a range of ultrasonic frequency from 100 kHz to 1 MHz in region of incident angle  $0^\circ$  to  $90^\circ$  as shown in Fig. 101. In region of incident angles from  $0^\circ$  to  $30^\circ$ , the transmission coefficients for longitudinal transmitted wave for the silicon wafer is about 43%, for a region of frequencies from 0.1 MHz to 1 MHz. This may be a good message for the design of a real solid acoustic emission microsensor because a constant transmitted energy may make the microsensor more easily process the signals of an acoustic emission in a solid if the incident angles of the acoustic emission are small.

The transmission coefficients for transmitted shear wave (vertically polarized) for silicon wafer between aluminum and copper is very low, less than 10% for incident angles less than  $50^\circ$ , and only 8% for incident angles less than  $30^\circ$  as shown in Fig. 102.

The energy ratios for the longitudinal reflected wave to longitudinal incident wave,  $E_{rp}/E_{inc}$  and the reflected shear wave to longitudinal incident wave,  $E_{rs}/E_{inc}$  are also given in Figs. 103-104. Less than 18% of the longitudinal incident wave energy is carried off by the longitudinal reflected wave on the surface of the silicon wafer between aluminum and copper when the incident angles are less than  $50^\circ$  for the region of frequencies from 0.1 MHz to 1 MHz as shown in Figure 96. Less than 6% of the longitudinal incident wave energy is carried off by the reflected shear wave on the surface of the silicon wafer when the incident angles are less than  $30^\circ$  for the region of frequencies from 0.1 MHz to 1 MHz as shown in Fig. 104. In a region of larger incident angles, the longitudinal reflected wave and reflected shear wave carry off more than 40% of the longitudinal incident wave energy at a frequency of 0.1 MHz. The reflected energy is decreased when the frequency of incident wave increases.

The materials selected in the above analysis are arbitrary. As materials information for our microsensor structure become more understood, additional modeling will be carried out.

The theoretical multi-layered model indicates that more than 80% of the longitudinal acoustic emission wave energy will go into the silicon wafer between aluminum and copper when incident angles are less than  $30^\circ$  in the region of frequencies from 0.1 MHz to 1 MHz. For the region of incident angles from  $30^\circ$  to  $70^\circ$ , still there is 70 to 30 % of the incident wave energy to go into the silicon wafer when frequencies of the incident wave are in the range from 0.1 MHz to 1 MHz.

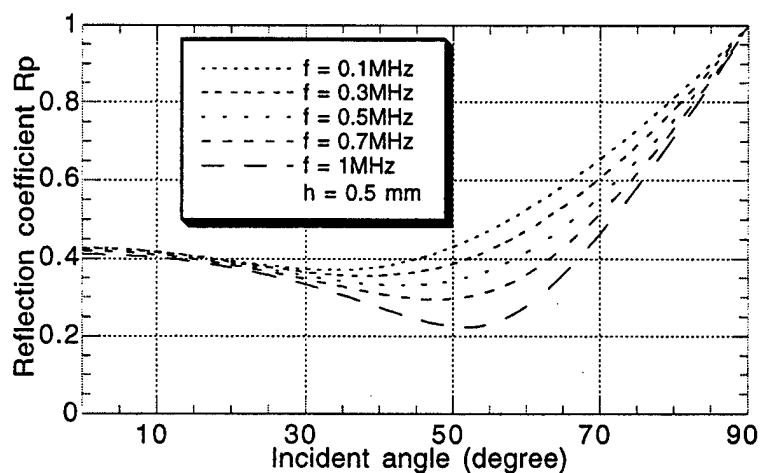


**Figure 99.** Theoretical reflection curves (Longitudinal reflected waves) for longitudinal incident wave in multi-layered solids.

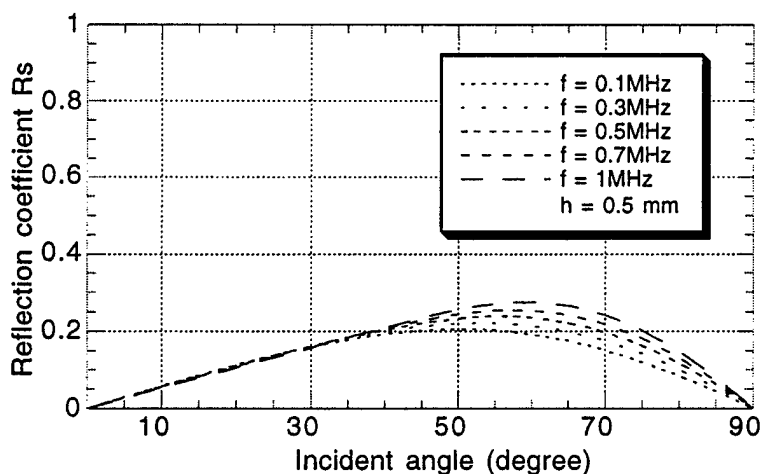


**Figure 100.** Theoretical reflection curves (vertical polarized shear reflected waves) for longitudinal incident wave in multi-layered solids.

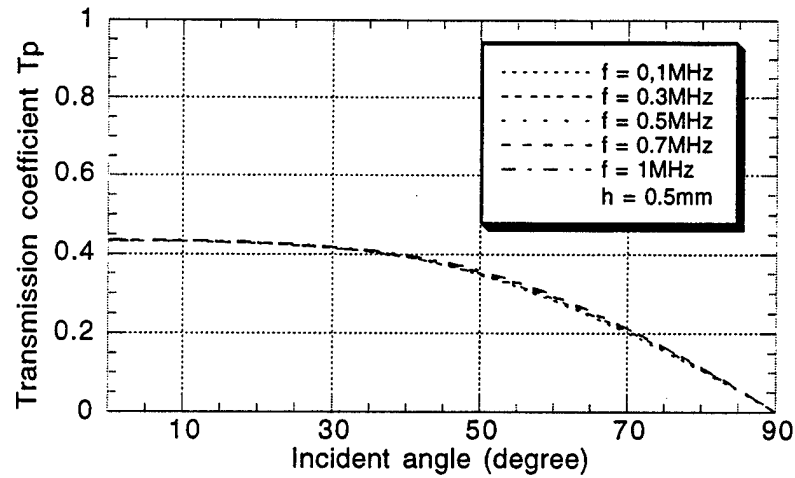


**Figure 101.** Theoretical transmission curves (Longitudinally transmitted waves) for longitudinal incident wave in multi-layered solids.

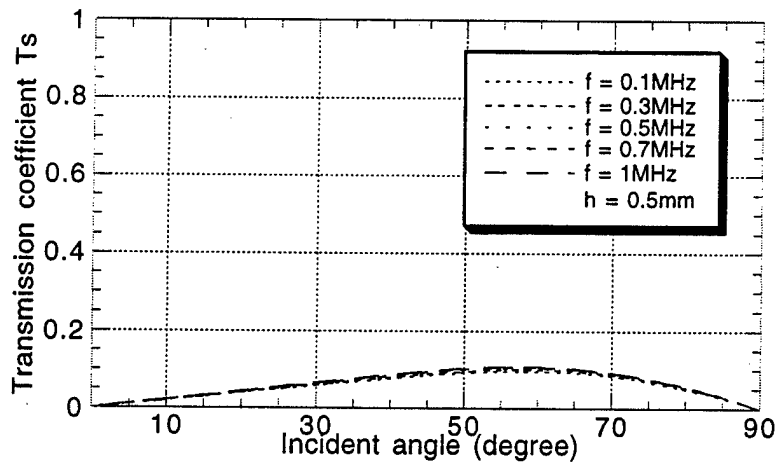


**Figure 102.** Theoretical transmission curves (vertically polarized transmitted waves) for longitudinal incident wave in multi-layered solids.

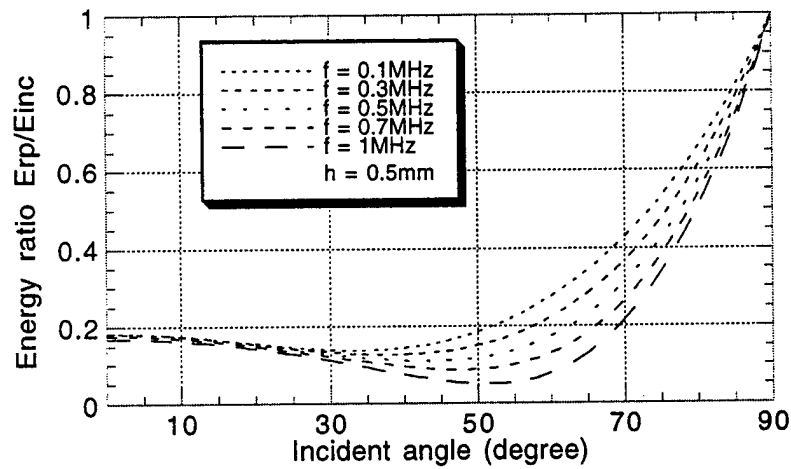


**Figure 103.** Energy ratio for longitudinal reflected wave to longitudinal incident wave in multi-layered solids.

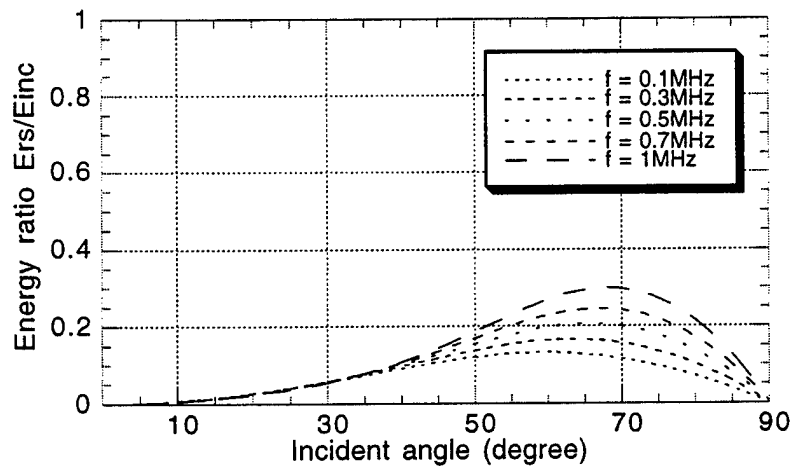


**Figure 104.** Energy ratio for reflected shear wave (vertically polarized) to longitudinal incident wave in multi-layered solids.



### **Microcrack Materials Physics and Reference Signal Calibration**

The second year of the mechanical testing portion of the microelectromechanical systems (MEMS) acoustic emission (AE) project focused on two main objectives. The first was identification of physical phenomena using the AE signal characteristics. The second objective was determination of the properties of the materials used in fabricating the actual MEMS AE sensor. Several goals have been met in both areas, along with determining areas of testing which require further investigation. The energy of an AE event can be directly linked to the elastic energy released in two types of failures, regardless of sample size and geometry. In addition, the modulus and hardness of each material used in the MEMS sensor and the mechanical properties of the entire package have been determined.

#### *Identification of Physical Phenomena via AE Signal Characteristics:*

Acoustic emission signals have been generated which correspond to film delaminations in thin film systems and the onset of plasticity in metals. Thin film failure characteristics are of interest for determining the type of signal which would correspond to a failure in a portion of the MEMS device other than the actual sensor. Plasticity in metals is of particular interest for this project, since fatigue crack extension is preceded by the persistent motion of dislocations in front of the crack tip.

Several features of the waveform of an AE event were considered for use as "signatures" of event types: the rise time of a signal, the frequency character of the signal, the initial rate of change of the signal with respect to time, and the total energy in the signal. A set of experiments were carried out

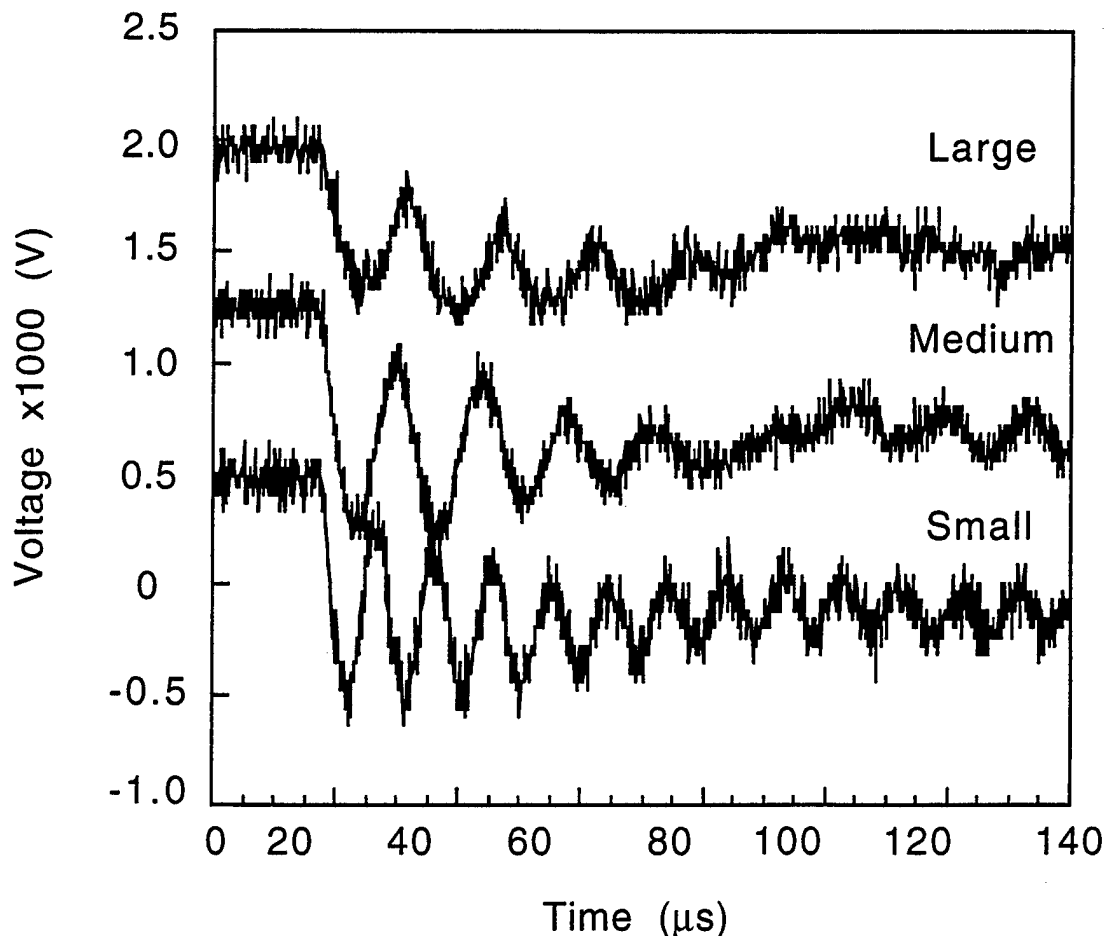


**Figure 105.** AE waveforms from initiation of plasticity in Fe-3% Si. Note the dependence of the rise time and frequency of the signal on the sample size.

to determine the effects of sample size on the signal characteristics [85]. An Fe-3% Si single crystal, which previously was shown to produce detectable acoustic emission events during nanoindentations, was cut to 25mmx4mm x4mm. The sample was indented in a micro-mechanical testing device (MMT) and reproducible yield excursions were obtained. The procedure was then repeated after cutting the sample to a 4 mm cube, and then sliced to 4 mm x 4 mm x 1 mm. Representative acoustic emissions corresponding to the indentations in the three sizes of crystal are shown in Fig. 105.

From this experiment and others [85], it has been determined that the sample size controls both the rise time and the frequency of the AE signal. Therefore, for general identification of physical phenomena, these parameters cannot be used to unambiguously determine the type of event which caused the AE signal. However, it has been shown that in the case of Ta<sub>2</sub>N films the AE sensor can be used in conjunction with the MMT to detect film delaminations which previously would not have been detected using only the loading information [86].

It has been known for quite some time that the energy of an AE signal from a bulk fracture event scales with the energy released in the fracture process [87,88]. Experiments in Fe-3% Si, W, and on Ta<sub>2</sub>N films on sapphire have shown that the same trend holds for microscopic events, such as thin film fracture or the onset of plasticity, as shown in Fig. 106 [85]. This scaling is independent of the sample size, composition, and geometry over the range of materials used in this study. Since nanoindentation

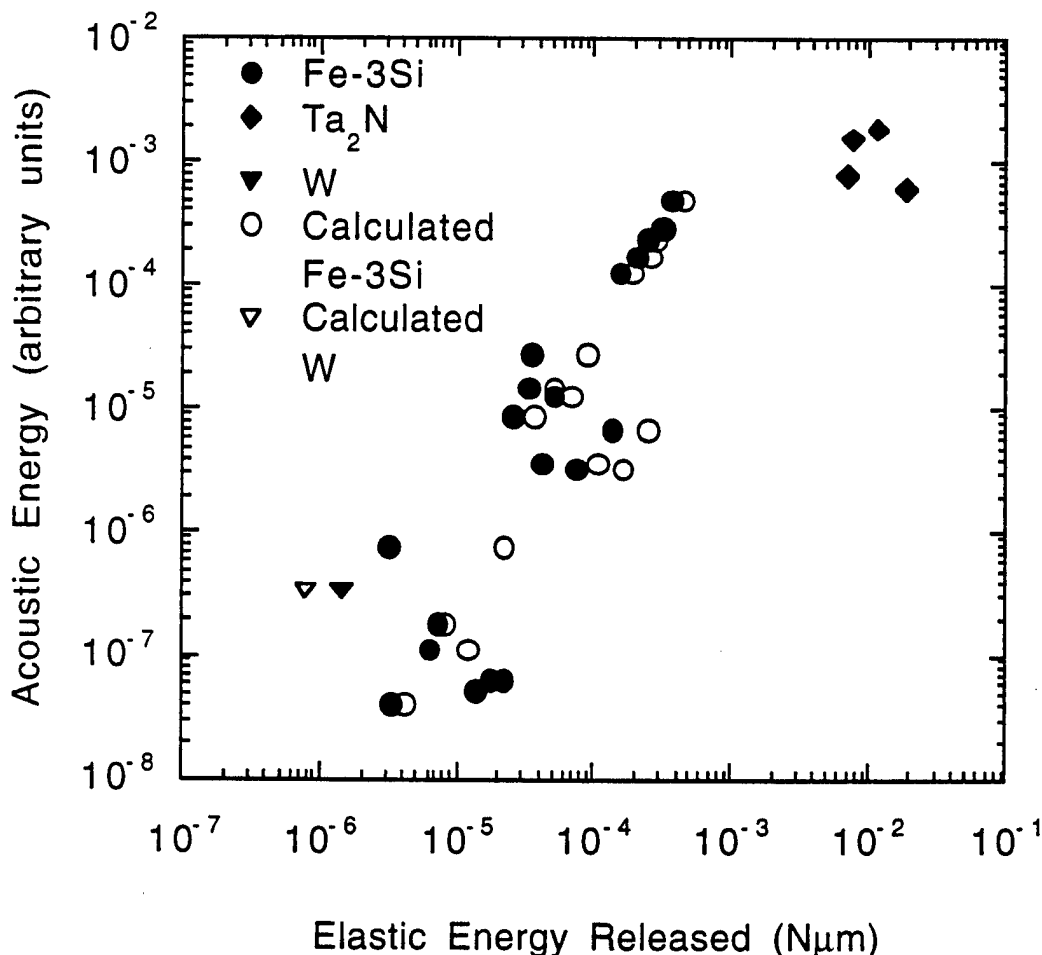


**Figure 106.** Relationship between measured acoustic energy and the elastic energy released from an event. The calculated elastic energies based on Hertzian contact mechanics are also shown.

can be used to quantitatively measure the elastic energy released in an event, it should be possible to calibrate AE sensors. From this, the actual amount of physical damage in a sample could be determined from an AE signal. It should be noted that as the sample size increases by orders of magnitude from the samples used in this study to actual structural parts a sample size calibration may also be needed.

Experiments are under way to test the relationship between the elastic energy released in an event and the AE energy in much larger samples. By fitting the MMT with a sample holder which can hold a long sample with multiple AE sensors attached, we can determine both the effects of distance and how the waveform changes with distance during the onset of plasticity.

#### *Mechanical Properties of Materials Used in Microsensor Fabrication:*

Since the materials used in fabricating a MEMS AE sensor are in the form of thin films, it is difficult to determine the mechanical properties using conventional techniques. Low load indentations have increasingly become a common method of evaluating the modulus and hardness of thin films. Therefore, indentations were made using a Nanoindenter II (located at SANDIA NATIONAL LABORATORIES, Livermore CA) to provide statistical sampling of the properties of each materials being considered for the sensor.

Initial studies of the mechanical properties of the materials used in the bottom electrode began with evaluating each individual layer deposited on a silicon (100) substrate [89]. The individual layers were deposited using the method by which they are deposited on the entire system. The  $\text{SiO}_2$  layer is grown using a wet thermal oxidation in  $\text{H}_2$  and  $\text{O}_2$  environment. The titanium and platinum were deposited by RF sputtering in argon.  $\text{TiO}_x$  was grown using reactive RF sputtering of titanium in an argon and oxygen environment.  $\text{Si}_x\text{N}_y$  and the polycrystalline silicon were deposited using low pressure chemical vapor deposition. The  $\text{SiO}_2$  layer was 526 nm thick; the Pt - 2% Cu layer was 1.6  $\mu\text{m}$  thick; the Ti layer was 1.7  $\mu\text{m}$  thick; and the remaining individual films were grown to nominal thicknesses of 1  $\mu\text{m}$ . The bottom electrode systems were made using the processes described above for each layer, and are shown in Table 6.

By using a substrate correction technique to subtract out the effects of the Si substrate on the measured mechanical response, the modulus and hardness of each film was determined. Details of the correction methods can be found in [89]. The results are shown in Table 7, and consist of an average of approximately 30 indentations per film. In addition to evaluating each material individually, the various bottom electrode configurations which were being evaluated were tested. It was found that for the bottom electrode system 3, the modulus of the electrode was approximately 140 GPa, and was relatively constant through the thickness of the electrode.

The actual sensor material, lead-zirconate-titanate (PZT), was also tested in the Nanoindenter. The PZT is deposited by solution chemistry routes onto the system 3 electrodes. With a relatively constant modulus for this system, we can again utilize the substrate correction method to determine the modulus and hardness of the PZT thin film. The results show that the modulus of the PZT thin film is approximately 175 GPa, with a hardness of approximately 12 GPa [90].

Both the PZT thin film and the Pt - Cu film have a higher elastic modulus than the bulk forms of the same material. Bulk Pt has a modulus of approximately 160 GPa, and bulk PZT has a modulus of approximately 60 GPa. The fact that our measured values of Ti,  $\text{SiO}_2$ , and Si correspond closely to the bulk values suggests that the indentation technique is valid. However, recently it has been suggested that indentation techniques are more sensitive to residual stress than previously expected. The Pt film is under a high state of tensile stress (approximately 700 MPa) and we expect the PZT to also be under a residual stress (though not quite as high as the Pt).

To examine the effects of the residual stress on modulus measurements, a set of experiments has been undertaken involving Pt films. Using an e-beam evaporator at the Microtechnology Laboratory, a series of Pt films will be deposited at various rates on 3 inch Si wafers. The residual stress should vary

with deposition rate, and will be measured using wafer bowing techniques. The films will then be indented and the modulus calculated. By indenting to the same depth in each film, errors caused by substrate corrections will be minimized. The measured modulus can be compared to the residual stress, allowing us to determine if the residual stress in the films can account for our previously measured "high" moduli.

**Table 6.** Bottom electrode materials thicknesses (nm) used for MEMS acoustic emission sensor. Either SiO<sub>2</sub> or Si<sub>x</sub>N<sub>y</sub> is in contact with the silicon wafer.

System	Pt	Ti	TiO <sub>x</sub>	Poly Si	Si <sub>x</sub> N <sub>y</sub>	SiO <sub>2</sub>
1	200	20	36	200	1500	-
2 *	200	20	36	200	1500	-
3	200	20	36	-	-	930
4	200	20	36	-	-	517

\* Annealed for 950 °C for 25 minutes in N<sub>2</sub> after polycrystalline silicon deposition.

**Table 7. Mechanical Properties of Materials Used in MEMS AE Sensor.**

Material /Thickness, nm	Elastic Modulus, GPa	Surface Hardness, GPa
Si substrate	181	13
Polycrystalline Si, 1000	172	8 - 13
Si <sub>x</sub> N <sub>y</sub> , 1000	267	30 - 33
SiO <sub>2</sub> , 526	78	10.5 - 12
TiO <sub>x</sub> , 1000	185	7 - 12
Ti, 1700	113	2.5 - 3.5
Pt-2% Cu, 1600	237	5 - 8

#### 2.3.3.2 Sub-Task II

### **SENSOR ELECTRONICS**

*D. Polla, R. Harjani*

In this section, current progress and future work is to be reported upon with respect to the sensor electronics of an aircraft fatigue and failure warning system. In particular, the progress related to acoustic emission sensor electronics, a temperature sensor and its related electronics, and telemetry circuitry are reported upon. The conceptual schematic for the fatigue/failure microsensor is shown in Fig. 91. This section addresses the system blocks enclosed in the gray hashed polygon.

Statements about the current status and future work are presented, with details about the various design blocks. Table 8 shows the status of this sub-task.

**Table 8. Current Status of Electronics**

- Acoustic emission electronics
  - Evaluated voltage amplifier versus charge amplifier tradeoffs.
  - Evaluated power and noise design tradeoffs.
  - Developed minimum bounds on power.
  - Developed charge amplifier that cancels 1/f noise, offsets and thermal effects.
- Temperature sensor and electronics
  - Developed and fabricated a MOS weak inversion based temperature sensor.
  - Developed circuit design for a novel switched-capacitor bandgap voltage-based temperature sensor.
  - Evaluated area power tradeoffs.
- Telemetry electronics
  - Developed overall design topology for telemetry.
  - Developed first pass circuit designs for system level blocks.
  - Simulated and evaluated performance based on completed layouts.

#### **Acoustic Emission Electronics**

The goal is to design low power signal conditioning electronics for the detection of cracks and unusual wear in aircraft and submarines. The inputs to our circuit will be the piezoelectric sensor output which will then be amplified and converted into its digital form. This amplified signal will then be sent to the base station via telemetry. The sensor types have been mentioned in brief, but more stress has been given to the acoustic emission sensors. The design of the charge amplifier along with some offset and noise reduction circuitry is given. Both MOS and Bipolar techniques have been considered for the design of the circuit and some design tradeoffs between power and noise has been explained. Simulation results are shown to prove our arguments.

#### **Sensor Types**

The three sensor types used in this project are:

- *Temperature and pressure sensors*: Temperature sensors are used for identification of excessive heating and also for temperature compensation and signal referencing.
- *Microbeam accelerators*: These sensors are used for detection of unwanted mechanical vibrations.
- *Acoustic emission sensors* : Used for the detection of cracks and unusual wear.

### Acoustic Emission Sensor

This sensor is used for the detection of cracks, and is the most important sensor from the sensor electronics point of view. When there is an acoustic emission event, the outgoing ultrasonic waves hit the thin film piezoelectric sensor which is coupled to the aircraft component and an output charge or voltage is produced. This magnitude of this output signal is proportional to the magnitude of the acoustic emission event.

#### Signal Characteristics:

The characteristics of the acoustic emission signal is as follows:

- *Signal bandwidth:* The experimentally measured acoustic emission signal bandwidth is from 50 kHz to about 1 MHz.
- *Noise frequency:* The vibration noise due to fretting of the mechanical parts and low frequency noise is less than 100 kHz.

The design bandwidth chosen is 5 MHz as it is better to design with some tolerance margin. The minimum frequency for the design was chosen to be 50 kHz. The advantages of choosing this frequency are that it cancels out most of the flicker and vibration noise as well as the thermal drift and offsets.

#### Amplifier Design:

There are two options for the amplifier design: a voltage amplifier (Fig. 107) or a charge amplifier (Fig. 108). The advantages of using a charge amplifier over a voltage amplifier are mentioned below :

- The piezoelectric sensor output is normally charge. Hence it makes sense to use a charge amplifier to amplify it.
- Secondly, the output voltage of the piezoelectric sensor is very small. This is because the piezoelectric material has a very high permittivity and hence the voltage is very small. This can be shown in the following equation.

$$V = \frac{Q}{C} = \frac{Q}{\epsilon \cdot \frac{A}{d}} \quad (16)$$

- Finally, a voltage amplifier will have a capacitance at its input which will cause loss of charge due to leakage.

The charge amplifier circuit shown in Fig. 108 is a simple basic design. The current  $I$  and capacitance  $C_s$  is used to model the charge. The inverting terminal of the operational amplifier is at virtual ground and so no charge flows through into the opamp. All the charge has to flow through the feedback capacitance  $C_f$ . If the value of  $C_f$  is made very small the voltage at the output  $V_o$  will be large and hence amplification of charge is achieved. The gain of the circuit is given by the ratio of  $C_s$  over  $C_f$ . Hence, to get a high gain,  $C_f$  is made much smaller than  $C_s$ .

Modifications to this basic design were done to cancel out low frequency noise and offset. The modified circuit diagram is shown in Fig. 109. In the modified circuit, a lowpass filter and a transconductance cell is connected in negative feedback. The lowpass filter passes only the low frequency components and the transconductance cell is used to convert the voltage into current which is then fed into the inverting node of the amplifier. This modification helps in canceling out the low frequency noise and offset. The transfer function for the entire circuit is shown below.

$$\frac{V_o(S)}{I_{in}(S)} = - \left[ \frac{S^3 \cdot C_s + C_{f1} \cdot C_{f2} \cdot R_2 \cdot (1 + A_2) - (1 + A_1) \cdot S \cdot C_{f1}}{C_{f1} \cdot C_{f2} \cdot R_2 \cdot C_s \cdot (1 + A_2) \cdot S^2} \right] \quad (17)$$

Simplifying this further, we get:

$$\frac{V_o(S)}{I_{in}(S)} = \left[ \frac{S \cdot C_s}{1 - \frac{S}{C_{f2} \cdot R_2}} \right] \quad (18)$$

From the transfer function it is clear that the circuit has a zero at the origin and a pole at the frequency,  $1 / C_{f2} \cdot R_2$ . Thus the circuit has the characteristics of a highpass filter which is exactly what is wanted. Both MOS and Bipolar transistor technologies have been considered and power and noise analysis have been done to see the difference between the two.

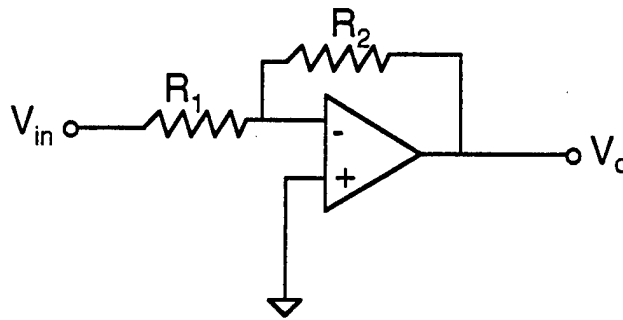


Figure 107. Voltage Amplifier

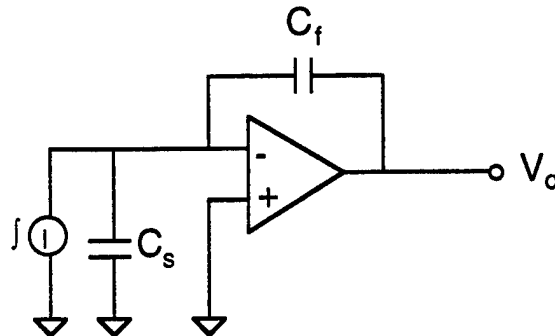


Figure 108. Charge Amplifier

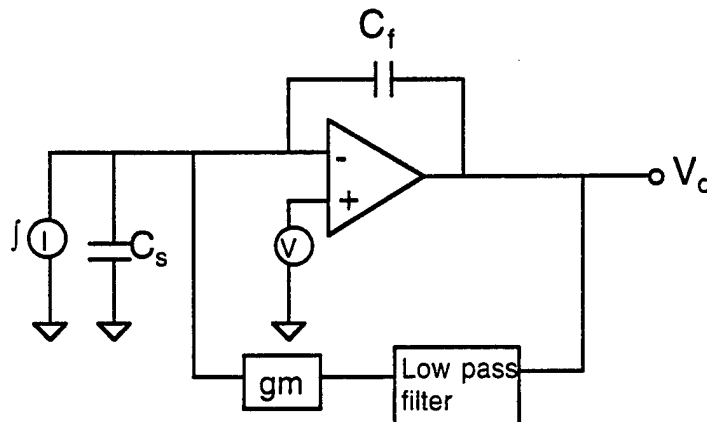


Figure 109. Modified Charge Amplifier

**Power Analysis:**

In MOS transistors, power is given by the equation:

$$P = V \cdot I = \frac{V \cdot (BW \cdot C)^2}{2 \cdot K \cdot \frac{W}{L}} \quad (19)$$

where BW is the bandwidth, C is the sensor capacitance, K is the transconductance factor, V is the voltage, I is the current, and W/L is the size of the transistor. From the above equation, we see that power is proportional to the square of the bandwidth and the sensor capacitance.

In Bipolar transistors, power is given by the equation:

$$P = V \cdot I = V \cdot BW \cdot U_T \cdot C \quad (20)$$

Here,  $U_T$  is 26 mV and all the other factors are the same as for MOS transistors. Thus, in bipolar transistors, power is linearly proportional to bandwidth and capacitance. This difference in power is shown in Fig. 110. In this graph, we see that MOS transistors consume more power than bipolar transistors in both strong and weak inversion regions by a factor of two.

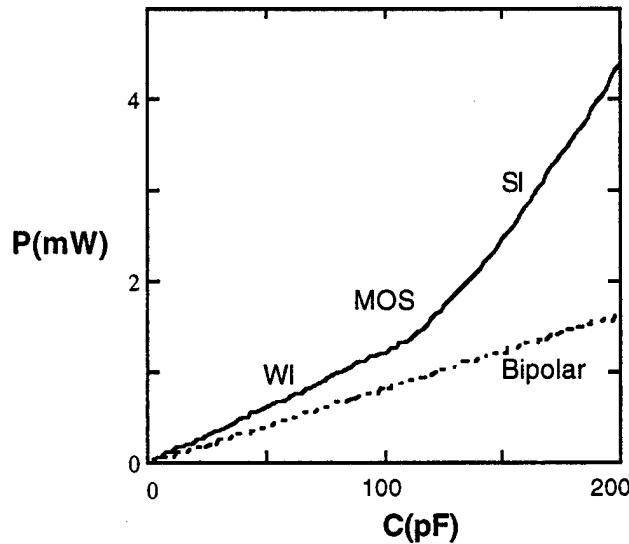


**Figure 110. Plot of Power versus Capacitance for MOS and Bipolar Transistors.**

**Noise Analysis:**

In MOS transistors, noise voltage is given by the equation:

$$V_{nT}^2 = \frac{8 \cdot K \cdot T \cdot gm}{3 \cdot gm \cdot C} = \frac{8 \cdot K \cdot T}{3 \cdot C} \quad (21)$$

Here, K is Boltzmann's constant, T is the temperature, gm is the transconductance and C is the sensor capacitance.

In bipolar transistors, noise voltage is given by:

$$V_{nT}^2 = \frac{2 \cdot q \cdot U_T}{C} = \frac{2 \cdot K \cdot T}{C} \quad (22)$$



In both MOS and bipolar, the noise voltage is independent of frequency. This can be seen in the plot of noise spectral density versus capacitance shown in Fig. 111. In this graph, it is shown that the noise spectral density in MOS and bipolar differ by a factor of two for a range of capacitances.

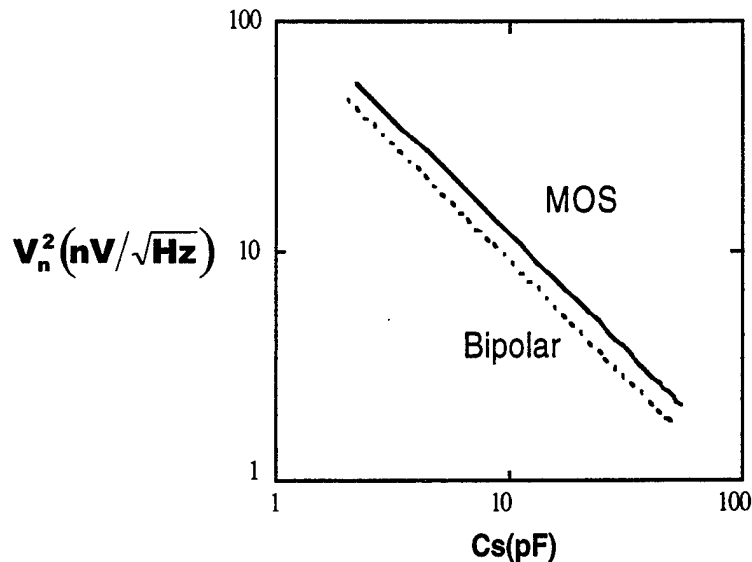


**Figure 111. Noise Spectral Density versus Capacitance**

#### *Design Tradeoff:*

The observations from power and noise comparisons can be summarized as follows:

- *Power analysis* - From the power analysis we see that the power in MOS transistors is proportional to the square of the capacitance whereas power in bipolar transistors is linearly proportional to capacitance.
- *Noise analysis* - From the noise analysis we see that the noise voltage in both MOS and bipolar transistors is inversely proportional to the sensor capacitance.

Thus, we see that there is a clear tradeoff between power and noise. If the capacitance is increased the noise reduces but the power increases and vice-versa. For 11 bits of accuracy and bandwidth of 5 MHz the minimum sensor capacitance for the charge amplifier is 5 pF and the minimum power is 1  $\mu$ W.

#### *Simulation Results:*

The simulation result of the charge amplifier with a sensor capacitance of 100 pF and a feedback capacitance of 10 pF is shown in Fig. 112. The ac response of the circuit is shown for an input voltage of 1V. The gain is 20 dB which is as expected.

#### *AE Circuit Conclusions:*

The design of the charge amplifier circuit for the acoustic emission sensors is explained in detail. The advantages of charge versus voltage amplifier is given. The power and noise analysis for the circuit is done and verified by simulation results. Finally simulation result for the charge amplifier circuit is also attached. Future work includes detailed circuit implementation of the charge amplifier and the bandpass delta-sigma A/D converter.

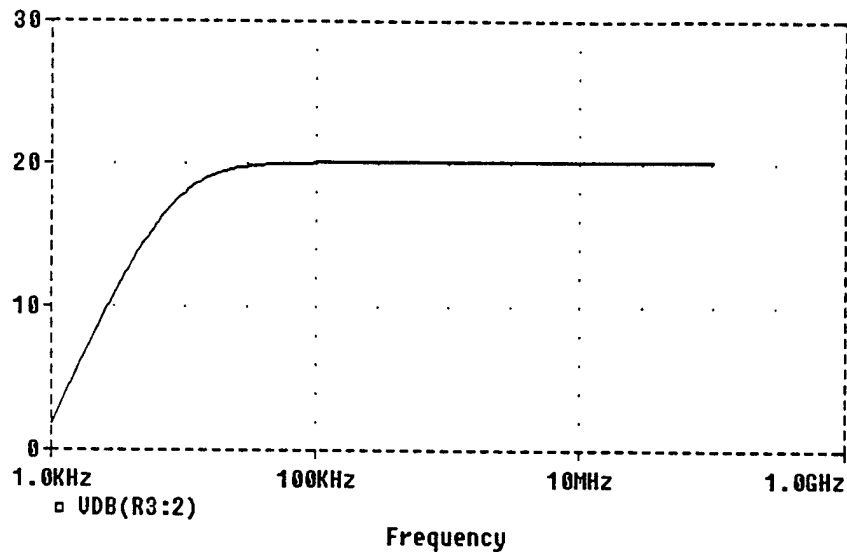


Figure 112. AC Response of the Charge Amplifier Circuit

### Temperature Sensor & Electronics

Most common temperature sensors are based on development of a PTAT (proportional to absolute temperature) cell and a reference voltage ( $V_{ref}$ ) cell. In general, a ratiometric measurement of the voltage produced by the PTAT cell in relation to  $V_{ref}$  is made and digitized with the help of data converters. A block diagram for such a circuit is shown below in Fig. 113. The PTAT voltage is generated by evaluating the difference between two exponentially related base-to-emitter voltages of a bipolar device. Unfortunately, CMOS does not include intrinsic bipolar devices, however, it does include parasitic lateral and vertical bipolar devices. It is easier to design circuits with the parasitic lateral bipolar transistor. However, it suffers from a low beta value and an overall sensitivity to process conditions. So, parasitic vertical bipolar transistors are preferred. They are not without problems either. Their collector is always connected to the substrate.

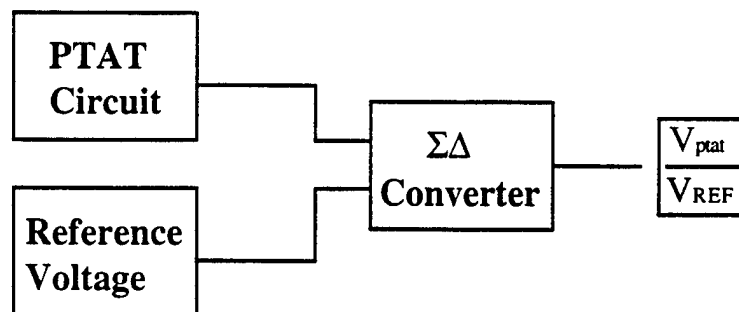
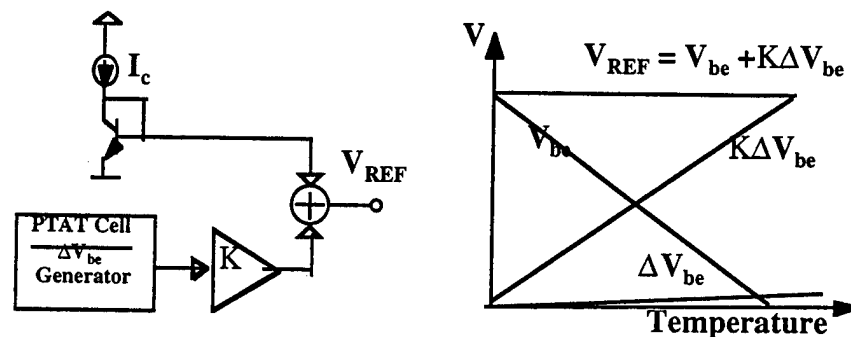


Figure 113. Temperature Sensor Block Diagram

Two temperature sensor circuits have been designed. One is based on exploiting the exponential characteristic of the parasitic vertical bipolar transistor available in CMOS technologies. The second is based on exploiting the exponential characteristics of a MOS device when operated in the weak inversion region.

A conceptual block diagram for system operation is shown in Fig. 114. Two voltages are added to create a temperature independent voltage reference. It can be shown that the forward biased  $V_{be}$  of a bipolar transistor has a negative temperature coefficient of approximately  $-2 \text{ mV}/^\circ\text{C}$ . Additionally, it can also be shown that the difference between two  $V_{bes}$  ( $\Delta V_{be}$ ) has a positive voltage coefficient of approximately  $+0.085 \text{ V}/^\circ\text{C}$ . In general, the  $\Delta V_{be}$  is proportional to the absolute temperature, and such is often called a PTAT (proportional to absolute temperature) cell. The output of the PTAT cell is multiplied with a constant ( $K \Delta V_{be}$ ) such that its positive coefficient matched the magnitude of the temperature coefficient of  $V_{be}$ . This generates a temperature independent voltage reference, where ( $V_{ref} = V_{be} + K \Delta V_{be}$ ). An external reading of the temperature can be provided by evaluating the ratio of  $(K \Delta V_{be})/V_{ref}$ . One of the primary advantages of this topology is that it provides both a voltage that is proportional to temperature and a reference voltage that is independent of absolute voltage.



**Figure 114. Bandgap Temperature Sensor Principles**

A linear resistance based circuit that performs the necessary functions mentioned in the previous paragraph are shown in Fig. 115. Unfortunately, there is direct tradeoff between low power and area for this circuit. To keep the current dissipation the resistance values have to be made large. However, this takes up extensive silicon area. Additionally, to design an accurate temperature reference, we are required to use poly-silicon integrated resistors which have extremely low resistivity and result in an increase in area. We propose to use a switched-capacitor version of the circuit shown in Fig. 115. The switched-capacitor version of the temperature sensor is shown in Fig. 116. However, before we consider the switched-capacitor implementation in Fig. 117 we plot silicon area consumed by the linear resistive version of the circuit shown in Fig. 115 vs. the switched-capacitor implementation of the circuit shown in Fig. 116. The X-axis shows the supply current and the Y-axis shows the silicon area in square microns. It is clear to see that for low power applications the switched-capacitor implementation is orders of magnitude smaller in area. Figure 118 shows the simulation results for the switched-capacitor implementation of the temperature sensor. Plots for the  $K \Delta V_{be}$  and  $V_{ref}$  have been shown.

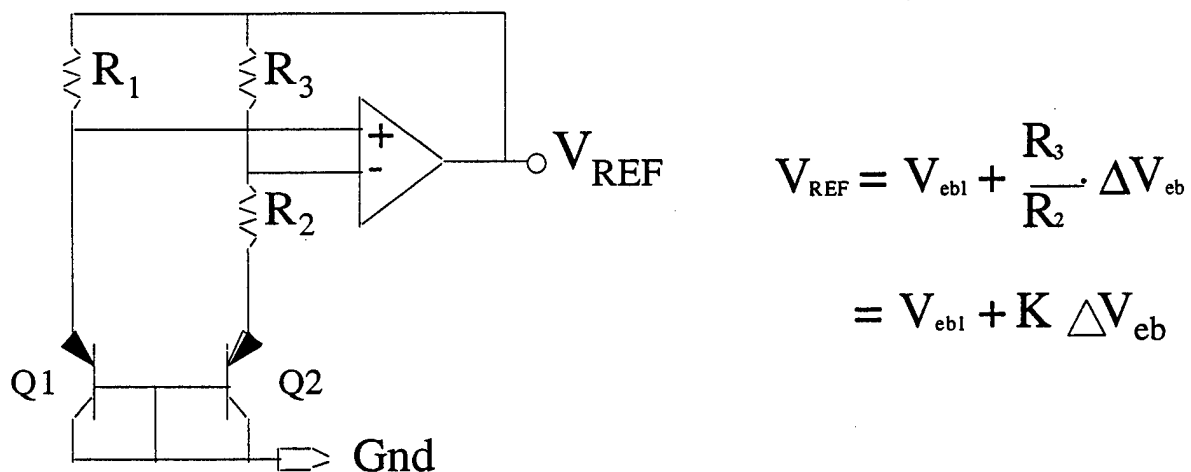


Figure 115. Linear Resistance Based Bandgap Voltage Reference.

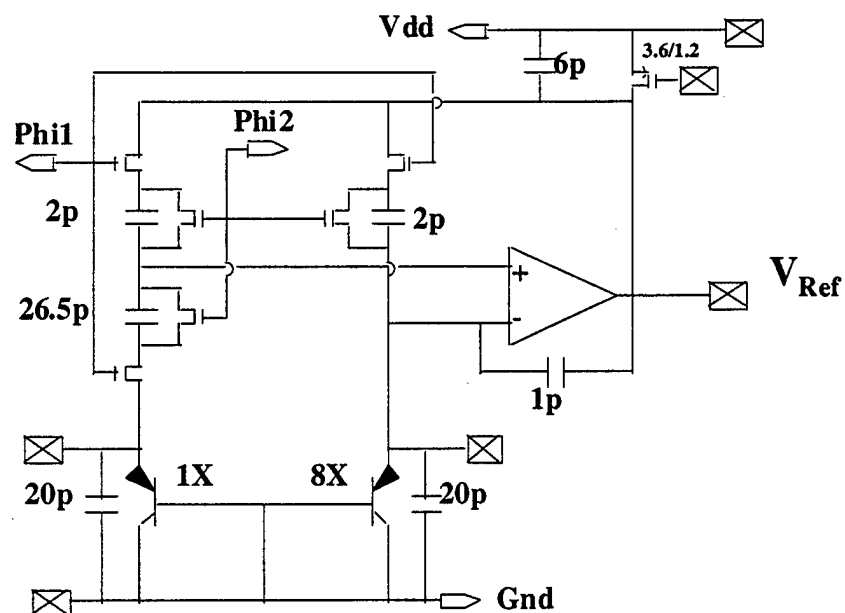


Figure 116. Switched-capacitor Implementation of Temperature Sensor

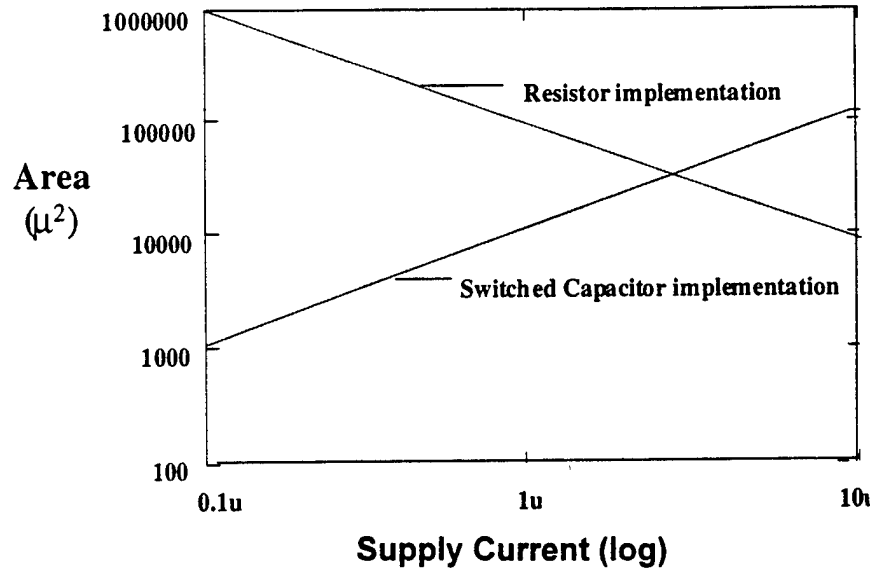


Figure 117. Comparison of Silicon Area for Linear Resistor vs. Switched-capacitor Implementation

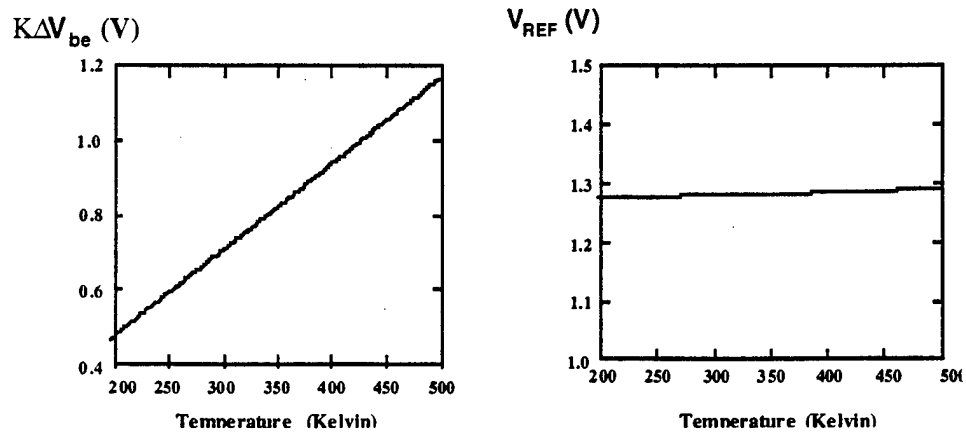


Figure 118. Simulation Results for Switched-capacitor Temperature Sensor

In Fig. 119, the circuit design for the weak inversion PTAT cell is illustrated. The expression for the output voltage is shown on the right, S1 and S2 are the device W/L ratios for the respective transistors. It is clear that the voltage is a function only of device size and temperature. A simulation of the circuit using the first order model is shown in Fig. 120. The simulation results include the results from the first order model shown in Fig. 119 as a well as a full model using SPICE BSIM models. The offset between the two results can be predicted by some second order effects. Forty copies of completed designs for this circuit have been sent out for fabrication.

In summary, two circuit designs have been presented for a novel bandgap temperature sensor and a weak inversion temperature sensor. The bandgap temperature sensor includes a voltage reference and as such does not require an external reference. A switched-capacitor implementation has been described for the circuit that should be orders of magnitude smaller in area and power compared to other implementations. Additionally, though not explicitly mentioned, the temperature coefficient of integrated capacitors is two orders of magnitude lower than the temperate coefficient of integrated resistors. It is expected that our design will have lower second order nonlinearity. Final designs for this circuit will be sent out to fabrication in early March. A weak inversion PTAT cell has also been presented. The design is extremely small, requiring low power. However, it requires the use of an external voltage reference. problems with offset and non-repeatable temperature coefficient reported by other researchers still need to be verified.

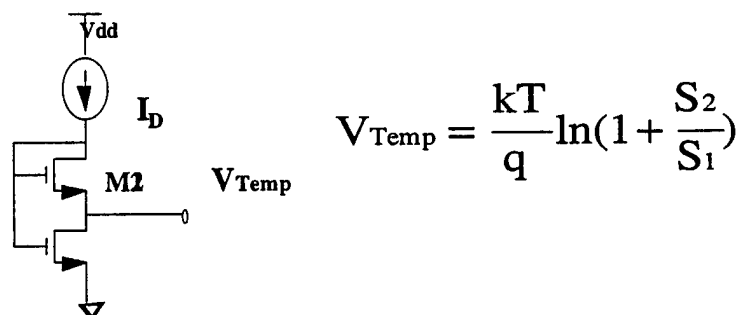


Figure 119. Weak Inversion PTAT Cell

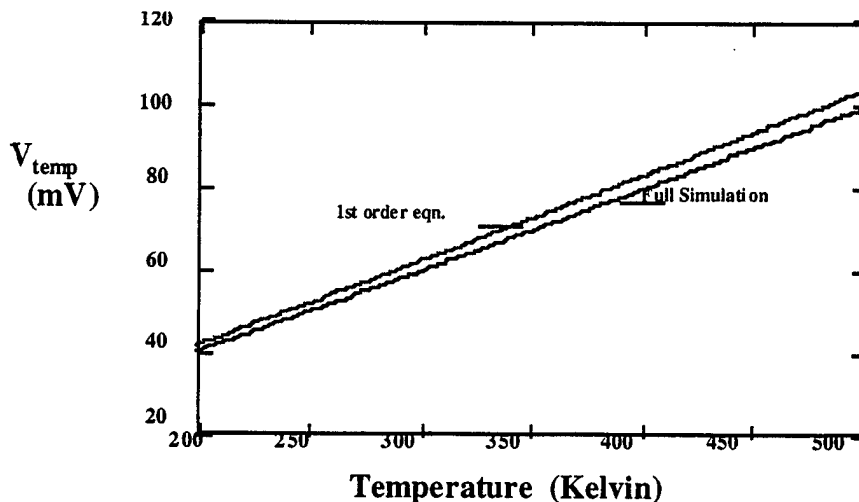


Figure 120. Simulation Results for Weak Inversion PTAT Cell

### Telemetry for an Aircraft Crack Detection Microsensor

A CMOS transceiver is being designed for wireless communication with the microsensors as shown in the telemetry block diagram of Fig. 121. Choosing to use 2-way communication with the microsensors, the base station can request data from one microsensor at a time by sending a unique identification code for the respective microsensor. The reason for doing this is that the raw bit-rate from each microsensor is about 50 MHz. This can be seen from Fig. 122, where the sensor signal with a total bandwidth of 5 MHz is amplified by the preamplifier and converted to digital data by a 8-10 bits Analog to Digital Converter (ADC). A Digital Signal Processor (DSP) will perform preliminary crack detection and store the data that was gathered in memory.

When a microsensor is contacted by the base-station, it will send a code back which either means that no possible cracks are detected, or that a possible crack is detected. If a possible crack is detected, the microsensor will also send all the stored crack-related data to the base-station.

The transceiver is optimally designed to work in the 902-928 MHz ISM band, but the same transceiver can be used at frequencies from 10 MHz up to 1 GHz. The transceiver is meant for short range communication (up to 20m), and therefore a simple modulation format (ASK) is chosen to minimize power. The transceiver is designed in a standard digital 3 layer metal 0.5  $\mu\text{m}$  CMOS process available through MOSIS.

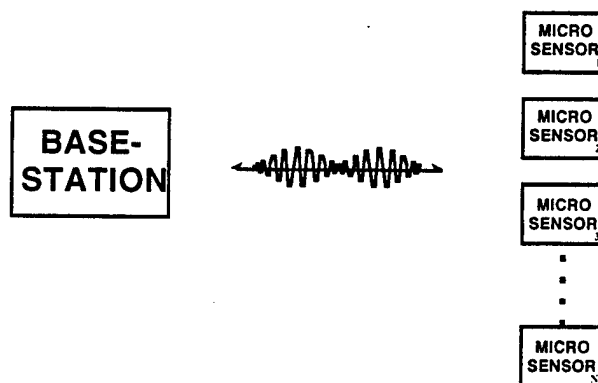


Figure 121. Telemetry Block Diagram

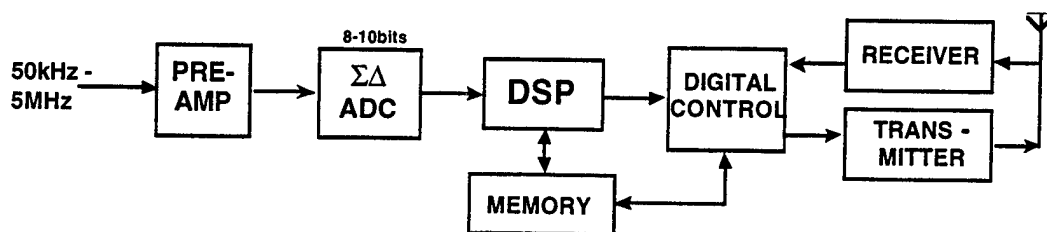


Figure 122. Microsensor Block Diagram

### Transceiver Operation:

The transceiver block diagram is shown in Fig. 123. The antenna is shown to the far left and it is shared by the receiver and the transmitter through a preselect filter. The receiver (RX) is the path above the Local Oscillator (LO), and the transmitter (TX) is the path below the Local Oscillator.

The objective of the preselect filter is to reject the image channel from the receiver, and to reduce the bandwidth of all the signals and noise that is available at the antenna terminals. The preselect filter does also reduce harmonic distortion from the transmitter. Our transceiver is not designed for full duplex, so the transmitter will never transmit at the same time as the receiver is receiving.

To minimize noise in the receiver and to obtain maximum power transfer from the transmitter to the antenna, the antenna impedance and the preselect filter should be matched with the input impedance of the receiver and the output impedance of the transmitter. The receiver and the transmitter can not be matched with the antenna for maximum power transfer without having the receiver input terminals disconnected while transmitting, and having the transmitter output terminals disconnected while receiving. This is incorporated by using an TX/RX switch between the preselect filter and the receiver and transmitter.

The local oscillator (LO) is shared by the receiver and the transmitter, and it oscillates with the frequency :

$$f_{LO} = f_{RF} + f_{IF} \quad (23)$$

where  $f_{RF}$  is the carrier frequency of the system. The intermediate frequency (IF),  $f_{IF}$  is chosen to be 10.7 MHz so that standard FM filters can be used during testing of the receiver. The IF frequency determines a major part of the power consumption in the transceiver, hence, a lower intermediate frequency, gives lower power. However, if the intermediate frequency is chosen too low, it becomes very difficult to make a preselect filter which can reject the image, since the image frequency is at

$$f_{image} = f_{RF} - f_{IF} \quad (24)$$

and the preselect must pass  $f_{RF}$  while rejecting  $f_{image}$ .

An intermediate frequency of 10.7 MHz is found to be about as low as practically possible using commercially available preselect filters in a heterodyne type receiver for frequencies in the 900 MHz ISM band.

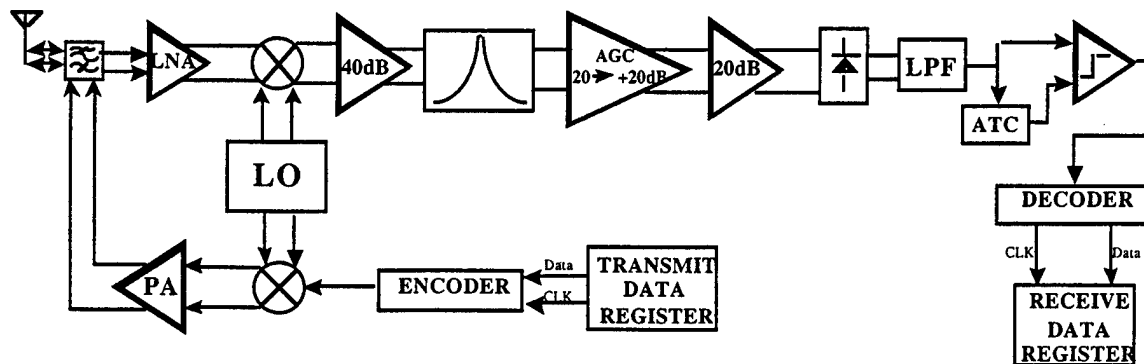
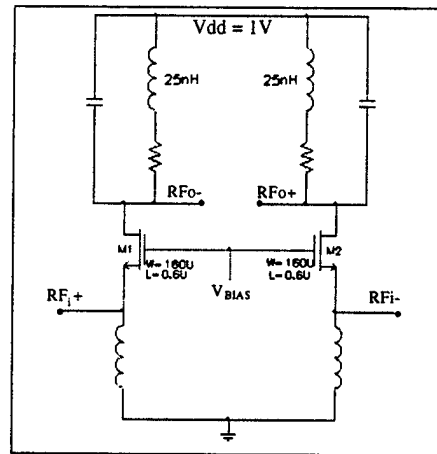


Figure 123. Transceiver Block Diagram



All circuits in the receiver are designed fully differential in order to keep the common mode noise down, such as the substrate noise. The low noise amplifier (LNA) is designed to give about 15 dB of gain around 950 MHz. The LNA is shown in Fig. 124. Low noise is obtained by using a single transistor amplifier with a matched input impedance and a low bias current. Also the series resistance of the on-chip spiral inductor is minimized to give lower noise and higher gain.

The LNA operates at a supply voltage of only 1 Volt to properly bias the down conversion mixer directly. This should not degrade the dynamic range since the received signals at the antenna terminals are in the microvolt to millivolt range. The LNA frequency response is shown in Fig. 125.



**Figure 124. Low Noise Amplifier Schematic**

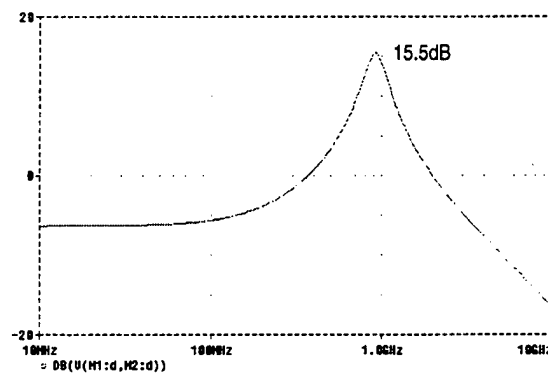


**Figure 125. LNA Frequency Response**

There are two 25 nH on-chip spiral inductors for the LNA designed in the 3<sup>rd</sup> metal layer as shown in Fig. 126. The inductors are designed with the objective to minimize the series resistance which lowers the gain and increases the noise, and to minimize the capacitance to the substrate which lowers the resonant frequency. The spiral inductors are designed and simulated using models verified by other research groups.

The down conversion mixer shown in Fig. 127 is a fully balanced Gilbert cell. This is an effective CMOS mixer that rejects common mode noise and cancels the local oscillator frequency and the rf input frequency at the output. The output IF spectrum will consist of the difference frequency,  $f_{LO} - f_{RF}$ , and the sum frequency,  $f_{LO} + f_{RF}$ , and the harmonics of these frequencies. It is important that the local oscillator signal at the input of the mixer has a large voltage amplitude to switch the M3, M4, M5, and M6 totally on and off. The downconversion mixer in Fig. 127 gives a conversion gain of about -3dB and uses about 1.5 mW of power.

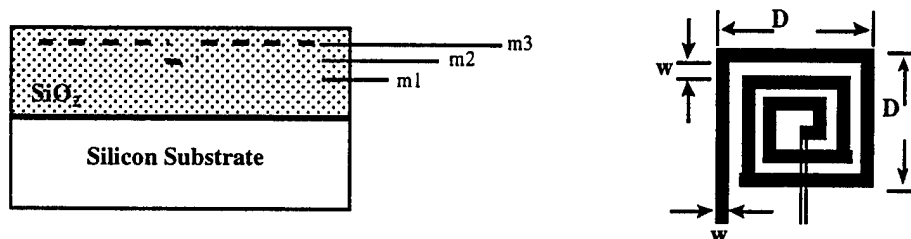


Figure 126. On-chip Spiral Inductors

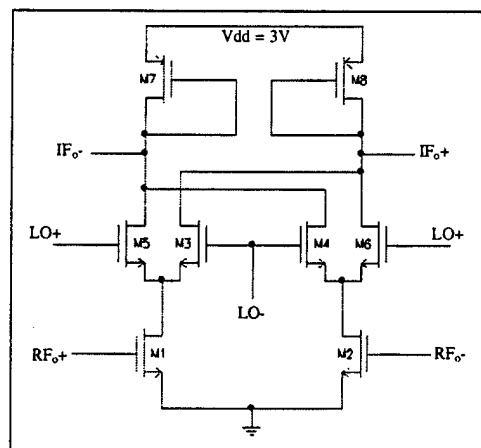


Figure 127. Downconversion Mixer

The intermediate frequency part of the receiver has a total gain from 40 - 80 dB to meet the specified dynamic range. The gain is controlled by an Automatic Gain Control (AGC) circuit shown in Fig. 128. The AGC is important since the signal received by individual microsensors will vary from location to location and by environmental effects.

The AGC was simulated in time domain with a input ASK modulated signal with a decreasing amplitude to see if the AGC can automatically keep the output amplitude constant. These simulation is shown in Fig. 129, where the upper signal is the input, and the lower signal is the output of the AGC. As one can see, the AGC does indeed keep the output amplitude constant, and this without effecting the modulation.

The ASK detection circuitry uses a multiplier circuit to square the IF signal for a full wave rectification. After rectification, the signal is low pass filtered and compared by a comparator with automatic threshold control (ATC). ATC is included for increasing the dynamic range of the receiver.

The transmitter consist of a modulator and a current amplifier (Power Amplifier (PA)). The transmitter is shown in Fig. 130, and the antenna impedance is matched with the output impedance of M1 and M2 for maximum power transfer to the antenna.

Transistors M3 and M4 modulates the Local Oscillator which is fed differentially in to the Power Amplifier. The modulating signal, shown as "data" in Fig. 130 should be a sine wave rather than a square wave to reduce harmonic signals to be transmitted.

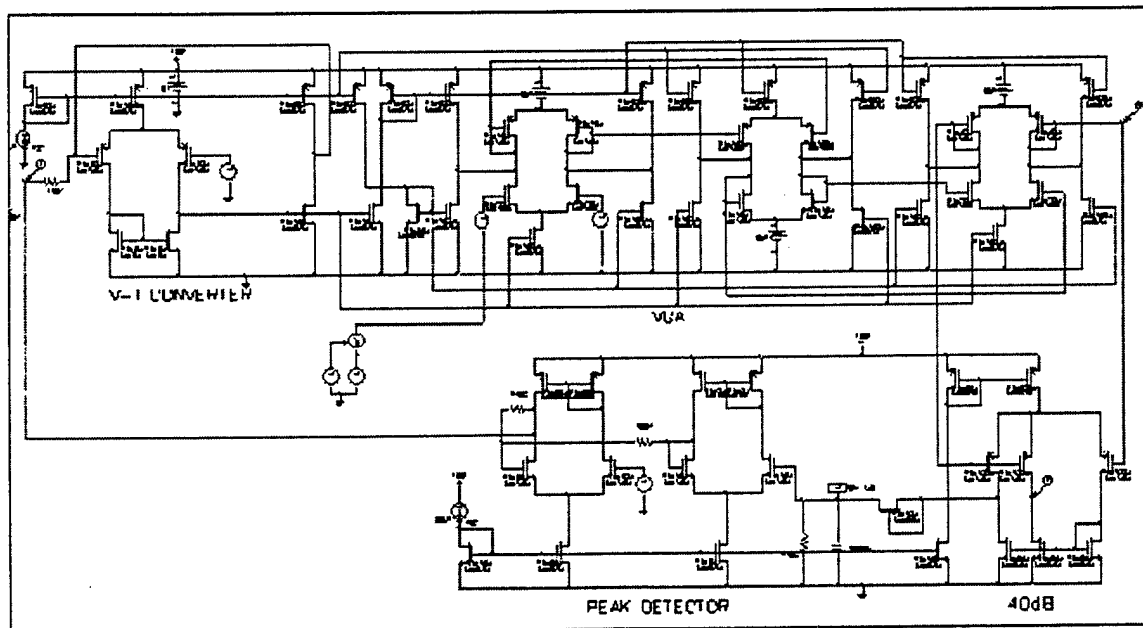


Figure 128. Automatic Gain Control Circuit

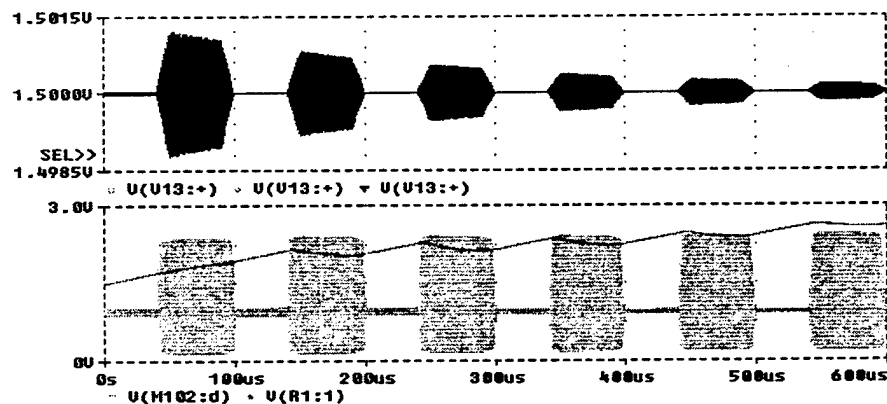


Figure 129. AGC Simulation

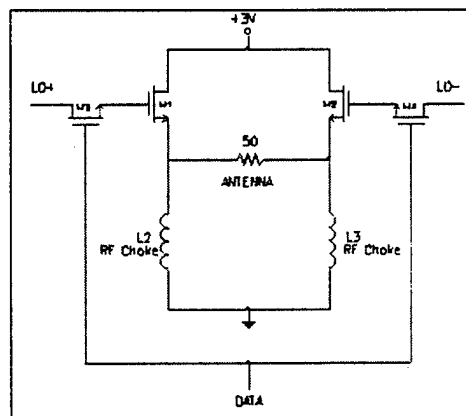
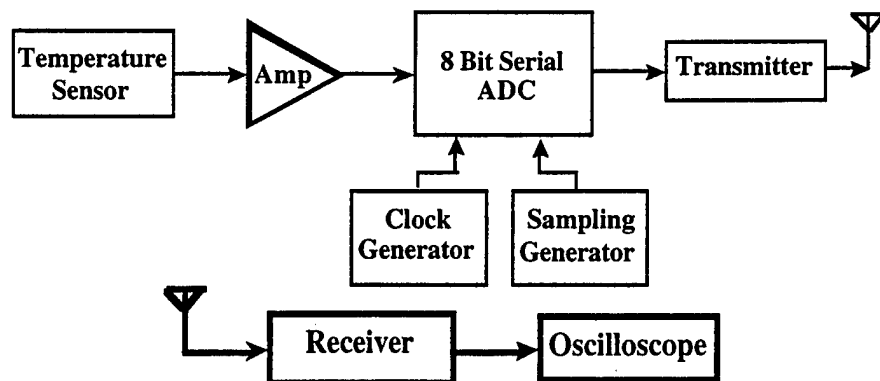


Figure 130. Transmitter Circuit

*Prototype:*

A prototype was designed and implemented to show that we could do RF transmission and reception. Data was sent from a temperature sensor wireless to a receiver, and the data was shown on a oscilloscope. The prototype block diagram is shown in Fig. 131.



**Figure 131. Prototype Block Diagram**

*Transceiver Conclusions:*

A low power transceiver for sensor telemetry is being designed in a digital CMOS 0.5 $\mu$ m process. The transceiver is designed fully integrated without the antenna, the preselect filter, and the channel select IF filter. The first test chip from the transceiver project will be sent for fabrication in February, and the second complete transceiver chip will be sent for fabrication in April 1997. A brief outline for additional transceiver and other electronics work is summarized in Table 9.

**Table 9. Future Electronics Work**

- Acoustic emission electronics
  - Develop final designs for charge amplifier and send to fabrication.
  - Evaluate and design high speed bandpass sigma-delta A/D converter.
- Temperature sensor and electronics
  - Finalize and complete designs for temperature sensors, and send for fabrication.
  - Test and evaluate fabricated designs.
- Telemetry electronics
  - Complete final designs including antenna design.
  - Develop designs for minimum power.

### 2.3.3.3 Sub-Task III

#### **SIGNAL PROCESSING**

*D. Polla, K. Buckley, M. Kaveh, A. Tewfik*

Periodic inspection and/or preventive maintenance of machines is time-consuming, expensive and requires substantial down time. Hence, automatic fault monitoring techniques provide an economical alternative, their feasibility being largely governed by the technique's ability to detect the fault with required certainty.

Acoustic Emissions (AEs) are stress waves emitted by stressed material undergoing deformation processes such as plastic deformation or crack growth. Diagnostics based on AEs is a passive, nondestructive evaluation (NDE) method and is, hence, an attractive option for automatic monitoring of faults in machines. These stress waves can be detected by piezoelectric transducers (PZT) placed strategically on the material specimen. Characteristics of AE signals from crack growth have been extensively studied (e.g., see [91] and references therein). Most of these studies were, however, done for isolated material specimens in controlled laboratory conditions at very high SNRs (signal to noise ratios). In a practical case, when the AE signal has to be detected while the machine is in operation, the AE is buried at very low SNRs under strong interference/noise caused by mechanical motion in the machine.

The objective in the signal processing component of this M-URI investigation is the detection and evaluation of helicopter rotor component cracks from AE signals generated during the formation/propagation of these cracks. In the case of a helicopter, the interference and noise due to mechanical motion is not only strong, as mentioned above, but also quite complex. It is highly nonstationary, and arises due to a number of factors that, other than vibration, may include fretting, hydraulic noise and electromagnetic interference [92]. Most of these noise events are transient and not unlike AE signals. Hence, the task of detection is not merely limited to the detection of transient signals in white noise [93]. It also becomes important to classify these detected transient events as AE signatures or otherwise. The problem is further compounded by the fact that in the case of complex material geometries of the rotor components, the characteristics of the AE signal is not, to a large extent, currently known *a priori*. Also, the noise is highly load dependent and it is not possible to fully characterize it under all possible permutations of the working environment. In consequence, the question is, given a knowledge of the structure of a machine and the characteristics of the noise under certain load conditions, can this partial *a priori* knowledge be effectively used to detect AE signals at very low SNRs with a very high probability of detection and low false alarm rates.

With the above problem in mind, the investigation was organized into three overlapping phases :

- A) PHASE 1: *Data Collection and Analysis* -- Collection of relevant noise/signal data from various sources and analysis of this data to gain a better understanding of the characteristics of the various types of signals and noise that would be observed in the given operating environment [94].
- B) PHASE 2: *Noise Suppression and Transient Detection* -- Development of suitable signal processing algorithms for suppressing noise and detecting transient signals for further analysis. Refinement of these algorithms will be ongoing, based on understanding developed in Phase 1.
- C) PHASE 3: *Transient Signal Classification* -- Development of signal processing algorithms to classify detected transient signals, that is to determine their source (e.g. microcrack, fretting, electromagnetic).

Several factors contribute to the difficulty of this objective. Noted above are noise levels and complexity, and uncertain AE signal characteristics. The nature of this particular problem suggests that representative data to analyze is difficult to obtain. Fortunately, through collaborations both initiated by this M-URI and developed to complement it, an understanding of the signals and noise is being gained. In years 1-3 of this M-URI investigation, this understanding will lead to the identification of a signal processing approach based on realistic assumptions. In M-URI Years 4 and 5, it is proposed to further refine the method and evaluate its effectiveness in an operating environment.

## A. Phase 1: DATA COLLECTION AND ANALYSIS

### ACCOMPLISHMENTS OF M-URI YEAR 2

Acoustic emission data is being collected from a number of sources, including:

- Prof. Bill Gerberich of the Material Science Department at the University of Minnesota, who has provided a number of examples of AE signals associated with different material types, geometries and crack characteristics. This data has helped gain an understanding of the AE signal characteristics for a wide range of scenarios ranging from thin film microcracks to macroscopic metal fracture.
- Researchers at Georgia Institute of Technology, who have provided data strengthening the understanding of AE signals associated with metal fractures.
- Researchers at the Honeywell Technology Center, Minneapolis, who have recently provided access to the data they acquired on the Boeing test bed facility in Philadelphia. The data has provided information on the characteristics of various kinds of transient noise associated with the helicopter rotor operation under different load conditions. Also, it has improved the understanding of the propagation of the AE signal through complex component geometries and joints.
- Prof. K. Buckley, who visited Cherry Point in September 1996, and collected data from an H-46 helicopter under various load and electromagnetic interference scenarios.

Interactions have also occurred with University of Minnesota's Microelectronics Lab and the Department of Electrical Engineering concerning the acquisition of data using the microsensors that they are developing for this project. We are also currently interacting with researchers from Northwestern University and Penn State University who will be sources for noise/signal data in the near future.

#### Preliminary Processing of Data

The preliminary processing stage (before digitizing of the data) of our data acquisition system currently consists of a 50 kHz high pass filter and preamplifiers with 60 dB gains used in conjunction with various Physical Acoustics Inc. sensors. The design and specifications of the preamplification stage might have to be revisited when the Physical Acoustics Inc. sensors are replaced with the microsensors being developed by Profs. Dennis Polla and Bill Robbins at the University of Minnesota.

#### Construction of Noise/Signal Models

Subsequent to the analysis of the AE signal data and the vibration data that we have acquired, we have constructed a model for the data expected to be measured under inflight conditions. The data that we received from Honeywell recently, agrees quite well with our proposed model.

Vibration data recorded from a rotor component in a helicopter exhibits some periodicity in its characteristics. A major proportion of the energy of this data is concentrated at the lower end of the spectrum, usually less than 50 kHz [93]. AEs, on the other hand, are transient in nature, with dominant spectral content over 100 kHz (and possibly extending to 2-3 MHz). Therefore, a high-pass filter with a cutoff of 50 kHz should be used at the preamplification stage before A/D conversion. Even after this preprocessing is done, AEs are still buried under higher frequency interference at low SNRs.

Figs. 132-133 show typical data observed over two time periods or cycles (one cycle corresponds to one full rotation of the rotor). The data for these two cycles was constructed from the data provided to us by Honeywell. The data provided by Honeywell contained only the background noise and the first dominant transient. The other periodic and random transients, which are fretting and electromagnetic noise respectively, were measured separately in our lab and added to the above data at expected SNRs. This was done because, the data from actual inflight conditions is expected to contain more transient noise than the data measured on the Boeing test bed under laboratory conditions. Note also that several AEs measured during microcrack growth in Tantalum Nitride specimens [94] have been added to the data shown in Fig. 133 at low SNRs. The efficacy of the proposed approach at detecting these weak AEs is illustrated below.

## DIRECT SENSING, ANALYSIS, REAL-TIME DIAGNOSIS

From Figs. 132-133, it can be noted that the data contains a number of strong transient signals whose durations are much less than one cycle. We will refer to these as transient noise. In addition to the above, "steady" lower level noise which we will refer to as background noise, is also present. On the basis of the time of occurrence of these transient noise events with respect to the start of the cycle (henceforth, in this discussion, time of occurrence will implicitly mean the time of occurrence with respect to, or referenced to, the start of the cycle under scrutiny), we have two categories:

- 1) quasi-periodic transient events, (labeled as 'p' in Fig. 132) that occur at approximately the same time in every cycle
- 2) periodic or random transient events.

Quasi-periodic transient events may arise due to frictional rubbing (or fretting) of surfaces. Random transient events may be caused, for example, due to electromagnetic interference or spurious fretting (e.g., from roller joints).

Some assumptions can now be made about the characteristics of the noise and AE signals based on our current understanding of the problem.

- 1) The spectral content of the AE signals are concentrated in a few spectral bands. The energy of the background noise in these bands is insignificant compared to its total energy. It is further assumed that the background noise is stationary over time durations much longer than that of the transient events.
- 2) Periodic noise transients occur at approximately the same time index (referenced from start of the cycle) at every cycle. Corresponding periodic transients over successive cycles are highly correlated.
- 3) AE signals are assumed to exhibit no periodicity. It is important to note that this assumption does not imply that AE signals cannot occur over two consecutive periods. We merely assume that the time of occurrence of the AE signals over consecutive periods are not correlated even though there might exist a high degree of correlation between the actual AE events over both periods. Also the characteristic decay rates of AE signals, though widely varying depending on the characteristic of the crack and its location with respect to the sensor, are in general, lower than that of electromagnetic transients and much higher than that of fretting transients. We will, therefore, exploit this *a priori* knowledge of the range of decay rates exhibited by AE signals at the eigenfiltering/denoising stage.
- 4) Crack formation/propagation is assumed to exhibit a sequence of transient events [95], the rate and characteristics of which is governed by material and crack characteristics.
- 5) Random transient noise events in the same cycle or over consecutive cycles may or may not be highly correlated, depending on the actual sources of these events.

### PLANS FOR M-URI YEAR 3

Over the next year, representative AE signal and noise data will continue to be acquired. This effort will include, but not be restricted to:

- 1) a visit to the Cherry Point Naval Aviation Depot in March 1997 to collect data from microsensors developed as part of this M-URI. Sensors will be affixed to a helicopter, in close proximity to the rotor, operating under various loads.
- 2) obtaining AE signals collected in laboratories at Georgia Tech and the University of Minnesota. This data will be collected using the microsensors referred to above. In March 1997, members of this M-URI team will meet at Northwestern University to coordinate this effort.
- 3) procuring crack growth AE sequence data collected at Northwestern University under this M-URI effort.

These data sets will be used to further our understanding of characteristics of AE signals generated from helicopter rotor microcracks under operating conditions, and of noise corrupting these signals in operating conditions.



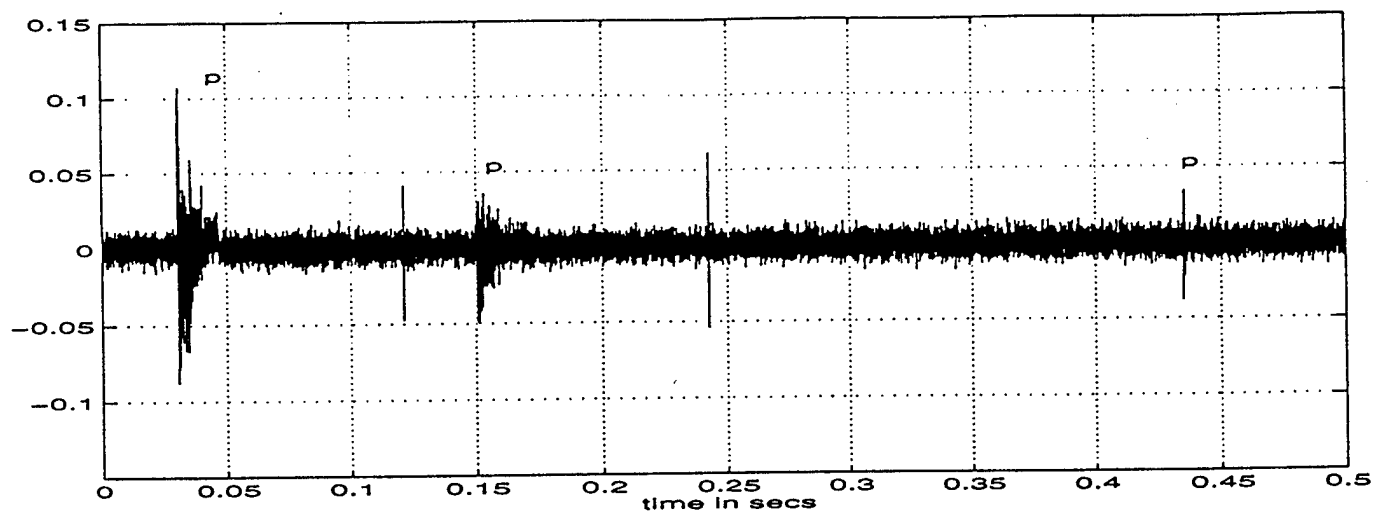


Figure 132. Data Recorded over One Cycle

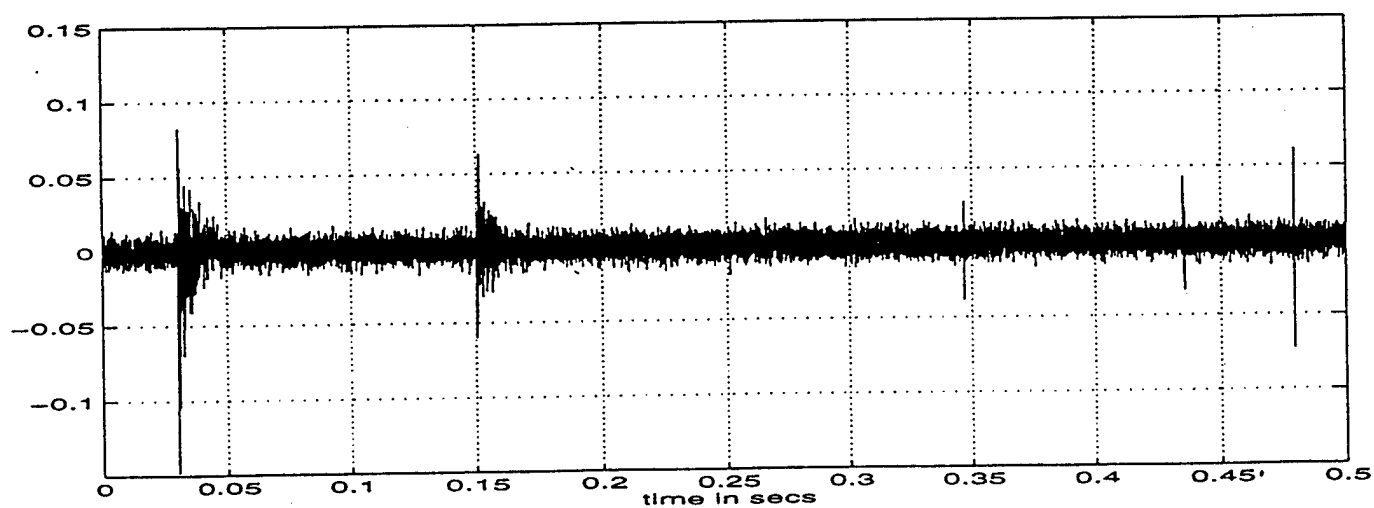


Figure 133. Data Recorded over the Next Cycle

## B. Phase 2: NOISE SUPPRESSION AND TRANSIENT DETECTION

Figure 134 shows the block diagram of the proposed approach for the above signal/noise models and assumptions. The basic methodology is to reduce the given data to a collection of transient events in white noise by filtering out the background noise. This is done in the prefiltering stage by fitting an AR model to the data using blocks of data chosen from the previous cycle, corresponding to time intervals that do not contain any transient events. Then a denoising of the time series is done to effectively pick out the transients, some of which might be buried in the white noise at low SNRs. In the classification stage, the quasi-periodic transient events are first discarded, following which a simple preliminary detection is done based on a history of the number of random transient events observed in every cycle. If AE signals are detected at the preliminary detector, then additional signal processing is done to localize/characterize the source of the AE signals. This would not only confirm the decision made in the previous stage, but also give some reasonable estimate of the criticality of the crack.

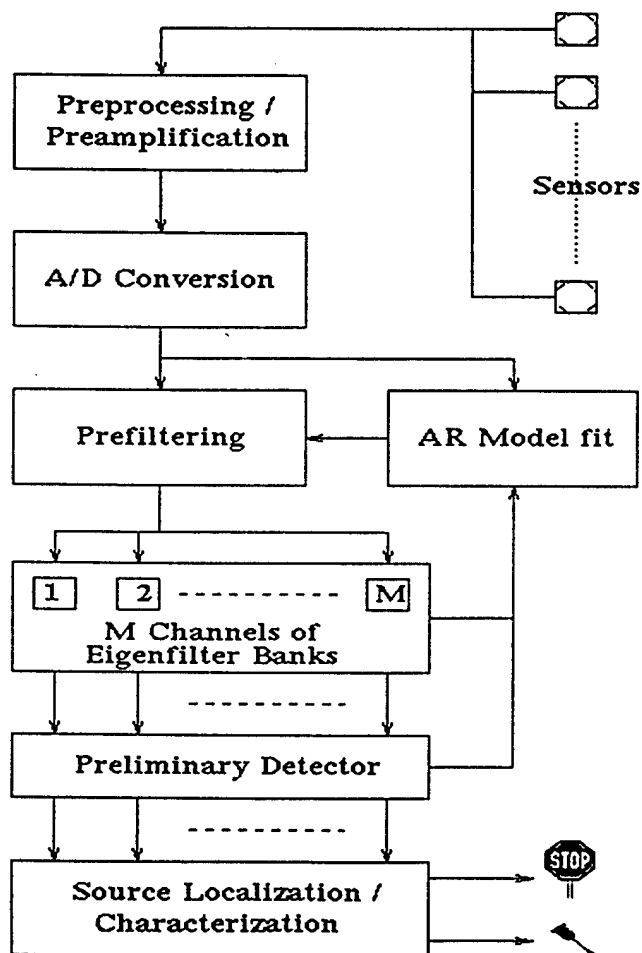


Figure 134. Block Diagram of Proposed Signal Processing Approach

## ACCOMPLISHMENTS OF M-URI YEAR 2

### Eigenfiltering/Denoising

The output of the prefilter is a collection of transient events in additive white noise. If the exact decay rate were known then optimal data tapers that have minimal spectral leakage outside the frequency range (or frequency bin) of interest can be found in closed form [96]. However, as mentioned above, we have no exact *a priori* knowledge of the decay rate of the AE signals. However, a range of decay rates that they might exhibit is known. Though, a closed form solution for the optimal tapers does not exist in this case, the tapers can still be computed numerically as a generalized eigenvector problem. The set of eigenvectors computed for each frequency bin are then used as the filter coefficients (with time index reversed) for the bank of filters corresponding to that frequency bin. The output of these eigenfilters are then combined as a weighted sum using the corresponding eigenvalues. As shown in Fig. 134, each of these eigenfilter banks correspond to one channel. Using a set of these eigenfilter banks, each corresponding to a given frequency bin of interest, decomposes the original time series into several components.

Using a partial knowledge of the range of expected decay rates for AE signals we numerically estimated the optimal tapers for frequency bins of 100 kHz width at low SNRs. Figure 135 shows a typical taper obtained for the frequency bin 50 to 150 kHz - the frequency bin containing the AE signals. Figure 136 shows the generalized eigenvalues that give a measure of the spectral compactness (the energy concentrated in the required frequency band) of the tapers. It can be seen that the spectral compactness drops off rapidly beyond a certain number of dominant tapers, corresponding to the number of Rayleigh frequency spacings present within the given frequency band of interest [96].

### Detection of Transients

Various algorithms have been evaluated for the detection of transients signals, of which principal component detection [92] and optimal taper filtering/denoising [93,97] are now considered the best suited for the given problem. These algorithms may, however, need to be modified if future data acquisitions dictate changes in the assumptions (listed on page 177) made on the noise and signal characteristics based on our current understanding of the problem.

Figure 137 shows the output of the channel containing the AE signals. The collection of time series' of all the channels can be thought of as a decomposition of the original time series on a highly redundant frame. Several techniques have been proposed for denoising of a time series data using thresholding of the frame coefficients. We will use the soft thresholding technique proposed in [98]. The threshold obtained using the above method is depicted in Fig. 137 with a dashed line. Figure 138 shows the denoised time series of the above channel. Figure 139 is a zoomed-in look at the denoising of a single AE event.

## PLANS FOR M-URI YEAR 3

Based on the enhanced understanding discussed above, refinements to noise filtering and transient detection algorithms will continue. The objective is to provide high probability of AE signal detection and low probability of false alarm (due to either random noise, or transients not due to microcracks).

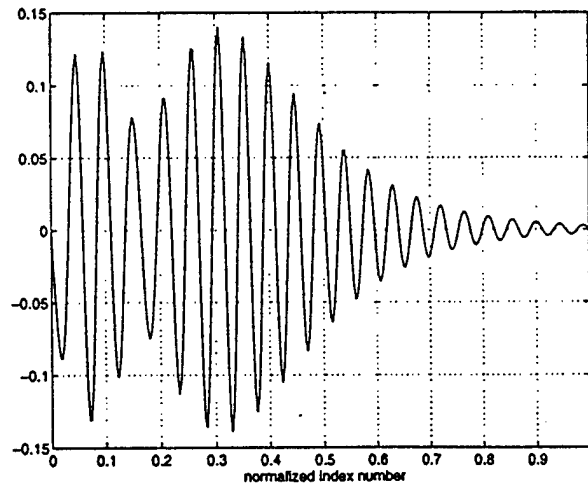


**Figure 135. An Optimal Taper**

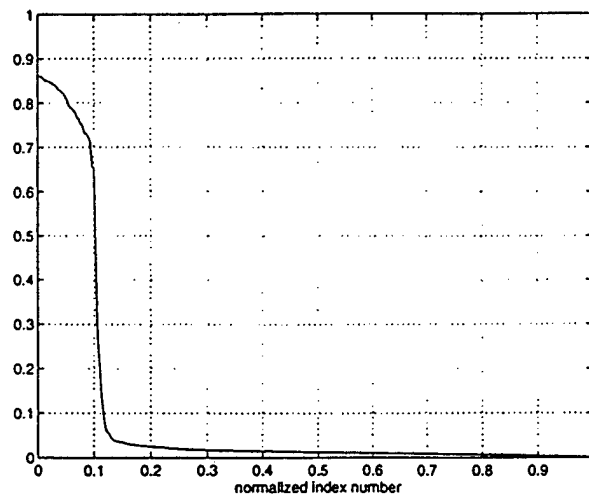


**Figure 136. Spectral Compactness of Tapers**

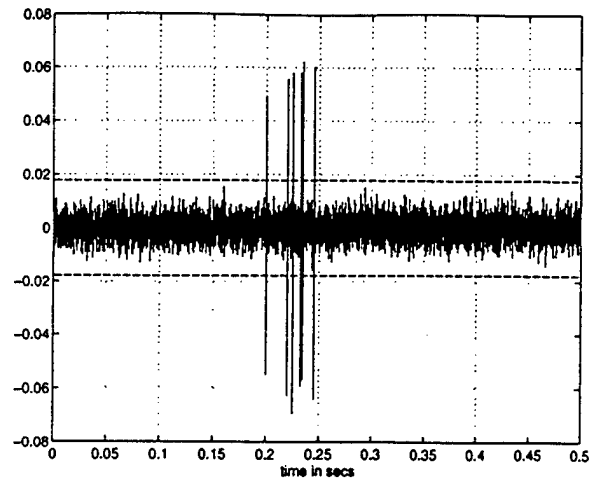


**Figure 137. Output of Channel that Contains the AE Signals**

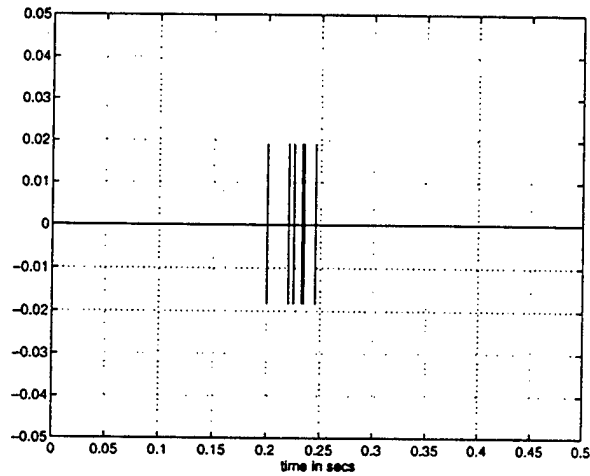


**Figure 138. Denoised Time Series of One Channel**

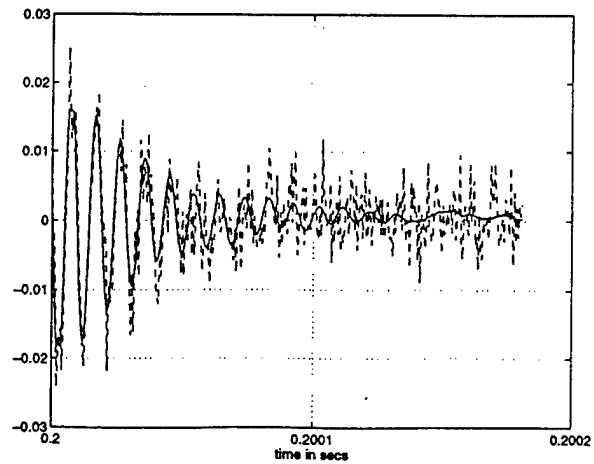


**Figure 139. Denoising of a Single AE Event**

### C. Phase 3: TRANSIENT SIGNAL CLASSIFICATION

#### ACCOMPLISHMENTS OF M-URI YEAR 2

##### Detection Using Count Statistics

The input to this function block is a collection of denoised transients. The first step is to separate the random transients from the quasi-periodic transient events that occurred over both cycles. The starting time indices of the transients are estimated from the denoised data using simple thresholding. A similar estimate is already available for the previous cycle. Due to inherent "jitter", caused due to load imbalances and thresholding variances, the time index of quasi-periodic events in the two cycles will not be identical. If a Stochastic model for this jitter is available then events corresponding to the same quasi-periodic process can be identified using a maximum likelihood criterion [97]. To distinguish between quasi-periodic/random events, we form the likelihood matrix given by  $L=[l_{ij}]$ , where  $l_{ij}$  is the likelihood that the  $i$ th transient from the current cycle and the  $j$ th transient from the previous cycle belong to the same periodic process. For a given transient of index  $I$  from the current cycle,  $\max_j l_{ij} > d$  gives the maximum likelihood of the index of the transient in the previous cycle that corresponds to the same periodic process, i.e., the column that contains the maximum value along each row gives the maximum likelihood estimate of the index. Note that this maximum value in each row should be above a certain threshold. If a maximum value in a row cannot be found above the given threshold, then the event corresponding to that row index is assumed to be a random occurrence.

At this stage of the project, the spectral characteristics of these random transient events have not yet been fully characterized. Hence, we propose a simple detection scheme using count statistics once the quasi-periodic transient events have been separated out. A count of the random transient events in every cycle is done. A history of these counts over a number of cycles is used to detect the occurrence of AE signals. Here we assume a simplistic case, wherein in the absence of the AE signals, randomly occurring transient events can be modeled as Poisson occurrences governed by a rate  $\lambda$ . The presence of a train of AE events in a cycle can hence be detected as non-stationarities of the underlying Poisson model [99].

Monte-Carlo simulations were done with synthetic data generated similar to the two cycles of data presented above. Figure 140 shows the ROC curves obtained for various values of  $k$  (5 to 15), where  $k$  is the number of AEs synthetically introduced into one cycle. Note that the false-alarm rates (FAR) in the figure are rates/cycle, and hence, for a cycle of 1 second duration a FAR of  $10^{-5}$  would be equal to about 28 hours. These ROC curves can be improved by incorporating *a priori* knowledge of the spectrum of the AE signals or the interference transient events. This preliminary detection can operate at higher than acceptable FARs, as the source characterization/localization stage succeeding this stage will provide a further reduction in FARs.

##### Source Localization/Characterization and Channel Identification

Preliminary work has been done with localizing and characterizing the AE signal source using the data provided to us by Honeywell. Initial results are quite encouraging and support the use of blind deconvolution techniques following preliminary detection, to decrease false-alarm rates while maintaining a high probability of detection of the crack signal.

A single source waveform propagates through different channels, and is subsequently received with additive noise at various sensors. Identification of the corresponding channel responses and the source waveform without any assumptions on the source/channel models of such a single-input multiple-output system has been studied. A number of methods exist for such "blind" identification and we are currently studying various modifications on the existing methods to enhance their performance in our specific scenario. In this report, we will present a simple least squares solution (LS) for the blind source

estimation problem. We will use a segment of the Honeywell data for the source estimation problem. In their test setup they introduced an artificial AE source, the "pinger", using a piezoelectric transducer driven by a transient electrical signal. This "pinger" signal was then measured at two sensors located some distance away from the source. Figure 141 shows the source waveform and the data recorded at the two sensors corresponding to the artificial AE event. Note that the two sensors were not located on same component as the "pinger", and hence, the propagation of the signal through joints is encouraging. Figure 142 shows the power spectrum of the actual and estimated source waveforms. The identification of the dominant modes of the source waveform by the LS algorithm is apparent.

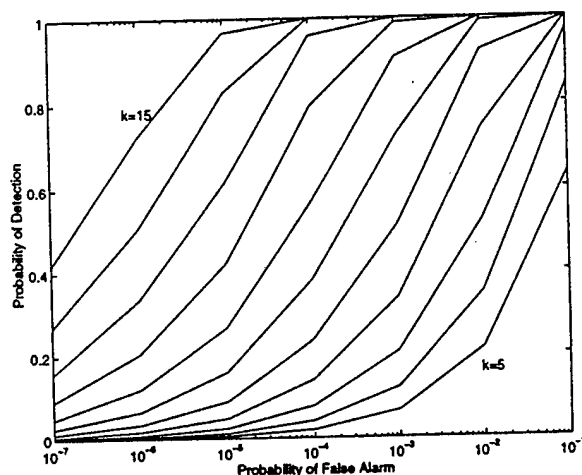


Figure 140. ROC Curves for  $k=5$  to 15

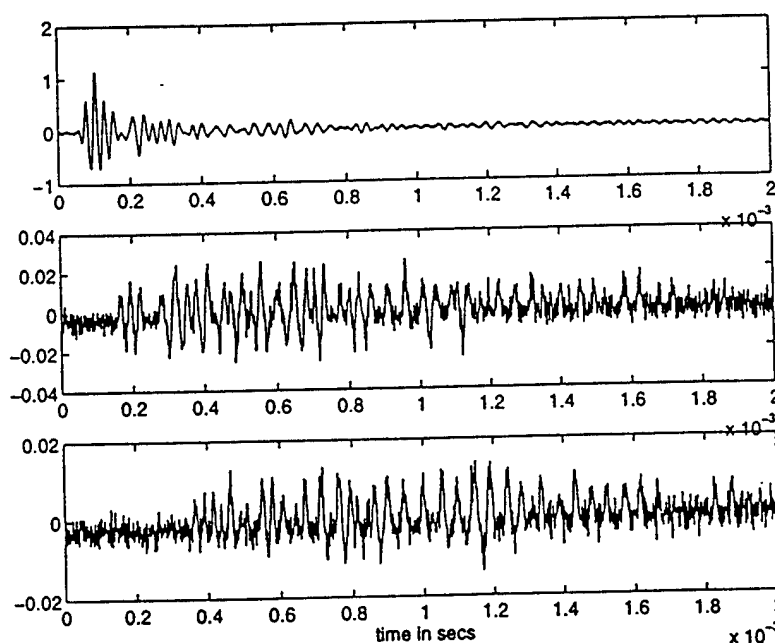
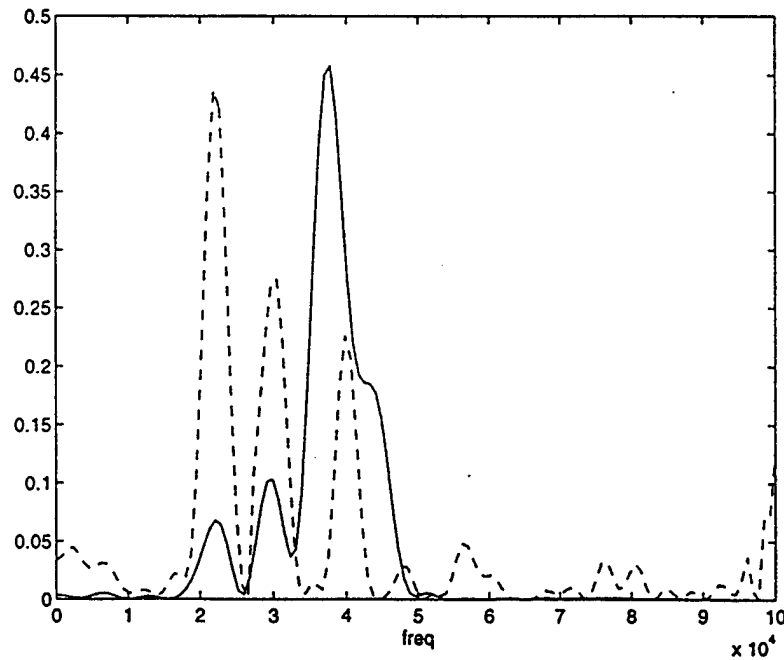


Figure 141. Source Waveform and Data Measured at Two Sensors



**Figure 142. Comparison of Power Spectra of Actual and Estimated Source Waveforms**

### **PLANS FOR M-URI YEAR 3**

Development of classification algorithms, which distinguish between microcrack generated AE signals and other transients, will be concluded. Source-localization/channel-identification based methods, and differentiation based on count statistics will continue to be considered. An assessment of the advantage of a multi-modal approach to transient signal classification (e.g., use of both AE and accelerometer data) will be made.

With the completion of Phases 1-3, the proposed AE signal processing based approach to helicopter rotor microcrack detection will have been evaluated. This evaluation is based on an understanding of the problem derived from the data described above, and from consultations with other members of this M-URI team.



#### 2.3.3.4 Integrated Microsensors for Aircraft Fatigue and Failure Warning **PROJECT PLANS FOR M-URI YEAR 3 and BEYOND**

At the time of this writing, nearly 21 months of contracted activity have been completed. According to the original proposal, this project is on-schedule. A substantial effort in the area of telemetry, which was originally planned for M-URI Years 4 and 5, has also been initiated. Areas of emphasis for Year 3 are summarized below.

1. Piezoelectric AE microsensors and vibration monitors in discrete silicon-based form have now been successfully developed. A working circuit, implementing a general-purpose charge amplifier to directly interface with piezoelectric microsensors, has also been developed. In M-URI Year 3, integration of these microsensors, charge amplifier, and other circuits blocks will occur on a single silicon chip, forming the key components of the integrated microsystem chip of Fig. 91.
2. Actual AE signals and noise background data has been acquired on several helicopter platforms. This data has helped in identifying signal processing methodologies and algorithms. In Year 3, these signal processing methods will be tested on the integrated microsystem chip described in #1 above. Additional real data acquired from helicopters using these chips will be acquired.
3. Several practical problems still need to be solved in order to have a useful deliverable at the conclusion of this program. A significant effort in extending circuit-sensor interface techniques has therefore been undertaken. We have started to address the problem of wireless telemetry of a real-time condition signal to a central processing unit. The reduction of a wireless telemetry technique for piezoelectric microsensors with a remote transceiver will be carried out in Year 3.
4. Pending availability of resources, on-chip energy strategies for our monitoring chips will be identified. Two approaches being considered include 1) the use of thin film batteries formed on the backside of our coupons, and 2) the use of energy scavenging methods such as converting excess mechanical energy into electricity via the piezoelectric effect.
5. Microsensor hardware has been delivered to other team members. We look to iteratively refining our microsensor technologies to best fit the needs of all M-URI and condition-based maintenance researchers.

A critical extension to the research of Sub-Task III *Signal Processing* is in the evaluation of the signal processing methods developed in PHASES 1-3 for a real-time actual situation. This would be a main objective for Years 4 and 5. An additional objective would be the further refinement of these signal processing methods, based on: 1) continuing data acquisition and analysis; 2) using AE signal Finite Element Models developed at Georgia Tech (for specific rotor components) as an extension of their current M-URI effort on stress modeling of these components (Section 2.2.1.1); and 3) understanding the crack growth generated AE sequences currently being developed at Northwestern University as part of this M-URI (Section 2.3.4).

### 2.3.4 ACOUSTIC EMISSION MODELING FOR INTEGRATED DIAGNOSTICS

Co-investigator: Isaac M. Daniel (Northwestern)

M-URI Year 2 Funding Allocation: 3.2%

#### PROJECT OVERVIEW

Acoustic emission (AE) consists of high frequency stress waves generated by the rapid release of energy due to fracture, plastic deformation, wear or interfacial friction [100]. Acoustic emission monitoring is a very sensitive method with a wide dynamic range and can be used as a diagnostic means of continuous assessment of damage in materials and components. Acoustic emission methods can be applied to metallic and nonmetallic components and specimens subjected to monotonic or fatigue loading. In general, acoustic emission can be used to monitor crack initiation and propagation, to locate the source of the emission and ultimately to predict the state of damage and life of the component.

Key factors in the successful application of the method are the selection of appropriate sensors, installation, means of transduction, and physical interpretation of output. Discrimination between signal and noise is of paramount importance. The background noise can be hydraulic, electrical or mechanical. Methods of noise suppression that have been used to date include high-pass frequency filtering, floating signal threshold, spatial filtering such as guard sensor array, time filtering (delta-time) and analysis of signal characteristics.

Numerous studies have been conducted dealing with correlations of AE output and fracture mechanics and fatigue damage parameters. It has been shown that under monotonic loading AE can detect yielding and that the cumulative AE output from a notched specimen is directly related to the stress intensity factor [101]. Acoustic emission is very useful in detecting crack initiation and propagation under fatigue loading [102-110]. In application of the AE method, discrimination between signal and noise is of paramount importance.

The objective of this project is to investigate and develop/adapt acoustic emission analyses for material flaw characterization, leading to the failure prediction of flight vehicle and other structural components of interest to the Navy. Materials of interest include 4340 steel and 13-8 PH stainless steel. Edge-notch and compact tension specimens are being tested under cyclic tensile loading. The investigation consists of signal/noise discrimination, direct crack growth monitoring, acquisition of acoustic emission data, analysis of AE data and correlation of AE data with damage growth. In the case of aluminum, the AE output consists of three characteristic parts corresponding to three stages of crack propagation; the first stage of high but decreasing AE rate, the second stage with a low and nearly constant rate and extending over 80% of the specimen lifetime and the third stage with increasing AE rate up to failure. The rate of AE output in the second stage can be described by a power law in terms of the stress intensity factor range, analogous to the Paris law for crack growth rate. In the case of steel, AE results from crack extension, notch tip plasticity and closure, and plasticity dominated rapid crack propagation. The various sources of AE activity have been analyzed based on the phase of the loading cycle at which they occur. A high rise in AE activity in the first half of the fatigue life has been attributed to a transition from plane strain to plane stress crack propagation. This type of analysis of AE data will lead to a correlation of AE activity, loading cycle phase and actual physical damage mechanisms in the specimens. Eventually, this approach will lead to a determination of the current state of damage of a specimen or component and prediction of its remaining life.

#### ACCOMPLISHMENTS OF M-URI YEAR 2

In pursuing this basic research, test materials have been selected based on their potential for use in actual applications. Most of the work during the past year was done on 4340 steel, a material used in an H46 helicopter connecting link. A 6.4 mm (0.25 in.) thick plate of 4340 steel was received from

Georgia Tech. In addition, a 12.7 mm (0.50 in.) thick 4340 steel plate was purchased for specimen fabrication.

The 4340 material was received in the annealed condition and heat treated according to specifications recommended for rotor components. The material was tested in uniaxial tension in the annealed and heat treated conditions. Stress-strain curves are shown in Fig. 143. In the heat treated condition the 4340 steel had the following properties:

Hardness: 38-40 Rc

Yield Stress: 1300 MPa (190 ksi)

Critical Stress Intensity Factor:  $K_{Ic} = 71.5 \text{ MPa}\sqrt{\text{m}}$  (65 ksi  $\sqrt{\text{in}}$ )

The primary specimen type used was a standard compact tension specimen (ASTM 399, Fig. 144). The specimens had overall dimensions of 9.53 cm (3.75 in.) by 9.14 cm (3.60 in.) and a thickness of 12.7 mm (0.5 in.). A crack of initial length  $a_0 = 30.5 \text{ mm}$  (1.2 in.) was machined by EDM prior to heat treatment. The crack had a 60° V-shaped tip and a crack tip radius of 0.102 mm (0.004 in.).

Various AE sensors were considered and it was decided initially to use 150 kHz resonance sensors (R15, Physical Acoustics). The data acquisition instrumentation was upgraded to a new system which is fully digital, multichannel, and performs simultaneous real-time extraction of AE features and recording of waveforms (MISTRAS 2001, Physical Acoustics Corp.). The system provides software selectable filters and is well suited for detecting multiple site or dispersed damage. It uses primarily high sensitivity resonance transducers. It is also well suited for neural network pattern recognition.

Various techniques were considered for direct monitoring of crack extension during fatigue testing. They include the use of conductive paint circuits, telemicroscope and crack propagation gages. The latter were found to be accurate and convenient for obtaining a direct real-time record of the crack length. Two such gages were mounted ahead of the initial crack, a higher resolution gage near the initial crack tip in order to better pinpoint crack initiation and the first stage of crack propagation and a coarser gage farther down the expected crack path (TK-09-CPA01-005/DP and TK-09-CPC03-003/DP, Measurements Group). The specimen with the AE sensors and crack propagation gages mounted is shown in Fig. 145.

As anticipated, signal/noise discrimination was identified as the most crucial problem. Various methods of noise suppression were considered. High-pass frequency filtering can filter out low frequency noise. Threshold filtering can suppress all lower amplitude noise. However, there may still be some higher frequency and higher amplitude noise reaching the transducers. Spatial filtering techniques based on guard sensors or differential time of arrival can be used to eliminate noise from external sources away from the notch. Noise can also be separated by analyzing the individual waveforms and identifying special characteristics attributed to noise. The method of noise suppression used was threshold filtering and spatial filtering based on the differential time of arrival (Fig. 146). Two 150 kHz resonance transducers (R15, Physical Acoustics) were placed at equal distances from the source (notch). Signals emanating from the source would arrive at the two sensors nearly simultaneously. Signals (noise) from external sources, such as one end of the specimen, would arrive at the sensors at times differing by approximately  $\Delta t = s/c$ , where  $c$  = wave speed and  $s$  = distance between transducers. Only signals with a difference in time of arrival of  $\Delta t < s/c$  need to be retained. This type of filtering can be performed automatically by the instrumentation system used. In the present case  $s/c \cong 19 \mu\text{s}$ , but only signals with a time difference of  $\Delta t < 2 \mu\text{s}$  were retained.

Fatigue tests were conducted on 4340 steel compact tension specimens in a servohydraulic testing machine at a stress ratio  $R = 0.1$ , and at a cyclic frequency of 2 Hz. During data acquisition, preamplifiers with 40 dB gain were used and a threshold of 34-37 dB was set. A number of fatigue tests were conducted at various initial peak stress intensity factors  $K_{max}$  ranging from  $K_{max} = 0.15 K_{Ic}$  to  $K_{max} = 0.35 K_{Ic}$  where  $K_{Ic}$  is the critical stress intensity factor of the material.

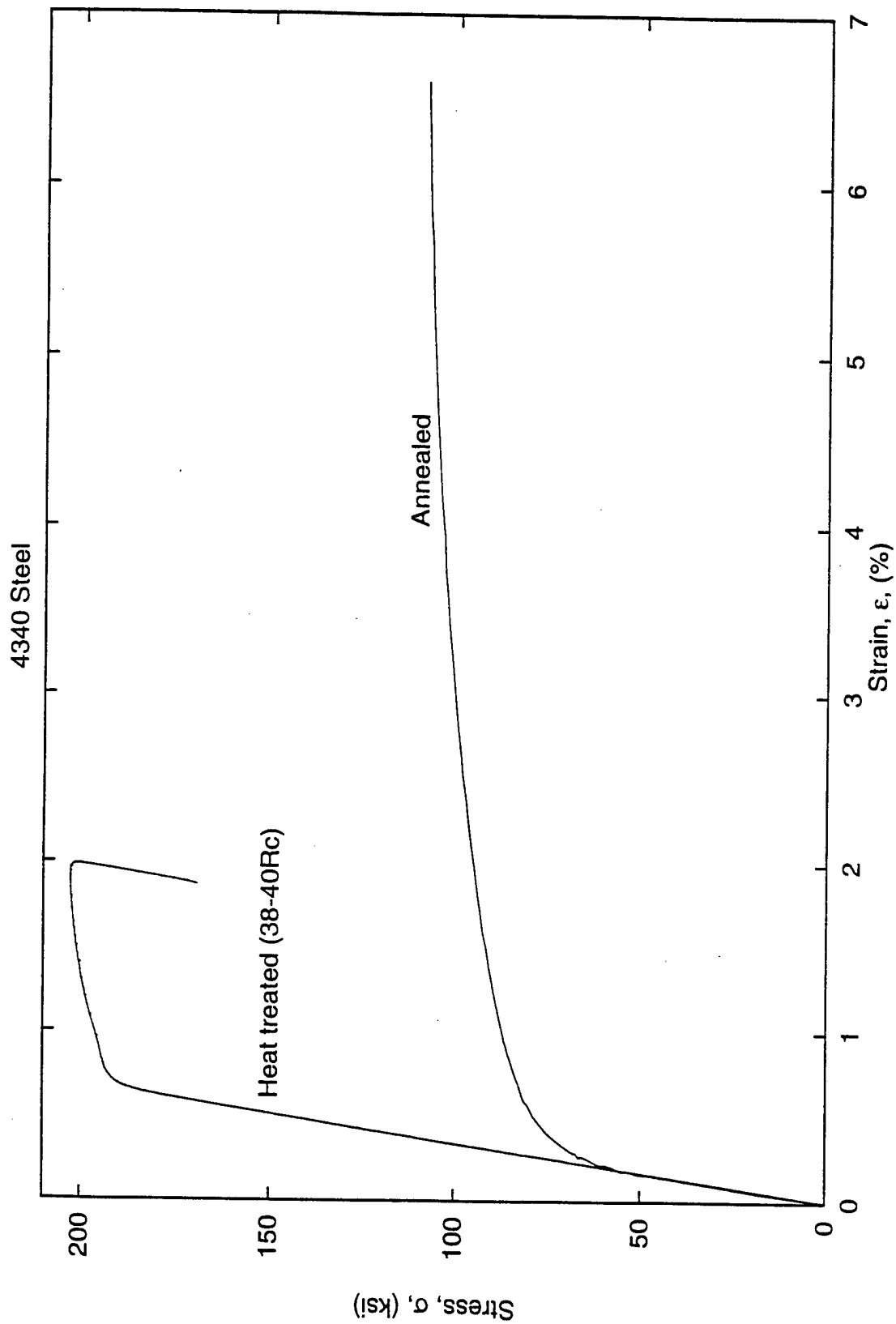
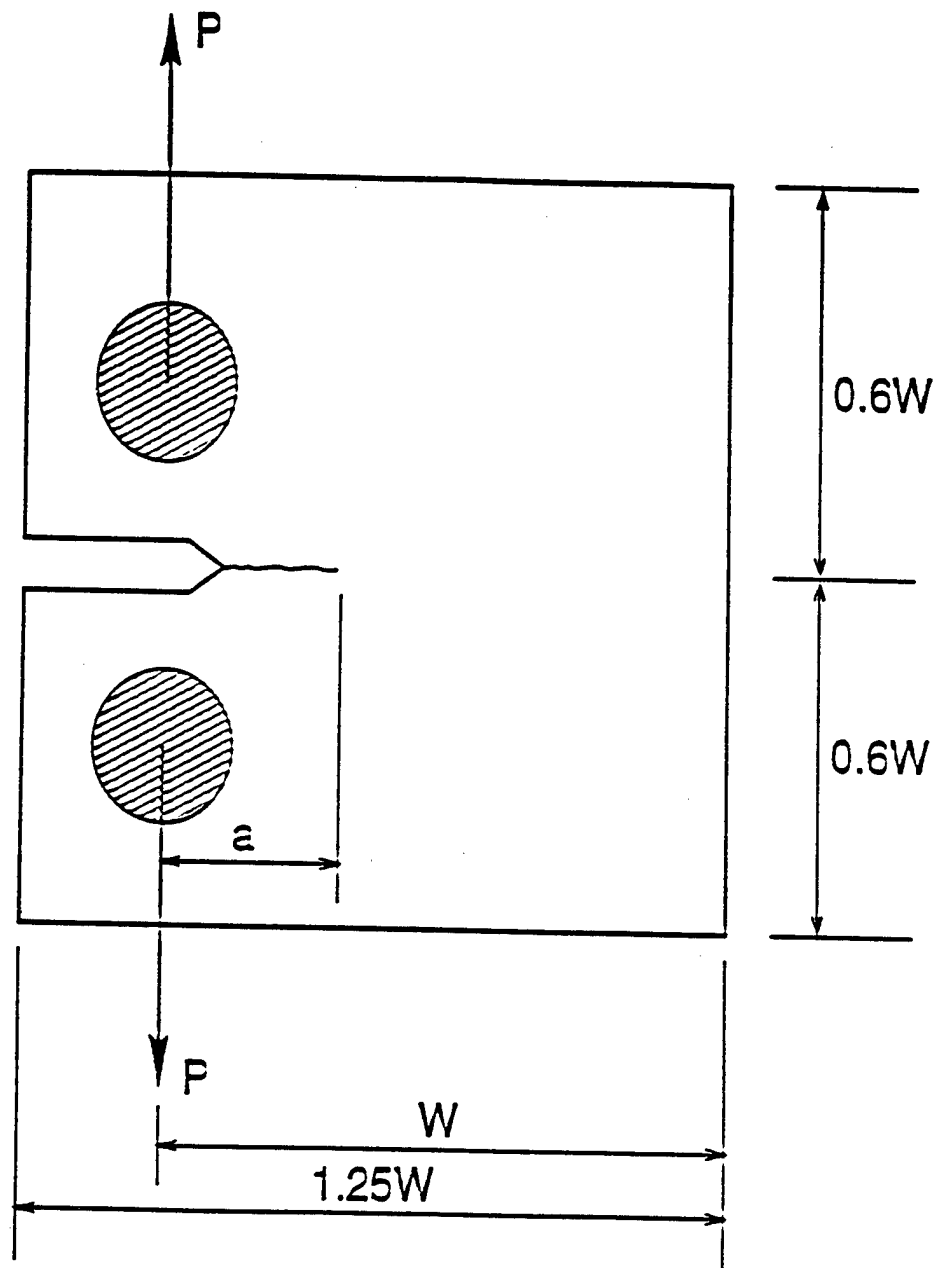
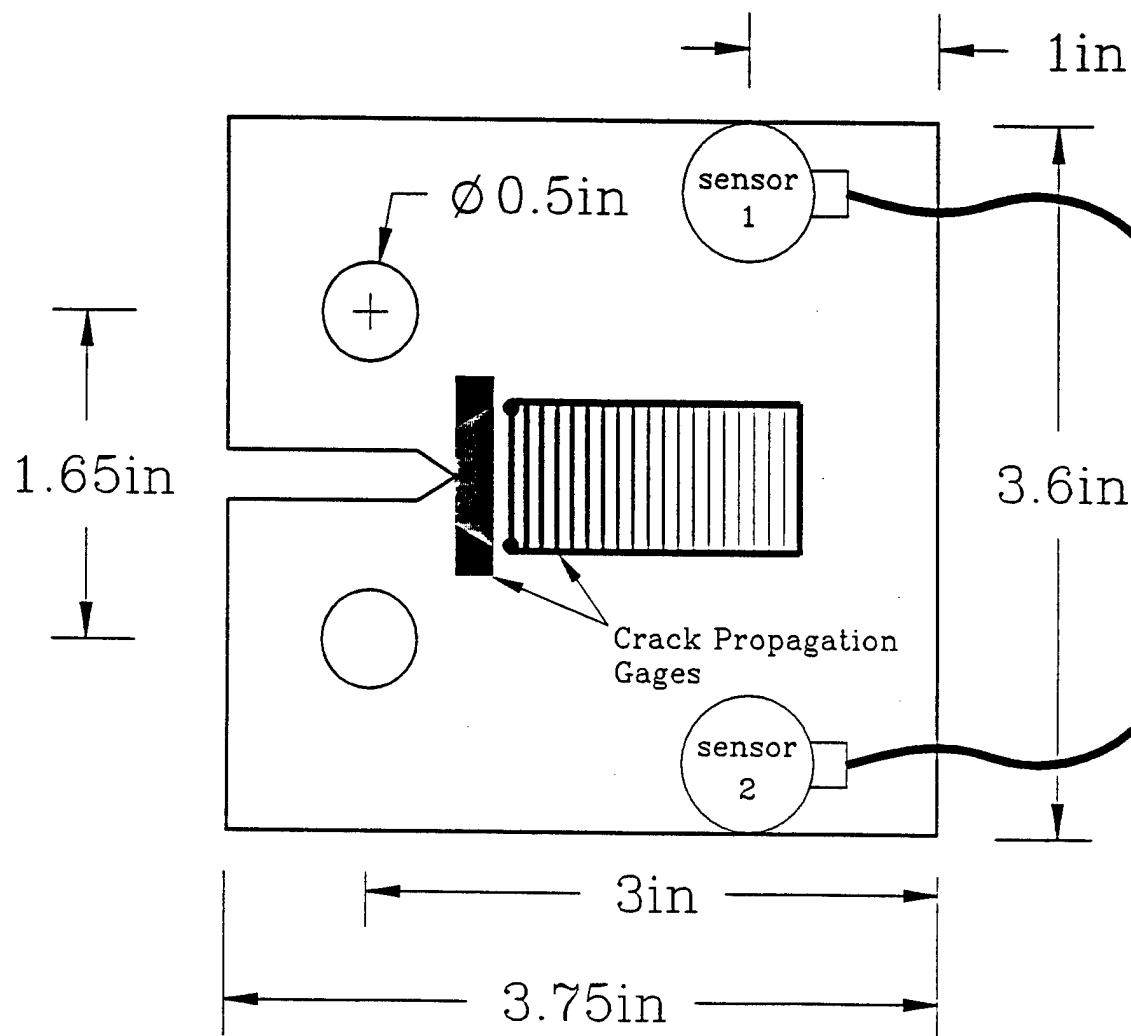


Figure 143. Stress-Strain Curves for Annealed and Heat Treated 4340 Steel



Thickness:  $B = \frac{W}{2}$

Figure 144. Compact Tension Specimen (ASTM 399)



**Figure 145. Compact Tension Specimen with AE Sensors and Crack Propagation Gages**

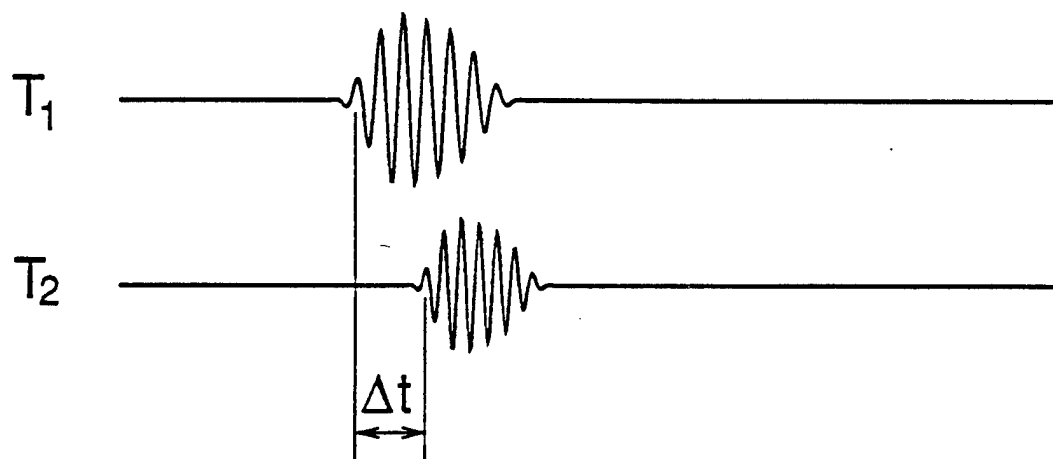
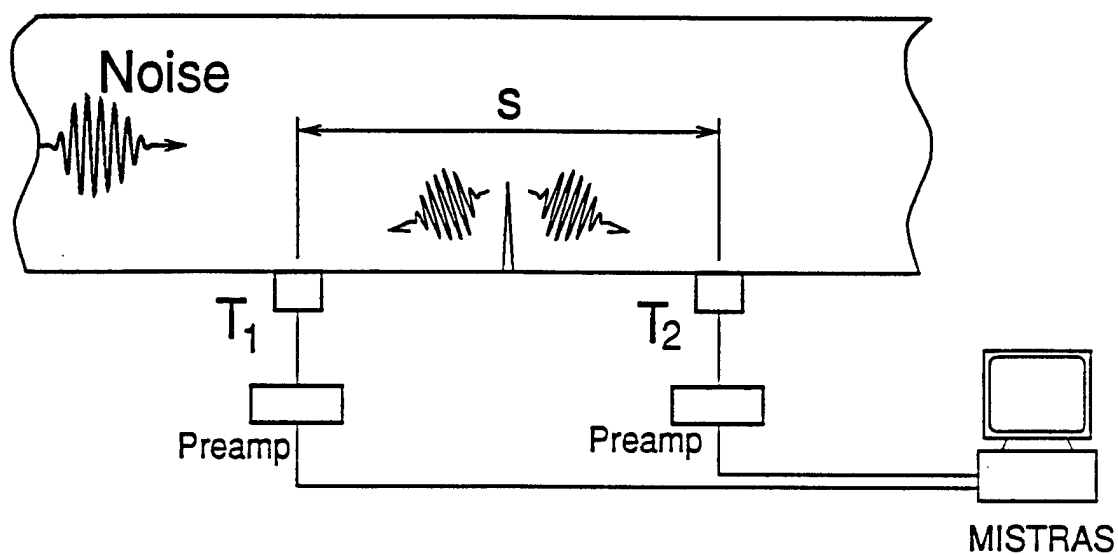


Figure 146. Spatial Filtering Technique for Noise Suppression

The cumulative number of AE counts and the crack length are plotted versus number of fatigue cycles for a typical specimen in Fig. 147. The AE curve is characterized by jumps in the first half of the fatigue life whereas the crack length increases smoothly. Several possible explanations for these jumps were considered. The possibility that the jumps are due to inherent material behavior including fracture modes (intergranular, intragranular) cannot be eliminated although the crack seems to grow gradually and smoothly especially at the time of the jumps. The possibility that the jumps are caused by noise from the load introduction points was eliminated, because such noise would occur throughout the fatigue test and would not be localized in time. This was checked experimentally by conducting a test with an unnotched compact tension specimen. Although the spatial filtering technique used eliminates noise signals coming from one end of the specimen (see Fig. 148) the remote possibility was considered of equal noise signals emanating simultaneously from the two ends of the specimens. This possibility was also excluded after conducting a test with a specially made asymmetric CT specimen with load introduction holes at different distances from the crack tip. Repeated testing confirmed that these jumps are consistent, repeatable and not attributable to noise. Normalized cumulative AE counts and crack length were plotted versus normalized fatigue cycles for four different tests conducted at two different initial loads (Fig. 148). All four AE plots display similar jumps, with those corresponding to higher initial  $K_{max}$  occurring earlier. The normalized crack extension curve is identical in all four cases.

It was observed that AE activity occurs at all levels and phases of the loading cycle, both during loading ( $\phi > 180^\circ$ ) and unloading ( $\phi > 180^\circ$ ). Cumulative AE counts were separated into loading and unloading phases and plotted versus fatigue cycles in Figs. 149-152. It is seen that AE counts during unloading increase gradually whereas loading AE counts display characteristic jumps.

The AE data were also analyzed on the basis of loading cycle phase by plotting histograms of the AE counts as a function of loading cycle phase, or stress level at various stages of the fatigue life (Figs. 153-158). These histograms represent the total number of AE events at a given phase (stress level) for all the cycles of the respective stage. These histograms were superimposed on the AE curve which was divided into six stages as shown in Fig. 159. It is seen that in the first two stages most of the AE activity occurs near the unloading end of the cycle. Later on the AE activity shifts toward the beginning of the loading cycle. Finally the AE activity becomes concentrated near the beginning, the peak and the end of the loading cycle, corresponding to plasticity dominated rapid crack propagation.

The loading phase distribution of the AE activity is illustrated graphically in Fig. 160. It is seen that the AE output can be separated into three groups or regions according to the phase of the loading cycle at which it occurs. AE signals in group A occur primarily during the first half of the fatigue lifetime and correspond to the end of the unloading cycle ( $\phi > 250^\circ$ ). AE signals in group B occur during the loading part of the cycle at a phase angle  $\phi$  decreasing with fatigue cycles. This activity, which takes the form of jumps, corresponds primarily to crack opening and crack propagation. AE signals in group C occur near the end of the fatigue lifetime near the peak of the loading cycle. They correspond to rapid crack propagation in the final stage.

The AE output variation with loading cycles was also correlated with crack extension, state of stress and fracture morphology (Fig. 161). The very initial stage consists of crack initiation and merging of the various initial crack planes. This is followed by a region of length comparable to the specimen thickness and dominated by plane strain crack propagation. This region corresponds to moderate AE activity. When the crack extends to several specimen thicknesses in length there is a transition from plane strain to plane stress with a concomitant change in fracture surface morphology from smooth to rough (Fig. 161). This transition corresponds to the intense AE activity recorded. The above region is followed by plane stress dominated crack propagation and finally by unstable crack propagation leading to ultimate failure (stage 6 in Fig. 159).

Similar results were obtained for a series of tests conducted at peak stress intensity factors  $K_{max}$  ranging from  $0.15 K_{Ic}$  to  $0.35 K_{Ic}$ . The loading phase distribution of AE activity, the cumulative number of AE counts and the crack length for these tests are plotted versus loading cycles in



Figs. 162-168. They all display similar characteristics, i.e., grouping of AE activity into three regions (A, B, C), jumps in the cumulative AE output, and smooth crack extension. In the case of the test conducted at  $K_{\max} = 0.175 K_{IC}$ , the variation with fatigue cycles of the cumulative AE counts by group or region is plotted in Fig. 169. In this case, the AE activity of region B corresponding to crack propagation is the dominant one.

### PLANS FOR M-URI YEAR 3

- *Instrumentation*: Utilize broad band transducers and analyze AE output in various frequency ranges. Investigate any possible relation between observed jumps in AE output and frequency range.
- *Data Analysis*: Continue analysis of AE data based on loading cycle phase. Investigate distribution of differences of time of arrival ( $\Delta t$ ) of the various groups of AE activity and thereby identify and screen out any noise in the data.
- *Crack Opening*: Measure crack opening load (or  $K$ ) during cyclic loading by direct measurement with gages and compare results with AE indications. The corresponding crack opening  $K_{op}$  will be determined as well as the effective stress intensity factor range  $\Delta K_{eff} = K_{\max} - K_{op}$ .
- *Specimen Geometry*: Consider different specimen geometries that will allow full control of crack propagation in fatigue tests under displacement control.
- *Interpretation of Results*: AE activity will begin to be correlated with physical failure mechanisms using pattern recognition schemes. AE activity of each individual group (based on loading cycle phase) will be correlated with the corresponding dominant crack propagation mechanism. The pattern of AE activity of each group will be correlated with the overall damage state or "age" of the specimen.

### VISION FOR YEARS 4 AND 5

- *Interpretation of Results*: AE activity will continue to be correlated with physical failure mechanisms using pattern recognition schemes. AE activity of each individual group (based on loading cycle phase) will be correlated with the corresponding dominant crack propagation mechanism. The pattern of AE activity of each group will be correlated with the overall damage state or "age" of the specimen.
- *Damage Modeling*: Damage accumulation models leading to life prediction will be sought based on AE signals.

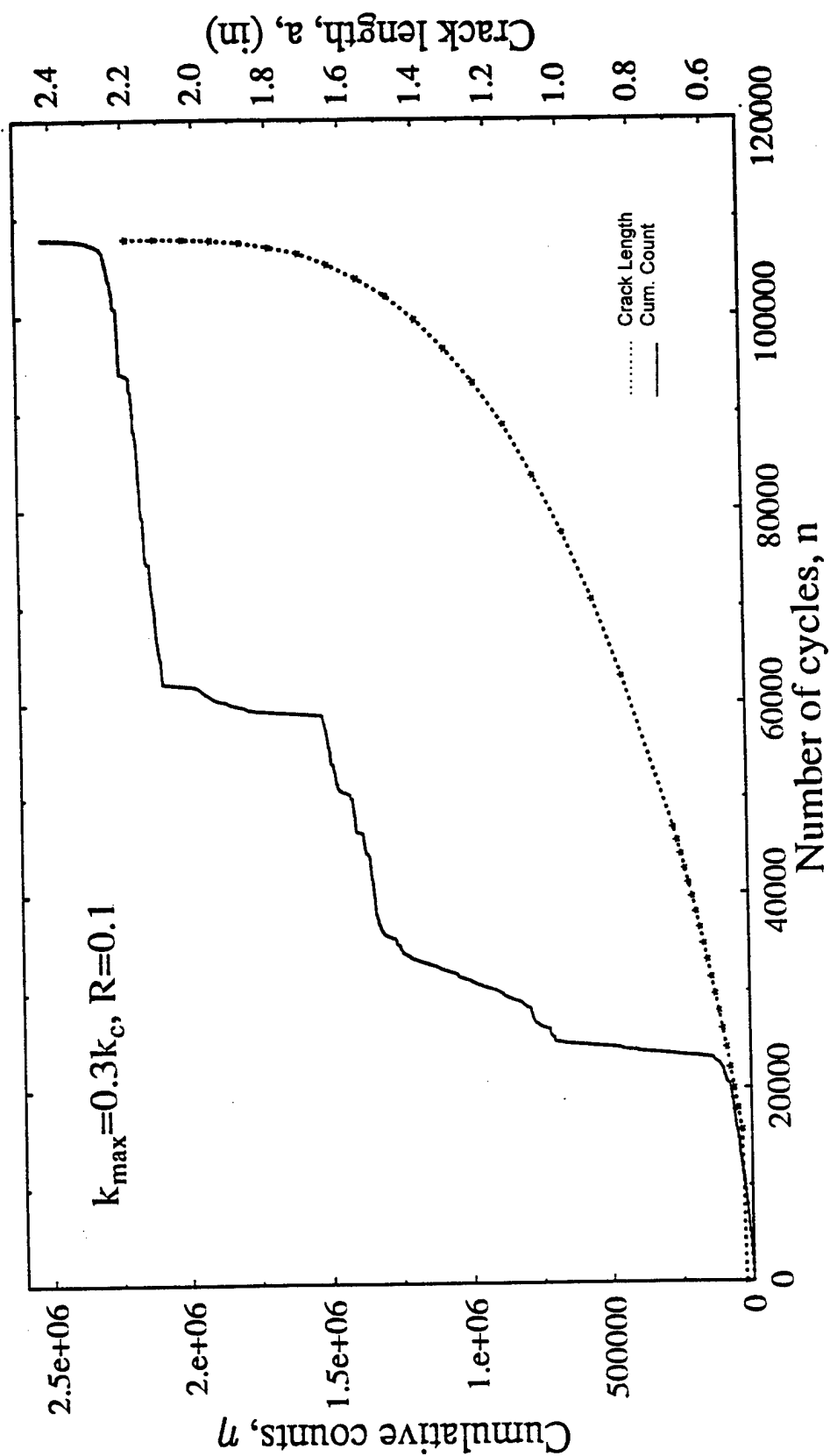


Fig. 147 Cumulative AE Counts and Crack Extension vs. Fatigue Cycles  
(4340 Steel; compact tension specimen)

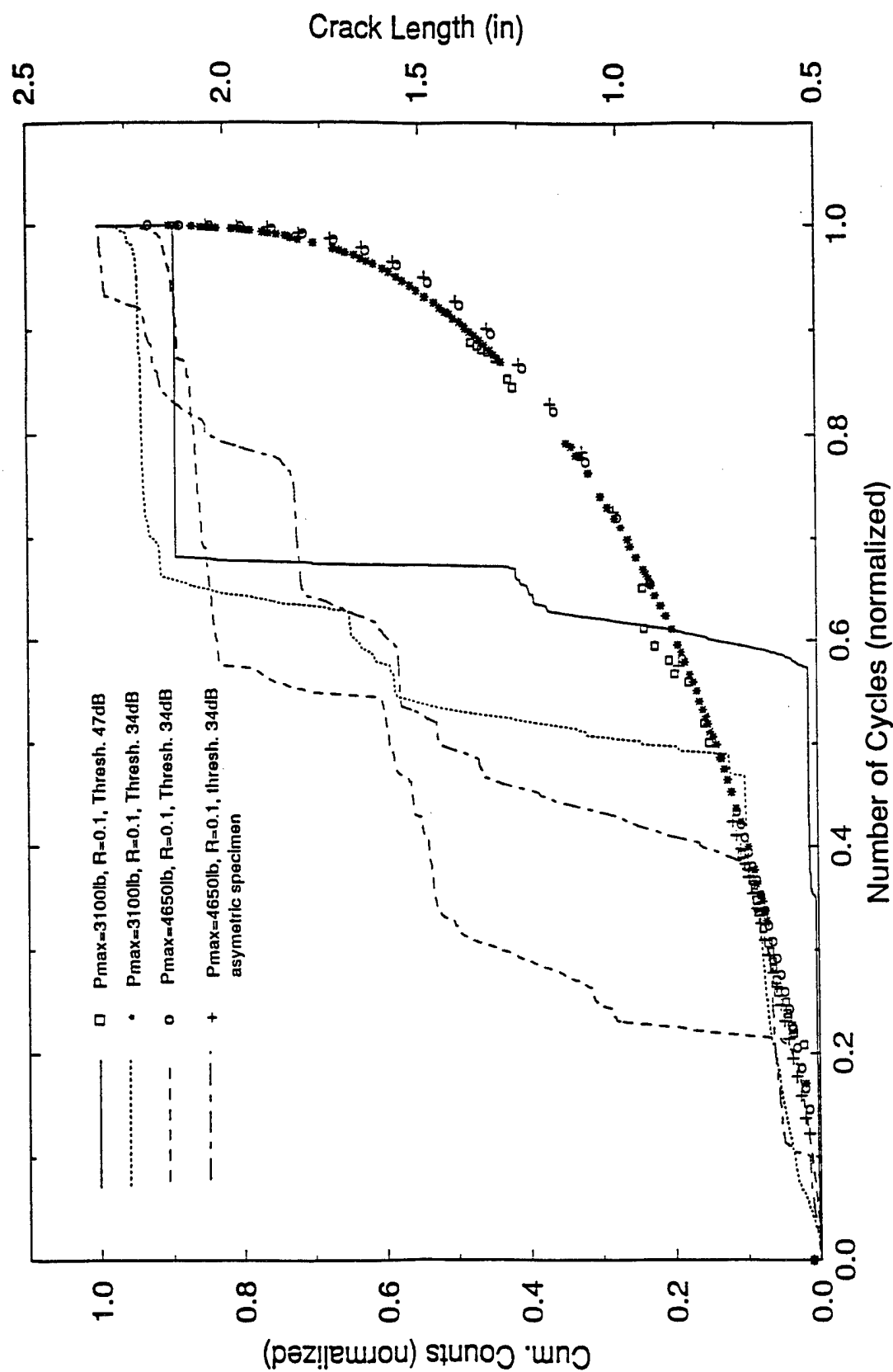


Fig. 148 Normalized Cumulative AE Counts and Crack Length vs. Normalized Number of Fatigue Cycles for Four 4340 Steel Specimens

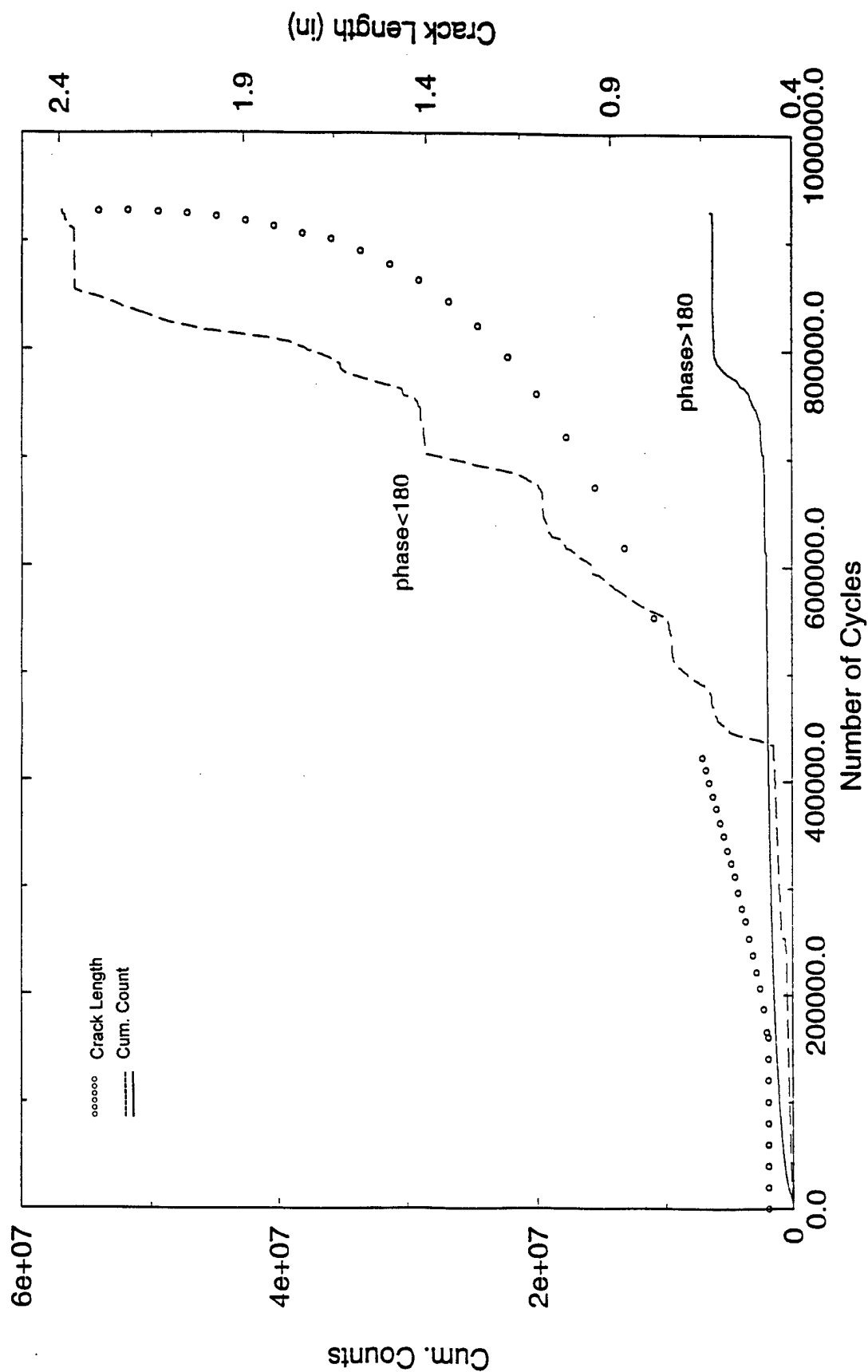


Fig. 149 Cumulative AE Counts and Crack Length vs. Number of Fatigue Cycles  
(4340 Steel,  $K_{max} = 0.15 K_{Ic}$ )

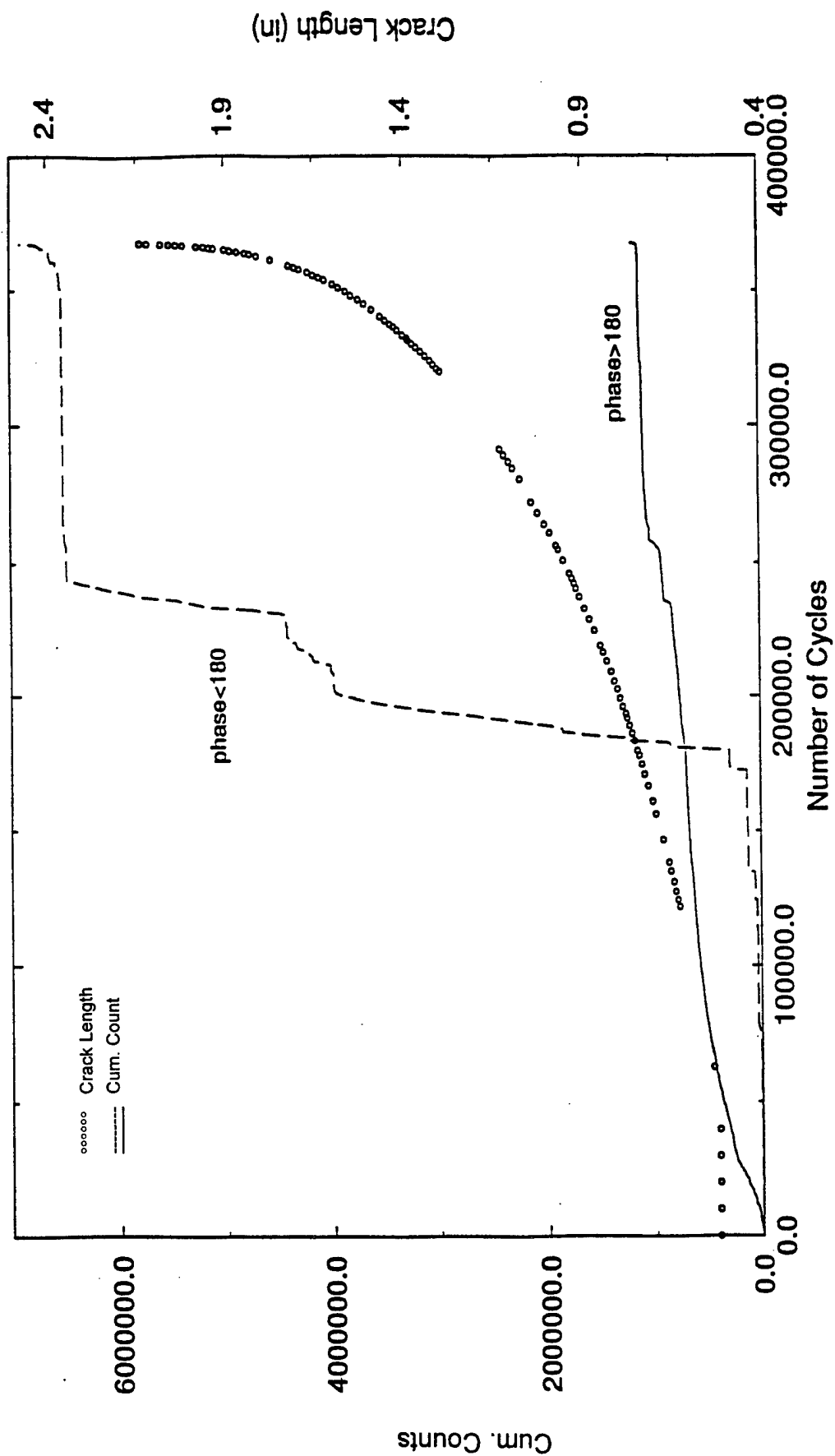


Fig. 150 Cumulative AE Counts and Crack Length vs. Number of Fatigue Cycles  
(4340 Steel,  $K_{max} = 0.20 K_{Ic}$ )

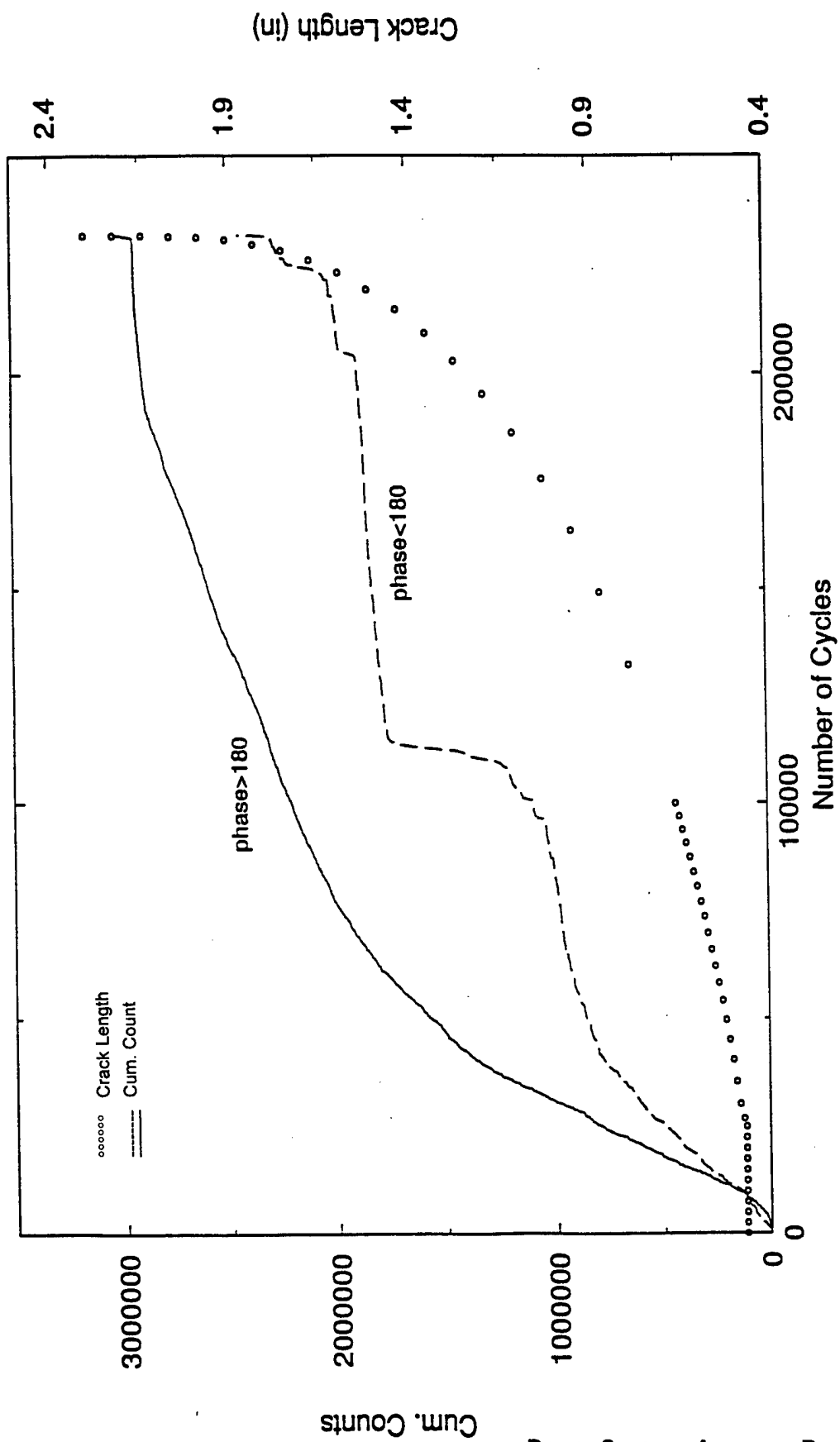


Fig. 151 Cumulative AE Counts and Crack Length vs. Number of Fatigue Cycles  
(4340 Steel,  $K_{max} = 0.25 K_{Ic}$ )

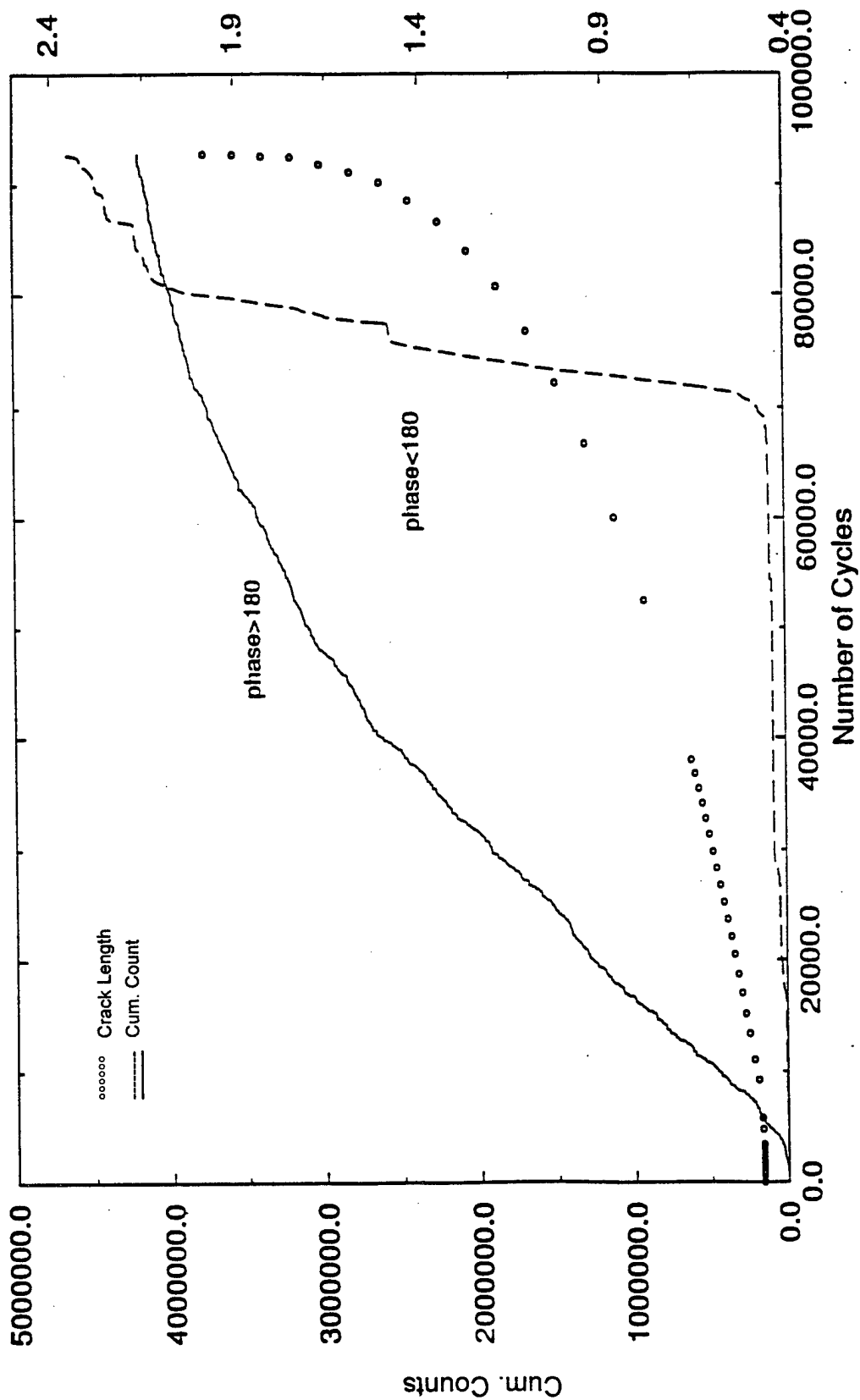


Fig. 152 Cumulative AE Counts and Crack Length vs. Number of Fatigue Cycles  
(4340 Steel,  $K_{max} = 0.35 K_{Ic}$ )

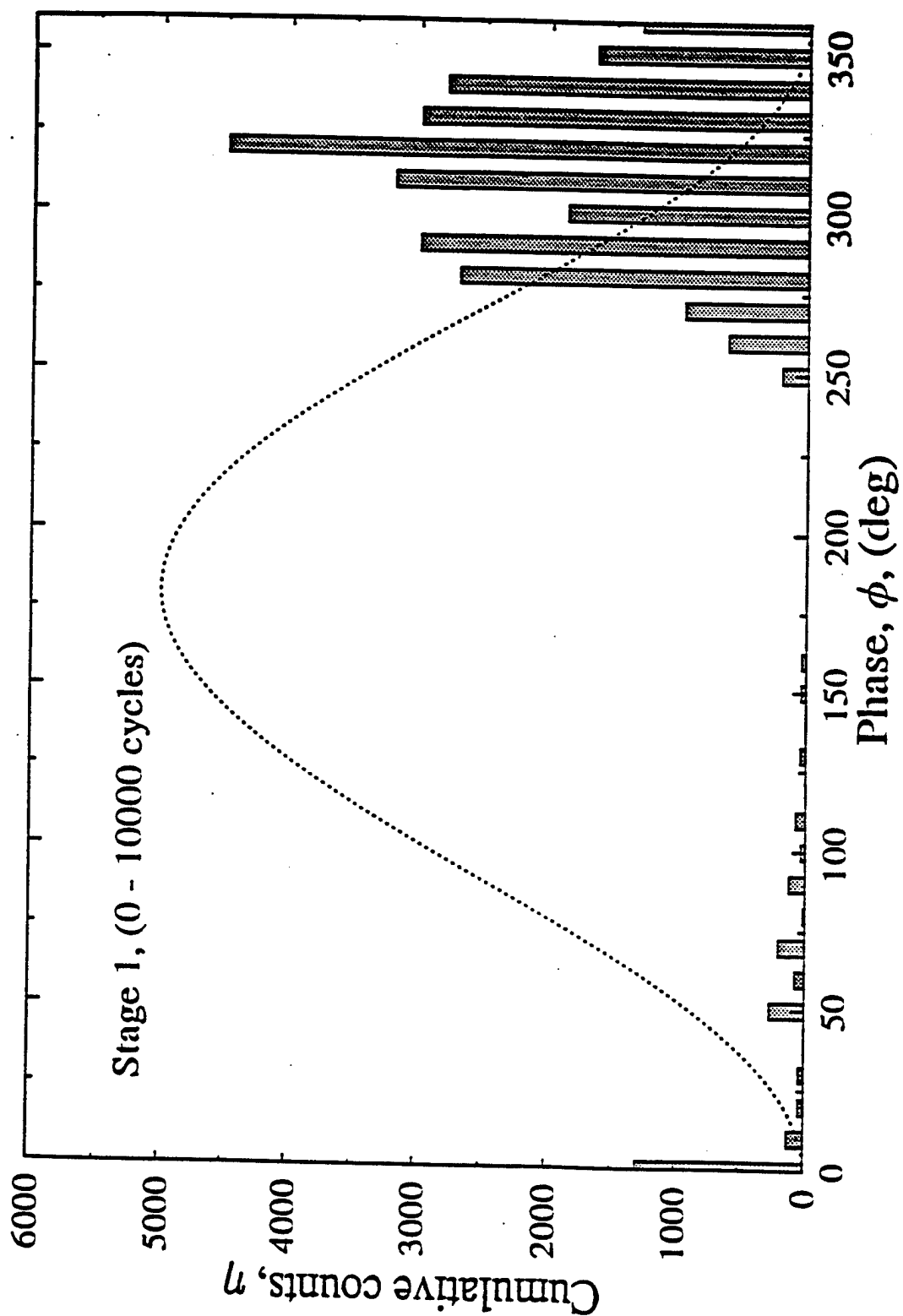


Fig. 153 Cumulative AE Counts vs. Loading Cycle Phase  
(4340 Steel, compact tension specimen)



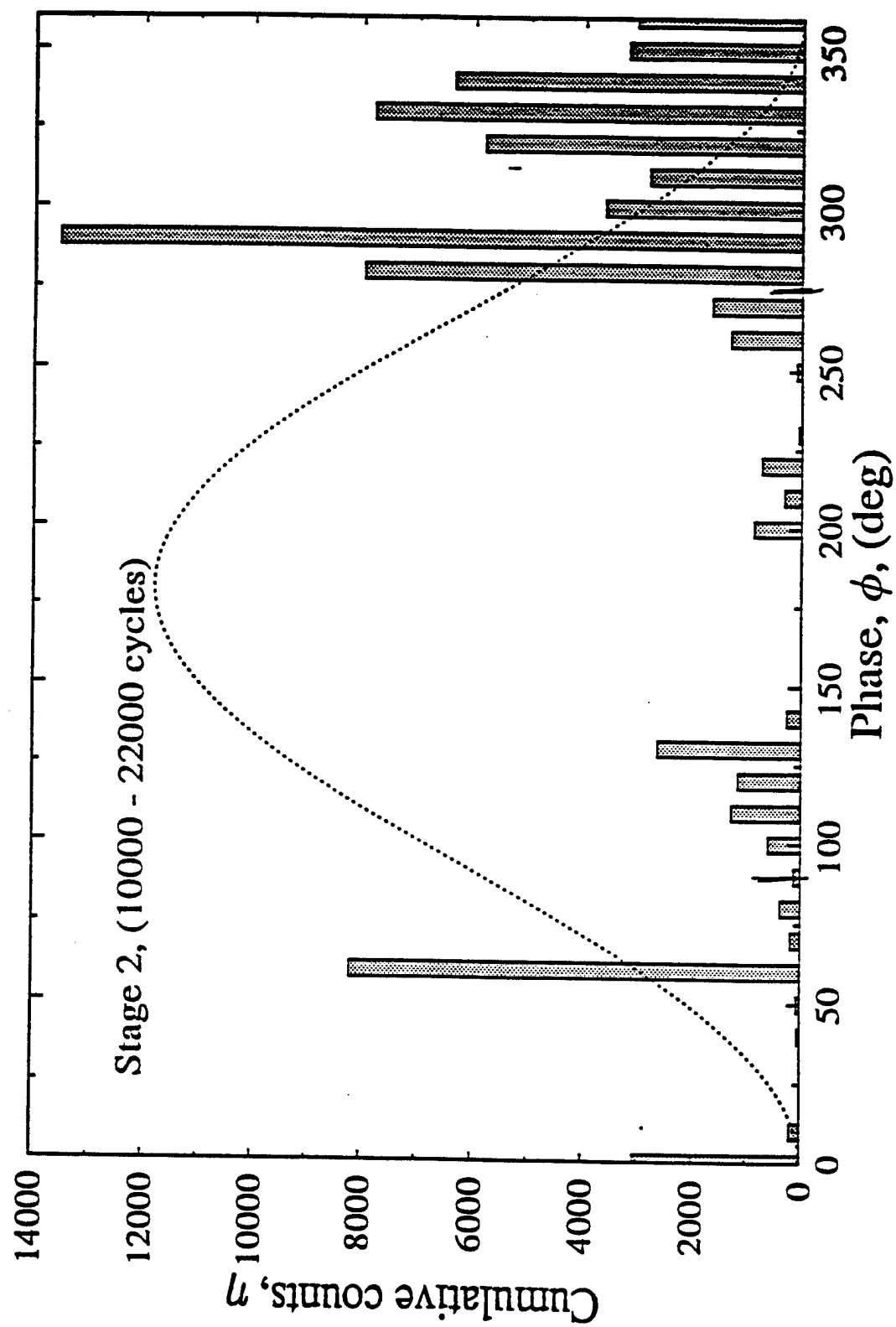


Fig. 154 Cumulative AE Counts vs. Loading Cycle Phase  
(4340 Steel, compact tension specimen)

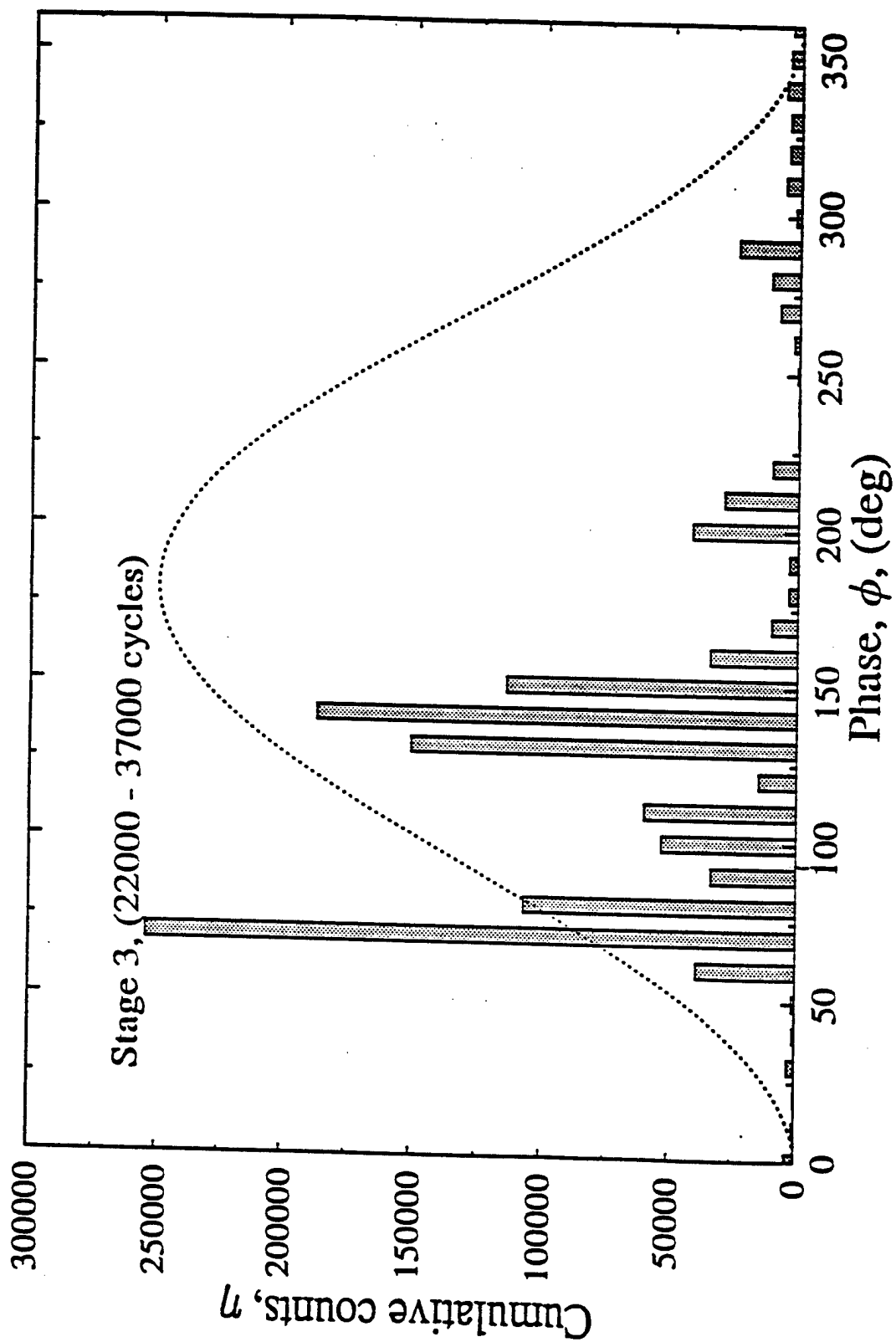


Fig. 155 Cumulative AE Counts vs. Loading Cycle Phase  
(4340 Steel, compact tension specimen)

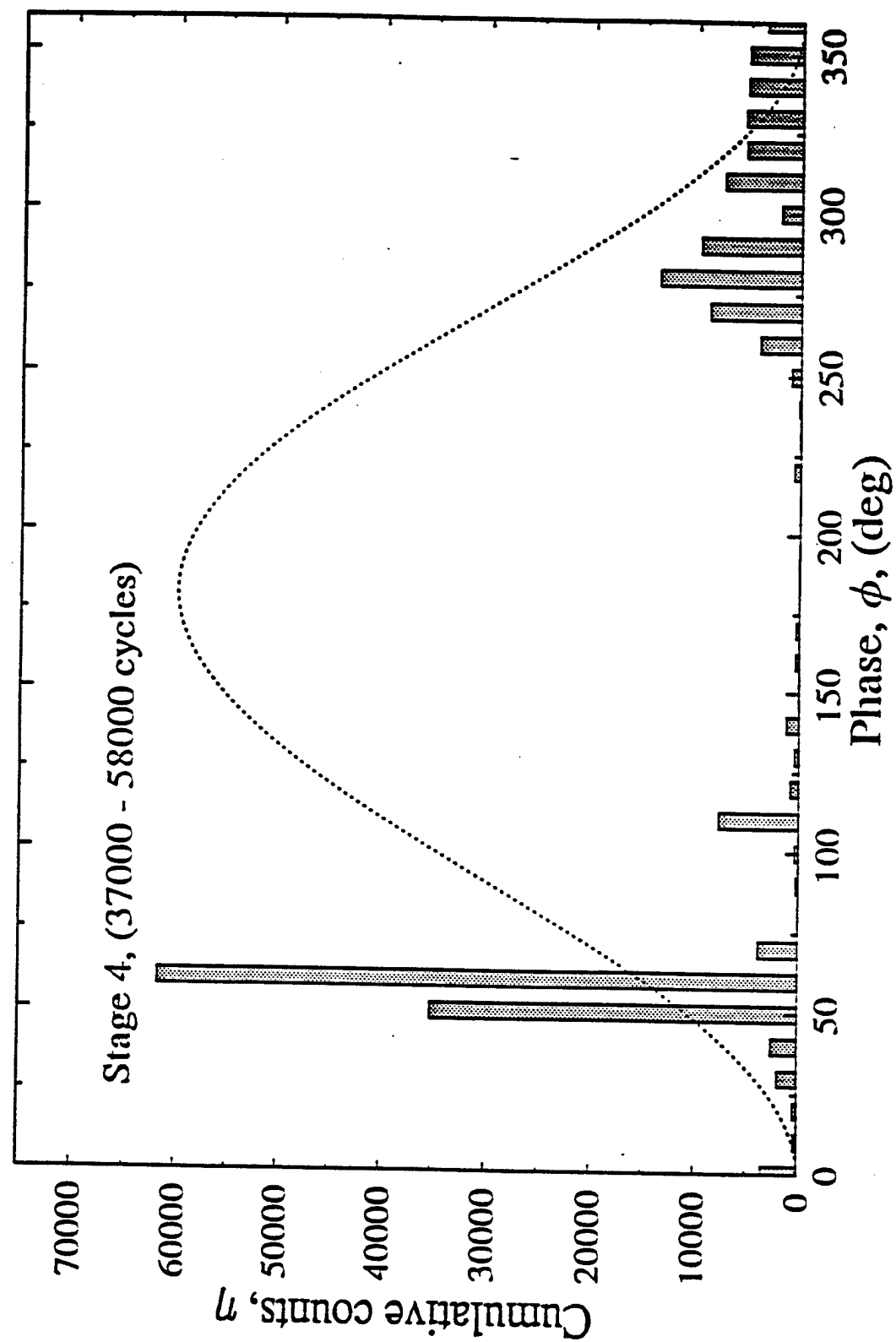


Fig. 156 Cumulative AE Counts vs. Loading Cycle Phase  
(4340 Steel, compact tension specimen)

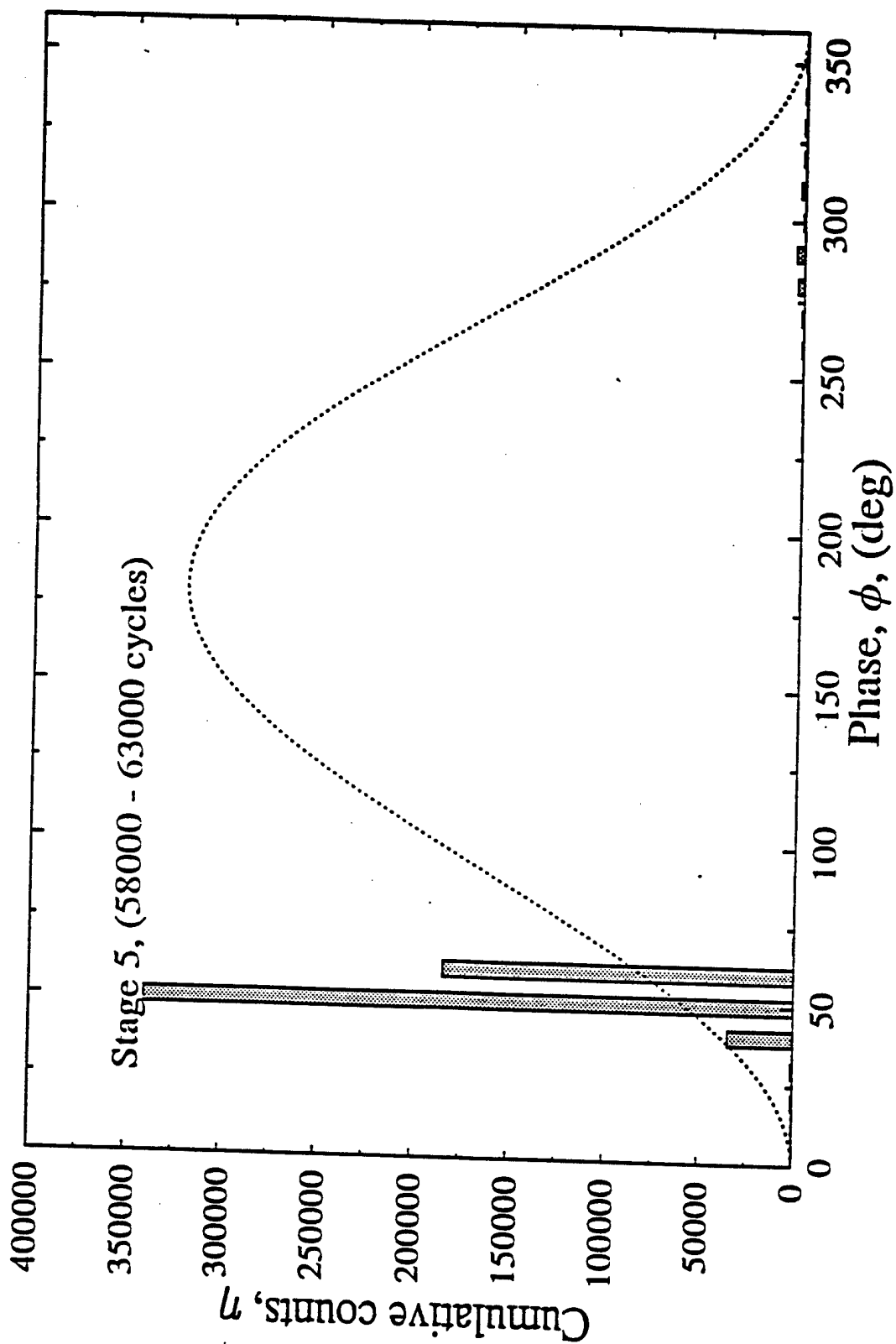


Fig. 157 Cumulative AE Counts vs. Loading Cycle Phase  
(4340 Steel, compact tension specimen)

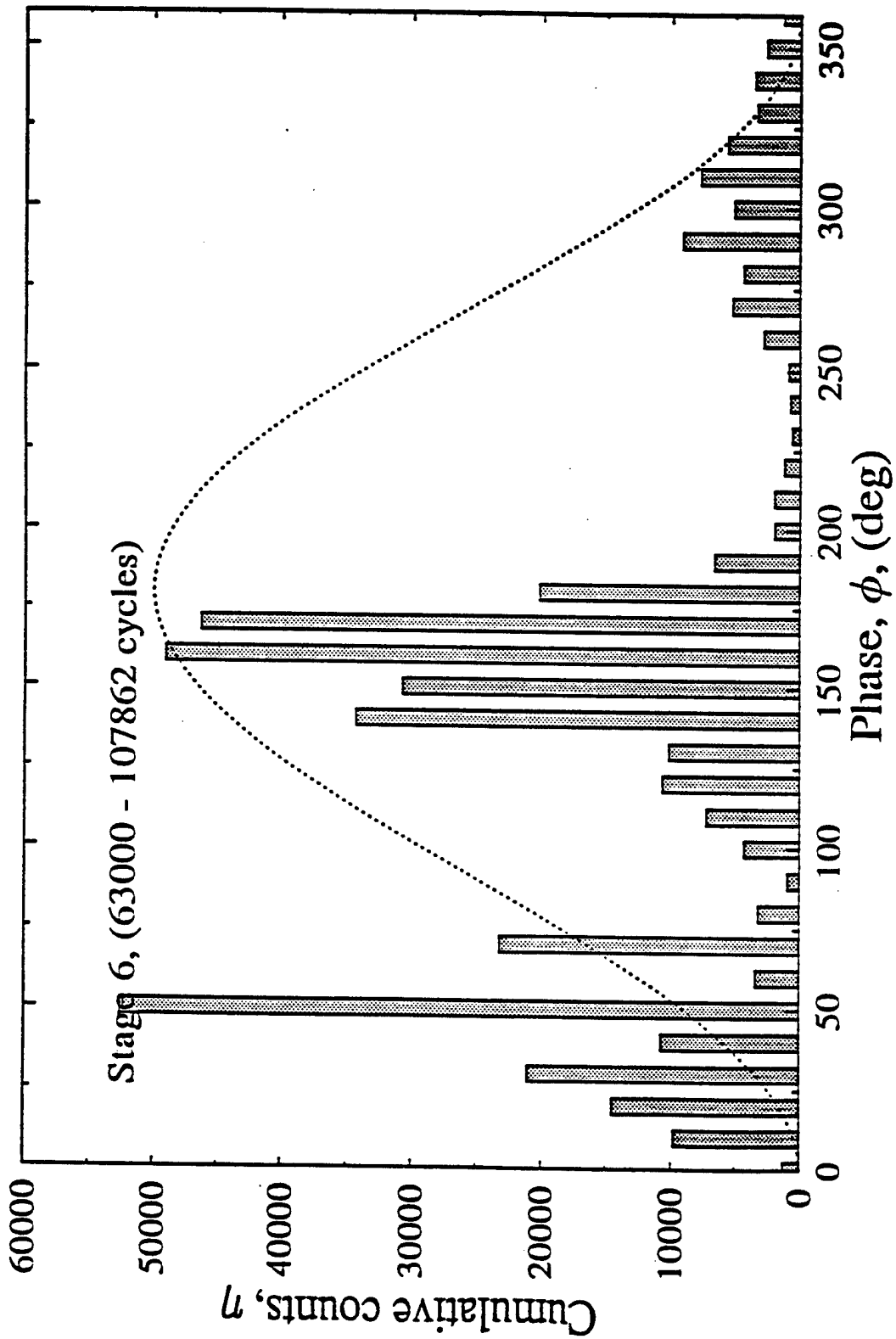


Fig. 158 Cumulative AE Counts vs. Loading Cycle Phase  
(4340 Steel, compact tension specimen)

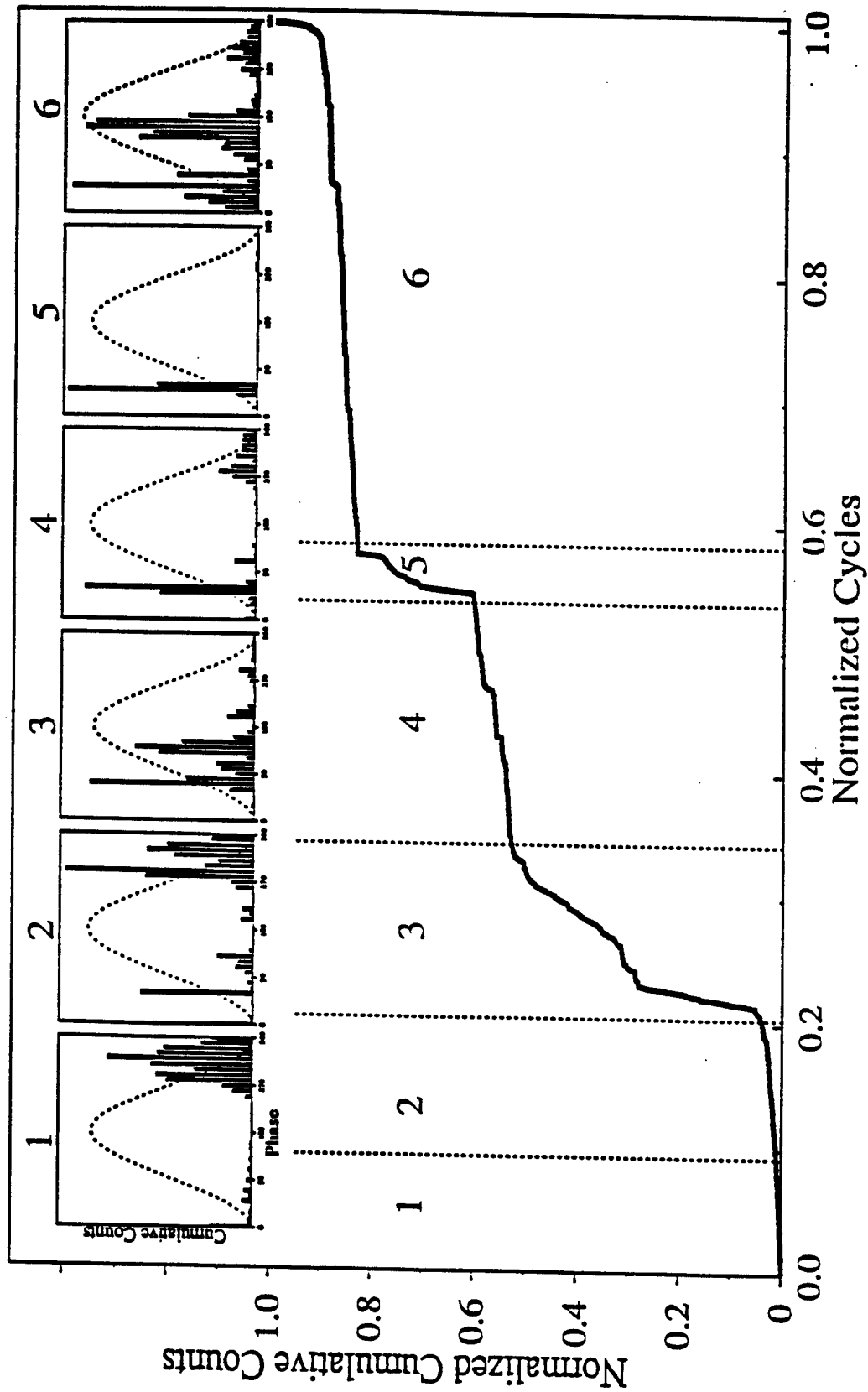


Fig. 159 Cumulative AE Counts and Corresponding Phase Distributions at Several Stages  
(4340 Steel, compact tension specimen)

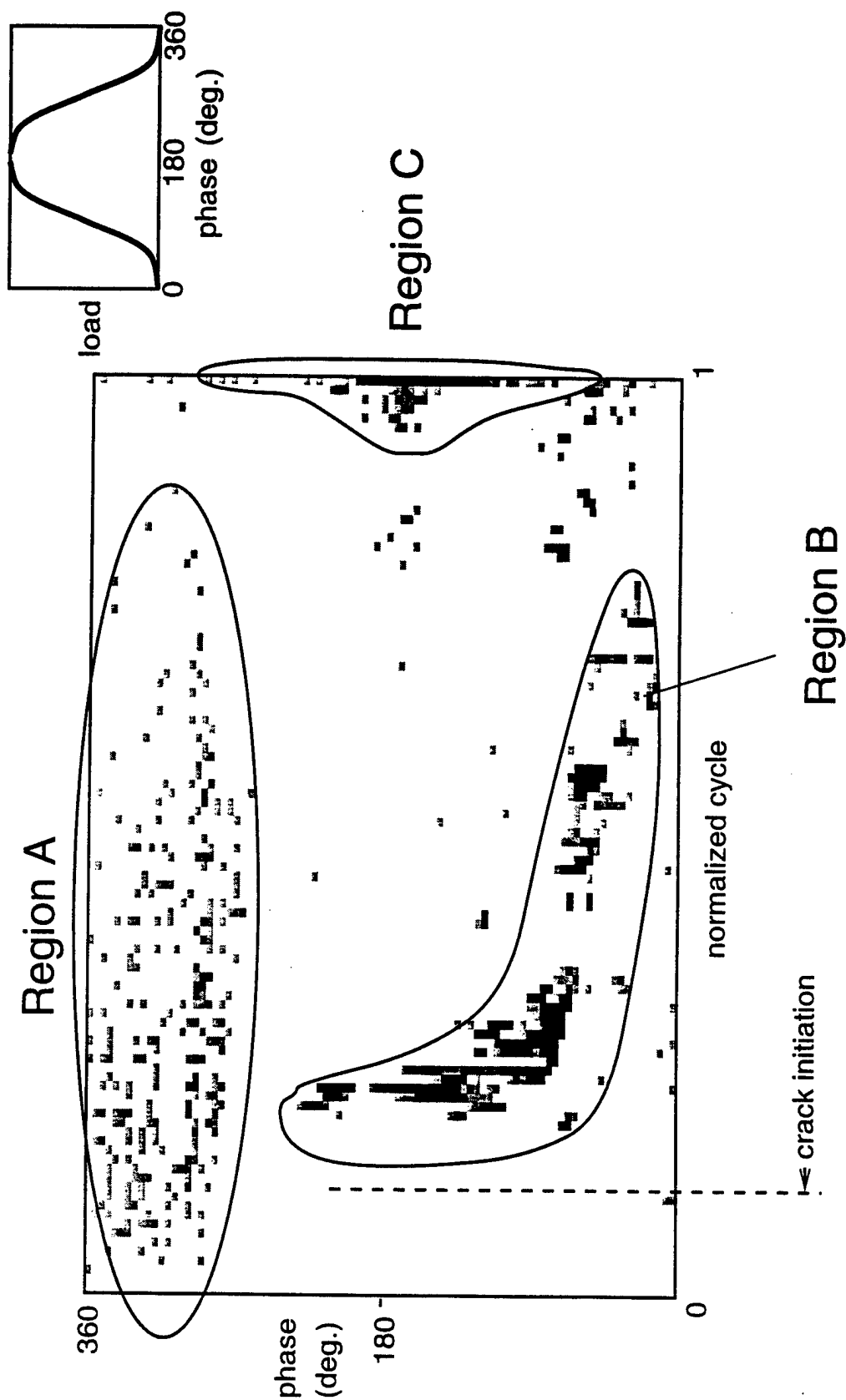
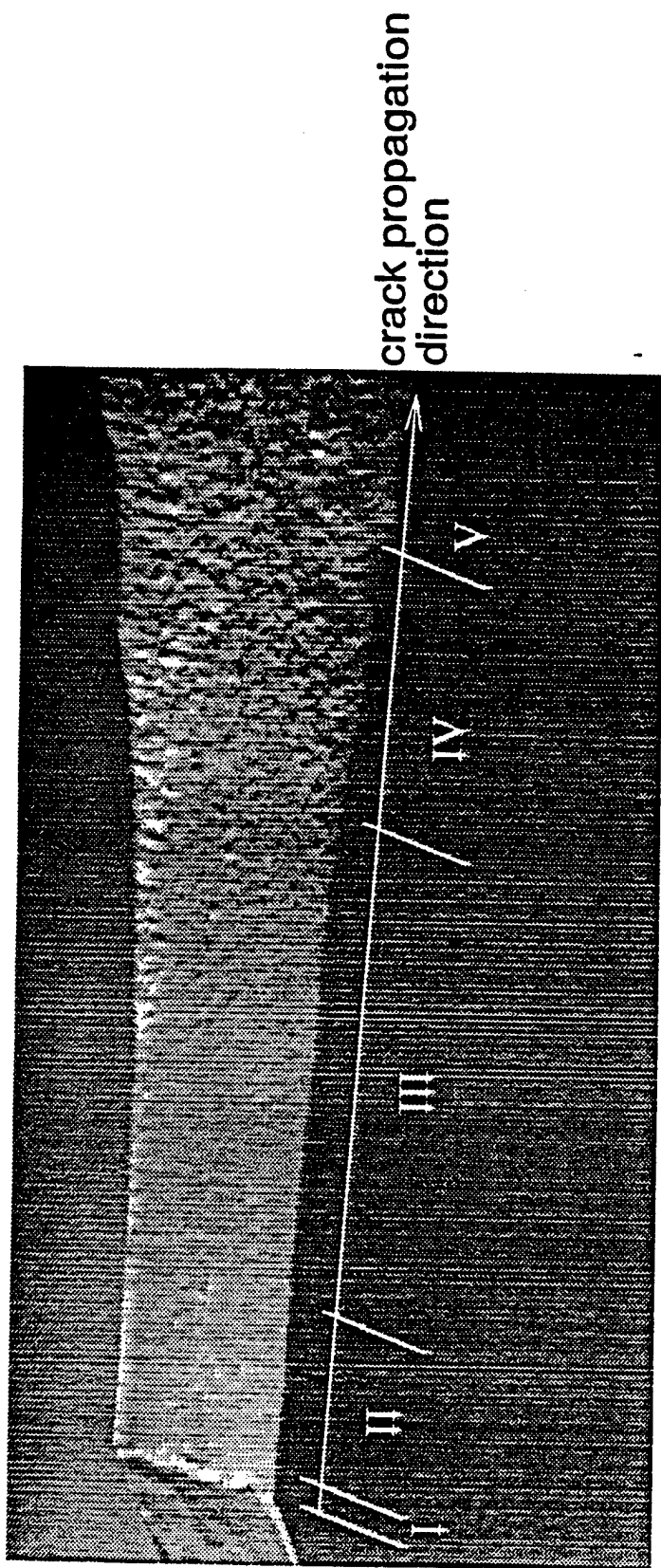


Fig. 160 Loading Phase Distribution of AE activity



- I. Crack initiation and crack planes merge
- II. Plane strain dominated crack propagation
- III. Transition from plane strain to plane stress
- IV. Plane stress dominated crack propagation
- V. Unstable crack propagation

Fig. 161 Fracture Morphology and Stages of Crack propagation  
(4340 Steel; CT Specimen)



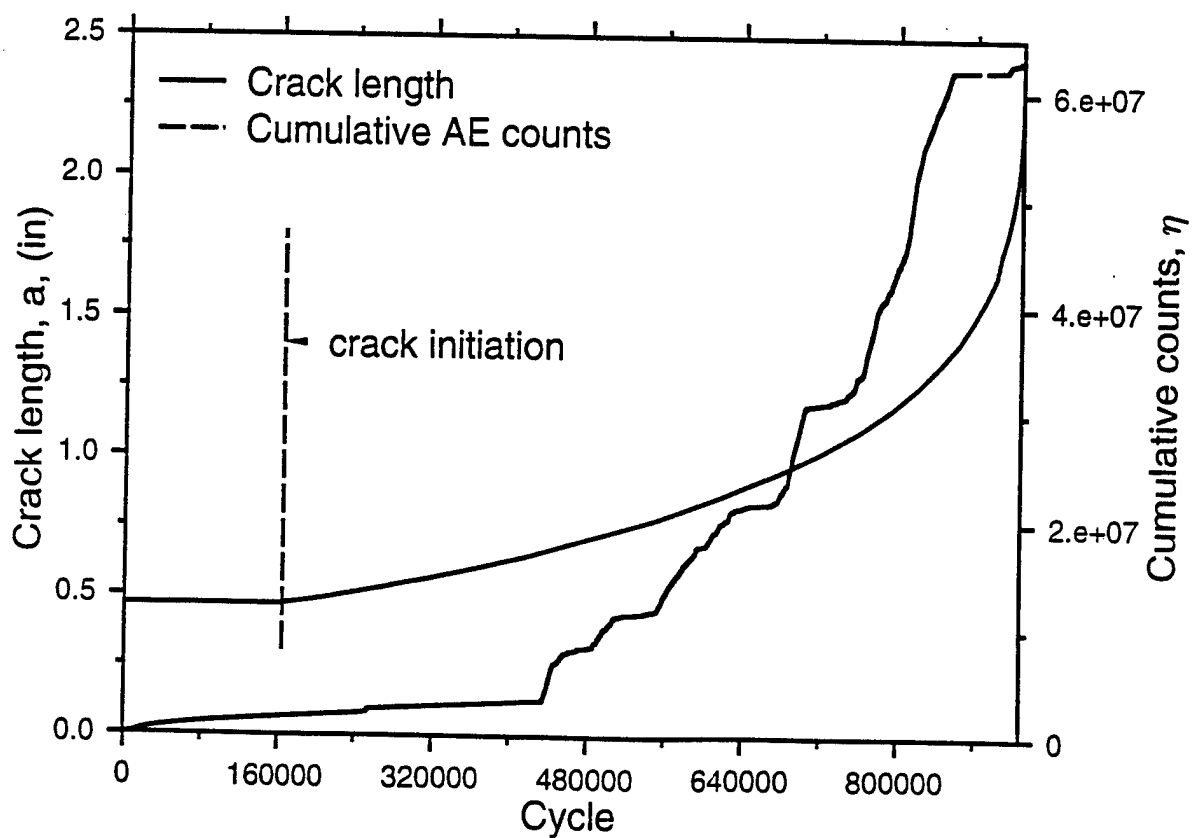
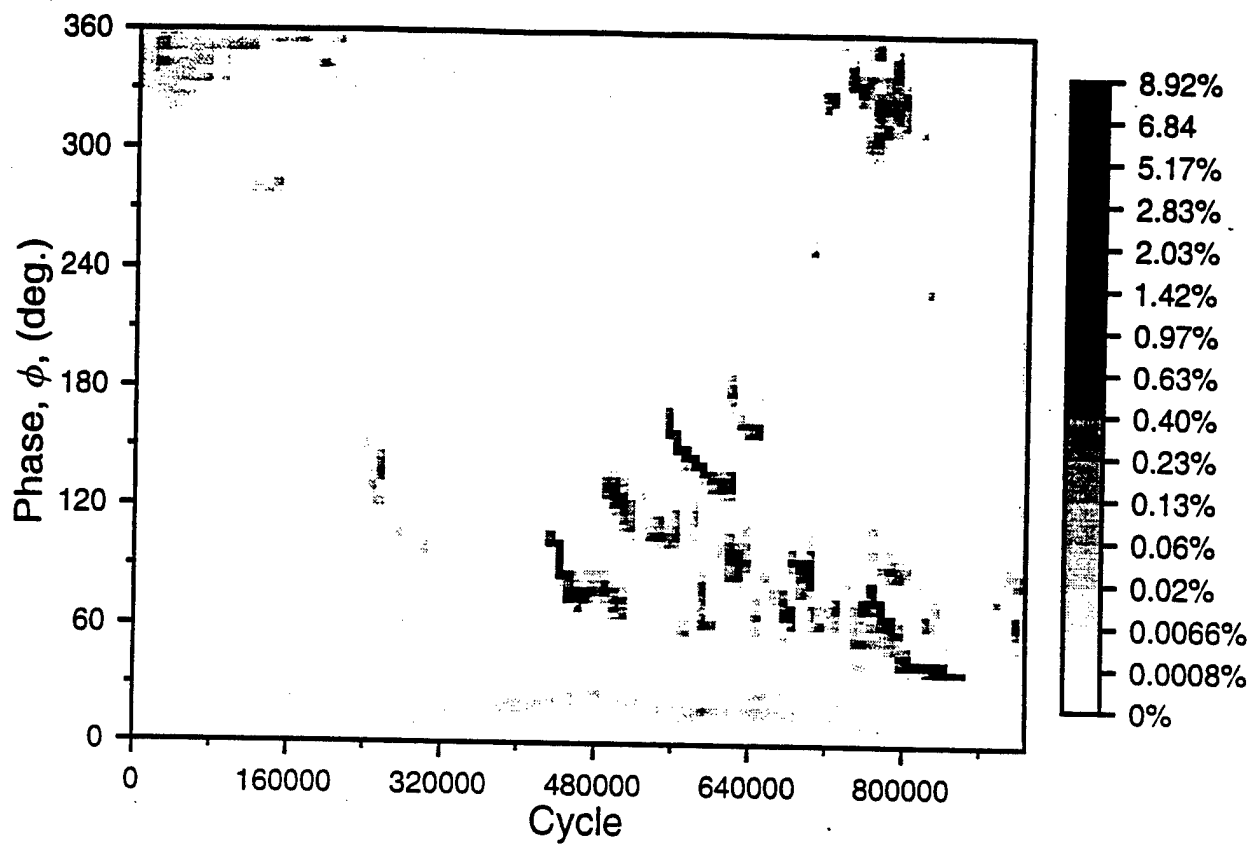


Fig. 162 Probability Density Function of AE Cumulative Counts for a 4340 Steel Compact Tension Specimen ( $K_{\max} = 0.15 K_c$ ,  $R = 0.1$ )

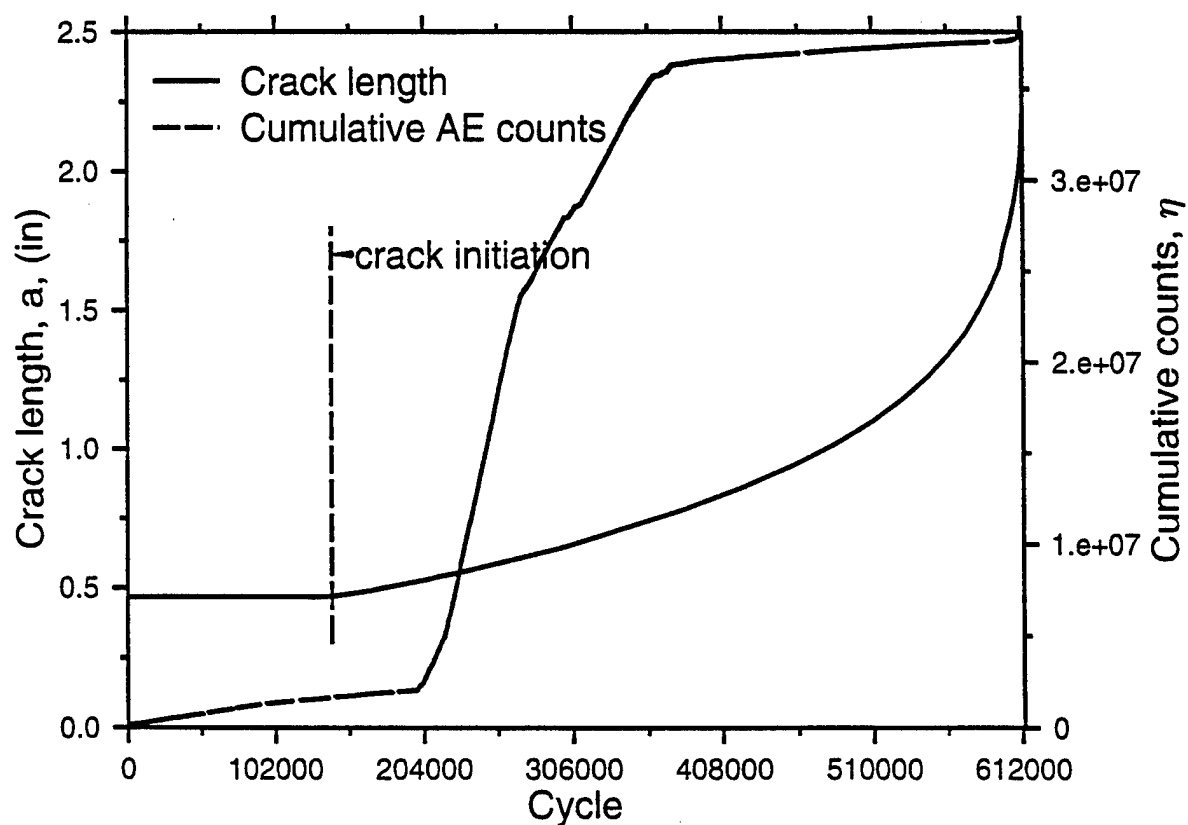
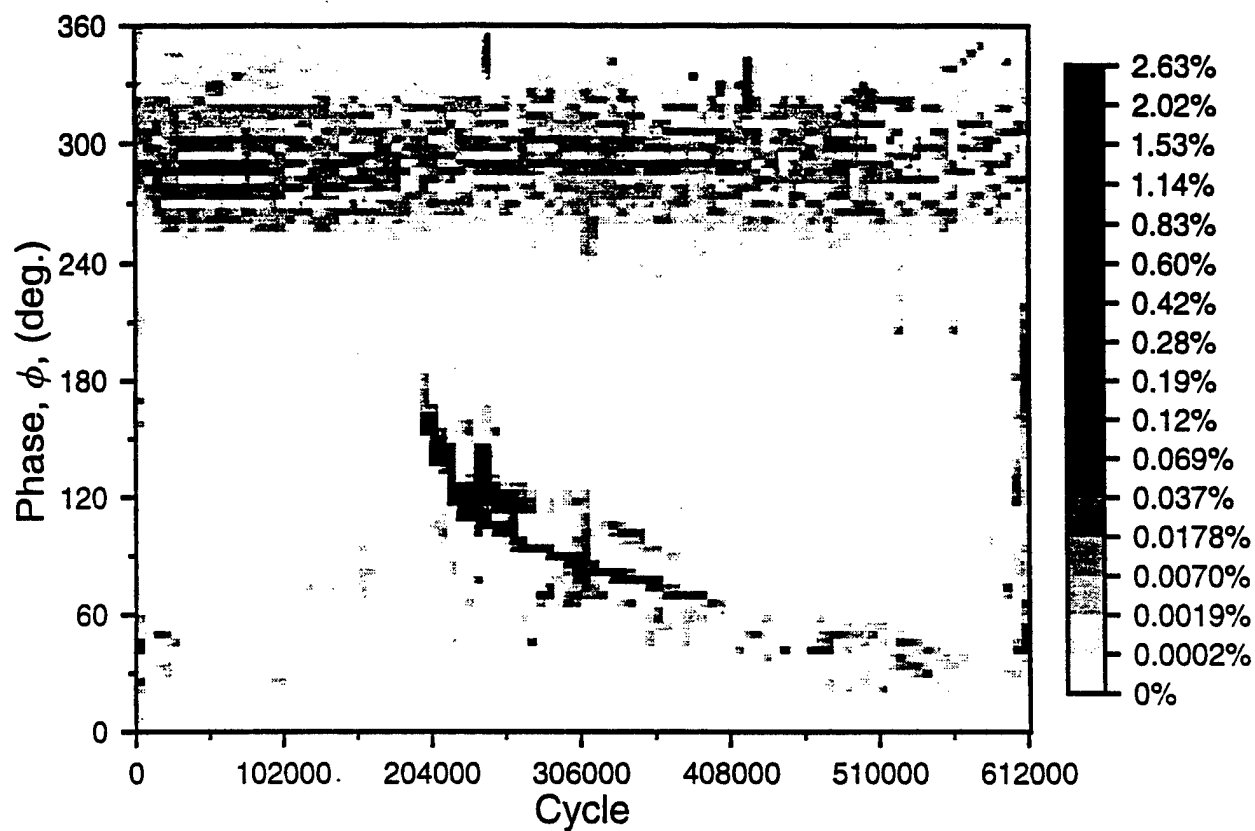


Fig. 163 Probability Density Function of AE Cumulative Counts for a 4340 Steel Compact Tension Specimen ( $K_{\max} = 0.175 K_c$ ,  $R = 0.1$ )

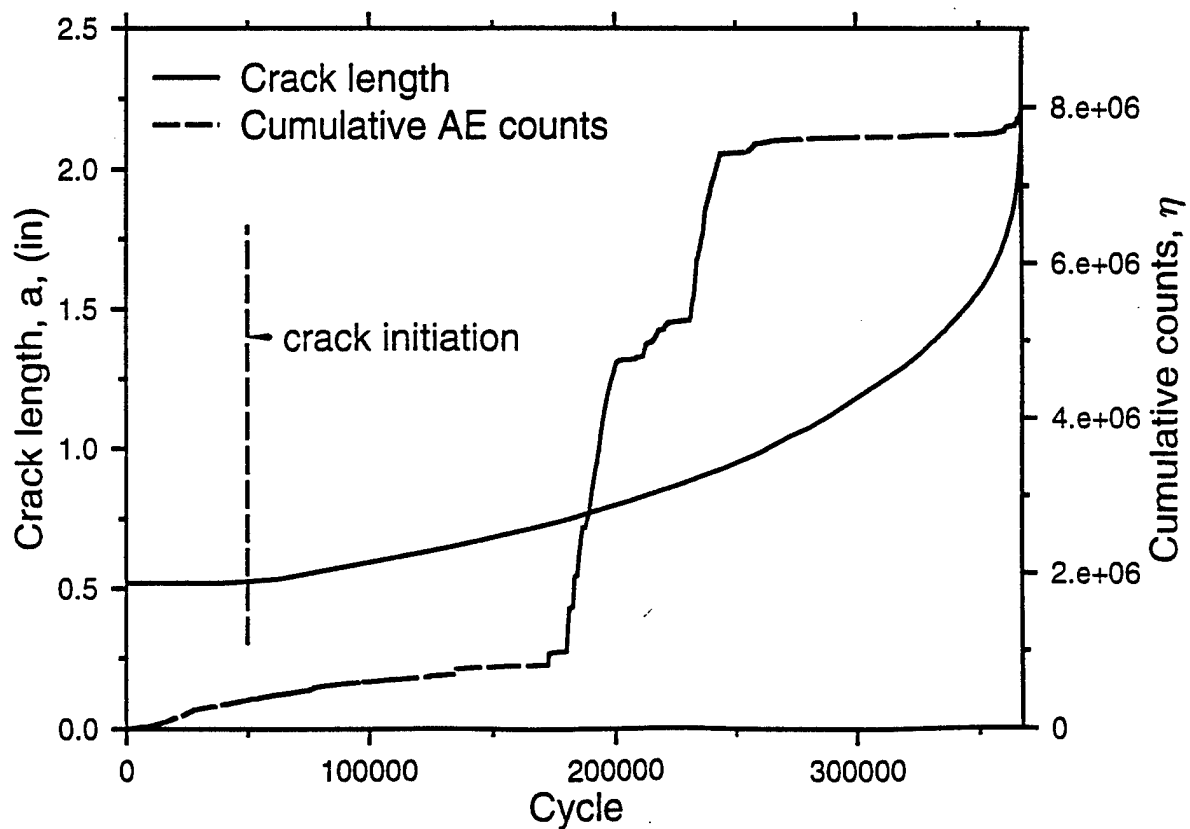
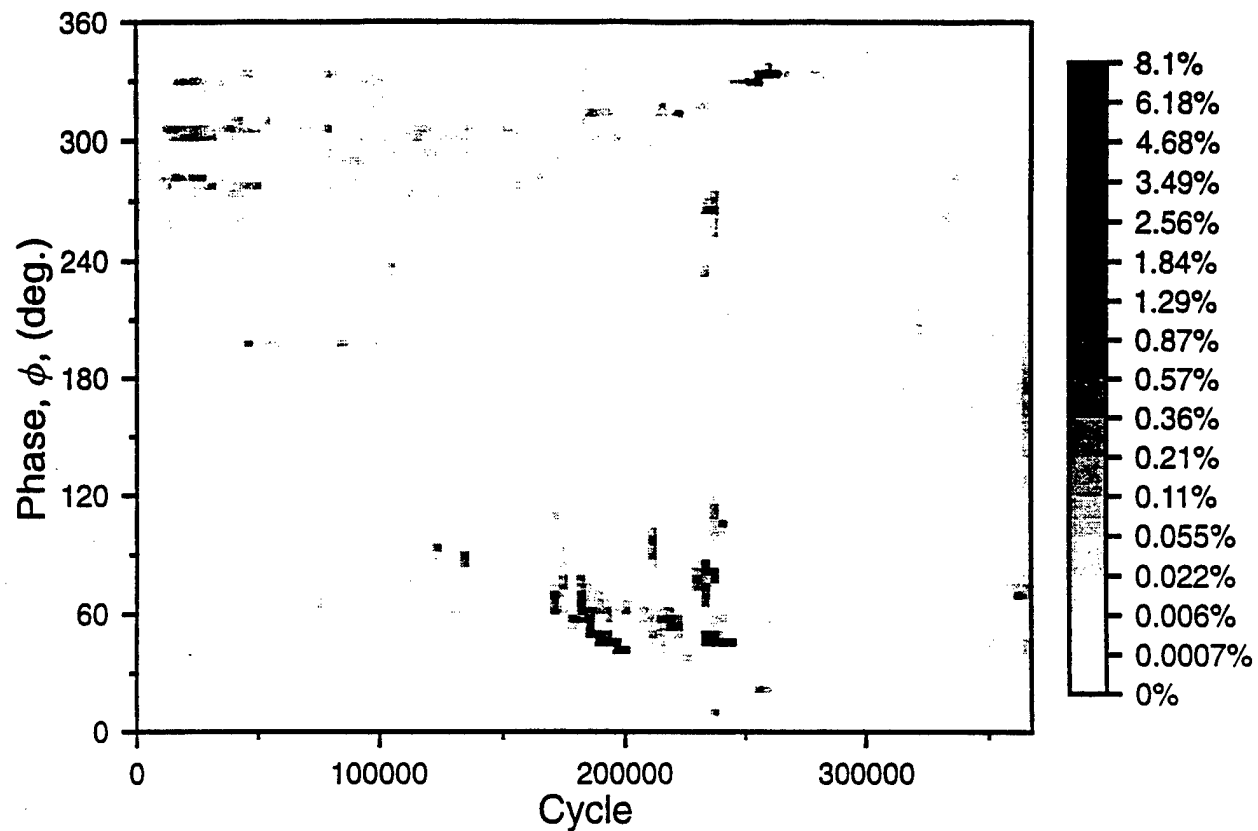


Fig. 164 Probability Density Function of AE Cumulative Counts for a  
4340 Steel Compact Tension Specimen  
( $K_{\max} = 0.2 K_c$ ,  $R = 0.1$ )

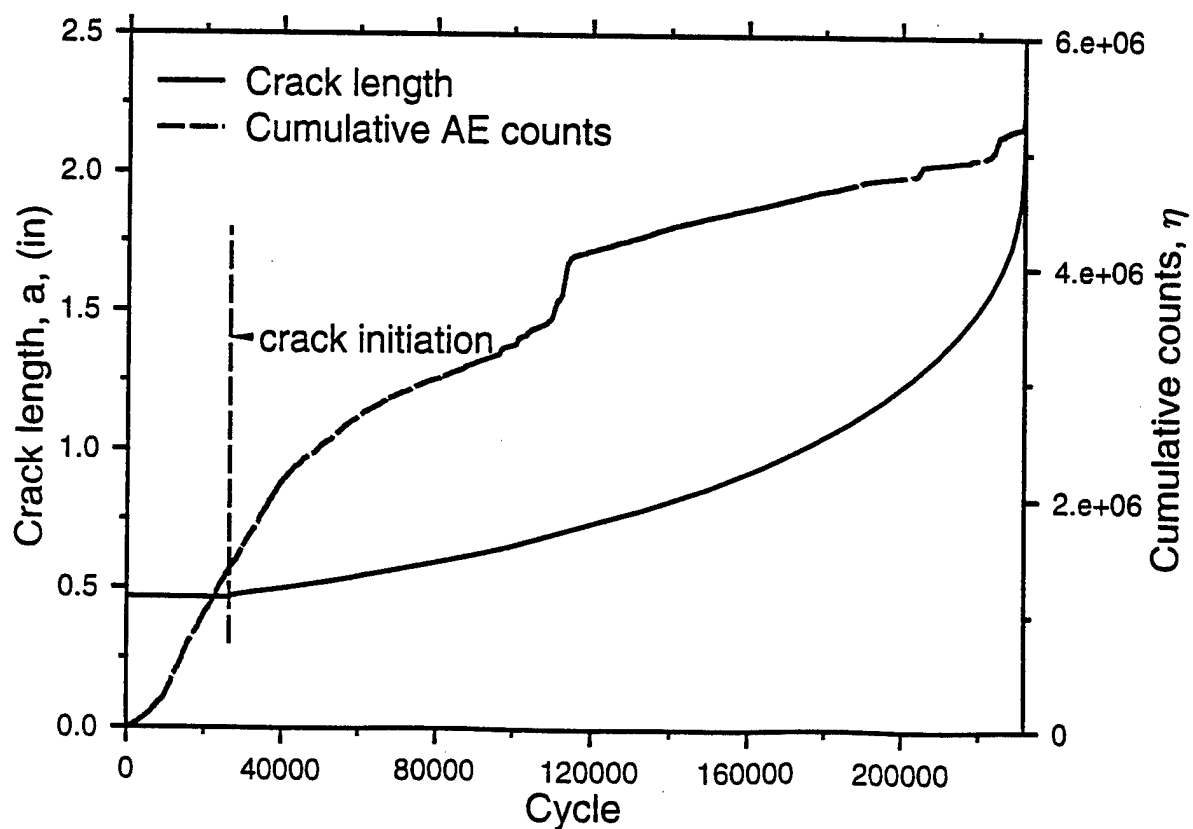
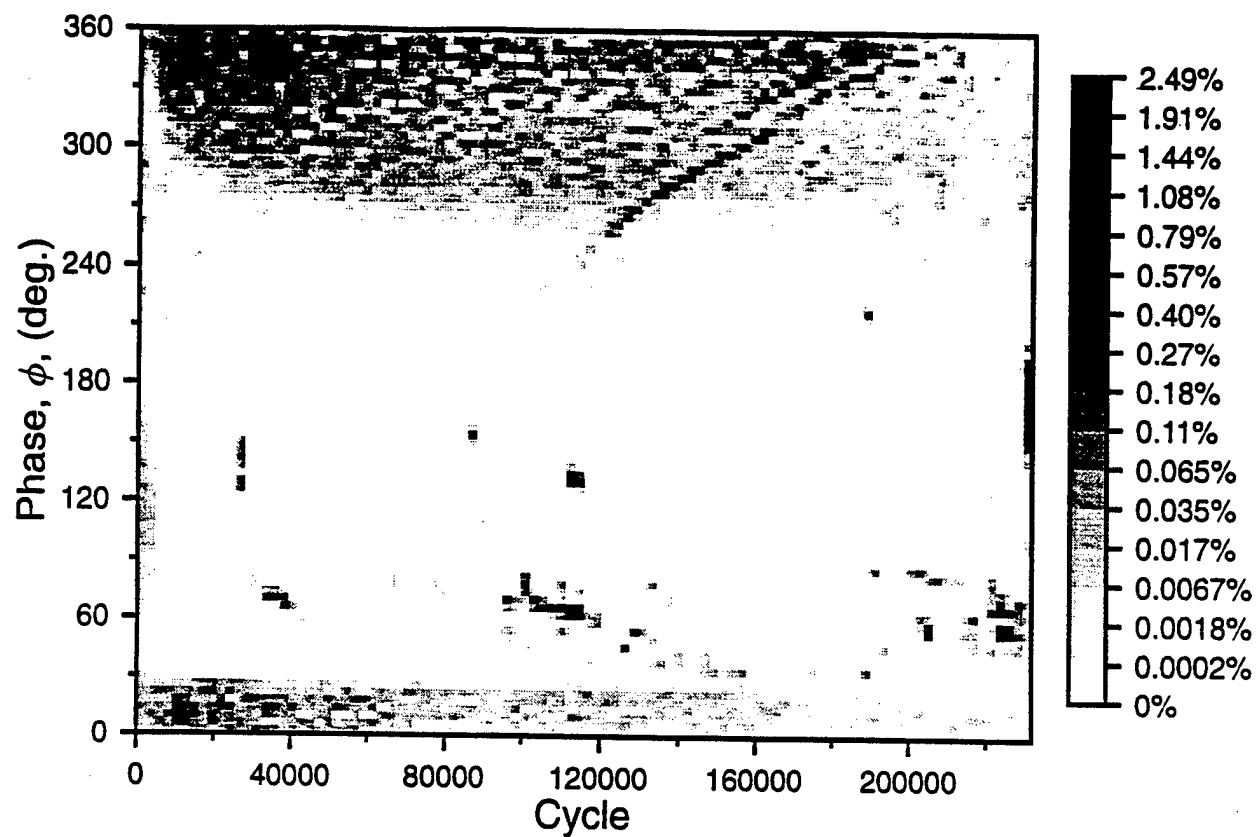


Fig. 165 Probability Density Function of AE Cumulative Counts for a 4340 Steel Compact Tension Specimen ( $K_{\max} = 0.25 K_c$ ,  $R = 0.1$ )

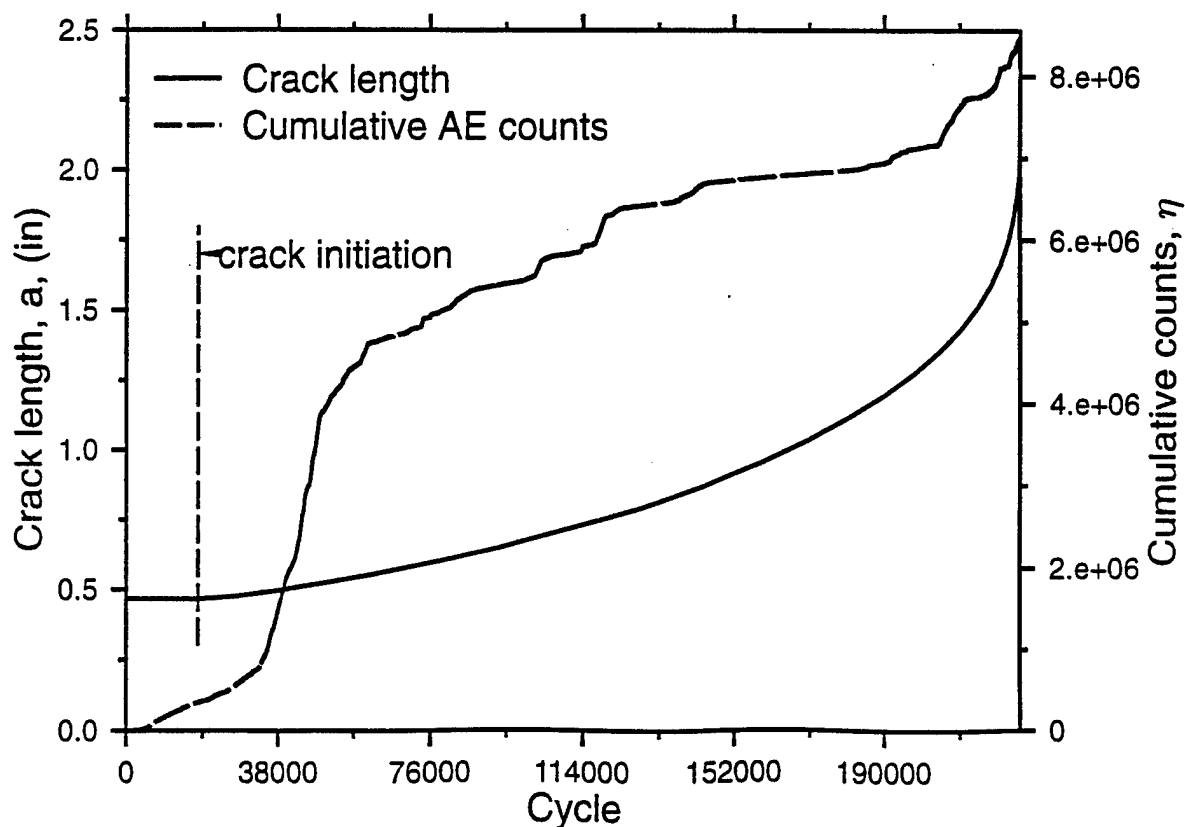
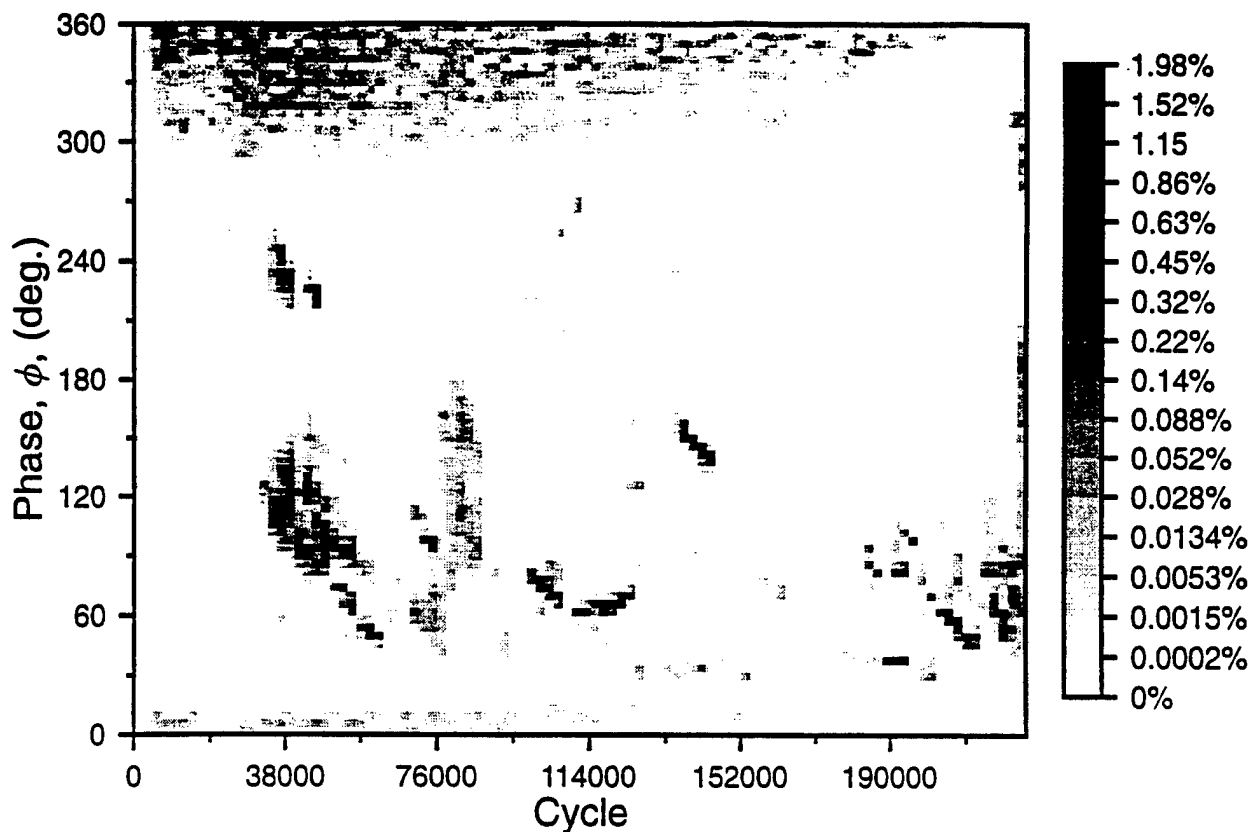


Fig. 166 Probability Density Function of AE Cumulative Counts for a 4340 Steel Compact Tension Specimen  
( $K_{\max} = 0.25 K_c$ ,  $R = 0.1$ )

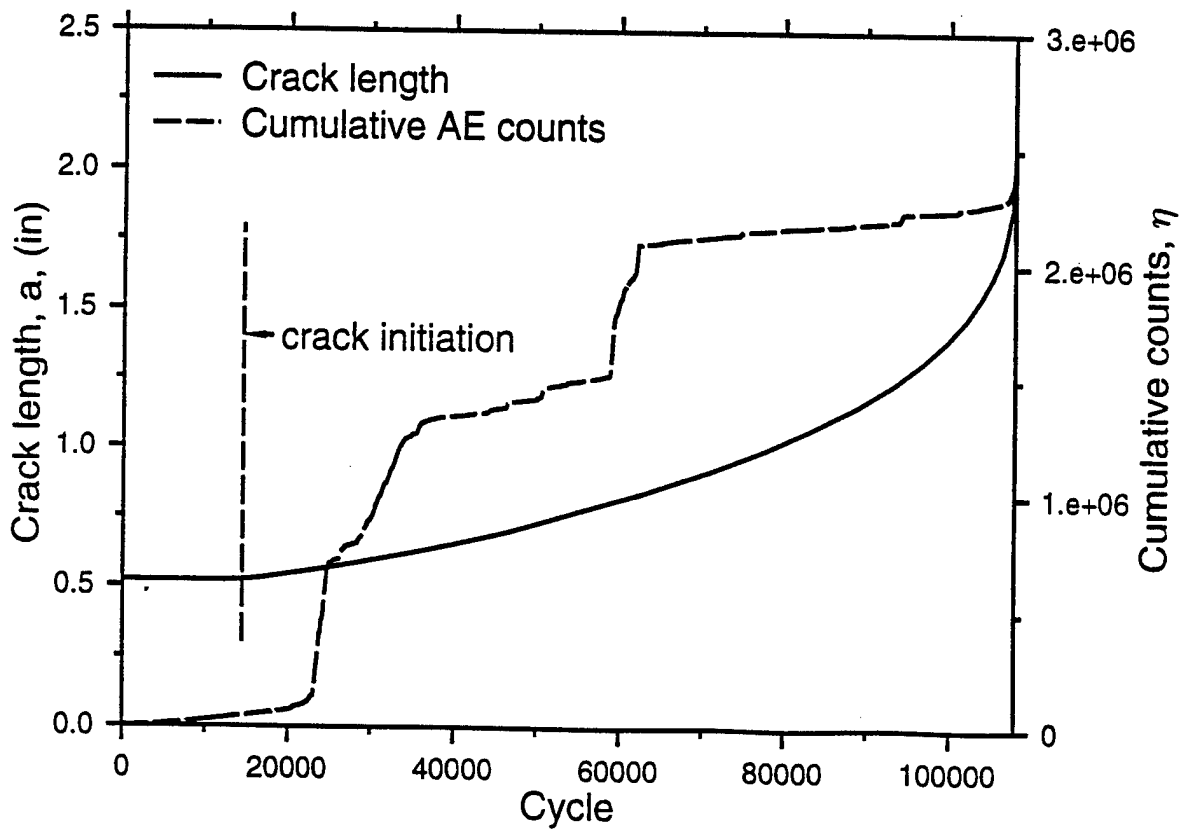
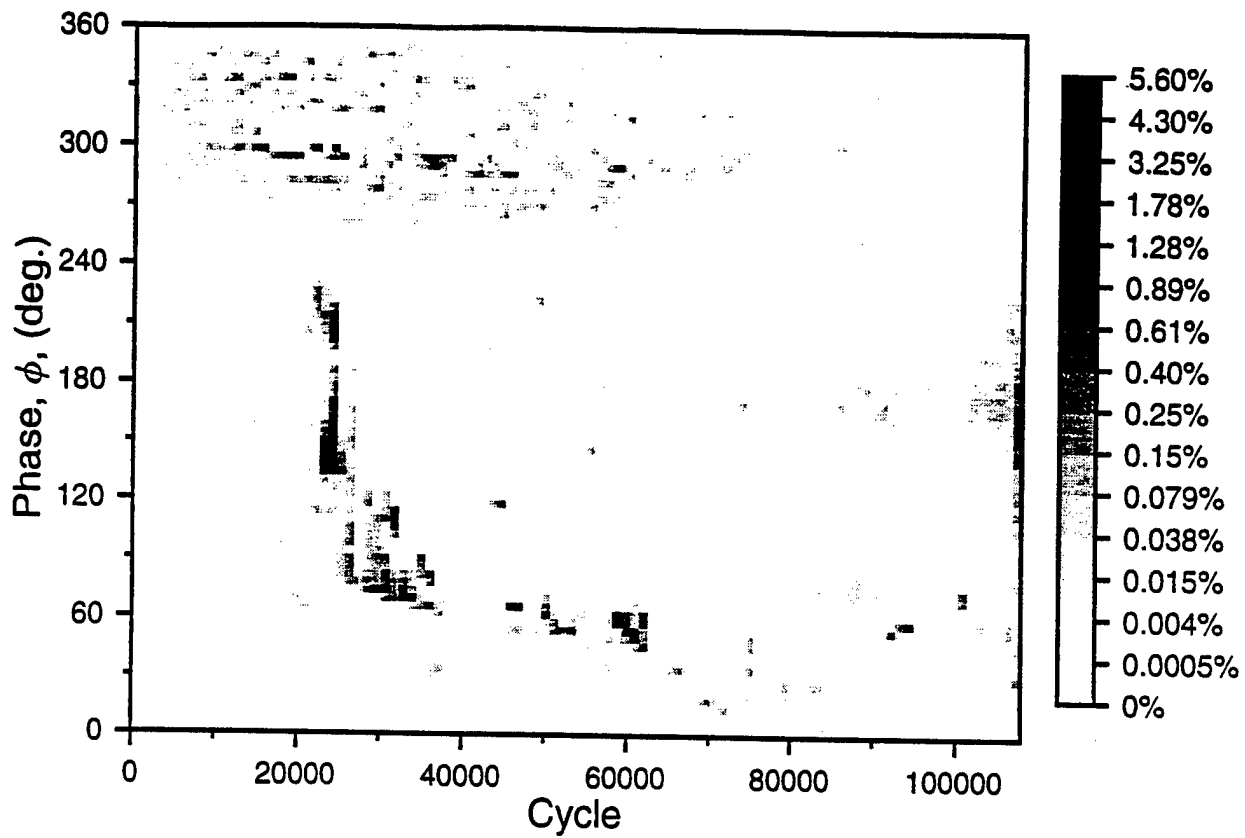


Fig. 167 Probability Density Function of AE Cumulative Counts for a 4340 Steel Compact Tension Specimen ( $K_{\max} = 0.3 K_c$ ,  $R = 0.1$ )

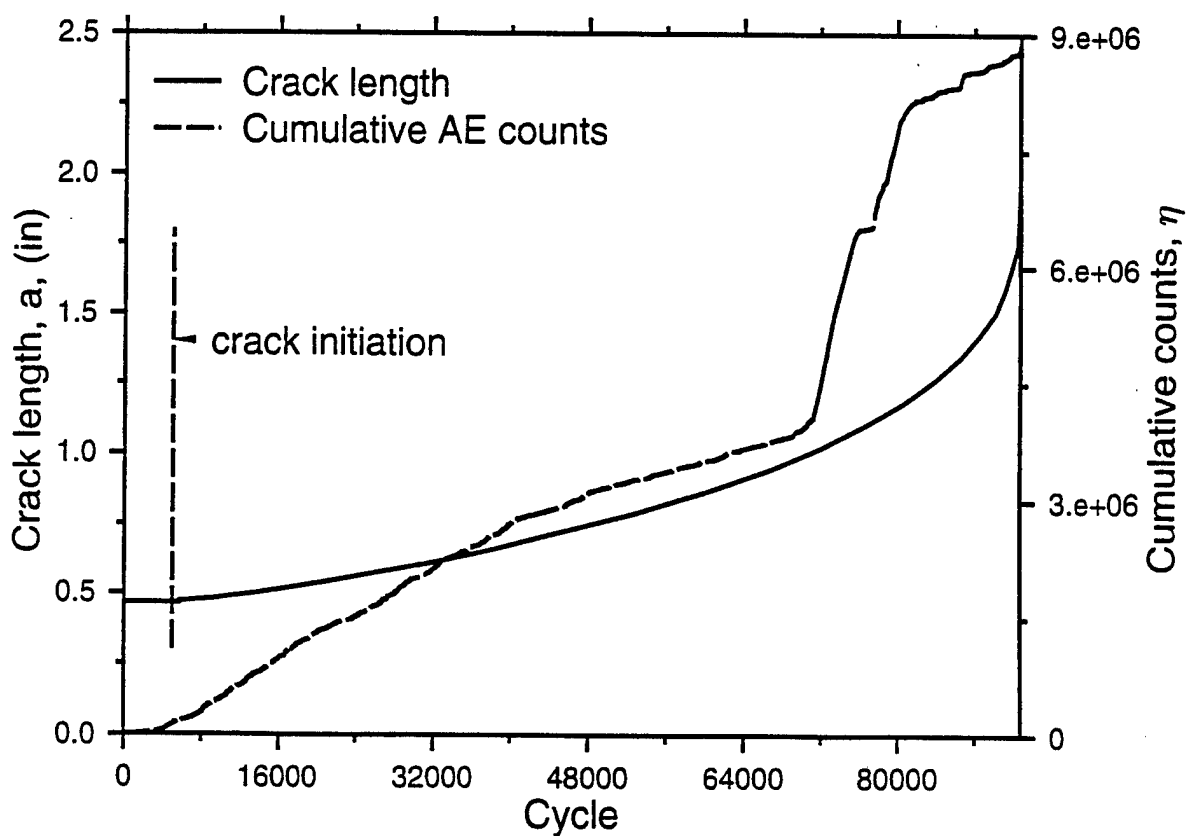
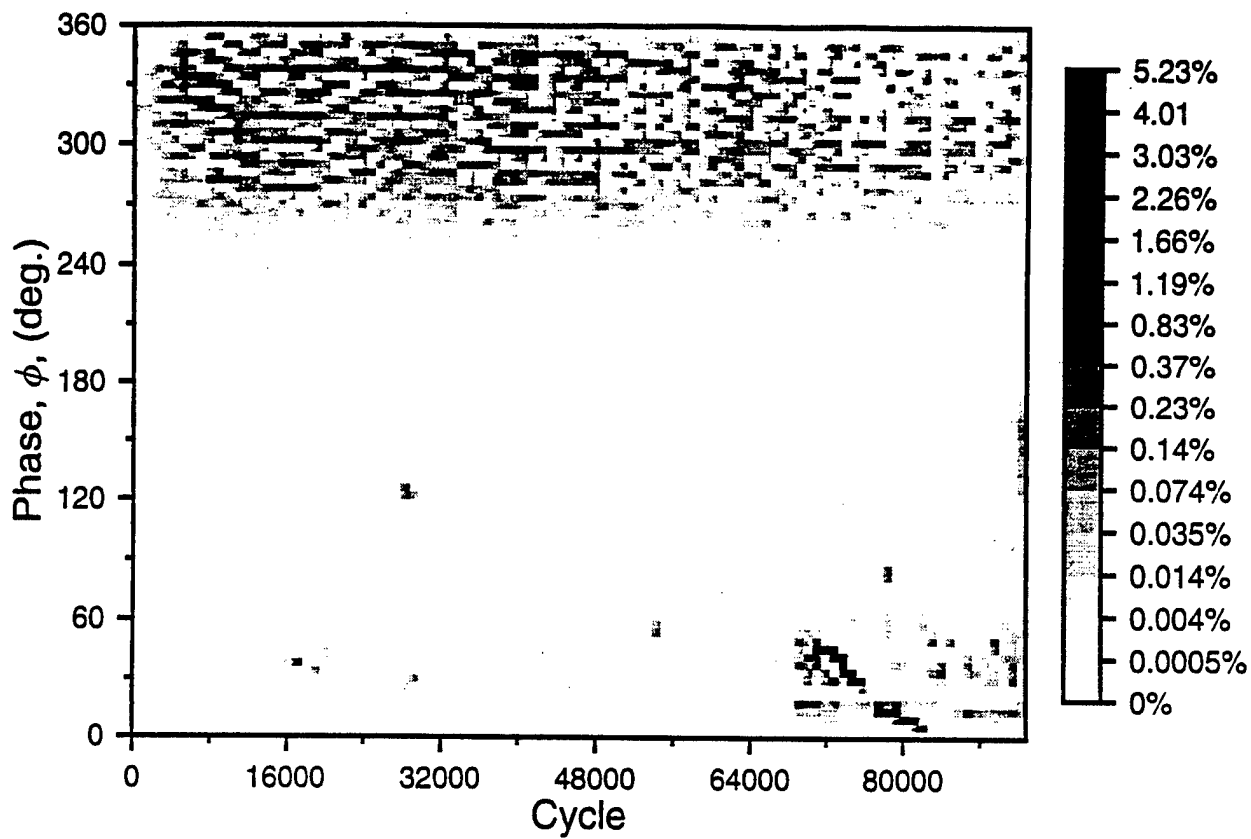


Fig. 168 Probability Density Function of AE Cumulative Counts for a 4340 Steel Compact Tension Specimen ( $K_{\max} = 0.35 K_c$ ,  $R = 0.1$ )

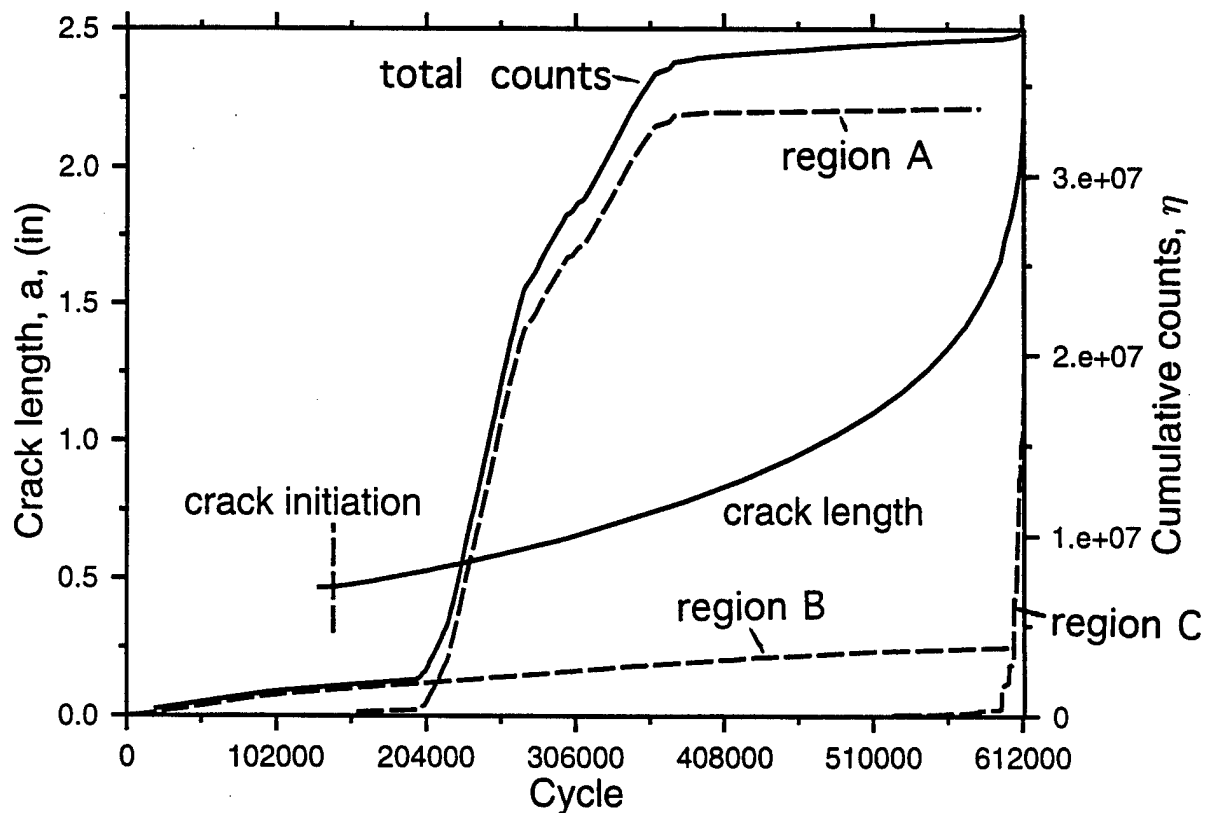
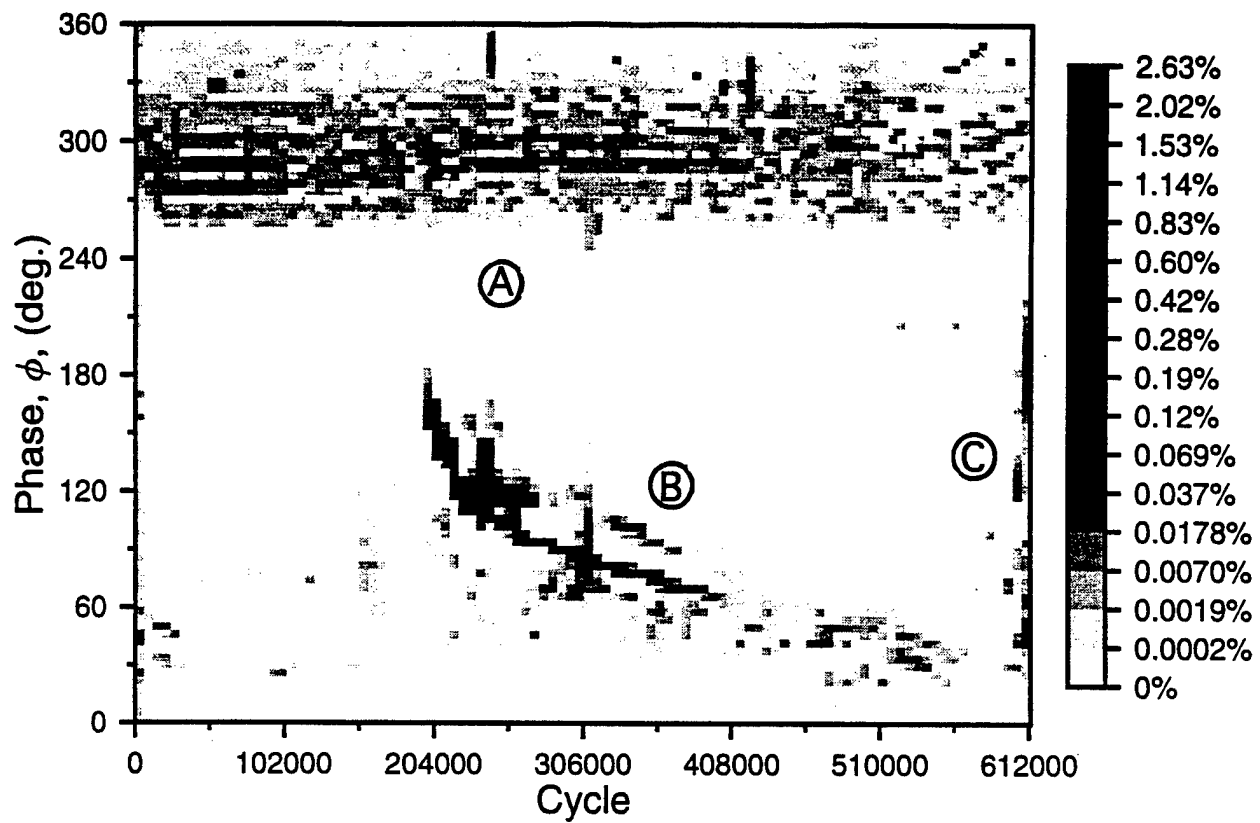


Fig. 169 Probability Density Function of AE Cumulative Counts for a 4340 Steel Compact Tension Specimen ( $K_{\max} = 0.175 K_c$ ,  $R = 0.1$ )



### **2.3.5 DYNAMIC METROLOGY AS A WEAR DIAGNOSTIC**

Co-investigators: Steven Liang, Thomas Kurfess, Steven Danyluk (Georgia Tech)

M-URI Year 2 Funding Allocation: 5.2%

#### **PROJECT OVERVIEW**

This project investigates dynamic measuring methodologies for rolling element bearing defects through sensor signature analysis. Specifically, the utility of a new signal processing combination of the High Frequency Resonance Technique (HFRT) and Adaptive Line Enhancer (ALE) is investigated. Two transducers, the accelerometer and the acoustic emission sensor, are used to acquire data for this analysis. Experimental results have been obtained for inner race and outer race defects of a rolling taper bearing. Results show the potential effectiveness of the signal processing technique to determine both the severity and location of a defect.

The HFRT utilizes the fact that much of the energy resulting from a defect impact manifests itself in the higher resonant frequencies of a system. Demodulation of these frequency bands through use of the envelope technique is then employed to gain further insight into the nature of the defect while further increasing the signal to noise ratio. If periodic, the defect frequency is then present in the spectra of the enveloped signal.

The ALE is used to enhance the envelope spectrum by reducing the broadband noise. It provides an enhanced envelope spectrum with clear peaks at the harmonics of a characteristic defect frequency. It is implemented by using a delayed version of the signal and the signal itself to decorrelate the wide band noise. This noise is then rejected by the adaptive filter that is based upon the periodic information in the signal [111].

Results have been obtained for inner race and outer race defects. The analyses of these defects shows the effectiveness of the methodology to determine both the severity and location of a defect. In two instances, a linear relationship between signal characteristics and defect size is indicated for accelerometer analysis.

#### **Objectives and Relevance**

The objectives of this work are to investigate the utility of a new combination of the High Frequency Resonance Technique (HFRT) and the Adaptive Line Enhancer (ALE) to effectively detect and diagnose the severity and location of bearing defects. Multiple sensors are used to determine the effectiveness of the methodology with both an accelerometer and an acoustic emission sensor. An evaluation is being done to determine the ability of each sensor to detect a relationship between key signal characteristics and defect size that enables a diagnostic relationship to be developed. Comparisons are being made to selected traditional methods of defect detection.

In the absence of effective defect detection capability, one traditional way of combating the untimely shutdown of machinery has been to institute scheduled maintenance of critical rotating elements based upon their historic life span. Some critical components are so important, helicopter rotor bearings for example, that they are replaced in such a timely fashion that virtually zero will fail. Though it can be argued that 99.9% of these parts would last substantially longer depending upon the amount of unused life. These components are often replaced early, and a significant savings may be realized if condition-based instead of scheduled maintenance were instituted. The successful continuation of this work will result in the diagnostic and prognostic capability to help realize these types of savings.

Most difficulties posed in bearing initial fault detection stem from the presence of a variety of noises and the wide spectrum of a bearing defect signal. Therefore, the success of bearing fault detection methods usually depends on increasing a bearing defect signal-to-noise ratio. Identification and quantification of key signal features dictating the condition of the element is then the main priority.

To date, most work only serves to identify the presence of a defect, or at best differentiate the defect based on qualitative measures such as light, medium, or heavy damage without practical, quantitative grounds for fault identification [112-119]. There has been a deficiency in the development of a relationship between various detection methodologies and defect size. A defect becomes a failed bearing when an applicable definition of failure has been satisfied. For example, a defect that has reached a size of  $0.0645 \text{ mm}^2$  ( $0.01 \text{ in.}^2$ ) is commonly defined to be a failure by industry standards [120]. To date, the development of such a diagnostic capability that lends itself to possible prognostics has not been addressed.

The methodology presented here serves to address these issues. First, the signal-to-noise ratio is greatly increased through processing. This allows defects of smaller magnitude to be detected, well before failure occurs. Second, results indicate a direct relationship between signal features and defect size, yielding a diagnostic tool that can be used to effectively quantify the defect.

## ACCOMPLISHMENTS OF M-URI YEAR 2

### Signal Processing Methodology

In this work, an adaptive line enhancer (ALE) is used to increase the detectability of a periodic defect signal. It enhances the spectrum of the envelope signal provided to it by the high frequency resonance technique (HFRT). Figure 170 displays a block diagram of the signal flow for the overall processing scheme. The HFRT takes advantage of the large amplitudes of a defect signal in the range of a high frequency system resonance, and provides a demodulated signal with a high defect signal-to-noise ratio in the absence of low frequency mechanical noise. The ALE is expected to reduce wide band noise of the obtained demodulated signal and, therefore, enhance the envelope spectrum of the defect signal with clear peaks at the harmonics of the characteristic defect frequency.

#### *High Frequency Resonance Technique:*

A bearing defect signal  $s(t)$  can be represented by bursts of exponentially decaying sinusoidal vibration at a system resonant frequency  $f_r$  [121]. The high frequency resonance technique [122,123] is illustrated in Fig. 170 and Fig. 171 and involves 3 steps. First, band pass a measured signal (Fig. 171a) around a selected high frequency band with the center at a chosen resonant frequency of system, resulting in Fig. 171b. Second, demodulate the band passed signal with a non-linear rectifier, resulting in Fig. 171c. Third, use a low pass filter to cancel high frequency components and retain the low frequency information associated with bearing defects, resulting in Fig. 171d.

In order to cancel the high frequency components and retain the low frequency information associated with a bearing defect,  $s_d(t)$  is passed through a low pass filter. A pure bearing defect signal,  $s(t)$  has nonzero magnitude only at the harmonics of a characteristic defect frequency. Therefore, the spectrum of  $s_d(t)$  will have nonzero values only at the harmonics of the characteristic defect frequency that are less than the bandwidth of a used band pass filter shown in Fig. 171d. The nonzero values of an envelope spectrum at the harmonics of a particular characteristic defect frequency indicate the occurrence of a defect, and the location of the defect can be determined by its unique defect frequency.

#### *Adaptive Line Enhancer:*

The envelope signal of a damaged bearing obtained by the above method is contaminated by broad band noise making it difficult to detect the early damage of the bearing. A real time envelope signal  $x(k)$  can be considered as the sum of narrow band signals  $s_e(t)$  spaced at the harmonics of a characteristic defect frequency but corrupted by broad band noise  $n(k)$ .

$$x(k) = s_e(k) + n(k) \quad (25)$$

Therefore, the adaptive line enhancer (ALE) can be used to separate the narrow band signals from the broad band noise. ALE was first introduced by [111] and its performance was studied by [124]. The delayed version of  $x(k)$  is used as the reference input of an adaptive filter. The output of the filter is then subtracted from the primary input signal  $x(k)$  to form an error sequence  $e(k)$ . The error sequence is fed back to adjust the filter weights, shown in Fig 170.

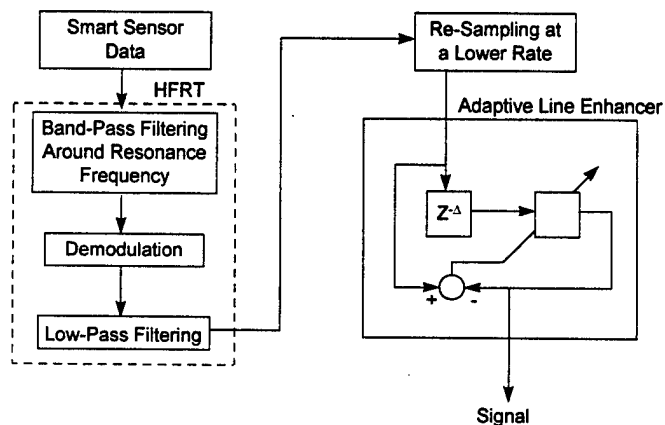


**Figure 170. Signal Processing Diagram**

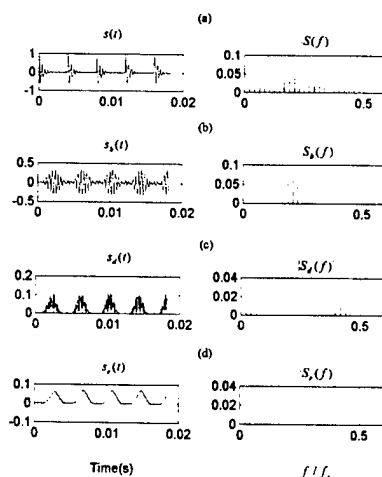


**Figure 171. High Frequency Resonance Technique Processing**

The principle of the adaptive line enhancer can be understood as follows. The delay of an input signal causes the decorrelation between the broad band noise components of reference input and primary input while the narrow band signal is still highly correlated. To minimize the error power of the filter, the adaptive filter compensates for the correlated signal so that it can be canceled at the summing junction. Since the filter can not compensate for the decorrelation of the broad band noise components, only the narrow band signal is output from the adaptive filter. In the frequency domain, the filter weights will tend to form a band pass function about the center frequencies of the narrow band input components. Therefore, the broad band noise components of delayed input are rejected while the narrow band signal information is retained. Here a recursive least mean squares (LMS) algorithm is used for this adaptive filter because of its computational simplicity. The output of the filter is:

$$y(k) = W_k^T X_k \quad (26)$$

where  $W_k^T$  is the weight vector of the filter and input vector  $X_k$  is

$$X_k = [x(k-\Delta) \quad x(k-1-\Delta) \quad \dots \quad x(k-L+1+\Delta)]^T \quad (27)$$

Then the error is:

$$e(k) = x(k) - y(k) \quad (28)$$

The mean square error (MSE) is the expected value of  $e(k)$ . The LMS algorithm controls the weight vector of the filter so that the mean square error is minimized. The optimal weight vector  $W^*$  that minimizes the MSE is

$$W^* = R^{-1}P \quad (29)$$

where the input signal autocorrelation vector  $P$  is

$$P = E \{x(k)X_k^T\} \quad (30)$$

and the autocorrelation matrix  $R$  is:

$$R = E \{X_k X_k^T\} \quad (31)$$

In practice,  $R$  and  $P$  are generally unavailable because they require an expectation operation ( $E$ ). The following recursive LMS algorithm is a practical method to find a approximate solution of Eqn. (29). The weights of the filter are updated by:

$$W_{k+1} = W_k + 2\mu e(k)X_k \quad (32)$$

where  $\mu$  is adaptive step size. The simulation results show that it is appropriate to let  $\mu$  satisfy the following stability condition in practice [125].

$$0 < \mu < \frac{1}{L \{power \ of \ input\}} \quad (33)$$

Therefore, given the input sequence  $x(k)$  and initial value of the weight vector, the values of filter output  $y(k)$ , the error  $e(k)$  and the weight vector  $W_k$  can be computed for all time by Eqns. (26), (28) and (32).

Without the requirement of a priori information, the ALE's self-tuning capability allows it to find weak narrow band signals in wide band noise. Therefore, it has the potential to detect the line spectrum of a defect bearing HFRT signal in a noisy environment. Figure 174 subplots 3 and 4 illustrate the increase in signal-to-noise ratio obtained by the ALE.

#### **Defect Determination:**

Given that defect location and the shaft speed together with bearing geometry dictate the frequency of impact generation, it is a simple matter to calculate these frequencies. The Timken LM501310 cup and LM501349 cone were chosen for all testing. This is a tapered roller bearing with a bore diameter of 41.275 mm (1.625 in.) and an outer diameter of 73.4314 mm (2.8910 in.). For a single type of defect, at one location on the cup, at 1200 RPM this yields defect frequencies of 164.64 Hz for a cup defect, and 215.36 Hz for a cone defect. These frequencies are often the focus of frequency domain analysis techniques, and are also critical to the combination of the HFRT and ALE presented in this work.

A peak ratio (P.R., Eqn. (34)) is defined as the sum of the peak values of the defect frequency, and harmonics, over the average value of the spectrum.

$$P.R. = \frac{N * \sum_{j=1}^n P_h}{\sum_{k=1}^N A_i} \quad (34)$$

$P_h$  is the amplitude value of the peak located at the defect frequency harmonic,  $A_i$  is the amplitude at any frequency, and  $N$  is the number of points in the spectrum. The number of harmonics in the spectrum,  $n$ , is found by  $600/f_d$ . Six hundred is used as the maximum frequency in the analyzed spectrum, and  $f_d$  is the characteristic defect frequency. The peak ratio is a dimensionless ratio determined for damaged and undamaged bearings, and is only used to indicate the presence of a defect. Then, the peak value of the first harmonic after HFRT is used to determine the magnitude of the defect. Therefore, once the peak ratio verifies that a defect is present, the peak value is then used to estimate the size of the defect. The effectiveness of the peak ratio is compared to that of other standard detection methods of kurtosis, RMS, and crest factor. This is done in the frequency domain after HFRT. Thus, all analyses and comparisons will be drawn from the same data sets after similar processing.

#### **Test System**

A schematic of the test system can be seen in Fig. 172. A four bearing system is contained within a test housing. A Wilcoxon 736T high frequency accelerometer is used to acquire vibration signals, and a Physical Acoustic Corporation type R15 acoustic emission sensor is used to detect high frequency stress waves. The resulting AE signal from the processor (ALM8) is a demodulated version that is very similar to a raw signal processed by the HFRT technique.

A Krohn-Hite #3384 programmable filter is used to prevent aliasing, and low pass filters the accelerometer data at 10 kHz (half the sampling frequency). The acoustic emission data are low pass filtered at 1 kHz because the ALM 8 already envelopes the signal, and information above 1 kHz is noise.

Since the premise of the HFRT technique is based upon proper selection of a resonant frequency band, the resonances of the bearing test system had to be determined. Several distinct bands were located through hammer impact testing, and experimentation revealed that the band between 7.5 and 9.2 kHz is more readily excited by defect impacts. Therefore, it is the focus of attention for accelerometer analysis.

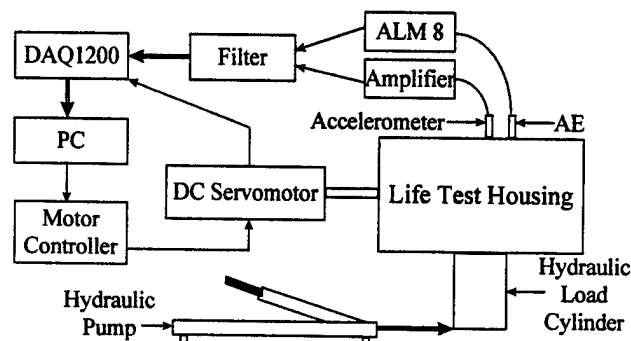


**Figure 172. Experimental Schematic**

### **Experimental Results and Conclusions**

In the testing, all damage takes the form of scratches made to the center of the raceways with a diamond scribe. All cup and cone scratches are controlled as to a length of approximately 2.54 mm (0.1 in.). The width of the damage created is controlled by the number of passes that a scribe makes over the raceway. The defect widths examined range from 15.40  $\mu\text{m}$  to 408.48  $\mu\text{m}$ . It is useful to note that all of these defect sizes are well below industry standards for the definition of a failure, as mentioned earlier.

#### **Outer Race Defects:**

Seven bearings of damage levels ranging to 349.32  $\mu\text{m}$  are examined. The most significant result obtained from outer race damage experiments is the determination of a relationship between peak value and defect width for accelerometer data. These results were obtained under 1200 RPM and 4911 N/bearing loading conditions. At least four data sets for each condition were taken. The tabulated averages of these experiments are found in Table 10. Figure 173 shows the relationship between peak value and defect width. All seven defect sizes appear on the graph because the peak ratio was able to determine the presence of defects in all cases. This can be seen from the table where the peak ratios for defective bearings are substantially higher than that for the good bearing. The vertical variation for a given defect size represents a confidence interval for measurements. Thus, in practice, a given peak value measurement has a window of accuracy in defect width prediction. Moreover, the y-intercept represents the noise level of the system. This directly affects sensitivity, which for this system lies somewhere between a defect of width 0.00  $\mu\text{m}$  and 15.40  $\mu\text{m}$ .

Unlike the peak value, the traditional signal features of RMS, kurtosis, and crest factor values do not follow a consistent trend. While the RMS and kurtosis values actually follow a generally increasing pattern, neither follow a continuously increasing pattern. Crest factor appears to be completely uncorrelated, randomly increasing and decreasing. It is possible that the resolution of these methods is insufficient to detect such small changes in defect size.

**Table 10. 1200 RPM Accelerometer Experiments for Cup Damage**

Defect Width ( $\mu\text{m}$ )	RMS (g)	Kurtosis	Crest Factor	P.R. with ALE	P.R. w/o ALE	Peak Value (g)
0.00	0.0051	3.025	4.228	12.85	5.78	$9.70 \times 10^{-5}$
15.40	0.0046	3.220	4.473	156.95	17.81	$2.12 \times 10^{-4}$
38.03	0.0051	5.141	5.319	238.78	64.17	$8.66 \times 10^{-4}$
75.40	0.0071	5.065	5.421	255.38	59.36	$1.00 \times 10^{-3}$
104.92	0.0068	5.168	5.165	281.49	58.84	$1.28 \times 10^{-3}$
111.87	0.0103	5.620	5.664	238.33	49.21	$1.52 \times 10^{-3}$
349.32	0.0172	7.137	4.719	252.14	112.77	$3.88 \times 10^{-3}$

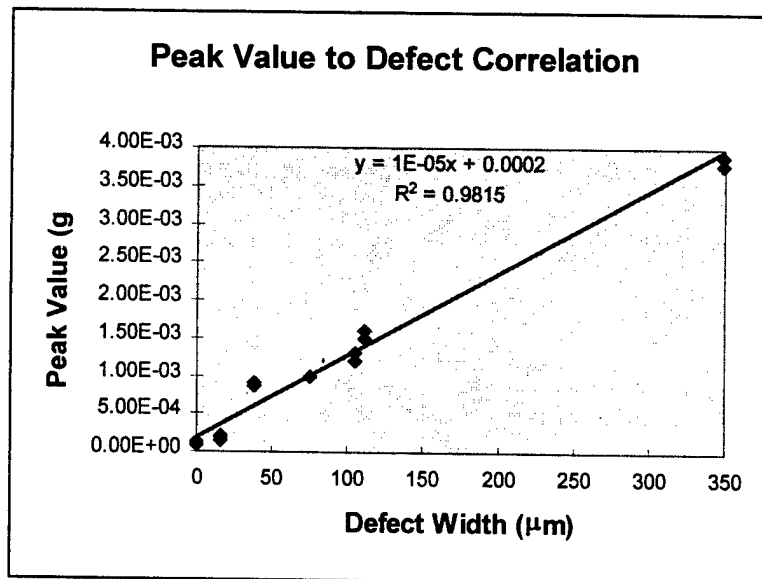


**Figure 173. Peak Value Relationship for Cup Damage, 1200 RPM**

Figure 174 and Figure 175 show results of analysis for 15.40  $\mu\text{m}$  and 349.32  $\mu\text{m}$  damage. These plots give raw data, raw spectrum, HFRT spectrum, and HFRT with ALE spectrum. The defect frequencies and related harmonics are quite clear at 164 Hz and higher. It is clear from the plots that the defect frequency becomes more prominent as damage increases, even to the point that it is visible in the raw time signal. Moreover, the advantage of the ALE routine is clearly seen in Fig. 174, where the defect peaks become quite prominent after noise cancellation.

The AE data were taken simultaneously under exactly the same conditions. Figure 176 shows results of AE data processing for a heavy 349.32  $\mu\text{m}$  cup defect. While an increased peak value trend was observed, no clear linear relationship exists in this case. Table 11 lists calculated averages for this AE data. The smallest defect detected was 38.03  $\mu\text{m}$ . As expected, in all cases when the peak ratio indicates a defect, the peak value is increased. However, the increased peak value does not follow an increasing trend, except to say that its levels are elevated. Additionally, for this speed, the acoustic emission sensor is not as sensitive as the accelerometer, whose detected sensitivity is 15.39  $\mu\text{m}$ . However, when the AE does detect a defect, it is clearly identified, with the peak ratio increasing an order of magnitude. Moreover, RMS, kurtosis, and crest factor follow no clear trend. In fact, they do not even experience significantly elevated levels as with the peak value.

Additionally, several conclusions can also be drawn by comparing the ability of the accelerometer and AE sensor. The accelerometer is more sensitive to cup defects than the AE sensor. The ability of each method is slightly diminished using the AE sensor, with the crest factor becoming insensitive. Given that the RMS does tend to increase, crest factor fails because the peak value of the time signal does not increase commensurately. Another observation is that typically the shaft speed (20 Hz) is clearer in the AE signal. This may be useful in verifying the speed, and thereby raising confidence in defect frequency calculations and conclusions.



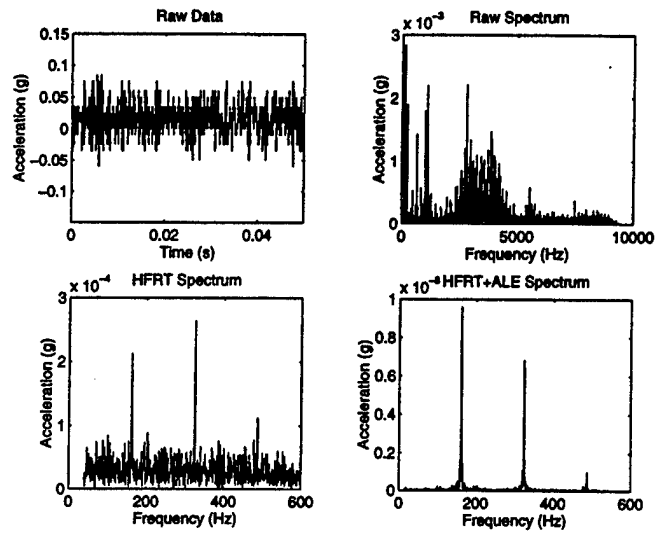


Figure 174. Accelerometer Data Analysis for 15.39 $\mu$ m Cup Scratch at 1200RPM

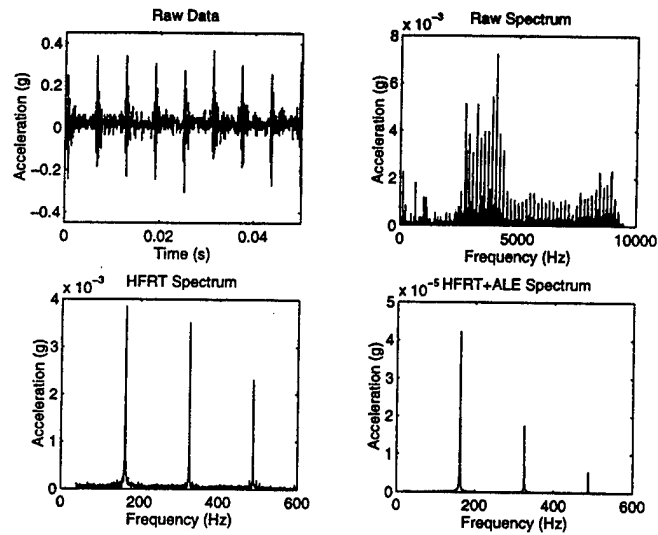
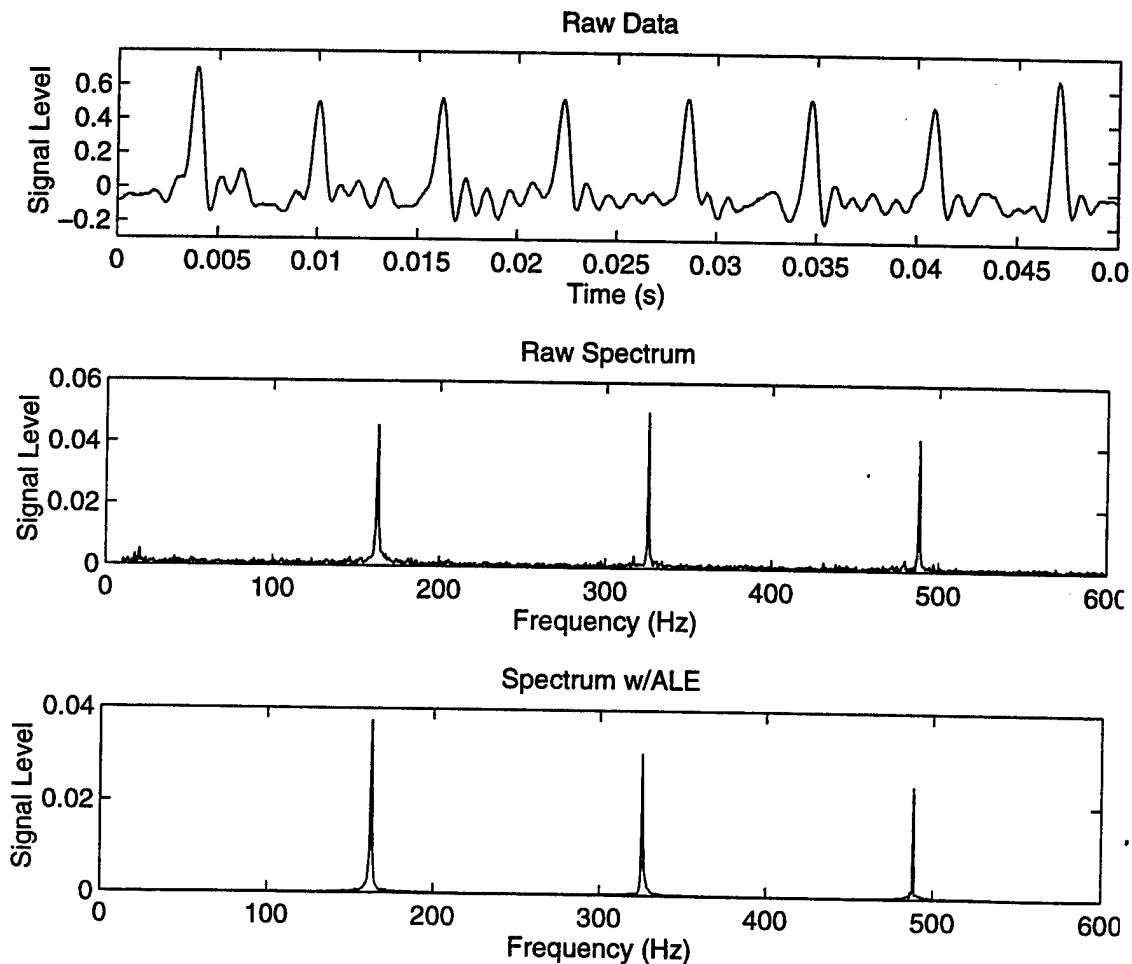


Figure 175. Accelerometer Data Analysis for 349.32 $\mu$ m Cup Scratch at 1200 RPM

**Table 11. 1200 RPM AE Experiments for Cup Damage**

Defect Width ( $\mu\text{m}$ )	RMS (g)	Kurtosis	Crest Factor	P.R. with ALE	P.R. w/o ALE	Peak Value (g)
0.00	0.0372	3.272	4.910	22.66	8.03	$2.50 \times 10^{-5}$
15.40	0.0278	3.059	4.326	21.90	8.49	$8.16 \times 10^{-6}$
38.03	0.0694	4.304	4.111	258.17	89.97	$7.90 \times 10^{-3}$
75.40	0.0631	3.901	4.323	251.36	64.91	$4.18 \times 10^{-3}$
104.92	0.0356	3.667	4.438	217.40	38.90	$3.57 \times 10^{-4}$
111.87	0.0673	3.763	4.375	234.28	51.41	$3.28 \times 10^{-3}$
349.32	0.1431	4.418	4.418	266.69	113.48	$3.79 \times 10^{-2}$



**Figure 176. AE Analysis for Cup Damage**

#### *Inner Race Defects:*

Experiments were conducted on bearings with six different levels of inner race (cone) damage. Table 12 shows the average results of this testing at 1200 RPM. The most interesting outcome is the relationship found between peak value and defect width. This is seen in Fig. 177 where a linear fit has been done to illustrate this relationship. However, as seen in the table, the peak ratio does not indicate the presence of a defect for the first defect width. As a result, these data do not appear on the linearization plot. As with the cup defect, the noise level can be seen reflected in the y-intercept, and a vertical window of uncertainty surrounds each defect prediction as a result of variation in test results.

From the table, it is clear that RMS is not correlated to defect size. However, kurtosis, crest factor, and the peak ratio are, but neither are related as closely as the peak value. This can be seen in Fig. 178, where linear fits are performed for both kurtosis and crest factor. The variances for both are higher than for peak ratio, although the kurtosis fit is reasonable.

The rotational frequency is easily identified for this defect type. This is because the defect is on the rotating race and revolves relative to the load region at 20 Hz. This results in not only the defect frequency of 215.36 Hz, but beat frequencies at 20 Hz on either side of the characteristic defect frequency. There are even 40 Hz and 60 Hz harmonics of the rotational frequency present. All of these features can be seen in Fig. 179 and are clear in this case because the defect is large.

Analysis of the acoustic emission data reveals that the acoustic emission sensor is not sensitive to any of the cone defects tested. No defect frequencies are identified in any of the cases, not even for the heaviest cone defect. Since the impacts are of the same nature, it is reasonable to assume that the same type of strain induced stress waves are generated. However, none of these emissions are transmitted to the AE sensor at a level strong enough to be recognized. There are a few reasons why this is possible. AE signals generated by an inner race defect have to travel farther and through more interfaces than those for any other type of defect. Also, signal strength may be diminished if the line of travel for the AE wave is not direct to the sensor. This will be influenced by the line created by the position of the defect, the roller, and the sensor placement. Additionally, it is also reasonable to assume that the farther any signal must travel, the weaker it will get.

**Table 12. 1200 RPM Accelerometer Analysis for Cone Damage**

Defect Width ( $\mu\text{m}$ )	RMS (g)	Kurtosis	Crest Factor	P.R. w/ALE	P.R. w/o ALE	Peak Value (g)
0.00	0.0051	3.028	4.288	9.23	4.77	$9.03 \times 10^{-5}$
34.57	0.0081	3.024	4.372	9.41	4.85	$1.34 \times 10^{-4}$
43.28	0.0070	3.186	4.822	17.84	6.04	$1.70 \times 10^{-4}$
81.46	0.0074	3.499	5.171	71.59	10.90	$3.13 \times 10^{-4}$
104.62	0.0070	4.217	5.880	49.96	10.27	$3.59 \times 10^{-4}$
408.48	0.0103	6.334	6.733	55.44	16.73	$8.37 \times 10^{-4}$

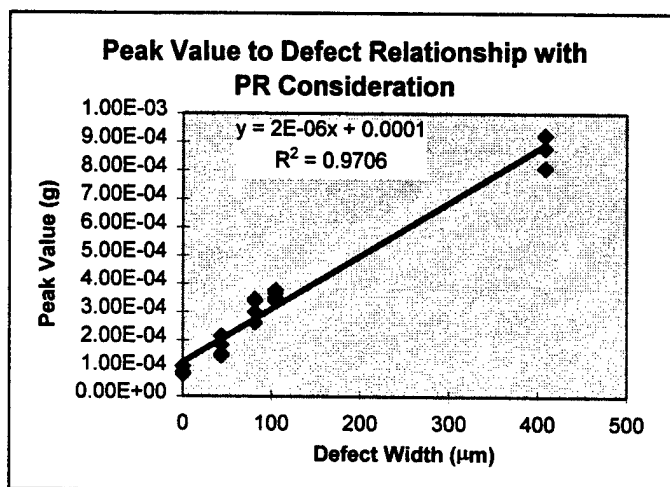


Figure 177. Accelerometer Relationship for Cone Defects with PR Consideration

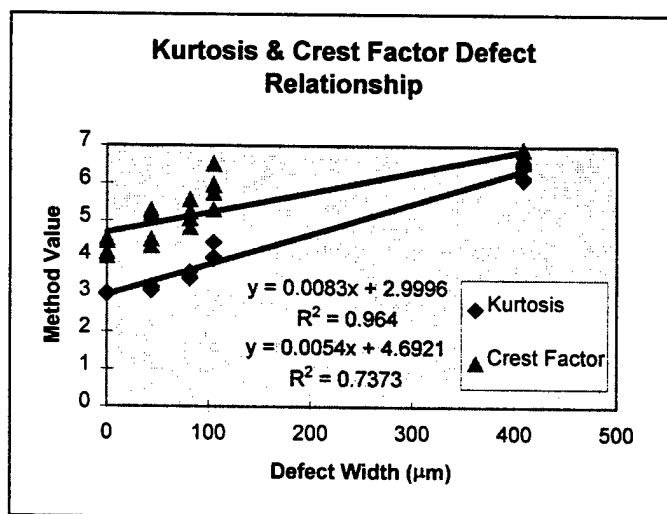
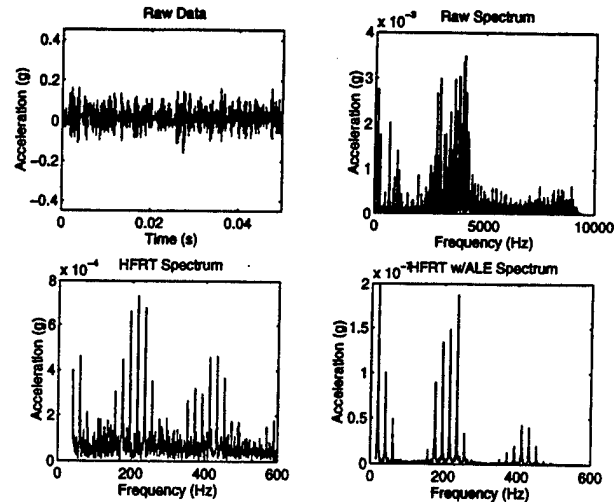


Figure 178. Kurtosis and Crest Factor to Defect Relationship for Cone Defects



**Figure 179. Accelerometer Analysis for 408µm Cone Defects**

### **Discussion**

The ability of both the sensors and signal processing methods to detect and diagnose two types of defects has been demonstrated to date. Overall, the accelerometer is comparable to or better than the AE sensor at detecting the defect types. The sensors are better able to detect outer race defects, but the AE sensor was not sensitive to the inner race defects tested.

The peak ratio is the most reliable indicator of localized defect presence out of the methods tested. It enjoys greater or equal success in every case. Kurtosis and RMS are a close second in their reliability. Crest factor is quite insensitive, being the most unreliable method tested. It failed to show a correlation to defect size in each case.

Moreover, after defect detection by the peak ratio, the peak value demonstrates a good correlation to defect size. A linear relationship between peak value and defect width of the accelerometer data at 1200 RPM has been outlined for both inner and outer race defects, with  $R^2$  correlation values of 0.9815 and 0.9706 found for cup and cone relationships. To date, prior work has not attempted to establish such a relationship. All previous work located has focused on the identification of the presence of a defect, with possible size differentiation based on categories such as light, medium, and heavy.

It is important to note that while the peak ratio excels at localized defect detection, it is not particularly capable of identifying other types of damage. Debris denting is a case in point because of the lack of a characteristic defect frequency. Results show that either sensor used with the RMS technique has the ability to differentiate between the good, light, and heavily debris dented bearings. Kurtosis and crest factor both failed for this case.

Kurtosis is a statistical measure based on the shape of the wave form. A good bearing with a random distribution of asperities has a theoretical kurtosis value of three, regardless of amplitude of the signal. A bearing with debris denting is essentially the same thing as a good bearing, only with asperities on a larger scale. Therefore the signal level is increased, and the kurtosis values remain unchanged. The crest factor values do not increase because they are based on the peak value of the time signal over the RMS level. It is true that the peak value of the time signal increases as increased debris denting takes place. However, since the RMS value also increases significantly the ratio of the two tends to remain the same, and crest factor gives no indication of a defect.

Therefore, a comprehensive defect detection scheme should incorporate the methodologies most effective in diagnosing the defects of interest. While the frequency based peak ratio is excellent for localized defect detection, a time domain method such as RMS is more suited for non-localized defect detection such as debris denting or insufficient lubrication.

### PLANS FOR M-URI YEAR 3

The two key areas of sensor integration and prognostics can offer significant capability relevant to the overall objective of condition-based maintenance. These two areas are strategically built upon the analytic basis already established in the work completed during the first two years. Future research will involve the extension of current signal processing and modeling results into a methodology to deterministically, probabilistically, and heuristically fuse input features from various sensors for enhanced diagnostics. Subsequently, the methodology to estimate the remaining utility of the mechanical system based on inverse mechanistic modeling and recursive production theory will be developed for remaining life estimation. Intelligently increasing the types of sensors and detection methods used to acquire information can improve detection capability and sensitivity. It has been demonstrated that the AE and accelerometer have different detection capabilities. Increasing sensor implementation could increase the different types of defects that can be detected by the system, as well as improve the sensitivity of the detection methods.

Developing a better understanding of the mechanisms behind signal generation and transmission can improve understanding of sensor capabilities. Information regarding the effect of materials and part interfaces on elastic wave propagation may lead to improved sensor selection and placement techniques. A better understanding of the excitation of particular resonant frequencies can reduce calibration difficulties and pass band selection. Improved understanding of the effects of RPM, loading, defect size, Hertzian regions, and defect location on system excitation may result in improved signal to defect relationships, as well as expand the scope of current relationships.

Figure 180 presents a flow chart for future research whose primary objectives are twofold. First bearing damage must be modeled based on basic scientific principles, this will provide a fundamental link between signals processed from multiple sensors and bearing health. Simultaneously, appropriate signal processing techniques must be developed to extract key features from the sensors' signals to determine bearing health as well as to update the empirical parameters used in the model formulation. At the end of the third year, a theoretical basis and implementation principles for the integration of various sensors for enhanced diagnostics will be developed.

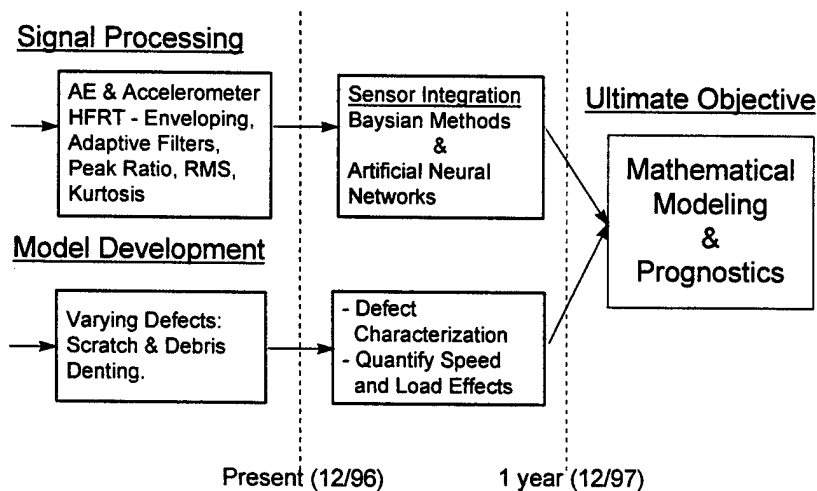


Figure 180. Flow Chart for Future Research

## **VISION FOR YEARS 4 AND 5**

The use of an intelligent system to detect and diagnose defects will greatly enhance the system's performance. It has been shown that different detection methods can have different usefulness depending on the type of defect present. For example using models that integrate information such as peak ratio, kurtosis, RMS, as well as other metrics into a model based diagnostic system should yield a highly sensitive and accurate system capable of adapting to various environments and operating conditions.

Finally, prognostics is the logical next step after an effective diagnostic system is developed. A life prediction system based on the diagnostic capability developed is the ultimate industrial application. The ability to not only to diagnose problems as they occur, but to predict time-to-failure. Instead of scheduled maintenance based on statistical data, maintenance could be scheduled based on real-time system condition information. Any of the improvements outlined here can help realize savings in terms of implementing condition based maintenance systems, but a prognostic system should be the ultimate goal.

The successful completion of this project is anticipated to provide the physical fundamentals and inverse mechanistic modeling for predictive prognostics at the completion of year 4, and to provide the prototype system development, testing, iterative modification, and deliverable documentation at the finish of year 5.

### 2.3.6 MONITORING OF SUB OR HIGHER HARMONIC OSCILLATIONS IN ROTATING MACHINE ELEMENTS

Co-investigator: Itzhak Green (Georgia Tech)  
M-URI Year 2 Funding Allocation: 5.6%

#### PROJECT OVERVIEW

Noncontacting mechanical face seals are being used increasingly in high performance rotating machinery. However, unpredictable mechanical face seal life is still a problem that remains to be solved. Although the exact cause of the seal failure is still not well understood, the intermittent contact between the rotor and the stator is believed to be one of the major causes of seal failure.

The objective of this research is to monitor and control the dynamic behavior of a flexibly mounted rotor noncontacting mechanical face seal in a seal test rig. In particular, the research focuses on detecting and control the contact between the rotor and stator that may cause severe face wear and sudden seal failure. Meaningful condition monitoring measures are taken by incorporating proximity probes and a universal controller board connected to a personal computer. The dynamic behavior of the noncontacting mechanical seal is monitored on-line. The monitoring system can display the orbit of the rotor angular misalignment in real-time where the shape of the orbit gives an indication of the seal dynamic behavior. Key dynamic parameters, such as seal clearance and relative angular misalignment between the rotor and the stator, are chosen to be monitored. Contact between the rotor and stator is detected by a combination of relative angular misalignment and seal clearance. A dominant indication of contact is the presence of higher harmonics oscillations, which are multiples of the rotating shaft speed. The monitoring system can detect seal contact during operation using orbit plots and signal processing, and suppress it by incorporating an active control strategy. The control strategy is to eliminate contact between the rotor and the stator by adjusting the air pressure in rotor chamber. The fluid film stiffness and damping coefficients change with the air pressure and these cause changes in rotordynamic response in both angular and axial modes.

#### Approach

An experimental test rig has been built to study the dynamic response of a flexibly mounted rotor (FMR) mechanical face seal. This rig is being used to study higher harmonic oscillations (HHO) because they have been detected under various operation conditions. The mechanical face seal was designed to operate in a noncontacting mode, but the detected HHO indicated the existence of contact between the rotor and stator. It is this contact that leads to damage, and hence must be avoided. The seal system operates under the balance of the opening force and the closing force. The opening force is provided by the pressure drop across the sealing interface, where the closing force is provided by the sealed hydraulic pressure, the initial spring compression and the air pressure in the rotor chamber. In previous experiments the air pressure was set manually by a pressure regulator and could not be automatically controlled. Currently an electro-pneumatic transducer which can adjust the closing force automatically is used to replace the air pressure gauge. A monitoring system based on eddy-current proximity probes and a flow meter has been constructed to monitor the rotordynamic behavior and to detect the existence of HHO. The flow meter can output a voltage that is proportional to the flow rate. A control algorithm on the closing force will be incorporated for the maximum reduction of HHO.



## ACCOMPLISHMENTS OF M-URI YEAR 2

### 1. Several design modifications have been made to the test rig system:

- We redesigned the water supply line of the test rig. The previous set up of water supply line was unable to prevent the water to flow backwards into the water pressure gauge. The new set up supplies pressurized water to the test rig directly from the water supply line and is separated from the air supply line.
- We installed another water filter in the water supply line in order to filter out debris from the water supply line.
- We added a draining system to the bottom of the housing.
- We replaced the manual air pressure regulator with an electropneumatic transducer that can convert voltage signal to pressure. This makes automatic control of air pressure possible. We also added necessary connections to the computer.
- We designed a new spring support system to the rotor. It includes two springs compressed at both ends of the rotor. This design is better in restricting the rotor angular disturbance than single spring.
- We machined another rotor supporting part with one O-ring groove of appropriate width and a spring holder. With similar supporting structure we can compare the seal dynamic behavior of one O-ring support and two O-ring support, with or without spring.

### Several changes have also been made to the data acquisition system:

- We replaced DAS16 data acquisition board with a dSPACE DS1102 board and installed corresponding software (TRI and TRACE). We also installed a Texas Instrument C compiler. This compiler compiles and links C code generated from Matlab's SIMULINK model. We have set up the environment for the dSPACE software and hardware system.
  - We changed the wire connections for the data acquisition system for use with the DS1102 board. We made connections between the dSPACE connection panel and the computer, the connections between the dSPACE connection panel and the proximity probes, the connections between the dSPACE connection panel and the electropneumatic transducer.
2. We calibrated the motor speed controller readings using TRACE software from dSPACE Inc. We can now determine the motor speed without adding a tachometer.
  3. We conducted test rig operation based on the operating parameters that previously produced higher harmonic oscillations (HHO) and successfully reproduced higher harmonic oscillations.
  4. We integrated the control setup in the test rig system. The strategy is to use proximity probes and flow meter as sensors to sense rotordynamic responses, use electropneumatic transducer as actuator, use Mathworks software Matlab and corresponding tool boxes to perform signal processing and controller design, and use the dSPACE DS1102 controller board for data acquisition and controller realization.
  5. We obtained the relationship between the seal clearance and the air pressure in the rotor chamber based on the static force balance in the axial direction of the shaft. It takes into account the stiffness of the spring and the secondary O-ring. This relationship can help determine the air pressure in the rotor chamber when a seal clearance is selected or can help in choosing the spring constant when the seal clearance is selected and there is a limit in the air pressure range in the rotor chamber.
  6. We have built a model based on the proximity probe signals that can calculate the rotor angular misalignment, stator initial misalignment and relative angular misalignment between the rotor and stator.
  7. We have developed an algorithm to display the orbit of the rotor angular misalignment in real-time.

Highlights with respect to the aforementioned accomplishments are detailed in the following sections.

## DIRECT SENSING, ANALYSIS, REAL-TIME DIAGNOSIS

### **Experimental Set-up**

A seal test rig has been built to study the dynamic behavior of the FMR noncontacting mechanical face seals. The schematic of the noncontacting FMR mechanical face seal test rig is shown in Fig. 181. The rotor is flexibly mounted on a rotating shaft through two elastomeric O-rings. This allows the rotor to track the stator misalignment and move axially. A carbon graphite ring is mounted on the rotor through an elastomeric O-ring. A groove is made at the rotor where the bottom of the carbon graphite ring touches the rotor face. The stator is fixed in the housing. The coning of the stator can be adjusted by adjusting the bolts distributed circumferentially throughout the rear holder of the stator (Fig. 182). Three micrometers mounted at the end of the housing are used to adjust the stator misalignment. The stator and the carbon graphite ring form the sealing dam. The seal operates at an equilibrium position with certain clearance between the rotor and the stator such that the opening force and closing force equal to each other. The opening force is contributed by the hydrostatic and hydrodynamic force acting on the sealing interface. The hydrostatic force is effected by the seal geometry, coning angle, the sealed pressure, the outside pressure, the fluid viscosity and the seal clearance. The closing force is composed of the support load contributed by the spring and the elastomer O-ring, the hydraulic force acting on the seal and the pressurized air pressure acting inside the rotor chamber. There is a direct relationship between the seal clearance and the air pressure acting on the back of the rotor chamber. Therefore, various seal clearances can be obtained by changing the air pressure acting on the back of the rotor chamber.

The shaft is screwed into a spindle that is connected through two wafer-spring couplings to a motor. The motor speed is controlled by a motor speed controller. The housing is made of three parts for conveniences of machining, maintenance, and adjustment of the test rig. All possible leakage paths are sealed by O-rings.

Air is supplied from the main air supply line to the rotor chamber through holes in the shaft and housing. It is sealed by a lip seal and separated from the water by a contacting seal. The air pressure is adjusted by the computer through a voltage to an electropneumatic transducer. Pressurized water is supplied from the main water supply line into the housing. The water pressure is manually controlled by a pressure regulator. A water pressure gauge in the water supply line displays the water pressure.

Three REBAM 7200 eddy current proximity probes mounted at the end of the housing are used to detect the dynamic response of the rotor. A low pass filter with a cut-off frequency of 1000 Hz is used to eliminate high frequency cross-talk noises among the probes. Each proximity probe can measure the static and dynamic distance between its tip and the rotor end surface. The calibrated distance-voltage relationship is  $39.44\mu\text{m/V}$ . The maximum output of each proximity probe is -24 Volts. A voltage divider is used to drop the maximum amplified voltage of the proximity probes from -24V to -10V. The reduced voltage is then sent to a DS1102 board (from dSPACE, Inc.) that resides in a personal computer.

### **Experimental Results**

Several experiments were performed to understand basic properties of the seal test rig system. We also investigated the difference of rotor behavior caused by one O-ring support and two O-ring support. The details are omitted here. We will discuss the theoretical background briefly in the following sections.

### **Seal Dynamic Response**

Several coordinate systems are used to describe the FMR noncontacting mechanical face seals (Fig. 183, Fig. 184). Detailed descriptions of these coordinate systems are omitted here.

Fig. 185 shows vector representation of the complete dynamic response of the seal system. The clearance  $C$  between the rotor and the stator is very small; thus, the rotor response,  $\vec{\gamma}_r^*$ , and stator misalignment,  $\vec{\gamma}_s^*$ , must also be very small. This allows all angles to be treated as vectors. The relative

misalignment between the rotor and the stator,  $\vec{\gamma}^*$ , is the vector subtraction of the rotor angular response,  $\vec{\gamma}_r^*$ , and the stator misalignment,  $\vec{\gamma}_s^*$ , i.e.,

$$\vec{\gamma}^* = \vec{\gamma}_r^* - \vec{\gamma}_s^* \quad (35)$$

The magnitude of  $\vec{\gamma}^*$  is:

$$\gamma^* = \sqrt{\gamma_r^{*2} + \gamma_s^{*2} - 2 \cdot \gamma_r^* \cdot \gamma_s^* \cdot \cos(\psi_r - \psi_s)} \quad (36)$$

The rotor response,  $\vec{\gamma}_r^*$ , is composed of two parts:  $\vec{\gamma}_{rs}^*$  and  $\vec{\gamma}_{ri}^*$ , where  $\vec{\gamma}_{rs}^*$  is the rotor response to the stator misalignment,  $\vec{\gamma}_s^*$ , and  $\vec{\gamma}_{ri}^*$  is the rotor response to the rotor initial misalignment,  $\vec{\gamma}_{ri}^*$ . Since  $\vec{\gamma}_{rs}^*$  is fixed in space, while  $\vec{\gamma}_{ri}^*$  rotates at speed  $\omega$ , the overall response  $\vec{\gamma}_r^*$  is a rotating vector with a time varying frequency,  $\dot{\psi}_r$ . The magnitude of both  $\dot{\psi}_r$  and  $\vec{\gamma}_r^*$  vary cyclically with a constant frequency,  $\omega$ . The relative misalignment between the rotor and the stator will be calculated from the experimentally measured rotor response,  $\vec{\gamma}_r^*$ , stator initial misalignment,  $\vec{\gamma}_s^*$ , rotor precession,  $\psi_r$ , and stator angle,  $\psi_s$ .

### **Seal Contact Criterion**

The dimensionless form of the local film thickness  $H$  can be written as follows (see Fig. 184):

$$H = 1 + \gamma \cdot R \cdot \cos\theta + \beta(R - R_i) \quad (37)$$

Where  $\gamma$  is the dimensionless relative misalignment,  $\gamma^* r_o / C_o$ , and  $\beta$  is the dimensionless coning,  $\beta^* r_o / C_o$ . Face contact will first occur at the minimum film thickness, i.e., at  $\theta = \pi$ , either at the inside or outside radius of the seal depending on the magnitude of  $\beta$ . From Eqn. (37), the conditions for face contact are:

$$1 - \gamma \cdot R_i = 0 \quad (38)$$

for contact at  $R = R_i$  when  $\beta > 1/R_i$ , and

$$1 - \gamma + \beta(1 - R_i) = 0 \quad (39)$$

for contact at  $R = 1$  when  $\beta < 1/R_i$ .

The smaller value of  $\gamma$ , as calculated from Eqns. (38) and (39), determines the critical condition of contact. It should be noted that for a properly designed seal that has a coning angle larger than the critical value,  $\beta_{cr} = 1/R_i$ , face contact would occur according to condition of Eqn. (38), i.e., when  $\gamma = 1/R_i$ .

### **Rotor Angular Response Orbit**

The relative misalignment between the rotor and the stator is calculated from the experimentally measured rotor response,  $\vec{\gamma}_r^*$ , stator initial misalignment,  $\vec{\gamma}_s^*$ , rotor precession,  $\psi_r$ , and stator precession,  $\psi_s$ .

An algorithm for calculating  $\vec{\gamma}_r^*$ ,  $\vec{\gamma}_s^*$ ,  $\psi_r$  and  $\psi_s$  was developed based on vector algebra. Consider the inertial coordinate system  $\xi\eta\zeta$  (Figs. 183, 185, and 186). Axis  $\xi$  can be arbitrarily chosen to reside in the XY shaft-fixed rotating plane. Axis  $\zeta$  coincides with the axis of shaft rotation. (Yet, axes  $\xi$  and  $\zeta$  are stationary.) Points A, B, and C are situated on the rotor plane where each has coordinates  $\xi$ ,  $\eta$ , and  $\zeta$  in that inertial system. Each of these points is chosen to coincide in the  $\xi\eta$  plane with the location

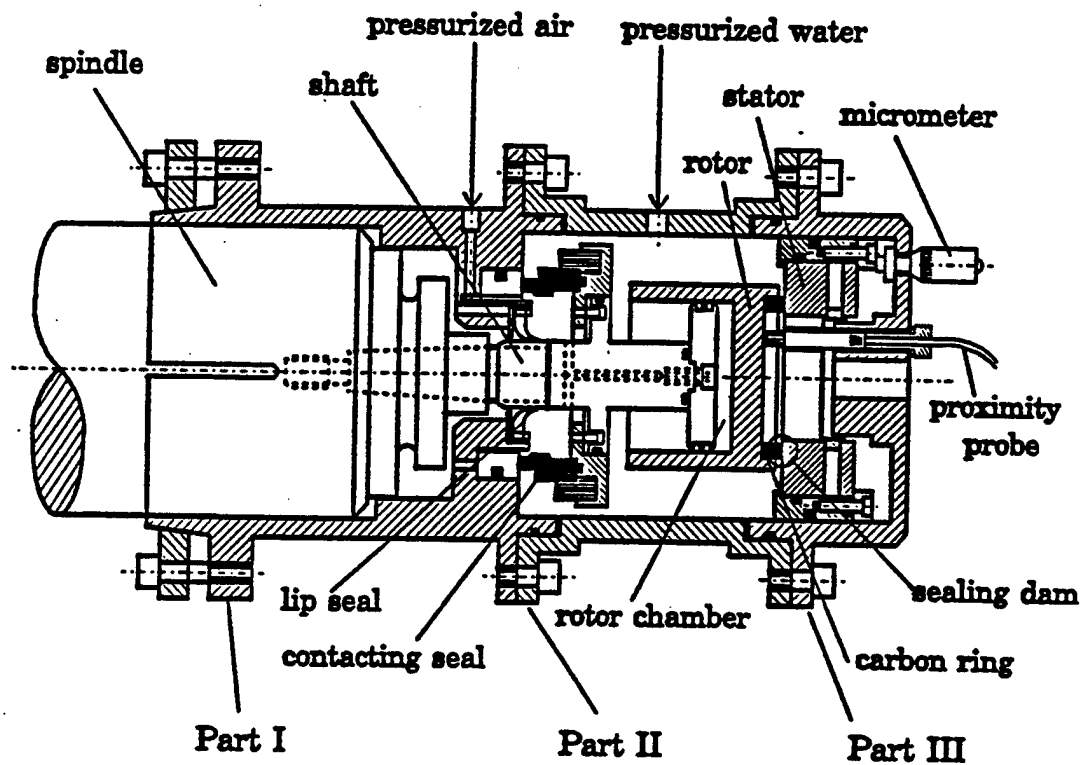


Figure 181. Schematic of the Noncontacting FMR Seal Test Rig

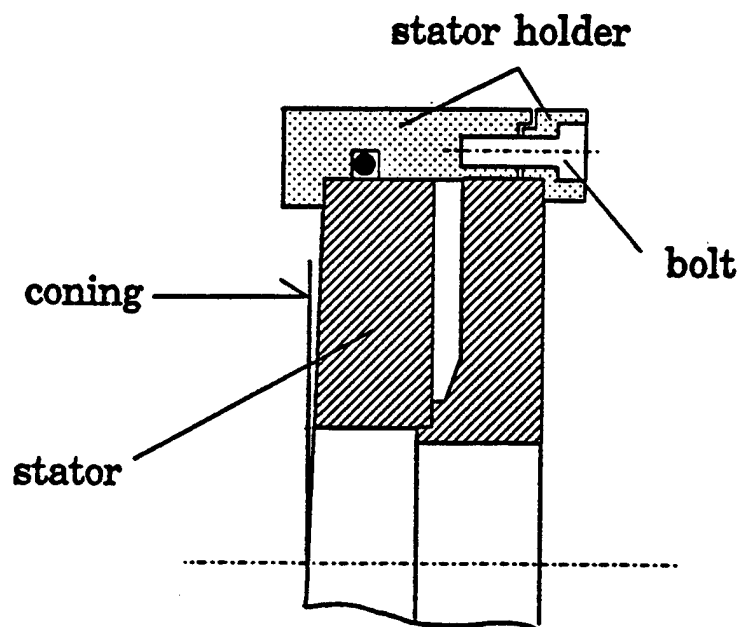


Figure 182. Stator Coning Mechanism





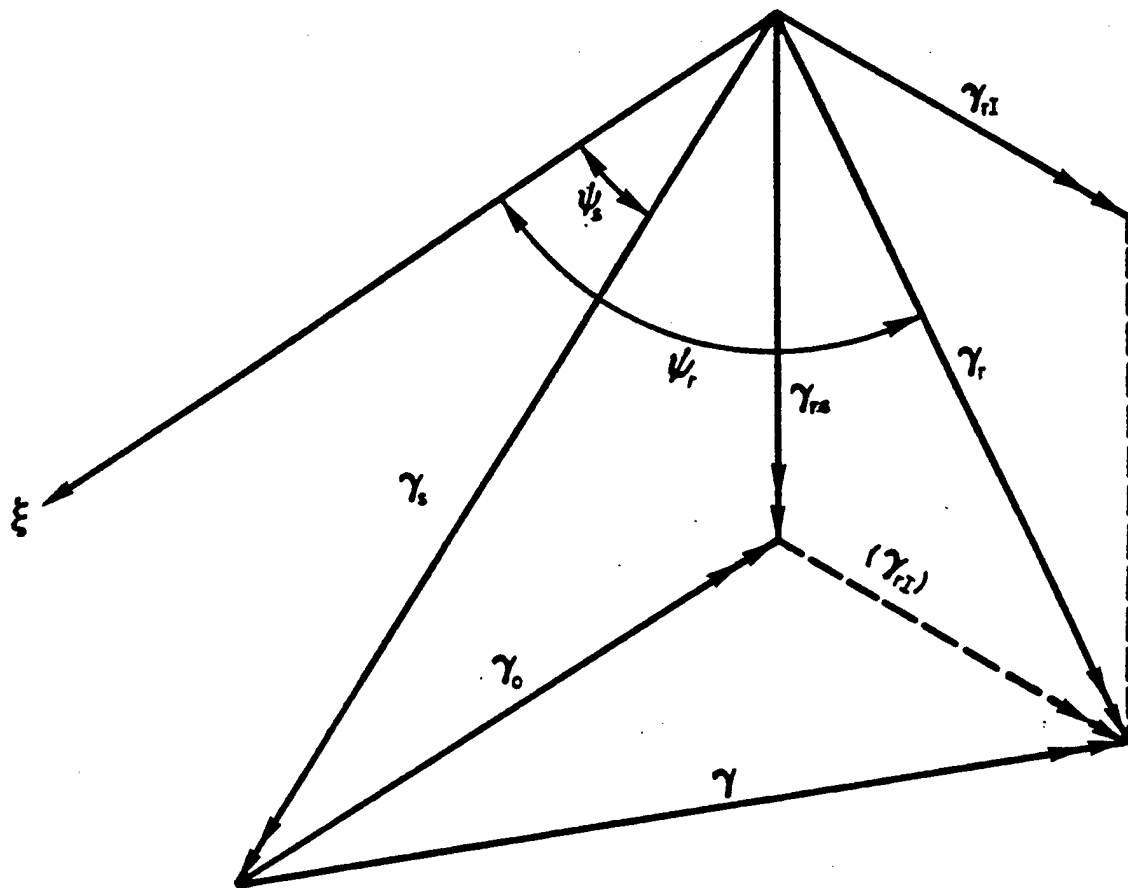


Figure 185. Vector Representation of the Complete Response

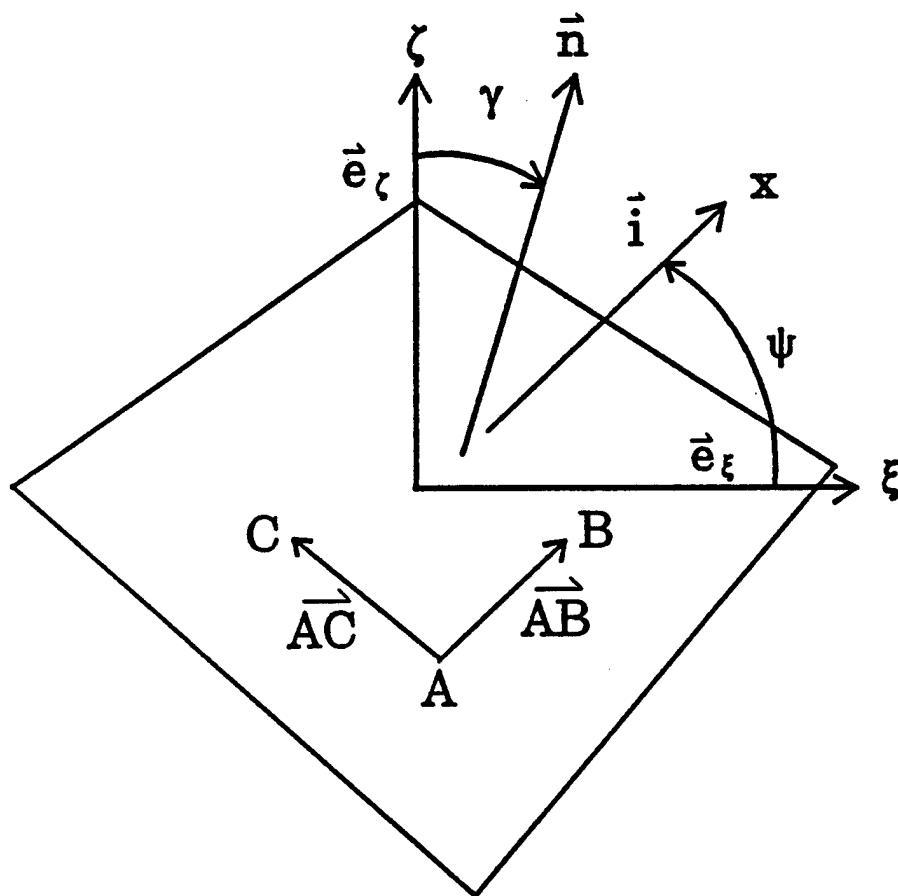


Figure 186. Misalignment and Precession of a Plane



of one of the three proximity probes that measures the distances to the rotor. Hence, the values of  $\xi$  and  $\eta$  for each point are unvarying. (Conveniently axis  $\xi$  was chosen to lie on the projected line connecting points C and B.) The value of  $\zeta$  for each point is provided by the instantaneous reading of that proximity probe. Hence, a unit vector out-normal to the rotor plane,  $\bar{n}$ , is defined by

$$\bar{n} = \frac{\bar{AB} \times \bar{AC}}{|\bar{AB} \times \bar{AC}|} \quad (40)$$

The misalignment of the plane,  $\gamma_r$ , is obtained by

$$\bar{e}_\zeta \cdot \bar{n} = \cos \gamma_r; \quad \therefore \gamma_r = \cos^{-1}(\bar{e}_\zeta \cdot \bar{n}) \quad (41)$$

The nutation axis,  $x$ , is defined by

$$\bar{i} = \frac{\bar{e}_\zeta \times \bar{n}}{|\bar{e}_\zeta \times \bar{n}|} \quad (42)$$

The precession angle,  $\psi_r$ , is the angle between  $\xi$  and  $x$ , and is obtained by

$$\bar{e}_\xi \cdot \bar{i} = \cos \psi_r; \quad \therefore \psi_r = \cos^{-1}(\bar{e}_\xi \cdot \bar{i}) \quad (43)$$

Because the rotor nutation,  $\gamma_r$ , is by definition positive, the computation resulting from Eqn. (41) is unambiguous. This, however, is not the case for the precession angle,  $\psi_r$ , which can take on any value from 0 to  $2\pi$ . Hence, Eqn. (43) needs to be used judiciously because of the ambiguity when calculating ArcCosine (MATLAB, as with all other computer languages, always produces results between  $-\pi/2$  and  $\pi/2$ ). To correctly determine the precession angle such that it has continuous motion between 0 and  $2\pi$ , the following procedure has been implemented:

When  $\cos^{-1}(\bar{e}_\xi \cdot \bar{i})$  is positive, then  $\psi_r$  could be in the first or the fourth quadrant. To uniquely determine  $\psi_r$ , we also check the sign of  $\cos(\bar{e}_\eta \cdot \bar{i})$ . Hence,

1. If the sign of  $\cos(\bar{e}_\eta \cdot \bar{i})$  is positive then  $\psi_r$  is determined to be in the first quadrant;
2. If the sign of  $\cos(\bar{e}_\eta \cdot \bar{i})$  is negative then  $\psi_r$  is in the fourth quadrant.

Similarly, when  $\cos^{-1}(\bar{e}_\xi \cdot \bar{i})$  is negative, then  $\psi_r$  could be in the second or the third quadrant. Once again we check the sign of  $\cos(\bar{e}_\eta \cdot \bar{i})$ . Here,

3. If the sign of  $\cos(\bar{e}_\eta \cdot \bar{i})$  is positive then  $\psi_r$  is determined to be in the second quadrant;
4. If the sign of  $\cos(\bar{e}_\eta \cdot \bar{i})$  is negative then  $\psi_r$  is in the third quadrant.

This procedure allows to present the rotor response,  $\gamma_r$ , in an orbit plot as shown in Fig. 187. The orbit represents the locus of the tip (i.e., magnitude) of the vector  $\gamma_r$  positioned at the instantaneous precession angle,  $\psi_r$ .

To obtain the stator initial misalignment,  $\gamma_s^*$ , and the stator angle,  $\psi_s$ , an analysis similar to the above (Eqns. (40) through (43)) can be performed. However, since the proximity probes target the rotor,

the objective here is to bring the stator into full contact with the rotor effectively making the rotor plane and the stator plane to be the same. Hence, the rotor is firmly pressed against the stator by imposing a high air pressure in the rotor chamber, keeping meanwhile the shaft stationary. Now the proximity probes effectively measure the stator plane as well.

A rotor reference plane perpendicular to the axis of shaft rotation needs to be defined in order to calculate the coordinates of the proximity probes in the  $\zeta$  direction. This rotor reference plane is defined by the mean values of the three proximity probes reading in one shaft rotation. The rotor response,  $\bar{\gamma}_r^*$ , stator initial misalignment,  $\bar{\gamma}_s^*$ , the rotor precession,  $\psi_r$ , and the stator angle,  $\psi_s$ , are all calculated with respect to the rotor reference plane.

As mentioned previously, the rotor angular response,  $\bar{\gamma}_r^*$ , is a rotating vector with a time varying frequency,  $\dot{\psi}_r$ . The magnitude of both  $\dot{\psi}_r$  and  $\bar{\gamma}_r^*$  vary cyclically with a constant frequency  $\omega$ . The change in magnitude and direction of the rotor angular response,  $\bar{\gamma}_r^*$ , in the  $\xi\eta$  plane forms the orbit of  $\bar{\gamma}_r^*$ . A major accomplishment in this work was the ability to present the orbit in **real-time** on the computer monitor. The component in  $\xi$  direction is  $\bar{\gamma}_r^* \cos \psi_r$ , while the component in  $\eta$  direction is  $\bar{\gamma}_r^* \sin \psi_r$ . The shape of the orbit of  $\bar{\gamma}_r^*$  can be used to detect seal face contact. An elliptical shape of the orbit centered at origin indicates no contact occurs (Fig. 187a). Any other orbit shape indicates that there is contact between the rotor and the stator (Fig. 187b).

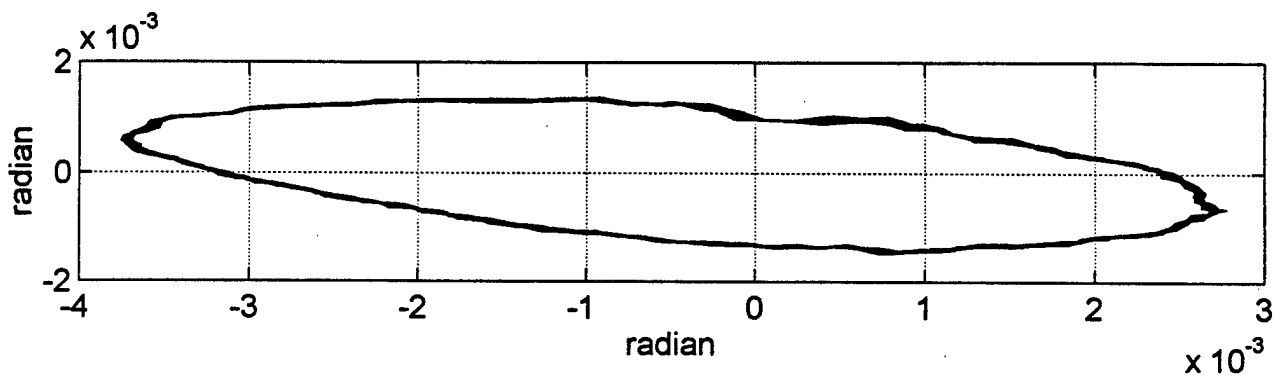
Figure 188 shows the time signals of the three proximity probe signals, their power spectrum densities (these were calculated off-line) and the orbit of the rotor angular misalignment. This is an ideal case because the tests were run without the stator, hence, by definition contact is an impossibility. It is clear that when contact does not exist the signals are pure sinusoidal and the orbit plot represents a consistent smooth locus of the tip of the rotor angular misalignment vector.

Figure 189 shows the time signals of the proximity probe, their power spectrum densities and the orbit of the rotor angular misalignment when there is contact between the rotor and the stator in three different situations. All were run at a shaft speed of 15 Hz, water pressure of 30 psi, and a coning angle of 7.2 mrad. Fig. 189a shows results for tests where the flexible support consisted of only one O-ring seal. A second higher harmonic is clearly visible. The orbit plot deviates considerably from its ideal elliptical shape. Figure 189b shows results for tests where the support had two O-ring seals. In which case the second higher harmonic is even more pronounced and is shown to exist in all three signals. The orbit plot deviates significantly from its ideal elliptical shape. While the air pressure in the rotor chamber was 7 psi for the test results shown in Figs. 189a and 189b, in the results shown in Fig. 189c that pressure was increased to 9 psi. Once again Fig. 189c shows results for tests where the support had two O-ring seals. In this case higher harmonics are shown to exist up to the 10<sup>th</sup> harmonic indicating severe face contact. The orbit plot not only deviates considerably from its ideal elliptical shape, it has a very erratic behavior. Regardless of the three test results reported above, it is clear that the orbit plot shows a consistent (also repeatable) behavior. This gives confidence that orbit plot can serve as an efficient real-time tool to reliably detect undesirable contacting operation and HHO.

## **Future Work**

### *Detecting HHO in Rotor Response By Means of Real-Time DSP:*

As indicated above, the presence of higher harmonic oscillations caused by face contact has been displayed in real-time through orbit plots. Evidently HHO can also be detected in the spectrum of the three proximity probes signals. However, the digital signal processing thus far had to be performed off-line. The possibility of implementing also real-time DSP will be investigated using the blockset package of Mathworks' Matlab and the DS1102 board from dSPACE, Inc.



**Figure 187a. Rotor Dynamic Response Orbit (noncontacting operation)**

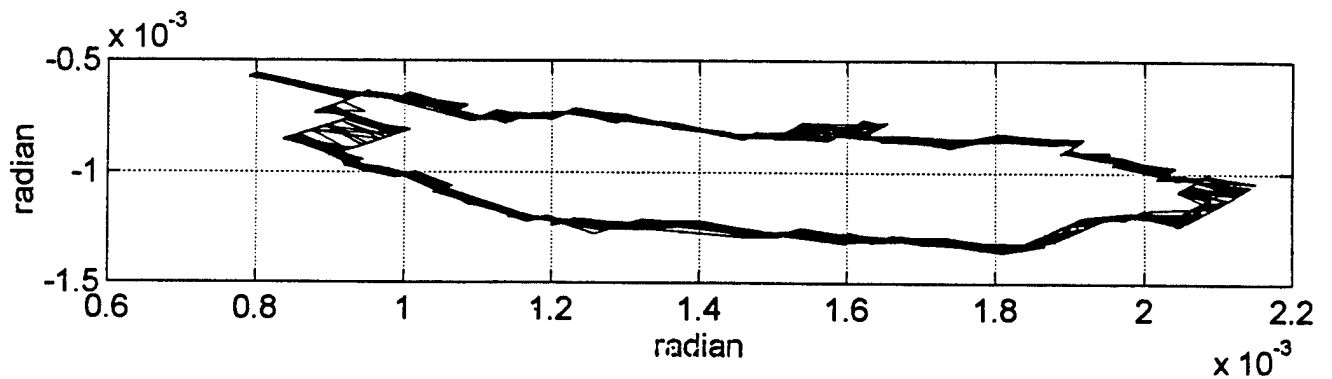


**Figure 187b. Rotor Dynamic Response Orbit (having seal face contact)**

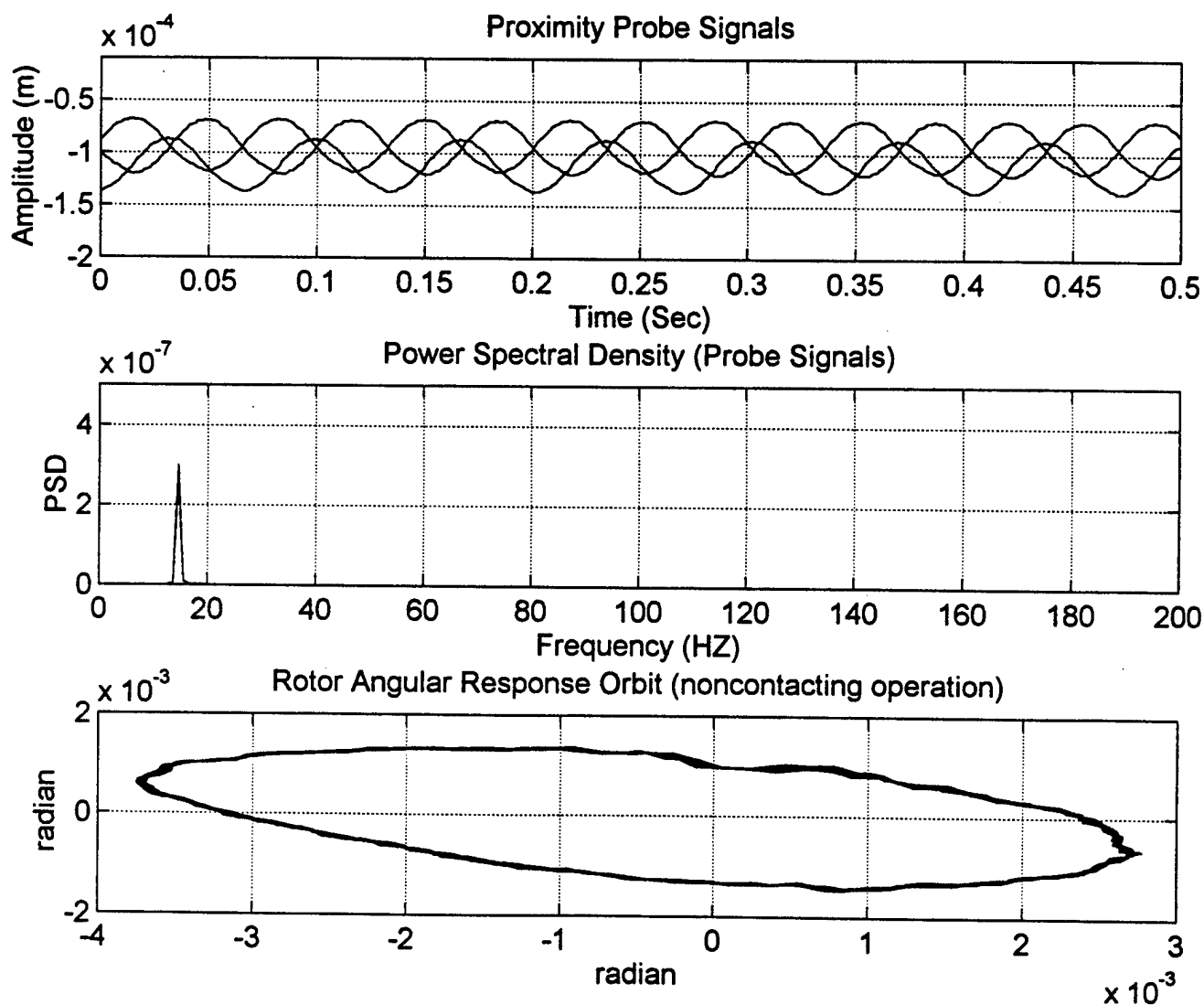


**Figure 188. Rotor Dynamic Response (noncontacting operation)**

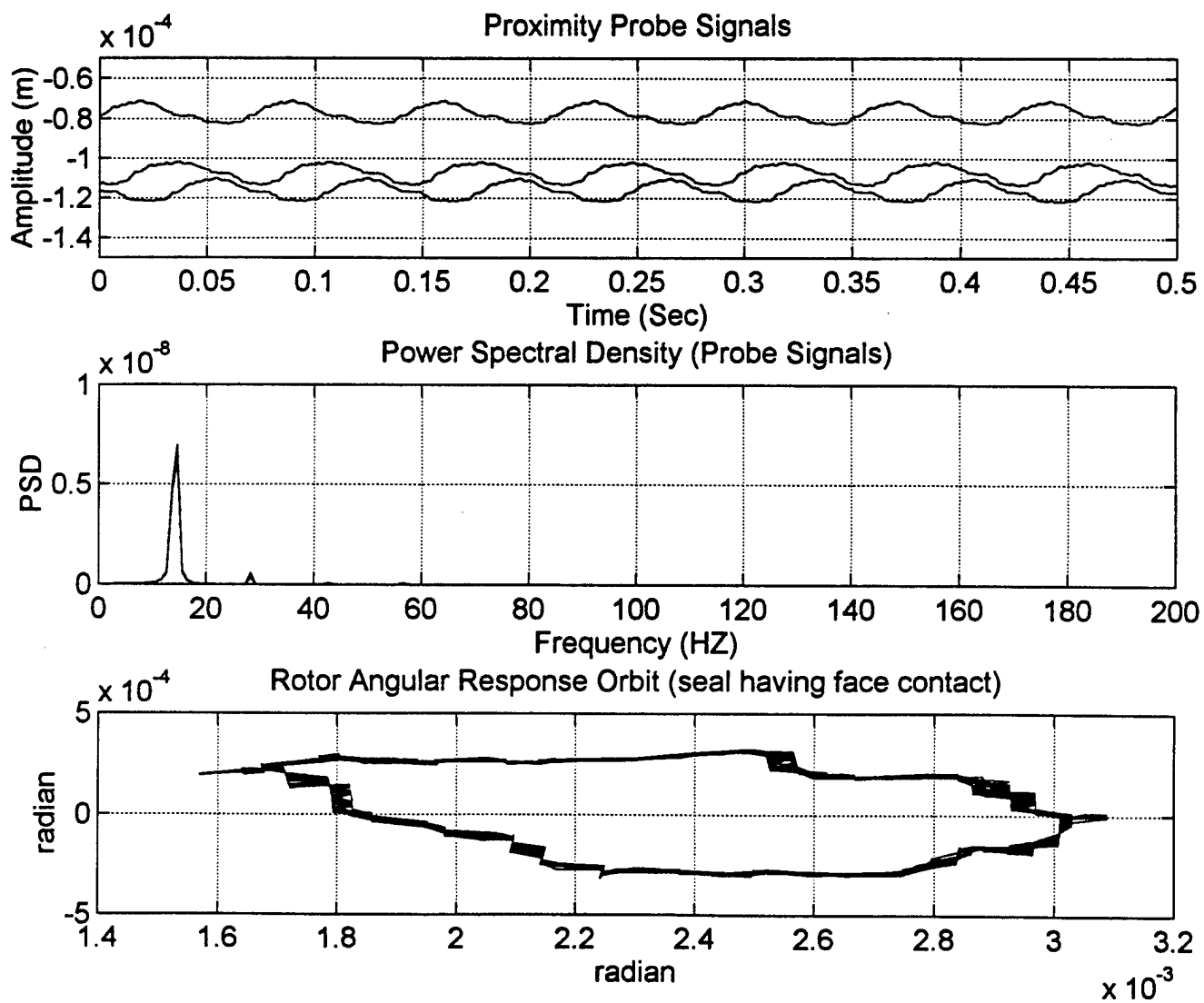


Figure 189a. Rotor Dynamic Response (seal having face contact)

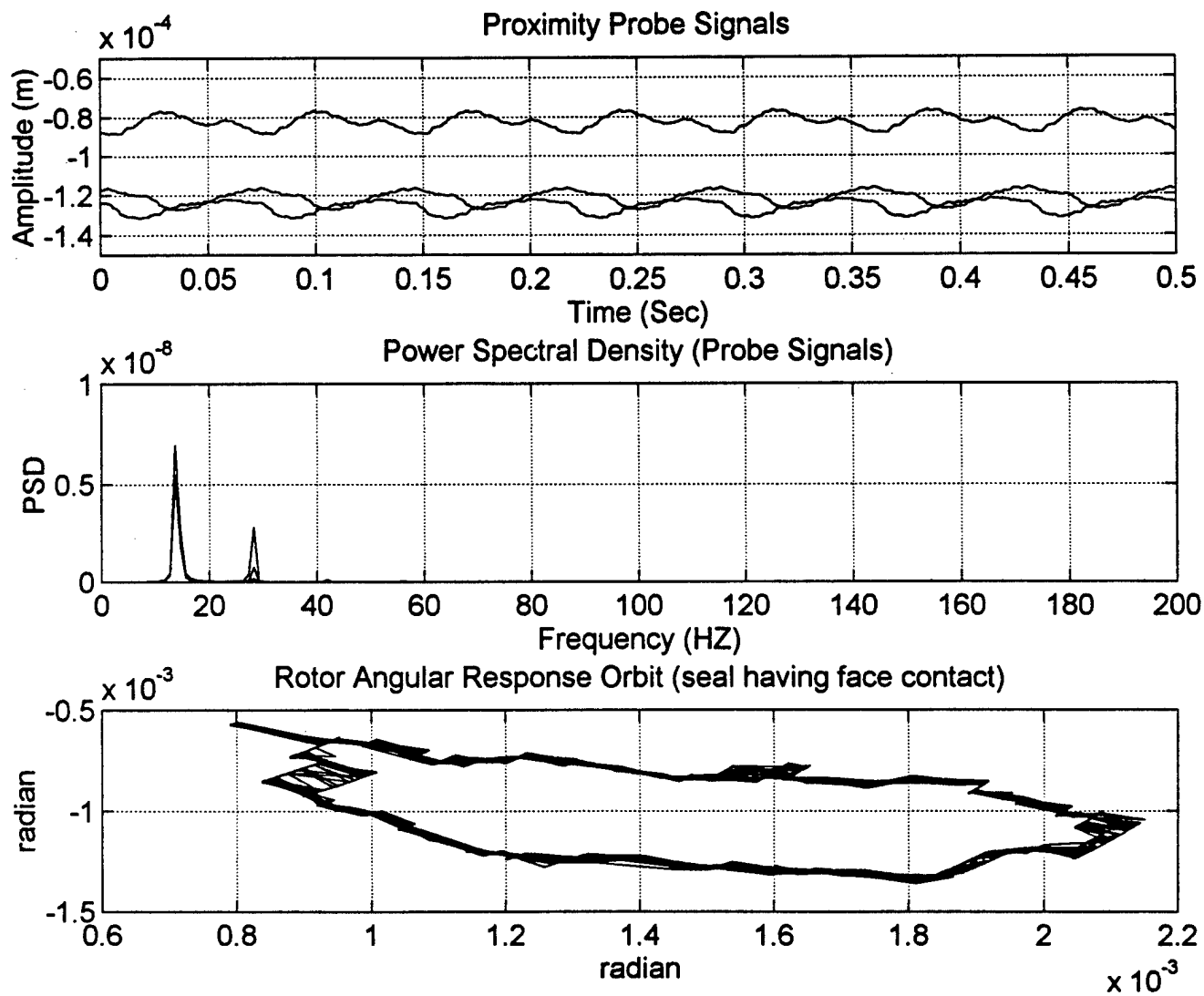


Figure 189b. Rotor Dynamic Response (seal having face contact)

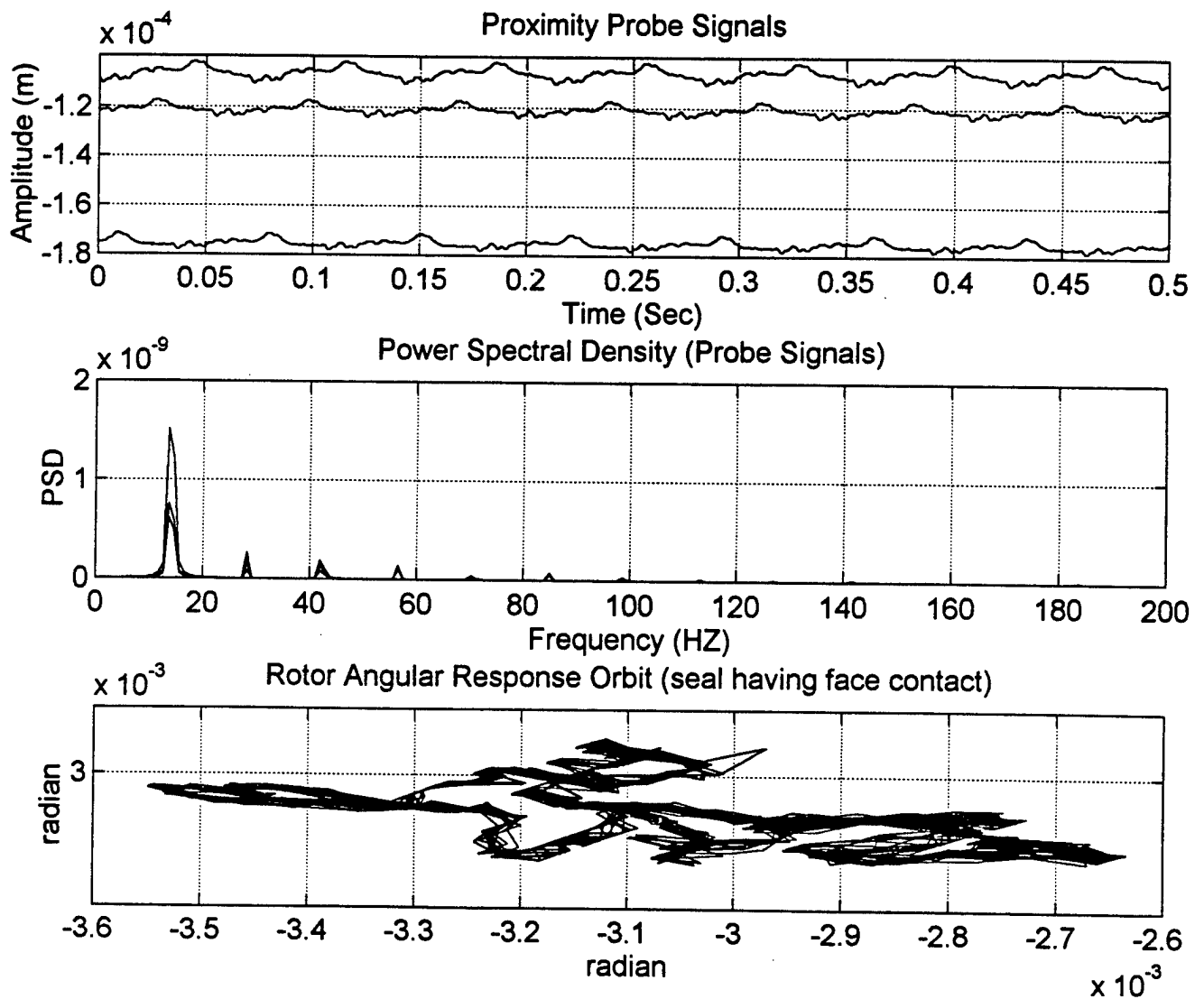


Figure 189c. Rotor Dynamic Response (seal having face contact)

### Seal Controller Design:

The need for a controlled mechanical seal has been expressed just recently in [126]. The control scheme has been based upon feedback signals that were either the temperature measured close to the sealing dam or the leakage rate. Generally, temperature or leakage rate can give some indication of the seal clearance. However, this can be misleading because the center line clearance could be large even when contact occurs as caused by a large misalignment between the rotor and the stator. Temperature will generally rise if rubbing contact occurs over the entire seal face area. However, temperature may or may not rise if there is local (i.e., point) face contact as caused by misalignment. First there must be severe face contact and the thermocouples must be located fairly close to the point of contact to detect a temperature change. Typically local contact happens when the misalignment is fairly large, hence, the leakage is larger too. This larger leakage will cool the faces and, therefore, the temperature may or may not change. Also, because of thermal inertia detection of temperature changes may not be detected immediately at the time when contact occurs (and by the time it is detected it may be too late to prevent serious face damage). In other words, the temperature may not be a reliable source of information if considered as a sole source of information. Some of this reasoning could be applicable when leakage rate is used as a feedback signal. It is the aim of this effort to develop a control system that once HHO are detected (as explained above) a control system will attempt to rectify the problem via feedback control and return FMR seal to noncontacting operation while maintaining the clearance and the relative misalignment as small as possible.

The linearized equation of motion of FMR mechanical face seals had been derived to be as follows:

$$I_t \ddot{\gamma}_\xi + I_p \dot{\gamma}_\eta + D \dot{\gamma}_\xi + B \gamma_\eta + K \gamma_\xi = \gamma_s (K_f \cos \psi_s + \frac{1}{2} D_f \sin \psi_s) + K_s \gamma_r \cos \omega t \quad (44)$$

$$I_t \ddot{\gamma}_\eta - I_p \dot{\gamma}_\xi + D \dot{\gamma}_\eta - B \gamma_\xi + K \gamma_\eta = \gamma_s (K_f \sin \psi_s - \frac{1}{2} D_f \cos \psi_s) + K_s \gamma_r \sin \omega t \quad (45)$$

$$m \ddot{Z} + D_{33} \dot{Z} + K_{33} Z = F_{air} \quad (46)$$

where:

$I_t$  : transverse moment of inertia

$I_p$  : polar moment of inertia

$D_f$  : fluid film angular damping coefficient

$D_s$  : support angular damping coefficient

$D$  : total angular damping coefficient,

$D_f + D_s$

$B : D_s + \frac{1}{2} D_f$

$K_f$  : fluid film angular stiffness coefficient

$K_s$  : support angular coefficient

$K$  : total angular stiffness coefficient,  $K_f + K_s$

$\gamma_\xi, \gamma_\eta$  : rotor tilt in the inertia system  $\xi\eta\zeta$

$\gamma_s$  : fixed stator misalignment

$\gamma_r$  : initial rotor misalignment

$\psi_s$  : angle between the  $X_s$  and  $\xi$  axes

$\omega$  : shaft rotating speed

$K_{33}$  : total axial stiffness coefficient,  $K_{f33} + K_{s33}$

$D_{33}$  : total axial damping coefficient,  $D_{f33} + D_{s33}$

$K_{f33}$  : fluid film axial stiffness coefficient

$D_{f33}$  : fluid film axial damping coefficient

$K_{s33}$  : support axial stiffness coefficient

$D_{s33}$  : support axial damping coefficient

$Z$  : seal axial displacement from equilibrium position

$m$  : rotor mass

$F_{air}$  : rotor chamber air force

$t$  : time



Equations (44) to (46) are linear with constant coefficients. They are based on a small perturbations analysis. As can be seen the axial mode Eqn. (46) is uncoupled from the angular modes Eqns. (44) and (45). Practical seals will always possess angular misalignment due to assembly tolerance and operation disturbance. The decoupling of axial and angular modes is true only if motions are limited about an equilibrium clearance and a stable system. When the seal clearance changes so do all fluid film rotordynamic coefficients. A quasi static force balance in the direction of the shaft axis shows that increasing the rotor back air pressure will decrease the seal clearance. This in turn will increase the fluid film stiffness coefficients (both axial and angular) and damping coefficients (both axial and angular). Increasing the fluid film stiffness and damping coefficients will reduce the maximum relative misalignment between the rotor and the stator and prevent rotor and stator contact. The control strategy proposed is to change the seal clearance by changing the air pressure in the rotor chamber and, therefore, change both axial and angular stiffness and damping coefficients of the fluid film. The change of the above fluid film coefficients will change the angular response of the rotor.

Experiments will be conducted to find the relationship between the rotor back air pressure and the seal clearance, the relationship between the rotor back air pressure the relative angular misalignment between the rotor and the stator. A controller will be designed to verify the control strategy.

### PLANS FOR M-URI YEAR 3

The following will be pursued in Year 3 by Graduate Student Min Zou:

1. The feasibility of performing on-line DSP/FFT on the proximity probe signals.
2. Detecting contact through the contact criterion (Eqns. (38) and (39)), and correlate with HHO.  
For this we need to know the clearance  $C_0$ . We plan to do the following:
  - (a) To further investigate the possibility of measuring  $C_0$  from proximity probes. (Others have found that this is difficult to accomplish because of drifting in the readings of the probe signals.)
  - (b) To estimate  $C_0$  from leakage measurement. i.e., use a leakage equation and a flow meter capable of measuring minute flows with A/D capabilities for sampling and real-time processing.
3. Modify test rig to reduce initial stator and rotor misalignments to examine cases of noncontacting operation.
4. Determine the motor speed on-line.
5. Develop control strategy.
6. Design a controller that can be used to reduce HHO during the test rig operation.
7. Perform exhaustive experiments with and without controller.

In the middle of Year 3 (September 1997), Dr. J. Dayan, will be joining this team to work on this project as a visiting Professor. Dr. Dayan is a senior member at the Faculty of Mechanical Engineering at The Technion, Israel Institute of Technology, with research expertise in Controls, System Identification, and Diagnostics. His stay has been secured through an independent grant and is cost shared with the Mechanical Engineering School at Georgia Tech.

Xiaoling He, a new graduate student, started to work on this project at the beginning of February 1997 and will become a Ph.D. student in the Spring Quarter, 1997. While Min Zou concentrates her efforts on working with the closing force for either generating or controlling HHO, Xiaoling He will work on similar aspects but will utilize the opening force. The closing force effects the seal clearance, which in turn effects the rotordynamics of system. However, through analysis it was discovered that the sealing dam coning has a more dramatic effect on the fluid film stiffness and damping coefficients. Hence, through an on-line change of the coning it will be possible to vary the opening force and fluid film moments in the sealing dam more easily due to the greater sensitivity to coning. Xiaoling He will also direct a major part of her work to analyze the dynamics of intermittent face contact and impact.

This stage is necessary for a thorough understanding of the mechanical and physical processes that generate and constitute HHO.

While the coning angle is preset and fixed for the current on-going effort, a new approach will be taken by varying the coning on-line by means of a moving piston that will reside in the stator assembly. Design modification of the stator will be made and a new stator will be manufactured. A complete analysis of a stepped sealing dam (caused by the piston that effectively provides a converging gap similar to coning) will be performed to allow an optimized design.

#### **VISION FOR YEARS 4 AND 5**

1. Continue activity with respect to addressing the new approach, i.e., the coning will be varied on-line by means of a moving piston that will reside in the stator assembly. Analysis of a stepped sealing dam (caused by the piston that effectively provides a converging gap similar to coning) will have been completed to permit an optimized design.
2. Incorporate the new stepped stator in the test rig, carry out experiments, detect HHO, and produce orbit plots. Repeat experiments with the same operational conditions as performed by Min Zou but now using opening forces/moments strategies instead.
3. Analyze the dynamics of intermittent contact and impact, and correlate with experimental data.

## 2.4 REFERENCES

### Section 2.1.1 Flaw Detection and Characterization

- [1] Wagner W. and Spicer, J. B., 1987, "Theoretical noise-limited sensitivity of classical interferometry," *J. Opt. Soc. Am.* 4, pp. 1316-1326.
- [2] Yang, Y., DeRidder, N., Ume, C. and Jarzynski, J., 1993, "Non-contact optical fibre phased array generation of ultrasound for non-destructive evaluation of materials and processes," *Ultrasonics* 31, pp. 387-394.
- [3] Bruinsma, A. J. A. and Vogel, J. A., 1988, "Ultrasonic noncontact inspection system with optical fiber methods," *Appl. Opt.* 27 (22), pp. 4690-1695
- [4] Cielo, P., Nadeau, F. and Lamontagne, M., "Laser generation of convergent acoustic waves for materials inspection," *Ultrasonics*, March 1985.
- [5] Fomitchov, P., Steckenrider, J. S, Krishnaswamy S. and Achenbach, J. D., 1996, "Low noise interferometric sensor for ultrasonic measurement," in *Review of Progress in Quantitative Nondestructive Evaluation* (D. O. Thompson & D. E. Chimenti, ed.), Vol 16.
- [6] Wang, L. S., Steckenrider, J. S. and Achenbach, J. D., 1996, "A fiber-based laser ultrasonic system for remote inspection of limited access components," in *Review of Progress in Quantitative Nondestructive Evaluation* (D. O. Thompson & D. E. Chimenti ed.), Vol 16.
- [7] Fomitchov, P., Wang, L. S., Steckenrider, J. S., Achenbach, J. D. and Krishnaswamy, S., "Laser-based ultrasonics for QNDE applications," International Conf. on Exp. Mech., Singapore, Dec. 4-6, 1996 (to appear in an *SPIE Proceedings*).

### Section 2.1.4 Study of Acoustic Emission and Transmission from Incipient Fatigue Failure

- [8] Hurlebaus, S., 1996, "Laser generation and detection techniques for developing transfer functions to characterize the effect of geometry on elastic wave propagation," M.S. Thesis, Georgia Institute of Technology, Atlanta, GA.
- [9] Hurlebaus, S., Jacobs, L. and Jarzynski, J., 1997, "Optical techniques to develop transfer functions to remove geometric features in acoustic emission signals," to appear in *Review of Progress in Quantitative Nondestructive Evaluation*, Vol. 16.
- [10] Gorman, M. R., 1991, "Acoustic Emission for the 1990s," *Proc. Ultrasonics Symposium*.

### Section 2.2.1 Structural Fatigue Investigation

- [11] Parks, D. M., 1974, "A Stiffness Derivative Finite Element Technique for Determination of Crack Tip Stress Intensity Factors," *International Journal of Fracture*, Vol. 10, No. 4, pp. 487-502.
- [12] Bakker, A., 1983, "On Local Energy Release Rates Calculated by the Virtual Crack Extension Method," *International Journal of Fracture*, Vol. 23, pp. R85-R90.
- [13] Claydon, P.W., 1992, "Maximum Energy Release Rate Distribution from a Generalized 3D Virtual Crack Extension Method," *Engineering Fracture Mechanics*, Vol. 42, No. 6, pp. 961-969.
- [14] Hussain, K., de los Rios, E.R. and Navarro, A., 1993, "A Two-Stage Micromechanics Model for Short Fatigue Cracks," *Engng. Fract. Mech.*, 44(3), pp. 425-436.
- [15] Wang, C.H., 1996, "Effect of Stress Ratio on Short Crack Fatigue Growth," *ASME J. Engng. Mater. Techn.*, 118, pp. 362-367.
- [16] Miller, K.J., 1993, "The Two Thresholds of Fatigue Behaviour," *Fatigue Fract. Engng. Mater. Struct.*, 16(9), pp. 931-939.

- [17] Nisitani, H., 1987, "Behavior of Small Cracks in Fatigue and Relating Phenomena. *Current Research on Fatigue Cracks*, T. Tanaka, M. Jono and K. Komai, Eds., Current Japanese Materials Research, 1, Elsevier, pp. 1-26.
- [18] Tanaka, K. and Akiniwa, Y., "Propagation and Non-propagation of Small Fatigue Cracks," in *Advances in Fracture Research, Proc. ICF7*, Vol. 2, Houston, TX, March 20-24, 1996, pp. 869-887.
- [19] Tanaka, K., 1987, "Short-Crack Fracture Mechanics in Fatigue Conditions," *Research on Fatigue Cracks*, eds. T. Tanaka, M. Jono and K. Komai, *Current Japanese Materials Research*, Elsevier, 1, pp. 93-117.
- [20] Hobson, P.D., 1985, "The Growth of Short Fatigue Cracks in a Medium Carbon Steel," PhD Thesis, University of Sheffield, Sheffield, UK.
- [21] Hobson, P.D., Brown, M.W. and de los Rios, E.R., 1986, "Two Phases of Short Crack Growth in a Medium Carbon Steel," in *The Behaviour of Short Fatigue Cracks*, eds. K.J. Miller and E.R. de los Rios, EGF Publ. 1, Inst. Mech. Engrs, London, pp. 441-459.
- [22] Newman, J.C., "FASTRAN II - A Fatigue Crack Growth Structural Analysis Program," *NASA Technical Memorandum 104159*, February 1992.
- [23] *Damage Tolerant Design Handbook*, Volume 2, WL-TR-94-4053, May 1994, pp. 6-260 to 6-264.
- [24] Friesel, M.A., 1989, "Application of Signal Analysis to Acoustic Emission from a Cyclically Loaded Aluminum Joint Specimen," *Materials Evaluation*, Vol. 47, pp. 842-848.
- [25] Vingsbo, O. and Soderberg, D., 1988, "On Fretting Maps," *Wear*, Vol. 126, pp. 131-147.
- [26] Spink, G.M., 1990, "Fretting Fatigue of a 2.5% NiCrMoV Low Pressure Turbine Shaft Steel: The Effect of Different Contact Pad Materials and of Variable Slip Amplitude," *Wear*, Vol. 136, pp. 281-297.
- [27] Mutoh, Y., 1995, "Mechanisms of Fretting Fatigue," *JSME International Journal, Series A*, Vol. 38, No. 4, pp. 405-415.
- [28] Endo, K. and Goto, H., 1976, "Initiation and Propagation of Fretting Fatigue Cracks," *Wear*, Vol. 38, pp. 311-320.
- [29] Edwards, P.R., 1981, "The Application of Fracture Mechanics to Predicting Fretting Fatigue," *Fretting Fatigue*, R.B. Waterhouse, ed., Applied Sci. Publ., London, pp. 67-97.
- [30] Nix, K.J. and Lindley, T. C., 1985, "The Application of Fracture Mechanics to Fretting Fatigue," *Fatigue and Fracture of Engineering Materials and Structures*, Vol. 8, No. 2, pp. 143-160.
- [31] Hattori, T., Nakamura, M., Sakata, H., and Watanabe, T., 1988, "Fretting Fatigue Analysis Using Fracture Mechanics," *JSME International Journal, Series 1*, Vol. 31, No. 1, pp. 100-107.
- [32] Faanes, S. and Fernando, U.S., 1994, "Life Prediction in Fretting Fatigue using Fracture Mechanics," *Fretting Fatigue*, ESIS 18, R.B. Waterhouse and T.C. Lindley, eds., Mechanical Engineering Publications, London, pp. 149-159.
- [33] Faanes, S. and Fernando, U.S., 1994, "Influence of Contact Loading on Fretting Fatigue Behaviour," *Fatigue and Fracture of Engineering Materials and Structures*, Vol. 17, No. 8, pp. 939-947.
- [34] Takeuchi, M., Satoh, T., Mutoh, Y., Waterhouse, R.B., and Kon, Y., 1994, "Fretting Fatigue of an Austenitic Stainless Steel in Seawater," *Fatigue and Fracture of Engineering Materials and Structures*, Vol. 17, No. 8, pp. 949-958.
- [35] Tanaka, T., Mutoh, Y., Sakoda, S., and Leadbeater, G., 1985, "Fretting Fatigue in 0.55 C Spring Steel and 0.45 C Carbon Steel," *Fatigue and Fracture of Engineering Materials and Structures*, Vol. 8, No. 2, p. 143.
- [36] *Damage Tolerant Design Handbook*, 1975.
- [37] Seetharaman, V., Sundararaman, M., and Krishnan, R., 1981, "Precipitation Hardening in a PH 13-8 Mo Stainless Steel," *Mat. Sci. & Eng.*, Vol. 47, pp. 1-11.
- [38] Cieslak, W.R., Brooks, J.A., and Garrison, W.M., Jr., 1986, "The Weldability, Microstructure and Properties of Precipitation Strengthened Martensitic Stainless Steels," *Advances in welding science and technology: proceedings of an International Conference on Trends in Welding Research*, Gatlinburg, Tennessee, USA, 18-22 May 1986, S.A. David, ed., ASM International, pp. 515-521.
- [39] Cieslak, M. J., Hills, C. R., Hlava, P.F., and David, S. A., 1990, "An Investigation of the High Temperature and Solidification Microstructures of PH 13-8 Mo Stainless Steel," *Metall. Trans. A*, Vol. 21A, pp. 2465-2475.

- [40] Munn, P. and Andersson, B., 1990, "Hydrogen Embrittlement of PH 13-8 Mo Steel in Simulated Real-Life Tests and Slow Strain Rate Tests," *Corrosion*, Vol. 46, No. 4, pp. 286-295.
- [41] Scully, J. R., Van Den Avyle, J. A., Cieslak, M. J., Romig, A. D., Jr., and Hills, C. R., 1991, "The Influence of Palladium on the Hydrogen-Assisted Cracking Resistance of PH 13-8 Mo Stainless Steel," *Metall. Trans. A*, Vol. 22A, pp. 2429-2444.
- [42] Hochanadel, P.W., Robino, C.V., Edwards, G.R., and Cieslak, M. J., 1994, "Heat Treatment of Investment Cast PH 13-8 Mo Stainless Steel: Part I."
- [43] Gaugh, R. R., 1987, "Stress Corrosion Cracking of Precipitation-Hardening Stainless Steel," *Material Performance*, pp. 29-34.
- [44] *MIL Handbook 5G*, November 1994.
- [45] McDowell, D. L., 1996, "Basic Issues in the Mechanics of High Cycle Metal Fatigue," *International Journal of Fracture*, Vol. 80, pp. 103-145.
- [46] Attia, M. H. and Waterhouse, R. B., 1992, *Standardization of Fretting Fatigue Test Methods and Equipment*, ASTM STP 1159, American Society for Testing and Materials, Philadelphia.
- [47] Swain, M.H., Everett, R.A., Newman, J.C. and Phillips, E.P., 1990, "Growth of Short Cracks in 4340 Steel and Aluminum-Lithium 2090," NASA Report N91-11247/4, NTIS.

### Section 2.2.2 Fatigue Reliability

- [48] Bowen J., et al., "Critical Equipment Failures and Maintenance Issues," Subgroup Report, *Proc. Workshop on Condition Based Maintenance*, Office of Naval Research and Georgia Institute of Technology, Atlantic Beach, NC, November 15-17, 1993.
- [49] Glaeser, B. A. and Wedeven, L. D., "Failure Models," Subgroup Report, *Proc. Workshop on Condition Based Maintenance*, Georgia Institute of Technology and Office of Naval Research, Atlantic Beach, NC, November 15-17, 1993.
- [50] Harkness, H., Fleming, M., Moran, B. and Belytschko, T. B., "Fatigue Reliability Method with In-Service Inspections," *Proc. FAA/NASA International Symposium on Advanced Structural Integrity Methods for Durability and Damage Tolerance*, Hampton, VA, May 4-6, 1994.
- [51] Harkness, H. H., Belytschko, T. B., and Liu, W. K., 1992, "Finite Element Analysis of Fatigue Life," *Nucl. Engng Des.*, Vol. 133, pp. 209-224.
- [52] Xu, Y. and Moran, B., 1997, "Limit State Surface Element Method for Reliability," Technical Report, Northwestern University, Evanston, IL, in preparation.
- [53] Xu, Y. and Moran, B., 1997, "Optimization Method for Inspection Planning," Technical Report, Northwestern University, Evanston, IL, in preparation.
- [54] Xu, Y. and Moran, B., 1997, "Inverse Problem Approach to NDE Technique and Parameter," Technical Report, Northwestern University, Evanston, IL, in preparation.
- [55] Moran, B., Zulfiqar, A. and Sukumar, N., "On the Direct Integration Method for Fatigue Reliability Calculations," Technical Report, Northwestern University, Evanston, IL, July 1996.

### Section 2.3.2 Eddy Current Micro Sensors for Integrated Diagnostics

- [56] Libby, H. L., 1971, *Introduction to Electromagnetic Nondestructive Testing Methods*, Wiley-Interscience, New York.
- [57] Blitz, J., 1991, *Electrical and Magnetic Methods of Nondestructive Testing*, Adam Hilger, Bristol.
- [58] Uesaka, M., Nakanishi, T., Miya, K., Komatsu, H., Aoki, K., and Kasai, K., 1995, *IEEE Transactions on Magnetism*, 31, pp. 870 - 876.
- [59] *Annual Report-MURI Year 1, Integrated Diagnostics*, ONR Grant N00014-95-1-0539, R. Cowan and W. Winer, eds., Georgia Institute of Technology, Atlanta, GA, February 1996, pp. 130-149.

## REFERENCES

- [60] Zheng, L., Xue, J. and Ramalingam, S., "Eddy Current Micro-Sensors for Flaw Imaging," *Monitoring Technology for Condition Based Maintenance*, R. Cowan, ed., ASME 96-TRIB-66, October 1996, pp. 25-31.
- [61] Dodd, C. V., 1967, *Solutions to Electromagnetic Induction Problems*, Doctoral Dissertation, University of Tennessee, Knoxville, TN.
- [62] Palanisamy, R., 1980, Doctoral Dissertation, Colorado State University, Fort Collins, CO.
- [63] Ida, N., 1983, *Three-dimensional Finite Element Modeling of Electromagnetic Nondestructive Testing Phenomena*, Fort Collins, CO.
- [64] Ranmuthu, K. T. M., Pohm, A. V., Daughton, J. M., and Comstock, C S., 1993, *IEEE Transactions on Magnetism*, **29**, pp. 2593 - 2595.
- [65] Daughton, J. M., and Chen, Y. J., 1993, "GMR Materials for Low Field Applications," *IEEE Transactions on Magnetism*, **29**, pp. 2705 - 2710.

### Section 2.3.3 Integrated Microsensors for Aircraft Fatigue and Failure Warning

- [66] Polla, D. L. and Francis, L. F., "Ferroelectric Thin Films in MEMS Applications," *Materials Research Society Bulletin*, **21**, No. 7, July 1996, pp. 59-65.
- [67] Polla, D. L., 1995, "Microelectromechanical Systems Based on Ferroelectric Thin Films," *Microelectronic Engineering*, **29**, pp. 51-58.
- [68] Hsueh, C.-C., Tamagawa, T., Ye, C., Helgeson, A., and Polla, D. L., 1993, "Sol-gel Derived Ferroelectric Thin Films in Silicon Micromachining," *Integrated Ferroelectrics*, **3**, p. 21.
- [69] Scruby, C. B., 1987, *J. Phys. E: Sci Instrum.*, **20** p. 946.
- [70] Jaffe, B., Cook, B. W. and Jaffe, H., 1971, *Piezoelectric Ceramics*, Academic Press, New York.
- [71] Wright, J. S. and Francis, L. F., to be submitted to *J. Mater. Res.*
- [72] Lin, C. T., Li, L., Webb, J. S., Lipeless, R. A. and Leung, M. S., 1993, *Integrated Ferroelectrics*, **3**, p. 333.
- [73] Lakeman, C. D. and Payne, D. A., 1991, *J. Am. Ceram. Soc.* **75** (11), p. 3091.
- [74] Schwartz, R. W., Boyle, T. J., Lockwood, S. J., Sinclair, M. B., Dimos, D., Buchheit, C., 1995, *Integrated Ferroelectrics*, **7** pp. 259-278.
- [75] Aegerter, M. A., 1992, *J. Non-Cryst. Solids*, **151** p. 195.
- [76] Tuttle, B. A. and Schwartz, R. W., 1996, *Mat. Res. Bulletin*, **21** (6), p. 49.
- [77] Li, J-F., Moses, P., and Viehland, D., 1995, *Rev. Sci. Instrum.*, **66**, p. 21.
- [78] Zhang, Q. M., Pan, W. Y., and Cross, L. E., 1988, *J. Appl. Phys*, **63** (8), p. 2182.
- [79] Schwartz, R. W., Voigt, J. A., Boyle, T. J., Christenson, T. A. and Buchheit, C. D., 1995, *Ceram. Eng. and Sci. Proc.*, **16** (5), p.1045.
- [80] Kwok, C. K. and Desu, S. B., *Journal of Materials Research*, **8** (2), p. 339.
- [81] Polla, D. L. and Schiller, P. J., 1995, "Integrated Ferroelectric Microelectromechanical Systems (MEMS)," *Integrated Ferroelectrics*, **7**, pp. 359-370.
- [82] Schiller, P. and Polla, D. L., "Integrated Piezoelectric Microactuators Based on PZT Thin Films," *Seventh IEEE International Conference on Solid-State Sensors and Actuators*, Yokohama, Japan, June 1993.
- [83] Kim, H.-S., Kim, J.-H., Zurn, S., and Polla, D. L., 1996, "Electrical and Mechanical Properties of PZT(54/46) Thin Films for Silicon Micromachined Devices," *IEEE Int. Symposium on Application Ferroelectrics*, Piscataway, N.J.
- [84] Beranek, L. L., 1996, *Acoustics*, Acoustical Society of America, Woodbury, N.Y.
- [85] Bahr, D. F. and Gerberich, W. W, 1997, "Relationships Between Acoustic Emission Signals and Physical Phenomena During Indentation," submitted to *J. Materials Research*.

- [86] Bahr, D. F., Hoehn, J. W., Moody, N. R and Gerberich, W. W., 1997, "Nanoindentation and Acoustic Emission of Nitride Films with Metal Interlayers " submitted to *Acta Materiala*.
- [87] Gerberich, W. W and Hartbower, C. E., 1967, *Int. J. Fract. Mech.*, **3**, p. 185.
- [88] Cai, H., Evans, J. T., Boomer, D., 1992, *Eng. Fract. Mech.*, **42**, p. 589
- [89] Bahr, D. F., Wright, J. S., Francis, L. F., Moody, N. R and Gerberich, W. W., 1996, "Mechanical Behavior of a MEMS Acoustic Emission Sensor " in Proceedings of the Materials Research Society, **444**, *Materials in Mechanical and Optical Microsystems*, in press.
- [90] Bahr, D. F., Wright, J. S., Francis, L. F., Moody N. R., and Gerberich, W. W., "The Mechanical Behavior of PZT Thin Films Deposited by A Sol-Gel Technique," presented at TMS Annual Meeting in *Evolution and Advanced Characterization of Thin Film Microstructures*, February, 1997.
- [91] Drouillard, T. F., 1996, "A History of Acoustic Emission," *J. of Acoustic Emission*, vol. **14**, no. 1, pp. 1-34.
- [92] Scala, C. M., McCardle, J. F. and Bowles, S. J., 1992, "Acoustic Emission Monitoring of a Fatigue Test of an F/A-18 Bulkhead," *Journal of Acoustic Emission*, **10**, no. 3/4, pp. 49-60.
- [93] West, D., Venkatesan, G., Tewfik, A., Buckley K., and Kaveh, M., 1996, "Detection and Modeling of Acoustic Emissions for Fault Diagnostics," *IEEE SSAP Workshop*, Corfu, Greece.
- [94] Buckley, K., Venkatesan, G., West, D. and Kaveh, M., "Detection and Characterization of Cracks for Failure Monitoring and Diagnostics," *ICASSP 96*, Atlanta, May 1996.
- [95] Mitrakovic, D., Grabec, I. and Sedmak, S., "Simulation of AE signals and signal analysis systems," *Ultrasonics*, Sept. 1985, pp. 227-232.
- [96] Park, J., Lindberg, C. R. and Thomson, D. J., 1987, "Multiple-taper Spectral Analysis of Terrestrial Free Oscillations," *Geophys. J. R. Astr. Soc.*, **91**, pp. 755-794.
- [97] Venkatesan, G. T., West, D., Buckley, K. M., Tewfik, A. H., Kaveh, M., "Automatic Fault Monitoring using Acoustic Emissions," *ICASSP 97*, Munich, Germany, April 1997.
- [98] Donoho, D. L., "Denoising by Soft Thresholding," *IEEE Trans. on Information Theory*, **41**, no. 3, May 1995, pp. 613-627.
- [99] Cox, D. R. and Lewis, P. A. W., 1966, *The Statistical Analysis of Series of Events*, John Wiley and Sons Inc., New York.

#### Section 2.3.4 Acoustic Emission Modeling for Integrated Diagnostics

- [100] Liptai, R. G., Harris, D. O., Engle, R. B. and Tatro, C. A., 1971, "Acoustic Emission Techniques in Materials Research," *Inter. Journal of Nondestructive Testing*, Vol. **3**, pp. 215-275.
- [101] Dunegan, H. L. and Harris, D. O., 1969, "Acoustic Emission - A New Nondestructive Testing Tool," *Ultrasonics*, Vol. **7**, No. 3, pp. 160-166.
- [102] Fang, D. and Berkovits, A., 1993, "Fatigue Damage Mechanisms on the Basis of Acoustic Emission Measurements," *Novel Exper. Techniques in Fracture Mechanics*, ed. by A. Shukla, AMD-Vol. 176, ASME, pp. 213-235.
- [103] *Acoustic Emission Testing in Nondestructive Testing Handbook*, 1987, Vol. 5, ed. by R. K. Miller and P. McIntire, Second Ed., American Soc. for Nondestructive Testing, Columbus, OH.
- [104] Morton, H. L., Harrington, R. M. and Bjeletich, J. G., 1973, "Acoustic Emissions of Fatigue Crack Growth," *Engineering Fracture Mechanics*, Vol. **5**, No. 3, pp. 691-697.
- [105] Lindley, T. C., Palmer, I. G. and Richards, C. E., 1978, "Acoustic Emission Monitoring of Fatigue Crack Growth," *Materials Science and Engineering*, Vol. **32**, pp. 1-15.
- [106] Hamel, F., Bailon, J. P. and Bassim, M. N., 1981, "Acoustic Emission Mechanisms during High Cycle Fatigue," *Engineering Fracture Mechanics*, Vol. **14**, No. 4, pp. 853-860.
- [107] Berkovits, A. and Fang, D., "An Empirical Design Model for Fatigue Damage on the Basis of Acoustic Emission Measurements," 17th ICAF Symposium, Stockholm, June 1993.

- [108] Sinclair, A. C., Connors, D. C. and Formby, C. L., 1977, "Acoustic Emission Analysis during Fatigue Crack Growth in Steel," *Materials Science and Engineering*, Vol. 28, , pp. 263-273.
- [109] Kohn, D. H., Ducheyne, P. and Awerbuch, J., 1992, "Acoustic Emission during Fatigue of Ti-6Al-4V: Incipient Fatigue Crack Detection Limits and Generalized Data Analysis Methodology," *J. of Materials Science*, Vol. 27, pp. 3133-3142.
- [110] Smith, S. and Morton, T. M., 1973, "Acoustic-Emission Detection Technique for High-Cycle-Fatigue Testing," *Exper. Mech.*, Vol. 13, pp. 193-198.

### **Section 2.3.5 Dynamic Metrology as a Wear Diagnostic**

- [111] Widrow, B. et al. 1975, "Adaptive Noise Canceling: Principles and Applications." *Proceedings of the IEEE*, v63 n12, pp. 1692-1716.
- [112] Alfredson, R.J. and Mathew, J. , 1985, "Time Domain Methods for Monitoring the Condition of Rolling Element Bearings", *Mechanical Engineering Transactions*, v10, n2, The Institution of Engineers, Australia, pp. 102-107.
- [113] Alfredson, R.J. and Mathew, J., 1985, Frequency Domain Methods for Monitoring the Condition of Rolling Element Bearings," *Mechanical Engineering Transactions*, v10, n2, The Institution of Engineers, Australia, pp. 108-112.
- [114] Carney, M., Mann, A. and Gagliardi, J., 1994, "Adaptive Filtering of Sound Pressure Signals for Monitoring Machinery in Noisy Environments," *Applied Acoustics*, v43, pp. 333-351.
- [115] Daadbin, A. and Wong, J.C.H., 1991, "Different vibration monitoring techniques and their application to rolling element bearings," *International Journal of Mechanical Engineering Education*, v19 n4, pp. 295-304.
- [116] Kim, P.Y., 1987, "Proximity Transducer Technique for Measuring Health Monitoring," *Journal of Propulsion and Power*, v3 n1, pp. 84-89.
- [117] Li, C.J. and Ma, J., 1992, "Bearing Localized Defect Detection Through Wavelet Decomposition of Vibrations," *Sensors and Signal Processing for Manufacturing*, ASME PED, v55, pp. 187-196.
- [118] Martin, H.R. and Hornarvar, F., 1995, "Application of Statistical Moments to Bearing Failure Detection," *Applied Acoustics*, v 44, pp. 67-77.
- [119] Margin, K.F. and Thorpe, P., 1992, "Normalized spectra in monitoring of rolling bearing elements," *Wear*, v159, pp. 153-160.
- [120] Lawrentz, D., 1996, The Timken Company, Canton, OH.
- [121] Braun, S. and Datner, B., 1979, "Analysis of Roller/ball Bearing Vibrations," *Journal of Mechanical Design Transactions*, v101, pp. 118-125.
- [122] McFadden, P.D. and Smith, J.D., 1984, "Vibration Monitoring of rolling Element Bearings by the High Frequency Resonance Technique-A Review," *Tribology International*, v17, pp. 1-18.
- [123] Su, Y.-T. and Lin, S.-J., 1992, "On Initial Fault Detection of a Tapered Rolling Bearing: Frequency Domain Analysis," *Journal of Sound and Vibrations*, v155, pp. 75-84.
- [124] Treichler, J.R., 1979, "Transient and Convergent Behavior of the Adaptive Line Enhancer," *IEEE Transactions on Acoustics, Speech, and Signal Processing* vASSP-27 n1, pp. 53-62.
- [125] Clarkson, P.M., 1993, *Optimal and Adaptive Signal Processing*, Boca Raton FL: CRC Press, pp. 166-173.

### **Section 2.3.6 Monitoring of Sub or Higher Harmonic Oscillations in Rotating Machine Elements**

- [126] Etsion, I., Palmor, Z., and Harari, N., 1991, "Feasibility Study of a Controlled Mechanical Seal," *Lubrication Engineering*, Vol. 47, No. 8, pp. 621-625.



### 3. TECHNOLOGY TRANSFER ACHIEVEMENTS

---

The pivotal objective of the Integrated Diagnostics program is to accommodate academia's commitment to explore and discover, and industry's need to develop and improve. To expedite the transfer of the knowledge obtained from academic research, information has been disseminated through a variety of means, including publications, monthly updates, meeting presentations, and the educational process.

#### 3.1 PUBLICATIONS

Faculty and students have been encouraged to publish their findings in such archival materials as publications, meeting transactions, and books. Current abstracting and computer search activities make such resources quite valuable to the world at large. Manuscripts from *Integrated Diagnostic* activity, submitted and/or published during this reporting period, are listed below with their respective abstracts.

##### Refereed Journal (8)

1. Bahr, D. F., Nelson, J. C., Tymiak, N. and Gerberich, W. W., "Mechanical Behavior of a Passivating Surface under Potentiostatic Control," *J. Materials Research*, submitted September 1996.

Continuous microindentation has been carried out on an iron-3% silicon single crystal in 1 M sulfuric acid. The ability of the material to support elastic loading is directly linked to the presence of thermally grown oxide films and passive films applied through potentiostatic control of the sample. When the passive film is removed, either by chemical or electrochemical means, the iron alloy can no longer sustain pressures on the order of theoretical shear strength of iron. Instead, the material behaves in a traditional elastic-plastic manner when no film is present. The oxide film at the edges of the indentation can sustain applied tensile stresses up to 1.2 GPa prior to failure. Indentation in materials undergoing dissolution must account for the rate of material removal over the remote surface and the resulting plastic deformation around the contact of the indentation.

2. Bahr, D. F. and Gerberich, W. W., "Relationships between Acoustic Emission Signals and Physical Phenomenon during Indentation," *J. Materials Research*, submitted January 1997.

A commercial acoustic emission transducer has been used in conjunction with nanoindentation techniques to study the relationship between acoustic emission signals and discrete physical events caused by nanoindentation. Indentations into tungsten and iron single crystals have been used to study dislocation nucleation and passive film failure. In addition, indentations made into a thin nitride film on sapphire have been used to generate film delaminations. Parameters such as signal rise time and frequency have been found to be related to sample geometry, and not to the type of event which caused the acoustic emission signal. As a possible calibration for AE sensors, the most meaningful parameter is the acoustic emission energy, which has been shown to scale with the elastic energy released during the event. The measured values of elastic energy released correspond very closely to those calculated using Hertzian contact mechanics.

3. Bahr, D. F., Hoehn, J. W., Moody, N. R., and Gerberich, W. W., "Nanoindentation and Acoustic Emission of Failures in Nitride Films with Metal Interlayers," *Acta. Mat.*, submitted February 1997.

Interfacial fracture has been induced between a tantalum nitride film with an aluminum interlayer on a sapphire substrate using nanoindentation. To identify failures for which a model calculation is valid, a commercial acoustic emission sensor has been used to study the details of the failure event. The interfacial fracture energy of the system with an aluminum interlayer is approximately 8 J/m<sup>2</sup>. Within narrow bounds, this toughness value is reproducible using three different theoretical approaches. The acoustic emission signal is used to determine a lower bound interfacial crack velocity of 5 m/s. The majority of the failure has been shown to be at the aluminum-sapphire interface, suggesting that the fracture energy and crack velocity determined are related to the toughness of this interface and not the nitride-aluminum interface. Time dependent failure of nitride films on 154 nm thick aluminum interlayers makes this system unsuitable for practical use.

4. Daniel, I. M., Luo, J-J, Sifniotopoulos, C., and Chun, H. J., 1997, "Acoustic Emission Monitoring of Fatigue Damage in Metals," *Nondestructive Test. and Evaluation*, to appear.

The objective of this study was to investigate and develop/adapt acoustic emission (AE) methods for detection and characterization of fatigue damage growth in metals. The materials investigated were 2024-T3 aluminum and 4340 steel. Edge-notch and compact tension specimens were tested under cyclic tensile loading. The investigation consisted of signal/noise discrimination, direct crack growth monitoring, acquisition of acoustic emission data, analysis of AE data and correlation of AE data and damage growth. In the case of aluminum, the AE output consists of three characteristic parts corresponding to three stages of crack propagation; the first stage of high but decreasing AE rate, the second stage with a low and nearly constant rate and extending over 80% of the specimen lifetime and the third stage with increasing AE rate up to failure. The rate of AE output in the second stage can be described by a power law in terms of the stress intensity factor range, analogous to the Paris law for crack growth rate. In the case of steel AE results from crack extension, notch tip plasticity and closure, and plasticity dominated rapid crack propagation. The various sources of AE activity were analyzed based on the phase of the loading cycle at which they occur. A high rise in AE activity in the first half of the fatigue life has been attributed to a transition from plane strain to plane stress crack propagation.

5. Hurlebaus, S., Jacobs, L. J., and Jarzynski, J., "Laser Techniques to Characterize the Effect of Geometry on Acoustic Emission Signals," *Nondestructive Test. And Evaluation*, submitted November 1996.

The finite geometry of a laboratory specimen changes a measured acoustic emission waveform because of reflections, transmissions, and mode conversions at the interfaces and boundaries of the specimen, thus making it difficult to interpret the measured signal. This paper develops a transfer function that removes these geometric effects from measured acoustic emission signals. This transfer function is developed using a repeatable, broad band (synthetic) acoustic emission source, a pulsed laser, and a broad band, high fidelity sensor, a laser interferometer. The steps in the development of the transfer function are as follows: an acoustic emission signal is generated and detected in a specimen whose geometry is being characterized; this experiment (same source) is repeated in a "geometry-less specimen," one that contains no geometric features, and the "geometry-less" signal is divided by the specimen signal (in the frequency domain) to form the transfer function. This transfer function can operate on an acoustic emission signal, measured in the same spectrum, but caused by a different source. The accuracy of this transfer function is demonstrated by operating on different acoustic emission sources such as a pencil lead break and removing unwanted geometric features.

6. McDowell, D. L. and Bennett, V. P., 1996, "A Microcrack Growth Law for Multiaxial Fatigue," *Fatigue Fract. Engng. Mater. Struct.*, Vol. 19, No. 7, pp. 821-837.

Critical plane approaches have gained increasing support based on correlation of experimentally observed fatigue lives and microcrack orientations under predominantly low cycle fatigue (LCF) conditions for various stress states. In this paper, an engineering model is further developed for microcrack propagation consistent with critical plane concepts for correlation of both LCF and high cycle fatigue (HCF) behavior, including multiple regimes of small crack growth. The critical plane microcrack approach of McDowell and Berard serves as a starting point to incorporate multiple regimes of crack nucleation, shear growth under the influence of microstructural barriers, and transition to linear crack length-dependent growth related to elastic-plastic fracture mechanics (EPFM) concepts. Microcrack iso-length data from uniaxial and torsional fatigue tests of 1045 steel and Inconel 718 are examined and correlated by introducing a transition crack length that governs the shift from nonlinear to linear crack length dependence of  $da/dN$ . This transition is related to the shift from strong microstructural influence to weak influence on the propagation of microcracks. Simple forms are introduced for both the transition crack length and the crack length-dependence of crack growth rate within the microcrack propagation framework introduced previously by McDowell and Berard, and are employed to fit the 1045 steel and IN 718 microcrack iso-length data, assuming pre-existing sub-grain size cracks. The nonlinear evolution of crack length with normalized cycles is then predicted over a range of stress amplitudes in uniaxial and torsional fatigue. The microcrack growth law is shown to have potential to correlate microcrack propagation behavior as well as damage accumulation for HCF-LCF loading sequences and sequences of applied stress states.

7. McDowell, D. L., 1996, "Basic Issues in the Mechanics of High-Cycle Fatigue," *Intl. Journal of Fracture*, **80**, pp. 103-145.

Extension of damage tolerance concepts to lower length scales and small cracks relies critically on deeper understanding of (a) small crack behavior including interactions with microstructure, (b) heterogeneity and anisotropy of cyclic slip processes associated with the orientation distribution with grains, and (c) development of reliable small crack monitoring techniques. The basic technology is not yet sufficiently advanced in any of these areas to implement damage tolerant design for high-cycle fatigue (HCF). The lack of consistency of existing crack initiation and fracture mechanics approaches for HCF leads to significant reservations concerning application of existing technology to damage tolerant design of aircraft turbine engines, for example. The intent of this paper is to focus on various aspects of the propagation of small cracks which merit further research to enhance the accuracy of HCF life prediction. Predominant concern will rest with polycrystalline metals, and most of the issues pertain to wide classes of alloys.

8. McDowell, D. L., "Mechanics of Small Fatigue Crack Growth in Metals, *Intl. Journal of Fatigue*, submitted September 1996.

Development of microstructure-sensitive fatigue crack propagation relies critically on deeper understanding of (a) small crack behavior including interactions with microstructure, (b) heterogeneity and anisotropy of cyclic slip processes associated with the orientation distribution of grains, and (c) local mode mixity effects on small crack growth. The basic technology is not yet sufficiently advanced to implement damage tolerant design for HCF. This paper introduces a new model which incorporates small crack blockage by microstructure barriers and is consistent with critical plane concepts for stage I growth of small cracks, standard cyclic stress-strain and strain-life equations, and the Kitagawa diagram for HCF threshold behaviors. The model is able to provide realistic predicted trends of small crack growth behavior, including the fatigue limit, load sequence effects, and stress state effects.

#### **Nonrefereed Publications (9)**

1. "Integrated Diagnostics," March 1995-February 1996 M-URI Year 1 *Annual Performance Report*, ONR Grant N00014-95-1-0539, Georgia Tech, Atlanta, 1996 (223 pages).

2. "Integrated Diagnostics-Monthly Progress Report," Vol. II, No. 1-10, Georgia Tech, Atlanta, April 1996 thru January 1997.

3. Bahr, D. F., Wright, J. S., Francis, L. F., Moody, N. R., and Gerberich, W. W., "Mechanical Behavior of a MEMS Acoustic Emission Sensor," *Proc. Materials Research Society*, Fall 1996 (in press).

The elastic modulus and hardness of materials used in a MEMS acoustic emission sensor were determined using nanoindentation techniques. In addition to testing each individual material, the behavior of four candidate bottom electrode structures, two based on nitride layers and two based on oxide layers, have been evaluated. The multilayer nitride bottom electrode is relatively unaffected by a 950°C annealing step; however, some evidence of second phase formation in the polycrystalline silicon layer has been observed. Increasing the thickness of the thermally grown silicon dioxide in the oxide based electrodes lowers the measured hardness of the top layer of the platinum while increasing the measured modulus of the entire electrode at depths corresponding to the oxide film. Errors of up to 25% in the calculated area of indentation based on the indenter shape function occur for indentations which penetrate both the platinum and oxide films.

4. Cowan, R. S. and Winer, W. O., "Adding Time to Aging Machinery with an Appropriate Maintenance Methodology," *Proc. 7th Nordic Symposium on Tribology*, Bergen, Norway, June 1996.

The maintenance of mechanical systems employing tribological elements is an area of activity that has received much attention in recent decades, given that it has enabled the technology that surrounds us to become more reliable, safer, and more economical. As various components of a mechanical system may be optimally maintained in different ways, this paper gives a brief review of the techniques presently available for cost-effective maintenance planning, and those that offer promise through integrated diagnostics.

5. Fomitchov, P., Wang, L-S, Steckenrider, J. S., Krishnaswamy, S., and Achenbach, J., "Laser-based Ultrasonics for QNDE Applications," *Intl. Conf. Mech. Engrg. Advances and Applications*, Singapore, December 1996.

Surface and plate acoustic waves are commonly used to nondestructively investigate the near-surface region of a solid component for cracks and other defects. An attractive method of generation and detection of ultrasonic waves is laser based ultrasonics (LBU). Because it is non-contact, LBU can be implemented for inspection of limited access components using optical fibers, requiring only a small cross-sectional area for access. The work presented here employs optical fibers to remotely generate and detect ultrasound with energy focused into a selected narrow frequency band. The generation system uses a binary diffraction grating to separate the single laser beam into 10 equal but spatially separated laser beams which are focused into 10 individual fibers, thereby maximizing optical throughput to the component surface. In addition, a low noise fiberized Sagnac interferometer for ultrasonic signal measurement is discussed. The main advantage of this interferometer is improved signal-to-noise ratio, which has been achieved using an optical frequency shifting technique for biasing quadrature and for elimination of parasitic interference between sampling beams and other unwanted beams in the interferometer. The Sagnac interferometer is truly path-matched, and as such is insensitive to low frequency thermal fluctuations and vibration noise. An acousto-optic modulator is included in the Sagnac loop, and serves a two-fold purpose: frequency shifting and quadrature biasing. Experimental results are presented for both the fiber-optic ultrasound generating array and the Sagnac interferometer.

5. McDowell, D. L., "Pushing the Boundaries: Remaining Life of Components in High Cycle Fatigue," *ASM Newsletter*, Vol. 2, No. 2, February 1997, pp. 3-4.

This article provides an overview of strategy with respect to the making of accurate remaining life estimates and the establishment of safe inspection intervals for critical structural parts of complex systems.

6. Moran, B., Zulfikar, A., and Sukumar, N., "On the Direct Integration Method for Fatigue Reliability Calculations," Technical Report, Northwestern, Evanston, July 1996.

This report describes and compares several techniques for determining fatigue reliability. Special emphasis is placed on the Direct Integration Method and techniques for improving computing speed with a view toward problems in 3D fracture mechanics. The Direct Integration Method has been applied to problems in fatigue reliability where the component is subjected to in-service NDE inspections according to a given schedule. The code capabilities include multiple inspections, arbitrary probability of detection (POD) curves, and multiple random variables. The fatigue reliability problem of an edge crack in a semi-infinite plate is considered to investigate the accuracy of the Direct Integration Method. This example shows that the results of the present methodology are in good agreement with results from Monte Carlo simulation and the First Order Reliability Method (FORM). The Direct Integration Method is also applied to fatigue reliability calculations of a semi-elliptical surface breaking crack and the results are compared to those obtained from FORM.

7. Venkatesan, G., West, D., Buckley, K., Tewfik, M., and Kaveh, M., "Automatic Fault Monitoring using Acoustic Emissions," *Proc. ICASSP97*, Munich, Germany, submitted January 1997.

Techniques for automatic monitoring of faults in machinery are being considered as a means to safely simplify or dispense with expensive periodic fault inspection procedures. This paper presents results from an ongoing investigation into the feasibility of using Acoustic Emissions for automatic detection of microcrack formation/growth in machine components.

8. West, D., Venkatesan, G., Tewfik, A., Buckley, K., and Kaveh, M., *Proc. IEEE*, 1996, pp. 303-306.

The formation of microcracks in a material creates propagating ultrasonic waves called Acoustic Emissions (AEs). These AEs provide an early warning to the onset of material failure. In practical cases, however, these AEs have to be detected at very low SNRs, amongst strong interference and random noise. This paper presents some preliminary results from an ongoing investigation into the modeling and detection of AEs as a viable technique for predictive diagnostics.

9. Zheng, L., Xue, J., and Ramalingam, S., "Eddy-current Microsensors for Flaw Imaging: Numerical Simulation and Experimental Evaluation," *Monitoring Technology for Condition Based Maintenance*, R. Cowan, ed., ASME 96-TRIB-66, October 1996, pp. 25-31.

To improve the spatial resolution of eddy-current NDE systems, micro-sensors and micro-sensor arrays built with silicon processing technology are proposed here. However, the reduced dimension micro-devices require an effective means for coupling the excitation power to produce adequate output signals. Output signal characteristics of flux-focusing probes have hence been investigated in this work with FEM simulations. It is shown that large improvements in power coupling are feasible with flux-focusing. Calculated results are evaluated with a scaled, macro-probe on test samples containing model flaws. Signals acquired by scanning test samples are presented. Process images presented show that small flaws can be mapped reliably. Micro-sensor designs based on the calculated results are presented.

### **Books, or sections thereof (3)**

1. Daniel, I. M., Luo, J-J, Sifniotopoulos, C., and Chun, H. J., "Acoustic Emission Monitoring of Fatigue Damage in Metals," *Proc. Review of Quantitative NDE*, **16**, Plenum Press, 1996 (to appear).

The objective of this study was to investigate and develop/adapt acoustic emission (AE) methods for detection and characterization of fatigue damage growth in metals. The materials investigated were 2024-T3 aluminum and 4340 steel. Edge-notch and compact tension specimens were tested under cyclic tensile loading. The investigation consisted of signal/noise discrimination, direct crack growth monitoring, acquisition of acoustic emission data, analysis of AE data and correlation of AE data and damage growth. In the case of aluminum, the AE output consists of three characteristic parts corresponding to three stages of crack propagation; the first stage of high but decreasing AE rate, the second stage with a low and nearly constant rate and extending over 80% of the specimen lifetime and the third stage with increasing AE rate up to failure. The rate of AE output in the second stage can be described by a power law in terms of the stress intensity factor range, analogous to the Paris law for crack growth rate. In the case of steel AE results from crack extension, notch tip plasticity and closure, and plasticity dominated rapid crack propagation. The various sources of AE activity were analyzed based on the phase of the loading cycle at which they occur. A high rise in AE activity in the first half of the fatigue life has been attributed to a transition from plane strain to plane stress crack propagation.

2. Hurlebaus, S., Jacobs, L. J., Jarzynski, J., "Optical Techniques to Develop Transfer Functions to Remove Geometric Features in Acoustic Emission Signals," *Proc. Review of Quantitative NDE*, **16**, Plenum Press, 1996 (to appear).

This work demonstrates the effectiveness of using laser ultrasonic techniques to develop transfer functions to quantify and remove geometric effects from measured acoustic emission waveforms. The effectiveness of these transfer functions is directly dependent upon the broadband, repeatable, noncontact, high-fidelity, point measurements that are possible with the laser based techniques used in this work. While very sophisticated experimental techniques are used in this study, the accompanying signal processing tools are somewhat naïve; the thrust of this effort is in making accurate experimental measurements of wave propagation in finite specimens.

3. Wang, L., Steckenrider, J. S., and Achenbach, J. D., "A Fiber-based Laser Ultrasonic System for Remote Inspection of Limited Access Components," *Proc. Review of Quantitative NDE*, **16**, Plenum Press, 1996 (to appear).

Surface and plate acoustic waves are commonly used to nondestructively investigate the near-surface region of a solid component for cracks and other defects. An attractive method of generation and detection of ultrasonic waves is laser based ultrasonics (LBU). Because it is non-contact, LBU can be implemented for inspection of limited access components using optical fibers, requiring only a small cross-sectional area for access. The work presented here employs optical fibers to remotely generate and detect ultrasound with energy focused into a selected narrow frequency band. The generation system uses a binary diffraction grating to separate the single laser beam into 10 equal but spatially separated laser beams which are focused into 10 individual fibers, thereby maximizing optical throughput to the component surface.

## Miscellaneous

### *Monthly Progress Updates:*

To keep the Integrated Diagnostic community (e.g., ONR Program Officer, M-URI Team Members) up-to-date and informed about the ongoing activities of the program, status reports from the program's researchers have been collected, edited, and distributed as a monthly progress report.

### *Informational Brochure:*

Intended for those interested in knowing more about the MultiUniversity Center for Integrated Diagnostics (e.g., potential collaborators, prospective students), a brochure, based on the theme "a safe tomorrow through innovation today" was developed. It describes the ONR M-URI goals, the research being conducted, and the educational opportunities available in Integrated Diagnostic disciplines.

### *Information Highway:*

To ensure a wide dissemination of Integrated Diagnostic information, electronic reporting is being utilized. A MultiUniversity Center for Integrated Diagnostics World-Wide-Web Homepage has been created, providing information with respect to four main themes: the Center's research objectives (or innovations), research accomplishments, technology transfer achievements, and a research faculty (staff) directory. Access can be achieved using the address <http://www.me.gatech.edu/Diagnostics/>.

## **3.2 PRESENTATIONS**

The process of technology transfer not only involves the recording of information, but also assisting in the understanding of that information and promoting its implications; hence, *Integrated Diagnostic* activity has been presented at a number of venues during this reporting period as listed below.

1. Achenbach, J. D., "A Fiber-Based Laser Ultrasonic System for Remote Inspection of Limited Access Components," *Review of Quantitative NDE*, Brunswick, ME, July 28-August 2, 1996.
2. Achenbach, J. D., "Laser Based Ultrasonics for QNDE Applications," *International Conference on Experimental Mechanics: Advances and Applications*, Singapore, December 1996.
3. Bahr, D. F., Kramer, D. F., Wright, J. S., Francis, L. F., and Gerberich, W. W., "Acoustic Emission as Identification of Physical Phenomena," *Materials Research Society*, Spring 1996.
4. Bahr, D. F., Hoehn, J. W., Moody, N. R., and Gerberich, W. W., "Indentation and Acoustic Emission in Nitride Films," *ASM/TMS Materials Week*, 1996.
5. Bahr, D. F., Wright, J. S., Francis, L. F., Moody, N. R., and Gerberich, W. W., "Mechanical Behavior of a MEMS Acoustic Emission Sensor," *Materials Research Society*, Fall 1996.
6. Bahr, D. F., Wright, J. S., Francis, L. F., Moody, N. R., and Gerberich, W. W., "The Mechanical Behavior of PZT Thin Films Deposited by a Sol-Gel Technique," *TMS Annual Meeting*, 1997.
7. Berthelot, Y., "Mode Control of Ultrasonic Guided Waves in Thick Cylinders for Crack Detection," *131st Mtg. of the Acoustical Society of America*, Indianapolis, IN, May 16, 1996.
8. Cowan, R. S. and Winer, W. O., "Adding Time to Aging Equipment with an Appropriate Maintenance Methodology," *7th Nordic Symposium on Tribology*, Bergen, Norway, June 1996.
9. Daniel, I., "Acoustic Emission Monitoring of Fatigue Damage in Metals," *Review of Quantitative NDE*, Brunswick, ME, August 1, 1996.
10. Hurlebaus, S., Jacobs, L. and Jarzynski, J., "Transfer Functions to Remove Geometry Effects from AE Signals," *Review of Quantitative NDE*, Brunswick, ME, July 28-August 2, 1996.

11. Hurlebaus, S., Jacobs, L. and Jarzynski, J., "Transfer Functions to Remove Geometry Effects from AE Signals," *Gordon Conference on Nondestructive Characterization of Materials*, Andover, NH, August 18-23, 1996.
12. Kim, J. H., Wang, L., Li L., Zurn, S., and Polla, D. L., "Device Characteristics of Piezoelectric Cantilever Beam Accelerometers Using Surface Micromachining Process," *Proc. 8th Intl. Symposium on Integrated Ferroelectrics*, Phoenix, AZ, March 1996.
13. Lim, T. H., Kim, J., Wright, J., Li, L., Polla, D. L., and Francis, L., "Direct Depositions of PbTiO<sub>3</sub>(PT) and PZT on Si/SiO<sub>2</sub> and Si Using Polyimide as a Diffusion Barrier," *Mtg. of the American Physical Society*, St. Louis, MO, March 1996.
14. Polla, D. L., "Integrated Ferroelectric MEMS: Technology Issues and Device Applications," *Proc. 8th Intl. Symposium on Integrated Ferroelectrics*, Phoenix, AZ, March 1996.
15. Qu, J., "Transverse Matrix Cracking," *ASME Mechanics and Materials Conference*, Baltimore, MD, June 12-14, 1996.
16. Saxena, A., "Fatigue Crack Growth in Power-Plant Materials and Components," *Fatigue '96 International Conference*, Berlin, Germany, May 1996.
17. Zheng, L., Xue, J., and Ramalingam, S., "Eddy Current Microsensors for Flaw Imaging: Numerical Simulation and Experimental Evaluation," *ASME/STLE Intl. Tribology Conf.*, San Francisco, CA, October 17, 1996.

### 3.3 EDUCATION

A primary mode of technology transfer is through students, who, trained in an aspect of integrated diagnostics, may subsequently apply such knowledge upon entry in an engineering profession. Post-doctoral, graduate, and undergraduate students have taken an active role in the research activities pursued during this reporting period. They are identified in Appendix A.

#### Graduate Education

Graduate education leading to M.S. and Ph.D. degrees is a major emphasis of the Integrated Diagnostics program. Thirty-five (35) research assistantships have been awarded during this reporting period, of which 19 are at Georgia Tech, 2 are at Northwestern University, and 14 are at the University of Minnesota. Six of these recipients have since received a graduate degree as listed below.

Tom Cooney, Ph.D. (5/96)	Electrical Engineering	U. of Minnesota	<i>Advisor:</i> Francis
Brian Gardner, MS (9/96)	Mechanical Engineering	Georgia Tech	Qu
Stefan Hurlebaus, MS (9/96)	Engineering Mechanics	Georgia Tech	Jacobs
Jason Shirioshi, MS (12/96)	Mechanical Engineering	Georgia Tech	Kurfess
Paul West, MS (12/96)	Civil Engineering	Georgia Tech	Jacobs
Fan Yang, Ph.D. (6/96)	Materials Science	Georgia Tech	Saxena

#### Undergraduate Education

The Integrated Diagnostics program has granted five internships at Georgia Tech and two at the University of Minnesota, providing part-time employment during the junior/senior college year. This unique opportunity to collaborate with faculty and graduate students provides these individuals with valuable experience and incentives as they seek future employment or continue their studies through graduate education.

### **Seminars**

To promote additional insight with respect to integrated diagnostic endeavors, speakers from academia and industry have been given the opportunity to address the faculty and staff of the MultiUniversity Center for Integrated Diagnostics. During this reporting period, four presentations occurred as summarized below.

- *Dr. Brian J. Roylance*, Dept. of ME, University of Swansea, Wales; April 15, 1996.

This seminar addressed the integrated diagnostic activities at the University of Wales, Swansea, where tribology is currently combined with condition-monitoring research in oil and wear-debris analysis.

- *Dr. Kenneth Holmberg*, VTT-Technology Research Center, Finland; April 19, 1996.

This seminar addressed a general approach developed and used for solving problems in the area of operational reliability. Some examples of developments and industrial applications on predictive maintenance were given.

- *Ms. Joanna Spanjaard*, Australian National University, Australia; June 10, 1996.

An overview of the university's Cooperative Research Centre was given, followed by a detailed description of the problem of variable speed condition monitoring for rotating machinery. In particular, bearing fault detection at a steel mill was discussed.

- *Mr. Tom Edwards*, Honeywell Technology Center, Minneapolis, MN; January 22, 1997.

An overview of Honeywell Technology Center research activity was provided, with special emphasis on Honeywell's involvement in an Office of Naval Research Accelerated Capabilities Initiative (ACI) in Condition-Based Maintenance.

### **3.4 PARTNERSHIPS**

Faculty and staff associated with the MultiUniversity Center for Integrated Diagnostics have initiated ties with various academic, industrial, and government organizations. Such partnerships have occurred to assure that the research being sponsored is conducted in an effective manner, and is of continued relevance to potential developers. Collaborations that have resulted during this reporting period are noted below with respect to the agency involved and the purpose intended.

- *Cherry Point Naval Aviation Depot, Cherry Point, NC* - This facility performs inspection and maintenance routines on an assortment of US defense assemblies including engines, carrier components, and aircraft. Information has been provided with respect to many areas, including the location and identification of critical components and failures, service environments, and material/design needs.

- *Honeywell, Inc., Minneapolis, MN* - A participant of the Air Vehicle Diagnostics System (AVDS) program through the development of a Rotor Acoustic Monitoring System (RAMS), the Honeywell Technology Center has provided pertinent information the MultiUniversity Center with respect to component failure, load-history, and sensor access for the H46 rotorhead assembly.

- *Timken Co., Canton, OH* - As a leading manufacturer of tapered roller bearings, this organization has provided the MultiUniversity Center with test material, hardware, and knowledge pertinent to bearing defect classification, and bearing-system diagnosis and prognosis.

- *Torrington Co., Norcross, GA* - Dedicated to the development of various mechanical systems, this organization has provided expertise with respect to the assessment and impact of rolling-element bearing surface damage.



## APPENDIX A. Program Participants

---

### PRINCIPAL INVESTIGATOR (1)

Ward O. Winer

Georgia Tech

Mechanical Engineering

### CO-PI'S (21)

Jan D. Achenbach	Northwestern	Quality Engineering
Scott Bair	Georgia Tech	Mechanical Engineering
Yves Berthelot	Georgia Tech	Mechanical Engineering
Isaac Daniel	Northwestern	Mechanical & Civil Engineering
Steven Danyluk	Georgia Tech	Mechanical Engineering
Itzhak Green	Georgia Tech	Mechanical Engineering
Laurence Jacobs	Georgia Tech	Civil & Environmental Engineering
Jacek Jarzynski	Georgia Tech	Mechanical Engineering
W. Steven Johnson	Georgia Tech	Materials Science & Engineering
Thomas Kurfess	Georgia Tech	Mechanical Engineering
Steven Liang	Georgia Tech	Mechanical Engineering
David L. McDowell	Georgia Tech	Mechanical Engineering
Brian Moran	Northwestern	Civil Engineering
Richard Neu	Georgia Tech	Mechanical Engineering
Dennis Polla	U. of Minnesota	Electrical Engineering
Jianmin Qu	Georgia Tech	Mechanical Engineering
S. Ramalingam	U. of Minnesota	Mechanical Engineering
Richard Salant	Georgia Tech	Mechanical Engineering
Ashok Saxena	Georgia Tech	Materials Science & Engineering
Waymond Scott	Georgia Tech	Electrical Engineering
George Vachtsevanos	Georgia Tech	Electrical Engineering

### SUPPORT FACULTY (12)

Kevin Buckley  
 Richard S. Cowan  
 Arthur Erdman  
 Lorraine Francis  
 William Gerberich  
 Ramesh Harjani  
 Mostafa Kaveh  
 Susan Mantell  
 William Robbins  
 Charles Stancil  
 Ahmed Tewfik  
 Yonglin Xu

#### *Collaborating with:*

Polla  
 Winer  
 Polla  
 Polla  
 Polla  
 Polla  
 Polla  
 Polla  
 Polla  
 Polla  
 Winer  
 Polla  
 Moran

U. of Minnesota  
 Georgia Tech  
 U. of Minnesota  
 U. of Minnesota  
 U. of Minnesota  
 U. of Minnesota  
 U. of Minnesota  
 U. of Minnesota  
 U. of Minnesota  
 U. of Minnesota  
 Georgia Tech Research Institute  
 U. of Minnesota  
 Northwestern

## PROGRAM PARTICIPANTS

### POST-DOCTORAL RESEARCHERS (10)

H. J. Chun (3/95-1/97)	<i>Sponsor:</i>	
Joon Han Kim (4/95-11/96)	Daniel	Northwestern
Guoli Liu (1/96-4/96)	Polla	U. of Minnesota
Chr. Sifniotopoulos	Qu	Georgia Tech
J. S. Steckenrider (7/95-5/96)	Daniel	Northwestern
Liusheng Wang	Achenbach	Northwestern
Nam Yun Woo	Achenbach	Northwestern
Fan Yang	Polla	U. of Minnesota
Young-Soo Yoon	Saxena	Georgia Tech
Shayne Zurn	Polla	U. of Minnesota
	Polla	U. of Minnesota

### UNDERGRADUATE STUDENTS (7)

Damian Aquilar	<i>Advisor:</i>	
Carribeth Bair	Ramalingam	U. of Minnesota
Angela Drexler	Jarzynski	Georgia Tech
Richard Hamm (1/96-6/96)	Polla	U. of Minnesota
Jennifer Hsieh (9/95-6/96)	Johnson	Georgia Tech
Todd Levine	Jacobs	Georgia Tech
Ryan Morrissey (6/96-8/96)	Neu	Georgia Tech
	McDowell	Georgia Tech

## PROGRAM PARTICIPANTS

### GRADUATE STUDENTS (35)

William Anderson  
 David Bahr  
 Valerie Bennett  
 Scott Billington  
 Orvid Birkenes  
 Tom Cooney (6/95-5/96)  
 Anne Gao (7/95-3/96)  
 Brian Gardner  
 Ken Hamall (10/96-12/96)  
 Richard Hamm  
 David Harris (9/95-3/96)  
 Xiaoling He  
 Lori Jenson (7/95-7/96)  
 Lei Jin (6/95-8/96)  
 Hyeon-Sang Kim  
 Maxim Koutsak  
 Yawei Li  
 Zongbao Li  
 J. J. Luo  
 Akshay Patel  
 Kyeonglan Rho  
 Aaron Schmidt  
 Zhiqiang Shi  
 Jason Shiroishi (9/95-12/96)  
 Christine Valle  
 Victor Vaysman  
 Gopal Venkatesan  
 Dennis West (3/96-12/96)  
 Paul West (3/96-12/96)  
 J. S. Wright  
 Jianhua Xue  
 Fan Yang (5/95-6/96)  
 Lanshi Zheng (3/95-8/96)  
 Min Zou  
 Ali Zulfiqar

#### *Advisor:*

Salant/Jarzynski  
 Gerberich  
 McDowell  
 Kurfess  
 Buckley/Kaveh  
 Francis  
 Polla  
 Qu  
 Danyluk  
 Johnson  
 Scott  
 Green  
 Polla  
 Francis  
 Polla  
 Jarzynski  
 Liang  
 Berthelot  
 Daniel  
 Neu  
 Polla  
 Robbins  
 Jarzynski  
 Kurfess  
 Jacobs/Qu  
 Scott  
 Buckley/Kaveh  
 Buckley  
 Jacobs  
 Francis  
 Ramalingam  
 Saxena/Johnson  
 Ramalingam  
 Green  
 Moran

Georgia Tech  
 U. of Minnesota  
 Georgia Tech  
 Georgia Tech  
 U. of Minnesota  
 U. of Minnesota  
 U. of Minnesota  
 Georgia Tech  
 Georgia Tech  
 Georgia Tech  
 Georgia Tech  
 U. of Minnesota  
 U. of Minnesota  
 U. of Minnesota  
 Georgia Tech  
 Georgia Tech  
 Georgia Tech  
 Georgia Tech  
 Northwestern  
 Georgia Tech  
 U. of Minnesota  
 U. of Minnesota  
 Georgia Tech  
 Georgia Tech  
 Georgia Tech  
 Georgia Tech  
 U. of Minnesota  
 U. of Minnesota  
 Georgia Tech  
 U. of Minnesota  
 Georgia Tech  
 Northwestern

# REPORT DOCUMENTATION PAGE

Form Approved  
OMB No. 0704-0188

Public reporting burden for this collection of information is estimated to average 1 hour per response, including the time for reviewing instructions, searching existing data sources, gathering and maintaining the data needed, and completing and reviewing the collection of information. Send comments regarding this burden estimate or any other aspect of this collection of information, including suggestions for reducing the burden to Washington Headquarters Services, Directorate for Information Operations and Reports, 1215 Jefferson Davis Highway, Suite 1204, Arlington, VA 22202-4302, and to the Office of Management and Budget, Paperwork Reduction Project (0704-0188), Washington, DC 20503

1. AGENCY USE ONLY (Leave Blank)		2. REPORT DATE 28 February, 1997		3. REPORT TYPE AND DATES COVERED Year 2 Performance: Mar. 1, 1996-Feb. 28, 1997	
4. TITLE AND SUBTITLE  Integrated Diagnostics				5. FUNDING NUMBERS  G N00014-95-1-0539	
6. AUTHOR(S)  Richard S. Cowan and Ward O. Winer (eds.)					
7. PERFORMING ORGANIZATION NAME(S) AND ADDRESS(ES) Georgia Institute of Technology MULTIUNIVERSITY CENTER FOR INTEGRATED DIAGNOSTICS G. W. Woodruff School of Mechanical Engineering 801 Ferst Drive Atlanta, GA 30332-0405				8. PERFORMING ORGANIZATION REPORT NUMBER	
9. SPONSORING/MONITORING AGENCY NAME(S) AND ADDRESS(ES)  Office of Naval Research 800 N. Quincy Street Arlington, VA 22217-5660				10. SPONSORING/MONITORING AGENCY REPORT NUMBER	
11. SUPPLEMENTARY NOTES  The information conveyed in this report does not necessarily reflect the position or the policy of the Government, and no official endorsement should be inferred.					
12a. DISTRIBUTION/AVAILABILITY STATEMENT				12b. DISTRIBUTION CODE	
13. ABSTRACT (Maximum 200 words) This document summarizes performance activity regarding basic research being conducted in the area of <i>Integrated Diagnostics</i> , a term associated with the technologies and methodologies used to determine how mechanical failures occur, and how they can be detected, predicted, and diagnosed in real-time. Objectives, set forth through the Department of Defense Multidisciplinary Research Program of the University Research Initiative (M-URI), are being addressed by faculty and staff from the Georgia Institute of Technology, Northwestern University, and the University of Minnesota. This activity is funded through the Office of Naval Research for a basic period of three years, with a potential for two additional years. Second-year accomplishments, plans, and technology transfer actions are reported upon. During this reporting period, experiments based on material, load, and vibration information from critical rotorcraft components have been designed and conducted so as to collect data of relevance in understanding the mechanisms of failure for use in developing failure models. These models can serve as a guide in the selection and development of sensors to detect faults and pending failures. Effort has been placed on micro-sensor development, and achieving the means to analyze and correlate reliable sensor output for operator use. Organizationally, this activity is being accomplished through (16) projects, categorized by three thrust areas.					
14. SUBJECT TERMS  Integrated Diagnostics; Condition-based Maintenance Failure Detection; Failure Prediction; Sensors; Direct Sensing				15. NUMBER OF PAGES 285	
				16. PRICE CODE	
17. SECURITY CLASSIFICATION OF REPORT  Unclassified	18. SECURITY CLASSIFICATION OF THIS PAGE  Unclassified	19. SECURITY CLASSIFICATION OF ABSTRACT  Unclassified	20. LIMITATION OF ABSTRACT  SAR		